CLRC

COUNCIL FOR THE CENTRAL LABORATORY
OF THE RESEARCH COUNCILS

Central Laser Facility

Rutherford Appleton Laboratory

Annual Report 1996-97

Contents

Acknowledgements

The production team for this Annual Report were as follows:

Editorial Board	Henry Hutchinson, Brian Wyborn
Overall Co-ordination	Alison Brown
Production	Katharine Hale, Chris Naboulsi, Dawn Sleep
Chapter Editors	Steven Rose, Tony Parker, Colin Danson
Section Editors	Colin Danson, David Neely, Peter Norreys, Abdes Djaoui, Pavel Matousek, Phil Taday, Kevin Henbest, Graeme Hirst, Mick Shaw, Andrew Langley
Technical Support	Chris Reason, Paul Jobbins, Edmund Jones, RAL CLEO Support.

For the first time the CLF Annual Report has been produced as an electronic document. All articles were provided as files by facility users and staff. Collating, editing and the final document production were carried out on the CLF's file server. There inevitably were a few compatibility problems: between different software; different versions of the same software; different hardware platforms; and different printers. However, the resulting publication has benefited overall. A number of lessons have been learned from this exercise which will stand us in good stead for the production of future annual reports.

This report is available on the CLF's Web Page Ref. http://www.nd.rl.ac.uk/lasers/.
It is also proposed to produce it on CD Rom.

The document has been reproduced by the RAL Reprographics Section.

Thanks to all the above for their contribution towards producing this report and of course to all the authors for their submissions.

Foreword

M H R Hutchinson

Rutherford Appleton Laboratory, Chilton, Didcot, Oxon, OX11 0QX, UK.

It is a pleasure for me as the new director of the Central Laser Facility (CLF) to introduce the annual report for 1996/97. It is a particular challenge to be given the opportunity of taking over the leadership of the facility at a time when the international reputation of the research carried out in the CLF, both by the academic user community and our in-house staff, is so high. For this I would like to pay tribute to the huge contribution made by my predecessor, Mike Key, who was instrumental in building up a laboratory of which the UK scientific community can be proud.

A particularly important aspect of the research programme over the past few years has been the development of high intensity lasers and the study of the interaction of laser radiation with matter at intensities which only a few years ago was only possible with much larger, multi-kilojoule lasers. This has become possible using the technique of chirped pulse amplification (CPA) on both the high power lasers at the CLF, Vulcan and Titania. The large-scale KrF Titania amplifier was commissioned in April '96 and during February and March '97, Vulcan, the Nd:glass laser system, has been undergoing an extensive upgrade as the first stage of a programme which will increase the power to 0.25 PW. A dramatic consequence of this was the complete refurbishment of target area west (TAW) and the installation of a new target chamber which will allow all eight beams from Vulcan to be used simultaneously in a wide variety of configurations.

In the Lasers *for* Science Facility (LSF), a dual tuneable parametric amplifier system has been developed for use in time-resolved resonance Raman spectroscopy (TR^3). This is a unique facility and will impact such areas as electron transfer in photosynthesis and the study of relaxation processes in intramolecular reactions.

The year has seen the introduction of a new funding arrangement with our principal funding council, EPSRC. This system links the level of funding of the facility to the quality of the scientific proposals submitted by the academic users. The result has been an unprecedented demand for laser time and it is the continuing responsibility of all of us, in the user community and in the CLF, to ensure that the quality of both the research facilities provided and the proposals submitted allow the new system to be fully effective.

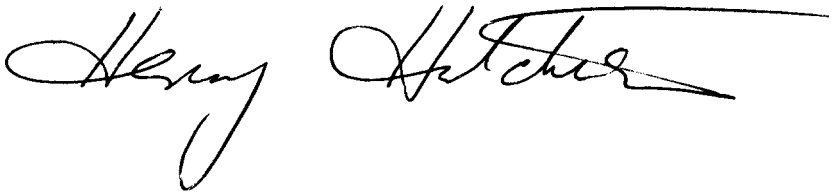

Overview of the Central Laser Facility

M J Shaw

Rutherford Appleton Laboratory, Chilton, Didcot, Oxon, OX11 0QX, UK.

INTRODUCTION

The Central Laser Facility (CLF) is one of the UK's major research facilities and is devoted to the provision of advanced laser systems for pure and applied research. Based at Rutherford Appleton Laboratory near Didcot in Oxfordshire, the CLF was set up twenty years ago to provide the UK university community with a world class high power laser system. The initial impetus behind the establishment of the CLF was the then recently released idea of laser induced thermonuclear fusion. These days, laser fusion is just one topic amongst many that is studied at the CLF and the extent and capabilities of the laser systems have expanded enormously as new discoveries in the rapidly changing field of laser science have been incorporated into the facilities provided. This overview looks at these facilities as they were at the end of March 1997.

FACILITIES AVAILABLE

The CLF runs operational facilities for two major programmes: The High Power Laser Programme and the Lasers *for* Science Facility Programme. The High Power Programme uses two, very different, high power laser systems: **Vulcan** and **Titania**.

Vulcan is a flashlamp-pumped Nd:glass laser system which has grown from the original two-beam laser of 1978 into a very versatile system. It delivers a maximum of 2.5 kJ of energy from its six 10 cm and two 15 cm beamlines to its two main target areas, TAE and TAW each of which is equipped with frequency conversion optics to enable both 1μm and 0.5 μm operation of all beams. A range of pulse durations are available from 100ps to 10ns in various geometries. An ultra-short pulse (700fs), ultra-high irradiance (10^{19}W cm^{-2} on target), chirped pulse amplification (CPA) capability is available, with vacuum propagation to target and reflective beam focusing optics to eliminate non-linear distortion of the beam profile at the highest intensities. In March 1997 a new large multi-purpose target chamber was installed in TAW as part of the Phase I Petawatt Upgrade (see Fig. 1). This chamber has been specifically designed to make best use of the ultra-high power Vulcan CPA beam.

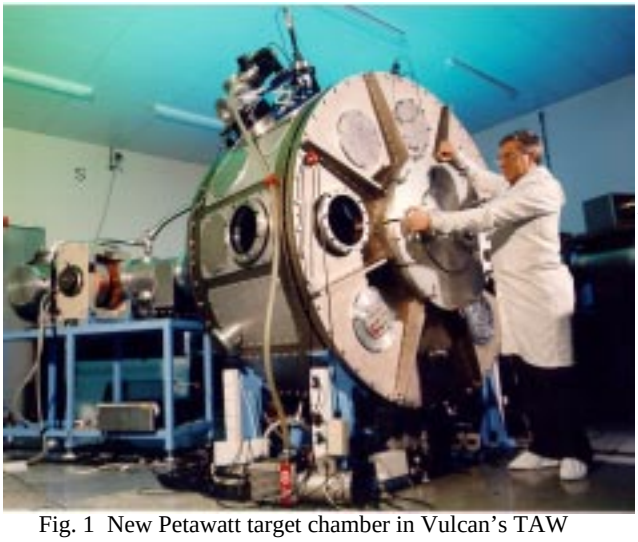

Fig. 1 New Petawatt target chamber in Vulcan's TAW

Titania is the CLF's newest high power laser system which only became operational in April 1996. It is based on electron-beam-pumped krypton fluoride lasers which operate in the UV at 248 nm. During the reporting year it was operated in CPA mode with a single beam recompressed to < 400 fs and a pulse energy of up to 0.5 J.

Both high power lasers are capable of heating high density matter to extreme temperatures and so principally attract physicists interested in fundamental studies at high energy density.

The Lasers *for* Science Facility provides a number of laboratories equipped with state-of-the-art table-top laser systems with a strong emphasis in spectroscopy. A wider field of research interests are catered for here ranging from atomic and molecular physics through chemistry, biochemistry and biology to materials science. The **Nanosecond Laboratory** is equipped with lasers for ns and ps Time-Resolved Resonance Raman spectroscopy (TR^3), and laser flash photolysis. The **Ultrafast Spectroscopy Laboratory** provides a unique dual wavelength, multi-kHz femtosecond synchronised pump-probe apparatus based on OPA technology which cover the spectral region from 220-2200 nm with a synchronisation of better than 150 fs (see front cover photo). The **Femtosecond Laboratory** is based on Ti:sapphire technology providing < 100 fs tuneable pulses amplified to near mJ level. The **X-ray Laboratory** developed at the CLF is the World's brightest laboratory laser-plasma soft x-ray source. Uses include: x-ray lithography, microfabrication, radiation biology. The range of operation of the x-ray source has been greatly extended this year by the development of a VUV capability which in some respects is close to that available from synchrotron radiation sources. The **Laser Microscopy Laboratory** comprises a fast gated 5-dimensional confocal laser microscope with sub-micron resolution. In addition to the laboratories based at RAL, the Lasers *for* Science Facility operates a **Laser Loan Pool** which provides stand-alone, commercial laser systems (YAG-pumped dye, excimer, argon-ion and Ti:sapphire) on loan for periods of up to 6 months at the user's home institution.

The above operational facilities are aided by a number of support groups which provide the essential services required to maintain ongoing operations. Principal amongst these is the engineering and technology group which provides mechanical, electrical and target fabrication support. This group also provides users with a high quality engineering design and construction service for the apparatus needed to run their experiments at the CLF. In addition, users benefit from the administrative support group which helps with arrangements for accommodation and transport and provides secretarial support. A small theoretical group provides advanced computer codes to help model experiments and an equally small research and development group works on keeping the facilities at the forefront of laser technology.

ACCESS

For researchers from UK universities access to the facilities is provided in the main via tickets associated with research grants from the major funding bodies. A limited amount of direct access is available for trial experiments. European researchers can gain access by application to the Large Facilities Access scheme of the EU TMR programme. Use by commercial enterprises or government bodies outside the EU is available at contract rates. Potential new users should contact the director of the CLF in the first instance for further information.

THREE DIMENSIONAL CHARACTERISATION OF HIGH-DENSITY NON-CYLINDRICAL PULSED GAS JETS FOR LASER-PLASMA INTERACTION

R Azambuja[1], M Eloy[1] , G Figueira [1] , D Neely [2]

1) GoLP/Centro de Física de Plasmas, Instituto Superior Técnico, Av Rovisco Pais, 1096 Lisbon Codex, Portugal.
2) Central Laser Facility, Rutherford Appleton Laboratory, Chilton, Didcot, Oxon, OX11 0QX, UK.

INTRODUCTION

Pulsed gas jets are commonly employed in a variety of research areas. Ionisation of such targets produces high electron density plasmas used in x-ray laser experiments[1-3] and laser-plasma interaction studies[4] . These kind of jets consist of either a spatially localised (<1mm) transversely uniform cylindrical column of neutral atoms in a low-density supersonic region or simple free-expansion jets extending for several millimetres in a high density gradient subsonic region, and have been fully characterised by several methods.[5-8]

For plasma-based acceleration schemes, such as the Laser Wakefield Accelerator (LWFA)[9-11], long regions (~ cm) of high electron density are required and can be achieved by using non-cylindrically symmetrical gas jets, such as rectangular-shaped nozzles. This geometry extends the interaction length and time between the pulse and the plasma and permits the creation of plasma channelling lengths at least one order of magnitude longer than those obtained with current cylindrical jets.

In the experiment described here we employed a double orthogonal Mach-Zehnder interferometer and Simultaneous Algebraic Reconstruction Technique (SART) algorithm to determine the three-dimensional density profile produced by rectangular nozzles of different dimensions and by the collision of two gas jets.

INVERSION METHODS - SART

Using interferometric techniques[12] we can determine the phase shift due to the propagation of a laser beam, with wavelength λ, through a medium, with refractive index n_o , by measuring the displacement of the interferogram fringes relative to their unperturbed position. The fringe shift, *h(j,z)*, as a percentage of the unperturbed interferogram, is:

$$h(j,z) = \frac{1}{\lambda}\int_L (n - n_0)\, d\alpha \qquad (1)$$

If we were to assume a cylindrically symmetric variation of the refractive index then *n(r)* could be determined using the inverse Abel transformation and a single projection of the object. However, in the case where no axial symmetries are present we must use tomographic methods and many projections. Several methods have been studied for image reconstruction. Literature[13,14] advises SART as the best choice of algorithm for the problem, with low-noise accurate image reconstruction and rapid convergence.

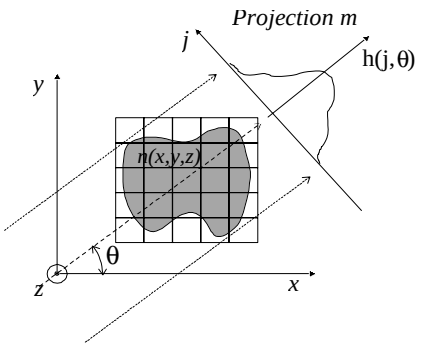

Fig 1. Cross Section of an assymmetrical phase object. The refractive index n(x,y,z) has an arbitrary distribution in the x,y plane.

Methods of algebraic reconstruction (ART) in computer tomography are based on a representation of the projection line integrals as discrete ray-sums. The problem of reconstruction then becomes one of solving a system of linear equations of the form:

$$p_{mn} = \sum_{i=1}^{I}\sum_{j=1}^{J} w_{ijmn}\, f_{ij} \qquad (2)$$

For the unknown values of the image function f_{ij} on a sampling grid of size I x J, the solution will be expressed in terms of the given projection data p_{mn}. The subscript *m* represents the projection index from a total of *M* projections. The subscript *n* represents the ray index among *N* rays within each projection. The summation coefficients w_{ijmn} represent the area of the cell (i,j) covered by the ray (m,n).

The simultaneous algebraic reconstruction technique is an iterative method for solving the system of equations (2). Estimates $\hat{f}_{ij}^{(q)}$ of the image function f_{ij} are updated so as to satisfy the ray-sum equation (2). The new estimate $\hat{f}_{ij}^{(q+1)}$ is determined from the estimate $\hat{f}_{ij}^{(q)}$ by an update-correction strategy combining terms from all rays within a particular projection before the image function is updated, defined as:

$$\hat{f}_{ij}^{(q+1)} = \hat{f}_{ij}^{(q)} + \lambda^{(q)} \cdot \frac{\sum_{n=1}^{N}\left(w_{ijmn} \cdot \frac{p_{mn} - \sum_{i=1}^{I}\sum_{j=1}^{J} w_{ijmn}\hat{f}_{ij}^{(q)}}{\sum_{i=1}^{I}\sum_{j=1}^{J} w_{ijmn}} \right)}{\sum_{n=1}^{N} w_{ijmn}} \qquad (3)$$

One iteration of the algebraic reconstruction is complete when all ray-sum equations of the system have been used exactly once. The scaling factor $\lambda^{(q)}$ is a relaxation factor and its value can vary between two consecutive steps and projections and may be chosen in the range from 0.0 to 2.0. The initial estimate $\hat{f}_{ij}^{(q)}$ representing the point of departure for the reconstruction method is chosen as a zero function.

EXPERIMENTAL CONFIGURATION

A double orthogonal Mach-Zehnder interferometer consisting of four Al mirrors and four 50/50 beamsplitters of surface flatness λ/20 was mounted inside the Target Area 2 vacuum chamber. The laser used was a low-power continuous-wave Green He-Ne (543nm) chopped at 50 Hz, giving rise to a pulse duration of 150 μs. Additional optics was employed for filtering, expanding and collimating the beam before entering the chamber. To ensure a smooth intensity variation, a diaphragm was used to apodise the beam contour.

The gas flow through the nozzle was controlled by a solenoid valve set to open for 4.8 ms connected to a high pressure N_2 reservoir at 900 psi. A He gas jet with equal backing pressure was also characterised. For every shot the chamber pressure was kept constant at 10^{-1} torr.

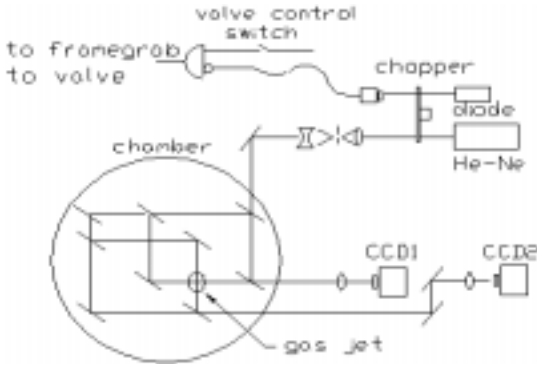

Fig 2. Experimental configuration.

Interference patterns were registered using two free-running CCD cameras and recorded with a framestore (CEO) system. Both the solenoid valve and the framegrabber were triggered by a low-power, 50Hz-chopped, diode laser focused onto a photodiode and a digital delay generator. Lenses with suitable focal lengths were used for imaging the gas jet zone onto the CCD sensors with different magnifications.

RESULTS AND CONCLUSION

We present the radial density profile obtained with N_2 for a cylindrical nozzle with diameter 1mm, (Figs. 3a., 3b.) for a rectangular nozzle, with dimensions 10 x 0.8mm^2 (Figs. 4a., 4b.) and for the collision of two nozzles with 5 x 0.65mm^2 and 5 x 1.1mm^2 (Figs. 5a., 5b), measured 28 milliseconds after the opening of the solenoid valve and for different distances, z, from the nozzle tip.

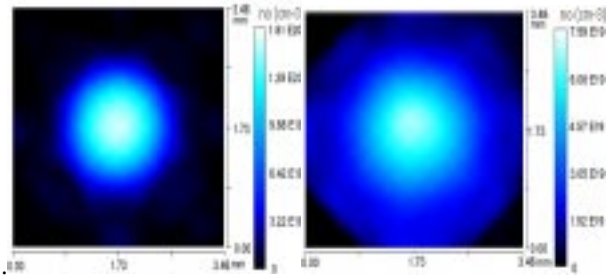

Fig 3a. Cylindrical nozzle, z=500 µm

Fig 3b. Cylindrical nozzle, z=1000 µm.

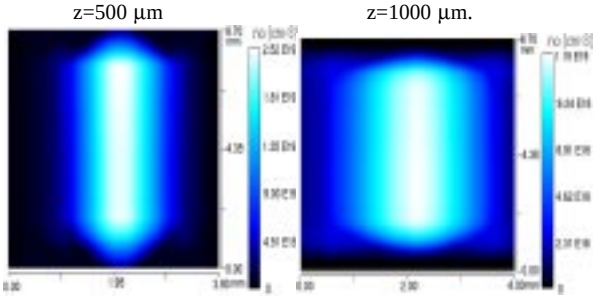

Fig 4a. Rectangular nozzle z=505 µm

4b. Rectangular nozzle z=1010 µm

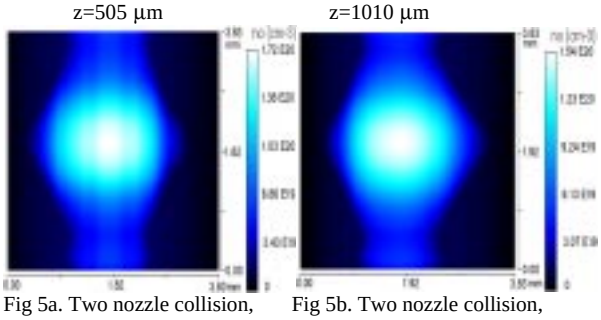

Fig 5a. Two nozzle collision, z=600 µm.

Fig 5b. Two nozzle collision, z=1200 µm.

The axial gas density decreases exponentially with the distance, z, from the nozzle tip with a scale length of approximately 1.4 mm and varies very little with time as shown in Fig 6., for the rectangular nozzle.

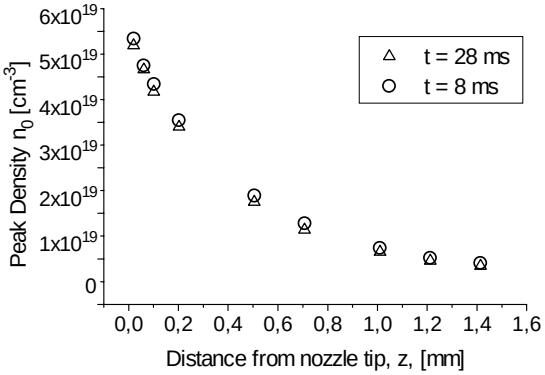

Fig 6.Peak density variation with distance from nozzle tip for two different instants after the opening of the solenoid valve.

We have fully characterized the three-dimensional density profile of non-cylindrical and cylindrical high-density pulsed gas jets by using a double orthogonal Mach-Zehnder interferometer and SART methods for inversion.

With rectangular gas jets we obtain similar densities as those produced by cylindrical nozzles, but persisting for much longer lengths. Colliding two rectangular nozzles allows for even greater densities, without increasing the backing pressure.

REFERENCES

1) N H Burnett and P B Corkum, J. Opt. Soc. Am. B, 6 1195, (1989)

2) N H Burnett and G D Enright, IEEE J. Quant. Electron , 26 1797, (1990)

3) H Fiedorowicz *et al.*, Phys. Rev. Lett., 76 415, (1996)

4) A Modena *et al.*, Nature, 377 606, (1995) and references therein

5) L Musinski *et al.*, Plasma Physics 24 731, (1982)

6) Y M Li and R Fedosejevs, Meas. Sci. Technol. 5 1197, (1994)

7) B Farizon *et al.*, Nuc. Inst. Meth. In Phys. Res. 101 287, (1995)

8) A Behjat, G J Tallents and D. Neely, CLF Annual Report (1996)

9) T Tajima and J M Dawson, Phys. Rev Lett. 43 267, (1979)

10) L M Gorbunov and V I Kirsanov, Zh. Eks. Teor. Fiz. 93 509, (1987) [Sov. Phys. JETP 93 260, (1987)]

11) P Sprangle *et al.* , Appl. Phys. Lett. 3 2146, (1988)

12) M Born and E Wolf, Principles of Optics, Pergamon Press (1970)

13) A H Andersen, IEEE Trans. on Med. Imag. 8 (1) 50, (1989) and references therein

14) R Gordon, IEEE Trans, on Med. Imag. (NS-21) 78, (1974)

FAST, HIGH RESOLUTION X-RAY CONTACT MICROSCOPY WITH AN ADVANCED EPOXY NOVOLAC RESIST

A C Cefalas[1)], P Argitis[1*)], Z Kollia[1)], E Sarantopoulou[1)], T W Ford[2),] A D Stead[2)], A Marranca[2)], C N Danson[3)], J Knott[3)], D Neely[3]

1) National Hellenic research Foundation, Theoretical and Physical Chemistry Institute, 48 Vas. Constantinou Av.Athens 11635 Greece. e-mail: ccefalas@eie.gr

2) Royal Holloway, University of London, Egham, Surrey TW20 0EX, UK. e-mail: T.W.Ford@rhbnc.ac.uk; A.Stead@rhbnc.ac.uk

3) Central Laser Facility, Rutherford Appleton Laboratory, Chilton, Didcot, Oxon. OX11 0QX, UK. e-mail: C.N.Danson@rl.ac.uk

*Permanent address: Institute of Microelectronics (IMEL) - NCSR "DEMOKRITOS" 15310 Ag.Paraskevi, Greece.

ABSTRACT

We report on the use of an epoxy novolac chemically amplified photoresist to produce X-ray images of living biological specimens in the water window using laser plasma generated soft X-rays (2.4 - 4.4 nm). The photoresist response was at least one order of magnitude "faster" than the standard PMMA (polymethyl methacrylate) previously used in soft X-ray contact microscopy (SXCM). After chemical development of the exposed resists, atomic force microscopy (AFM) of the relief images obtained of biological specimens clearly showed the flagella of the motile green alga, *Chlamydomonas*, suggesting a lateral resolution better than 300 nm, whilst the AFM was capable of discriminating height features of 20 nm in depth profiles.

INTRODUCTION

Soft X-ray contact microscopy (SXCM) is an interdisciplinary technique that has many applications in both life and material sciences. For life sciences SXCM enables the ultrastructure of living hydrated specimens to be studied without the need of dehydration or other chemical pretreatment of the living specimen by using suitable pulsed X-ray sources such as laser plasmas[1,2)]. The interest in using soft X-rays, in the so called "water window" (2.3 - 4.4 nm or 280 - 530 eV), is based on the low attenuation at these wavelengths caused by water as compared to the attenuation caused by organic matter. Indeed, just below the oxygen K edge (2.4 nm), 1 m water has only 20% absorption while the carbon containing proteins have distinctively higher absorbance[3)]. Therefore, images with good contrast can be produced by SXCM, provided that a high contrast photoresist is available. Furthermore, the shorter wavelength of the X-ray light, relative to visible light, allows for better resolution than with light microscopy whilst the path length of the 3 - 4.4 nm X-ray photons is 20 times higher than that of the 10 KeV electrons. Thus, unlike electron microscopy, images of specimens up to 10 µm thick can be obtained if their carbon content is low.

To be successful the technique requires the development of sensitive photoresist materials for image recording; these should have optimized contrast, high resolution and an extended grayscale. Up to now the only known photoresist used successfully in SXCM has been polymethyl methacrylate (PMMA). This is a high resolution photoresist with good contrast but it is a relatively slow photoresist and therefore requires a very large fluence of X-rays for imaging. This has limited the range of X-ray sources that can be used, mainly to those of large national facilities.

Laser plasma sources are devices that can efficiently generate X-rays. The intensity and the spectral distribution of the X-ray emission from the plasma depends on many parameters, such as the energy of the laser pulse, its wavelength, its pulse duration, the focusing of the beam on the target and the atomic number of the target. In this experiment we used the Nd:glass laser facility at Rutherford Appleton Laboratory at 1.06 µm to generate soft X-rays in the water window. Using the same geometry and development procedure for all of our photoresist samples, we have compared the performance of PMMA (a positive resist) to two forms of a novel negative, epoxy novolac photoresist, which we call EPR (Epoxy resist)[4)].

MATERIAL AND METHODS

The experimental apparatus for producing soft X-ray contact images consisted of the laser source and the vacuum chamber (Target Area 4), where the holder containing the biological samples and the photoresist was placed[5)]. The laser source was the Nd:glass laser of the Rutherford Appleton Laboratory that can deliver 16 J at 1.06 µm. The vacuum chamber was evacuated at a pressure of 10^{-5} mbar and the laser beam was focused with a lens of 40 cm focal length on a planar yttrium foil target (Goodfellow, Cambridge, UK). The X-rays were monitored with a pin photodiode and an X-ray diode array[6)]. After initial tests to compare the sensitivity of PMMA and EPR in the absence of either water or a biological specimen cells of the motile green alga, *Chlamydomonas*, were placed in a droplet of medium on the silicon nitride window (120 nm thick; FaSTec, Silverstone, UK). The photoresist was placed onto this and the holder assembled and tightened to ensure that the specimens were in close contact with the photoresists[1)]. The thickness of the water was monitored by light microscopy prior to placing the specimen holder into the vacuum chamber. To filter out the 1 KeV photons a thin (0.1 µm) aluminium film was placed in front of the silicon nitride window. Throughout the experiments the distance between the target and the front surface (i.e. silicon nitride window) was maintained at 15 mm.

A Du Pont Elvacite 2041 (MW 443,000) polymer was used for PMMA resist formulation. 500 nm films were spun from a propylene glycol methyl ether acetate solution and prebaked at 160^{o} C for 60 mins. Methyl isobutyl ketone/ Isopropanol 1:1 was used as developer at developing times from 45 secs to 105 secs. The EPR resist formulation described elsewhere[4)] was used as the standard EPR. The modified epoxy novolac resist version was formulated with a higher MW polymer (MW 3300 vs MW 2250). For both the EPR and modified EPR resists, a 4 min post exposure bake at 90^{o} C was used, and methyl isobutyl ketone was used as developer (1 min) followed by a rinse with isopropanol (45 secs). The developed photoresists were examined with a Burleigh SPM atomic force microscope with a 75 µm scan head.

RESULTS

Initial images taken either without a silicon nitride window or, when a window was present, without a biological specimen, revealed that the negative, epoxy novolac photoresist, which we call EPR[4)], is at least one order of magnitude more sensitive in getting useful images than PMMA. A fluence of 50 mJcm^{-2} in the water window, was found to be the threshold for a blank image to appear on the PMMA, although such images were very shallow, with just 20 nm maximum depth difference; this agrees with previously published figures[7,8)]. In comparison the threshold for EPR in a similar experiment was only 3 - 5 mJcm^{-2} and fluences such as this were obtained with a laser energy of just 300 mJ (Fig. 1). This value was even lower for a slightly modified epoxy novolac based resist (0.5 mJcm^{-2}) which was produced using a related material formulated with a higher MW polymer.

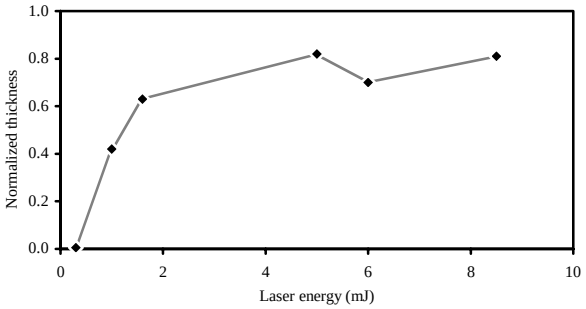

Fig.1 Normalized thickness as a function of the input laser energy for the EPR resist.

Images of *Chlamydomonas* cells were successfully obtained using the negative epoxy novolac photoresist (Fig. 2), these images clearly show the cell body and the flagella. Using PMMA in conjunction with a similar source to specimen distance, biological imaging was not possible when the specimen was behind an 0.1 µm aluminium filter even at the maximum energy pulse obtained from the laser. This suggests that in previous imaging experiments[9,10] a significant contribution to image formation may have been from higher energy photons or from UV which is also filtered out by an aluminium coating[11].

The biological images (Figs. 2,3) recorded with EPR suggest a lateral resolution considerably better than 300 nm as the diameter of flagella are approximately 600 nm but these are clearly distinguishable. For successful biological imaging it is also necessary to be able to distinguish adjacent areas of the specimen which may differ only marginally in their ability to absorb soft X-rays, this is in effect the contrast characteristics of the photoresist. The present images, unlike previous studies using PMMA[12,13], show no ability to discriminate structures within the cell, that is to say the absorption by the cell body was sufficient to result in the complete dissolution of the photoresist when it was developed. However, the response of the photoresist was able to differentiate between a single flagellum and areas where two flagella overlapped (Fig. 3). In this case the photoresist area corresponding to the overlapping regions was c.80 nm deep, whereas images of single flagella were only c.20 nm. Since the depth of the images of the cell body were c.100 nm deep it is concluded that two flagella also absorbed sufficient X-rays to produce a maximum response.

In conclusion we have therefore demonstrated that the novel photoresist used in this study are significantly more sensitive than the traditionally used PMMA and, whilst their range of sensitivity may not be as great as PMMA, such materials can be used in imaging experiments. Perhaps, more significantly however, is that such photoresists could be used with less intense X-ray sources and could therefore be the basis of development of a small scale soft X-ray microscope using a small commercial laser.

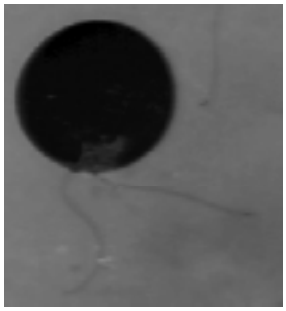

Fig. 2 Image of *Chlamydomonas* using the EPR resist. The laser energy was 10.6 J and the development time was 1 min. The cell body and the flagella are distinct but no structural details are visible within the cell body.

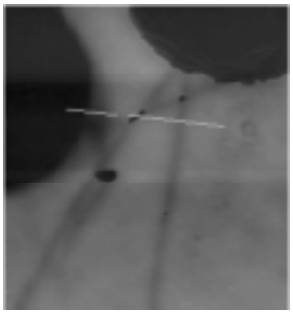

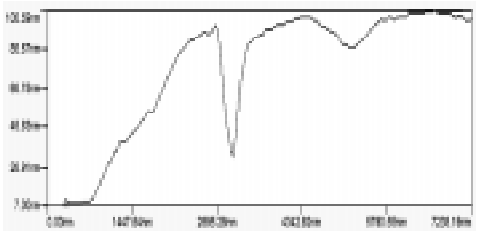

Fig. 3 Image of *Chlamydomonas* (a) using the EPR resist. The laser energy was 10.6 J and the development time was 1 min. The depth of the area (b) corresponding to single flagella is approximately 20 nm deep (open arrow) whereas those of overlapping flagella are 80 nm (closed arrow).

REFERENCES

1). T W Ford, A D Stead and R A Cotton
Electron Microscopy Reviews, 4 269, (1991)
2). J Kirz, C Jacobsen and M Howells
Quart. Rev. Biophysics, 28 33, (1995)
3). R A Cotton, J H Fletcher, C E Webb, A D Stead and T W Ford SPIE Proceedings, 2015 86, (1994)
4). P Argitis, I Raptis, C J Aidinis, N Glezos, M Baciocchi, J Everett and M Hatzakis
Journal of Vacuum Science & Technology, B13 (6), 3030, (1995)
5). A D Stead, T W Ford, C Danson, D Pepler and M Ebbage
Annual Report to the Laser Facility Committee, Rutherford Appleton Laboratory. pp. 47, (1995)
6). G Eker, G J Tallents, A Behjat, D Neely, E Wolfrum, A D Stead and T W Ford
Annual Report to the Laser Facility Committee, Rutherford Appleton Laboratory. pp. 111, (1996)
7). T Tomie, H Shimizu, T Majima, M Yamada, T Kanayama, H Kondo, M Yano and M Ono
Science, 252 691, (1991)
8). R A Cotton, A D Stead, T W Ford, J H Fletcher and C E Webb SPIE Proceedings, 1741 204, (1993)
9). T W Ford, R A Cotton, A M Page and A D Stead
Annual Report to the Laser Facility Committee, Rutherford Appleton Laboratory. pp. 52, (1993)
10). A D Stead, R A Cotton, A M Page, C G Steele, R Bagby and T W Ford
Annual Report to the Laser Facility Committee, Rutherford Appleton Laboratory. pp. 64, (1994)
11). T W Ford, R A Cotton, A M Page and A D Stead
Annual Report to the Laser Facility Committee, Rutherford Appleton Laboratory. pp. 52, (1993)
12). T W Ford, R A Cotton, A M Page and A D Stead
In: X-Ray Microscopy IV, (Eds. V.V. Aristov & A.I. Erko). Inst. Microelectronics Technology, Chernogolovka, Russia. pp. 276, (1994)
13). A D Stead, T W Ford, J A Catcheside, C P B Hills and A Ridgeley
Journal of X-Ray Science & Technology 2 172, (1990)

OPTICAL SPECTROSCOPY OF FREE AND CONFINED LASER PRODUCED PLASMAS

D.J. Heading, J.S. Wark

Department of Physics, Clarendon Laboratory, University of Oxford, Parks Road, Oxford, OX1 3PU

Recent advances in laser ablation has lead to a refocussing of attention upon optical spectroscopy of plasmas as a means for diagnosing the conditions[1,2] . The requirement of a diagnostic for plasmas is that the probe should be non-invasive and not cause any perturbation to the environment. The observation of light emitted from the plasma fulfils this criterion admirably.

Recent interest has focused on the inference of conditions in laser produced plasmas in a confined mode[3] . We have developed confined laser ablation as a means of obtaining tractable plasma conditions for understanding plasma processes in strongly coupled plasmas. In this report we show some recent data we have obtained for confined laser ablation. We also show how the major features of such plasmas can be modelled using a modified version of the Medusa hydrodynamic code[4] , coupled to spectroscopic post processor[3] .

Experimentally the set up is simple. A target is irradiated with the TA4 beam from Vulcan, and observed with a prism spectrometer. The output from the spectrometer is incident on the input slit of a optical streak camera, in this case an Imacon 500. The time resolved spectrum is recorded by a Darkstar CCD camera and the image saved on a computer for later analysis. The target is made of a 30 thick layer of Al, deposited on a quartz plate. A second quartz plate is held around 250 micron away from the deposited laser. The laser passes through the second plate (the confining wall) and generates a plasma on the Al layer. The plasma expands and fills the gap. The shock waves passing through the plasma ensure a high degree of plasma homogeneity.

The hydrodynamic code Medusa has been modified to permit the calculation of the spectra. The original ionisation balance package was not correct at the low temperatures encountered in these plasmas, and so it was substituted for our Saha-Boltzmann solution. This is consistent with our spectral calculation code, which was modified to act as a post processor for the density, temperature and cell width the Medusa simulation generates. The code must also be modified for taking the gap into account. As a Lagrangian code, any cell in the gap will be compressed and its temperature will be driven extremely high. This is unacceptable in this case, as thermal conduction from that cell will distort the temperature profile of the ablating plasma. Thus the code has to be run in two stages, firstly the laser target interaction, and free ablation of the plasma, and secondly the confining of the plasma by the outer wall, and its shock heating. Currently the effect of the outer wall is only taken into account by allowing thermal conduction across it. This almost certainly underestimates the thermal conductivity through the confining wall.

In a confined geometry, the plasma crosses the gap and then impacts the confining wall. In this case the plasma then is shock heated by the exchange of kinetic energy for heat, and the ionisation is higher. A typical streak is shown in figure 1a. In this case 3 J of laser energy hit a 30 nm Al foil, which expanded into a 250 micron wide gap. The spectral lines in this streak are wide and merge into each other. The main feature is found at 450 - 500 nm, and is identified as the Al II and Al III features at 452 and 466 nm. No evidence of neutral resonance lines is observed, and the Al III 570 nm line in the wing of the broad, main feature. This suggests that the plasma is both hot and dense

The simulation of the target is shown in figure 1b. Clearly there are significant differences between the data and the simulation, but the gross structure of the two spectra are similar. For example, the time between the initial ablation emission and the peak of emission from the first impact on the wall is measured experimentally to be ~12 ns, whereas the simulation predicts 15 ns. Also, the observed spectral lines are present in the simulated spectrum. The Al I resonance line at 395 nm is visible in the simulated spectrum but not in the data.

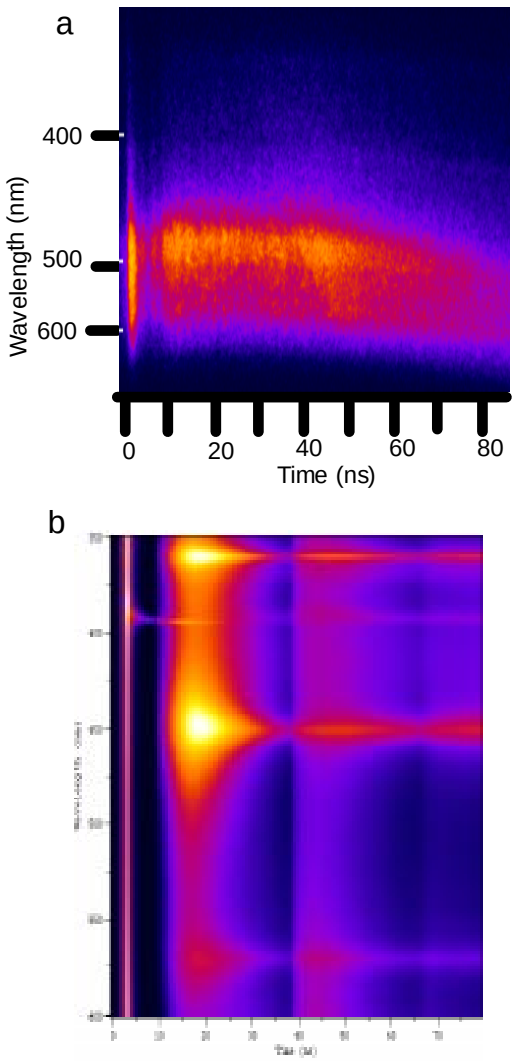

Figure 1a Experimental Spectrum for 3 J on Target, 250 micron gap, 30 nm thickness of Aluminium.
1b Simulation of the Spectrum at the same conditions

The major problem with the simulation is that the shock waves have a much greater influence on the emission than is observed in the data. After the initial transit of the plasma, no major increase of emission is observed, whereas in the simulation, the returning shock wave clearly reheats the plasma at around 40 ns and 65 ns. This is probably due to the low thermal conductivity into the walls and through the plasma, the standard Medusa values, based on Spitzer rates[5] are too small for solid quartz and for plasmas of the anticipated density and temperature. A higher thermal conductivity would ensure that the shock wave was more dissipated on impact and interaction, and thus that the returning shock wave would be weaker.

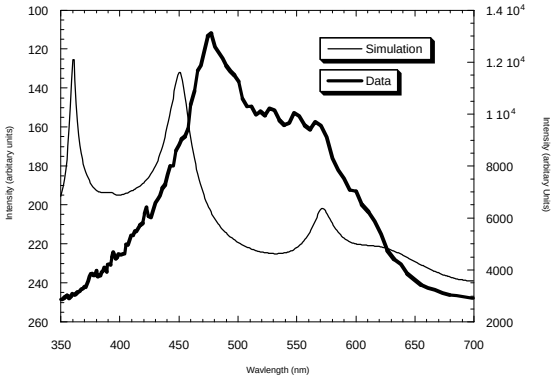

Figure 2: Comparison of Experiential and Simulated spectra 40 ns after the laser pulse.

Other differences between the two spectra can be accounted for by the fact that the data has not been corrected for the non-linear wavelength response of the prism spectrometer the intensity response of the cameras.

A comparison of the two spectra taken at 40 ns is shown in Figure 2. Clearly in the wings of the spectrum the response of the camera is rapidly falling off. However, the two main features are reasonably well represented, and the width of the lines are commensurate. The centre of the simulation is much lower than that found in the data. The reason for this is unclear, but it may be due to weaker Al lines which are not included in the database used to generate the spectrum.

Further work is clearly needed on the simulation of the spectral emission. This can be approached in a number of ways. The code can be stopped and then restarted with an outer wall added, to permit a realistic simulation of the wall-plasma interaction. The thermal conductivity of the walls should be modified to give the correct value for quartz. Further work is probably needed on the initial ionisation and absorption of the laser beam. Currently, the energy is assumed to be dumped at the critical density, apart from that which is absorbed via inverse bremstrahlung. In fact, during the absorption, multiphoton processes can be important, and the ionisation during this phase may not be the same as that given by LTE. This could have important consequences for the period at least up until the plasma has expanded to fill the gap. Further work is also necessary on the image processing of the experimental data, to correct for the intensity response, camera distortions and non-linear wavelength scale.

REFERENCES

1) D.J. Heading, G.R. Bennett, J.S. Wark, R.W. Lee.
Novel plasma source for dense plasma effects
Phys. Rev. Lett., **74** (18), 3616-3619 (1995).
2) A.N. Mostovych, L.Y. Chan, K.J. Kearney, D. Garren, C.A. Iglesias, M. Klapisch, F.J. Rogers.
Opacity of dense, cold, and strongly coupled plasmas
Phys. Rev. Let., **75** (8), 1530-1533 (1995).
3) D.J. Heading, G.R. Bennett, J.S. Wark, R.W. Lee.
Simulations of Spectra from Dense Aluminium plasmas
J.Q.S.R.T., **54** (1/2), 167-180 (1995).

4) J.P. Christiansen, D.E.T.F. Ashby, K.V. Roberts.
Medusa: A One-Dimensional Laser Fusion Code
Computer Physics Communications, **7** 271-287 (1974).
5) L. Spitzer.
Physics of Fully Ionised gases; ed.2nd ; Interscience: (1965)

X-RAY LASER MEASUREMENTS OF DIRECT DRIVE IMPRINT ON VULCAN

D. H. Kalantar[1)], E. Wolfrum[2)], J. Zhang[3)], M. H. Key[1)], L. B. DaSilva[1)], A. Demir[4)], N. S. Kim[2)], C. L. S. Lewis[5)], J. Lin[4)], A. MacPhee[5)], D. Neely[2)], B. A. Remington[1)], J. E. Rothenberg[1)], R. Smith[4)], G. J. Tallents[4)], J. Wark[3)], J. Warwick[5)], and S. V. Weber[1)]

[1)]Lawrence Livermore National Laboratory, Livermore, California 94550
[2)]Rutherford Appleton Laboratory, Chilton, Didcot, United Kingdom
[3)]Clarendon Laboratory, University of Oxford, Oxford, United Kingdom
[4)]Department of Physics, University of Essex, Colchester, United Kingdom
[5)]School of Mathematics and Physics, Queen's University of Belfast, Belfast, United Kingdom

INTRODUCTION

High gain direct drive inertial confinement fusion requires very uniform irradiation of a hollow spherical shell with a layer of fusionable deuterium and tritium on its inner surface. The intensity of laser irradiation builds up in several nanoseconds from an initial 'foot' at ~10^{13} W/cm^2 to more than 10^{15} W/cm^2 during the main drive pulse. Laser ablation of the capsule surface produces a high pressure, accelerating the shell radially inward, and resulting in Rayleigh-Taylor (R-T) growth of surface perturbations originating from both the initial surface roughness of the capsule and from imprint of spatial non-uniformities in the laser drive intensity early in the laser pulse.

The uniformity of illumination on a direct drive implosion capsule is determined on a large scale by the multi-beam irradiation geometry, and on a small scale by beam smoothing techniques. By using a large number of beams (such as the 60 beams of the Omega laser[1] or 48 beam clusters for the NIF[2]), large scale non-uniformities due to the overlap of the laser focal spots are adequately reduced. Random phase plates (RPPs)[3] are introduced to smooth the individual beam focal spots. The spatial intensity variations of the individual beam speckle patterns may be smoothed by spectral dispersion (SSD)[4] with induced spatial incoherence (ISI)[5] or by using partially coherent light.[6]

We performed experiments to study the imprint under conditions simulating the low intensity foot of the pulse on an ignition target, such as designed for the NIF. We used a 0.53 µm laser wavelength, and considered the imprint in thin Al foils due to both a broadband distribution of modes such as those in smoothed speckle patterns, and a single mode optical intensity variation. We characterized the laser imprint using a Ge x-ray laser and multilayer imaging optics, as described previously.[7] In this paper we summarize and compare the multiple and single mode imprinting results.

X-RAY LASER RADIOGRAPHY

To measure early time imprinting prior to the onset of R-T growth, we use the Ge x-ray laser, which lases at 19.6 nm. Since the mass absorption coefficients of all materials are high for this wavelength, we use Al foils, with an L absorption edge at a photon energy just above the x-ray laser energy. With this configuration, we are able to probe 2 µm foils with a high sensitivity to modulation in optical depth. A 50 nm variation in the foil thickness corresponds to a 10% variation in the transmission of the x-ray laser.

We use the x-ray laser as a source of radiation for face-on radiography, as described in reference 7. We image the modulation in optical depth of the directly driven foil target using molybdenum-silicon multilayer optics.[8] A single spherical reflecting optic is used at near normal incidence in combination with a flat mirror at 45° incidence that serves to spectrally filter the image. The multilayer optics relay an image of the transmission of the x-ray laser backlighter through the directly drive foil onto a 16-bit Peltier cooled back-thinned (CCD) with high magnification and high resolution. We characterized the modulation transfer function using gold grid targets, and determined that the resolution is equivalent to that from a 5 µm full width at half maximum (fwhm) Gaussian point spread function.

OPTICAL IRRADIATION PATTERN

We show sample far field images of the irradiation patterns used in these imprint experiments in Fig. 1. These images were recorded as an equivalent focal plane image during the experimental series using photographic film that was pulse calibrated at the 0.53 µm laser wavelength. These images are displayed as fractional modulation in the exposure to represent the time integrated optical smoothing level. In addition, we show the 2-D Fourier transforms of the speckle patterns, which we will discuss later.

In Figs. 1a-c, we show the multimode speckle patterns used for the experiments. We show a static speckle pattern, together with SSD smoothed and ISI smoothed speckle patterns at 0.53 µm. The Vulcan beam was f/10, which provides a speckle size of about 10 microns. The imprint beam was incident on the Al foil at 16° off-normal, and the pulse shape was 1.0 ns square with a ~100 ps rise. The average intensity within the fwhm spot size was in the range 2-6x10^{12} W/cm^2.

In Fig. 1d, we show a sample optical intensity pattern used for the single mode imprint experiments. This intensity pattern was achieved by interfering the Airy pattern focal spots of two beam segments that were transmitted through 4 x 10 mm rectangular apertures in a beam block inserted into the beam path. The average intensity was 3-10x10^{12} W/cm^2.

The static speckle pattern is an interference pattern from the random phases of the RPP elements. The Fourier transform shown in Fig. 1a is azimuthally symmetric, and it has a theoretical value for the rms modulation of 1.0. We measured an rms modulation of 0.93.

Smoothing by spectral dispersion reduces the modulation of the speckle pattern by spatially dispersing the time varying spectral components of the broadband laser in one dimension. The speckle pattern fluctuates rapidly in one direction, smoothing of the short wavelength structure in that direction, as indicated by the one-dimensional nature of the Fourier transform of the SSD smoothed speckle pattern. We measured a value of 0.25 for the modulation of the SSD smoothed speckle pattern with 0.5 THz bandwidth (measured with a spectrometer at the 0.53 µm laser wavelength).

Spatial incoherence is induced on the 0.5 THz Vulcan beam by inserting a 5x5 array of varying thickness glass plates into the beam path, in addition to the RPP, introducing delays of up to 220 ps on different segments of the beam. The resulting speckle pattern shows a reduction in the Fourier power for short wavelengths in all directions, but not for the longer wavelengths that are determined by the speckle size for the beamlets from each segment of the glass plate array. We measured an rms modulation of 0.27 for the ISI smoothed speckle pattern.

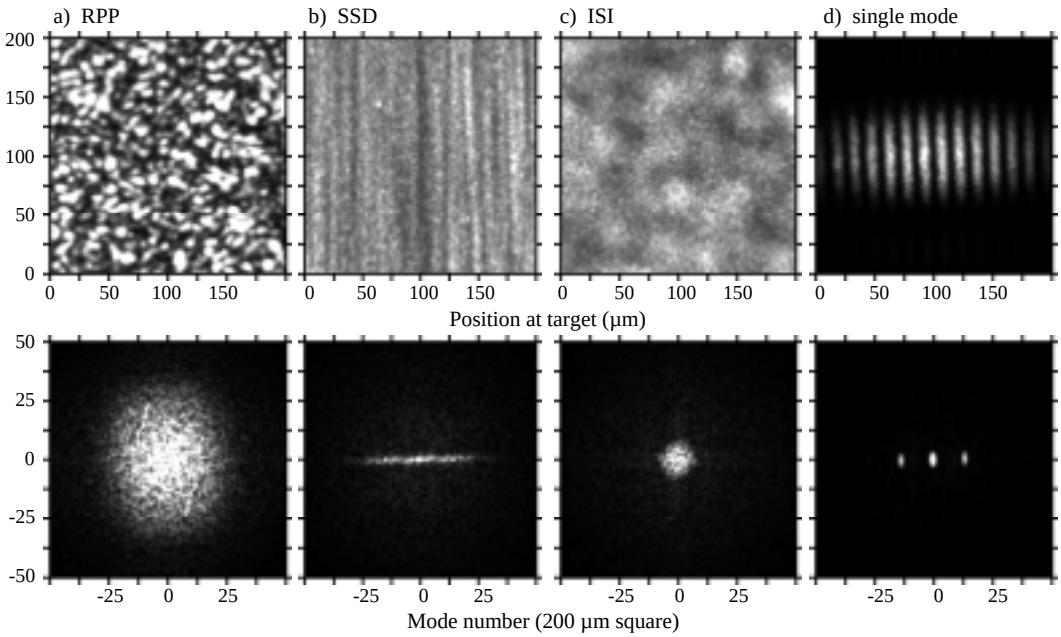

Figure 1: Optical irradiation patterns used for the imprint experiments. The patterns shown are a) static RPP speckle pattern, b) SSD smoothed speckle pattern, c) ISI smoothed speckle pattern, and d) 15 μm single optical mode. Each is displayed as modulation in exposure on the film. The 2-D Fourier transforms are shown for reference.

The differences in the speckle patterns are illustrated with lineouts in Fig. 2 of the 2-D Fourier spectra shown earlier in Fig. 1. Lineouts of Fourier power parallel and perpendicular to the dispersion direction show that the power in the perpendicular direction is only slightly reduced from the static speckle pattern, whereas the power in the parallel direction is significantly reduced by the time-varying dispersion. For the case of ISI smoothing, the power is reduced for wavelengths shorter than about 50 μm (mode 4) in all directions.

LASER IMPRINTED MODULATION

A. 0.53 μm irradiation at 2-6x10^{12} W/cm^2

We irradiated 2 μm thick Al foils with a 1 ns laser pulse at intensities varying from 2-6x10^{12} W/cm^2 at 0.53 μm. The typical shock breakout time is about 0.20 ns. We recorded XUV radiographs of the modulation in optical depth in the foil using the Ge x-ray laser. An extensive data set was obtained including both imprint and subsequent R-T growth by recording radiographs at various times relative to the imprint laser pulse.

We show sample XUV radiographs in Fig. 3 that were recorded for each smoothing scheme on Vulcan. These are all shown at about 0.45 ns into the optical drive pulse, following 0.25 ns of R-T instability growth. In the case of static speckle, the modulation in optical depth of the foil is very pronounced. For the SSD and ISI smoothed cases with measured optical exposure rms modulations of 0.25-0.27, however, the modulation is close to the level of the background resulting from the surface finish of the Al foils and the intrinsic speckle pattern of the x-ray laser at the plane of the thin foil.

Two-dimensional Fourier transforms of the optical depth modulation are also shown in Fig. 3, corresponding to the XUV radiographs. These show structure that reproduces the structure of the optical speckle patterns, shown earlier in Fig. 1. Lineouts of these 2-D Fourier power are shown in Fig. 4. Two lineouts are shown for the SSD smoothed beam parallel and perpendicular to the dispersion direction, whereas the lineouts for the static and ISI smoothed imprint are azimuthally symmetric and are shown averaged for the two directions. The modulation imprinted by an SSD smoothed beam shows power at short wavelengths only in the direction perpendicular to the dispersion direction. For the example of ISI, the lineout shows power at long wavelengths characteristic of the speckle from the individual echelon segments, but there is little power in short wavelength modulations in all directions, as shown previously for the lineouts of the Fourier transform of the optical speckle pattern.

By imaging the optical depth modulation of the thin Al foil at a range of times, we record the R-T growth of perturbations in the foil. We show a time sequence of lineouts from the Fourier analysis of the static speckle imprinted modulations in Fig. 5. This shows the growth of perturbations at all wavelengths. Note that because the Fourier transforms are azimuthally symmetric, we can multiply these curves by 2^1n, where n is the mode number, to obtain Fourier power per mode. This then provides a technique for measuring of the instability growth, resolved as function of mode number.

Since we do not yet have detailed simulations of this experiment that include opacity effects ($\kappa=\kappa(\rho)$), we empirically normalized our measurements to correct for the average change in opacity due to compression (discussed in the following section). This normalized rms is plotted in Fig. 6 for the various cases of laser smoothing. Details of the change in rms as a function of time depends on the Fourier composition of the speckle pattern. However, as a first order approximation, we assume the growth rate is the same for the different cases, and an exponential fit to the static imprint data is applied with a constant multiplier to the other two cases. We observe

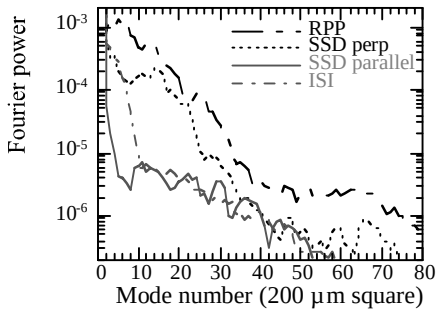

Figure 2: Lineouts of the 2-D Fourier transforms showing the reduction in power per mode due to SSD and ISI smoothing of the laser speckle pattern.

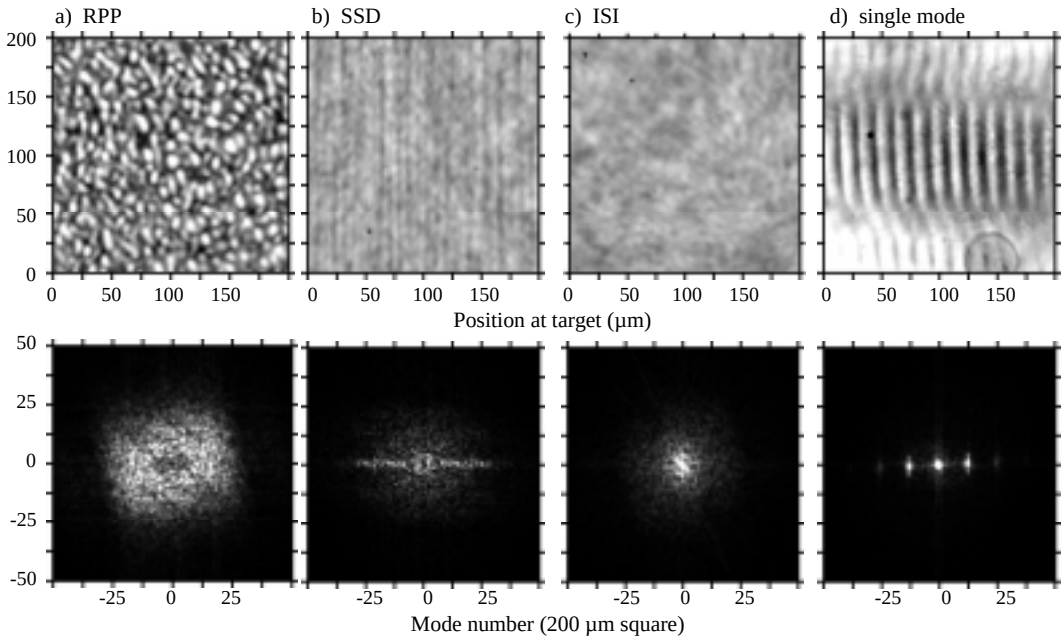

Figure 3: XUV radiographs of modulation in the Al foil recorded with the x-ray laser. These are shown as modulation in optical depth at t=0.45 ns for the cases a) static speckle imprint, b) SSD smoothed imprint, and c) ISI smoothed imprint. The modulation in optical depth imprinted by a single 15 μm mode is shown at t=0.58 ns. Two-dimensional Fourier transforms are shown for reference.

significant imprint of the static speckle. Interpolating at the shock breakout time of about 0.20 ns, we observe that the fractional rms modulation in mass per unit area is 0.053±0.009.

The SSD smoothed case shows little change in the rms above the noise early in time. We can see the 1-D modulation characteristic of the residual speckle pattern due to SSD smoothing, but the isotropic noise due to the surface finish of the foil and the intrinsic speckle pattern of the x-ray laser dominates the rms. The surface roughness of the Al foils is about 20 nm, which corresponds to a level of 0.01 in Fig. 6.

At late time, the modulation imprinted by SSD grows above the noise level. If we look at t=1.0 ns, and extrapolate back to shock breakout at 0.20 ns by assuming the same R-T growth history as for the static RPP speckle case (curve shown in Fig. 6), then we obtain an rms modulation in fractional mass per unit area of 0.018±0.002. The growth rate does depend weakly on the distribution of modes, but we have not included this in our initial analysis of the data.

Performing a similar analysis on the data obtained by imprinting with ISI, we observe that the rms modulation in fractional mass per unit area is about 0.008±0.001 at t=0.20 ns. The ISI smoothed speckle pattern imprints the least in these targets. Note that in this case the pulse shape has a rise time that is >0.2 ns due to the glass plate beam delays. The different pulse shape may affect the overall hydrodynamics, but relative to the 50% rise point on the laser pulse shape, the shock breaks out at the same time (0.2 ns).

B. Single mode 0.53 μm irradiation

By introducing a beam block with two small apertures, as described separately,[9] we imprinted a hydrodynamic perturbation into the foil with a single wavelength. We used this to characterize single mode imprinting and R-T growth, and also to characterize the opacity increase for shock compressed Al. Although we conducted a sequence of tests, using single mode optical perturbations with wavelength of 15-90 μm, and at 1-10x10^{12} W/cm^2, we discuss here only a summary of the results from the 15 μm single optical mode imprinting at 3-5x10^{12} W/cm^2, and we compare the results with the multiple mode imprinting. Detailed analysis of the different cases is shown in more detail by Wolfrum et al.[9]

An XUV radiograph of a thin Al foil imprinted with this λ=15 μm single mode pattern at about 3x10^{12} W/cm^2 is shown in Fig. 3d, along with the two dimensional Fourier transform. The zero order interference fringe intensity pattern has an Airy pattern envelope with fwhm dimension of the central peak of about 125 μm x 320 μm. This image, recorded at 0.58 ns into the optical drive pulse, shows a single mode modulation in the optical depth of the foil.

The x-ray laser probe allows us to radiograph a large area of the foil that includes both shocked and unshocked regions when we use a small irradiation pattern such as that generated with the

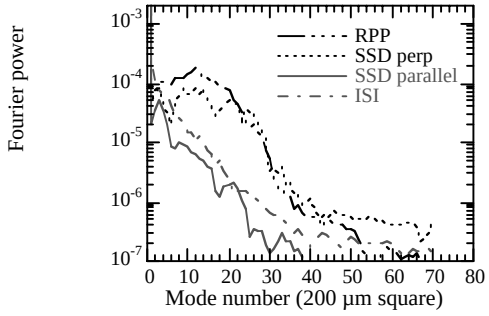

Figure 4: Lineouts of Fourier power from XUV radiograph of multiple mode laser imprint shown earlier in Fig. 3.

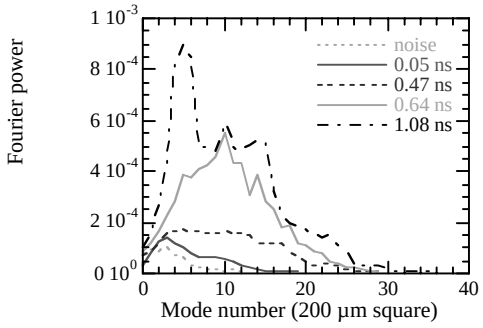

Figure 5: Fourier power per mode plotted at a range of times, showing the growth per mode.

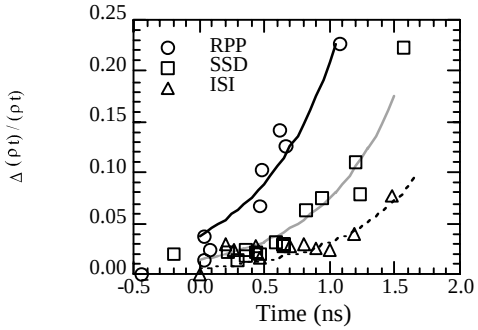

Figure 6: Modulation in optical depth as a function of time imprinted by the different smoothing techniques.

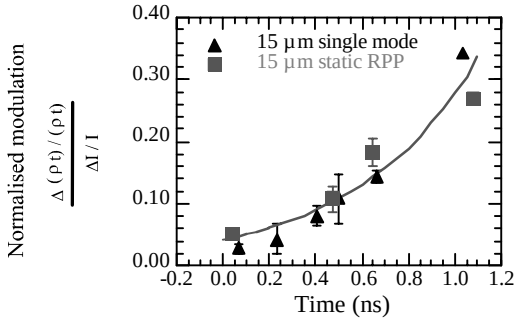

Figure 7: Imprint efficiency measured from both single mode and multiple mode optical modulations for λ=15 µm.

two apertures. We observe in the radiographs that the shocked region is more opaque than the unshocked region (the region with the ripples in Fig. 3d is darker on average than the surrounding edges), which is due to a shock enhancement in the opacity.

We quantify the shock change in opacity using a time-sequence of radiographs, and empirically remove the effect of time-dependent opacity from the rms modulation of the imprinted foil, as shown earlier in Fig. 6. We apply this correction as:

$$\frac{\delta(\rho t)}{(\rho t)} = \frac{\delta(\ln(\text{exposure}))}{(\kappa\rho t)_o + \Delta(OD)},$$

where $(\kappa\rho t)_o$ is 4.48 for 2 µm thick cold Al at the 19.6 nm Ge x-ray laser wavelength, and $\Delta(OD)$ is the difference in average optical depth in the shocked region vs. the unshocked region. In these experiments, the average change in optical depth, $\Delta(OD)$, is <1.3 in the shocked region, which means that this effect represents a correction to the fractional modulation of mass per unit area less than 25%.

Note that once the shock breaks out from the Al foil at 0.20 ns, the effect of shock enhancement of the opacity is reduced because the foil decompresses. Calculations with OPAL result in a change in the opacity of the Al of 25% during the shock transit phase, in agreement with the experimental result. After shock breakout, however, simulations that included x-ray preheat suggested the foil decompressed faster than the opacity data indicates. At the time of shock breakout, the simulations indicated that the ratio of P/P(Fermi) at the high pressure limit was about 1.03. Several hundred ps after the shock breaks out, x-ray preheat has a larger effect, but this does not affect the comparison of imprinted modulation due to the different smoothing schemes since they are affected identically. This effect of preheat is a complication of the experiments, but it does not invalidate them as a test of the modelling.

We Fourier analyzed the modulation imprinted by the single mode optical pattern for the experiments, and plotted the Fourier amplitude of the 15 µm mode as a function of time. This is shown in Fig. 7, corrected for the change in opacity due to shock compression, and normalized by the laser intensity modulation of the 15 µm mode obtained by Fourier analyzing the optical intensity pattern shown earlier in Fig. 1d. This corresponds to an imprint efficiency.

The single mode and multimode perturbations are imprinted in the foil with similar efficiency relative to the optical intensity modulation, demonstrating the linearity of the imprint process in these experiments. On the graph, we include a fit to the full set of data, including the single mode and multiple mode results at average intensities of 3-5x10^{12} W/cm^2. The growth rate plotted here is 1.9±0.2 ns^{-1}, where the growth is of modulation normalized to the laser intensity modulation.

SUMMARY AND CONCLUSIONS

We have used the XUV radiography technique to study imprint in thin foils. We made measurements of the temporal development of the imprinted modulation including Rayleigh-Taylor growth of the modulations imprinted by low intensity 0.53 µm irradiation on a 2 µm Al foil under various laser smoothing schemes. We have used a single mode intensity pattern to characterize the imprint at single perturbation wavelengths. This allows a direct comparison of single vs. multiple mode imprinting.

ACKNOWLEDGMENTS

We gratefully acknowledge the support from the Vulcan laser support staff throughout these experiments. This work was funded by the Engineering and Physical Sciences Research Council. It was also partially supported under the auspices of the US DOE by LLNL under Contract No. W-7405-ENG-48, and EW was supported by the Austrian Fonds zur Förderung der wissenschaftlichen Forschung under Project No. P10844 NAW.

REFERENCES

1) J. M. Soures,
J. Fusion Energy **10**, 295 (1991).

2) S. W. Haan *et al*,
Phys. Plasmas **2**, 2480 (1994).

3) Y. Kato *et al*,
Phys. Rev. Letters **53**, 1057 (1984).

4) S. Skupsky *et al*,
J. Appl. Phys. **66**, 2456 (1989).

5) R. H. Lehmberg *et al*,
Opt. Commun. **46**, 27 (1983);
D. A. Peplar *et al*,
Proc. SPIE **1840**, 76 (1993).

6) H. Nakano *et al*,
J. Appl. Phys. **73**, 2122 (1993);
N. Miniyaga *et al*,
to appear in Proc. 15th IAEA Conf., Vienna.

7) D. H. Kalantar *et al*,
Rev. Sci. Instrum. **68**, 802 (1997);
D. H. Kalantar *et al*,
Phys. Plasmas **4**, 1985 (1997).

8) D. G. Stearns *et al*,
J. Vac. Sci. Technol. A **9**, 2662 (1991);
T. W. Barbee, Jr. *et al*,
Appl. Opt. **32**, 4825 (1993).

9) E. Wolfrum *et al*,
submitted to Phys. Plasmas;
E. Wolfrum *et al*,
these proceedings.

EXPERIMENTAL STUDY OF SHORT-WAVELENGTH RAYLEIGH-TAYLOR MODE COUPLING

C.Meyer, L.Barringer, S.Nurruzaman, R.Taylor, O.Willi

Imperial College, London, SW7 2BZ, UK

INTRODUCTION

In the context of inertial confinement fusion (ICF), a high degree of spherical symmetry of the imploding capsule is required in order to compress sufficient deuterium-tritium fuel to high density and temperature to trigger fusion reactions. However, implosions are subject to a variety of hydrodynamic instabilities that amplify small departures from spherical symmetry. Imperfections in the target manufacture, non-uniformities present across the spatial profile of laser beam focal spots or radiation fields asymmetry created in hohlraums seed these hydrodynamic instabilities. The Rayleigh-Taylor (RT) instability [1] is considered as being the principal physical mechanism which limits the performance of fusion targets. In the classical case, the RT instability arises at the interface of two incompressible fluids of unequal density, when the heavy fluid is supported above the light fluid in a gravitational field. Small perturbations at the interface between the two fluids grow exponentially in time and lead to the formation of a nonlinear bubble-and-spike structure. In ICF, the RT instability occurs whenever the density and pressure gradients have opposite signs. That is, at the ablation front during the acceleration phase when the hot, low-density ablating plasma is pushing against and accelerating the remaining unablated material, and at the inner shell-fuel interface during the deceleration phase, when the cold, dense shell is compressing the lower density but higher pressure D-T fuel. Furthermore, the motions of the outer and inner surfaces of the shell are strongly coupled, so that amplified surface perturbations present at the ablation front feed through to provide inner surface perturbations. Mixing of material at the inner surface between the shell and fuel degrades fuel compression to values below those required to achieve high gain. But, if perturbations at the ablation front grow sufficiently then the shell will buckle or even break up, preventing ignition altogether.

Data recently obtained [2] suggest that short wavelengths, below 18µm, are fully stabilised owing to ablation and finite density gradients effects. In this experiment an intense, approximately Planckian soft x-ray source was used to accelerate ablatively the targets. This soft x-ray source production involved the use of millimetre size high-Z cylindrical cavities called hohlraums. When multiple laser beams enter the case through holes, a large fraction of the laser energy is converted into x-ray radiation. The x-rays are thermalised and confined through multiple absorption and re-emission inside the cavity, producing an highly isotropic and thermal x-ray flux. It was proven necessary to use this indirectly driven scheme to avoid laser nonuniformities, which may result in artificially accentuating instability formation which can detract from a clean and controlled study of the RT instability being made.

Much of the previous work has concentrated on the growth of single wavelength perturbations. But, in practical applications, the RT instability will evolve from random perturbations where many different wavelength modes are present. The purpose of the present experiment is to find out if and how the short wavelength modes couple to long wavelength modes. These longer wavelength disturbances may have larger growth rates and may be more damaging for shell break-up. When two perturbations with wave numbers k_2 and k_3 are initially present they couple to excite a long-wavelength perturbation and a short-wavelength perturbation with wave numbers $k_1=k_3-k_2$ and $k_5=k_3+k_2$, respectively [3]. A novel soft x-ray imaging technique with a spatial resolution of the order of one micron has recently been developed by the Imperial College team [4]. This resolution is an order of magnitude better than that obtained with the conventional soft x-ray pinhole camera assembly, which was found to be essential to resolve the shorter wavelengths and their harmonics. This technique was employed to measure the time dependent growth of the optical depths.

EXPERIMENTAL SETUP

Six 1.2ns square pulse VULCAN beams, three per side, were focused through the laser entrance holes (LEH) onto the walls of a gold cavity (see figure 1). The beams were separated from one another by a 13° angle and were incident on the horizontal plane. The hohlraum was rotated by 30° with respect to its axis to prevent beams normally incident on the hohlraum from passing through the two opposite LEH without depositing their energy in the cavity. The nominal size of the cavity was 1mm diameter, 1.3mm long, and the wall thickness was typically about 30µm. The cavity consisted of three 500µm diameter holes: two laser entrance holes (LEH) were used to inject the energy into the cavity and the other as a diagnostic hole. Polycarbonate foils were mounted across 50µm thick washers which were then stuck across the diagnostic hole on the wall of the hohlraum with foil perturbations facing inwards. The six beams delivered an overall energy of about 550J at a wavelength of 527nm in a 1.2ns pulse. The focus of each beam was located in the plane of the LEH.

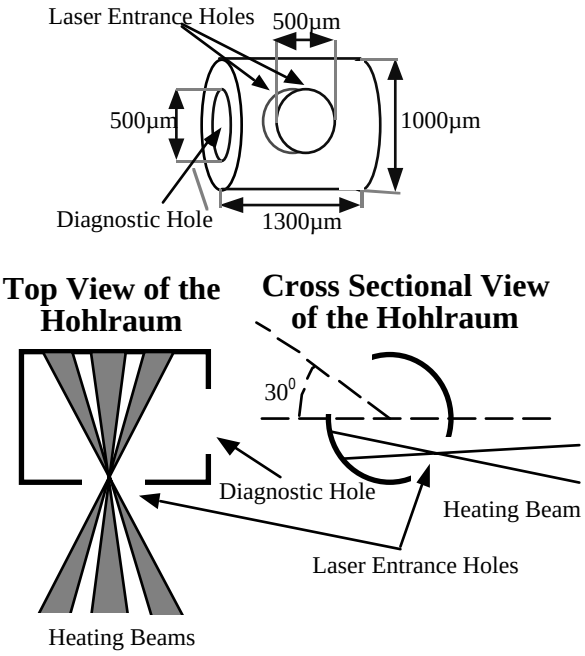

Figure 1: *Experimental geometry for the indirect drive planar RT instability experiment.*

The imaging system consisted of a spherical multi-layered mirror which reflected a narrow band (±5eV) of soft x-ray radiation at a central wavelength of 50Å (250eV). The magnification achieved with the system was about 90× (see figure 2). The imaging system was employed in a face-on, on-axis configuration and was relayed to a 2D gated microchannel plate imager, monitoring the relative transmission of the foil to the probe x-rays. Four temporally separated images were recorded on each shot with a 120ps temporal resolution.

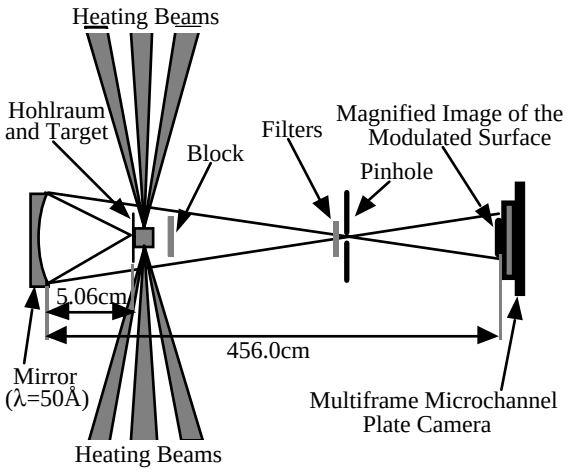

Figure 2: *Experimental arrangement of the soft x-ray imaging system.*

To measure the spatial response of the system consisting of the soft x-ray mirror and SLIX detector, a fine copper mesh (750 lines per inch), placed in the target position, was backlit with a large area spot of x-rays generated by hitting a 550µm backlighter disk with one of the VULCAN beams. The transmitted modulated signal obtained, provided a direct measure of the modulation transfer function (MTF) of the overall system (see figure 3). The MTF is well approximated by a curve of the form $1/(1+(2\pi\sigma/\lambda)^2)$ with σ=0.48. The MTF at 0.6 is found to be better than 4µm.

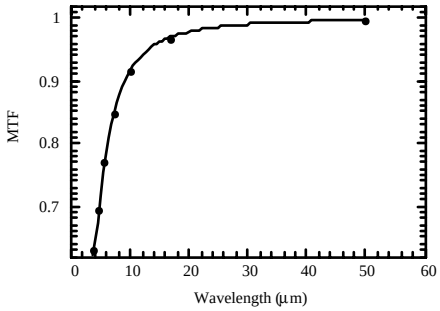

Figure 3: *The instrument MTF as a function of wavelength. The data points represent the measured MTF. The solid curve represents a best fit with the function* $1/(1+(2\pi\sigma/\lambda)^2)$*, where* σ*=0.48.*

TARGET DESCRIPTION

Indirectly driven capsules surrounding the DT fusion fuel employed in ICF consists generally of low-Z materials [5]. Low-Z materials are used because they are good absorbers and therefore lead to high transfer efficiencies. On top of this, they give excellent hydrodynamic efficiencies due to their low ionisation energies. It turns out that the atomic number *Z* has to be high enough to ensure sufficient x-ray absorption by K-shell ionisation. Planckian radiation of about 100eV temperature, value characteristic for the hohlraum targets used in this experiment, contains photons predominantly in the energy region hn=100-900eV, especially where the K-edge limit of elements *Z*=6-8 is contained. Figure 4 displays the normalised spectral energy of a 100eV blackbody compared to an approximate spectrum taken from reference [6]. It is seen that ablator materials composed of mixtures of *Z*=6-8 can be employed. Following the above discussion, polycarbonate was chosen as our target material ($C_{16}H_{14}O_3$, ρ=1.2gcm^{-3}). Mean free path (MFP) spectrum in cold polycarbonate is also displayed [7].

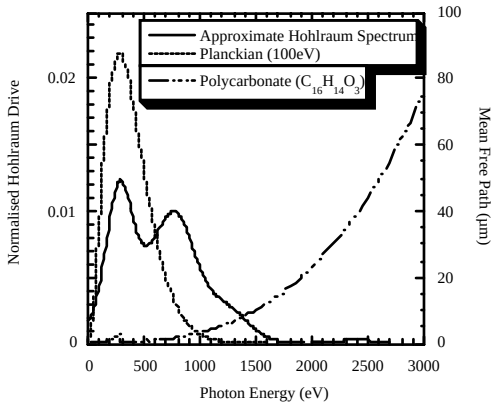

Figure 4: *The normalised spectral energy of the approximate spectrum is compared to the 100eV blackbody spectrum. The photons MFP in cold polycarbonate is plotted as well.*

This indicates that photons with energies below 800eV will deposit their energy within a few microns from the target surface, while at higher photon energies, the bulk of the target is likely to be preheated. The approximate spectrum differs from a blackbody because some x-rays generated within the cavity will escape the plasma without being absorbed, giving rise to the creation of three distinct emission bands characteristics of the gold spectrum, namely the O, N and M bands located at 275, 750 and 2400eV, respectively. The M band radiation is emitted in the laser-irradiated part of the cavity walls, and represents 1-2% of the x-ray conversion efficiency. The O band is produced in a re-emission zone while the N band is formed in a mixed region between the two regions cited above. It also appears from the plot that a substantial amount of x-ray energy is located in the energy band of 250±5eV reflected by the multi-layered mirror, and this was proven to be sufficient to probe the target through the entire interaction. A target thichness of about 15µm was used and with a cold opacity of 3785cm^{2}g^{-1} for polycarbonate, a relative probe transmission of 0.1% is obtained. This latter value drops in time as the target is progressively heated. Three types of multimode targets were investigated with the following form

$$\eta(x) = \sum_{n=1}^{m} \eta_n \cos\left(\frac{2\pi x}{\lambda_n}\right).$$

The characteristics for each type of target are indicated in table 1.

Type	Wavelength (µm)	Amplitude (µm)
1	λ_1=33.5	η_1=0.35
	λ_2=16.7	η_2=0.65
	λ_3=11.2	η_3=0.32
2	λ_2=25	η_2=0.90
	λ_3=16.7	η_3=0.61
3	λ_2=14.5	η_2=1.03
	λ_3=9.7	η_3=0.39

Table 1: *Characteristics of each type of multimode target used in the experiment.*

However, in this paper, the analysis will be confined to the last type (i.e. 3) of multimode target.

GRATING MANUFACTURE

The gratings used in the experiment were produced through the technique of optical interferometry. The interferometer was set up at the required pitch and exposure trials were conducted for each type of grating to determine the conditions that give the required depth. The glass plate coated with the photoresist was first exposed to produce a first pitch and exposed again to the second fringe pattern. After development two superimposed gratings were obtained. A small region along the edges of the gratings was exposed to only one grating in order that the depth of each component could be measured independently. To minimize Moiré patterns (due to the exposure of two close periods) and Vernier Moiré fringes of high frequencies (due to the change in space of the phase between the two gratings) care was taken to ensure good parallelism between the two exposure patterns. The last operation consisted of replicating the molds in silicone rubber. The silicon rubber substrate was a square with a 25mm side so that large quantities of modulated foils can be produced. This material was chosen because it is pretty robust and inert to solvents. The silicon rubber was cast onto the photoresist and the modulations were accurately reproduced. The manufacture of the foil was achieved by first dissolving granulated polycarbonate in di-chloro methane. The silicon rubber substrate was dipped into the dissolved polycarbonate for the casting of the foils and left next for a few minutes in the vapor of the solvent to slow down the drying process, which avoids the irreversible clouding of the foil. As a result, a clean foil of good quality was produced. Several trials were carried out to obtain the thickness desired. The thickness was measured to an accuracy better than one micron with the help of a thickness monitor. The characterisation of the initial perturbations was critical for proper interpretation of the RT growth. The multimode gratings were characterised at NPL. To measure the grating groove profiles a step height measuring machine called "Talystep" was employed. The modulated foils were characterised at the atomic weapon establishment (AWE, Reading) with the atomic force microscope technique (AFM). Figure 5 shows the multimode grating profile measured together with the curve fit (14.5µm and 9.7µm wavelengths only), where the upper side of each curve corresponds to the grating (the lower side then corresponds to the foil). In the same figure a histogram representing peak-to-valley amplitudes of the Fourier transform of the grating trace and target profile is also shown.

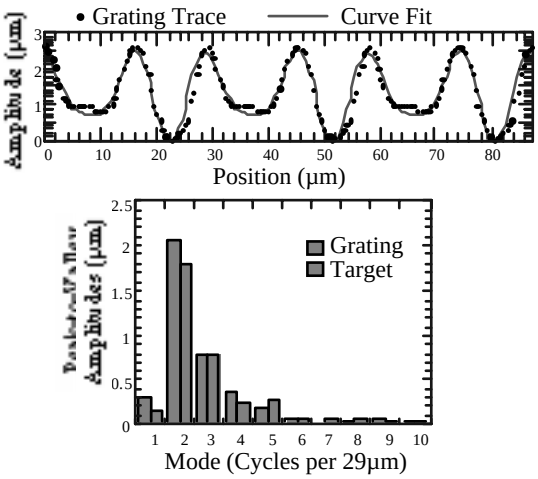

Figure 5: *Grating trace and curve fit along with the grating and target mode spectra.*

The Fourier modes are enumerated as harmonics of the longest repeating pattern (29µm). We can clearly see that the curve fit follows closely the grating trace. Ideally, we wanted to produce a grating with the two preexisting modes k_2 (λ_2=14.5µm) and k_3 (λ_3=9.7µm) only, to generate via coupling mode k_1. However, after inspection of the histogram, presence of mode k_1 and its subharmonics is evident. Note that the grating and target spectra are nearly identical.

ANALYSIS

The gated images taken in the experiment were all recorded on negative Ilford HP5 photographic film and subsequently converted to digital form with the help of a spinning drum scanner. Because of the nonlinear response curve of the film the digitised images were corrected through the use of an absolutely calibrated intensity step wedge exposed on the same piece of film. The optical density of the signal recorded on film was subsequently converted to intensity. The face-on radiographic technique is based on the fact that transverse modulations in foil optical depth *OD* generate modulations across the transmitted backlighter signal. These intensity modulations are directly related to the optical depth of the foil through the following relation:

$$I(x) = I_0 e^{-OD(x)}.$$

Here, *I(x)* is the intensity measured on film. The optical depth is defined as

$$OD(x) = \rho_{av}\kappa_{av} z(x),$$

where r_{av} represents the average mass density, k_{av} is the average opacity, and *z* is the absorbing region thickness along the line of sight, i.e., along the normal to the foil at position *x*. The optical depth lineouts were then obtained by taking the -ln(*I(x)*) since $I(x) \propto e^{-OD(x)}$. They were finally deconvolved through the use of the MTF measured experimentally. Each lineout was Fourier transformed to obtain the associated spectrum. It is critical for a proper interpretation of the data to determine the sensitivity of the detector. Small amplitudes perturbations are detectable by face-on radiography because of the combination of high material opacity (k=3785cm^{2}g^{-1}) and a signal-to-noise ratio $R_{S/N}$ of 25 for the detector. From the following equation, the minimum detectable optical depth then evaluates to 0.039

$$\Delta(OD)_{min} = \Delta(\rho\kappa z)_{min} = \ln\left(\frac{R_{S/N}+1}{R_{S/N}}\right).$$

A gated 2-D face-on radiograph taken at 1250ps is shown in figure 6.

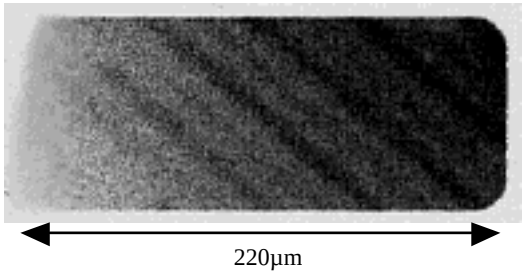

Figure 6: *Raw gated image at t=1250ps.*

The intensity lineouts displayed in figure 7 show that early in time, the foil is still opaque to the soft x-ray probe. The fluctuations are solely attributed to the quantum noise of the detector. Later in time, however, the foil becomes transparent, as a result of preheat from the x-rays generated inside the cavity. The contrast increases progressively in time and we clearly observe the intensity modulations. The histogram representing the Fourier transform of the optical depth profiles, clearly reveals the presence at 750ps of a 29µm wavelength

component inceasing in time. Furthermore, it can be seen that components up to the fifth harmonic are also present in this spectrum, which is in sharp contrast to the singlemode data obtained under the same experimental conditions, where no modulations have been observed at all below 18µm. The subharmonics of all optical depth values less than 0.039 are unphysical, since, as explained earlier, this value corresponds to the minimum detectable optical depth.

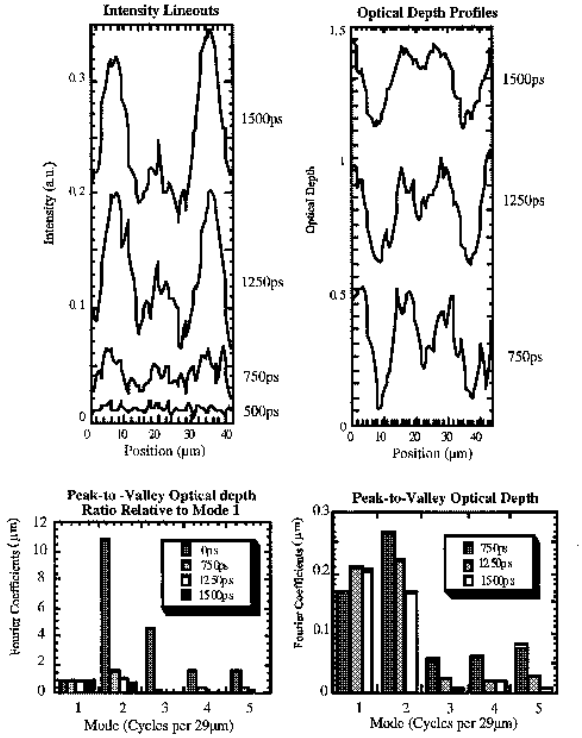

Figure 7: *Intensity lineouts and optical depth lineouts. The lineouts are artificially offset vertically from bottom to top in order of increasing time. Also shown is the histogram of the peak-to-valley optical depth along with the histogram of the peak-to-valley ratio relative to mode 1 (29µm).*

To emphasise the growth of mode 1, the peak-to-valley optical depths are also represented in terms of ratio relative to mode 1, and the associated histogram shows that the relative growth of mode 1 with respect to its harmonics is substantially higher, with for instance, a decrease by a factor of 10 in optical depth for mode 2 with respect to mode 1, 750ps after the start of the interaction.

CONCLUSION

This preliminary analysis suggests that some coupling occurred to produce the seeded 29µm component. Detailed simulations are currently carried out to investigate the degree of coupling present in the experiment as the 29µm component was also present in the original Fourier spectrum.

REFERENCES

[1] S. Chandrasekhar, *Hydrodynamicand Hydromagnetic Stability* (Oxford University Press, London, 1968), Chap 10.

[2] R. Taylor, S. Nurruzaman, C. Meyer, and O.Willi CLF, RAL, Annual Report 1995-96.

[3] S.W. Haan Phys. Fluids B 3, 2349 (1991).

[4] O. Willi *et al*., Rev. Sci. Instrum. 69, 4818 (1992).

[5] M. Murakami, J. Meyer-ter-vehn, Nuclear Fusion 7, 1315 (1991).

[6] D. R. Kania *et al*., Phys. Rev A 46, 7853 (1992).

[7] B. L. Henke, E. M. Gullikson and J. C. Davis, *Atomic Data and Nuclear Data Tables* 54, No.2 (July1993).

MEASUREMENT OF A SINGLE MODE IMPRINT IN LASER ABLATIVE DRIVE OF A THIN AL FOIL BY XUV LASER RADIOGRAPHY

E.Wolfrum[1)], D.Kalantar[2)], J.Warwick[3)], J.Lin[4)], R.Smith[4)], J.Zhang[1)], A.Demir[4)], M.H.Key[2)], C.L.S.Lewis[3)], A.MacPhee[3)], D.Neely[5)], B.A.Remington[2)], S.Rose[5)], G.J.Tallents[4)], J.Wark[1)], S.V.Weber[2)]

1) Clarendon Laboratory, University of Oxford, Oxford, UK. e-mail: e.wolfrum@rl.ac.uk
2) Lawrence Livermore National Laboratory, Livermore, California, USA
3) School of Mathematics and Physics, Queen's University of Belfast, Belfast, UK
4) Department of Physics, University of Essex, Colchester, UK
5) Central Laser Facility, Rutherford Appleton Laboratory, Chilton, Didcot, UK

INTRODUCTION

A critical factor influencing the feasibility of ignition of direct drive inertially confined thermonuclear fusion (ICF) is the seeding of Rayleigh Taylor (RT) growth of surface perturbations by imprint from laser intensity variations[1)]. Smoothing techniques are used to minimise the optical perturbations resulting in a temporally fluctuating speckle pattern of high time averaged uniformity[2)]. Large imprinted amplitudes have been recorded after RT growth for multimode speckle using radiography with either thermal x-rays or x-ray lasers as backlighter[3,4)]. Such experiments give valuable information on the root mean square (rms) amplitude and spectrum of the imprinted perturbations but are difficult to relate to theoretical modelling because of the complexity of the multimode speckle patterns. The study of imprinted modulations due to a single mode optical intensity pattern offers better insight into the physical processes of imprinting and is the subject of this paper.

The growth rate of a single mode of wavelength λ is roughly proportional to $k^{1/2}$ ($k=2\pi/\lambda$)[5)] and the saturation amplitude is expected to be $\lambda/10$[6)]. The most damaging modes are those wavelengths that can most easily cause a break up of the shell in an ICF target, i.e. $2 \le \lambda/\Delta R \le 8$[7)], with ΔR being the in-flight thickness of the shell. Longer wavelengths grow too slowly and shorter wavelength modes saturate before they grow to a large enough amplitude to affect the implosion. In current target designs modes with λ = 40-160 µm are of special interest. Here we investigate modulation growth due to single mode optical intensity perturbations with λ = 15, 30, 70 and 90 µm wavelength.

EXPERIMENTAL SETUP

The experimental setup is shown in fig. 1. Six beams of the VULCAN Nd:glass laser at 1.05 µm were used in a standard off-axis line focus geometry, where two 18 mm long, 100 µm wide Ge stripe targets were irradiated from opposite sides to form a refraction compensated lasing medium. The x-ray laser drive pulses were 75 ps long with a 10% prepulse delivered 2.2 ns before the main pulse. Under these conditions, the x-ray laser beam was saturated with an output energy of ~ 0.9 mJ. It had a divergence of about 30 mrad along the x-ray laser target surface, and 6.6 mrad normal to the surface[8)].

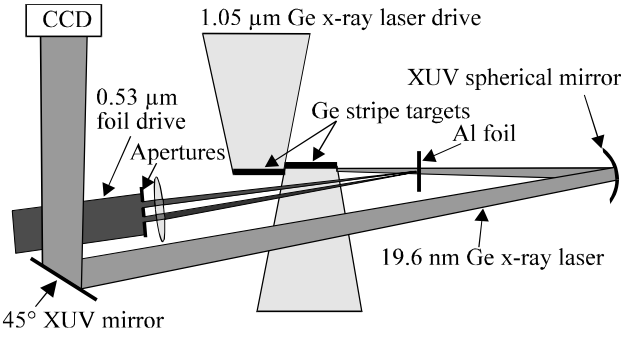

Fig.1: Experimental setup

We used Al foil targets since Al has the lowest opacity for the Ne-like Ge x-ray laser wavelength of 19.6 nm. The Al is still highly attenuating, which limits the experiment to thin foils. It also means, however, that the technique is sensitive to small modulations in the thickness of the foil. At 19.6 nm, the cold absorption coefficient for Al is 2.24 μm^{-1} [9)]. With this high an opacity, a thickness variation of only 50 nm results in a 10% change in signal intensity.

A 2 µm thick Al foil was placed about 3 cm away from the output aperture of the Ge x-ray laser. We then used two multilayer mirrors to image the Al foil in the x-ray laser wavelength onto an XUV sensitive charge coupled device (CCD). A spherical mirror with a 1 m radius of curvature was placed 53 cm from the Al foil, providing a 17.5X magnified image of the foil on the CCD (5 µm resolution) at near normal incidence (<0.6°) to minimise spherical aberrations. The CCD was filtered with an additional 0.8 µm Al foil to reduce thermal emission from the foil, and a 45° angle of incidence planar mirror was used to relay the image onto the CCD and spectrally isolate the image from the thermal background noise.

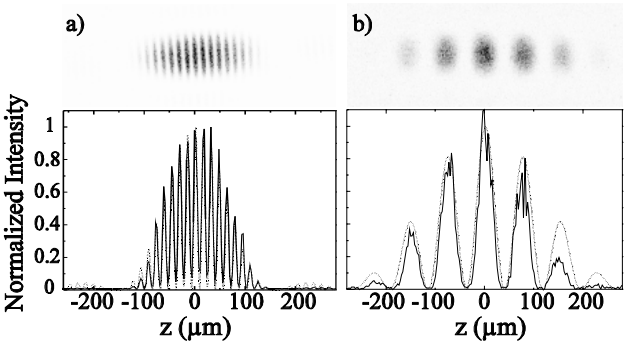

Fig.2: Intensity patterns for a) 15µm and b) 70 µm single modes recorded on film together with horizontal lineouts through the centre. The dotted lines represent the calculated intensity distributions.

The single mode interference patterns were generated in the focal plane of a lens by double rectangular slit apertures. The two selected uniphase wavefront elements interfere to create single mode perturbations of 15, 30, 70 and 90 µm periodicity. The fringe pattern is created under an Airy function envelope, determined by the dimensions of the rectangles. The 2 µm thick Aluminium foils were irradiated with a frequency doubled beam of the VULCAN laser (λ = 527 nm) at irradiances 0.5 - $1.5 \cdot 10^{13}$ W/cm^2. The incident angle was 16º. The trapezoidal pulse with a risetime of typically 0.1 ns had a FWHM of 1 ns. An equivalent plane monitor (EPM) was used to record the imprinted intensity pattern. The EPM consisted of a 10 m focal length lens that focused the selected wavefront elements onto calibrated film with a magnification of 8.25x. Figs. 2a and 2b show the calculated patterns and the EPM recorded intensity patterns for both 15 micron and 70 micron modes. Horizontal lineouts through the centre of the patterns are compared with the calculated prediction and show excellent agreement.

As the internal jitter of the timing between the XRL drive beams and the Al foil drive beam could exceed 0.2 ns, we recorded them simultaneously with an optical streak camera for every shot. In our convention t = 0 denotes the time when the imprint drive beam has risen to 50% of its maximum.

MODELLING

Extensive studies[10] have addressed ablation front RT instability growth in planar laser ablative acceleration of thin foils, essentially establishing RT growth rates which agree with numerical modelling. The numerical modelling has led to a widely accepted dispersion relation for direct drive that includes the ablative stabilisation effect which is the so called Takabe formula[5], $\gamma = 0.9(ka)^{-0.5} - 3kv_a$, where γ is the growth rate, k is the wave number of the perturbation, a is the acceleration and v_a is the velocity across the ablation front. We use the Takabe relationship to estimate RT growth factors in the present work by obtaining values for the acceleration and ablation velocity from one-dimensional numerical modelling of the ablative drive process. Estimates of the shock transit time during which the imprinting occurs prior to acceleration and RT growth were also obtained from the simulations. The 1D Lagrangian code MED103 was used to determine an average value for acceleration, a, and the average flow velocity across the ablation front, v_a, during the main drive phase.

For the long wavelength perturbations, i.e. small k, additional considerations are appropriate. Following Taylor's original paper[11] for the case of a liquid sheet of finite thickness D we consider a perturbation with wavenumber k growing exponentially in time so that the initial elevations of the disturbances above their mean levels are of the form

$\eta_U = \alpha \cos kx$ at the upper surface

$\eta_L = 0$ at the lower surface.

i.e. an initial amplitude perturbation is present on the upper surface (corresponding to the initially imprinted modulation in our case) then the elevations of the upper and lower surfaces become (as given by Taylor):

$$\eta_U = \alpha\left\{\frac{\cosh \gamma t - e^{-2kD}\cos \gamma t}{1-e^{-2kD}}\right\}\cos kx$$

$$\eta_L = \alpha\left\{\frac{\cosh \gamma t - \cos \gamma t}{1-e^{-2kD}}\right\}e^{-kD}\cos kx\ .$$

If k is small, the upper and lower surface perturbations simplify to

$$\eta_U = \alpha\left(1+\frac{1}{2D}at^2\right)\cos kx$$

$$\eta_L = \alpha\frac{1}{2D}at^2\cos kx$$

Hence the amplitude at both the upper and lower surface perturbations are each increased by the amount $1/(2D)\ at^2\ \alpha$ cos(kx), i.e. equal perturbations on the upper and lower surfaces cancel to give no growth. These long wavelength approximations are valid for $\lambda > 20$ D, which is in our case $\lambda >$ 40 µm. Using the output of MED103 the amplitudes of both surfaces are estimated to be still well within the linear regime of RT growth.

RESULTS AND DISCUSSION

Radiographs were recorded at different times during the drive phase. Figures 3a and b show 15 µm mode radiographs together with their horizontal lineouts taken at t=0.04 ns and t=0.35 ns. The irradiance for these shots averaged over the sinusoidal pattern at the FWHM of the Airy pattern was 7 10^{12} W/cm^2.

The first image (fig. 3a) is taken in the very early stage of imprint, i.e. where a shock wave is just launched into the target. Nevertheless, the increase in density causes a clearly visible change in the mass absorption coefficient, appearing as dark area in the radiograph. The amplitudes of the areal density perturbations are still close to the noise level of the measurement.

The response of the shocked target visible in the radiographs is comprised of a change in opacity due to the compression of the target and areal density perturbations driven by the single mode. While both effects are convolved in the 70/90 µm mode case, the envelope in the 15 µm mode pattern produces a region of shocked material that can be compared to unshocked regions, thus allowing us to quantify the change in opacity of the shock compressed Al foil.

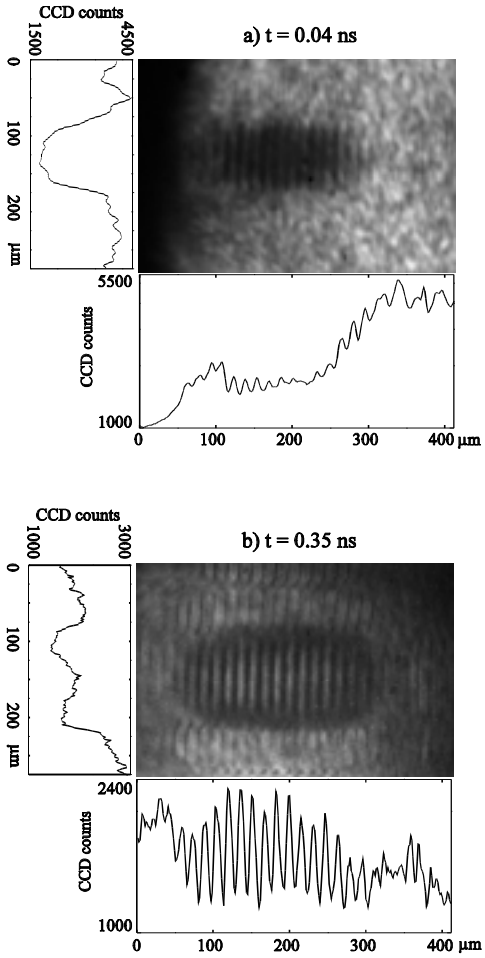

Fig. 3: Typical radiographs of 15 µm single mode imprint at a) t=0.04 ns (before shock breakout) and b) t=0.35 ns (after shock breakout together with horizontal and vertical lineouts.

The second image (fig 3b) taken at a time t=0.35 ns, i.e. 0.15 ns after shock breakout, exhibits significant perturbation amplitudes due to RT growth. The average mass absorption coefficient in the shocked region is still slightly increased compared to the undriven regions of the Al foil.

The change in opacity $\Delta\tau_c$, with $\tau_c = \kappa\rho d$, κ the mass absorption coefficient, ρ the density and d the thickness, was evaluated by $\Delta\tau_c = \ln(I/\langle I\rangle)$, where I is a linear fit to the radiograph intensities for uncompressed areas and $\langle I\rangle$ the average intensity in the centre of the shocked area. Assuming that the average areal mass density ρd stays constant, i.e. $\rho d = \rho_0 d_0$, with ρ_0 the cold density and d_0 the initial thickness of the

foil, the changed opacity $\tau_c+\Delta\tau_c = (\kappa+\Delta\kappa)\rho d$, yields a corrected mass absorption coefficient, $\kappa' = \kappa+\Delta\kappa$. This was used in the evaluation of the single mode amplitudes in order to empirically remove the opacity effect.

The rms areal density amplitudes $\Delta(\rho d)$ of the single modes have been derived from the minima and maxima of the fringe pattern in the radiographs, I_{min}, I_{max}:

$$(\rho d)_{\max} - (\rho d)_{\min} = \ln\left(\frac{I_{\min}}{I_{\max}}\right) * \frac{1}{\kappa'} = 2.86\Delta(\rho d)$$

where the factor 2.86 stems from conversion of maximum amplitude to rms for a sinusoidal curve.

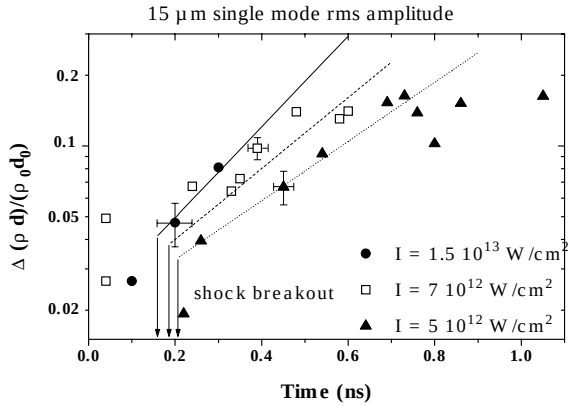

Fig.4: Relative 15 µm single mode rms amplitudes for different irradiances. A saturation effect can be observed for t > 0.8 ns. The lines are the calculated growth curves using the Takabe formula.

Fig. 4 shows the relative amplitudes $\Delta(\rho d)/(\rho_0 d_0)$ for 15 µm modes versus time for different irradiances. The solid and dashed lines are exponential growth curves $\Delta(\rho d)/(\rho_0 d_0)$ (t) = $\Delta(\rho d)_{ini}/(\rho_0 d_0)$ *exp[γ*(t-t_{sb})], with γ the growth rate and t_{sb} the shock breakout time. The values for initial imprint, i.e. imprinted modulation at shock breakout time, $\Delta(\rho d)_{ini}$, have been derived from a fit of the growth curves to the relevant experimental data. For irradiances of 5 10^{12} W/cm^2, 7 10^{12} W/cm^2 and 1.5 10^{13} W/cm^2 the values for initial imprint $\Delta(\rho d)_{ini}/(\rho_0 d_0)$ are 0.034, 0.039 and 0.041 rms, respectively. Errors for these values are < 10%. For irradiances below 7 10^{12} W/cm^2 there is some evidence of saturation for $\Delta(\rho d)/(\rho_0 d_0)$ = 0.15 rms.

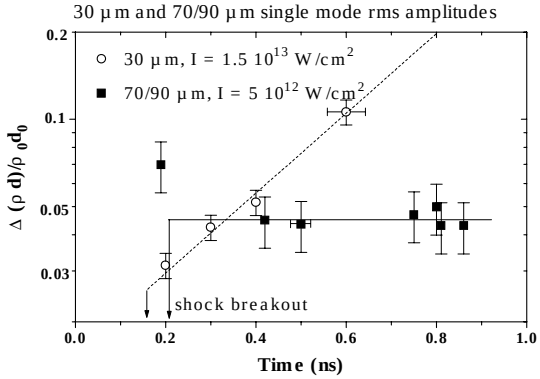

Fig. 5:Relative rms amplitudes for 30 µm and 70/90 µm single modes for I=1.5 10^{13} W/cm^2 and I = 5 10^{12} W/cm^2, respectively. The dashed line is the calculated growth curve using the Takabe formula, the solid line indicates no growth as expected for λ > 40 µm.

Fig. 5 shows the relative amplitudes $\Delta(\rho d)/(\rho_0 d_0)$ for 30 µm modes and 70/90 µm modes versus time for I = 1.5 10^{13} W/cm^2 and I = 5 10^{12} W/cm^2, respectively. The dashed line is the calculated growth curve for λ = 30 µm using the values given in Tab.1. For the 30 µm mode the fit through the data yields an initial imprint $\Delta(\rho d)_{ini}/(\rho_0 d_0)$ = 0.026. As described earlier the long wavelength approximations may be applied for wavelengths > 40 µm, yielding equal perturbations on the upper and lower surfaces, which cancel, to give no growth. The expected growth of the 70 and 90 µm mode perturbations thus being 1, both data sets have been combined, and a value for initial imprint $\Delta(\rho d)_{ini}/(\rho_0 d_0)$ = 0.045 can be derived from the data. Although the measured data have been corrected for the change in opacity due to shock compression as described earlier, underestimation of the increase in opacity during shock transit is a likely cause for the rather high data point at ~0.2 ns.

SUMMARY AND CONCLUSIONS

Initial imprint due to single mode direct laser drive has been determined for 15, 30, 70 and 90 µm modes at various intensities, ranging from 5 10^{12} W/cm^2 to 1.5 10^{13} W/cm^2. In those cases, where the Takabe formula could be fitted, values for initial imprint, i.e. modulation in the Al foil at shock breakout time, could be derived with high accuracy (error < 10%). The 15 µm mode causes relative initial imprint $\Delta(\rho d)_{ini}/(\rho_0 d_0)$ of 0.034, 0.039 and 0.041 rms for irradiances of 5 10^{12} W/cm^2, 7 10^{12} W/cm^2 and 1.5 10^{13} W/cm^2, respectively. In case of the 70/90 µm modes, long wavelength approximations apply, giving no growth, which can be seen in the measurements. Relative initial imprint has been determined to be 0.045 for an irradiance of 5 10^{12} W/cm^2.

ACKNOWLEDGEMENTS

We gratefully acknowledge the support from VULCAN Laser and Target area staff as well as the skilful fabrication of the targets by the RAL target preparation group. We would also like to thank Dr. D.Youngs of AWE, Aldermaston, for very helpful discussions. This work was partially supported by grants from the Engineering and Physical Sciences Research Council and under the auspices of the U.S. Department of Energy by the Lawrence Livermore National Laboratory under Contract No. W-7405-ENG-48.

REFERENCES

1) J.Nuckolls, L.Wood, A.Thiessen, and G.Zimmerman. Nature 239, 139 (1972)
2) M.H.Emery, J.H.Gardner, R.H.Lehmberg, and S.P.Obenschain. Phys.Fluids B3, 2640 (1991)
3) M.Desselberger, T.Afshar-rad, F.Khattak, S.Viana, and O.Willi, Phys.Rev.Lett. 68, 1539 (1992)
4) D.H. Kalantar, M.H. Key, L.B. DaSilva, S.G. Glendinning, J.P. Knauer, B.A. Remington, F. Weber and S.V. Weber. Phys. Rev. Lett. 76, 3574 (1996)
5) H. Takabe, K. Mima, L. Montierth and R.L. Morse. Phys.Fluids 28, 3676 (1985)
6) D.H.Sharp. Physica 12D, 1 (1984)
7) M.H.Emery, J.H.Gardner and J.P.Boris. Appl.Phys.Lett. 41, 808 (1982)
8) J.Zhang, P.J.Warwick, E.Wolfrum, M.H.Key, C.Danson, A.Demir, S.Healy, D.H.Kalantar, N.S.Kim, C.L.S.Lewis, J.Lin, A.G.MacPhee, D.Neely, J.Nilsen, G.J.Pert, R.Smith, G.J.Tallents, and J.S.Wark. Phys.Rev. A54, R4653 (1996)
9) B.L.Henke, P.Lee, T.J.Tanaka, R.L.Shimabukuro and B.F. Fujikawa. At. Data Nucl. Data Tables 27, 1 (1982)
10) J.D.Kilkenny, S.G.Glendinning, S.W.Haan, B.A.Hammel, J.D.Lindl, D.Munro, B.A. Remington, S.V.Weber, J.P.Knauer, and C.P.Verdon. Phys.Plasmas 1, 1379 (1994)
11) Sir G.Taylor, F.R.S., Proc.Roy.Soc. A201, 192 (1950)

X-RAY SCATTERING FROM A RADIATIVELY HEATED PLASMA

N C Woolsey [1] , D Riley [1] , and E Nardi [2]

1) School of Mathematics and Physics, Queens University of Belfast, Belfast BT7 1NN, E-mail n.woolsey@qub.ac.uk
2) Department of Particle Physics, Weizmann Institute of Science, Il-76100 Rehovot, Israel

We describe the first experimental results of kilo-volt x-ray scattering from a plasma[1]. We show x-ray scattering is potentially a powerful diagnostic tool. The technique is particularly useful when applied to strongly coupled plasmas, i.e. if the strong coupling plasma $\Gamma>1$, and $\Gamma=(ze)^2/(ak_BT)$ where Z is the effective charge, e is the electronic charge, a is the ion-sphere radius, k_B is Boltzmann's constant and T is the temperature. Collective effects due to ion-ion coupling lead to an angle dependent increase in the scattering cross-section. The extreme case is a crystalline solid where collective effects lead to diffraction phenomenon. The theoretical basis of x-ray scattering from a plasma has been described[2] and shows that scattering cross-sections are sensitive to the Coulomb coupling between the plasma particles and the two-particle radial distribution function.

The total x-ray scattering cross-section is determined by measuring the number of x rays scattered out of a collimated x-ray probe as it propagates through a plasma. A spectrometer records the number of photons incident on the plasma, N_{ph}, and a CCD counts the number of scattered photons, N_s, as a function of angle. The ratio of these two measurements, accounting for the number of ions in the plasma, N_a, the solid angle subtended by the CCD, ½, attenuation of the probe in the plasma and CCD filtering and detection efficiency, D, yields the total cross-section $I(\theta)$. I.e. $N_s(\theta)=I(\theta)N_{ph}N_aD½$.

The experimental geometry is shown in Fig. 1. Seven beams of VULCAN were used. The six beam cluster with f/10 lenses operating at 532 nm with a 1 ns laser pulse duration were focused on to a Au x-ray conversion foil with 0.75 mm focal spot RPP plates. The 1000 Å thick Au conversion foil was supported by a 0.5 µm thick CH film. Laser light striking the Au foil at an irradiance of ~10^{14} W/cm^2 is up-converted to soft x-rays[3], x rays emitted from the rear, unirradiated surface heat a 5 µm thick Al foil placed 7 mm away. The seventh laser beam was delayed 0.5 ns to the cluster and tightly focused (<100 µm diameter) using f/5 optics onto a 6 µm thick Ti foil placed 20 mm from the Al foil. Temperatures are sufficient to created a He-like plasma[4] and the 1-2 resonance line radiation (Heα, the $1s^2$-$1s2p\ ^1P_1$ transition centred at 4.749 keV[5]) is used to backlight the Al plasma. Line emission from the Ti plasma closely follows the laser temporal pulse shape[4]. In addition, the angle of incidence of the laser on the backlighting foil was less than 15° to suppress resonance absorption. Heα radiation from the unirradiated surface of the Ti foil is collimated using two pinholes to form a 5° divergent x-ray probe. The pinholes are concentric and 0.4, and 0.8 mm in diameter placed at 4 and 7.9 mm from the Ti foil respectively. Accurate, reproducible positioning of the target components was ensured by alignment with microscopes, the target assembly was kinematically located in the target chamber. Background radiation was limited by placing the target assembly in a mylar-lined aluminum box, holes are cut into the box to allow laser and diagnostic access.

Incident laser energy, the backlighter focal spot were monitored on each shot. The number of Heα photons created were measured using a Si(111) spectrometer couple to a cooled 16-bit CCD. Scattered radiation was recorded at 41.5±3.5° and 48.5±3.5° to the probe beam direction with an Oriel IntaSpec IV, single stage, cooled CCD operated at -10 °C. The CCD was tailored for kilo-volt sensitivity and consisted of a front illuminated, deep depletion CCD, area of 27.64 by 6.9 mm, with 1024 by 256 pixels and 16 bit resolution. The CCD detection efficiency, QE, at 4.749 keV is approximately 85%[6].

The CCD was filtered with 250 µm of Be, 200 µm of mylar and 16 µm of Al resulting in a considerable reduction in background signal, with, approximately 5 % of the scattered photons being detected. The number of Heα photons interacting

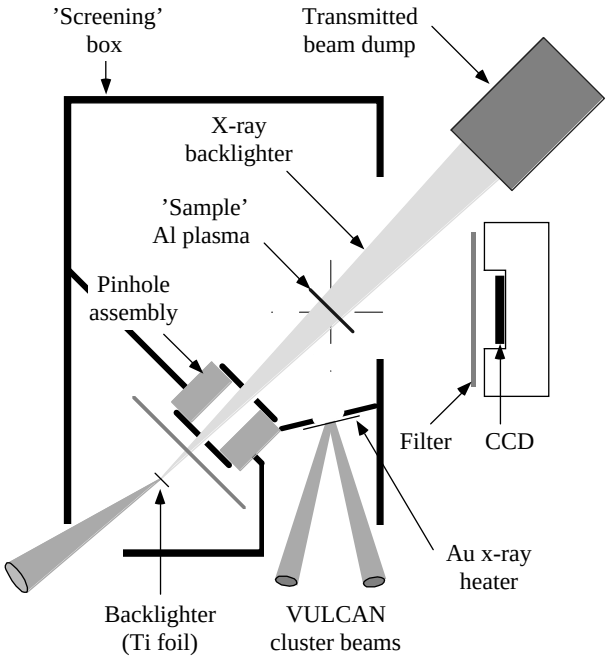

Fig. 1 Schematic of the experimental setup

with the CCD was small (typically 200). Photons incident on the CCD were spectrally resolved by histogramming the CCD records and recognising a single electron-hole pair is created with each 3.65 eV deposited in the detector[7], the CCD sensitivity was 10 electron-hole pairs resulting in an energy resolution of 36.5 eV. Histograms taken between 41.5±3.5° and 48.5±3.5° are shown in Figs. 2a and b, (also in Figs. 3a and b, 4a and b) respectively. In these figures the abscissa is the photon energy (equivalently number of counts), between 0 and 6 keV, corrected for dark current noise; and the ordinate is the number of pixels containing that number of counts.

Figure 2 shows data taken when the backlighting laser beam only was fired, these histograms show the scattered spectrum from a cold Al foil. The peaks at 4.8 keV are identified as the scattered Ti Heα signal and are superimposed on a background spectrum. The background spectrum results from scattered soft x rays, and recombination radiation emitted as the backlighter is absorbed in the scattering foil. When the foil thickness was reduced the level of background intensity is also reduced. Background is removed by fitting a low order polynomial to the spectrum either side of the scattered peak and interpolating under the peak. The interpolated fit is subtracted from the spectrum, and the area under the peak represents the number of scattered photons. The number of photons in the peak, N_s, and the peak full-width-half-maximum (FWHM) are shown in columns 2 and 3 of Table 1. Note the peak FWHM is larger than the FWHM measured at 0 keV, in addition the FWHM appears to be greater at higher scattering angles. The width at zero counts represents the natural broadening of the CCD.

In Fig. 3 the lasers striking the Au conversion foil only were fired, indicating the contribution from the heating Au x-ray source, and from the Al plasma to the scattered data. These are typical spectra due to absorption and scattering of heating x rays from the Au conversion foil. The spectra are characterised by a large signal around 0 keV and broad peak between 3 and 4 keV. The broad peak results from scattering of Au M-band,

the filter response results in the apparent peak centred at ~3.5 keV, a similar feature is seen in Fig. 4.

In Fig. 4 spectra from a radiatively heated Al foil probed with a Ti Heα backlighting radiation source are shown. The peaks at 4.8 keV (c.f. Figs. 2) are the scattered Ti Heα photons, the scattered Ti Heα signal sits on background spectra due to recombination radiation generated in the Al foil and scatter of Au conversion foil radiation. The sources of background noise and the scattered signal are identified by analysing each set of results. The complete target was assembled for each experiment.

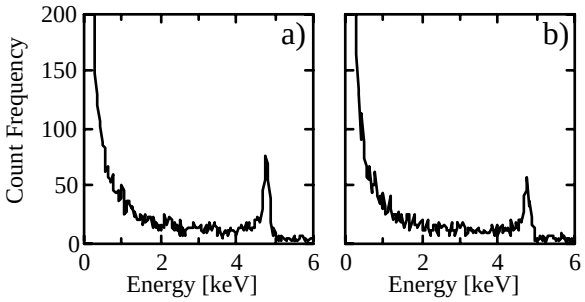

Fig. 2 Scattered backlighter spectra from a cold 5 µm thick Al foil.

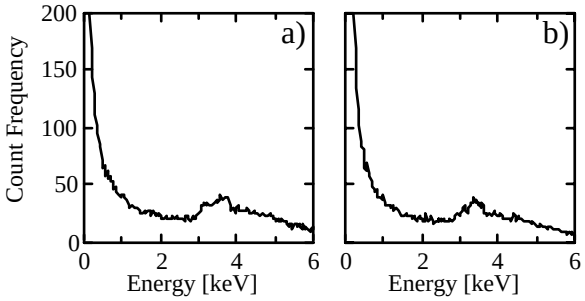

Fig. 3 Background spectra Peak centred at 3.5 keV due to Au M-band.

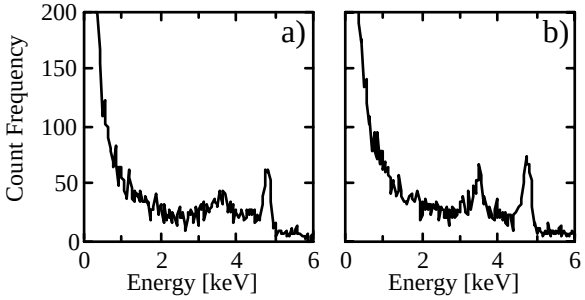

Fig. 4 Scattered data from radiatively heated Al foil.

The calculation of the total scattering cross-sections for 4.8 keV x rays at 42±3.5° and 48±3.5° are shown in Table 1. With current experimental accuracy the cross-sections in the cold and heated foil can not be distingushed. For example, the number of photons detected gives a statistical uncertainty of about 6 %, experimental uncertainties contribute a further random error of 10 % and possible systematic errors (including spectrometer accuracy) approaching 25 % are present. Calculations[1,8] of scattering from a cold Al gas with 4.8 keV x rays at 45° result in total x-ray scattering cross-sections of 5.4×10^{-23} cm^2 in agreement with measured values.

The scattered peaks have a finite FWHM which result from the natural broadening of the CCD and the spectral width of the backlighting source. The backlighter consists of 2 He-like lines; the resonance line $1s^2$-$1s2p\ ^1P_1$ at 4.749 keV and the inter-combination line $1s^2$-$1s2p\ ^3P_1$ at 4.727 keV[5], and a series of Li-like dielectronic satellites centred at 4.700 keV[9].

At present these measurements are qualitative, but demonstrate the scattering technique. For example, the Al foil is 5 µm thick, too thick to heat uniformly; using the Au conversion foil data[3] and cold opacity tables[10] we estimate 7 eV/atom is deposited at the foil centre. In this estimate the results of Ref. 3 were scaled to laser parameters used here and a dilution factor due to experimental geometry was included[11]. We conclude a significant fraction of the heated foil was in a plasma state.

	Fig. 2 (cold Al)		Fig. 4 (plasma)	
	38-45°	45-52°	38-45°	45-52°
'Zero' FWHM (eV)	111	114	110	112
Ti Hea FWHM (eV)	143	186	147	171
N_s	332	309	331	252
N_{ph}	1.60×10^{11}		1.87×10^{11}	
N_s	9.45×10^{17}		9.45×10^{17}	
½ (str)	0.0079		0.0079	
Filter transmission	0.0572		0.0572	
CCD sensitivity	0.85		0.85	
I(θ) ($\times 10^{-24}$ cm^2)	5.7	5.2	4.9	3.7

Table 1.

Improvements in the cross-section measurements are being investigated by considering; 1) reducing the Al foil thickness from 5 to 1 µm, 2) reducing backlighter duration from 1 to 0.1 ns, 3) reducing the background radiation by suppressing the Au M-band, 4) increasing the backlighter energy, 5) redesign of CCD housing and target components, and 6) improving target alignment accuracy.

In summary kilo-volt x-ray scattering as a dense plasma diagnostic is demonstrated. Total x-ray cross-sections from a cold Al foil and the radiatively heated foil were measured using a Ti Heα radiation source at ~45° and within experimental accuracy agree with calculation. These were single laser-shot measurements from a radiatively heated plasma recorded with a temporal resolution of ~1 ns. The total x-ray cross-sections are small and measurement requires an ultra-bright x-ray source such as a high temperature plasma and CCD based photon counting methods. The background radiation levels limited the accuracy of these experiments, methods of reducing the background levels are being implemented and show experimental accuracy can be improved and will enable the measurement of strong coupling effects in the future. Future work will be directed at the measurement of cross sections from strongly coupled plasmas created by radiative heating and shock compressed foils, and will be directed at improving the accuarcy of the experiments.

We thank the staff of the CLF for their assistance during the experiments, and Dr. A. G. MacPhee for discussions on CCD's. This work is funded by EPSRC grant number GR/K95543.

1) N C Woolsey, D Riley and E Nardi
In preparation (1997)
2) E Nardi
Phys rev A 43 1997 (1991)
3) C A Back et al
J Quant Spectro Radiat Trans 51 (1994)
4) D W Phillion and C J Hailey
Phy Rev A 34 4886 (1986)
5) J H Scofield
LLNL UCID-16848 (1975)
6) A G MacPhee and C L S Lewis
Eds D Eder, D Matthews, AIP Proc 332, Williamsburg (1994)
7) G W Fraser et al
Nucl Instr and Meth A 350 368 (1994)
8) R W James
The Optical Principles of the Diffraction of X-rays, Bell and Sons, London (1948)
9) R L Kelly
J Phys and Chem Ref Data 16 (1987)
10) B Henke, E M Gullikson and J C Davis
Atomic and Nuclear Data Table 54 181 (1993)
11) R W Lee and J T Larsen
J Quant Spectro Radiat Trans (1996)

COMPARISON OF SIMULATED NE-LIKE AND F-LIKE GE RESONANCE LINE SPECTRA WITH EXPERIMENTAL RESULTS

A. Demir[1)], G.J. Tallents[1)], A. Behjat[1)], J. Warwick[2)], C.L.S. Lewis[2)], G.J. Pert[3)], J. Zhang[4)], E. Wolfrum[5)], P. Nickles[6)]

1) Department of Physics, University of Essex, Colchester, CO4-3SQ, UK
2) Department of Pure and Applied Physics, The Queen's University of Belfast, Belfast, BT7 1NN, UK
3) Department of Physics, University of York, York, YO1 5DD, UK
4) Clarendon Laboratory, Department of Physics, University of Oxford, OX1 3PU, UK
5) Central Laser Facility, Rutherford Appleton Laboratory, Chilton, Didcot, Oxon, OX11 OQX, UK
6) Max-Born Institut, Rudower Chaussee 6, 12489 Berlin, Germany

INTRODUCTION

Reducing the pumping energy is one of the main challenges of x-ray laser research. To reduce the required driving energy for collisional x-ray lasers, pre-pulse and multi-pulse techniques have been applied[1-4)]. Hydrodynamic simulation[5)] and experiments[6)] show that using a short pulse superimposed on a long pre-pulse reduces the driving energy and increases the lasing output of collisional x-ray lasers. A low intensity long pulse produces Ne-like ions and then a high intensity short pulse creates population inversion. In this report, experimental results of resonance line emission with a short laser pulse (~6 ps) superimposed on a long pulse (600 ps) pumping Ne-like Ge undertaken with travelling wave irradiation at the Rutherford Appleton Laboratory is presented. The Ne-like and F-like Ge resonance line emissions have been modelled using an hydrodynamic code EHYBRID[7)]. Additional coding to calculate the emitted Ne-like and F-like spectral line intensities has been written to enable the calculation of artificial spectra. The artificial spectra for the resonance line emission of Ne-like and F-like Ge are here compared to experimental emission.

EXPERIMENTAL METHOD AND RESULTS

The experiment was undertaken in the Target Area West experimental room of the Vulcan laser at Rutherford Appleton Laboratory. To perform the experiment, two beams of the Vulcan laser were focused to 100 μm width in a 10 mm long line. One of the beams had a pulse length ~ 600 ps. The other beam was chirped pulse amplified (CPA) with a pulse length on target ~8 ps. Both beams of long and short pulses were focused onto the Ge stripe targets. The long pulse intensity was ~$5x10^{12}$ W/cm^2. The short pulse intensity ~$6x10^{14}$ W/cm^2.

The long pulse beam was focused using a cylindrical refracting lens and an off axis spherical mirror focusing system. The CPA short pulse beam was focussed using an off-axis parabolic and an off axis spherical mirror system.

To diagnose the Ge x-ray laser media transversely, a KAP (2d = 26.632 Å) curved crystal spectrometer was placed with a space resolving slit of 200 μm width 15 cm away from the target surface. The 200 μm slit enabled spatial resolution along the line focus with a 0.6 magnification. To protect the CCD detector from visible light, a 25 μm Be filter was used in front of the CCD. Figure 1 shows an example of the time-and space integrated Ne-like and F-like resonance line spectrum with filter transmission and reflectivity effects considered.

MODELLING

Figure 2 shows the space- integrated emissivity of Ne-like and F-like Ge resonance lines between 7 and 10.2 Å wavelength range at 606 ps of the laser irradiance. The emissivities were calculated by multiplying the spontaneous emission rates by the excited level densities and integrating over every cell. In the calculation 123 Ne-like and 133 F-like resonance lines were considered. The original EHYBRID code was modified to calculate the spontaneous emission rates from the EHYBRID tabulated absorption oscillator strengths.

Resonance lines are often optically thick, since they have strong oscillator strengths. Therefore it is necessary to take into account opacity for the resonance line intensity calculations. An escape factor approximation has been developed by Demir et al[8)]. The emissivity of the resonance lines has been multiplied by the escape factor. In the calculation, the Doppler decoupling effect has been considered by only integrating the absorption coefficient over the Doppler decoupling length[9)] in the calculation of the relevant optical depth. Figure 3 shows the time-integrated theoretical Ne-like and F-like Ge resonance spectrum. The spectrum is dominated by the Ne-like resonance lines as observed experimentally (see figure 1) with only small

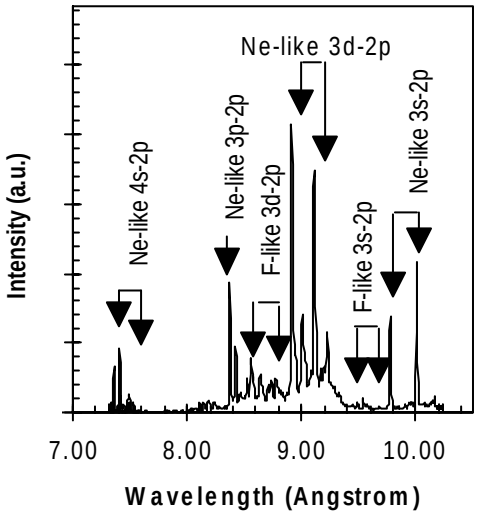

Figure 1 A typical Ge keV spectrum recorded by a curved KAP (2d = 26.6 Å) spectrometer. Filter transmission and crystal reflectivity effects have been taken into account.

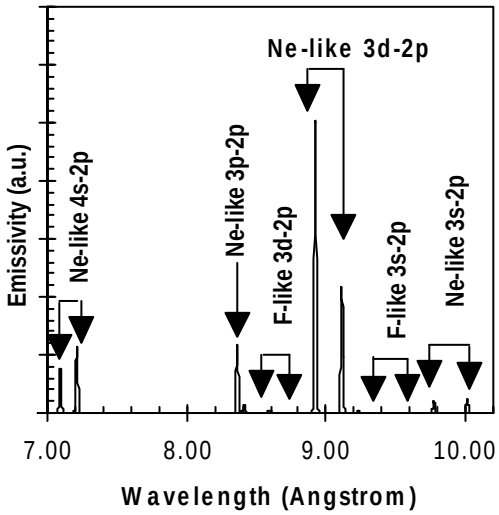

Figure 2 The space-integrated emissivity of the Ne-like and F-like resonance lines between 7 and 11 Å calculated at time 606 ps
(6 ps after the start of the short laser pulse).

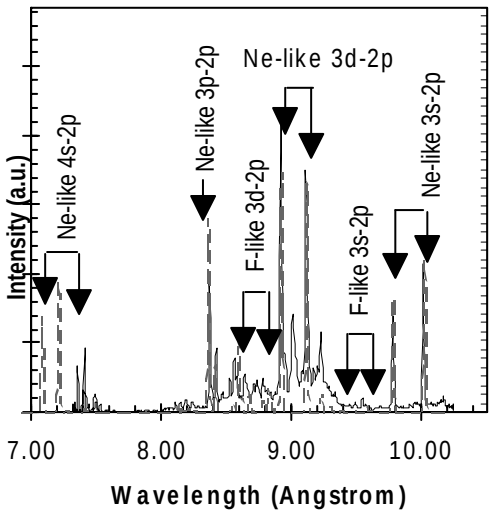

Figure 3 The time-integrated Ne-like and F-like Ge resonance line spectrum. Here the solid curve shows the experimental spectrum and the dashed curve shows the theoretical spectrum.

F-like emission. The theoretical calculations are fitted to the experimental spectrum. If opacity is not considered, the Ne-like resonance lines are much more intense (for example the Ne-like 3d-2p line is 19x stronger) and it would probably be impossible to see the F-like lines with a typical experimental spectrometer dynamic range (~100).

Figure 4 shows the Ne-like and F-like resonance lines intensities as a function of time. There is almost no resonance line emission from the 600 ps long pulse. The resonance line emissions effectively starts after the main 6 ps pulse. The F-like emissions peaks ~20 ps later than the Ne-like emissions and drops rapidly. Most of the emission occurs at ~620 after the onset (~603 ps) and peak (~606 ps) of the x-ray laser gain at 196 Å.

Figure 5 shows the ratio of the F-like 3s-2p to Ne-like 3s-2p and the ratio of the F-like 3d-2p to Ne-like 3d-2p line groups as a function of time. The peak ratio for the F-like 3s-2p to Ne-like 3s-2p line ratio is ~0.08. The peak ratio for the F-like 3d-2p to Ne-like 3d-2p is ~0.32. The peak for both of the line ratios is around 620 ps. Several authors[10] have shown that space- and

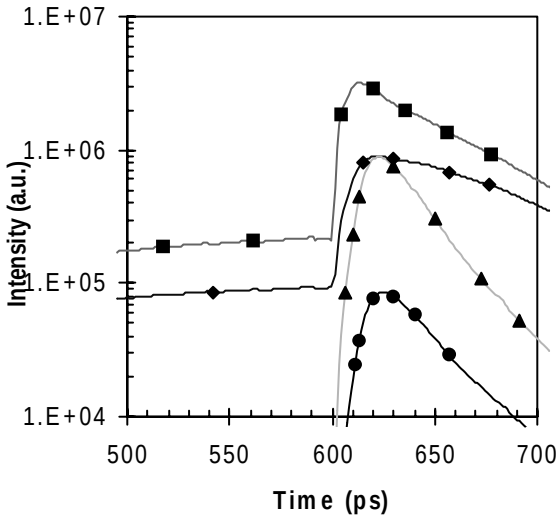

Figure 4 The Ne-like and F-like resonance line intensities as a function of time. ◆ Ne-like 3s-2p, ■ Ne-like 3d-2p, ▲ F-like 3d-2p, ● F-like 3s-2p.

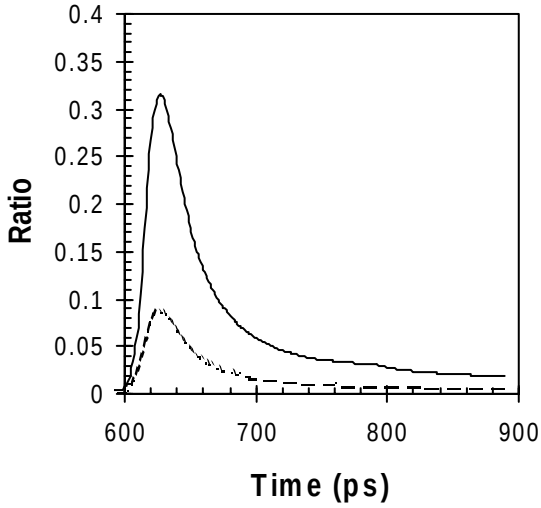

Figure 5 The ratio of the space-integrated F-like 3s-2p to Ne-like 3s-2p and the F-like 3d-2p and Ne-like 3d-2p line groups as a function time. The solid curve shows the ratio of the F-like 3d-2p to Ne-like 3d-2p line intensities and the dashed curve represents the ratio of the F-like 3s-2p to the Ne-like 3s-2p line intensities.

time-averaged F-like 3s-2p to Ne-like 3s-2p ratios of $^{3}0.1$ are needed to observe gain. With the long and short pulse pumping configuration it is apparent (Fig. 5) that this ratio can be less. For the condition of the simulation of figure 5, a peak gain of 55 cm^{-1} is predicted for the 196 Å lasing line.

CONCLUSION

A Ne-like Ge x-ray laser experiment performed with (~6 ps) short pulse and (600 ps) long pulse has been analysed. The Ne-like Ge x-ray laser media was modelled using the EHYBRID code. Artificial spectra have been calculated and found to be in good agreement with the experimentally measured emission.

REFERENCES

1) Zhang et al
Phys. Rev. A, 54 (6) R4653, (1996)

2) Behjat et al
Optics Commun.,135, 49, (1997)

3) G.F.Cairns et al
Optics Commun.123 777, (1996)

4) Tallents et al
Proceedings of the 5th Int. Conf. on X-ray lasers, eds. S. Svanberg and C-G Wahlstrom 151 372, (1996)

5) Healy et al
Optics Commu., 132 442, (1996)

6) Nickles et al
Phys. Rev. Lett., 78 (14) 2748, (1997)

7) Nickles et al
SPIE Proceedings 2520 373,. (1995)

8) Pert
Fluid Mech. 131 401, (1983)

9) Demir et al
Phys. Rev. E, 55, 1827, (1997)

10) Rybicki and D.G. Hummer,
Astrophys. J. 219 654, (1978)

11) Al-Hadidithi
Ph.D thesis (1994) (University of Essex).

PRELIMINARY STUDIES OF PLASMA DENSITY DIP GENERATION FOR X-RAY LASER WAVEGUIDING

A.G. MacPhee[1], C.L.S. Lewis[1], J.Y. Lin[2], G.J. Pert[3], P.A. Simms[3], G.J. Tallents[2], P.J. Warwick[1], E. Wolfrum[4], J. Zhang[4]

1) School of Mathematics and Physics, Queen's University of Belfast, Belfast, BT7 1NN
2) Department of Physics, University of Essex, Colchester, CO4 3SQ
3) Department of Physics, University of York, York, YO1 5DD
4) Department of Physics, University of Oxford, Oxford, OX1 3PU

INTRODUCTION

Optically pumped X-ray lasers are generated with the greatest efficiency when a pre-pulse is used compared to schemes where a target at room temperature is directly heated with a single pulse to provide lasing action in a single step[1]. The low temperature 'pre-plasma' produced in this way absorbs the subsequent pump energy more strongly and generates reduced density gradients transverse to the target surface. Refraction of the X-ray laser beam out of the gain region is reduced, which when optimized maximises the useful length of the available gain volume. Our recent efforts have been directed at extending this technique to provide a method of controlling X-ray laser refraction parallel to the target surface. The technique depends on the generation of a plasma density dip along the length of the pre-formed plasma through which the X-ray laser beam is constrained to propagate.

DENSITY DIP GENERATION

Modelling shows that using a combination of appropriately tailored pump pulses, a plasma density dip can be formed with dimensions suitable for X-ray laser wave-guiding[2]. Using the pump pulse configuration described in figure 1, the germanium density dip described in figure 2[3] was generated using the 2D fluid code POLLUX[3,4]. The first pulse loosely focused to a 200μm wide line pre-formed the plasma, whilst the second pulse focused to a 15μm wide line promoted the density dip. To verify that the scheme was capable of producing a useful output, the density structure produced in this way was post-processed for atomic detail using the hydro-atomic code EHYBRID[3,5] and the results of this further post-processed for X-ray laser propagation and gain with a full 3D ray-trace of the system[3]. The density dip had an approximately linear gradient of ~5×10^{22} cm^{-3}/cm through the symmetry axis as shown in figure 2, with plasma temperature in the region 900-1200 eV. This is typical of the conditions found in the gain region of a pre-pulsed germanium X-ray laser. From the contour plots, a similar gradient is observed parallel to the target surface through the central ~3×10^{20} cm^{-3} contour. This gradient provides the refractive effect suitable for guiding the X-ray laser beam in the vertical direction.

The density dip produced in this way evolves and decays over a period of the order ~100 ps, whilst the time for which conditions are suitable for wave-guiding with gain is only a few 10s of ps. This compares well with the ~40ps pulse duration of the Ge^{23+} *J*=0-1 196Å X-ray laser, based on the conventional 100 ps pulse scheme with a 10% pre-pulse arriving 2 ns early.

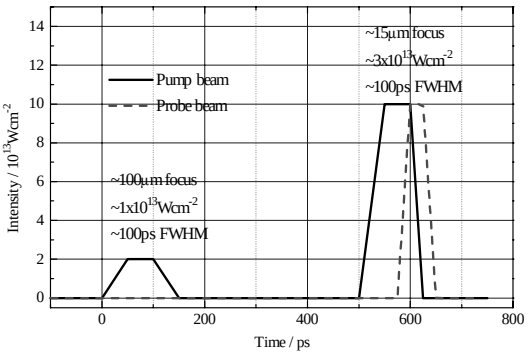

Figure 1 Pumping scheme for density dip generation.

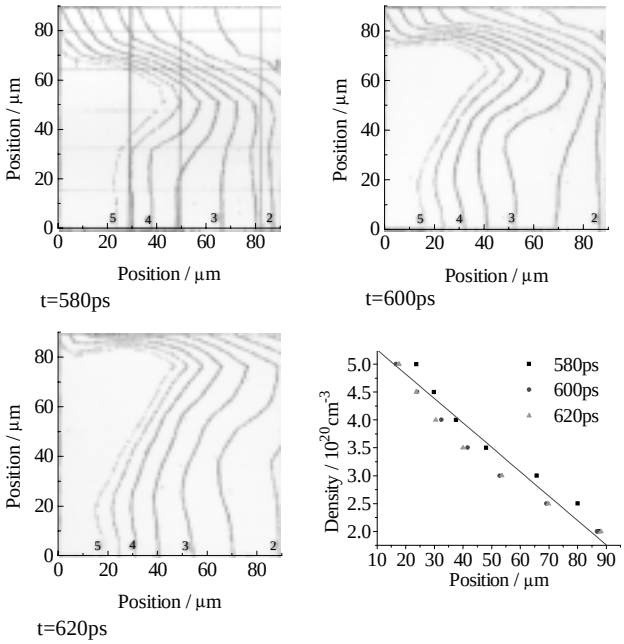

Figure 2 Electron density contours during dip evolution and horizontal line-outs through symmetry axis (position=0 μm).

EXPERIMENTAL DETAILS

To observe evidence of a channel in the plasma suitable for allowing X-ray laser propagation and guiding, a 3mm long density dip plasma was generated using the above pump characteristics. The plasma was back-lit with the Ge X-ray laser beam as shown in figure 3. The X-ray laser beam was timed to arrive at the entrance of the density dip at the time corresponding to t=580 ps in figure 1 (dashed line).

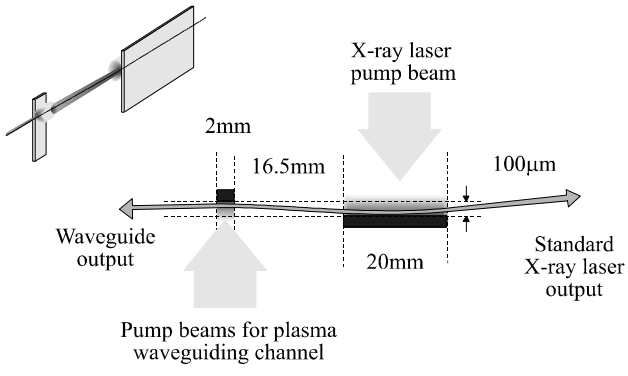

Figure 3 Schematic diagram of density dip back-lighting set-up.

~2 μm resolution was required in the object plane to over-sample the structure expected from the detailed modelling by a factor of ~2.5. This was achieved using a 25 cm focal length, 196 Å X-ray mirror with 22× magnification. ≤2 μm resolution was confirmed by measuring the average distance over which the transmission changed from 10%-90% across a binary object. The image was recorded when the object was back illuminated with the 196 Å X-ray laser as shown in figure 4.

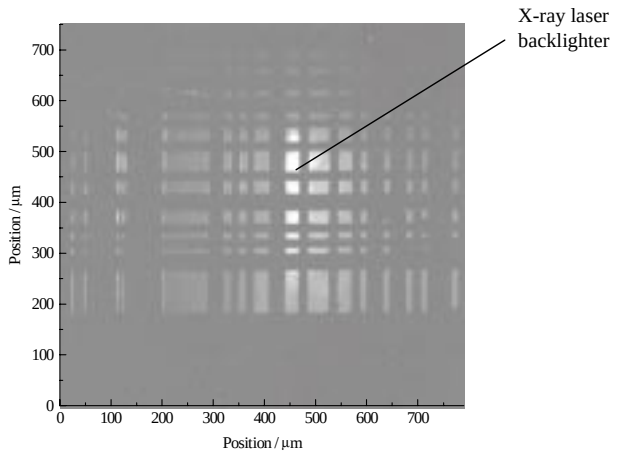

Figure 4 XUV image of gold test chart.

RESULTS

Figures 5-7 illustrate that a localised source of intense radiation was produced in the region of the proposed density dip, when back-lit with the X-ray laser during the period 580 ps-620 ps after the start of the pre-pulse. In figure 5, both the broad focus beam and the narrow focus beam forming the density dip

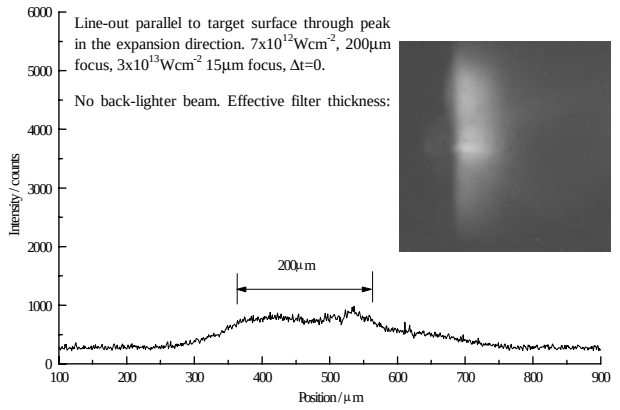

Figure 5 No delay, no back-lighter.

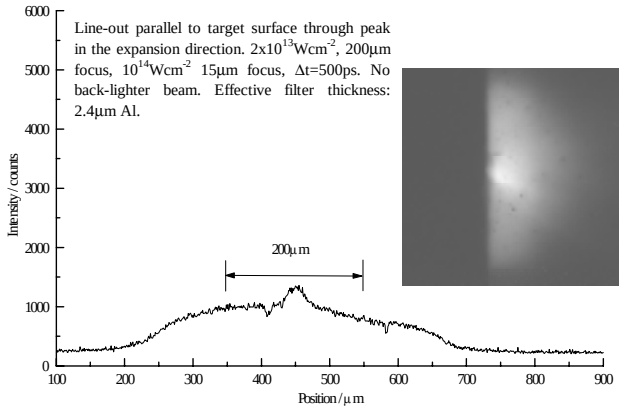

Figure 6 500ps Delay, no back-lighter.

arrived simultaneously, with no X-ray laser back-lighter. In figure 6, a 500 ps delay was introduced to the narrow focus beam. In figure 7, the X-ray laser back-lighter was introduced at 580 ps-620 ps after the pre-pulse. In this case, a channel of intense radiation was observed ~50μm from the target surface.

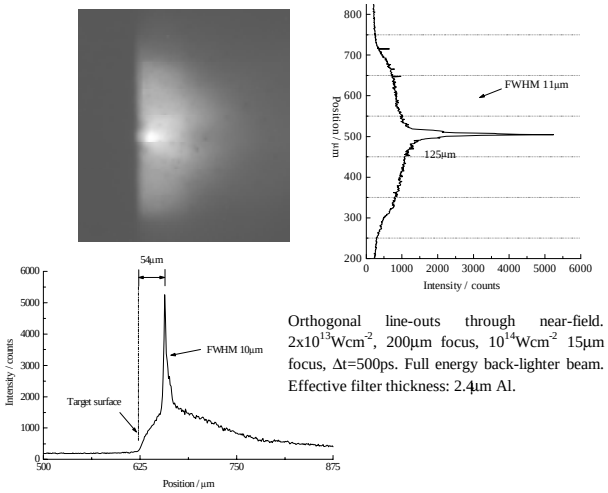

Orthogonal line-outs through near-field. 2x10^{13}Wcm^{-2}, 200μm focus, 10^{14}Wcm^{-2} 15μm focus, Δt=500ps. Full energy back-lighter beam. Effective filter thickness: 2.4μm Al.

Figure 7 500 ps Delay, with back-lighter.

CONCLUSION

Figures 5 and 6 illustrate that the intrinsic emission of the density dip target is not sufficient to produce a source of radiation equivalent to that observed in figure 7, where the back-lighting X-ray laser has been introduced. The narrow channel of intense radiation in figure 7 is approximately a factor of 2 brighter than the brightest back-lighting beam shot on its own under these conditions. This indicates that the density dip plasma column may also have exhibited gain, with a gain of the order 2-3 cm^{-1}, although the shot to shot variation in the back-lighter intensity may also have accounted for this.

A full length ~2-4 cm X-ray laser working under these conditions is expected to exhibit significantly increased brightness compared to the non-guided scheme through enhanced spatial coherence in the output beam. The present results make a good case for a full systematic study of the density dip plasma, to establish the practical merits of the system as an X-ray laser scheme and to attempt to optimise its performance. This will include pico-second optical and/or X-ray interferometry to measure the 2D electron density distribution in a sequence of time steps as the density dip evolves and measurements of the output efficiency of full length X-ray laser targets.

REFERENCES

1) See for example A G MacPhee et al, 'Improving the efficiency of collisionally excited X-ray lasers using multiple 100ps pulses'
Inst Phys Conf Ser No 151: Section 7, 250 (1996)

2) G J Pert et al, 'Effects of density structures and pulse temporal shaping'
Inst Phys Conf Ser No 151: Section 7, 260 (1996)

3) G J Pert, P A Simms
Private Communication, Department of Physics, University of York, York Y01 5DD

4) G J Pert, 'Fluid codes'
Proc 20th SUSSP, Laser-plasma interactions', ed R A Cairns, J J Sanderson, p323, St Andrews, (1979)

5) P B Holden et al, 'A computational investigation of the Ne-like Ge collissionally pumped laser
J Phys B, 27 341 (1994)

SATURATED TRANSIENT GAIN X-RAY LASER EXPERIMENT AT VULCAN CPA LASER

P.V. Nickles[1], M. Schnürer[1], M.P. Kalachnikov[1], W.Sandner[1], V.N. Shlyaptsev[2], C. Danson[3], D. Neely[3], E. Wolfrum[3], J. Zhang[3], A.Behjat[4], A. Demir[4] , G. Tallents[4] , J. Warwick[5] and C. Lewis[5]

[1] Max-Born-Institut, Rudower Chaussee 6, D-12489 Berlin, Germany
Tel.: 0049-30-63921310, Fax: 0049-30-63921329, e-mail: kalashni@mbi.fta-berlin.de
[2] Colorado State University, Fort Collins, Colorado 80523, USA
[3] Rutherford Appleton Laboratory, Chilton, Didcot, Oxfordshire OX11 0QX, U.K.
[4] University of Essex, Colchester, CO43SQ, U.K.
[5] Queens University Belfast, Belfast, U.K.

INTRODUCTION

Recently a collisionally excited transient gain X-ray laser in Ne-like Ti with a gain value of 19 cm^{-1} on the 3p-3s 32.6 nm line at a drastically reduced pump level of only a few Joules was demonstrated by the MBI group[1)]. The new two pulse scheme, which was proposed theoretically some years ago[2,3)], comprises the creation of a neon like plasma of the desired target atoms by a ns pulse followed by short (ps) pulse heating of the preformed plasma to produce a population inversion on the Ne-like ions. Due to the ps pulse excitation, a transient inversion occurs[2-6)], which is related to the different population rates of the levels via collisions and not determined by the slower relaxation rates of the excited levels relevant in the quasi-steady state (QSS) regime. It was shown, that transient inversion is characterised by a short life time and favourably yields much higher small signal gain values (10-100 cm^{-1}) as obtained in the QSS regime (several cm^{-1}) with long pulse pumping. However, as a result of the restricted experimental conditions at the MBI last year, neither gain saturation nor significant shifting to shorter wavelengths could be demonstrated.

Therefore, a joint experiment was carried out based on the high energy resources of the Vulcan CPA laser and the well proven RAL diagnostics to investigate some key parameters of this new transient excitation scheme for Ne-like ions. The aims were: 1. getting saturation in a Ti X-ray laser and 2. demonstrating the practicality of scaling the scheme to higher Z materials, in order to reduce the XRL wavelength. Based on theoretical modelling [Pert)], Ge was selected as the best candidate.

In this joint work, the amplification characteristics of the 3p-3s (J=0-1) transition at λ= 32.6 nm and the 3d-3p (J=1-1) transition at λ= 30 nm were studied with plasma column lengths up to 10 mm. Also, the dependence of the X-ray lasing signal on the optical laser pump energy was measured, the X-ray beam divergence was determined and the total output energy of the X-ray laser pulse was estimated. For the first time saturation of the low pump energy X-ray laser utilising transient gain on the 3p-3s transition in Ne-like Ti at 32.6 nm and Ge at 19.6 nm was demonstrated. In the following, a brief description of the experimental conditions as well the presentation of the results and their discussion are given.

EXPERIMENTAL SET-UP

The experiments were carried out with the Vulcan Nd:glass laser using a CPA-laser beam[7)] of up to 40 J laser energy (E_L) with a pulsewidth of several ps (2-3 ps at low E_L and 6-8 ps at high E_L) together with a second synchronised ns-laser beam. The short pulse was timed at the falling edge of the long 1 ns pulse which had a flat top temporal shape. The line foci of the two pulses with a length of 10 mm and a width of 100 µm were superposed on the target. Due to the irradiation geometry of the short pulse, a travelling focus with a phase velocity of about two times the speed of light was always established in one direction (to the spectrometer set-up). Figure 1 shows the schematics of the experiment.

Titanium and Germanium stripes on glass, with a thickness between 0.6 and 1.0 µm and a width of about 200-300 µm as well as massive slab targets were used. The amplification length was varied by changing the target length. The targets were centred in the line focus. The primary diagnostic along the target axis was a common flat-field grazing incidence XUV-spectrometer with a 1200 line/mm aperiodically ruled grating. Focusing, perpendicular to the dispersion direction was provided by a cylindrical mirror. The time integrated spectrum was recorded with a back-thinned cooled 16 bit CCD-camera. At higher X-ray laser signals Al- filters were used in front of the spectrometer to prevent saturation of the X-ray CCD camera. The corresponding absorption values were taken into account to

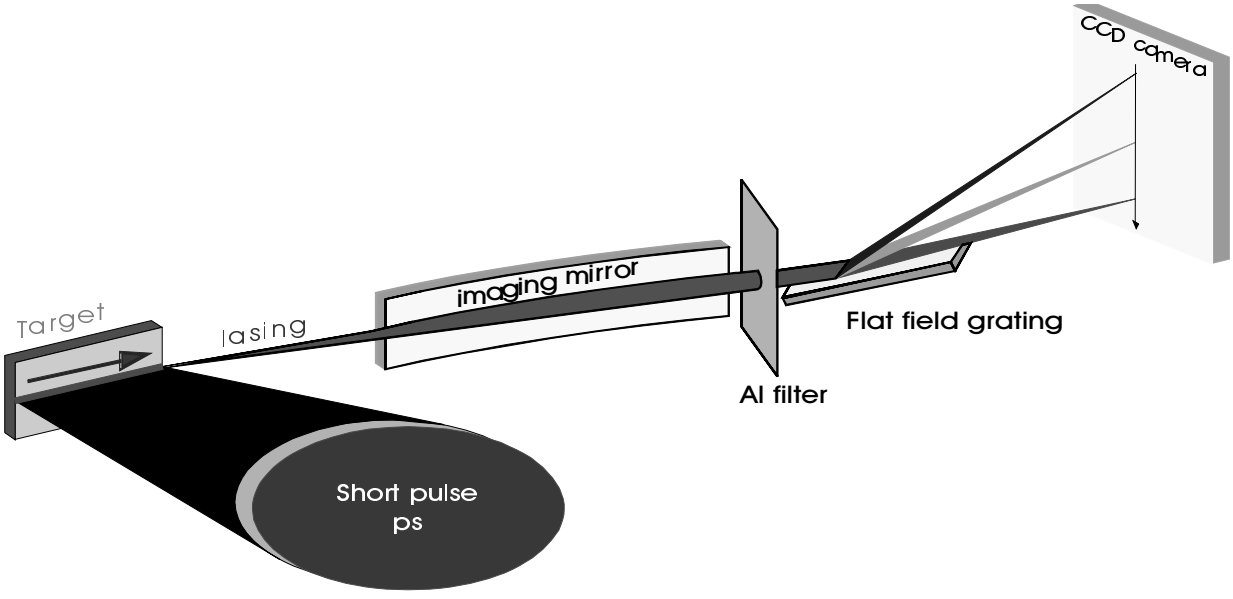

Figure 1 Schematic diagram showing the experimental set-up for the transient X-ray laser investigation.

estimate the lasing signal intensity.

RESULTS AND DISCUSSION

In figure 2 the XUV-signals at λ=32.6 nm and λ=30.1 nm are shown as a function of the length of the Ti-plasma column. For the plot we have taken the integrated line signals above the recorded plasma background emission near the wings of the two lasing lines. This amplification series was carried out at a pump energy level in the long pulse of 20 J ($1.4*10^{12}$ W/cm^2) and in the short pulse of 18 J ($2.2*10^{14}$ W/cm^2). As visible from the obtained data, the lasing signals can be fitted (Linford et al.[7]) with a gain g=35 cm^{-1} up to target lengths L= 4 mm. The corresponding gl is about 14. With further increases in target length, the rate of increase of the output signals reduces. This is an experimental sign that the X-ray laser is saturating rather than a result of x-ray beam refraction out of the gain region. Our RADEX calculation for the 3p-3s titanium line have revealed that saturation should take place at a gl ~15[1], which provides good confirmation that our assertion about saturated output is correct. Simultaneously, a second strong signal at about 30 nm was recorded which is determined to be the 3d-3p line. This lasing signal was already observed in previous experiments[1] but no amplification measurement could be made. In X-ray laser experiments using the QSS regime this line was not observed in Ne-like Ti but only in Ne-like Ar[9]. Now, for the first time, a gain value of g=15 cm^{-1} was determined for this line. However, as visible from figure 2, the 3d-3p line does not show such a pronounced saturation like behaviour within the data fluctuations up to a target length of 10 mm, even if the modelling predicts saturation too. Probably the amplification of this line is more sensitive to the excitation inhomogenities in the plasma and additional data is required to resolve to situation.

Due to the special irradiation geometry of the short pump pulse, the corresponding focus had a intrinsic velocity along the plasma column with a phase velocity of about two times the speed of light in the direction of the spectrometer. Additionally, we also tested an extra travelling excitation for the ps-pulse with a speed of the running focus matched to the speed of light by inserting a grating in the CPA beam line. Within the data fluctuation no systematic difference could be found in the output lasing signals. Therefore, all of the data set is included in fig.2.

In another series of experiments we determined the minimum pump energy necessary for lasing in titanium at 32.6 nm as depicted in fig.3. As visible, pump energies as low as E_{long} = 1 J for the long 1 ns pulse and E_{short} = 1.5 J for the short 3 ps pulse yield strong amplified emission. The target length was 3 mm. The corresponding pump intensities are I_L= $7*10^{10}$ W/cm^2 in the long pulse and I_L= $5*10^{13}$ W/cm^2 in the short pulse. So, we conclusively verified that X-ray lasing in the Ne-like Ti system is possible with table top class pump lasers. With E_{short} = 5 J which corresponds to $I_p \approx 10^{14}$ W/cm^2 one achieves already maximum XRL signal output in that pumping geometry. Also, an increase in the long pulse intensity up to an factor of more than 10 did not give a higher output signal. Using the short or the long pulse alone definitely no lasing was visible with the maximum energies in this experiment.

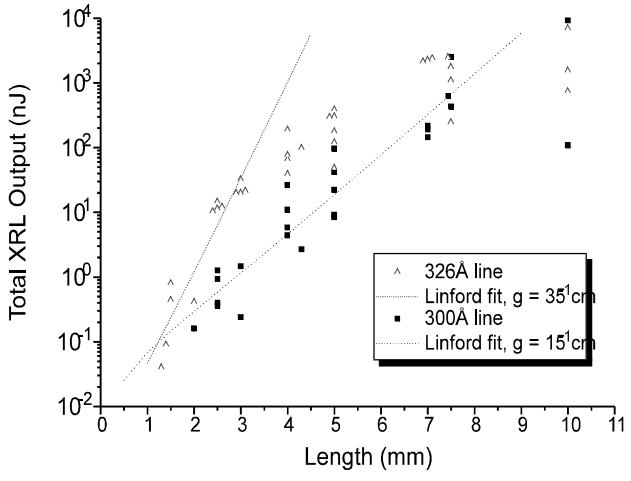

Figure 2 Saturated Ti XRL Peak output signals at 32.6 nm and 30 nm (crosses only) as a function of target length with pump intensities of $1x10^{12}$ Wcm^{-2} in the long and $2x10^{14}$ Wcm^{-2} in the short pulse.

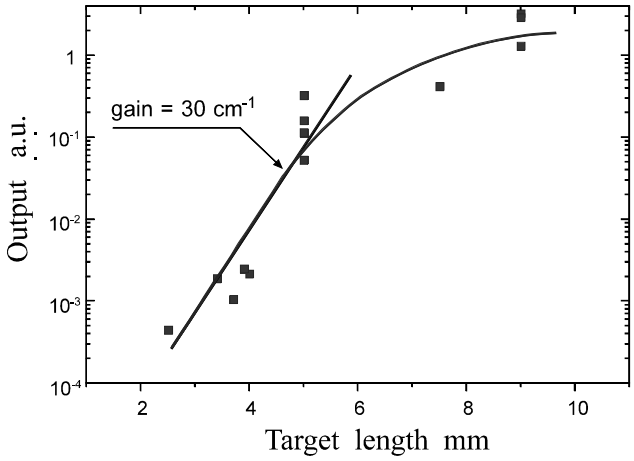

Figure 3 Saturated Ge XRL at 19.6 nm. Peak output signals versus target lengths.

The applicability of the efficient transient excitation scheme for higher Z-material to reach shorter wavelengths lasing was convincingly demonstrated for neon like Ge. Due to the large energy range delivered by the Vulcan CPA-beam it was possible to investigate the amplification behaviour of this Ge XRL also for target length up to 10 mm. The recorded lasing signal for the 3p-3s transition at 19.6 nm is displayed in fig. 4, showing both a high small signal gain value of about 30 cm^{-1} for targets with ≤ 5 mm, and a clear evidence of a saturation-like behaviour for ≥ 6 mm correspondingly. It is worth mentioning that strong lasing signals have been recorded with only 10 J pump energy in the short CPA beam as well in the long pulse beam.

Divergence measurements of the Ti X-ray laser beam at 32.6 nm from 9 mm long Ti-stripe targets have yields 2 to 3 mrad if the long pulse was 600 ps. For a 1 ns long pump pulse the divergence was 6 to 8 mrad. This suggests the longer pulse duration creates a more extended region of the inversion in the plasma column.

From our experimental results we also tried to get more confidence in the wavelength determination of the 3d-3p (J= 1-1) lasing transition in Ti at 30 nm. Theoretical calculations[1,6,13] cover the wavelength range between 29.1 and 30.0 nm. From our first transient inversion Ti experiments [1] with the MBI CPA-Glass laser we estimated (restricted by the limited spectral resolution of the equipment) a wavelength at about 30 nm. Now, taking 32.65 nm for the 3p-3s line, 19.6 nm for the 3p-3s lasing line in Ge and 17.065 nm for the Al-L absorption edge (visible in first and second order in the spectra) which we recorded without changing the set-up, we estimate with a quadratic fit concerning the dispersion characteristic in that region a wavelength for the 3d-3p line of (30.15±0.05) nm.

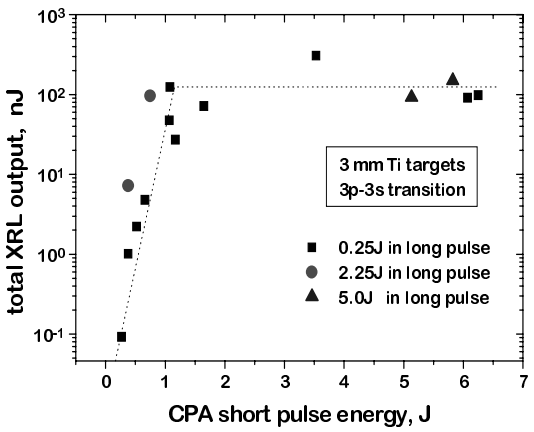

Figure 4 Peak output signals at 32.6 nm of 3 mm targets versus pump energy in the short pulse at fixed pump energies in the long pulse.

The time integrated spectrally resolved CCD-signals can be used to obtain the total output pulse energy of the XRL. Up to a final absolute calibration of the X-ray spectrometer- CCD camera set-up at least a rough estimation is possible. For the Ti XRL output energy values of about 40 μJ in both lines at 32.6 nm and 30.15 nm correspondingly for the highest signals are estimated per single X-ray laser pulse. This corresponds to an energy efficiency of about 10^{-5}, one of the highest ever reached for an soft X-ray laser.

CONCLUSION

Summarising we can state, that as a result of the excellent optical parameters and the operational reliability of the pump laser, the complex diagnostic and the technical support, accessible at the RAL during the campaign the results have surpassed our aims. It was shown for the first time that the new transient gain excitation scheme can be brought into saturation on the 3p-3s line in Ti at 32.6 nm (and very high gain for the 3p-3s line at) as well as on the 3p-3s line in Ge at 19.6 nm with only several Joules of pump energy required. This is 1- 2 orders of magnitude in pump energy reduction as compared to common quasistationary XRL systems. Additionally, the XRL divergence was determined to be about 5-10 mrad. The output energy in the range of several tens of uJ corresponds to a very high Ti XRL efficiency of ~10^{-5}. Finally, it is worth mentioning that the new efficient XRL excitation is not only restricted to neon like schemes but should be also attractive for nickel like as well innershell transitions opening a route to short wavelength low sized X-ray laser. Therefore, related experiments will be a matter of future experiments.

This work was supported by the European Union Large Scale Facility Programme. The authors gratefully acknowledge the support of laser operation, and engineering support groups of the Central Laser Facility of the RAL.

REFERENCES

1) P.V. Nickles, V.N. Shlyaptsev, M.P. Kalachnikov, M. Schnürer, I. Will, W. Sandner SPIE 2520, (1995) 373; P.V. Nickles, V.N. Shlyaptsev, M.P. Kalachnikov, M. Schnürer, I. Will, W. Sandner, PRL 78, (1997) 2748; P.V. Nickles, V.N. Shlyaptsev, M. Schnürer, M. Kalachnikov, T. Schlegel, W. Sandner. Optics Commun., in press

2) Y.V. Afanasiev, V.N. Shlyaptsev. Sov. J. Quant. Electr. 19, (1989) 1606.

3) L.B. DaSilva, B.J. MacGowan et al SPIE 1229, (1990) 128. M.D. Rosen, D.L. Matthews US Patent Nu. 5016250, (1991).

4) V N Shlyaptsev, P V Nickles, Th Schlegel, M P Kalachnikov, A L Osterheld. SPIE 2012, (1993) 212

5) S.B. Healy, K.A. Janulewicz, J.A. Plowes, G.J. Pert. Opt. Comm. 132, (1996) 442

6) J Nilsen. Phys. Rev. A54, (1996) 4539

7) C.N. Danson et al. Opt. Comm. 103, (1993) 392.

8) G.J.Linford et al. Appl.Opt. 13, (1974) 397.

9) H. Fiedorowicz and A. Bartnik, Y. Li, P. Lu and E. Fill, Phys. Rev. Lett. 76, (1996) 415.

10) Koechner. Solid State Laser Engineering, Springer- Verlag, (1992)

11) T Boehly, M. Russotto, R.S. Craxton, R. Epstein and B. Yaakobi, L.B. DaSilva, J. Nilsen, E.A. Chandler, D.J. Fields, B.J. MacGowan, D.L. Matthews, J.H. Scofield, and G. Shimkaveg. Phys. Rev. A42, (1990) 6962.

12) J. Zhang, S.T. Chunyu, Y.L. You et al.. Phys. Rev.A 53, (1996) 3640

13) A.K.Bathia, U. Feldman, and J.F: Seely. Atomic Data and Nuclear Tables 32 (1985) 435

14) J Zhang priv. comm.

15) Y Li, G.D. Tsakiris, and R. Sigel. Rev. of Scient. Instrum. 66, (1995) 80.

TIME RESOLVED MEASUREMENT OF THE ANGULAR DISTRIBUTION OF LASING AT 25.5 NM IN NE-LIKE IRON

R Smith[1)], A MacPhee[3)], G Tallents[1)], Ph. Zeitoun[2)], F. Albert[2)], A. Carillon[2)], P. Jaegle[2)], G. Jamelot[2)], C. L. S. Lewis[3)], A. Klisnick[2)], M.Maillard[2)], D. Ros[2)], S. Sebban[2)]

1) Department of Physics, University of Essex, Colchester CO4 3SQ, UK
2) Laboratoire de Spectroscopie Atomique et Ionique, Bât. 350, Université Paris-Sud, 91405 Orsay, France
3) Department of Pure and Applied Physics, Queens University of Belfast, Belfast BT7 1NN, UK

INTRODUCTION

X-ray laser output from laser produced plasmas has been observed in collisionally pumped Ne-like ions ranging from chlorine (Z=17) to silver (Z=47). Efforts to increase the efficiency of these schemes have been hindered by the extreme conditions of the plasma environment. For example, steep density gradients cause refraction effects which result in the premature loss of photons from the channel of x-ray amplification. Refraction can also serve to reduce collimation and coherence in the beam. It has been shown experimentally[3] and theoretically[3] that the inclusion of a prepulse preforms the plasma which relaxes the density gradients in the plane perpendicular to the target surface when the main heating pulse or pulses associated with the production of population inversion are incident. Reduced refraction because of lower density gradients leads to better beam guiding for the x-ray laser through the channel of amplification. In this paper, we present the angularly and temporally resolved x-ray laser emission from a Ne-like Fe plasma and demonstrate the effect that the density gradients have on the direction of the output beam through changes in the refraction of the active medium.

A time dependence in the angular distribution of soft x-ray laser output was first observed by Kodama et al[1] in Ne-like germanium where a significant reduction in the refraction was shown to occur during the irradiation by a single 700ps drive pulse.

The time dependence of the angular distribution of soft x-ray lasing at 255 Å in Ne-like Iron has been measured using a flat field spectrometer coupled to a streak camera. Slabs of iron have been irradiated over a length of 20 mm with the 1.06 μm output from the Nd-glass laser at LULI using a single pre-pulse and double main pulse driving configuration. The recorded change in deflection angle with time of the x-ray laser beam is in agreement with theoretical models which predict favourable reduction of refraction and on x-ray laser beam propagation with multi-pulse irradiation.

EXPERIMENTAL SETUP

The experiment was carried out using the LULI Nd-glass Laser system at Ecole Polytechnique in Paris. Three beams at 1.06 μm wavelength were irradiated in a line focus geometry onto an iron slab target. Lasing at 255 Å was achieved with a gain coefficient of 15 +/- 3 cm^{-1} for 20mm long targets. A single prepulse and double main pulse configuration was used for the driving beams as illustrated in figure 1.

The time resolved angular distribution of the output from the plasma was diagnosed by using a slit-less flat field spectrometer (FFS) coupled to a Kentech x-ray streak camera (figure 2). Within the FFS, gold reflection filters and an aluminium foil filter were used to spectrally isolate the Ne-like lasing line of 255 Å. An aberration-corrected concave grating with an average spacing 1200 lines/mm was tilted at ~3° off axis in order to focus the target plane onto the entrance of the x-ray streak camera. A time integrated spectrum from the Ne-like iron plasma shows that the lasing line at 255 Å dominates the axial output (figure 3).

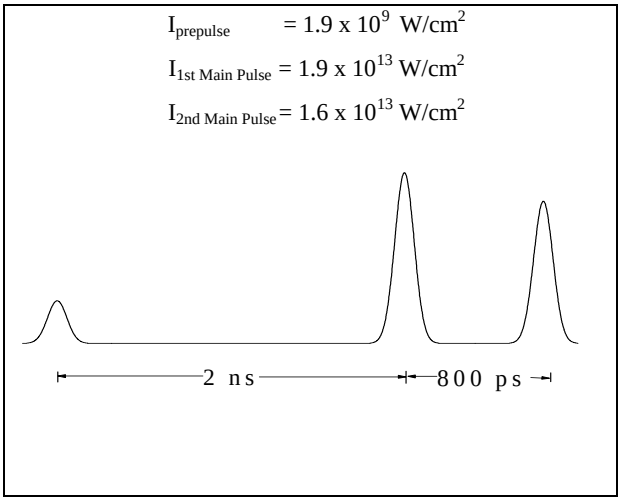

Figure 1 - Driving pulse configuration.

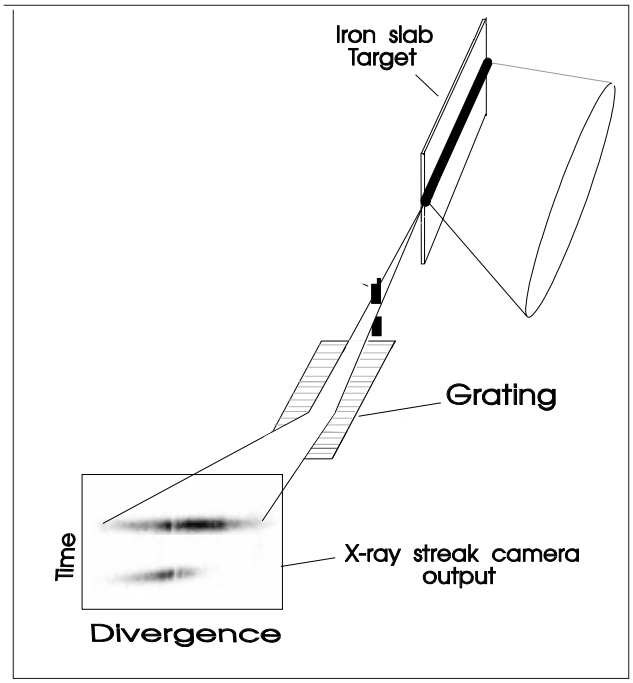

Figure 2 - Experimental set-up to obtain angularly resolved information as a function of time from the output of the Ne-like Iron x-ray laser.

The x-ray streak camera was positioned at the focal plane of the flatfield spectrometer to give temporal and angular resolution of the x-ray laser. The temporal resolution of the streak camera was therefore limited by the width of the 255 Å spectral line of Ne-like iron. The aperture at the entrance of the FFS limited the vertical collection angle to 1.5 mrad and so the collected x-rays were integrated vertically across 1mm coverage of the grating. At this distance, the streak camera output shows the x-ray laser

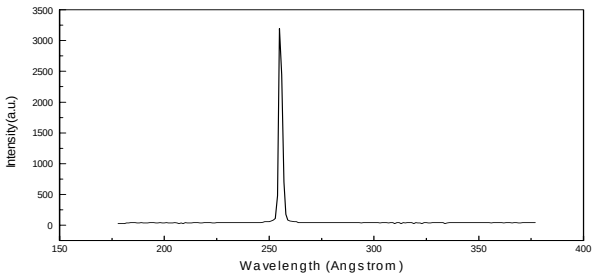

Figure 3 - Spectrum of Ne-like Iron x-ray laser resolved by a flat-field spectrometer shows dominant emission on the 25.5 nm spectral line.

beam profile variation from the target surface as a function of time. We refer to the direction of the peak of the x-ray laser be the 'pointing' of the beam and the full width at half maximum of the x-ray laser profile as the 'divergence'. The streaked image data was recorded using a 16 bit CCD camera butt-coupled to the image intensifier with a fibre optic face-plate.

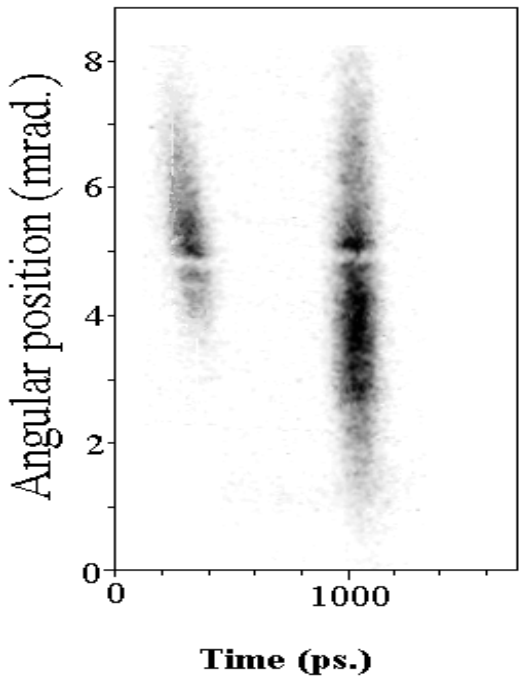

Figure 4 - Time and angularly resolved x-ray laser emission from the Ne-like Iron plasma irradiated by two laser pulses (at times of the above x-ray lasing) and a prepulse.

In figure 4, time and angle resolved emission from the Ne-like Fe plasma is shown. The two x-ray lasers pulses recorded were generated by the double optical drive pulse. Pin-cushion distortion in the 50/40 image intensifier is negligible in the middle of the screen where the image was recorded[2] and hence has minimal effect on the measurements of the beam pointing and divergence. Lasing does not occur during the prepulse. A reduced refraction from the target axis with time is observed for the first pulse, but not the second (figure 5).

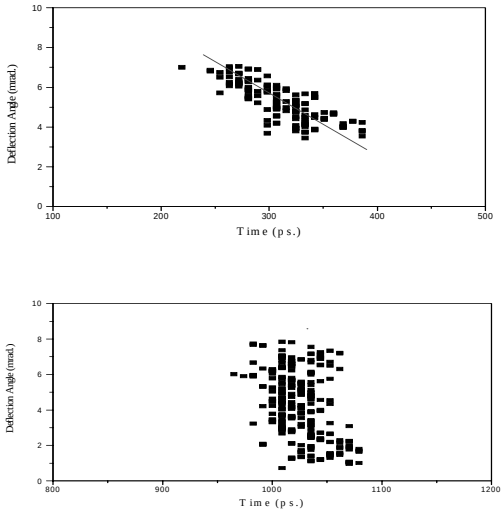

Figure 5 - X-ray laser pointing angle from the target surface as a function of time for (a) the first lasing pulse and (b) the second lasing pulse.

It can be seen from figure 5(a) that the pointing angle to the target surface for the first x-ray pulse decreases with time at a rate of ~0.03 mrad/ps. As time increases, the density gradients perpendicular to the target surface should decrease. This produces reduced refraction effects as illustrated by the movement of the first x-ray laser pulse closer to the target surface with time (figure 5(a)). By the time the second pulse is emitted the density gradients have already been established and so the beam pointing does not change with time during the pulse (figure 5(b)). This allows the x-ray photons to remain in the gain medium longer and hence the intensity of the lasing line is greatest in the second pulse (figure 4).

CONCLUSIONS

Refraction effects in an x-ray laser plasma medium have been shown to lessen in the final pulse of a multi-pulse drive experiment, in this scheme. The x-ray emission pointing moves closer to the target surface with time indicating that the density gradients have also relaxed with time. This reaffirms previous theoretical work which predicts that the inclusion of a prepulse relaxes density gradients, reduces refraction of the propagating x-ray laser and allows the beam to remain in the high gain region of the plasma. This results in higher x-ray laser output and pointing angles closer to the target surface.

REFERENCES

1) R. Kodama, D. Neely, L. Dwivedi, M.H. Key, J. Krishnan, C.L.S. Lewis, D. O'Neill, P. Norreys, G.J. Pert, S.A. Ramsden, G.J. Tallents, J. Uhomoibhi, J. Zhang Optical Comm. 90, 95 (1992)

2) A. Ridgley, 'Evaluation of 50/40 Image Intensifiers', Rutherford Appleton Laboratory (Nov. 1987)

3) A Behjat, J Y Lin, G J Tallents, A Demir, M Kurkcuoglu, C L S Lewis, A G MacPhee, S P McCabe, P J Warwick, D Neely, E Wolfrum, S B Healy and G J Pert. Optics Comm. 135, 49, (1997)

HIGH GAIN TRANSIENT PUMPED NE-LIKE X-RAY LASERS

P.J. Warwick [1)], A. Behjat [2)], A. Demir [2)], M.P. Kalachnikov [3)], C.L.S. Lewis [1)],
D. Neely [4)], P.V. Nickles [3)], M. Schnürer [3)], G.J. Tallents [2)], E. Wolfrum [4)], J. Zhang [5)]

1) School of Mathematics and Physics, Queen's University of Belfast, Belfast, BT7 1NN
2) Department of Physics, University of Essex, Colchester, CO4 3SQ
3) Max-Born-Institut, Rudower Chaussee 6, D-12489 Berlin, Germany
4) Rutherford Appleton Laboratory, Chilton, Didcot, Oxon, OX11 0QX
5) Clarendon Laboratory, University of Oxford, Oxford, OX1 3PU

INTRODUCTION

The brightest and most robust X-ray lasers to date rely on electron collisional excitation to pump electrons into the upper laser state, a quasi-steady state (QSS) population inversion being formed due to the rapid radiative decay of the lower laser level with respect to the upper one. The most efficient schemes still require 100's of Joules of drive laser energy on target[1)] and in order to become practical and accessible for applications, X-ray lasers must become more compact and efficient. One problem with QSS schemes is that the regime in which Ne-like ions dominate is of too low an electron temperature to support optimum excitation rates.

A novel scheme, utilising a transient population inversion was proposed theoretically a number of years ago[2,3)]. It involves a combination of ns and ps duration optical pulses. The ns pulse is low intensity and preforms a column of plasma, heated sufficiently to produce an abundance of Ne-like ions. Once the Ne-like fraction is optimised, the high intensity ps pulse rapidly heats the plasma in a time-scale shorter than that of the relaxation processes of the excited states, and before any significant further ionisation can occur. The inversion is formed due to the different collisional excitation rates of the 3p and 3s levels, as opposed to their radiative decay rates.

High transient gain has been reported in Ne-like Ti[4)] at 326 Å with a small signal gain coefficient of 19 cm^{-1} and a duration ≤ 20 ps. The experiments were motivated by simulations of the transient pumped Ti XRL which show peak local gain coefficients of up to ~200 cm^{-1} [3,5)]. By comparison, the most efficient QSS (long pulse driven) gain coefficient yet measured for Ti is 3.3 cm^{-1} [6)], requiring substantially higher drive energy.

Simulations of the Ge X-ray laser have also shown ultra-high gains on a number of transitions[7)]. A peak local gain coefficient of 140 cm^{-1} has been predicted for the J = 0-1, 196 Å transition, which when ray traced to take account of refractive effects gives a ray averaged gain of ~30 cm^{-1}.

The aims of this work were thus to repeat the Ti experiment under the higher irradiance conditions available using Vulcan, utilising a travelling wave pump (see later) to sample longer targets, and extend the scheme to higher Z, producing lasing in Ge if possible.

EXPERIMENTAL DETAILS

The experiment utilised two 1ω beams incident on a single target in the Target Area West interaction chamber. A CPA beam provided up to 22 Joules on target in a ~7ps duration pulse, coinciding temporally with the half maximum point on the falling edge of the long pulse. Different irradiance conditions were used for Ti and Ge targets. For Ti shots the long pulse was a roughly trapezoidal, 1 ns FWHM duration pulse, delivering an average of 20 Joules on target for an average intensity of 1.7×10^{12} W cm^{-2}. The short pulse delivered an average of 16 Joules on target for an average intensity of 2.2×10^{14} W cm^{-2}. For Ge the long pulse was a 600ps FWHM Gaussian pulse delivering an average of 40 Joules for an average intensity of 5.6×10^{12} W cm^{-2}. The short pulse delivered an average of 21 Joules for an average intensity of 3.0×10^{14} W cm^{-2}.

The primary axial diagnostic was a flat field, grazing incidence spectrometer with a 1200 lines per mm, aperiodically ruled grating, incorporating a cylindrical mirror for spatial resolution perpendicular to the dispersion direction. An XUV sensitive, back-thinned CCD was used to record time integrated spectra. Other diagnostics included a crossed slit camera and a space resolving crystal spectrometer to monitor uniformity of illumination and ionisation balance.

Because of the transient nature of the gain it is not advantageous to heat the entire target length simultaneously with the short pulse. Instead we need to create a plasma which travels from one end of the target to the other at the speed of light (c) and allows photons originating at one end to propagate to the other, whilst all the time experiencing gain. This is known as a travelling wave (TW) pump[8,9)] and is achieved in practice by introducing a path difference across the beam equal to the line focus length.

Because of the off axis geometry of the line focus optics there was an intrinsic path difference from one side of the beam to the other with respect to reaching the target, for both long and short pulse beams. This intrinsic path difference results in a focus running along the target at a velocity of about 2.7 c. A 300 lines per mm grating was inserted in the short pulse beam-line to provide the extra path difference necessary to slow this running focus down and give a travelling wave velocity of c. The effect of the TW velocity on the X-ray laser output is illustrated in a separate article in these proceedings, using a simple analytic model. Since the transit time of a 10 mm target is 33 ps the long pulse intrinsic running focus is not a problem.

RESULTS

In Figure 1 the XUV lasing signals at 326 and 301 Å are shown as a function of the length of the Ti plasma column. The 326 Å line is the 3p $^1S_0$ - 3s $^1P_1$ line, analagous to the 196 Å line in Ne-like Ge. The 301 Å line was first observed using the transient pump scheme[10)] but no gain measurement was

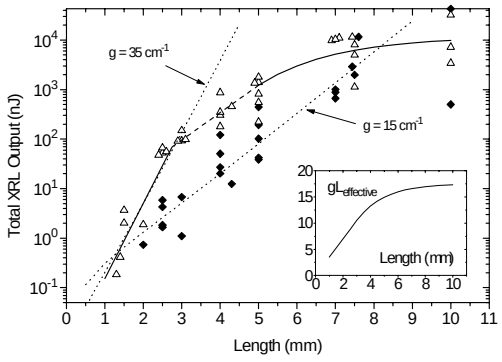

Figure 1 Output signals at 326 Å (Δ) and 301 Å (◆) as a function of target length for pump energies of 1.7 J/mm and 1.6 J/mm for the long and short pulses respectively. The inset shows how the effective gain-length product increases with target length, reaching "gL" ~ 15 at 5 mm.

possible and only a crude wavelength identification made. It has been suggested that it is a self-photo-pumped 3d $^1P_1$ - 3p $^1P_1$ transition[11)].

The 326 Å lasing signals can be fitted[12] with a gain coefficient g = 35 cm^{-1} up to target lengths L ~ 3 mm. With further increase of target length the rate of increase of the output signal drops indicating a falling effective gain coefficient, an effect typical of a laser entering the saturation regime. Calculations for the 3p-3s Ti line have indicated[4] that saturation should take place at a $\int g(l)dl \sim 15$. As seen later, this occurs at L ~ 5 mm supporting the assertion of saturated output.

Further evidence of saturation is the behaviour of the 3d-3p line at about 301 Å. For the first time a gain coefficient g = 15cm^{-1} has been determined for this line. However, the 3d-3p line shows no saturation-like behaviour within the data fluctuations up to a target length of 10 mm. If it were refraction causing the drop in the effective gain coefficient of the 3p-3s line with increasing target length, then it would be expected that the 3d-3p line would also suffer a similar effect as simulations show both lines having their peak gain in similar plasma regions. The influence of any refraction on the X-ray beam should be nearly the same as a result of the small difference in the wavelength between the two lines. Temporally resolved measurements have also shown[4] a simultaneous appearance and a comparable duration of these transient lasing emissions, revealing similar plasma conditions for them.

This is the first observation of fully saturated operation of the 326 Å line in Ne-like Ti. Small gain-length products ($gL < 9$) were observed on other long pulse (QSS) Ti lasers at 326 Å but the 3d-3p line was not observed[6,13,14].

It is worth noting that the saturation of gain observed in the experimental data for the 326 Å line can be described approximately by a simple relationship of the form

$$g(L) = \frac{g_0}{1 + \frac{i(L)}{i_s}} \qquad (1)$$

where $g_o = 35\ cm^{-1}$ is the small signal gain coefficient determined from signal growth for lengths up to ~ 3 mm, $i(L)$ is the signal strength after amplification through a length of plasma L, i_s is the saturation intensity level of the signal, causing the small signal gain coefficient to be halved in magnitude and $g(L)$ is the effective local gain coefficient as the XRL pulse propagates along the plasma column. Self consistency is obtained with $i_s \sim 500$ (arbitrary units but corresponding to the numerical labels used in Figure 1) at L ~ 4 mm. The decreasing gain coefficient can be roughly estimated as $g(L) \sim 35 \exp[-(L-3)/2]$ for $L \geq 5$ mm from local fits to the data. Using these two expressions for $g(L)$ and extrapolating in the region $3 \leq L \leq 5$ mm we can construct a fit for $i(L)$ as shown in Figure 1. The general agreement is good. Assuming that $g(L) = 35\ cm^{-1}$ for targets $L \leq 3$ mm and $g(L) = 35 \exp[-(L-3)/2]$ for $L > 3$ mm, we can make an estimate of the effective gain-length product (i.e. $\int g(l)dl$) as a function of target length. This is shown as an inset to Figure 1 and it may be seen that an effective gL of 15 occurs for a target length of 5 mm. This is consistent with the saturation gL predicted from calculations as mentioned earlier.

Within the data fluctuation no systematic difference could be found in the output Ti lasing signals with or without the travelling wave grating in place. This suggests the inversion period was a significant fraction of the 33 ps transit time of a 10 mm target. For clarity only data recorded without the travelling wave (i.e. with the grating removed) are included in figure 1.

In another series of experiments we determined the threshold pump values for lasing at 326 Å as depicted in Figure 2, which shows outputs from 3 mm targets.

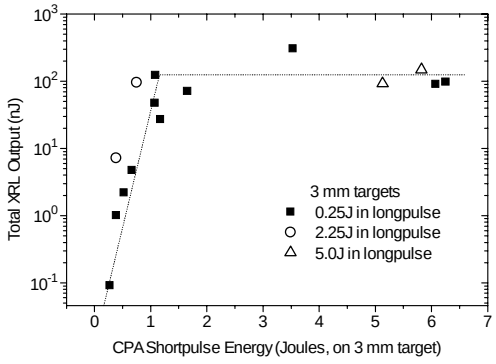

Figure 2 Output signals at 326 Å from 3 mm targets as a function of pump energy in the short pulse. The data points marked Δ correspond to the standard pump conditions used in Figure 1.

With E_{short} = 1.5 J for the short pulse and E_{long} = 0.25 J for the long pulse we observe the same output signal strength as recorded for Figure 1 conditions. This indicates that the gain coefficient is comparable and that we achieved a gain-length product of 10.5 for these reduced input energies. Pump energies as low as E_{long} = 0.25 J and E_{short} = 0.25 J yield measurable amplified emission. This verifies that X-ray lasing in the Ne-like Ti system is possible with table top class pump lasers. With E_{short} = 1.5 J one achieves the maximum XRL signal output in this pumping geometry. An increase in the long pulse intensity up to a factor of more than 10 did not give a higher output signal providing E_{short} was greater than 1.5 J. However, within the threshold region (E_{short} < 1.5 J) the lasing output was sensitive to E_{long}. Using the short or long pulse alone, no lasing was visible with the maximum energies used in this experiment.

From our experimental results we also tried to get more confidence about the wavelength of the 3d-3p lasing transition in Ti at 301 Å. This line has not been measured accurately before but is expected at 301 Å with an uncertainty of over 1 Å[5]. Fitting a quadratic through known wavelength markers we can estimate the dispersion, and obtain a wavelength for the 3d-3p line of 301.5 ± 0.5 Å.

The transient scheme was also successful in pumping the Ne-like Ge X-ray laser on the $3p\ ^1S_0$ - $3s\ ^1P_1$ (J = 0-1) transition at 196 Å. The rapid increase of X-ray laser signal with target length is illustrated in Figure 3. For lengths up to 5mm this growth is exponential and can be fitted using a small signal gain coefficient of 30 cm^{-1}. Signals from lengths greater than 5 mm deviate from this trend of exponential growth, the rate of increase of output slowing. As mentioned previously this is a characteristic feature of a laser going into saturation, the inversion being significantly reduced by the number of stimulated transitions. However in this case the curling over effect is not due to saturation. When the energy in both beams was halved for one shot we saw no lasing signal. For all shots illustrated the target was positioned in the centre of the line focus. However, when a 5 mm target was positioned to one side of the 10 mm line focus lasing signal was reduced by an order of magnitude. These shots indicate that the lasing signal is strongly dependent on the incident intensity, an effect already observed around the threshold incident intensity for Ti. We believe that for targets longer than 5 mm the intensity towards the ends of the target was low enough compared to the centre to decrease the local gain coefficient and prevent continued exponential growth with target length. However, 5 mm targets exhibit a gain-length product of 15 which is approaching that required for saturation. Also, taking the average energy output from 9 mm targets (13 μJ) and assuming a 20 ps pulse duration from a gain zone area measuring 100 μm by 100 μm, gives a conservative output intensity estimate of 6.5×10^9 W cm^{-2}. This

is close to the calculated saturation intensity of 2.0×10^{10} W cm^{-2}, although the different plasma conditions imply a different recovery time, t_{rec}, and hence the two values are not directly comparable.

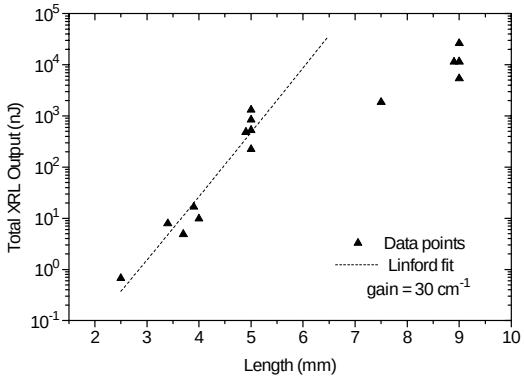

Figure 3 The integrated energy output of the Ge, 196 Å X-ray laser as a function of target length for pump energies of 3.3 J/mm and 2.1 J/mm for the long and short pulses respectively, using a travelling wave pump.

Shots where the TW grating was removed showed between one and two orders of magnitude less lasing output from 9 mm targets. Null shots, where only one of the two beams was fired, confirmed that lasing only occurred when the target was irradiated by both pulses. No Ne-like resonance line emission was visible on the crystal spectrometer from the long pulse alone. Figure 4 shows the spectrum obtained when both beams irradiated the target (bold line). For comparison a spectrum obtained with the same instrument from a typical QSS pumping scheme is shown also (fine line). The QSS scheme used was[1)] two 75 ps FWHM duration pulses, separated by 2.2 ns, the first pulse having 20% the intensity of the second, which had an intensity on target of 4×10^{13} W cm^{-2}. However, very similar spectra are obtained using ns pulses. The Ne-like 3d-2p lines in the QSS spectrum (the two brightest lines) had a time integrated intensity of 5 times that obtained using the transient scheme. The QSS spectrum has thus been scaled down to make the intensity on the Ne-like 3d-2p lines the same. Comparing the two spectra we see that F-like and O-like lines have been suppressed by using the transient scheme rather than the QSS scheme. Compared to the Ne-like emission, the brightest F-like 3d-2p line at 8.56 Å is relatively three times weaker under the transient scheme. We have thus created a large population inversion without wasting so much energy over-ionising the plasma.

EXPERIMENTAL SUMMARY

Reliable X-ray lasing has been demonstrated utilising a novel excitation scheme which requires exceptionally low input pump energies. Saturation of the 326 Å line in Ne-like Ti has been achieved for the first time due to a gain coefficient of 35 cm^{-1}. Measurable amplified emission was observed from 3 mm targets for a total pump energy of 0.5 J, representing a truly table-top system. A second 3d-3p laser line has been identified at 301.5 ± 0.5 Å and a gain coefficient of 15 cm^{-1} measured.

With less than 30 Joules of energy incident on a 5 mm Ge target we have achieved a gain coefficient of 30 cm^{-1} and a gain-length product of 15, which is approaching the saturation limit of this laser. This gain coefficient is the highest ever observed in Ne-like Ge and demonstrates the effectiveness and efficiency of the transient excitation scheme. With its predicted ultra-short pulse length this laser has applications for high temporal resolution probing of other laser produced plasmas.

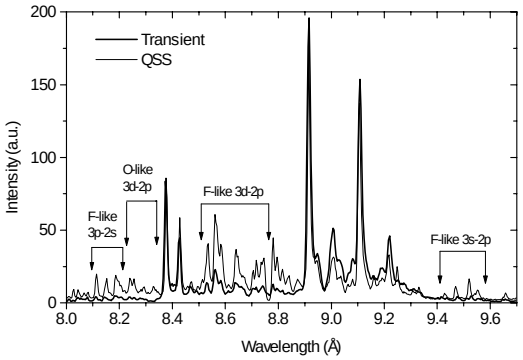

Figure 4 Resonance line spectra obtained using a KAP crystal spectrometer. The bold line is the spectrum obtained using the transient pump scheme. The fine line was obtained by the same instrument from a Ge target pumped with the QSS scheme.

REFERENCES

1) J Zhang, P J Warwick, E Wolfrum, M H Key, C Danson, A Demir, S Healy, D Kalantar, N S Kim, C L S Lewis, J Lin, A G MacPhee, D Neely, J Nilsen, G J Pert, R Smith, G J Tallents, J S Wark
Phys Rev A 54 R4653 (1996)

2) Yu V Afanas'ev and V N Shlyaptsev
Sov J Quantum Electron, 19 1606 (1989)

3) V N Shlyaptsev, P V Nickles, T Schlegel, M P Kalachnikov, A L Osterheld
SPIE, 2012 111 (1993)

4) P V Nickles, M Schnurer, M P Kalachnikov, I Will, W Sandner, V N Shlyaptsev
SPIE 2520 373 (1995)

5) J Nilsen
Phys Rev A, 55 3271 (1997)

6) J Zhang, S T Chunyu, Y L You, Q R Zhang, S J Yang, W Z Huang, D Y Wu, X Q Zhuang, S P Liu, Y Q Cai, F Y Du, X D Yuan, S F Wei, Y K Zhao, H S Peng, J Nilsen
Phys Rev A, 53 3640 (1996)

7) S B Healy, K A Janulewicz, J A Plowes, G J Pert
Optics Comm, 132 442 (1996)

8) J D Shipman, Jr
Appl Phys Lett, 10 3 (1967)

9) Z Bor, S Szatmari, A Muller
Appl Phys B, 32 101 (1983)

10) P Nickles, private communication.

11) J Nilsen
Phys Rev A, 53 4539 (1996)

12) G J Linford, E R Peressini, W R Sooy, M L Spaeth
Appl Optics, 13 379 (1974)

13) T Boehly, M Russotto, R S Craxton, R Epstein, B Yaakobi, L B DaSilva, J Nilsen, E A Chandler, D J Fields, B J MacGowan, D L matthews, J H Scofield and G Shimkaveg
Phys Rev A, 42 6962 (1990)

14) J Nilsen, G J MacGowan, L B DaSilva, J C Moreno
Phys Rev A, 48 4682 (1993)

EFFECTS OF DRIVE PULSE CONFIGURATION ON THE SAMARIUM X-RAY LASER

J. Zhang [1)], J.Y. Lin [2)], E. Wolfrum [1)], A. Djaoui [3)], A.G. MacPhee [4)], G.F. Cairns [4)], C.L.S. Lewis [4)], D. Neely [3)], G.J. Pert [5)], R. Smith [2)], G.J. Tallents [2)], J.S. Wark [1)]

[1)] Clarendon Laboratory, Department of Physics, University of Oxford, Oxford, OX1 3PU, UK
[2)] Department of Physics, University of Essex, Colchester, CO4 3SQ, UK
[3)] Central Laser Facility, Rutherford Appleton Laboratory, Chilton, Oxon, OX11 0QX, UK
[4)] School of Mathematics and Physics, Queen's University of Belfast, Belfast, BT7 1NN, UK
[5)] Department of Physics, University of York, York, YO1 5DD, UK

INTRODUCTION

Because of their favourable scaling to short wavelengths, collisionally excited Ni-like x-ray lasers have been extensively investigated using single long pulse [1-3)] and multipulse drive configurations [4-8)]. Recently, saturation was observed in the Ni-like Ag x-ray laser at 14 nm [9)]. Sm slab targets were also demonstrated to be able to provide saturated Ni-like x-ray laser output at 7.3 nm, when driven by an optimised double 75 ps laser pulse at 4.0×10^{13} Wcm^{-2} [10)]. In contrast, when driven by a single 600 ps laser pulse at similar irradiance, Sm slab targets could only produce very weak lasing signal. There has been much effort to reveal the reasons for different performances of Ne-like x-ray lasers driven by single pulse and multiple pulse [11-14)], however there is little research comparing of the performances of Ni-like x-ray lasers under such different drive configurations. It is our objective here to study the different performances of the Ni-like Sm x-ray lasers and thus provide a further understanding of the underlying physical processes.

In this paper, keV spectroscopy of laser plasmas is used to study x-ray emission from the double pulse driven plasma and from the single 600 ps pulse driven plasma in the wavelength range between 0.6 and 1.2 nm. Identification of spectral lines from Sm ions isoelectronic with Ni, Co and Fe is made using atomic physics calculations of the wavelengths and oscillator strengths. The relative abundances of the different ionisation stages, as inferred from the intensities of the 4f-3d transitions, compare favourably with the calculated ionisation distribution using a one-dimensional hydrodynamic code MED103 [15)]. Significant differences in temperatures and relative abundance of the ionisation stages are found for the two different drive pulse configurations. This may help explain the much improved performance of the Sm laser driven by the double pulse, compared to that driven by the single pulse configuration at similar irradiances on targets.

EXPERIMENTAL SETUP

The experimental set-up is similar to that described in Ref. [9-10)]. Three beams of the VULCAN Nd:glass laser at 1.05 µm were used in a standard off-axis focus geometry, which provided a line focus with 25 mm length and 100 µm width, giving an irradiance of ~ 4.0×10^{13} Wcm^{-2} on targets. Deploying the other three beams 180° opposed in a second line focus produced a plasma with an opposed density gradient, which helps compensate for the refraction of the x-ray laser beam from the first plasma [9-10)].

Flat slab targets used in the experiment were 18 mm long with 100 µm wide Sm stripes coated on glass substrates. Both ends of the slab target were placed well within the line focus to avoid generation of cold plasmas at the ends of the targets. The targets were aligned so that they were parallel with an optimised separation of 150 µm (in the direction perpendicular to the target surfaces) between the surface planes and an axial separation of 500 µm between the two targets. Traveling wave excitation for the two successive targets was designed to achieve maximum amplification. To approximate this condition, the three drive beams for the first slab target were therefore timed 60 ps earlier than the three beams for the second target.

This experiment used a pair of 75 ps pulses separated by 2.2 ns, with 10% energy in the first pulse and 90% in the main pulse. Results from an earlier Sm laser experiment [3)] using a single 600 ps pulse driver are used here for comparison. The irradiances on targets for both experiments were similar ~ 4.0×10^{13} Wcm^{-2}.

The primary diagnostics were two spatially resolved, time integrated KAP curved-crystal spectrometer with a radius of curvature of 30 cm and a KAP flat-crystal streaked spectrometer. They recorded the spectral range from 0.6 nm to 1.2 nm on InstaSpec IV x-ray CCD detectors. The space resolving spectrometers monitor the ionisation balance and uniformity along the line focus. An x-ray streak camera was coupled to the flat-crystal spectrometer to record the time history of the plasma emission.

RESULTS

Figure 1 compares the performances of the Sm laser at 7.3 nm driven by the double 75 ps short pulses (Fig. 1A) and that driven by the single 600 ps laser pulse (Fig. 1B). It is apparent

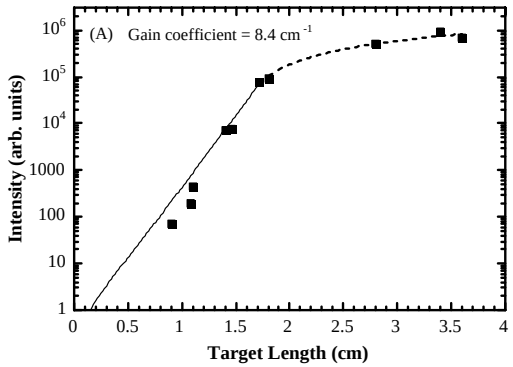

Figure 1A. Intensity dependence of the Sm laser on plasma length driven by a pair of 75 ps pulse separated by 2.2 ns at 4.0×10^{13} Wcm $^{-2}$.

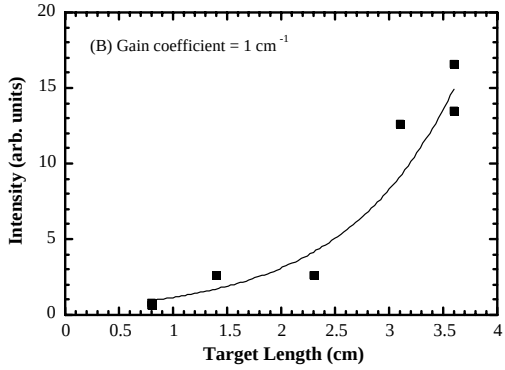

Figure 1B. Intensity dependence of the Sm laser on plasma length driven by a single 600 ps pulse at 4.0×10^{13} Wcm^{-2}. The dashed line shows the fit to the Linford formula.

that the Sm laser driven by the double pulse performs much better. The gain coefficient was determined by fitting the Linford formula to those data in the exponential region, to be 8.4 cm^{-1} in Fig. 1A. The output intensity saturates at a gain-length product ~16. By contrast, the gain coefficient of the Sm laser driven by the single 600 ps pulse configuration at the same irradiance has a very small gain ~ 1 cm^{-1}, as shown in Fig. 1B.

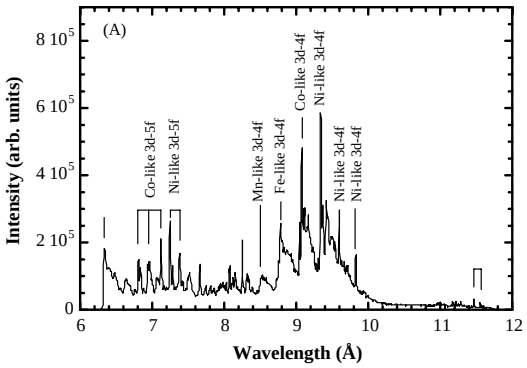

Figure 2A. KeV spectrum of Sm plasma emission under the same drive conditions as that in Fig. 1A. The spectral lines of Ni-like, Co-like and Fe-like ions are clearly visible.

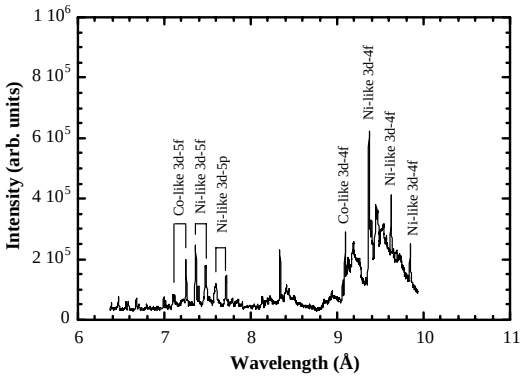

Figure 2B. KeV spectrum of Sm plasma emission under the same drive condition as that in Fig. 1B.

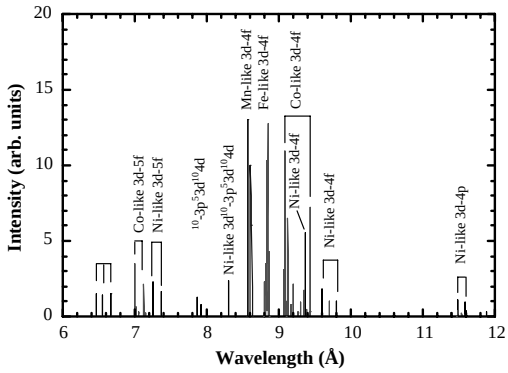

Figure 2C. Calculated Sm spectrum with an assumption of equal populations on different ionisation stages.

In figure 2 we show the comparison between the keV spectrum of the plasma driven by the double 75 ps pulse and that driven by the single 600 ps pulse. The spectra were corrected for the response of the CCD detector, the crystal reflectivity, the filter transmission and geometrical factors. The prominent lines of Sm transitions visible in Fig. 2A are due to 4f-3d transitions from Ni-like, Co-like, Fe-like and Mn-like ions respectively. The strong unresolved transition arrays observed in the long wavelength region arise from 4f-3d transitions. For the single 600 ps drive pulse configuration, the emission from Fe-like and Mn-like Sm ions is not present in Fig. 2B. This implies that the temperatures of plasmas driven by the double 75 ps configuration are higher than those driven by the single 600 ps configuration. The theoretical identifications of Ni-like, Co-like, Fe-like and Mn-like lines are drawn in figure 2C based on the oscillator strength for each transition. The calculated values in Fig. 2C are the results of a relativistic Dirac-Fock calculation of the average of configuration energies and potentials [16]. The calculations were carried out including all couplings of states with a given number of n=3,4 and n=5 electrons of a fixed angular momentum and parity. The oscillator strengths were calculated using the relativistic-length form of the electric dipole interaction which includes the effects of retardation.

Without detailed information on the population mechanisms for the excited states, the relative abundances of the ionisation stages from the 3d-4f emission are difficult to be determined quantitatively. However, as a zero-order approximation, we can compare the ionisation abundances inferred from the relative intensities of the 3d-4f emission with the ionisation distribution predicted by the one-dimensional hydrodynamic code MED103 simulation [15]. Since the 4f levels are very close together in energy, we can assume they are in local thermodynamic equilibrium (LTE). Then the experimental intensity ratio should be the same as the ratio of the oscillator strengths taking into account of the degeneracy factors, if we assume that all of the levels are equally populated, as shown in Fig. 2C. In order to obtain similar ratio of different ionisation stages as in the experimental data in Fig. 2A, we have multiplied the Co-like, Fe-like and Mn-like lines by factors of 0.4, 0.14 and 0.055 respectively. Similarly, we have to multiply the Co-like, Fe-like and Mn-like lines by factors of 0.25, 0.03 and 0.013 to get a similar ratio as the case in Fig. 2B. These give us an indication of time-integrated relative abundances of different ionisation stages.

One effect which could influence this approximation is opacity. It is obvious that the Co-like and Fe-like lines are all optically thin. Bailey et al. [18] estimated the opacity of the Ni-like lines and concluded that this is also negligible even in high-irradiance cases.

SIMULATIONS

In order to determine the plasma conditions produced in these experiments, numerical simulations were preformed with the one-dimensional hydrodynamic code MED103 [15]. The codes solves the hydrodynamic equations self-consistently with a time dependent average atom model which describes the ionisation of the plasma. Energies involved in excitation and ionisation processes are explicitly included in the free electron energy equation at each time step. Laser energy absorption by inverse bremsstrahlung and resonance processes is included together with flux-limited heat conduction. In figure 3 we show the calculated temporal evolution of electron density, electron temperature and percent Ni-like fraction for the following experimental conditions: A) For the double 75 ps pulse drive configuration, a 10% prepulse 2.2 ns in advance of a main pulse at $4x10^{13}$ Wcm^{-2} on targets; B) For the single 600 ps drive pulse configuration, the irradiance on targets is $4x10^{13}$ Wcm^{-2}. The temporal zero points were set at the peak of the main pulse in Fig. 3A and at the peak of the single pulse in Fig. 3B.

For the double 75 ps drive pulse configuration, MED103 predicts T_e = 1400 eV, and Z_{eff} = 34.5 (Z_{eff} is the average ionisation state) at the peak of the main laser pulse (Fig. 3A). The relative abundances of the ionisation stages are 1 : 0.32 : 0.1 : 0.03 for Ni-like:Co-like:Fe-like:Mn-like. For the single 600 drive pulse configuration, it predicts T_e = 800 eV, and Z_{eff}

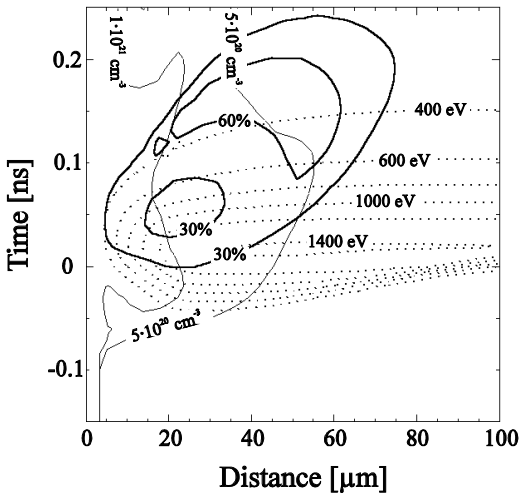

Figure 3A. Simulated temporal evolution of electron density (thin solid), electron temperature (dotted) and percent Ni-like ions (thick solid) as functions of space for the drive conditions in Fig. 1A. The time zero is set at the peak of the main pulse.

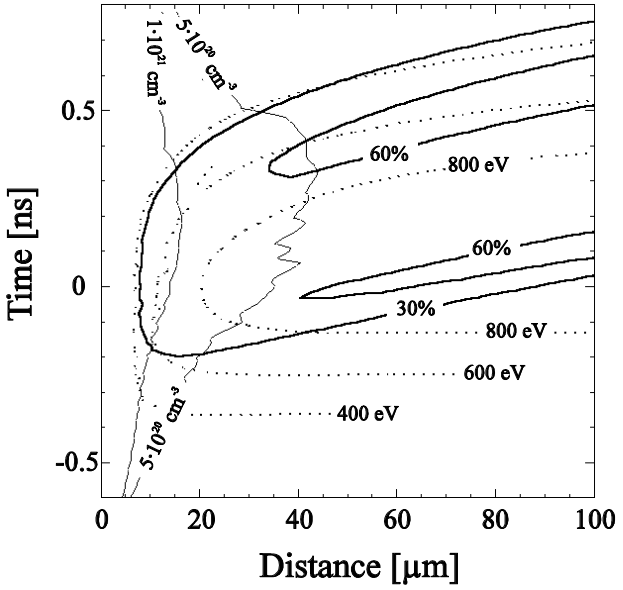

Figure 3B. Simulated temporal evolution of electron density, electron temperature and percent Ni-like ions as functions of space for the drive conditions in Fig. 1B.

=34.2 at the peak of the laser pulse (Fig. 3B). The relative abundances of the ionisation stages are 1 : 0.2 : 0.04 : 0.01 for Ni-like: Co-like: Fe-like:Mn-like. Because MED103 is a one-dimensional hydrodynamic code, the predicted electron temperatures are possibly too high. However, the basic characteristics and relative relationship predicated by the code agree qualitatively with the experimental observation.

It is plausible that the higher electron temperature can be achieved for the double drive pulse configuration, because the volume of the plasma is determined by the level of the prepulse [12]. Less energy from the main pulse is required to heat the smaller volume plasma, generated by the prepulse, to a high electron temperature, which is favourable for high gain operation. Previous Ni-like experiments performed at Lawrence Livermore National Laboratory (LLNL) also suggested that x-ray laser gain can only be observed when significant Co-like line emission is present [1,2,17]. This is consistent with our results in this respect.

The ion temperatures also play an important role in laser performances. The ion temperature at the peak of the main pulse is 200 eV with density of Ni-like ions of 8.3×10^{18} cm^{-3} for the double pulse driven plasma, whereas the ion temperature is 350 eV with density of Ni-like fraction of 7.5×10^{18} cm^{-3} for the single 600 ps driven plasma. Gain coefficient is proportional to the electron temperature and is inversely proportional to the square root of the ion temperature. Therefore, both of the lower ion temperature and higher electron temperature would enhance the gain in the double pulse driven plasma. Figure 3 also shows the more relaxed density gradients in the double 75 ps pulse driven plasma. That allows the x-ray laser beam to propagate a longer distance in the gain region and therefore obtain sufficient amplification for saturation to occur.

CONCLUSIONS

In summary, we have compared the keV spectra from the Sm plasma driven by a double 75 ps laser pulse and that driven by a single 600 ps laser pulse at similar irradiance on targets. The double 75 ps drive pulse configuration has been found to be able to provide higher electron temperature, which, together with lower ion temperature and reduced density gradient, lead to the much improved performance of the Sm laser.

REFERENCES

1) B.J. MacGowan et al.,
Phys. Rev. Lett. 59, 2157 (1987).

2) B.J. MacGowan et al.,
Phys. Fluids B4, 2326 (1992).

3) C.L.S. Lewis et al.,
X-Ray Lasers 1992, E.E. Fill, Editor, IOP Publishing, Conf. Series No. 125, 23 (1992).

4)S. Basu et al.,
Appl. Phys. B57, 303 (1993).

5)H. Daido et al.,
Phys. Rev. Lett. 75, 1074 (1995).

6) J. Nilsen and J.C. Moreno,
Opt. Lett. 20, 1387 (1995).

7) H. Daido et al.,
Opt. Lett. 21, 958 (1996).

8) Y. Li et al.,
Phys. Rev. A 53, R652 (1996).

9) J. Zhang et al.,
Phys. Rev. Lett. 78, 3856 (1997).

10) J. Zhang et al.,
Science 276, 1097 (1997).

11) J. Nilsen and J.C. Moreno.
Phys. Rev. Lett. 74, 337 (1995).

12) J. Zhang et al.,
Phys. Rev. A53, 3640 (1996).

13) J. Zhang et al.,
Phys. Rev. A54, R4653 (1996).

14) Y. Li et al,
Phys. Rev. A51, R4341 (1995).

15) A. Djaoui and S.J. Rose,
J. Phys. B: At. Mol. Opt. Phys. 25, 2745 (1992).

16) K.G. Dyall, et al.,
Comput. Phys. Commun. 55, 425 (1989).

17) L.B. Da Silva, et al.,
SPIE Proceedings 1229, 128 (1990).

SATURATED OPERATION OF A NICKEL-LIKE X-RAY LASER AT 7.3 NM

J. Zhang [1)], A.G. MacPhee [2)], J. Lin [3)], E. Wolfrum [1)], R. Smith [3)], C. Danson [4)], M.H. Key [5)], C.L.S. Lewis [2)], D. Neely [4)], J. Nilsen [5)], G.J. Pert [6)], G.J. Tallents [3)], J.S. Wark [1)]

1) Clarendon Laboratory, Department of Physics, University of Oxford, Oxford, OX1 3PU, UK
2) School of Mathematics and Physics, Queen's University of Belfast, Belfast, BT7 1NN, UK
3) Department of Physics, University of Essex, Colchester, CO4 3SQ, UK
4) Central Laser Facility, Rutherford Appleton Laboratory, Chilton, Oxon, OX11 0QX, UK
5) Lawrence Livermore National Laboratory, Livermore, CA 94550, USA
6) Department of Physics, University of York, York, YO1 5DD, UK

INTRODUCTION

An important objective in the development of X-ray lasers is to deliver a coherent, saturated output at wavelengths shorter than 10 nm [1)]. Such saturated X-ray lasers are required for holography [2)] and microscopy [3)] of biological specimens and for deflectometry [4)], interferometry [5)] and radiography [6)] of dense plasmas relevant to inertial confinement fusion and laboratory astrophysics [5)]. Saturated operation is very important because it means that the maximum power possible for a given volume of excited plasma is extracted by the stimulated emission. Saturated X-ray lasers also ensure an output energy sufficient for most applications and tend to produce a consistent output with little variation from shot to shot. Lasers are characterized by the product of the laser gain coefficient and the length of the laser region (gain-length product). Saturation requires a gain-length product exceeding 15, which means millions fold amplification by the stimulated emission.

The development of X-ray lasers has been marked by a progression toward successively shorter wavelengths. Saturation has been observed at wavelengths $\lambda > 15$ nm in neon-like X-ray lasers (lasers from ions with the electron configuration of neutral neon atoms) on the $J = 2 \rightarrow 1$ transitions in plasmas of Ge [7)], Se [8)] and Y [9)] and on the $J = 0 \rightarrow 1$ transition in Zn [10)] and Ge [11)] plasmas driven by the largest optical laser facilities in the world. However, these X-ray lasers are difficult to scale to the shorter wavelengths $\lambda < 10$ nm required for most applications, with the currently available laser driver energy, because the driver energy required to produce the gain-length product approaching saturation increases very rapidly in neon-like X-ray lasers for shorter wavelength operation. Nickel-like X-ray lasers, in principle, have a more favourable scaling of laser wavelength with drive laser energy but have difficulties in providing a saturated output. Much effort has been devoted toward developing nickel-like X-ray lasers [12-14)], but the resulting gain-length products and efficiency were low. Recent experiments have shown that the intensity and the efficiency of nickel-like X-ray lasers can be greatly enhanced by use of multiple equal intensity short pulses with 400 ps intervals [15-18)]. A significant gain-length product of ~8 has been reported [15-17)], which, however, is still too low for saturated operation.

In the multipulse mode, the first pulse heats and ionises the plasma but the density gradients are too steep for laser propagation. The plasma then expands creating a larger scale length plasma and producing a larger, more uniform gain region that allows for good laser propagation [19-21)]. Aiming at improving efficiency and enhancing the gain-length product, we took a different pulse configuration, compared to the experiments by other groups [15-18)], to drive nickel-like X-ray lasers. Because it is not necessary to have a pre-plasma in an ionization stage as high as nickel-like, a low intensity (10% ~ 30% of total energy) laser pulse (prepulse) was used to create a preplasma with a lower ionization. The preplasma was then allowed to cool down for a much longer time (> 2 ns) until it became not as transparent to the following laser pulse (main pulse) and the plasma region, where laser gain generates, can directly absorb more energy from the main laser pulse before it hits the critical density surface of the plasma. The long delay also provides an excited plasma column with much reduced density gradient to enable the X-ray laser beam to propagate a longer distance at higher density and therefore obtain sufficient amplification for saturation to occur [11,21)]. In this report, we present the first demonstration of a saturated X-ray laser beam at wavelengths $\lambda < 10$ nm, specifically the nickel-like samarium X-ray laser at 7 nm from a refraction compensating double target illuminated by a low-intensity prepulse 2.2 ns before the main drive laser pulse.

EXPERIMENTAL SETUP

The experimental set-up is similar to that described in Ref. [11,21)], as schematically shown in figure 1. Three beams of the VULCAN Nd:glass laser with a 75 ps duration at 1.05 µm were used in a standard off-axis focus geometry, which provide a line focus with 25 mm length and 100 µm width, giving an irradiance of ~ 4.0×10^{13} Wcm^{-2} on targets. Deploying the other three beams 180° opposed in a second line focus produced a plasma with an opposed density gradient, which helps compensate for the refraction of the X-ray laser beam from the first plasma [7,11,21)].

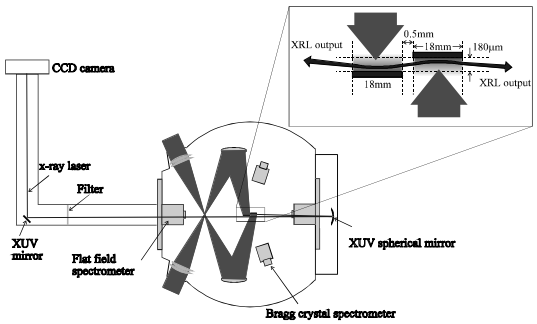

Figure 1. Schematic experimental setup.

Flat slab targets used in the experiment were 18 mm long with 100 µm wide samarium stripes coated on glass substrates. Both ends of the slab target were placed well within the line focus to avoid cold plasmas at the ends of the targets. The targets were aligned so that they were parallel with an adjustable separation (in the direction perpendicular to the target surfaces) between the surface planes and an axial separation of 500 µm between the two targets. Because the X-ray laser pulse duration is comparable to the propagation time, travelling wave excitation for the two successive targets is desirable to achieve maximum amplification. To approximate this condition, the three drive beams for the first slab target were therefore timed 60 ps earlier than the three beams for the second target. The primary diagnostics along the target axis were two flat-field grazing incidence X-ray spectrometers with 1200 line/mm aperiodically ruled gratings [11,21)]. They recorded the spectral range from 5.0 nm to 30.0 nm on InstaSpec IV X-ray charge-coupled device (CCD) detectors (Oriel Instruments, Stratford, CT USA). Radiation at wavelengths shorter than 6.0 nm was eliminated by use of two parallel silver mirrors at 10° grazing incidence angle. Boron and parylene (CH) plastic filters were used to provide

variable attenuation up to 10^3 and absorption edges for wavelength calibration. The axial spectra in a given axial direction were recorded in either of two ways. Time averaged spectra with angular resolution were obtained using an X-ray CCD detector in the focal plane. Alternatively, the Sm laser line at 7.3 nm was focused by the grating of the flat field axial spectrometer into the entrance of an X-ray streak camera so that the streak displayed the temporal variation of the angular distribution of the Sm laser line [21]. The laser line width was less than 50 µm at the streak entrance plane so the temporal resolution is limited by the streak camera operation to ~ 10 ps. A CCD detector recorded the time-resolved angular distribution. In order to measure the output energy, the on-axis spectrometers were cross-calibrated with a near field imaging system consisting of calibrated multilayer mirrors and an X-ray CCD detector [22,23], using the Ge laser at 19.6 nm [11] and the Ag laser at 14.0 nm [21] as the laser sources. This calibration assumes that the collection solid angle (50x50 $mrad^2$) of the multilayer mirror system overfills the angular distribution of the X-ray lasers. The response of the CCD detector and the transmission of filters were calibrated using X-ray radiation from a laser-produced plasma source coupled to a grating spectrometer [24]. Ionisation balance and uniformity along the axial direction of both plasmas were monitored using space resolving crystal spectrometers observing the resonance line emission of Ni-like and Co-like ionisation stages in the 6 ~ 12 Å region.

RESULTS

Figure 2 shows the measured time integrated on-axis output spectrum from a 18 mm long single flat target. The output is completely dominated by the nickel-like samarium 4d→4p, J=0→1 laser transition at 7.3 nm. The other weak 4d→4p, J=0→1 laser line at 6.8 nm is also visible. The intensity of the J=0→1 laser line at shorter wavelength will take over that at longer wavelength for higher Z elements [12,15]. The intensity of the laser lines were attenuated by a combination of boron and CH filters by a factor of 50 to avoid saturation of the CCD detector.

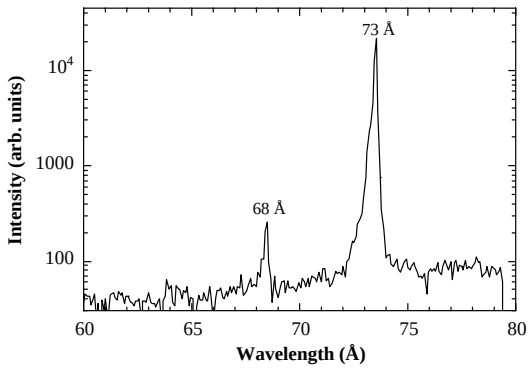

Figure 2. Axial spectrum from two coupled 18 mm long samarium targets separated by 175 µm. The laser line at 7.3 nm is clearly observed to completely dominate the spectrum. The other weak laser line at 6.8 nm is also visible.

In figure 3 the variation of the output intensity of the laser line at 7.3 nm versus the perpendicular separation between the double target is shown. The solid diamonds show the measured output intensity and its uncertainty. These measurements show that the coupling is optimized at a perpendicular separation near 175 µm between the double target. Using the calibrated flat-field spectrometers, the output energy of the samarium laser can be estimated by integrating the total photons emitted from the X-ray laser. The maximum output energy of the Sm laser was found to be 313 µJ, corresponding to a conversion efficiency $2x10^{-6}$, which is the highest efficiency achieved for Ni-like X-ray lasers. The estimated uncertainty in this measurement is within a factor of 3 and is due predominantly to uncertainty in the filter attenuation. The output intensity of the Sm laser is plotted in figure 4 against the target length. The maximum length of single target used in the experiment was 20 mm. It is apparent that the coupling efficiency at the optimised separation was quite high due to the small deflection and divergence angles to be described in the following paragraph. For target plasmas with lengths < 18 mm, the increase in output intensity of the laser line is a simple exponential form. The gain coefficient was determined, by fitting the Linford formula to those data in the exponential region, to be 8.4±0.6 cm^{-1}. The output intensity no longer increases exponentially with target length for targets longer than 18 mm, which corresponds to a gain length product ~ 15, beyond which the output intensity only increases linearly and varies very little from shot to shot.

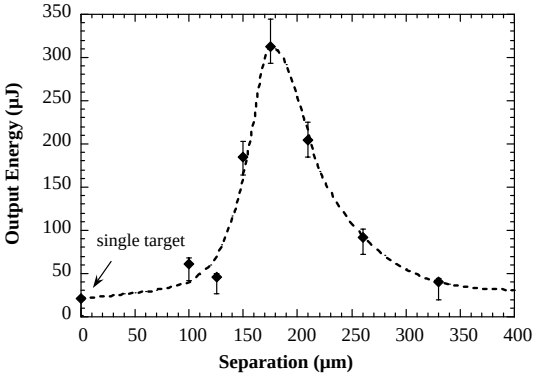

Figure 3. Output energy of the samarium X-ray laser versus the perpendicular separation between two opposing 18 mm long plasmas.

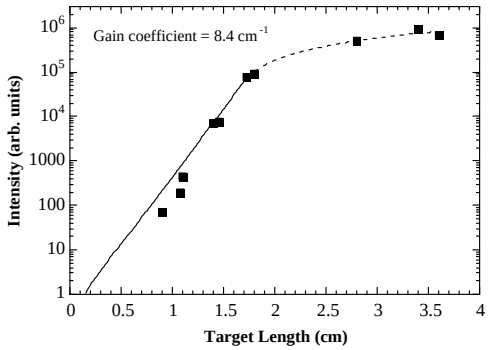

Figure 4. Peak intensities as a function of target length. The solid line shows exponential increase of the output intensity and the broken line shows the linear increase of the output intensity in the saturation region. Solid squares are from single target data and solid diamonds from coupled target shots. Saturation intensity is reached at an approximate gain-length product of 15.

Figure 5 presents streak images showing the temporal behaviour of the angular distribution perpendicular to the target surface of the Sm laser from a single flat target and a coupled double flat target with a separation of 175 µm. The grey levels of the two graphs were normalized to the same level to clearly show the distributions for the different target geometries. The peak emission from the double 18 mm target is about 10 times stronger than the emission from a single 18 mm long flat target. The laser emission from the single target has a broad divergence of 1.8 mrad and peaks at 2.5 mrad off-axis. This small divergence and deflection angles provide an evidence of much improved density gradient due to our special drive pulse configuration. This also resulted in the efficient coupling between the two targets. The laser emission lasts about 37 ps. This is one of the shortest-pulse X-ray lasers yet produced. By

comparison, the laser emission from a coupled double target shows a strong coupling effects both angularly and temporally. Its pulse duration is somewhat longer (49 ps) due to the contribution from two targets and its divergence is only 1.2 mrad, implying an ~ 5 µm spatial coherence length at the exit plane of the X-ray laser. The Sm X-ray laser beam from the double target is almost parallel to the target surface with a deflection angle as small as about 1 mrad. This is certainly an advantage to applications. The angular distribution of the Sm laser in the direction parallel to the target surface was also measured to spread over about 3.5 mrad and peaks at 2.0 mrad off-axis in the parallel direction. The angle of the peak intensity and divergence are influenced by refraction of the beam in the plasma. It is obvious that both deflection and divergence angles of the Sm laser (Fig. 5b) from a double target were compensated by the refraction compensating double target geometry. It should be noted that the pulse durations shown at right hand side are single scans through the angular peaks of the laser emission. The angularly integrated durations are about 10% longer. Similarly, the angular scans are single traces through the temporal peaks of the laser emission. The temporal integrated angular divergence are not very different from that measured by single traces.

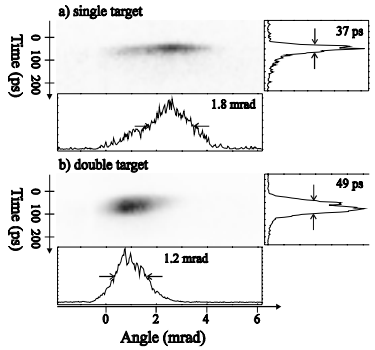

Figure 5. Typical X-ray streak images of angular distributions of the samarium laser line at 7.3 nm from single target, and a double flat target with a perpendicular separation of 175 µm. At the right hand side are the temporal traces. At the bottom are the angular traces.

Given our estimate of the upper limit of the source size (50 µm by 60 µm) from the knowledge of other similar X-ray lasers [11,21], the output intensity of the Sm laser was determined to be $2x10^{11}$ Wcm^{-2}. The estimated uncertainty in this measurement is less than a factor of 2. It is of interest to compare the output intensity with the saturated intensity calculated for typical plasma conditions using XRASER kinetic simulations [19]. The spontaneous emission rate of the upper laser level to the lower is calculated to be 0.35 ps^{-1}. Most of the upper level destruction rate is due to collisional mixing. The total destruction rate of the lower laser level is 4.5 ps^{-1}. In the simulations, typical plasma conditions for the samarium laser at 7.3 nm were used: an electron temperature of 700 eV, and an electron density of $1x10^{21}$ cm^{-3}. The saturated intensity is then calculated to be $1.3x10^{11}$ Wcm^{-2}, which agrees with the measured output. Taking into account the beam divergence (1.2 mrad by 3.5 mrad), a brightness of $2x10^{25}$ (photons·$s^{-1}mm^{-2}$ $mrad^{-2}$) is determined for the samarium laser at 7.3 nm. This is one of brightest X-ray lasers.

CONCLUSIONS

In conclusion, we have demonstrated the first saturated operation of an X-ray laser at wavelengths $\lambda < 10$ nm using only about $4.0x10^{13}$ Wcm^{-2} intensity on target, that is a focused intensity which can be achieved by many other smaller scale laser facilities. With the full ability of the VULCAN laser, saturated X-ray lasers at even shorter wavelengths near the water window would be possible and such an experiment has already been scheduled.

REFERENCES

1) R.C. Elton,
X-ray Lasers (Academic Press, New York, 1990).

2) J.E. Trebes et al.,
Science 238, 517 (1987).

3) L.B. Da Silva el al.,
Science, 258, 269 (1992).

4) D. Ress et al.,
Science, 265, 514 (1994).

5) R. Cauble et al.,
Science, 273, 1093 (1996).

6) D.H. Kalantar et al.,
Phys. Rev. Lett. 76, 3574 (1996).

7) A. Carillon et al.,
Phys. Rev. Lett. 68, 2917 (1992).

8) J.A. Koch et al.,
Phys. Rev. Lett. 68, 3291 (1992).

9) L.B. Da Silva et al.,
Opt. Lett. 18, 1174 (1993).

10) P. Jaegle et al.,
X-ray Lasers 1994, AIP Conf. Proc. 332, 25.

11) J. Zhang et al.,
Phys. Rev. A 54, R4653 (1996).

12) B.J. MacGowan et al.,
Phys. Fluids B 4, 2326 (1992).

13) C.L.S. Lewis et al.,
in X-ray Lasers 1992, E.E. Fill, Editor, IOP Publishing, Conf. Series No. 125, 23 (1992).

14) S. Basu et al.,
Appl. Phys. B 57, 303 (1993).

15) H. Daido et al.,
Phys. Rev. Lett. 75, 1074 (1995).

16) J. Nilsen and J.C. Moreno,
Opt. Lett. 20, 1387 (1995).

17) H. Daido et al.,
Opt. Lett. 21, 958 (1996).

18) Y. Li et al.,
Phys. Rev. A 53, R652 (1996).

19) J. Nilsen and J.C. Moreno,
Phys. Rev. Lett. 74, 337 (1995).

20) J. Zhang et al.,
Phys. Rev. A 53, 3640 (1996).

21) J. Zhang et al.,
Phys. Rev. Lett. 78, 3856 (1997).

22) G. Cairns et al.,
Appl. Physics B 58, 51 (1994).

23) J. Zhang et al.,
Phys. Rev. Lett. 74, 1335 (1995).

24) I. Weaver,
Ph.D. thesis, Queen's University of Belfast, Belfast (1996).

CHARACTERISATION OF A SATURATED X-RAY LASER AT 14 NM

J. Zhang[1)], A.G. MacPhee[2)], J. Nilsen[3)], J. Lin[4)], E. Wolfrum[1)], T.W. Barbee, Jr. [3)], C. Danson[5)], M.H. Key[3)], C.L.S. Lewis[2)], D. Neely[5)], R.M.N. O'Rourke[2)], G.J. Pert[6)], R. Smith[4)], G.J. Tallents[4)], J.S. Wark[1)]

1) Clarendon Laboratory, Department of Physics, University of Oxford, Oxford, OX1 3PU, UK
2) School of Mathematics and Physics, Queen's University of Belfast, Belfast, BT7 1NN, UK
3) Lawrence Livermore National Laboratory, Livermore, CA 94550, USA
4) Department of Physics, University of Essex, Colchester, CO4 3SQ, UK
5) Central Laser Facility, Rutherford Appleton Laboratory, Chilton, Oxon, OX11 0QX, UK
6) Department of Physics, University of York, York, YO1 5DD, UK

INTRODUCTION

Saturation has been observed in Ne-like x-ray lasers on the J = 2→1 transitions in plasmas of Ge [1)], Se [2)] and Y [3)] and on the J = 0→1 transition in Zn [4)], Ar [5)], Ge [6)] plasmas. Saturated operation is very important because it means that the maximum power possible for a given volume of excited plasma is extracted by the stimulated emission. Saturation also tends to produce an output energy sufficient for applications and ensures the production of a consistent output with little variation from shot to shot. Such saturated operation of x-ray lasers at shorter wavelengths are required for holography, microscopy, interferometry, radiography and many other applications [7-10)].

Although Ne-like x-ray lasers have shown large gains and gain length products, they are difficult to scale to the shorter wavelengths required for most applications, with the currently available laser driver energy. Ni-like x-ray lasers, in principle, work at much shorter wavelengths for the same amount of driver energy but have difficulties to provide saturated output. There have been significant achievements in developing Ni-like x-ray lasers at shorter wavelengths [11-17)]. A gain-length product of ~8 has been reported [14-16)] by using multi-pulse drive configurations. This, however, is still too low for saturated operation.

In the multi-pulse drive configuration, the first pulse heats and ionises the plasma but the density gradients are too steep for laser propagation. The plasma then expands creating a larger scale length plasma and produces a larger, more uniform gain region which allows for good laser propagation.

Aiming at improving efficiency and enhancing the gain-length product, we used a different drive pulse configuration compared to previous Ni-like experiments carried out by other groups [13-17)]. Since it is not necessary to have a pre-plasma in an ionisation stage as high as Ni-like, a low intensity (10% ~ 30% of total energy) laser pulse (prepulse) was used to create a preplasma with a lower ionisation. The preplasma was then allowed to cool down for a much longer time (> 2 ns), than those used in other experiments [13-17)], until it became not as transparent to the following laser pulse (main pulse) and the plasma region, where laser gain generates, can directly absorb more energy from the main laser pulse before it hits the critical density surface of the plasma. A larger separation (> 1 ns) between the prepulse and main pulse produces a larger gain region with lower gradients which allows for better propagation and therefore higher laser output [6)].

In this report, we present the first demonstration of saturation in a Ni-like x-ray laser, specifically, the Ni-like Ag laser at 14 nm from a refraction compensating double target.

EXPERIMENTAL SETUP

The experimental set-up is similar to that described in Ref. [6)]. Three beams of the VULCAN Nd:glass laser with a 75 ps duration at 1.05 μm were used in a standard off-axis focus geometry, which provide a line focus with 25 mm length and 200 μm width, giving an irradiance of ~ 20 TW·cm^{-2} on targets. Deploying the other three beams 180° opposed in a second line focus produced a plasma with an opposed density gradient which helps compensate for the refraction of the x-ray laser beam from the first plasma.

Flat slab targets used in the experiment were typically 18 mm long with 200 μm wide Ag stripes coated on the glass substrates. For some shots, targets with 20 or 22 mm length were used for gain measurements. Both ends of the slab target were placed well within the line focus to avoid cold plasmas at the ends of the targets. The targets were aligned so that they were parallel with an adjustable separation (in the direction perpendicular to the target surfaces) between the surface planes and an axial separation of 500 μm between the two targets. For some shots, curved targets with a 100-cm radius of curvature were used to make a comparison with the performance of flat slab targets.

Since the x-ray laser pulse duration is comparable to the propagation time, travelling wave excitation for the two successive targets is desirable to achieve maximum amplification. To approximate this condition, the three drive beams for the first slab target were therefore timed 60 ps earlier than the three beams for the second target.

The primary diagnostics along the target axis were two flat-field grazing incidence x-ray spectrometers with 1200 line/mm aperiodically ruled gratings [6)]. They recorded the spectral range from 5.0 nm to 30.0 nm on InstaSpec IV back-thinned soft x-ray CCD detectors (Oriel Instruments, Stratford, CT USA). Radiation at wavelengths shorter than 6.0 nm was eliminated by use of two parallel Ag mirrors at 10° grazing incidence angle. Si and C filters were used to provide variable attenuation and absorption edges for wavelength calibration. The axial spectra in a given axial direction were recorded in either of two ways.

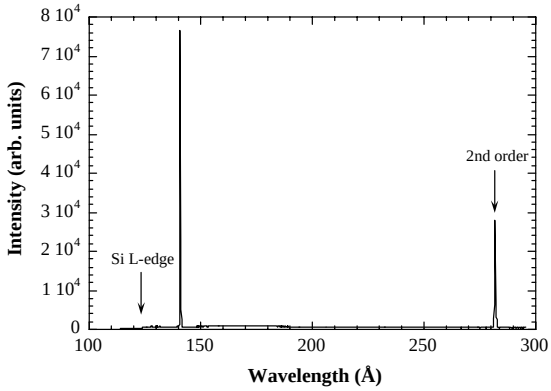

Figure 1. Axial spectrum from a 18 mm long single curved Ag target showing that the 14-nm laser line and its second order completely dominate the spectrum. The laser line has been attenuated by a factor of 100 to avoid saturation of the CCD detector.

Time averaged spectra with angular resolution were obtained using an x-ray CCD detector in the focal plane. Alternatively,

the Ag laser line at 14 nm was focused by the grating of an axial flat field spectrometer into the entrance of a streak camera so that the streak displayed the temporal variation of the angular distribution of the Ag laser line [1]. The laser line width was less than 50 µm at the streak entrance plane so the temporal resolution is limited by the streak camera operation to ~ 10 ps. A fibre-optic coupled CCD detector (Oriel Instruments) recorded the time-resolved angular distribution.

In order to measure the output energy and the spatial profile of the Ag x-ray laser, a near field imaging diagnostic [6,18,19] was used consisting of multilayer mirrors, Al and C filters and an x-ray CCD detector. The two mirrors had a combined measured peak reflectivity of about 20% at a central wavelength 14 nm with a Full Width at Half Maximum (FWHM) bandwidth around 1.5 nm. The concave multilayer mirror had 25 cm focal length and was positioned to image the output end of the Ag x-ray laser which was relayed off a 45° planar multilayer mirror onto the x-ray CCD detector at a magnification of 22X.

RESULTS

Fig. 1 shows the measured time integrated on-axis output spectrum from a 18 mm long single curved target. The output is completely dominated by the Ni-like Ag J = 0→1 laser transition at 14 nm and its second order. The intensity of the laser line was attenuated by a combination of Si and C filters by a factor of 100 to avoid saturation of the CCD detector. There are a few tenths of a nm uncertainty in the measured wavelength of the laser line. This line was predicted to be at 14.0 nm [20].

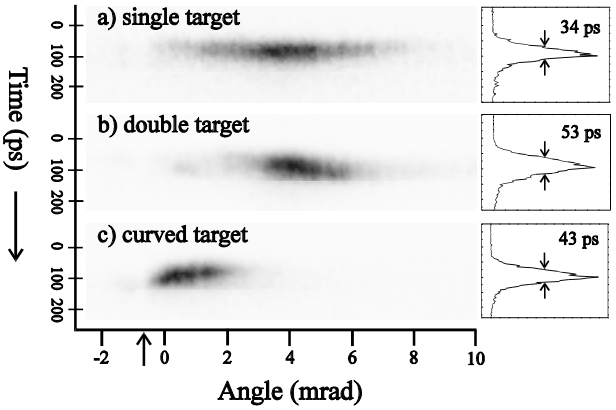

Figure 2. Typical x-ray streak images of angular distributions of the Ni-like Ag 14 nm laser line from a) a single flat target, b) a double flat target with a perpendicular separation of 150 µm, and c) a single curved target with 100-cm radius of curvature. At the right hand side are the temporal traces. The arrow at the bottom indicates the fiducial wire at - 0.5 mrad from the target surface.

Fig. 2 presents streak images showing the temporal behaviour of the angular distribution in the exit plane perpendicular to the target surface of the Ag laser from a single flat target, a coupled double flat target with an optimised separation of 150 µm and from a single curved target. The grey levels of the three graphs were normalised to the same level to show the angular and temporal distributions for the different target geometries. The peak emission from the double target is about 200 times stronger than the emission from a single flat target and about 80 times stronger than that from a curved target. The laser emission from the single target has a broad divergence of 3.4 mrad and peaks at 4.5 mrad off-axis. It lasts about 34 ps. By comparison, the laser emission from a coupled double target shows a strong coupling effect both angularly and temporally. Its pulse duration is somewhat longer due to the contribution from two targets and its divergence is 2.1 mrad. The emission from a curved target has the smallest divergence (~1.7 mrad) and peaks at only 0.8 mrad from the target surface. The pulse duration from the curved target is about 43 ps. It is apparent that the angle of the laser beam from the curved target sweeps in time towards the target surface. The angle of the peak intensity is influenced by refraction of the beam in the plasma. The pulse durations shown in Fig. 2 are a single scan through the angular peaks of the laser emission. The angularly integrated durations are somewhat longer.

The output intensity of the Ag laser is plotted in Fig. 3 against plasma length. For those single target plasmas with lengths < 22 mm, the increase in output intensity of the laser line is a simple exponential form. The gain coefficient was determined by fitting the Linford formula to those data in the exponential region, to be 7.2±0.4 cm^{-1}. The output intensity no longer increases exponentially with the plasma length for targets longer than 22 mm, beyond which the gain-length product is greater than 16 and the output intensity increases linearly and varies little from shot to shot.

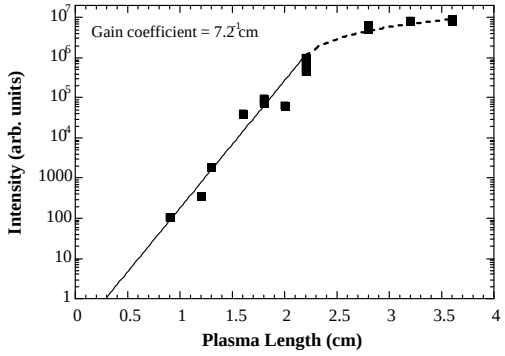

Figure 3. Peak intensity as a function of plasma length. The solid line shows exponential increase of the output intensity and the broken line shows the linear increase in the saturation region. Saturation is reached at an approximate gain-length product of 16.

Images of the spatial distribution of the Ag laser at the output aperture of the Ag laser from single, double and curved slab targets were recorded to study the laser output pattern and mode structure. The characteristics at the near field of a single flat target and double flat target were similar to those observed at near field of the Ne-like Ge J = 0→1 laser [6]. The output aperture of the Ag laser from a curved target was, however, smaller. Fig. 4 shows the near field image from a double flat Ag target with a perpendicular separation of 150 µm. The horizontal axis in the figure is the expansion direction perpendicular to the target surface and the vertical axis parallel to the target surface. The VULCAN laser beams are incident from left and right respectively on the two targets, with the line foci along the line of sight (out of the page). The target surface position was determined using the peak of the thermal emission from the target surface. The individual contributions from both targets are visible at the left and bottom part of the image. Most of the energy is concentrated in the coupled region. The FWHM extent in the transverse direction is about 43 µm. In the perpendicular direction, there is much structure in the laser pattern. The beam pattern peaks in the region around 150 µm from the target surface.

Since the collection solid angle of the multilayer mirror system overfills the angular distribution of the Ag laser beam, the output intensity can be estimated by integrating the total photons emitted from the output aperture and using an absolute calibration for the CCD detector, the calibrations for the x-ray multilayer mirrors, filters and the measured angularly integrated x-ray laser pulse duration. The output intensity of the Ag laser for an optimised separation (150 µm) between the two targets was estimated to be ~ 90 µJ, corresponding to a conversion

efficiency of $6x10^{-7}$, which is the highest efficiency achieved for Ni-like x-ray lasers. The maximum intensity of the Ag laser is about 69 GW·cm^{-2}. The estimated uncertainty in this measurement is a factor of 1.5 and is due predominantly to uncertainty in the filter attenuation. Given our best estimates of the source size (43x57 μm^2), and the beam divergence (1.5 mrad perpendicular by 3.5 mrad parallel), a brightness of $1.1x10^{25}$ photons·s^{-1}·mm^{-2} ·mrad^{-2} is calculated.

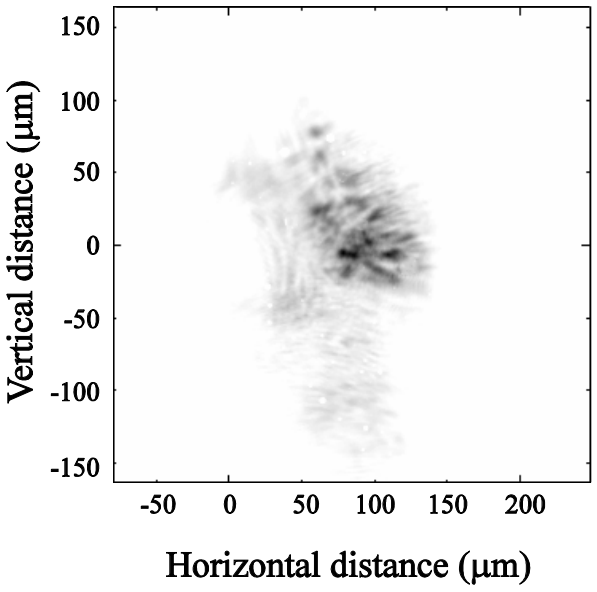

Figure 4. The end-on view of the Ni-like Ag x-ray laser from a coupled double target with a separation of 150 μm. The zero position on the horizontal axis is the target surface while the zero position on the vertical axis shows the centre of the line focus on the target.

It is of interest to compare the output intensity of the Ag laser with the saturated intensity estimated from the Einstein relations between spontaneous and stimulated emission [3,6]. The decay rate of the upper laser level is calculated from XRASER [21] kinetic simulations to be 6.31 ps^{-1} and the spontaneous emission rate of the upper laser level to the lower is 0.215 ps^{-1}. Most of the upper level destruction rate is due to collisional mixing. The total destruction rate of the lower laser level is 7.46 ps^{-1}. In the simulations, typical plasma conditions for the Ag laser were used: an electron temperature of 700 eV, and an electron density of $5.7x10^{20}$ cm^{-3}. The saturated intensity is then calculated to be 28 GW·cm^{-2}, which is about one third of the measured value. It should be noted that the saturation intensity is not an upper bound on the output but just the starting point at which the energy extraction becomes efficient for the laser operation.

CONCLUSIONS

In conclusion, we have demonstrated the first saturated Ni-like x-ray laser using only about 20 TW cm^{-2} intensity on targets, that is a focused intensity which can be achieved by many other smaller scale laser facilities. The narrow divergence, short pulse duration, high efficiency and high brightness of the Ag laser make it an ideal candidate for many x-ray laser applications. Using the available energies of the VULCAN laser on a narrower line focus, saturated output in Ni-like x-ray lasers can be achieved at much shorter wavelengths. This is an important step towards saturated operation of x-ray lasers at the water window.

ACKNOWLEDGEMENTS

We gratefully acknowledge the support from VULCAN Laser operation and target preparation groups.

REFERENCES

1) A Carillon, et al,
Phys Rev Lett 68, 2917 (1992)

2) J A Koch, et al.,
Phys Rev Lett. 68, 3291 (1992)

3) L B Da Silva, et al,
Opt Lett 18, 1174 (1993)

4) P Jaegle, et al,
X-ray Lasers 1994, AIP Conf Proc 332, 25

5) J J Rocca, et al,
Phys Rev Lett 77, 1476 (1996)

6) J Zhang, et al,
Phys Rev A 54, R4653 (1996)

7) J E Trebes, et al,
Science 238, 517 (1987)

8) L B Da Silva, et al,
Phys Rev Lett 74, 3991 (1995)

9) D H Kalantar, et al,
Phys Rev Lett 76, 3574 (1996)

10) A S Wan, et al,
Soft X-ray Lasers and Applications, Proc Soc Photo-Opt Instrum Eng 2550, 268 (1995)

11) B J MacGowan, et al,
Phys Fluids B 4, 2326 (1992)

12) C L S Lewis, et al,
X-ray Lasers 1992, E E Fill, Editor, IOP Publishing, Conference Series No 125, 23 (1992)

13) S Basu, et al,
Appl Phys B 57, 303 (1993)

14) H Daido, et al,
Phys Rev Lett 75, 1074 (1995)

15) J Nilsen and C Moreno,
Opt Lett 20, 1387 (1995)

16) H Daido, et al,
Opt Lett 21, 958 (1996)

17) Y Li, et al,
Phys Rev A 53, R652 (1996)

18) G Cairns, et al,
Appl Physics B 58, 51 (1994)

19) J Zhang, et al,
Phys Rev Lett 74, 1335 (1995)

20) J H Scofield and B J MacGowan,
Physica Scripta 46, 361 (1992)

21) J Nilsen,
Radiative-Hydro Modeling and Atomic Data Bases, edited by Allan Hauer and A L Merts, AIP Conf Proc No 168 (American Institute of Physics, New York, 1988)

MEASUREMENT OF X-RAY SPECTRUM FROM SOLID TARGETS AT HIGH INTENSITY, PICOSECOND LASER

F.N.Beg[1] , A.R. Bell[1], A.E.Dangor[1], A.P. Fews[2], P. Lee[1],P. Norreys[3] and M. Tatarakis[1]

1). Blackett Laboratory, Imperial College, London SW7 2BZ, UK.
2). H. H. Wills Physics Laboratory, University of Bristol, Royal Fort, Bristol, UK.
3) Central Laser Facility, Rutherford Appleton Laboratory, Chilton, Oxon OX11 0QX, UK.

INTRODUCTION

The development of the technique of chirped pulse amplification (CPA) has enabled high power lasers to produce multi-terrawatt femtosecond and picosecond laser pulses which can be focused at intensities that were previously inaccessible. Many new interesting physical phenomena are predicted in this regime. It has been demonstrated that x-rays in MeV can be produced using short pulse lasers[1) 2)]. Hard x-rays are produced by the fast electrons moving into the solid target. Recently, Malka and Miquel[3)] have shown that the electron temperature is dominated by the ponderomotive potential for those electrons directed along the axis of the laser beam and temperatures of 1 MeV have been measured.

Conversion to fast electrons with pico and sub picosecond pulses is due to non linear processes like vacuum heating or resonance absorption (see review by P. Gibbon[4)]). Absorption of >10% of the laser energy into fast electrons has been reported by many workers [5) 6)]. Schnurer *et al.*[6)] measured hard x-rays in the range of 100 keV from solid targets with ps laser pulses up to 7 x 10^{17} Wcm^{-2}. The x-ray data above 50 keV scales as $i_x \propto I_L^{2.8}$. Kmetec *et al.*[1)] showed that the detected x-ray yield increases as $E^{3/2}$ at the laser intensities of 10^{18} Wcm^{-2}, where E is the laser energy. In this experiment, it was also found that the x-ray yield is proportional to the target atomic number and the spectral distribution of x-rays was not found to depend on atomic number. Beg et al.[2)] measured the x-ray energies exceeding 10 MeV range at 5 x 10^{18} Wcm^{-2}.

EXPERIMENTAL SETUP

The experiments used CPA beam-line of the VULCAN Nd:glass laser . This laser delivered pulses on target of up to 30 J with pulse lengths ranging from 700 fsec to 1.3 psec. A 95% turning mirror located after the recompression gratings was used to steer the beam onto an f/4.2, 44 cm focal length off axis parabolic mirror onto target. A turning mirror allowed 5% transmission of the laser energy for measurements of the laser spectrum, the pulse duration by a single shot autocorrelator and the focal spot quality by an equivalent plane monitor. The contrast ratio was measured by a third order auto-correlator to be 10^{-6}.

The p-polarised laser light was focused at an angle of 30^o to the normal. Figure 1 shows a schematic of the target chamber in the horizontal plane and the principle diagnostics that were employed. Different target material viz., CH, CD, Mg, Cu, Mo. Pd, Sn and Ta were used but the results presented here are only from plastic targets.

The x-ray bremsstrahlung radiation from the target was measured with an array of eight filtered PIN diodes together with four photomultiplier/scintillator detectors. In addition to this filtered fibre dosimeter were also used. To eliminate bremsstrahlung radiation from energetic electrons and ions impinging on the wall of the chamber,

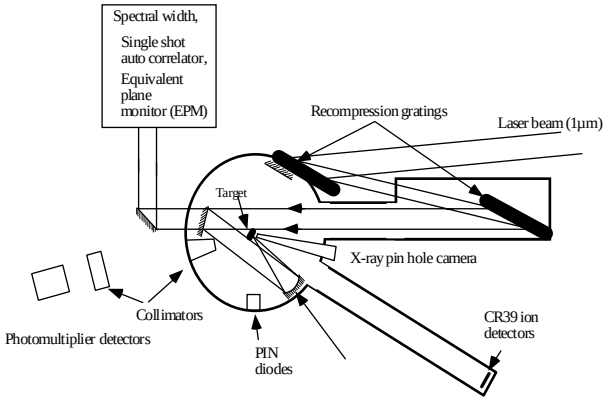

Figure1. Schematic layout of the target chamber.

collimating apertures for each scintillator/pmt were placed 20 cm from the target inside the vacuum chamber. These consisted of 1.0 cm holes drilled through 20 cm of lead angled to point the target at 4^o. The photomultipliers (XP 2008) were located 3.0 m from the target encased in 10 cm thick lead blocks with four 1.0 cm holes (angled to the target) and aligned with the collimating apertures in the vacuum chamber. The pmt detectors were filtered with a variety of materials viz. 1 to 50 mm lead, 50 and 100 mm stainless steel and 1 mm tantalum. To eliminate fluorescence from g-ray traversing the filters, 1.0 cm thick Al blocks were placed behind the filters. Two photomultipiers were fitted with NaI(Tl) crystals of diameter 2.54 cm and length 5 cm . Other two had plastic NE102A scintillate 10 mm thick and 30 mm diameter. For some shots, 1 mm NE102A scintillator was also used which is sensitive to relatively lower energies. On one photomultiplier 50 mm lead filter was used for all the shots to observe shot-to-shot variation. The calibration of the detectors as positioned in the experiment was not possible due to safety problems. So scint./photomultipliers were calibrated by placing g-ray source in front of each detectors with a 1.25 MeV ^{60}Co and a 665 keV ^{137}Cs source.

Filter Pair	Peak Energy (keV)	Energy Window (keV)
1) 10 μm Cu+20 μm Al 2) 37 μm Ti+20 μm Al	8	6 to 9
1) 2 mm Al 2) 250 μm Cu+1 mm Al	14	9 to 20
1) 250 μm Cu+1mm Al 2) 1 mm Cu+1 mm Al	42	28 to 60
1) 250 μm Ta+100 μm Al 2) 1 mm Ta+100 μm Al	67	55 to 250

Table 1. X-ray filters for PIN diodes.

Each of the eight Quantrad PIN diodes with a 100 mm^2 active area was biased to -300V. These were placed at 40 cm from the target. The active layer varied in thickness from 125 µm to 500 µm to increase the sensitivity of the detectors to higher x-ray energy. The response time of diodes is limited by the capacitance and the mobility of the charge carriers to ns time scale. The calibration of each detector was obtained from the manufactures data. The PIN diodes were also cross calibrated. These were checked with work of Corallo *et al.* [7]. The filters were defined to chose energy window. A 1 mm aperture was used for softer filter PIN diodes and 5 mm aperture for harder filter PIN diodes. Table 1 shows the x-ray filters used for the PIN diodes and the energy range measured.

EXPERIMENTAL RESULTS

Figure 2 shows a plot of x-ray spectrum obtained from the PIN diodes and scintillator/pmt combination. The spectrum plotted in figure 2 is the result of a number of shots at intensity 5.0±(3.0) x 10^{18} Wcm^{-2} for plastic targets. The spectrum suggests the presence of at least two electron temperatures. The curve fit through first three points in figure 2 suggests an electron temperature of 1-3 keV. A fit through last three points indicates an electron temperature of 300-400 keV. But this is a lower limit of temperature due to the lack of spectral resolution of the detectors at higher intensities.

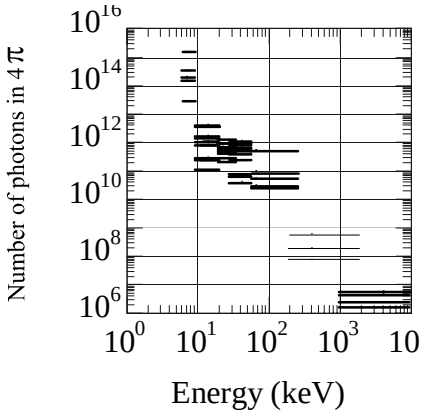

Figure 2. X-ray spectrum for CD and CH targets at an average intensity 5 x 10^{18} Wcm^{-2}.

Figure 3 shows the hot electron temperature vs the intensity on the target. A curve fit to data points shows a scaling of $T_{hot} \alpha (I\lambda^2)^{0.35\pm0.1}$.

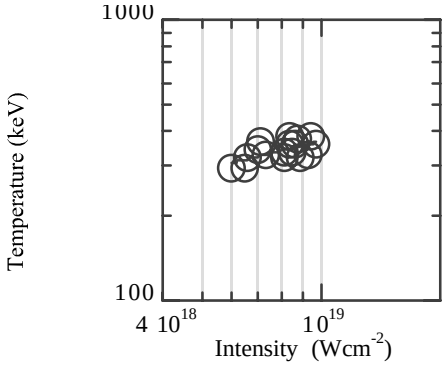

Figure 3. Electron temperature vs the incident intensity on the target.

This scaling is similar to the results obtained by Gitomer et al.[8] from the compiled data observed at a number of different laboratories. Our experimental results follows the curve fit as shown in figure 4 and are consistent with an extrapolation to higher values of $I\lambda^2$. It is interesting to note that the measurements shown by Gitomer et al. [8] are for long laser pulse lengths. In our experiment, the error bars in the intensity scaling make it difficult to distinguish between the resonance absorption and vacuum heating which are $T_{hot} \sim I^{0.3}$ and $T_{hot} \sim I^{0.5}$ respectively. However, the absolute value of the hot electron temperature T_{hot} ~ 400 keV at 10^{19} Wcm^{-2} suggests that resonance absorption is a dominant mechanism because much higher temperature is needed for the vacuum heating [3].

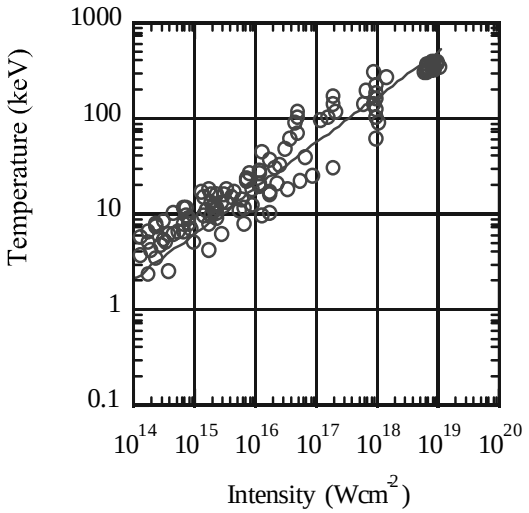

Figure 4. The x-ray determined temperature vs $I\lambda^2$.[8]. The temperature at the higher irradiance is from our experimental data.

REFERENCES

1) J. D. Kmetec et al
Phys. Rev. Lett. 68, 1527 (1992).

2) F. N. Beg et al
Phys of Plasmas 4, 453 (1997).

3) G. Malka and J. L. Miquel
Phys. Rev. Lett. 77, 75 (1996).

4) P. Gibbon and E. Forster
Plasma Phys. Controlled Fusion 38, 769 (1996).

5) D.D. Meyerhofer et al
Phys. Fluids B5, 2584 (1993).

6) M. Schnurer et al
Phys. of Plasmas 2, 3106 (1995).

7) D. M. Corallo et al
J. Phys. E: Sci. Instrum. 13, 623 (1980).

8) Gitomer et al
Phys. Fluids 29, 2681(1986).

SELF-CHANNELLING OF LASER PULSES AT RELATIVISTIC INTENSITIES IN PREIONIZED PLASMAS

M.Borghesi[1)], A.J.Mackinnon[1)], L.Barringer[1)], R.Gaillard[1)], L.Gizzi[2)], C.Meyer[1)], O.Willi[1)], A.Pukhov[3)], J.Meyer-ter-Vehn[3)]

1) The Blackett Laboratory, Imperial College of Science Technology and Medicine, London
2) Istituto di Fisica Atomica e Molecolare - CNR (Pisa), Italy
3) Max-Planck-Institut für Quantenoptik, Garching (Germany)

INTRODUCTION

The study of the interaction of intense laser pulses with plasmas is relevant for applications such as particle acceleration by plasma waves[1)] and the fast ignitor scheme[2)] for Inertial Confinement Fusion. These applications require the pulse to propagate over several Rayleigh lengths without considerable energy loss. For sufficiently powerful, spatially uniform laser pulses, self-guiding of the pulse can be achieved due to relativistic effects[3)]. Indeed, channelled propagation at relativistic intensities through initially neutral gases has been already observed in various experiments[4)], while observations of relativistic channelling in pre-ionised plasmas of near critical density, particularly relevant for fast ignitor applications, have been reported only recently[5)]. In particular, for laser pulses far above the threshold for relativistic filamentation, three-dimensional particle-in-cell (3D PIC)[6)] predicted the formation of a narrow, single propagation channel. The simulations revealed the importance of relativistic electrons travelling with the light pulse and generating multi-megagauss magnetic fields that pinch the electrons.

Here we report about a series of experiments performed at the Rutherford Appleton Laboratory to study the relativistic channelling of ultra-intense picoseconds pulses in pre-ionised plasmas[7)]. Some of the data here discussed have been already presented in last year's RAL annual report[8)].

EXPERIMENTAL SET-UP

The experiment was performed using the Vulcan Nd:glass laser in the chirped pulse amplification (CPA) mode. The targets were plastic (CH or Formvar) films with a thickness between 100 and 500 nm. The plasma was preformed by a 400 ps pulse, frequency doubled in a KDP crystal to λ=0.527 μm, which was focused onto target, in a spot between 200 and 300 μm in diameter, at an irradiance below 10^{13} W/cm^2. A 1.054 μm CPA interaction pulse of 1-3 ps in duration was focused into the preformed plasma. Both the heating and the interaction pulse were focused onto target by the same F/4.5 off-axis parabola (OAP). The green heating beam was injected into the short pulse beamline through the back of the last turning mirror before the OAP. A small divergence was imposed on the heating beam before the interaction chamber by a telescope in order to obtain a larger focal spot. The beam was focused in a 12 - 15 μm full width at half maximum (FWHM) focal spot. With an average interaction power of 10 TW, an incident irradiance between 3 and 9x10^{18} W/cm^2 was obtained. The delay between heating and interaction pulses was varied, allowing interaction with the plasma at different stages of its evolution. The plasma was diagnosed with a temporally independent probe pulse which was split-off from the uncompressed interaction beam. The probe beam was compressed by a pair of gratings and frequency doubled in a KDP crystal resulting in a probe wavelength of 0.527 μm and a pulse duration of a few picoseconds. The spatial resolution determined by the optical system was around 2 - 3 μm. Time resolved density maps of the plasma (limited to densities lower than 10^{20}/cm^3 due to refraction) were obtained with a Nomarski modified interferometer. The optical emission from the plasma was also imaged, in a direction transverse to the propagation axis. The magnetic fields generated in the plasma during the interaction were measured using a time-resolved polarimetric technique. For these measurements, particularly sensible to emission noise, the probe wavelength was Raman-shifted to λ=620 nm. Also, spectra of the backscattered radiation were collected with an optical grating spectrometer, using a 1200 lines/mm grating (linear dispersion 15 Å/mm).

EXPERIMENTAL RESULTS AND SIMULATIONS

Self-channelling of the CPA pulse appeared to be a typical feature of the interaction in the investigated experimental conditions and was detected via optical probe measurements. In fig.1 the spatially resolved second harmonic radiation emitted during the interaction of a 10 TW pulse with the preformed plasma is shown. The measured density profile is also presented (1-D simulations predict that the plasma is fully ionised, with a peak density of about 5x10^{20}/cm^3). The channel-like emission is time-integrated and is due to second harmonic (2ω) light emitted during the interaction, produced via non-linear processes in correspondence with the large density and intensity gradients present inside the channel. It can therefore be interpreted as a signature of the spatial extent of the interaction beam in the plasma. The average diameter of the channel is about 5 μm and its length about 130 μm. The channel changes in size periodically over distances of 15 - 20 μm with the transverse dimension varying within a few microns. From comparison with the preformed plasma profile, it can be seen that the laser pulse focuses down to 5 μm in size at a density of around 0.05 times the critical density n_c (n_c~1x10^{21}cm^{-3} for λ=1 μm). It should also be noted that the laser power was about 25 times the threshold power for relativistic self-focusing, $P_{th}=17\omega^2/\omega_p^2 \approx 0.4$ TW at this density.

Evidence of channelling was also obtained from interferometric measurements. The interferogram of fig.2 was taken at about 5 ps after the interaction (the preformed plasma density profile is also shown). A front (due to the shock wave expanding in the preformed plasma) produced by the short pulse while focusing down into the channel is clearly visible.

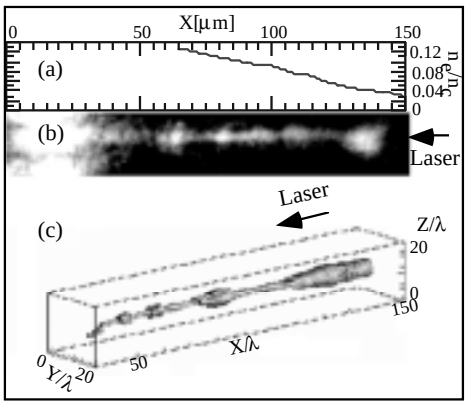

Fig.1. Channelling of a ps, 1.054 mm, 10 TW pulse during propagation through a preformed plasma: (a) preformed plasma density; (b) second harmonic emission channel; (c) 3-D PIC simulation: a perspective snapshot of the self-focusing pulse after 150 laser cycles (i.e. about 0.5 ps); the plotted surface corresponds to 67% of the cycle-averaged maximum intensity $<I_{max}>$. X is the distance from the original target position.

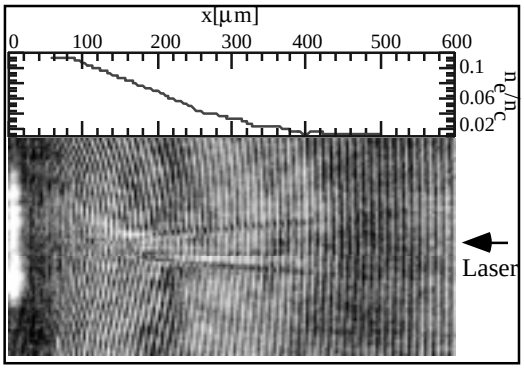

Fig.2. Interferogram taken 5 ps after the interaction of a 1.5 ps, 10 TW pulse with a preformed plasma. The density profile of the preformed plasma is also shown.

The laser pulse appears to be focused with an F/4.5 cone up to a background density of approximately 0.07 n_C at a distance of about 200 mm from the original target position. Beyond that density, it self-focuses into the channel. The experiment has been simulated with the 3D PIC code VLPL (Virtual Laser Plasma Laboratory), recently developed at the Max Planck Institute (Garching) for massive parallel processing (MPP). The simulation results are presented in figs. 1(c) and 3. The intensity distribution $<I>$ is shown in fig.1(c) for a time close to the peak of the pulse. After an initial unstable phase, the incident beam self-focuses into a narrow single channel at a density of about 0.07 n_C, according to the process described in ref.6. The channel width pulsates as the pulse defocuses and refocuses with a characteristic period of 15 -30 l. The maximum intensity $<I_{max}>$ varies accordingly with peaks up to 10 I_0. These results closely reproduce the experimental observations. The channel of fig.1(c) is further analysed in fig.3 by plotting the electron density for a Y,Z cross-section at $X = 80\ l$ and also as a line profile, normalised to the critical density n_C. One observes that electrons are expelled from the channel region and form a radially outgoing shock. An important feature governing the channel dynamics are currents of relativistic electrons travelling with the light beam and generating quasi-stationary magnetic fields[6]. The relativistic electrons modify the index of refraction n_r in the neighbourhood of the channel.

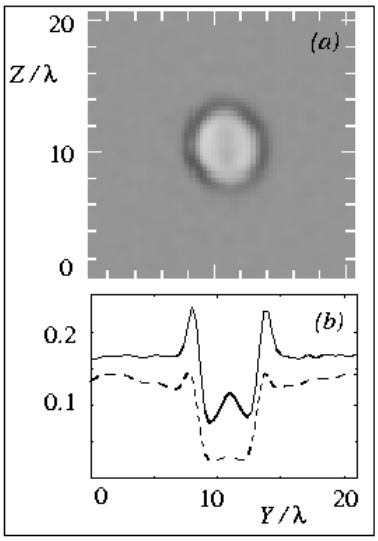

Fig.3. 3-D PIC simulation: electron density in units of the critical density n_C for Y,Z plane at $X=80\lambda$, after 150 laser cycles: a) 2D plot using linear grey scale; b) cut through centre in Y direction: n_e/n_C (solid line), $n_e<\gamma^{-1}>/n_C$ (dashed line).

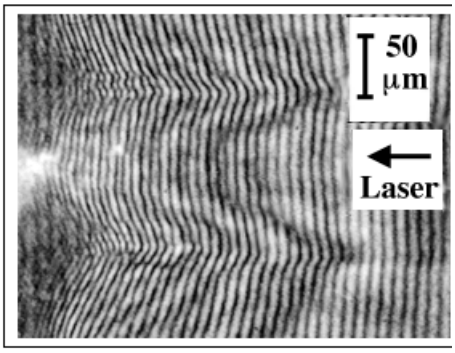

Fig.4. Interferogram recorded 65 ps after the interactic

This can be seen in fig.3, where the quantity $n_e<\gamma^{-1}>/n_C = 1 - n_r^2$ is plotted as a dashed line (the factor $<\gamma^{-1}>$, locally averaged, accounts for the mass increase). A "relativistic valley" has formed, about 20 λ wide. At its centre, a deeper density depression is produced by both electron expulsion and relativistic effects, and most of the light is guided into it.

The main feature observed in the 2ω backscattered spectra was a red-shifted broadening typically up to 40-50 nm. The broadening of the 2ω spectra can be explained as a Self Phase Modulation effect in the context of the channelling assumption discussed above. During the channel formation, the pulse travels through a medium in which the refractive index is rapidly varying. As a consequence, its phase is modulated. Since the derivative of the refractive index stays positive during the pulse propagation, the broadening is on the red side of the spectrum. The order of magnitude of the broadening expected, $\Delta\lambda/\lambda$, can be estimated supposing that the pulse propagates, during the channel formation, in an initially uniform plasma : $\Delta\lambda/\lambda \approx L\Delta n_r/(c\tau)$, where L is the length of the channel, Δn_r the maximum variation of refractive index, c the speed of light, τ the cavitation time. Using parameters close to the experimental ones, such as L=130 μm, τ=0.5 ps, Δn_r=0.07 (as in fig.3(b)) and λ=0.5 μm, one obtains Δλ≈30 nm, which is of the same order of magnitude of the measured broadenings.

After the pulse has traversed the plasma, the channel boundaries quickly expands. In fig.4 an interferogram of the channel after 65 ps is shown, when it has expanded to a radius of about 60 μm. At this time the density inside the channel is still about 40% of the background density. The temporal evolution of the channel size is shown in fig.5.

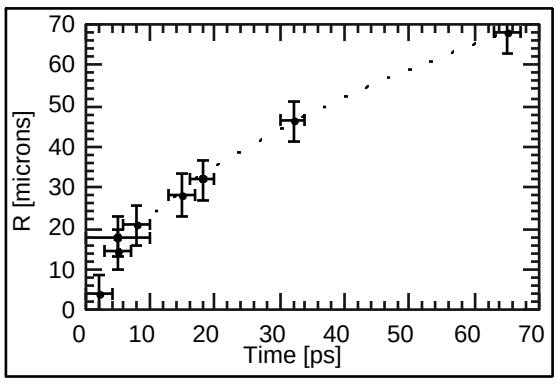

Fig.5. Temporal evolution of the channel radius (solid circles). The dashed line represents the best fit using a function proportional to $t^{1/2}$, while the empty squares represent the spatial extent of the inner Faraday rotation patterns in the polarigrams in fig.6.

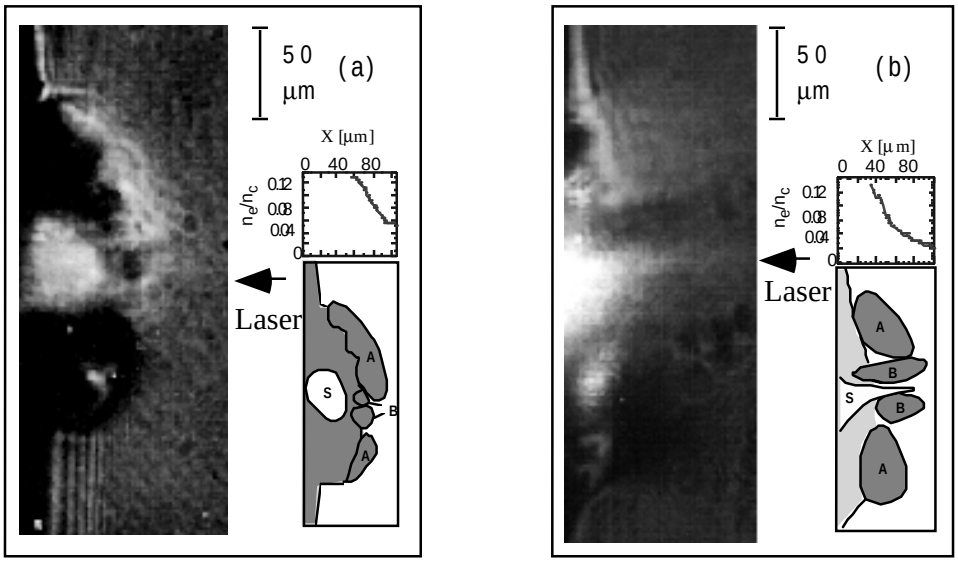

Fig.6. Polarigrams taken: (a) during the interaction of a 3 ps , 8 TW pulse, with the preformed plasma (probe duration Å 5 ps, with a maximum timing error of 8-10 ps); (b) 18 ps after the interaction of a 1.5 ps, 10 TW pulse with the preformed plasma (probe duration 2 ps , timing precision comparable with the probe pulse duration). The preformed plasma density profiles are also shown in the figure. In the sketches the outer dark-bright pattern are indicated with "A", the inner dark-bright pattern with "B" and the self-emission with "S".

The channel boundaries move out with an initial speed of about 5 10^8 cm/s, and expand with time following a $t^{1/2}$ dependence, as predicted from shock waves theory.

An important issue also investigated during the experiment was the generation of magnetic fields in the plasma as a consequence of the interaction (see also ref.9). The polarigrams shown in fig.6 were taken respectively during and 18 ps after the interaction, in two separate experiments. The Faraday rotation patterns detected show that two different types of toroidal fields are generated in the plasma as a consequence of the interaction. A "dark-bright " pattern (brighter than the background above the laser axis, darker below) is visible in the outer region of the plasma, as indicated in the figure. Another similar rotation pattern, but reverted with respect to the outer one, is visible close to the laser axis. While the outer rotation corresponds to a B-field directed as conventional thermoelectric field, the inner pattern corresponds to a toroidal field of opposite direction, with an amplitude that can be estimated to be in the range 1-10 MG [9], and consistent with the generation mechanism described in ref.6-7, i.e. with a current of fast electrons travelling on axis together with the laser pulse, and spatially separated return currents. During the expansion this field appears to stay confined within the expanding channel walls and affects the plasma behaviour, as it has been observed experimentally. In the interferogram of fig.7, taken 5 ps after the interaction, a density spike on axis, at the centre of the expanding channel suggested (as also observed in combined PIC + Magneto-hydrodynamic simulations[9]) that, within the shot-to-shot variability of the plasma conditions, the magnetic pressure may dominate over the thermal pressure in the region where the B-field peaks, and pinch the plasma on axis.

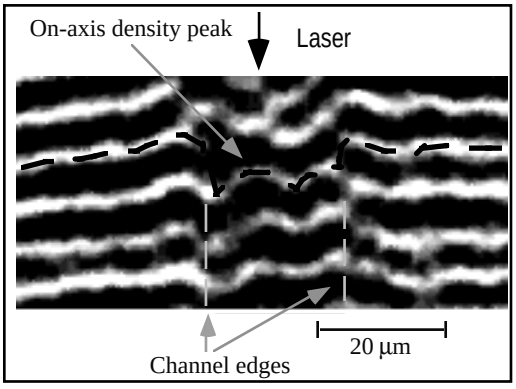

Fig.7 Interferogram taken 5 ps after the interaction. A fringe shift at the centre of the channel, corresponding to a density spike, is clearly visible.

CONCLUSION

The results of a series of experiment performed using the CPA Vulcan pulses indicate that the propagation of pulses at relativistic intensity through pre-ionised plasmas is characterised by relativistic self-channelling. This phenomenon was detected using optical probing diagnostics, and modelled using 3-D PIC simulations, that closely reproduced the experimental results and contributed to the understanding of the complex interaction scenario.

REFERENCES

1) E.Esarey *et al.*
IEEE Trans. Plasma Sci. 24, 252 (1996)

2) M. Tabak *et al.*
Phys. Plasmas 1, 1621 (1994)

3) P. Sprangle and E. Esarey
Phys. Fluids B 4, 2241 (1992)

4) A.B.Borisov *et al*
Phys. Rev. Lett. 68, 2309 (1992); P.Monot *et al.*, Phys. Rev. Lett. 74, 2953 (1995)

5) P.E.Young and P.R.Bolton
Phys. Rev. Lett., 77, 4556 (1996)

6) A. Pukhov and J. Meyer ter Veh
Phys. Rev. Lett. 76, 3975 (1996)

7) M.Borghesi *et al*
Phys. Rev. Lett. 78, 879 (1997)

8) M.Borghesi *et al*
Rutherford Appleton Laboratory Annual Report 1995-1996, RAL-TR-96-076, p.16 (1997)

9) M.Borghesi *et a*
in preparation (1997)

SELF-GENERATED MAGNETIC FIELDS IN ULTRAINTENSE LASER INTERACTION WITH SOLID TARGETS

M.Borghesi, A.J.Mackinnon, A.R.Bell, R.Gaillard, O.Willi

The Blackett Laboratory, Imperial College of Science Technology and Medicine, London

INTRODUCTION

A number of mechanisms can be responsible for the generation of large spontaneous magnetic fields during the interaction of a powerful laser pulse with a solid target[1)]. Up to now, experimental measurements of fields (up to about 1 MG) have been obtained with laser pulses ranging from a few tens of picoseconds[2)] to nanoseconds[3)], using optical Faraday rotation probing (*polarimetry*). Due to the availability of novel laser systems and their exciting applications , the attention of the scientific community has recently focused on the study of the interaction of ultra-intense picosecond and subpicosecond pulses with plasmas. In particular, the fast ignitor scheme for Inertial Confinement Fusion has generated great interest in the study of magnetic fields in short-pulse interactions, and particularly of their effects on the pulse propagation. Magnetic field generation in ultraintense interactions have hence been investigated through analytical and computational studies[4)], that predict very large fields, up to hundreds of MG in the overdense region of an irradiated solid target.

This report presents measurements of magnetic fields resulting from the interaction of a picosecond laser pulse with Al solid targets[5)], at irradiances exceeding 5 10^{18} W/cm^2.

EXPERIMENTAL SET-UP

The experiment was performed using the Vulcan Nd:glass laser operating in the Chirped Pulse Amplification mode (CPA). The experimental set-up is shown in fig.1. The targets were Al foils with a thickness of about 25 μm. The 1.054 μm CPA interaction pulse, about 1.5 ps in duration, was focused onto target by an F/4.5 off-axis parabola (OAP), in a 12 - 15 μm full width at half maximum (FWHM) focal spot, at an incident irradiance between 5 and 9x10^{18} W/cm^2. The plasma was diagnosed with a temporally independent

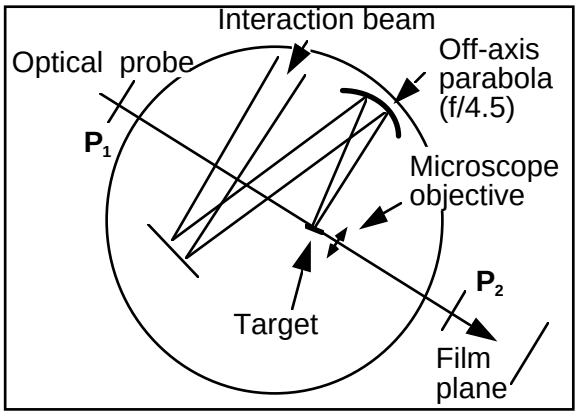

Fig.1. Experimental set-up

probe pulse which was split off from the uncompressed interaction beam. The probe beam was recompressed by a pair of gratings and frequency doubled in a KDP crystal resulting in a probe wavelength of 0.527 μm and a pulse duration of the order of a picosecond. A microscope objective, with an F-number of 4, imaged the plasma onto photographic film, with a magnification of about 45 and a spatial resolution of about 2 - 3 μm . A polarimetric Faraday rotation technique[1)] was used to detect the magnetic fields present in the plasma. For these measurements, in order to reduce the emission noise on film, the probe beam was Raman shifted in ethanol, to a wavelength λ=0.622 μm. The probe beam, linearly polarised by a polariser P1, was incident on the plasma in a direction transverse to the interaction beam axis (i.e. parallel to the target surface). A second polariser P2 was used after the imaging lens as an analyser (see also ref.6). The density profiles of the plasma, necessary to extract the magnetic field amplitude from the polarigrams, were obtained in separate measurements with a Nomarski modified interferometer.

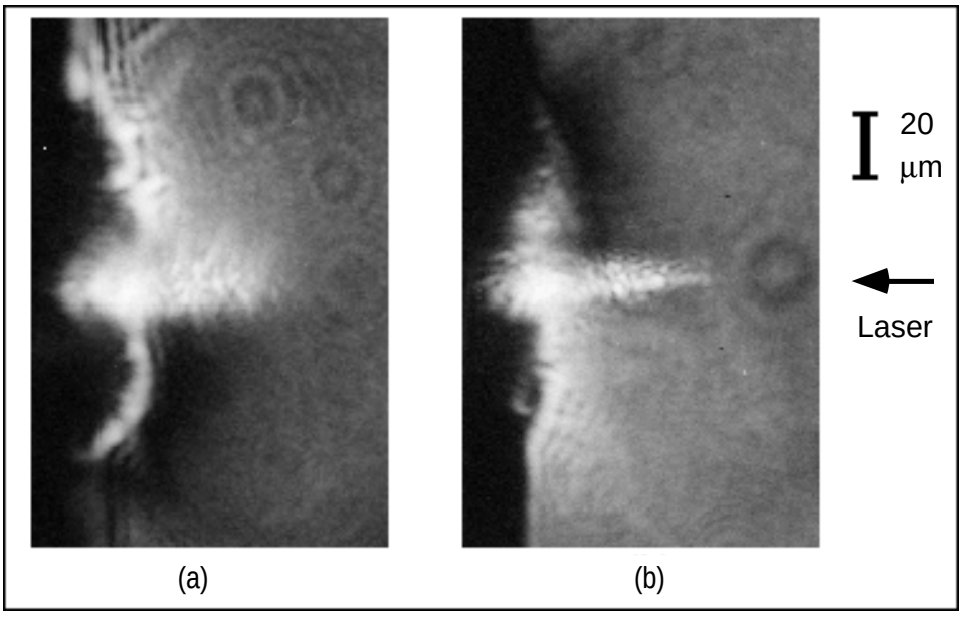

Fig. 2 (a), (b): Polarigrams taken 13 ps after the interaction of a 10 TW, 1.5 ps laser pulse with a solid Al target, with the polarisers respectively set -9° and +12° degrees off crossed.

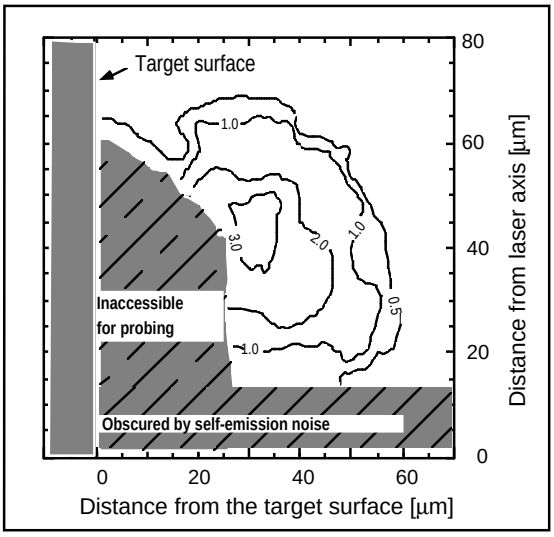

Fig.3. Magnetic field distribution extracted from the polarigram of fig.2(a). The magnitude is in units of megagauss. The plasma region either obscured by self-emission or not accessible for probing is shown.

Due to refraction off the steep gradients present in the denser region of the plasma, only densities lower than 1-2 10^{20} /cm^3 could be probed.

EXPERIMENTAL RESULTS

Magnetic fields with a maximum amplitude up to a few MG were detected in the experimental measurements. The fields observed were transient, with a lifetime of a few tens of picoseconds. No Faraday rotation was detected immediately after the interaction, when the field was probably still limited to regions not accessible for probing. After 5 ps the typical signatures corresponding to a toroidal field surrounding the laser axis (i.e. a dark and a bright pattern on the opposite sides of the axis, in the proximity of the target surface) began to appear. The strongest rotations were detected between 6 and 12 ps after the interaction. Two polarigrams obtained 12 ps after the interaction, with the polarisers set -9° and +12° degrees off normal are shown in figs.2(a) and (b). As expected, the dark-bright pattern reverses as the angle between the polarisers is changed from a value below 90° to a value above 90°. The sense of rotation is the same as observed in previous measurements in longer pulse regimes[2),3)], and is consistent with fields generated by the thermoelectric mechanism[1)].

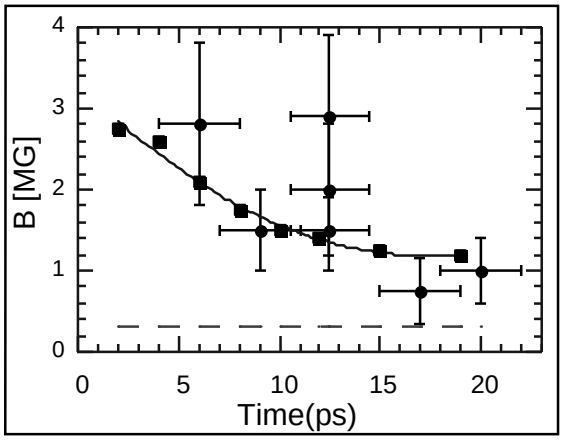

Fig.4 Temporal evolution of the maximum magnetic field detected at n_e = 4 10^{19}/cm^3 (full circles). The maximum fields predicted at the same density by MHD simulations are also shown (as squares and a solid line). The dashed line corresponds to the sensitivity of the diagnostic.

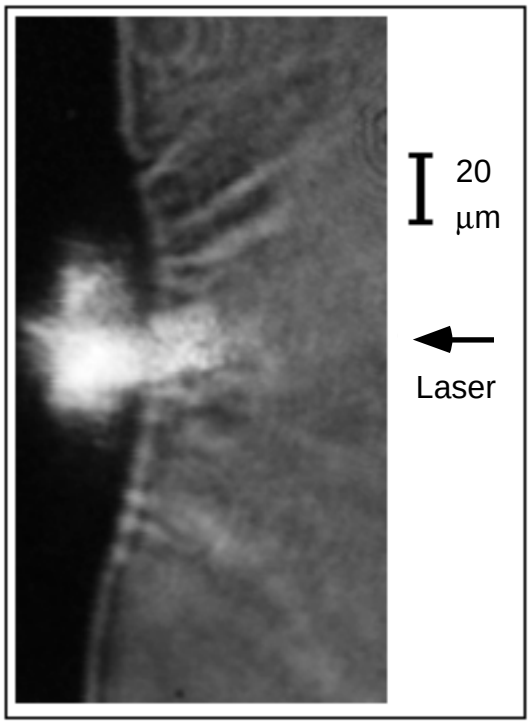

Fig.5. Polarigram taken 40 ps after the interaction (analyser set +12 degrees off normal).

A map of the product n_eB (electron density times magnetic field) in the plasma was obtained by Abel inverting the rotation angle measured off the polarigrams. The B-field amplitude could then be inferred by using an independent measurement of the density. For this purpose, a similar temporal sequence of interferograms, from which the evolution of the plasma density with time could be obtained, was acquired in separate measurements. The magnetic field contour obtained from the polarigram of fig.2(a) is shown in fig.3. The largest fields detected at this time were of the order of 2-3 MG, measured at an electron density of 3-5 10^{19}/cm^3.

The high temporal resolution of the diagnostic allowed the temporal evolution of the B field to be measured. The maximum field measured at a fixed density (4 10^{19}/cm^3) versus time is shown in fig. 4. Within the uncertainties of the measurement, the observed field decreases with time. At 20 ps after the interaction, small scale structures (possibly shocks due to fast electrons streaming back into the target) begin to appear, breaking up the uniformity of the rotation pattern, as visible in fig.5. Due to this, and also to the overall decrease of the rotation angle, it becomes difficult to extract a value for the field amplitude from data taken after 20 ps. At 50-60 ps after the interaction, no rotation is detectable anymore above the background noise, meaning that no field larger than 200-300 KG (i.e. the sensitivity of our diagnostic in these experimental conditions) is present in the region of the plasma accessible for probing.

An important feature immediately evident from the polarigrams (particularly in fig.2(b)) is a characteristically elongated self-emission plume, extending up to 100 μm from the target surface, with a transverse dimension of 10-20 μm. This time-integrated emission at λ=0.622 μm can be interpreted as bremsstrahlung radiation from a dense, collimated plasma plume. Similar structures have previously been reported in different interaction regimes, in x-ray images[7)] and interferograms[2)]. The formation of a plume structure in the

plasma has also been observed interferometrically. A localised fringe shift, corresponding to a high density jet, is clearly visible in the interferogram

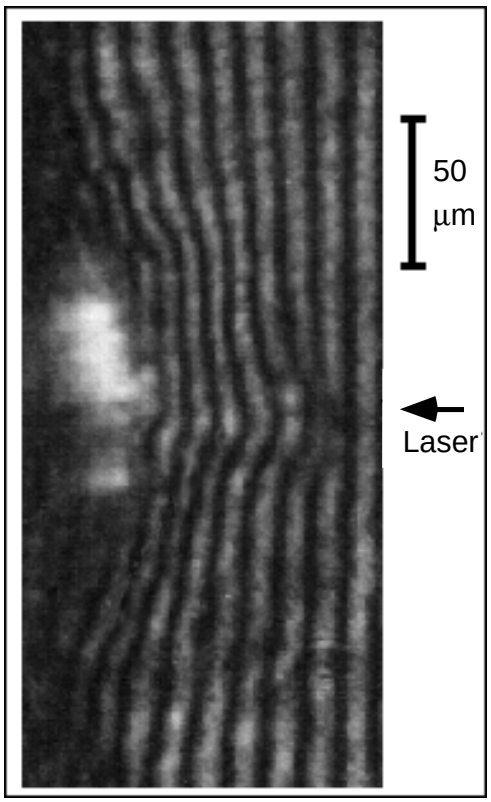

Fig.6 Interferogram recorded 15 ps after the interaction

of fig.6, obtained 15 ps after the interaction. The corresponding density distribution (fig.7 (a)) shows that the density inside the plume is as high as 10^{20}/cm^3 out to 80 μm from the target surface.

COMPARISON WITH SIMULATIONS

The experiment has been simulated using the computer code MH2D[7] that solves the magnetohydrodynamic (MHD) equations in cylindrical geometry. The code includes the pressure-driven magnetic source term, resistive diffusion of the magnetic field, and Spitzer thermal conduction with magnetic inhibition. A more detailed description of the simulation runs can be found in ref.5. In these runs, magnetic inhibition was imposed using the Bohm transport reduction term[7]. The maximum reduction allowable had however to be limited, in order to avoid complete inhibition of the thermal flux from the laser spot[5),7)]. The bulk properties of the plasma expansion seem to be described adequately by the code and, with the chosen conditions, a remarkable agreement with some of the experimental observations was obtained. The order of magnitude of the fields observed in the simulations, and also their temporal evolution, is comparable with the experimental observations. The maximum predicted values at the fixed density of 4 10^{19}/cm^3 are plotted for different times in fig.4 together with the experimental data. As it can be seen, the simulations are in good agreement with the magnitude and the decay of the magnetic field. In the simulation the overall peak field (6 MG) is observed at the end of the laser pulse, at densities between 1 and 5 n_c.

Also, the formation of a jet-like structure in the simulations is characteristic of the interaction in the intensity regime investigated, and the features of the experimental data are overall well reproduced in the computational results, as evident from fig.7(b). The simulations confirm that the jet is formed due to pinching of the plasma by the self-generated magnetic fields. In fact, if in the code the baroclinic sourceterm for the B-field is turned off, no jet formation is observed.

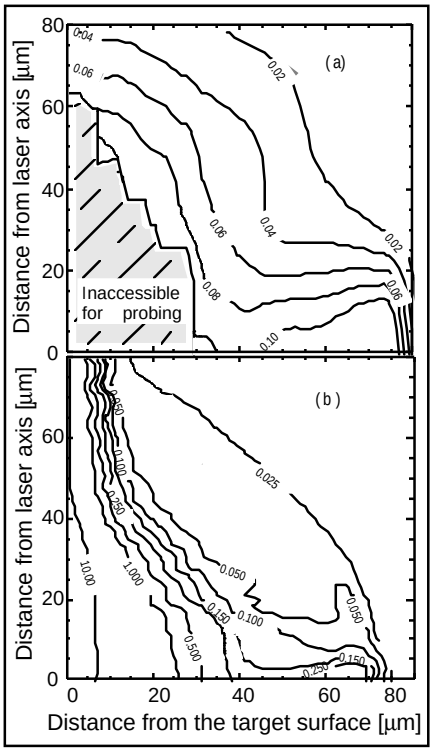

Fig.7 (a) Electron density distribution extracted from the interferogram of fig. 2 (c). (b) MHD code prediction for the density distribution. The densities given are in units of the critical density (1.1 10^{21}/cm^3)

CONCLUSION

MG magnetic fields generated during the interaction of a 10 TW, ps pulse with Al solid targets have been measured, using a polarimetric technique with picosecond temporal resolution. The fields, consistent with the thermoelectric generation mechanism, are transient, with a lifetime of a few tens of picoseconds and affect the plasma expansion, confining it into a collimated plume. Simulations performed with a 2D MHD code for the conditions of the experiment reproduced the main features of the experimental observations, and related the jet formation to the presence of the magnetic fields in the plasma.

REFERENCES:

1) J.A.Stamper
Laser & Particle Beams 9, 841 (1991) and references within
2) M.D.J.Burgess *et al*
Phys. Fluids 28, 2286 (1985)
3) J.A.Stamper and B.H.Ripin
Phys.Rev.Lett. 34, 138 (1975); A.Raven, O.Willi, P.T.Rumsby, Phys.Rev.Lett. 41, 554 (1978)
4) R.N.Sudan
Phys. Rev. Lett. 70, 3075 (1993); S.C.Wilks, W.L.Kruer, M.Tabak and A.B.Langdon, Phys. Rev. Lett. 69, 1383 (1992)
5) M.Borghesi et al
submitted to Phys. Rev. Lett. (1997)
6) M.Borghesi et al
Rutherford Appleton Laboratory Annual Report 1995-1996, RAL-TR-96-076, p.19 (1997)
7) A.R.Bell et al.
Phys.Rev.E 48, 2087 (1993)

EXPERIMENTAL STUDY TO TEST THE VIABILITY OF HIGH HARMONIC GENERATION FROM SOLID TARGETS WITH SHORT WAVELENGTH LASERS

D. M. Chambers[1)], P. Norreys[2)], A. E. Dangor[3)], R. S. Marjoribanks[4)], S. Moustaizis[5)], D. Neely[2)], S. G. Preston[1)], J. S. Wark[1)], I. Watts[3)] , M. Zepf[3)]

1) Department of Physics, Clarendon Laboratory, University of Oxford, Parks Road, Oxford, OX1 3PU, United Kingdom
2) Rutherford Appleton Laboratory, Chilton, Didcot, Oxon, OX11 0QX, United Kingdom
3) Blackett Laboratory, Imperial College of Science, Technology and Medicine, Prince Consort Road, London, SW7 2AZ, U.K
4) Department of Physics, University of Toronto, 60 St. George Street, Toronto, M5S 1A7 Ontario, Canada,
5) IESL/FORTH, University of Crete, P.O. Box 1527, 711 10 Heraklion, Crete, Greece

INTRODUCTION

There is currently great interest in the production of extreme ultraviolet (XUV) radiation by high harmonic generation. One method of generating the harmonics is from the interaction of intense sub-picosecond laser pulses with solid targets[1) 2)]. The electrons oscillate at close to relativistic velocities across the solid-vacuum boundary (for ultra-short laser pulses with negligible pre-plasma formation) or across the boundary of a ponderomotively-steepened density profile in the case of pre-plasma formation. The harmonic production mechanism can be viewed simplistically either as due to rectification of the acceleration of electrons[3)], or by treating the boundary layer as an oscillating mirror driven by the ponderomotive force[4)]. Both odd and even harmonics are produced due to the non-symmetric nature of the boundary layer.

The first experimental work in this area was carried out using CO_2 lasers (10.6 µm) in the late 1970's by Burnett et al.[5)] . The highest harmonic eventually produced was the 46th harmonic in 1981 by Carman et al.[6)], though this relates to a harmonic wavelength of only 230 nm, far from the XUV region. Recently there has been a resurgence in this work due to rapidly increasing optical laser intensities [1, 7)] made possible by the development of chirped-pulse-amplification (CPA) technology[8)]. Importantly, simulations performed by Paul Gibbon show that both the order and efficiency of harmonic production is only dependent on $I\lambda^2$ (where I is the intensity and λ the fundamental laser wavelength) and that over 60 harmonics can be produced with efficiencies over 10^{-7} at 10^{19} Wcm^{-2} μm^{2} [, 3)]. Experimental work carried out by Norreys *et al*. has demonstrated the production of the 75th harmonic at 14 nm from the Vulcan 1.053 µm Nd:Glass laser in good agreement with particle-in-cell (PIC) code simulations[1)].

If Gibbon's predictions are correct, this method of harmonic generation may provide a means of production of high brightness coherent XUV radiation in the so-called water window, between 4.4 and 2.3 nm. For a KrF-pumped Raman laser, starting with a wavelength of 268 nm, the water window is reached at the 62nd harmonic. Using Gibbon's $I\lambda^2$ scaling [3)] , and the results of Norreys *et al*.[1)] we could expect this harmonic to be obtained with an intensity of approximately $1.6\times10^{20}Wcm^{-2}$. This should be within reach of the forthcoming upgrade to the Titania KrF-pumped Raman laser[9)].

It is therefore timely to investigate the production of harmonics from the interaction of short-pulse UV laser radiation with solid targets. In the experiments described here, with the Titania CPA laser, the intensity on target was limited to 2×10^{18} Wcm^{-2}, and thus wavelengths of extremely high order are not expected. However, the experiments are still of significant interest, as they allow us to make comparisons with both the experimental results obtained using longer wavelength lasers, and with code calculations, thereby contributing to our overall understanding of the harmonic production process.

EXPERIMENTAL ARRANGEMENT

The experiment was performed using the TITANIA KrF laser[10)] in CPA configuration to give 1 ps pulses at 248.6 nm. Energies on target varied between 150 and 200 mJ, focused with an f/3.3 off-axis parabola to give intensities up to 2×10^{18} Wcm^{-2} at the target in a ~5× diffraction limited spot of 4 µm at full width half maximum. The targets consisted of optically polished slabs of fused silica, the beam was p-polarised with respect to the target.

The harmonic radiation was collected with a slitless flat field grazing incidence XUV spectrometer (based around a Hitachi 1200 l/mm grating at 4°), utilising a grazing incidence gold coated focusing mirror for increased collection efficiency. The grating and mirror were orientated so that their grazing incidence reflections gave perpendicular astigmatic line images of the focus of the laser at the detector plane. The XUV radiation was detected with a Galileo double micro channel plate (MCP), coupled to a Photonic Science DarkStar intensified charge-coupled-device (CCD) camera via a 4:1 reducing fibre optic coupler. The response of the MCP and CCD camera were calibrated in a separate experiment with respect to Illford Q-Plate film[11)]. The acceptance solid angle of the grating and gold mirror was 5.76×10^{-6} sr. A beam block was inserted in the zero order position to eliminate scattered fundamental and XUV radiation. The spectrometer viewed the interaction region at an angle of 56º to the incident laser beam.

RESULTS AND DISCUSSION

Figure 1 shows a typical line-out of the single-shot data showing the 3rd and 4th harmonics and rising plasma emission to shorter wavelengths. This data was obtained with the spectrometer viewing in specular reflection, i.e. an angle of incidence of the laser of 28º. The 4th harmonic signal was the highest order detectable, and only seen at the higher laser intensities.

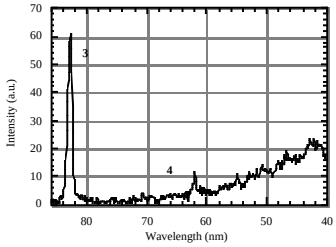

Figure 1. Typical lineout of the data taken with a laser intensity of 2×10^{18} Wcm^{-2} , at an incidence angle of 28º, with the spectrometer in the specular reflection direction.

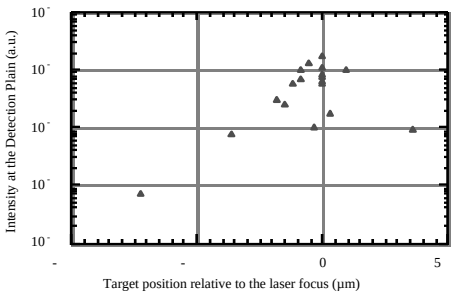

Figure 2. Third harmonic intensity at the detector, as a function of target position relative to the laser focus

The dependence of the collected third harmonic energy with incident laser intensity was investigated by moving the target through the laser focus. The results are shown in figures 2 and 3. The intensity at focus was calculated assuming a five times diffraction limited spot, consistent with equivalent-plane far field images taken from leakage through the penultimate turning mirror before the target. Intensities for all the other data points have been calculated assuming the beam to be in the geometrical limit, being at least three Rayleigh ranges from focus. As can be seen in figure 3 when the collected energy is now plotted against $I\lambda^2$ an interesting feature develops around 10^{16} $Wcm^{-2}\mu m^2$. For the reasons outlined below we identify this feature as the transition from specular to diffuse emission of the harmonic radiation.

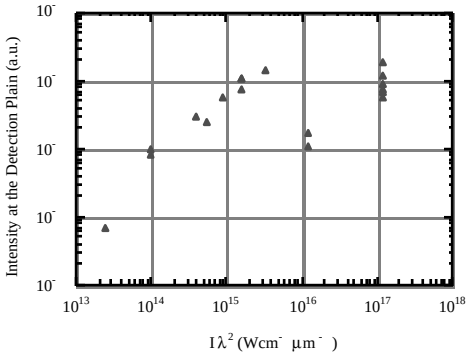

Figure 3. Third harmonic intensity at the detector as a function of $I\lambda^2$

In previous experiments, using Ti:Sapphire lasers (800 nm) with pulse lengths of between 60 and 150 fs giving intensities up to 1×10^{18} Wcm^{-2}, it was assumed (though not experimentally verified) that the harmonic emission was specular - i.e. confined to the cone angle of the reflected laser pulse[7,12] . This assumption was made because the component of the wavevector parallel to the surface is conserved in coherent non-linear processes at the steep solid-vacuum interface. However, in contrast, both the work of Norreys *et al.* using picosecond pulses at close to 10^{19} Wcm^{-2}, [1], and the early work utilising nanosecond CO_2 radiation[5,6] , demonstrated diffuse harmonic emission. This broad angular emission has been attributed to rippling of the critical density surface by Raleigh Taylor like instabilities as the expanding plasma is pushed back by the ponderomotive force[13] .

Importantly, in their recent studies of second harmonic radiation of clean, pre-pulse free,1μm, 1ps, Nd:Glass CPA laser pulses, Marjoribanks *et al.*[14] , demonstrated that the second harmonic emission was specular over incident values of $I\lambda^2$ ranging from $10^{14}Wcm^{-2}\mu m^2$ to the mid $10^{16}Wcm^{-2}\mu m^2$. However, with the removal of a saturable absorber (introducing a pre-pulse 1.5 ns before the main pulse at ~10^{-4} of I_{peak}) they observed a transition from specular to diffuse emission as the irradiance was increased from approximately $10^{15}Wcm^{-2}\mu m^2$ to $10^{16}Wcm^{-2}\mu m^2$. All of the above observations are consistent with the view that if the laser interacts with a pure solid-vacuum interface, the harmonic emission is specular, but if it interacts with a plasma (with the interface being formed via ponderomotive steepening) at sufficiently high intensity, diffuse emission occurs due to an intensity-dependent instability at the critical surface.

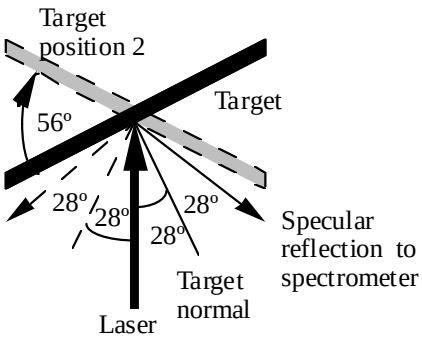

Figure 4. Schematic of the targets angular position with respect to the incident laser beam. The black target and solid lines represent the normal target position 1, with the spectrometer in the specular reflection direction. The grey target and dashed lines represent target position 2 with the angle of incidence, at 28º, and the spectrometer position remaining the same, but with the specular reflection direction being 112º from the previous direction.

In order to demonstrate that the emission at the higher intensities was indeed diffuse in this regime, the target was rotated, such that the laser was incident on target at the complementary position, i.e. keeping the incidence angle at 28º, but now with the spectrometer viewing far from the specular direction at an angle of 84º to the target normal, 112º from the specular reflection direction, as shown as position 2 in figure 4. In this new spectrometer position, strong 3rd harmonic emission was still detected at tight focus, of a comparable intensity to that observed in the specular direction. Further credence to this interpretation is afforded by plotting the third harmonic conversion efficiency as a function of irradiance, whilst assuming that the emission is into 2π for values of $I\lambda^2$ in excess of $10^{16}Wcm^{-2}\mu m^2$, but into an f/3.3 cone for irradiances below this value. The results are shown in figure 5. The consistent fit of all the data plotted gives weight to the interpretation that between $2\times10^{15}Wcm^{-2}\mu m^2$and $2\times10^{16}Wcm^{-2}\mu m^2$ the angularly-integrated conversion efficiency continues to rise, but the collected energy temporarily decreases (see figure 3) due to the transition from specular to diffuse emission. Similar conclusions have been reached previously by Marjoribanks and co-workers[14]

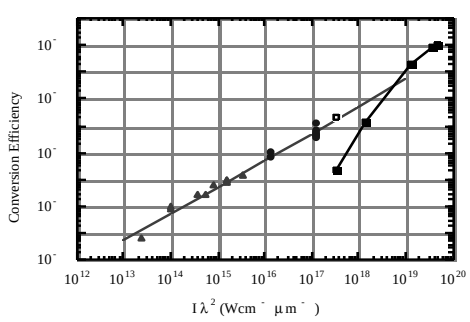

.

Figure 5. Conversion efficiency into the third harmonic versus incident laser irradiance. Triangles represent emission into the laser cone angle only, the circles emission into 2π steradians. The straight line fit represents $5.2 \times 10^{-22} \times I\lambda^2$ The solid black squares and fit represent the PIC code simulation results of Lichters *et al*. for a step-like density function. The open square represents the PIC code result for a density scale length of 0.8 λ, to match the experimental conditions. Lichters results are taken from figures 2 and 9 in reference 15).

In addition to studying the intensity dependence of the harmonic emission at a given angle of incidence described above, we also investigated the influence of incidence angle of the laser on the harmonic emission. For these studies the target was rotated, leaving the spectrometer position fixed. In all cases the target was placed in the focal plane of the laser beam, and thus the incident intensities were of order 1×10^{18}Wcm^{-2}. The results are shown in figure 6, where we have assumed diffuse emission for all angles of incidence in calculating the conversion efficiency. It can immediately be seen that there is an extremely strong dependence of the emission on the angle of incidence of the laser, with the peak conversion occurring for angles of incidence around 30º. At an incidence angle of the laser of 56º and with the spectrometer in the specular reflection direction no harmonic emission was detected. Thus there is a strong angular dependence of the harmonics, showing a reduction in conversion efficiency of greater than 3 orders of magnitude from a change in incidence angle from 28º to 56º.

This optimum angle of incidence is consistent with previous measurements of energy absorbed via resonance absorption made by Borghesi and co-workers using almost identical irradiance conditions on the Rutherford KrF laser system[16)] . Their results are shown for comparison in figure 7. The resonance absorption clearly peaks around the same angle as the harmonic radiation maximises. Borghesi's measurements would indicate that at an angle of incidence of, say, 10 degrees, the absorbed fraction decreases by a factor of 2 or so from the peak. Comparison with figure 6 would indicate that this decrease in absorbed energy is insufficient on its own to account for the factor of a few drop in harmonic conversion efficiency observed in moving from an angle of incidence of 30 to 10 degrees, though considering the error bars associated with this data, further work is obviously needed to verify this conclusively.

Finally it is of interest to compare the experimental conversion efficiencies with computational predictions. Recently, Lichters et al. have shown with a fully relativistic one dimensional PIC code, including a step-like density function, that strong oscillations are generated at the critical density surface by the ponderomotive force. They proceed from this to show that the harmonic generation process can be understood in terms of the light being reflected from an oscillating mirror[4,15)]. This "oscillating mirror model" was first proposed by Bulanov et al. in 1994 [17)] . The predicted harmonic conversion efficiencies, from the PIC code simulations with a step-like density function, are shown alongside the experimental data in figure 5.

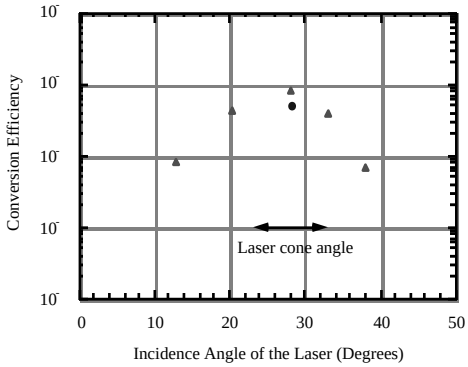

Figure 6. Conversion efficiency into the third harmonic versus angle of incidence of the laser with respect to the target normal. The triangles represent the average of at least 2 data points, with the target in position 1. The circle represents emission collected with the target in position 2, see figure 4. The black arrow represents the angular divergence of the laser

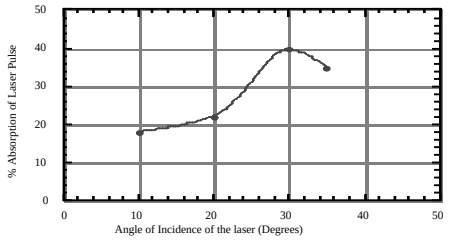

Figure 7. Percentage of the laser pulse absorbed by resonance absorption versus incidence angle of the laser, as measured by Borghesi *et al.* [(16)] .

More sophisticated PIC code simulations, using a density ramp to simulate different plasma density scalelengths, again provided by Lichters, go on to show for the lower harmonics, that an increase in conversion efficiency occurs with increasing density scalelength up to the order of a wavelength[15)] . Lichters et al. have suggested an explanation for this in terms of the oscillating mirror model, i.e. that the laser can drive larger oscillations of the critical density surface due to the weaker plasma restoring force. Obviously though, with too long a density scale length, the idea of a reflecting surface becomes somewhat blurred, and as expected the simulations show that the harmonic efficiencies are reduced with scalelengths over a wavelength. This explanation is backed up by the PIC code simulations, including step-like density functions, which also predict increased harmonic intensities with reduced plasma densities.

In order to make more consistent comparison with the Lichters sinmulations, an estimate of the plasma scalelength present in the experiment can be made from our knowledge of the angular dependence of the resonance absorption. The standard results of resonance absorption allows the plasma density scale length to be estimated from the formula[18)] .

$$\sin\phi = 0.8(\omega L/c)^{-1/3}$$

Where ϕ = the laser incidence angle for maximum absorption, ω = the fundamental laser frequency and L = the plasma density scale length in units of the laser wavelength. This implies the plasma density scale length to be 0.8 ($\pm$0.1) λ, i.e. 0.20 ($\pm$0.02) μm. Indeed, for this plasma density scalelength Lichters PIC code simulations predict a conversion efficiency of 2×10^{-4} at an irradiance of 3×10^{17} Wcm$^{-2}\mu$m^2. This point is also

shown alongside the experimental data in figure 5. The good agreement is now striking, and gives confidence that theoretical models can provide reasonable indicators of expected conversion efficiencies.

In conclusion we have investigated the generation of the third harmonic of a picosecond KrF laser interacting with a solid target. Both the intensity and incidence angle dependence of the conversion efficiency have been explored. The conversion efficiency has been shown to vary almost linearly with $I\lambda^2$ from about 10^{-8} at 10^{13} to 10^{-4} at 10^{17} $Wcm^{-2}\mu m^2$ with evidence of angular broadening from specular to diffuse emission between 2×10^{15} $Wcm^{-2}\mu m^2$and 2×10^{16} $Wcm^{-2}\mu m^2$. This broadening is consistent with previous studies of the second harmonic of a Nd:Glass CPA laser performed by Marjoribanks and co-workers[14]. The conversion efficiency as a function of angle of incidence was investigated at values of $I\lambda^2$ of order 10^{17} $Wcm^{-2}\mu m^2$ showing a strong dependence on the incidence angle of the laser. Harmonic generation peaked at an angle of incidence close to 30 degrees, consistent with the angle at which maximum resonance absorption was found by Borghesi and co-workers using similar irradiance conditions. Most encouragingly, these results are in agreement with theoretical simulations using a fully relativistic, one dimensional PIC code with appropriate plasma density scale lengths [15]. These results are therefore very encouraging for forthcoming KrF experiments with ultra high intensities, where if the theoretical predictions are correct, water window harmonics should be within reach.

The authors would like to acknowledge the help and support of the staff of the Rutherford Appleton Laboratory, U.K. This work was jointly funded by the United Kingdom Engineering and Physical Science Research Council (EPSRC) and the European Communities Large Access Programme. D. M. Chambers would like to acknowledge funding from the EPSRC and A.W.E., Aldermaston, U.K. S. G. Preston would like to acknowledge support from Merton College, Oxford, U.K.

REFERENCES

1) P.A. Norreys et al
Physical Review Letters, 76 (11), 1832-1835 (1996).

2) D.M. Chambers et al
Journal of Applied Physics, 81 (5), 2055-2058 (1997).

3) P. Gibbon
Physical Review Letters, 76 (1), 50-53 (1996).

4) R. Lichters et al
Physics of Plasmas, 3 (9), (1996).

5) N.H. Burnett et al
Applied Physics Letters, 31 172 (1977).

6) R.L. Carman et al
Physical Review A, 24 (5), 2649-2663 (1981).

7) S. Kohlweyer et al
Optics Communications, 117 431-438 (1995).

8) D. Strickland et al
Optics Communications, 56 219-222 (1985).

9) S. Angood et al
Rutherford Appleton Laboratory Technical Report No. RAL-TR-94-014, (1994).

10) E.J. Divall et al
Journal of Modern Optics, 43 (5), 1025-1033 (1996).

11) M. Zepf et al
Rutherford Appleton Laboratory Technical Report No. RAL-TR-95-025, 113-114 (1995).

12) D. Von der Linde et al
Physical Review A: Rapid Communication, 52 (1), R25-R27 (1995).

13) S.C. Wilks et al
Physical Review Letters, 69 (9), 1383-1386 (1992).

14) R.S. Marjoribanks et al
Bull. Am. Phys. Soc., Denver (1996).

15) R. Lichters et al
In Multiphoton Processes, IOP Publishing Ltd, 221-230 (1997).

16) M. Borghesi et al
Physical Review E, To be published. (1997).

17) S.V. Bulanov et al
Physics of Plasmas, 1 (3), 745 (1994).

18) C.E. Max
Physics of Laser Fusion, 1 Lawrence Livermore Laboratory Report (1981).

DETECTION OF PLASMA WAVES GENERATED BY A RELATIVISTICALLY INTENSE SELF-CHANNELLED LASER BEAM

C. E. Clayton[1], A. E. Dangor[2], C. Joshi[1], D. Gordon[1], K. A. Marsh[1], V. Malka[3], A. Modena[2], P. Muggli[1], D. Neely[4], F.N. Walsh[4], Z. Najmudin[2]

1) University of California Los Angeles, CA, USA 90095
2) Imperial College of Science and Technology, London, U.K. E-mail zn1@ic.ac.uk
3) Ecole Polytechnique, Palaiseau, France
4) CLF, Rutherford Appleton Laboratory, Chilton, Didcot, Oxon

INTRODUCTION

Short-pulse high-intensity lasers have generated much interest in recent years, due to their possible use for applications as diverse as X-ray lasers, particle accelerators and in fusion. Many of these possible applications, however, require enhanced interaction lengths to be successful. So it has become almost a holy grail in the community to find processes which can increase the length of laser propagation at high intensity.

Fortunately high intensity lasers propagating through plasmas may be able to overcome this problem themselves, through the process of relativistic / ponderomotive self-focusing[1]. Self-focusing occurs when the plasmas index of refraction has a radial dependence, such that there is a maximum on axis, which causes the laser to act as a positive lens. If this rate of focusing matches the natural diffraction of the beam, a steady state or channel is formed. The relativistic mass increase of electrons (due to the high quiver velocity in the electric field of an intense laser) and a density decrease (for example due to the ponderomotive push-out of an intense laser pulse) are two possible mechanisms which can create a suitable variation of refractive index. In practice in short-pulse high-intensity laser experiments, these two processes occur simultaneously. Indeed it is found that there is a theoretical critical laser *power* above which self-focusing takes place, $P_{cr} > 17\bullet(\omega_0/\omega_p)^2$ GW.

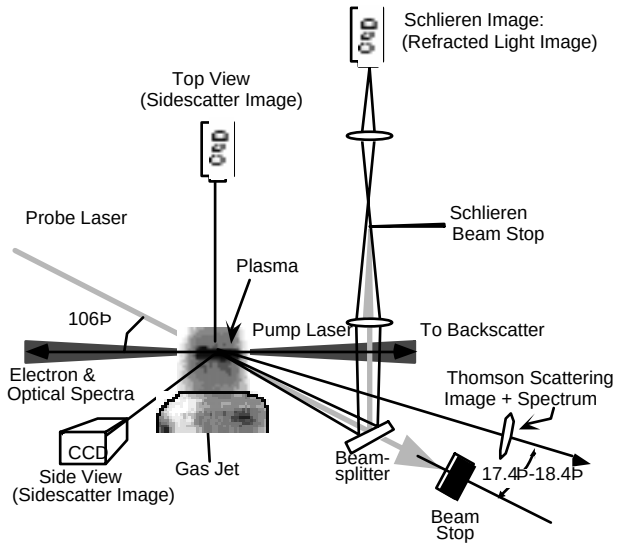

Figure 1 Experiment lay-out

EXPERIMENT

The lay-out of an experiment to investigate self-focusing is shown in figure 1. The Vulcan CPA beam is focused onto the edge of a supersonic gas jet, which provides a reasonably collimated flow of densities around 1×10^{19} cm^{-3}. The Å1ps, 24J (on target) laser beam was focused into a spot of diameter 20 µm. This gives intensities at focus greater than 5×10^{18} Wcm^{-2}. Note that with these parameters we are well above the theoretical threshold for self-focusing, PÅ12•P_{cr}. A transverse probe beam, of size 1 cm^2 and intensity Å 10^{11} Wcm^{-2}, is used for schlieren probing and Thomson scattering. The schlieren imaging provides qualitative information about density gradients within the plasma, and hence about the laser beam creating those gradients. The Thomson scattering was arranged so as to frequency match with forward travelling plasma waves, created by the self-modulational instability (or Raman Forward Scatter). Though this geometry cannot directly wavenumber match with the 'fast wave' that is responsible for energetic electrons, it does give a qualitative measure of its amplitude. This is because the waves measured will have decayed from the fast wave, and is a measure of its non-linearity as it approaches wave-breaking.

The transmitted laser beam is deflected away by a pellicle and recorded to validate the presence of plasma waves due to Self-Modulated Wakefields. Electrons accelerated and emitted in the forward direction are recorded with an electron spectrometer. To complete the diagnostics imaging cameras were provided in two directions mutually orthogonal to the main beam. One of these had a 2 l/mm transmission grating placed in front of it to allow simultaneous measurement of the spectrum of the scattered light. The combined use of the diagnostics makes this one of the most complete studies of self-focusing yet undertaken.

RESULTS

Figure 2 below shows an image of the sidescattered light. As can be seen the laser beam has appeared to break into two filaments. The upper one is shorter in length, but the lower one extends the full length of the gas jet, (as indicated by the faintly glowing background light). Noticeably the amount of scatter actually seems to increase towards the end of the filament. These filaments, though remarkable, have been observed now in many other similar experiments.[2]

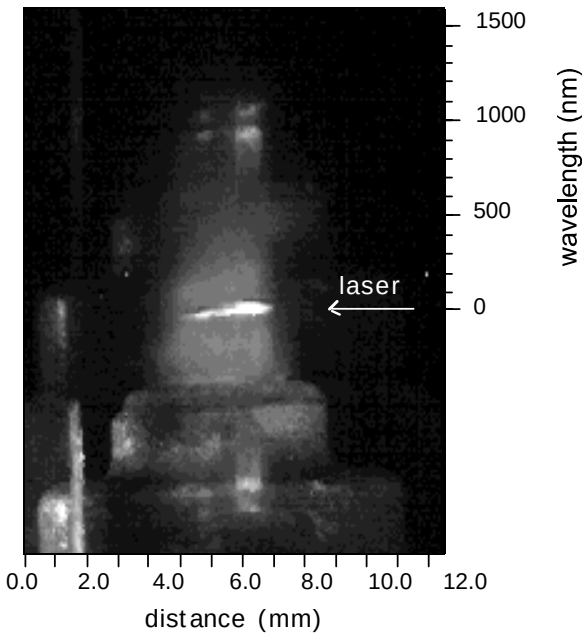

Figure 2 CCD image of sidescattered light, with spectrally dispersed image directly above it.

The spectrum of the image can be discerned directly above the undispersed image. As can be seen there are two main features, one at λ_0 and one shifted from it by λ_p to the blue. The plasma frequency is confirmed by the spectrum of the transmitted light which is modulated at the same frequency. The equivalent satellite to the red is surprisingly not seen, but this maybe due to the falling sensitivity of the Si CCD camera at that wavelength. The fundamental (λ_0) feature appears to be somewhat blue-shifted as the laser propagates into the plasma. Remarkably though the sidescatter decreases in amplitude initially on entering the gas jet, it actually brightens Å 3 mm into the jet. This corresponds to the bright point of the filament in the spectrally integrated image.

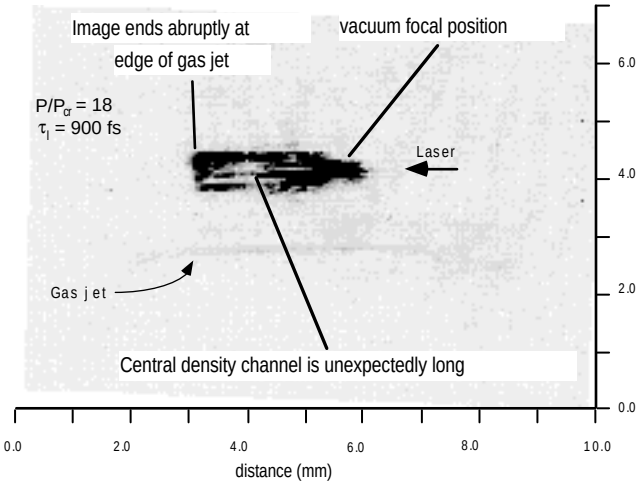

Figure 3 Schlieren image of long filament

A schlieren image, Figure 3, shows the density gradients created by a shot under similar conditions. Again a remarkable long filament is seen, which only terminates at the edge of the gas jet boundary. The peculiar rectangular shape of the plasma created, is in contrast to the fan like shape in shots without long filaments, and are indicative of severe modification of the propagation properties of the laser.

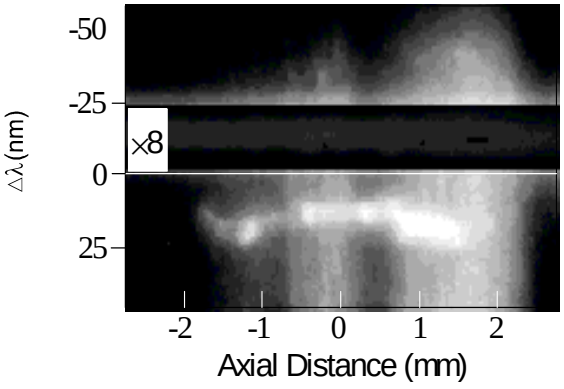

Figure 4 Imaging Thomson Scattering performed with same probe beam as the schlieren

Figure 4 shows light scattered from the 2ω probe beam which intersected the gas jet at 90_ to the driver CPA beam. The light has been imaged along the axial direction of the laser (horizontally in the figure) and spectrally dispersed perpendicularly. One can see that a lot of light is scattered at 2ω, and this has been attenuated in the picture. Around this is a diffuse glow over a large wavelength range. This is bremsstrahlung light. Recombination lines, which could be a nuisance around this wavelength with the helium medium used, have been reduced by optically gating the detection apparatus. This was done by using an optical gated imager with a gate time of 1 ns centred in time on the arrival of the laser pulse at the gas jet. The bright long feature blue shifted (i.e. down in the figure) from the 2ω of the probe is due to scattering from the plasma wave created by the self-modulational instability.

On most shots this feature is of length on the order of the Rayleigh length, the propagation length over which the maximum intensity drops by a factor of Ã2. This is as expected since high intensities are required for the self modulational instability. Indeed a drop of intensity of only around 2 significantly reduces the amplitude of this wave, as seen by the Thomson scattering diagnostic.

The amplitude of the plasma wave has been estimated by considering the energies to which electrons have been accelerated due to self-trapping[3]. From this it is apparent that in figure 4 not only is the plasma wave of high amplitude right across the gas jet, but also the laser amplitude must also be high (of the order 10^{18} Wcm^{-2}).

The shots with the longest filaments did not necessarily produce the highest energy electrons in the forward direction (40 MeV as opposed to 100 MeV). Though initially surprising, it must be remembered that the dephasing length for electrons, i.e. the distance over which they out-run the plasma wave, is of the order of hundreds of microns in this experiment. Therefore channelling may actually have an adverse effect on the most energetic electrons, by decelerating or deflecting them away from our detector.

CONCLUSIONS

In this experiment, the laser was focused with an Åf4 focusing off-axis parabola. As a result, the Rayleigh length in vacuum is of the order 200µm. Indeed due to natural refraction, if one focuses on the edge of our Å 3.5 cm gas jet, then the intensity at the other end should be of the order of 10^{16} Wcm^{-2}. This is barely enough to fully double ionise the helium medium we use, never mind making the 1 ps long laser pulse susceptible to instabilities such as Raman side scattering and the self-modulational instability. However as is clearly demonstrated in our images these instabilities are clearly taking place right across the gas jet.

In addition by finding the plasma wave amplitude of the wakefield created by the self-modulation instability, we were able to estimate the intensity within the laser filament at around 10^{18} Wcm^{-2}. To our knowledge this is the first time this measurement has been made in such experiments. All the evidence suggests channelling of much of the laser energy in a high intensity channel. We suspect that a combination of relativistic / ponderomotive self-focusing is responsible for the channelling[3].

REFERENCES

1) C. Max et al.
Physical Review Letters, 33, 209 (1974)

2) A. B. Borisov et al., P. R. L., 68, 2309 (1993); P. Monot et. al,. P. R. L., 74, 2953 (1995); M. Borghesi et al., P. R. L., 78, 879 (1997); K. Krushelnik et al.., P. R. L., 78, 4047, (1997); R. Wagner et al., P. R. L., 78, 3125 (1997).

3) C. E. Clayton et al.,
Submitted to Physical Review Letters.

POLARISATION AND ANGULAR DEPENDENCE OF THE ENERGY ABSORPTION OF INTENSE SUBPICOSECOND KRF PULSES ON SOLID TARGETS

R. Gaillard, A.J. Mackinnon, and O. Willi

Imperial College of Science, Technology and Medicine, London, UK

INTRODUCTION

The recent improvements in the development of sub-picosecond and picosecond, high intensity laser pulses have allowed for the production of hot, high-density plasmas which are of great interest for many applications such as the generation of coherent and incoherent x-ray sources[1]. Furthermore, an understanding of the mechanisms by which ultra-intense and ultra-short laser pulses are absorbed by a high-density plasma is of paramount importance in the context of the Inertial Confinement Fusion (ICF) program[2]. Therefore, in order to study the energy absorption mechanisms occurring in such plasmas, our group performed in the past few years several experiments using 12ps and 350fs KrF laser pulses on solid targets[3) 4)]. It was found that the experimental data from the 12ps pulse experiment were reasonably well modelled by a combination of resonance and collisional absorption. Absorption was measured as a function of incident angle at a laser intensity of $5x10^{16}$ Wcm^{-2}. The second experiment measured the amount of absorbed energy of KrF pulses focused at intensities up to 10^{17} Wcm^{-2} for angles of incidence ranging from 0° to 40°. We present here, absorption measurements performed with laser intensities exceeding 10^{17} Wcm^{-2} onto solid targets at incident angles as high as 80°.

EXPERIMENTAL ARRANGEMENT

This experiment was performed on the SPRITE / TITANIA laser facilities. The KrF laser used in the Chirped Pulse Amplification (CPA) mode[5] delivered up to 250mJ onto target in a pulse of 450fs duration at a wavelength of 248nm. The laser pulse was focused with an F/3.5 Off Axis Parabola (OAP) in a 12µm diameter UV focal spot. The resulting laser intensities achieved on target were ranging from $3x10^{17}$ to $5x10^{17}$ Wcm^{-2}. The short pulse was superimposed on an Amplified Spontaneous Emission (ASE) pulse. The ASE prepulse level was found to be of about $2x10^{8}$ Wcm^{-2}[6], resulting in a prepulse to main pulse contrast ratio of $2x10^{9}$. The targets used were 125µm and 250µm thick Aluminium layers. The target rotation axis was modified during the experiment from the vertical to the horizontal direction allowing s- and p-polarisation configurations to be studied. These rotations were operated under vacuum using a calibrated stepper motor. The use of a high-magnification television alignment system allowed us to control the target position and hence, to maintain constant the laser irradiance onto target. The fraction of energy absorbed by the target was determined indirectly by measuring the reflected fraction of energy from the target surface. These measurements were performed using a time integrated Ulbricht sphere and a UV sensitive calorimeter connected to a digital oscilloscope. The laser energy scattered by the target surface and thereafter re-emitted by the inner surface of the Ulbricht sphere was measured by the calorimeter collecting a fraction of it. Also, the direct backscattered energy into the OAP was evaluated by a calibrated photodiode connected to a second oscilloscope. To do so, we used one side quartz coated pellicle along the backscattered line in order to direct the reflected UV light towards the photodiode located outside the target chamber. A schematic of the experimental setup used in this experiment is shown in Figure 1:

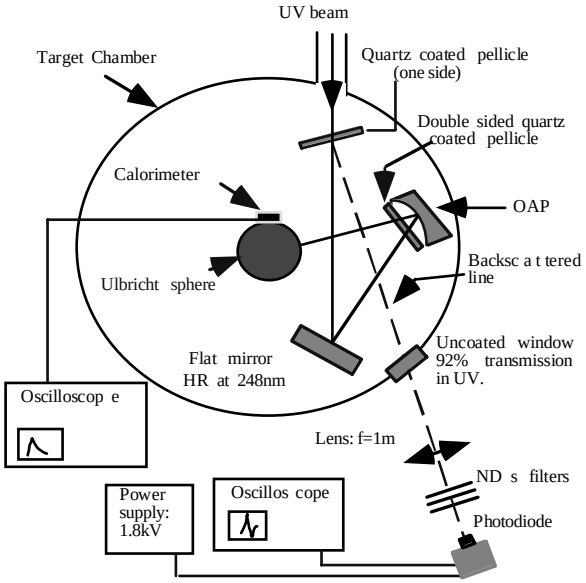

Figure 1: Schematic of the experimental setup.

EXPERIMENTAL RESULTS AND DISCUSSION

The fraction of absorbed energy was measured as a function of the incident angle of the laser beam on target. At high incident angle, it is obvious that the focal spot size increases resulting in a decrease of the laser irradiance achieved on target. In order to maintain constant the irradiance, measurements performed at 80° were obtained by increasing the beam energy up to 500mJ. Two sets of measurements obtained for s- and p-polarised light are presented below, in Figures 2 and 3. We used 125µm and 250µm thick aluminium targets during the s-polarisation set and the p-polaristion set respectively.

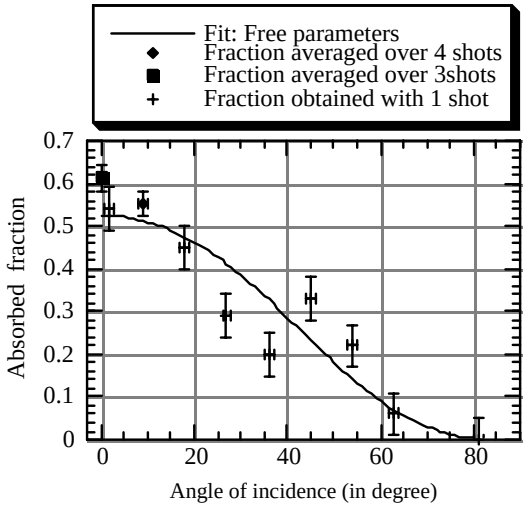

Figure 2: Fraction of energy absorbed as a function of the angle of incidence for s-polarised light. A curve fit is also plotted with the experimental data.

At normal incidence, the energy absorbed can be as high as 62%. As the angle of incidence increases, the absorption reduces from 62% at 0° to less than 10% at an angle of 60°. Furthermore, the absorption drops off to 0% at 80°. The stepper

motor which rotated the target axis was ±1° accurate. Thus, error bars can been introduced on each data point to account for this accuracy. In terms of absorption level, the error is a lot more difficult to evaluate and consequently a systematic error of 10% is introduced. As some data points are averaged over several laser shots, the error bars are reduced to 5%.

In the s-polarisation geometry investigated here, the laser electric field lies perpendicular to the plasma density gradient at all angles of incidence and consequently, the electric field cannot give rise to the generation of plasma waves in the critical density region. Therefore, the s-polarisation measurements provide us with a direct estimation of the fraction of energy absorbed by inverse bremsstrahlung since resonance absorption does not occur. The laser light is absorbed through collision processes taking place on its way up to the critical density (n_c=1.78x10^{22} cm^{-3} at λ_L=0.248μm) and on its way back to vacuum after reflection on the critical surface. However, at high angle of incidence the laser light does not penetrate high densities as it does at lower angle, leading to a lowering of the electron-ion collision frequency which depends linearly on the electron density. Hence, the inverse bremsstrahlung absorption decreases when the angle of incidence increases as seen in Figure 2.

The curve fit plotted in Figure 2 has been calculated according to the classical collisional theory of absorption which puts forward an exponential decrease of the absorbed fraction with respect to the plasma collisional frequency. The analytical fit function of the absorbed energy fraction A_{IB} can be expressed as follows in terms of the incident angle θ:

$$A_{IB} = 1 - e^{-C_{IB}\cos^{u}\theta}$$

where C_{IB} depends on the collisional frequency ν_{ei} and the density scalelength L_n. According to the classical theory, the exponent u is related to the plasma density profile and is equal to 3 and 5 respectively for exponential and linear density profiles. The constant C_{IB} and the exponent u were then set as free parameters in order to reproduce as close as possible the absorption behaviour over the range of angles investigated. As a result, the exponent u worked out to be 2.97. This value differs from the one used with exponential profile by less than 1%. This result reveals that the plasma profile might be better approximated by an exponential density profile, however, this will have to be confirmed with further works such as 1D simulations of the interaction.

The most striking feature observed in this s-polarisation plot is the high level of absorption obtained over the angles of incidence at a laser intensity of about 4x10^{17} Wcm^{-2}. This suggests that in this high intensity regime collisional absorption is still an important process, which is in sharp contrast with the well-known classical theory of inverse bremsstrahlung. However, several mechanisms which unfortunately cannot be quantified, may come into play increasing the absorption fraction measured. Firstly, the finite focusing cone of the parabola leads to a p-polarised component in the nominally s-polarised beam. It is known that there is a significant amount of p-polarised light in the focal spot due to diffraction effects even for normal incidence[7) 8)]. Therefore, this might explain a high absorption level measured at intermediate angle of incidence where the resonance absorption is more effective. The surface roughness of the target may also alter the effective polarisation and again, this would lead to a mixture of some p-polarised light to the s-polarised laser beam. Moreover, backscattered photodiode voltage measurements may confirm our assumptions about the high surface roughness. The fraction of the incident energy backscattered into the F/3.5 focusing lens (OAP) reached a maximum of 8% at normal incidence, however, for all other angles investigated here this was of about 2% up to 10° and even dropped off to less than 1% at larger angles. This small percentage of directly backscattered radiation suggests a diffuse scattering surface. In any case, this low backscatter signal also suggests that stimulated back-reflection was not significant in our measurements and consequently, parametric instabilities such as Brillouin intability did not occur. This can be well understood since in this short pulse regime ions are nearly at rest during the interaction.

For the p-polarised light, the component of the laser electric field which now lies parallel to the electron density gradient allows the resonance absorption mechanism to be switched on. Figure 3 is then an addition of the amount of energy absorbed due to inverse bremsstrahlung and collisionless processes as resonance absorption.

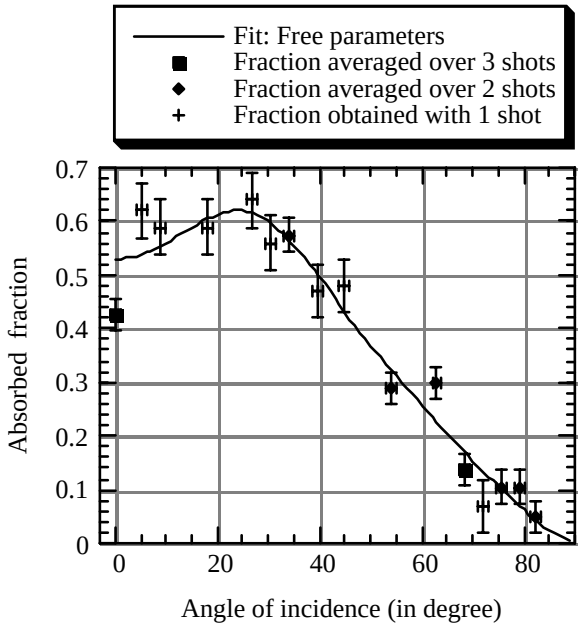

Figure 3: Fraction of energy absorbed as a function of the angle of incidence for p-polarised light. A curve fit is also plotted with the experimental data.

Errors bars introduced in Figure 3 were calculated the same way as for the s-polarisation case. The amount of laser energy absorbed increases from 45% at normal incidence up to 64% at an angle of about 30°. Consequently, the most efficient laser-plasma coupling is achieved at this optimum angle of incidence. At larger angles typically ranging from 30° to 82° the fraction of energy absorbed decreases from 64% to 5%. It is obvious that at intermediate angle of incidence inverse bremsstrahlung cannot be considered as the main absorption process occurring in the plasma. Moreover, the fraction of absorbed energy at 40° is twice that observed at the same angle in the s-polarisation graph which was about 25%. Numerical calculations performed by Milchberg and Freeman[9)] revealed that resonance mechanism presented at intermediate angles a peak absorption over a wide range of density scalelengths and hence, over a wide range of intensities. Thus, resonance absorption would be a good candidate to account for the relatively high absorption level measured here in this range of angles.

The curve fit plotted in Figure 3 corresponds to the best fit of the experimental data obtained by setting the parameters free. The fit function applied to the p-polarisation absorption data A_p was a combination of the two absorption mechanisms involved here:

$$A_p = A_{IB} + A_r$$

where A_{IB} is the collisional absorption fraction introduced earlier, and A_r is the fraction due to resonance absorption which can be expressed according to analytical results obtained by Landen [10]. In the limit of $k_0L_n >> 1$, where L_n is the plasma density scalelength, he found that numerical results tend towards an analytical solution for the resonant absorption of p-polarised light which could be written as a function of the incident angle θ:

$$A_r = C_{r1}\sin^2(\theta)e^{-C_{r2}\sin^3(\theta)}$$

where C_{r1} and C_{r2} will also be set as free parameters in order to obtain the best fit. The use of this analytical solution proposed by Landen for p-polarised light absorption implies relatively long density scalelengths which might not be the case of the intensity regime investigated here. This point will be discussed hereafter in this letter.

Substracting the absorption fraction for s-polarised light A_{IB} from that for p-polarised light A_p, it is then possible to deduce the absorption fraction due to resonant absorption as shown in Figure 4 versus the angle of incidence:

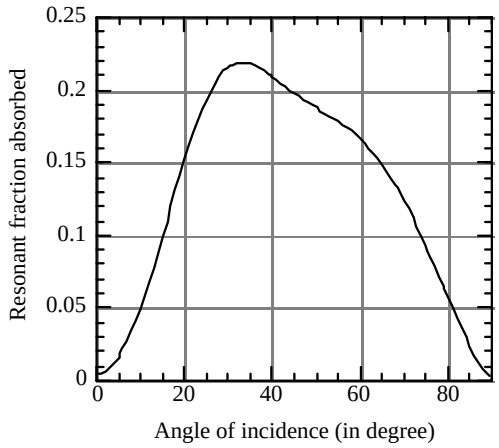

Figure 4: Fraction of energy absorbed by resonant absorption as a function of the angle of incidence deduced by substracting the best fits obtained for the s- and p-polarisation measurements.

The resonant absorption fraction remains under 15% at low angles of incidence since the laser electric field component lying in the plane of incidence is too small to efficiently generate plasma waves at the critical density. However, this mechanism becomes more efficient as the angle increases and presents a maximum of 22% at 33°. At higher angle, the component of the electric field parallel to the density gradient has however to tunnel a larger distance from the turning point to the critical density than at low angle of incidence, leading to a lowering of the resonant absorption mechanism. We observe a decrease of the absorbed fraction from 22% at 33° to 5% at an angle of 82°, and hence our data seem to be in good agreement with the model of resonant absorption. Furthermore, the resonance absorption peak seems to be confirmed by numerical calculations performed by Forslund [11] which shows a resonant peak of about 50% obtained for a value of the parameter function $\zeta = (k_0L_n)^{1/3}\sin\theta$ equal to 0.77. He made the hypothesis of a linear density profile and then verified that the resonant peak was still nearly 50% even over a wide range of angles, density gradient scalelengths and electron temperatures. Let us assume for now that in the intensity regime investigated here, the density profile can be better approximated with a linear density profile than with a solid-vacuum step-like profile, and that k_0L_n is large compared to unity. We point out that these assumptions will have to be confirmed with a complete investigation of the plasma density profile by means of simulation runs. Assuming this theory is applicable, the electric field which may excite plasma waves at the critical density has been expressed by Denisov in terms of the laser electric field in vacuum and the parameter function ζ [12]. Then, resonance absorption is optimum when ζ works out to be 0.8:

$$\zeta = (k_0 L_n)^{\frac{1}{3}}\sin\theta = 0.8$$

Thus, the density scalelength L_n can be inferred from the resonant peak measured experimentally at 33°. The plasma density scalelength turns out to be 0.12μm. We notice here a slight disagreement with the condition of validity of the resonant theory since L_n is of the order of the laser wavelength resulting in a k_0L_n value of about unity.

CONCLUSION AND FURTHER WORK

Absorption measurements of 450fs KrF laser pulses focused at an intensity of $4x10^{17}$ Wcm^{-2} on solid target have revealed an absorption level as high as 60% and 64% for s- and p-polarised light respectively. For both polarisations investigated here, absorption behaviour with respect to the angle of incidence are closely reproduced by curve fits proposed by the classical theory of absorption. However, further works will have to confirm whether or not the resonant absorption theory, firstly elaborated by Denisov and thereafter used by Landen, can be still applied to the data corresponding to plasma density scalelength of about 0.1μm. Detailed simulations will be performed by the author in order to estimate the density profile obtained during the interaction of the short pulse with the target. The role of the background ASE prepulse has not been discussed here, however, one of its effects would be an enhancement of the density scalelength due to the creation and expansion of a preformed plasma before the main short pulse reaches the target. According to the plasma formation threshold for UV laser pulses on metal target which is of $8x10^7$ Wcm^{-2} [13], it is reasonable to believe that a preplasma is created. The consequences of a preformed plasma on the absorption level measured will be evaluated by means of simulations and are the subject of ongoing studies carried out by the author. The high absorption level measured for s-polarised light might also be explained by the presence a preformed plasma.

REFERENCES

1) D. Riley, L.A. Gizzi, F.Y. Khattak, A.J. Mackinnon, S.M. Viana and O. Willi,
Phys. Rev. Lett. 69, 3739, (1992).

2) M. Tabak et al,
Phys. Plasmas 1 (5), 1626, (1994).

3) D. Riley, L.A. Gizzi, A.J. Mackinnon, S.M. Viana and O.Willi,
Phys. Rev. **E** 48, 4855, (1993).

4) M. Borghesi et al,
Rutherford Appleton Laboratory annual report (1994).

5) J.M.D. Lister, E.D. Divall, S.W. Downes, C.B. Edwards, G.J. Hirst, C.J. Hooker, M.H. Key, I.N. Ross, M.J. Shaw, W.T. Toner
Journal of Modern Optics, 41, 1203-1215, (1994).

6) Private communication with Jim Lister
Rutherford Appleton Laboratory, (1997).

7) R.P. Godwin
Appl. Opts. 33, Number 6, 1053, (1994).

8) A. Boivin and E. Wolf
Phys. Rev. E, 138, 1561, (1965).

9) H.M. Milchberg and R.R. Freeman
Opt. Soc. Am. B, 6, 1351, (1989).

10) O. Landen, D. Stearns, E. Campbell
Phys. Rev. Lett., 63, 1475, (1989).

11) Forslund, J. Kindel, K. Lee, E. Lindman, R.L. Morse,
Phys. Rev. A 11, 679, (1975).

12) N.G. Denisov
Soviet Physics JETP 4, 554 (1957).

13) R. Sauerbrey, et al.
Phys. Plasmas 1, 1635, (1994).

MEASUREMENT OF ELECTRONS SELF TRAPPED AND ACCELERATED TO 100 MEV BY A LASER-EXCITED RELATIVISTIC PLASMA WAVE

D. Gordon[1)], K. A. Marsh[1)], C. E. Clayton[1)], A. E. Dangor[2)], C. Joshi[1)], V. Malka[3)], A. Modena[2)], P. Muggli[1)], Z. Najmudin[2)]

1) University of California Los Angeles, CA, USA 90095
2) Imperial College of Science and Technology, London, U.K. E-mail zn1@ic.ac.uk
3) Ecole Polytechnique, Palaiseau, France

INTRODUCTION

The advent of short pulse high power lasers (such as Vulcan), has re-ignited interest in plasma waves as a source of high gradient electric fields. Such devices are of interest not only from a physics point of view, but also because they can be used as accelerating media for subatomic particles[1].

Previously with nanosecond pulses, it was necessary to precisely frequency match to the plasma wave using two synchronised beams, to resonantly excite it - the beatwave mechanism. Not only is this experimentally tricky, but the long time scale of the experiment allows significant plasma motion, which counters the precise frequency match and so limits the maximum accelerating field that can be achieved[2]. Short pulse lasers have many advantages. With the much higher intensities, the growth rate of the plasma wave is much greater. This means not only is it possible to grow a large plasma wave in a short time scale (Å picoseconds), so that plasma motion and other such instabilities are rendered impotent; but it also means that the plasma wave, by means of a feedback cycle, can grow from noise a second electro-magnetic wave which is exactly frequency matched to the plasma wave and pump laser. This in turn can further promote the plasma wave to grow. Hence avoiding the need for a second synchronised laser pulse. This method of growing plasma waves has been called the Self-Modulated Wakefield.

In a previous experiment[3], we were able to do a proof of principle demonstration of the self-modulated wakefield. In particular we were able to measure electrons trapped from the plasma and accelerated to beyond the cut-off of our detector, which was at that time 44 MeV. These results were correlated with optical diagnostics which provided evidence for the existence of the large amplitude plasma wave.

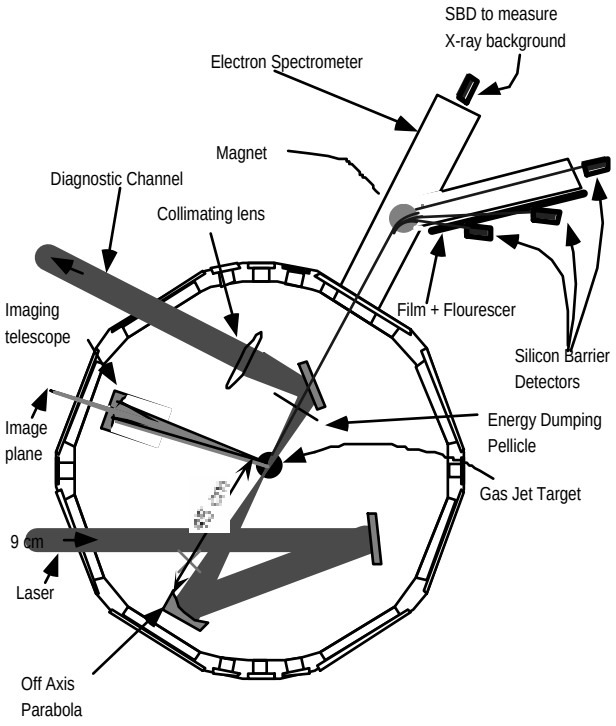

Figure 1 Experiment Set-Up

EXPERIMENT

The lay-out of the experiment is shown in figure 1. The Vulcan CPA beam is focused onto the edge of a supersonic gas jet, which provides a reasonably collimated flow of densities around 1×10^{19} cm^{-3}. The Å1ps, 24J (on target) laser beam was focused into a spot of diameter 20 µm. This gives intensities at focus greater than 5×10^{18} Wcm^{-2}. Not shown in the diagram is a transverse probe beam which is used for schlieren probing and Thomson scattering, (these diagnostics are reported on in a separate report). The transmitted laser beam is deflected away by a pellicle and recorded to validate the presence of the plasma wave.

The accelerated electrons were passed through an $f100$ lead collimator and dispersed using a Brown and Buechner electron spectrometer. The electron flux at a predetermined energy was measured using silicon barrier detectors of area 50 mm^2. A detector in the 'straight through' position acted as an indicator of the X-ray flux (since no electrons will have sufficient energy to reach this detector).

RESULTS AND CONCLUSIONS

Three typical electron spectra from "good shots" are shown in figure 2. As can be seen electron detectors placed to detect energies around 100 MeV, detect an electron flux double the X-ray noise level. The number of electrons in the lower energy 30 MeV channel is consistent with previous runs, in which our detection cut-off was at a lower energy. (In this experiment, the cut-off was greater than 200 MeV).

The 100 MeV electrons are interesting not only because they represent the highest energy yet confirmed from such a plasma based accelerator; but also because this is beyond the energy expected from a simple linear treatment of the acceleration process. With this assumption, the electrons should 'out-run' the plasma wave at an energy of 64 MeV. Theoretical work we have undertaken, indicates that the relativistic dependence of the plasma wave group velocity, allows electrons to be accelerated for longer distances and so provide greater final energies[4].

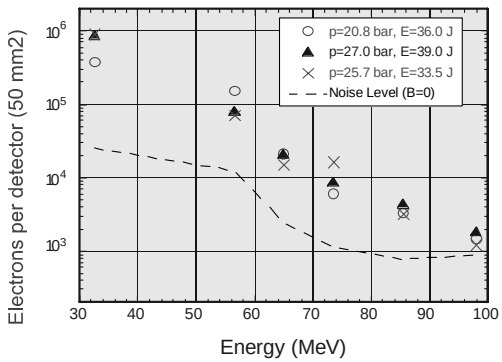

Figure 2 Electron spectra for three shots

REFERENCES

1) Tajima and Dawson, Phys. Rev. Lett., 43, 267 (1979)
2) F. Amiranoff et al., Phys. Rev. Lett., 68, 3710 (1992)
3) A. Modena et al., Nature, 377, 606 (1995)
4) D. Gordon et al., submitted to Phys. Rev. Lett.

FAST ELECTRON DEPOSITION IN LASER SHOCK COMPRESSED PLASTIC TARGETS

T A Hall[1], S Ellwi[2] , M Koenig[3] J Krishnan[4] , V Masella[2], F Pisani[2] , D Batani[3] , A Bernardinella[3] P Norreys[4] D Neely[4], S Rose[4] , M H Key[4] and A.P. Fews[5].

1) University of Essex, Colchester, CO4 3SQ. UK
2) LULI, Ecole Polytechnique, Palaiseau, France
3) Dipartimento di Physica, Universita di Milano, Italy
4) Rutherford Appleton Laboratory, Chilton, Didcot, OXON OX11 0QX, UK
5) Department of Physics, University of Bristol, Bristol, UK

INTRODUCTION

The fast ignitor scheme[1] gives a possible route to reducing the energy required to achieve break-even and gain in laser driven ICF. This scheme requires that an intense, short (~10^{19}Wcm^{-2}, 10 ps) laser pulse produces fast electrons which are then absorbed in a small region of dense compressed plasma in order to produce local heating and ignition. Experiments have been conducted to measure the fast electron production and the deposition of their energy in solid density targets and reasonable agreement has been obtained with models[2].

In this report we describe experiments using the VULCAN laser to extend these measurements to the study of fast electron production and deposition in shock compressed plasmas using k-alpha emission spectroscopy. The use of k-alpha emission from buried layer fluors is now an established technique and has been widely used in the study of fast electrons from femto second laser plasma interactions[3].

EXPERIMENT AND RESULTS

Fast electrons were produced on the "front side" of plastic foil targets by focusing the VULCAN CPA beam to a focal spot of 100 µm diameter using an f/10 off axis parabola (OAP). The energies of the CPA beam used in these experiments was in the range 2.5 to 15 J and the pulse length was 4 ps. Maximum irradiances on target were approximately 1 - 2x10^{16} Wcm^{-2}. These irradiances were chosen to make sure the electron range was matched to the target thickness for the shock compressed case, and that quasi-one dimensional irradiation conditions were maintained. The foil targets were compressed using three, 108 mm diameter frequency doubled long pulse beams (1 ns) of the VULCAN laser with a total energy of up to 160 J focused onto a spot of diameter 200 µm using random phase plates (RPA). The shock compression laser pulses were incident on the targets from the "rear side" i.e. from the opposite side from the CPA beam. The targets in these experiments consisted of a PVC plastic fluor layer (mostly of 13.5 µm thickness) sandwiched between two thicknesses of polyethylene. The thickness of the polyethylene layer on the front side of the target was varied from 10 µm to 150 µm. The rear side polyethylene overlayer was normally 20 µm except on some shots where there was no laser shock compression this layer was omitted.

The chlorine k-alpha spectra were recorded on DEF film using three PET flat crystal spectrometers. Two spectrometers were placed on the rear side, one at near normal incidence and the other at approximately 60° incidence and one spectrometer was placed on the front side at about 30° incidence. These positions and angles were mainly determined by beam constraints. Initial experiments were carried out using the long pulse beams alone to time the breakout of the shock by imaging the shock breakout region on the front of the target onto the slit of a visible streak camera[4] (using our definitions of "front side" and "rear side", the long pulse beams are incident on the "rear side" and the shock breakout is observed on the "front side"). The breakout was timed for various thicknesses of target and for a range of laser energies. The results that the shock wave is slowing down towards the rear of the thicker targets. This arises for two reasons, firstly the laser pulse does not sustain the drive pressure throughout the shock transit and the rarefaction wave follows rapidly. Secondly, two dimensional effects become important for the thicker targets where the thickness is of the same order as the focal spot diameter. Using these values of shock breakout, the short pulse beam was now timed to be incident on the front side 100 ps before shock breakout. This ensured that no expansion occurs from the front side and all but approximately 1 µm of plastic is compressed. For the thickest targets, no optical emission at breakout was observed due to the weakening of the shock and in these cases timing was achieved by extrapolation. This could be done with reasonable confidence because the results for the thinner targets are in very good agreement with code predictions.

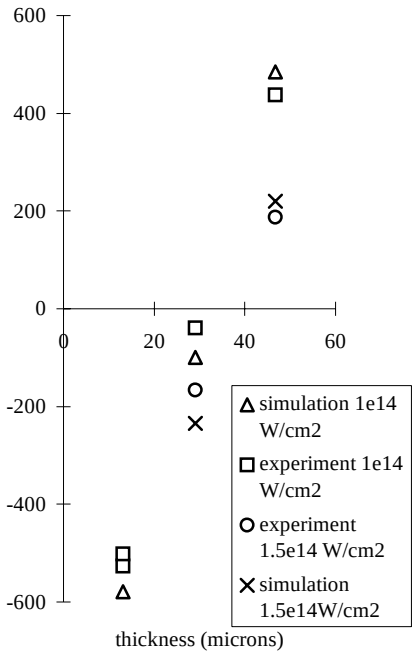

Figure 1 Experimental and simulation shock breakout times for various target thicknesses.

K-alpha spectra were obtained for a range of CPA laser pulse energies from about 3 J up to 15 J, corresponding to irradiances up to 2x10^{16}Wcm^{-2} on target. At higher irradiances than this the fog level on the DEF film masked the line spectra and made it impossible to obtain reliable results. The spectra were obtained for targets with and without shock compression and in the case of uncompressed targets some results were obtained when there was no rear side polyethylene layer covering the fluor layer.

On some laser shots, CR39 filtered track detector plastic was used in the chamber in order to measure the proton energy spectrum.

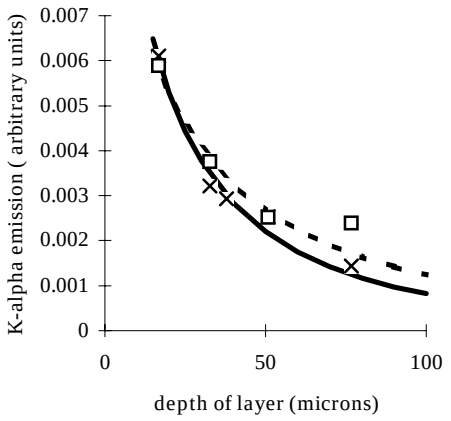

Figure 2 Uncompressed and compressed k-alpha yields. The continuous(30 keV) and broken lines(50keV) are the predictions of the model of Harrach and Kidder for the two hot electron temperatures.

The k-alpha x-ray intensity is plotted in figure 2 against the laser energy for one depth of buried fluor layer (16.5 µm). Although there is some scatter on this data, it is clear that there is a dependence on laser energy. The simplest assumption that the intensity is proportional to the laser energy is reasonable. With this scaling, the k-alpha emission is plotted in figure 4 as a function of depth of fluor layer for the uncompressed plastic. The continuous curve is derived from the work of Harrach and Kidder[5] where the deposition is of the form:

$$e(z) \mu \exp\left(-b\sqrt{\frac{z}{R_o}}\right)$$

with the value of b taken for carbon as 1.85. These values give the range, R_o, as 30±5 µm which, using the form from Harrach and Kidder:

$$R_o(kT_{hot}) = 3.8\times10^{-2}\,(kT_{hot})^{1.78} \quad \mu m$$

(where kT_{hot} is in keV) corresponds to a hot electron temperature of ~ 45 keV. This is not too different from the value obtained from the CR39 measurements which gives the value of kT_{hot} in the range 25 - 50 keV. These values are consistent with the hot electron temperature scaling given by Beg et al. which suggests that resonance absorption was the dominant absorption process.

The yields for the compressed plastic shows a significant scatter on the results which encompass the values obtained for the uncompressed plastic. The reasons for this scatter are not clear. Nevertheless a reasonably large number of shots were obtained for some thicknesses and average values can be taken. Figure 4 also shows the averaged values of the k-alpha yields of the uncompressed and compressed plastic together with a fit to the model of Harrach and Kidder. In this case the best fit to the experimental points gives an equivalent range for compressed material of 40 ± 10 µm.

The difference between the compressed and uncompressed targets is within the range of uncertainty of the results, however, the larger range of scatter of the results in the case of the compressed targets suggests in itself that there is a small but real difference. This could be from a variety of reasons.

The production of fast electrons could be affected by the shock compression if shock preheat were to cause some of the front side to spall or evaporate in advance of the shock arrival. Such an evaporation would provide a low density gas in front of the target prior to the arrival of the CPA pulse and thereby influence the absorption mechanism and hence fast electron production. The form of the thermal emission at shock breakout suggests from previous experiments [4] that there is no significant preheat but we did not take any particular efforts to measure preheat in these experiments.

A recent paper by Bell et al. [6] describes the conditions when flux inhibition can restrict the penetration of fast electrons. The penetration depth, z_o , given by Bell can be written in the form:

$$z_o = 3\times10^{-3}\,(kT_{hot})^2\ s_6\ I_{17} \quad \mu m$$

where s_6 is the conductivity of the material in units of 10^6 W^{-1} m^{-1}. The conductivity of the material inside the front surface of the target is likely to change very dramatically in space and time. The heat front from the CPA pulse will produce significant ionisation to a few microns depth (at these irradiances) but the shock compression will produce a relatively low degree of uniform ionisation. We would not expect the effective conductivity to exceed that of a good metallic conductor at room temperature. For the hot electron temperatures and irradiances appropriate to these experiments and assuming $s_6 < 1$, then

$$z_o < 1.6 \quad \mu m$$

Thus, flux inhibition will be important in the surface layers and the penetration of the electrons will be strongly dependent on the background material conductivity. The relatively small number of electrons that penetrate the surface layers will thus be dependent on the conductivity of the plasma near to the front surface. A change in effective conductivity of a factor of two is needed to explain the k-alpha results presented here.

The further possibility for the reason for the difference is due to dense plasmas effects on the cross section for fast electron excitation of the k shell electrons.

REFERENCES

1) Tabak M. et al
Phys. Plasmas, 1, (5), 1626, (1994)

2) Beg, F.N. et al
Phys. Plasmas, 4, 447, (1997)

3) Mancini, R.C. et al
J. Phys. B27, 1671, (1994)

4) Benuzzi, A. et al
Phys. Rev. E. , (1997)

5) Harrach, R.J. and Kidder
R.E. Phys. Rev. A, 23 ,2, 887, (1981)

6) Bell, A.R. and Davies, J.R.
Plasma Phys. Control Fusion, 39, 653, (1997)

CHARACTERISATION OF A SELF-MODULATED WAKEFIELD USING SELF GENERATED SECOND HARMONIC LIGHT

V. Malka[1)], C. E. Clayton[3)], A. E. Dangor[2)], K. A. Marsh[3)], A. Modena[2)], D. Neely[4)], F.N. Walsh[4)], Z. Najmudin[2)]

1) Ecole Polytechnique, Palaiseau, France
2) Imperial College of Science, Technology & Medicine, London, U.K. E-mail zn1@ic.ac.uk
3) University of California Los Angeles, CA, USA 90095
4) CLF, Rutherford Appleton Laboratory, Chilton, Didcot, Oxon

INTRODUCTION

Second harmonic generation in laser-plasma interaction is usually attributed either to the interaction of light with density gradients ($I \bullet \nabla n_e$) or intensity gradients with density ($n_e \bullet \nabla I$). As a consequence, second harmonic generation is useful in diagnosing non-linear propagation of laser pulses, in particular it is a common characteristic of filamentation instabilities.

For short-pulse high intensity laser-plasma interaction, second harmonic generation is expected to be a significant mechanism, not only due to the extremely high laser intensities, but also due to the extremely rapid form of plasma creation that results from such high intensities. For in these reactions, especially in the under-dense regime, the plasma is created predominantly by optical-field ionisation. This is the process whereby the intrinsic electric field of the laser is sufficiently high to strip atomic electrons from their ions. Since this mechanism is highly dependent on the laser electric field strength, there is a 'threshold' intensity at which ionisation is almost instantaneous. Hence the plasma creation follows contours of laser intensity.

EXPERIMENT

An experiment to investigate second harmonic generation in the underdense regime was conducted with the Vulcan CPA laser. The beam is focused onto the edge of a supersonic gas jet, which provides a reasonably collimated flow of densities around 1×10^{19} cm^{-3}. The gas jet is used to prevent ionisation defocusing reducing the intensity on focus. With a Å1ps, 24J (on target) laser beam, focused into a spot of diameter 20 µm, we obtained vacuum focused intensities greater than 5×10^{18} Wcm^{-2}. The transmitted laser beam is deflected away by a pellicle and recorded to validate the presence of plasma waves due to Self-Modulated Wakefields. One of the mirrors which transports this transmitted beam, allowed second harmonic to leak through. This is then passed through an optical spectrometer and recorded separately. Some of this transmitted green light was collected and passed into a calorimeter to give a calibration for the energy in the second harmonic. Electrons accelerated and emitted in the forward direction are recorded with an electron spectrometer. To complete the diagnostics imaging cameras were provided at 30° to the main beam, with a narrow band pass filter obstructing light at all frequencies except either the laser frequency ω or the second harmonic 2ω.

RESULTS

The spectrum of the transmitted green light, though centred at 2ω, has prominent satellites either side separated by the plasma frequency. The fact that the satellites are at $2\omega\pm n\omega_p$ and not $2(\omega\pm n\omega_p)$ shows that the second harmonic is generated and then scatters off a plasma wave, rather than being the second harmonic of already modulated light. The plasma wave is created by the self-modulated wakefield instability. Since the 2ω in our experiment is in the forward direction, by phase matching considerations, it must have scattered directly off the fast plasma wave left by the instability. So by considering the relative amplitude of satellites we can estimate the amplitude of the plasma wave. We obtain amplitudes close to the wave breaking amplitude for the plasma wave ($\nabla n_e / n_0 \approx 1$ - n_0 is the ambient density). This implies an electric field associated with the plasma wave of 100 $GeVm^{-1}$, and shows why such devices are candidates for next generation particle accelerators[1].

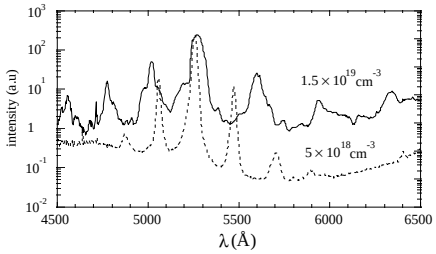

Figure 1 Spectrum of transmitted second harmonic

That the plasma wave is close to wave breaking comes as no surprise, since we observe copious energetic electrons[1] at densities around 1.5×10^{18} cm^{-3}. Signs of wave breaking are also apparent in the transmitted 2ω spectra at that density. The satellites appear broader and less smooth than at lower densities, which would be consistent with a turbulent disruption of the plasma wave, as would result from the excessive beam loading due to wave breaking.

The efficiency of second harmonic generation is found to be as high as 0.1% of the incident laser energy[2], and is found to increase linearly with the power of the driver laser. This is many orders of magnitude higher than found in similar (though lower power) experiments[3].

Images of the interaction in second harmonic light suggest that the 2ω is generated throughout the interaction region. Many shots do demonstrate that the second harmonic is generated in a hollow cone away from the focus. This is due not only to density gradients created by the nature of the ionisation (as mentioned above), but also enhancement of the density near the edge of this cone, due to ponderomotive blow-out of density in the higher intensity centre. However as shown in figure 2 some shots, particularly with a helium gas-jet, show sign of a filament within this cone. It is suspected that this is due to high intensity channelling of the laser beam. This observations has been supported by more recent investigations[4].

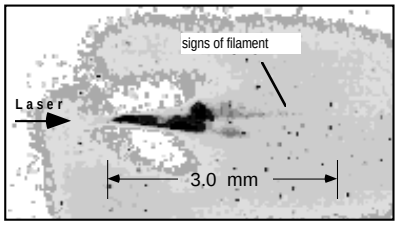

Figure 2 Image of scattered light through 2ω band-pass filter

REFERENCES

1) A. Modena et al
Nature, 377, 606 (1995)
2) V. Malka et al
Phys. of Plasmas, 4, 1127 (1997)
3) K. Krushelnick et al
Phys. Rev. Lett., 75, 3681 (1995)
4) C. E. Clayton et al
submitted to Phys. Rev. Lett.

RELATIVISTIC EFFECTS IN HIGH INTENSITY LASER-PLASMA INTERACTION

A. Modena[2)], C. E. Clayton[1)], A. E. Dangor[2)], C. Joshi[1)], K. A. Marsh[1)], V. Malka[3)], Z. Najmudin[2)]

1) University of California Los Angeles, CA, USA 90095
2) Imperial College of Science and Technology, London, U.K. E-mail zn1@ic.ac.uk
3) Ecole Polytechnique, Palaiseau, France

INTRODUCTION

Advances in short-pulse high power lasers has led to the possibility of obtaining relativistic intensities. By this we mean that the quiver velocity of electrons in the intrinsic electric field of the laser approaches the speed of light *c*. Such high-intensity lasers have generated much interest in recent years, due to their possible use for applications as diverse as X-ray lasers, particle accelerators and in fusion. However direct validation of the relativistic nature of the created plasma has proved more elusive. Here we report on measurements of the Forward Raman Scatter Instability (FRS) which provide evidence for relativistic electron quiver velocities.

EXPERIMENT

The Vulcan CPA beam is focused onto the edge of a well collimated supersonic gas jet, of densities around 10^{19} cm^{-3}. It has been found that the accuracy of focusing is significant. A movement of 500µm either into or out of the jet is found to degrade the results significantly. The ~1ps, 24J (on target) laser beam was focused into a spot of diameter 20 µm. This gives intensities at focus greater than 5×10^{18} Wcm^{-2} in vacuum. Note that with these parameters, the normalised vector potential a_0~2. At lower intensities, a_0 is equivalent to v_q/c, the quiver velocity. Hence we expect relativistic effects to be highly significant in this experiment.

The transmitted laser beam is deflected away by a pellicle and spectrally dispersed to look for Forward Raman Scattering. Raman scattering is the creation of plasma waves by the laser light at frequency ω_0 and a smaller amplitude electro-magnetic wave at $\omega_0\pm\omega_p$, usually generated from noise. The interaction of the laser with the plasma wave serves to amplify the lower amplitude satellite, so resulting in a feedback loop. Hence the signature of FRS is the electromagnetic sideband. These sidebands modulate the laser beam, hence the alternative name for this process; the self-modulational instability. At the high intensities in this experiment, the high growth rates for FRS lead us to expect FRS to be an important mechanism. The large amplitude plasma wave generated by the FRS is also responsible for the high energy electrons emitted in the forward direction which have also been recorded in such experiments [1)].

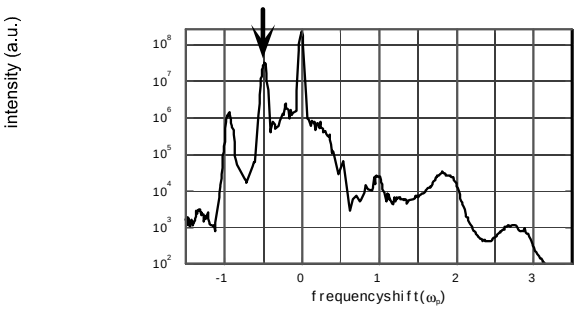

Figure 1 Transmitted laser spectrum showing signature of FRS as well as half harmonic (indicated by arrow)

RESULTS

A spectrum (normalised to the plasma frequency ω_p) of the light transmitted through a plasma of density 1×10^{19} cm^{-3}, is shown in figure 1. It clearly shows the cascade of satellites that are created by FRS. Noticeably there is also a prominent satellite at ω_0-$\omega_p/2$. Multiple harmonics are not rare in non-linear laser plasma interactions, but half harmonics are more difficult to explain. An explanation for this phenomenon has been provided by G. Shvets[2)]. At very high laser intensities, one must consider higher order terms for the relativistic change in electron mass. The second order term of the ponderomotive force ($\propto(a^2)^2$) introduces a term $\propto(a_0\bullet a_1)^2$, where a_1 is the scattered vector potential, in the equation of motion of the electrons. Thus e-m components differing in frequency by $\omega_p/2$ from the laser frequency can resonantly match with plasma oscillations at frequency ω_p, so allowing the half-harmonics to grow rapidly.

The appearance of the half harmonic is found to be difficult to predict, though it is observed only above densities of 8×10^{18} cm^{-3}. This is maybe not surprising since it requires both a high laser intensity and a large plasma wave amplitude to seed it. This effect has been called the Explosive Raman Instability.

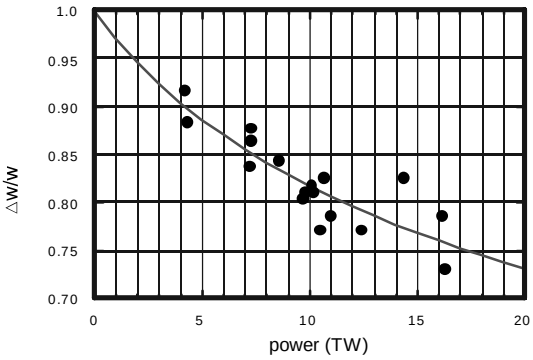

Figure 2 Sideband frequency separation/plasma frequency as a function of laser power.

A more direct measurement of the change of electron mass with laser intensity is shown in figure 2. The relativistic mass increase is proportional to $\gamma_{osc}=[1-(v_{osc}/c)^2]^{-1/2}$ the Lorentz factor, where v_{osc} is the oscillating velocity of the electrons in the laser field. As ω_p is inversely proportional to the electron mass the actual separation of the sidebands should decrease with intensity, as is observed in the figure. The continuous curve is a best fit with the formula $\omega_p/\omega_{p0} = (1+a_0^2/2)^{-1/4}$. The fit gives ω_p/ω_{p0} = 0.102 and a maximum intensity at 16 TW of 5×10^{18} Wcm^{-2}. Of course at such high intensities ponderomotive expulsion of electrons could also account for the decreasing effective plasma frequency. However recent simulations have shown that thermal pressure due to heating by FRS can prevent cavitation. Hence ponderomotive blow-out is not expected to be significant in the case of a plasma susceptible to FRS[3)].

REFERENCES

1) A. Modena et al, Nature, 377, 606 (1995)
2) G. Shvets et al.
Physics of Plasmas, 3, 3, 209 (1996); A. Modena et al., IEEE Trans. Plas. Sci., 24, 2, 289 (1996)
3) A. Modena
PhD thesis, Imperial College (1996); K-C. Tzeng, W. B. Mori, *private communication*

THE TITANIA KRYPTON FLUORIDE LASER: A SOURCE OF BRIGHT, EXTREME-ULTRAVIOLET HARMONIC RADIATION

S.G. Preston[1)], D.M. Chambers[1)], R.S. Marjoribanks[2)], P.A. Norreys[3)], D.Neely[3)], M. Zepf[1)†], J. Zhang[1)], M.H. Key[1),3)§], J.S. Wark[1)].

[1]Department of Physics, Clarendon Laboratory, University of Oxford, Parks Road, Oxford, OX1 3PU, UK.

[2]University of Toronto, Department of Physics, McLennan Physical Labs, 60 St. George Street, Toronto, Ontario, M5S 1A7, Canada.

[3]Rutherford Appleton Laboratory, Chilton, Didcot, Oxon, OX11 0QX, UK.

† Current address: Blackett Laboratory, Imperial College, London, SW7 2BZ, UK.

§ Current address: Lawrence Livermore National Laboratory, Livermore, CA 94550, USA.

INTRODUCTION

Recent advances in short pulse, high power laser technology have stimulated much interest and great research effort into the generation of coherent extreme ultraviolet (XUV) radiation by the non-linear process of high harmonic generation in a gaseous medium to generate wavelengths as short as 67 Å [1)]. Such a source can provide intensities that, until recently, were only available from optical laser systems and show great promise for use in applications such as interferometry, holography, opacity measurements, radiography and pump-probe spectroscopy.

It is now well known that the harmonic spectrum forms a plateau of odd-integer harmonics of the incident laser frequency, extending to a maximum photon energy of (where I_p is the ionisation potential of the atomic species, and is the ponderomotive potential of a laser field of frequency ω). The $3.17U_p$ term is the maximum possible kinetic energy of an electron returning to the core. Above this cut-off, the harmonic emission rapidly falls off to a negligible level.

The $1/\omega^2$ dependence of the ponderomotive potential implies that a long wavelength laser is needed to generate the highest harmonic order for a given ionisation stage. This is of great interest for studying and understanding the physical processes involved, but has the practical disadvantage that to generate harmonic radiation at a given frequency, one must produce a higher harmonic order than if a shorter wavelength were used. This is detrimental to the efficient production of XUV radiation by high harmonic generation through both phase matching and the single atom response[2) 3)]. With the recent commissioning of the TITANIA Krypton Fluoride laser, it is timely to investigate whether using a short wavelength laser does indeed lead to an increase in the harmonic generation efficiency over that from a longer wavelength laser.

THE EXPERIMENT

TITANIA was used in CPA mode[4)] to deliver up to 200±20 mJ to target, with a pulse length of ~350 fs and a wavelength of 248.6 nm. The data presented here are the result of the first experiments to be performed on this new laser. The 8 cm diameter laser beam was focused with a 100 cm focal length off-axis parabolic mirror (OAP) to a 10-30 times diffraction limited spot (with considerable internal structure on the scale of the diffraction limit).

The laser focus was positioned 1 mm above a solenoid-valve gas jet fitted with a 1 mm diameter, circular cross-section output nozzle. Gas targets of Helium and Neon were provided at a range of densities using backing pressures between 0.5 and 12 bar, although we only present results from 1.25 bar Neon here. (A more complete review of the data has been submitted for publication[2)]). A (triple mirror) imaging XUV spectrometer, placed in the cone of the laser beam behind the gas jet, was used to relay the laser focus onto a 1024 x 1024 pixel back-thinned CCD detector. Aluminium filters were placed in front of the spectrometer to block the KrF beam. A focal scan was performed by moving the gas jet along the direction of the laser beam while keeping the (vacuum) focal position of the OAP fixed. This ensured that the spectrometer always sampled the nominal laser focus.

HARMONIC GENERATION EFFICIENCIES

Figure 1 shows the variation of the generation efficiencies of the 7th to 13th harmonics in Neon, at a backing pressure of 1.25 bar, as a function of the position of the gas jet with respect to the vacuum laser focus (positive numbers indicate that the laser is focused before the gas jet).

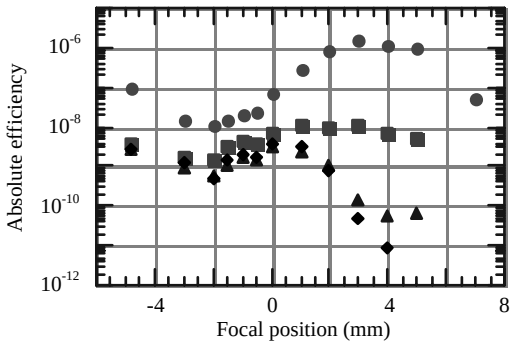

Figure 1. The variation of harmonic generation efficiencies with gas jet position for Neon at 1.25 bar. The harmonics shown are the 7th (circles), 9th (squares), 11th (triangles), and 13th (diamonds).

These generation efficiencies were calculated by taking into account the transmission of the Aluminium filters[5)], the response of the CCD camera[6)], and the reflectivity of the Hitachi grating[7)]. The total harmonic energy in the laser beam was calculated by multiplying the energy per unit solid angle collected by the first (axial) and the second mirrors by the solid angle of an annulus defined by the inner and outer angles subtended by the mirrors (by the beam in the case of the second mirror). The (third) outer mirror was outside the cone of the laser beam, and so did not collect any harmonic emission.

It should be noted that the conversion from the solid angle of the spectrometer to the solid angle of the annulus for the second mirror uses the outer angle of the beam. This is done as an approximation, as we do not know how the beam divergence is affected by passing through the gas target. If the emerging beam is refracted to cover the whole of the second mirror, then the maximum estimated energies would be increased to about 170% of the values presented.

The highest conversion efficiency of 3×10^{-6} for Neon was achieved using a backing pressure of 3 bar with the laser focused 3 mm before the gas jet. This conversion efficiency was achieved for laser shots with energies on target of between 190 and 220 mJ. This corresponds to a total harmonic yield of 700 nJ (or 1.2 µJ if calculated assuming the beam covers the full aperture of the middle mirror). The energy of the 9th

harmonic is two orders of magnitude less than the 7th harmonic under these conditions.

The maximum harmonic yield is lower at pressures below and above the optimum pressure of ~1.25-3 bar. Such a density dependence has been seen in other experiments[8]. The harmonic yield rises with gas density as the overall increase in the number of atoms within laser beam area and within a coherence length, despite the shortening of the coherence length caused by the higher density of free electrons as ionisation occurs. The data taken at 1.25 bar and 3 bar are essentially the same when errors due to shot-to-shot variation is accounted for. However, shots taken at sub-atmospheric backing pressures (not shown) produced lower efficiencies than the 1.25 bar data.

The data is symmetric about the -2 mm focal position. We attribute this offset to the harmonic signal coming from the last coherence length of the laser before it leaves the gas target, but it is also possible that the effective focal position of the laser is translated axially by refraction effects. (A full characterisation of the gas jet will be published at a later date). Within the extent of the focal scan, the harmonic generation efficiency appears to increase to a local maximum (at +3 mm) and then to rapidly fall off. This behaviour can easily be described by a simple model.

SIMULATIONS

The axial intensity profile of the laser is modelled as that of a non-diffraction limited beam with a focal spot radius, r_0, chosen to produce the best fit to the experimental data within the laser confocal parameter, which is chosen to match the correct f-number (f/12.5), in the geometric limit, using the relation $b = 2fr_0$.

The focal spot radius is then expected to vary axially (along the z-axis) as that of a Gaussian beam, i.e.

$$r(z)^2 = r_0^2\left(1+\frac{z^2}{b^2}\right)$$

So, the mean laser intensity of a beam of power, P, at an axial position, z, is

$$I(z) = \frac{Pb^2}{\pi r_0^2\left(b^2+z^2\right)},$$

over an area

$$A(z) = \frac{\pi r_0^2\left(b^2+z^2\right)}{b^2}.$$

The single atom harmonic response at varying intensities through the focus is obtained by solving the time-dependent Schrödinger equation in one spatial dimension using the Crank-Nicholson method. In common with most 1D calculations, the atomic core is represented by the soft-core (Rochester) potential [9), 10)] given by

$$V(x) = \frac{-Z}{\sqrt{a^2+x^2}}$$

where Z is the charge state (set to unity for a neutral atom), x is the spatial dimension, and a is a fitting parameter chosen to closely match the ionisation potential of neutral Neon (Z = 1, a = 0.82). The laser field is represented as a sinusoidally varying electric field (248.6 nm wavelength) enveloped by a 128 cycle sine-squared profile (~100 fs). Using a 100 fs pulse envelope does not significantly alter the results from using the longer (~350 fs) pulse, but does considerably reduce the runtime of the simulation.

We would expect the total harmonic yield to be proportional of the number of atoms within a volume determined by the beam area and the coherence length, and so we multiply the single atom response by the effective beam area, $A(z)$, and by the coherence length. The coherence length is assumed to be entirely due to the dephasing effects of the free electron density, which is calculated from the level of ionisation predicted by the single atom simulation. The level of ionisation was taken at the peak of the electric dipole acceleration of the atom. The simulated results must then be shifted by -2 mm to allow for the experimental offset and multiplied by a constant factor to match the magnitude of the experimental data.

Figure 2 compares the experimental data (7th harmonic from 1.25 bar Neon) with the simulated harmonic yield. The three lines represent the single atom response alone (dashed line); the single atom response weighted by the beam area alone (dotted line); and the single atom response weighted by both the beam area and the coherence length (solid line).

The best fit for the focal spot radius, r_0, was found to be about 30 µm - which is consistent with equivalent plane monitor measurements of the TITANIA focal spot. The mean laser intensity in a focal spot of this size is approximately 2 x 10^{16} W/cm^2. The form of the simulation only depends on the chosen value of the minimum focal spot size, r_0, within approximately one confocal parameter of the laser focus. After this, the axial dependence of the beam area asymptotically approaches that determined by the geometric limit - the f-number of the focusing parabola.

Neon 7th harmonic focal scan.

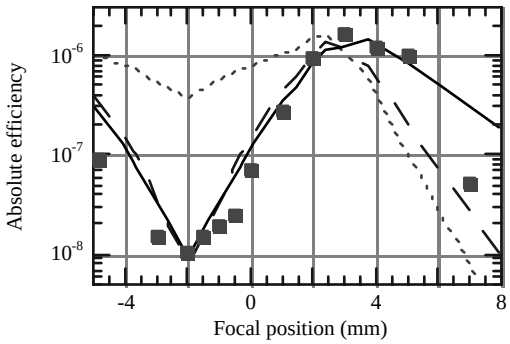

Figure 2. A comparison of the generation efficiency of the 7th harmonic in 1.25 bar Neon (squares) with the single atom response (dotted line), and with the volume weighted single atom response assuming a constant coherence length (dashed line), and assuming a coherence length determined by the free electron density (solid line). The data is plotted as a function of the focal position of the laser relative to the gas jet.

The correlation between the experimental data and the simulation is remarkably good over the entire focal scan, demonstrating the accuracy of the one-dimensional code when combined with simple volume effects. (A similar close agreement - over the whole harmonic spectrum - between volume weighted, one-dimensional simulations and experiment was demonstrated in previous publications[1) 3)]). The simulated response including dephasing effects appears to follow the experimental data most closely, until we move beyond the peak of the harmonic yield. After this the reduction in laser intensity causes the ionisation rate to rapidly fall off to a negligible level, resulting in an unphysically long coherence length. Therefore, dephasing in this region will be determined by the smaller of the coherence length determined by dispersion in the neutral gas target and phase effects in the beam, or the length of the gas target. This is why the simulation weighted by just the area

(where we assume the coherence length to be constant) better describes the experimental results in this low intensity region.

Figure 3 shows the experimental and simulated harmonic responses as functions of the intensity inferred from the fit of the simulation to the data. The experimental data peaks at a slightly lower intensity than the single atom response. This is because the beam area is a faster varying function of intensity than the single atom response at intensities from about 4-8 x 10^{14} W/cm^2.

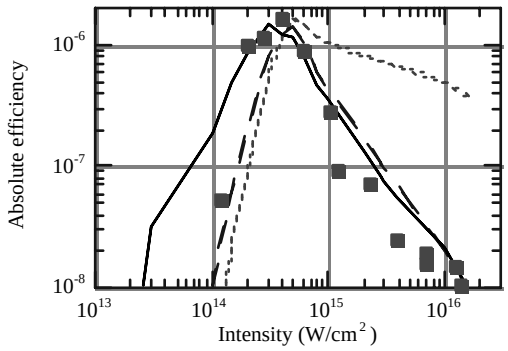

Figure 3. The same data as in figure 2, plotted against the intensity inferred from the simulations.

SOURCE BRIGHTNESS

Making the conservative assumption that harmonic emission occurs from the full area of the laser beam as it passes through the gas jet and then follows the (f/12.5) divergence of the laser; and that harmonic emission occurs for half of the laser pulse (~175 fs), we can calculate a lower bound on the spectral brightness of the 7th harmonic (355 Å) source. The (instrument limited) upper bound on the fractional bandwidth of the source, $\Delta\omega/\omega$, is ~3 x 10^{-3}, giving a minimum spectral brightness of more than 2 x 10^{15} W.steradian^{-1}.cm^{-2}$(\Delta\omega/\omega)^{-1}$.

This spectral brightness compares well with that recently produced from a source of harmonic radiation at the same wavelength from a laser-solid interaction (estimated to be ~6 x 10^{14} W.steradian^{-1}.cm^{-2}$(\Delta\omega/\omega)^{-1}$ at a laser intensity of 4 x 10^{18} W/cm^2, and extrapolated to ~8 x 10^{15} W.steradian^{-1}.cm^{-2}$(\Delta\omega/\omega)^{-1}$ at 10^{19} W/cm^2)[11]. These 'solid harmonic' results required a 20J, 20 TW laser system, rather than the 200 mJ, 0.5 TW of the TITANIA laser system.

However, the gas harmonic spectral brightness is significantly lower than the best current value for an X-ray laser (3 x 10^{18} W.steradian^{-1}.cm^{-2}$(\Delta\omega/\omega)^{-1}$ at the shorter wavelength of 19.6 nm [12]). However, the harmonic source has the advantage of having a sub-picosecond pulse length (compared to ~40 ps for the X-ray laser), and is potentially tuneable over all frequency space up to the harmonic cut-off [13]

We also note that the TITANIA laser will soon reach its full design specification and deliver up to 1.5 J in 350 fs, with three times diffraction limited divergence. The latter criterion has already been achieved and will enable focusing of the beam to the same spot size with a much longer f-number, which could increase the harmonic brightness by an order of magnitude or more.

CONCLUSION

We have measured the harmonic conversion efficiency from Helium and Neon as a function of the axial focal position of the laser with respect to the centre of the gas target and as a function of the gas density determined by the backing pressure of the gas jet valve used. The experiments produced conversion efficiencies into the 7th harmonic (355 Å) of over 3 x 10^{-6}, which are (to our knowledge) the highest demonstrated to date. The axial variation of the harmonic yield can be explained by a very simple model incorporating a one-dimensional, single atom harmonic generation code.

We have placed a conservative lower bound on the brightness of the harmonic source, at the optimum focal position and gas density, of 2 x 10^{15} W.steradian^{-1}.cm^{-2}$(\Delta\omega/\omega)^{-1}$. Such a source shows great promise for use in novel, high intensity XUV applications.

ACKNOWLEDGEMENTS

This work was funded by a grant from the Engineering and Physical Sciences Research Council (EPSRC) of the UK. The authors would gratefully like to acknowledge help received from the staff of the Rutherford Appleton Laboratory, UK, and especially from the TITANIA laser operations staff. S.G. Preston acknowledges support from Merton College, Oxford. D.M. Chambers acknowledges support from the EPSRC, and from AWE, Aldermaston.

REFERENCES

1) S.G. Preston, A. Sanpera, M. Zepf, W.J. Blyth, C.G. Smith, K. Burnett, M.H. Key, J.S. Wark, D. Neely, A.A. Offenberger
Physical Review A, 53 (1), R31-34 (1996).

2) S.G. Preston, D.M. Chambers, R.S. Marjoribanks, P.A. Norreys, D. Neely, M. Zepf, J. Zhang, M.H. Key, J.S. Wark
Submitted to Physical Review A, (1997).2

3) S.G. Preston
D. Phil Thesis, University of Oxford, (1995)

4) E.J. Divall, C.B. Edwards, G.J. Hirst, C.J. Hooker, A.K. Kidd, J.M.D. Lister, R. Mathumo, I.N. Ross, M.J. Shaw, W.T. Toner, A.P. Visser, B.E. Wyborn
Journal of modern optics, 43 (5), 1025-1033 (1996).

5) B.L. Henke, P. Lee, T.J. Tanaka, R.L. Shimabukuro, B.K. Fujikawa
Atomic Data and Nuclear Data Tables, 27 (1), 1-144 (1982).

6) T. Ditmire, J.K. Crane, H. Nguyen, L.B. DaSilva, M.D.†Perry
Physical Review A, 51 (2), R902-R905 (1995).

7) D. Neely, D.M. Chambers
RAL-TR-96-74 (1997).

8) C. Altucci, T. Starczewski, E. Mevel, C.-G. Wahlstrom, B.†Carre, A. L'Huillier
Journal of the Optical Society of America B, 13 (1), 148-155 (1996).

9) A. Sanpera, P. Jonson, J.B. Watson, K. Burnett
Physical Review A, 51 (4), 3148-3153 (1995).

10) Q. Su, J.H. Eberly
Physical Review A, 44 (9), 5997-6008 (1991).

11) D.M. Chambers, S.G. Preston, M. Zepf, M. Castro-Colin, M.H. Key, J.S. Wark, A.E. Dangor, A. Dyson, D. Neely, P.A. Norreys
Journal of Applied Physics, 81 (5), 2055-2058 (1997).

12) J. Zhang et al
Physical Review A, 54 (6), R4653-R4656 (1996).

13) S.G. Preston, J.B. Watson
Submitted to Physical Review A, (1997).

CALCULATIONS OF POPULATION DENSITIES IN NON-MAXWELLIAN LASER-PRODUCED PLASMAS

J M A Ashbourn[†] and N N Ljepojevic[‡]

Centre for Computer and Mathematical Modelling, School of Electrical, Electronic and Information Engineering,
South Bank University, 103 Borough Road, London SE1 OAA, England

INTRODUCTION

Many laboratory and astrophysical plasmas have been found to have non-Maxwellian electron distributions. It is of some interest to study the influence that the high energy tail of the electron energy distribution function (EEDF) has on the population densities of various ions in such plasmas. In this paper, we present a brief account of the effects of non-Maxwellian electron energy distributions on the population densities of excited atomic levels for hydrogen-like ions in a "self-plasma", such as would be produced by a laser. We model the electron energy distribution function by two Maxwellian finite elements, one approximating the bulk distribution with temperature T_b and the other the tail distribution with temperature T_t. We present results for various T_b/T_t ratios for AI XIII, which is commonly employed in laser-produced plasmas.

CALCULATION OF NON-MAXWELLIAN POPULATION DENSITIES

In this paper, we consider electron distributions which can be described by two finite Maxwellian elements at two different temperatures, one being the bulk temperature, T_b and the other being the tail temperature, T_t, for the tail of the distribution function. The first represents the distribution in the energy region $0 \le E \le E_c$ and the second that in the energy region $E_c \le E \le \infty$, where E_c, is the joining point of the two regions. At $E = E_c$ the distribution is continuous. We have modified the program COLRAD[1)] to include the effect of electrons having different temperatures in different energy regions. We consider the tail temperature to only affect transitions from the n = 1 level to all other levels and the bulk temperature to affect all other transitions from levels i to j where $i \neq 1$. We assume that E_c is less than the first inelastic threshold $|E(1S_{1/2})-E(2P_{1/2})|$.

The program uses a collisional-radiative model and the processes which are affected by the tail temperature are all electron collision transitions from the ground state, $1S_{1/2}$, to any other allowed level:

- Excitation by electron impact

$$H(1S_{1/2}) + e \rightarrow H(j) + e$$

- Ionization by electron impact

$$H(1S_{1/2}) + e \rightarrow H^+ + 2e$$

where j labels the atomic levels. All other processes involve only the bulk temperature for the calculation of the rate coefficients for each process. The rate coefficients for the inverse transitions back down to the ground state from all allowed levels are normally calculated by the principle of detailed balance from the rate coefficients for the original transitions from $1S_{1/2}$ to these levels. Since, however, the rate coefficients for the inverse processes depend on the bulk temperature, and not the tail temperature used for the original rate coefficients for the ground state, the calculations need to be repeated using the temperature T_b.

RESULTS FOR HYDROGEN-LIKE AL XIII

In this section, we present the results for calculations of the population densities of the fine structure levels, $1S_{1/2}$ to $3D_{5/2}$, as calculated by COLRAD, for the hydrogen-like ion, AI Xlll, in a "self-plasma", i.e. in a plasma produced using pure aluminium as the laser target. We consider electron temperatures at which it is reasonable to assume that all the aluminium atoms are ionized to the hydrogen-like state or are fully stripped bare nuclei. The bulk electron temperature considered in this brief report, T_b, is 1 keV, while the tail electron temperature for the non-Maxwellian distribution function, T_t, is varied around this bulk temperature by increasing it by a factor of 2 and then decreasing it by a factor of $\frac{1}{2}$. The ion temperature is set equal to the bulk electron temperature for the cases considered below.

Table 1 shows the results for the excited level population densities considered as described above, and it can be seen that using a non-Maxwellian distribution affects the population densities of each fine structure level quite markedly. If the tail temperature is twice as large as the bulk electron temperature, T_b= 1 keV, it can be seen from Table 1 that the non-Maxwellian population density is decreased from the Maxwellian population density by nearly a factor of 4 for the ground state, $1S_{1/2}$, and is decreased by nearly a factor of 2 for most of the other excited levels. When the tail temperature is half the bulk temperature, T_b= 1 keV, the non-Maxwellian population densities are seen to be increased by nearly one and a half orders of magnitude for the $1S_{1/2}$ level. As in the previous case, most of the other excited levels are increased by over a factor of 2 from the Maxwellian population densities, which is approximately the same as is observed when the tail temperature is twice the bulk temperature.

When $T_t = 2T_b$ for a hydrogen base plasma with hydrogen-like AI XIII, the reduction in the population densities for all the levels for a bulk temperature of 1 keV is smaller than it is when these are calculated for a bulk temperature of 500 eV, which in turn is smaller than that for a bulk temperature of 250 eV. The

[†] Email address: J.M.A.Ashbourn@damtp.cam.ac.uk

[‡] Email address: N.N.Ljepojevic@damtp.cam.ac.uk

inverse effect for the enhancement in the population densities for the case when $T_t = \frac{1}{2} T_b$ is seen as the bulk temperature is reduced to 500 eV and then to 250 eV.

CONCLUSION

When T_b and T_t are large, increasing T_b depletes the $1S_{1/2}$ state which results in all excited level populations being decreased with increasing T_t and being increased with decreasing T_t. When T_b is low, then the population density of the $1S_{1/2}$ state is large and not very sensitive to T_t, so that the behaviour of the excited levels due to T_t reverses. However, for such low temperatures our assumption that atoms are all in the hydrogen-like ionisation state is no longer valid, so we cannot quantitatively consider such cases.

When the Lyman-α intensity ratios are calculated for the non-Maxwellian case, the values do not vary much from those for the Maxwellian case, but this slight variance increases with increasing electron density so that for the higher electron densities, n_e, considered in this paper, the percentage difference between the two sets of values has become about 5%.

Table 1: Table of population densities for the fine structure levels $1S_{1/2}$ to $3D_{5/2}$ ratios for Al XIII in a Al "self-plasma" with the bulk electron temperature equal to 1 keV. The tail electron temperature is multiplied by factors of 2 and 1/2 so that the three cases of the tail electron temperature considered are 1 keV (Maxwellian), and 500 eV and 2 keV (non-Maxwellian). The electron density range, n_e, is as shown.

n_e (cm^{-3})	10^{18}	10^{19}	10^{20}
Level			
		T_t = 1000 eV	
$1S_{1/2}$	6.757 x 10^{16}	6.314 x 10^{17}	5.544 x10^{18}
$2S_{1/2}$	5.487 x 10^{11}	6.053 x 10^{12}	1.347 x 10^{14}
$2P_{1/2}$	1.143 x 10^{10}	1.072 x 10^{12}	9.264 x 10^{13}
$2P_{3/2}$	1.394 x 10^{10}	1.313 x 10^{12}	1.179 x 10^{14}
$3S_{1/2}$	1.349 x 10^{10}	5.610 x 10^{11}	3.286 x 10^{13}
$3P_{1/2}$	5.268 x 10^{9}	4.827 x 10^{11}	3.242 x 10^{13}
$3P_{3/2}$	6.350 x 10^{9}	5.615 x 10^{11}	4.918 x 10^{13}
$3D_{3/2}$	4.442 x 10^{9}	5.299 x 10^{11}	4.898 x 10^{13}
$3D_{5/2}$	5.052 x 10^{9}	5.664 x 10^{11}	6.533 x 10^{13}
		T_t=2000 eV	
$1S_{1/2}$	1.855 x 10^{16}	1.787 x 10^{17}	1.659 x 10^{18}
$2S_{1/2}$	3.031 x 10^{11}	3.467 x 10^{12}	8.336 x 10^{13}
$2P_{1/2}$	6.571 x 10^{9}	6.353 x 10^{11}	5.813 x 10^{13}
$2P_{3/2}$	8.206 x 10^{9}	7.969 x 10^{11}	7.577 x 10^{13}
$3S_{1/2}$	8.830 x 10^{9}	3.829 x 10^{11}	2.419 x 10^{13}
$3P_{1/2}$	3.493 x 10^{9}	3.304 x 10^{11}	2.387 x 10^{13}
$3P_{3/2}$	4.287 x 10^{9}	3.942 x 10^{11}	3.690 x 10^{13}
$3D_{3/2}$	3.128 x 10^{9}	3.746 x 10^{11}	3.678 x 10^{13}
$3D_{5/2}$	3.715 x 10^{9}	4.187 x 10^{11}	4.978 x 10^{13}
		T_t=500 eV	
$1S_{1/2}$	7.757 x 10^{17}	6.849 x 10^{18}	5.415 x 10^{19}
$2S_{1/2}$	1.376 x 10^{12}	1.430 x 10^{13}	2.823 x 10^{14}
$2P_{1/2}$	2.794 x 10^{10}	2.473 x 10^{13}	1.924 x 10^{14}
$2P_{3/2}$	3.361 x 10^{10}	2.987 x 10^{12}	2.410 x 10^{14}
$3S_{1/2}$	2.462 x 10^{10}	9.624 x 10^{11}	5.007 x 10^{13}
$3P_{1/2}$	9.568 x 10^{9}	8.271 x 10^{11}	4.939 x 10^{13}
$3P_{3/2}$	1.141 x 10^{10}	9.441 x 10^{11}	7.386 x 10^{13}
$3D_{3/2}$	7.623 x 10^{8}	8.846 x 10^{11}	7.350 x 10^{13}
$3D_{5/2}$	8.243 x 10^{9}	9.010 x 10^{11}	9.673 x 10^{13}

REFERENCES

1) N N Ljepojevic, R J Hutcheon, and J Payne Comput. Phys. Comm. **44,** 157 (1987).

DIRECT FORWARDS SCATTERING FROM LASER PULSES AT UP TO 10^{20}W/CM^2

H C Barr , S J Berwick, P Mason

Department of Physics, University of Essex, Colchester, Essex CO4 3SQ, UK. Email barrhc@essex.ac.uk

INTRODUCTION

Relativistically intense laser pulses which are many plasma wavelengths in extent are unstable in one dimension to stimulated Raman direct forward scattering (SRFS) and the relativistic modulational instability (RMI)[1-4]. This leads to rapid pulse break-up, generation of large amplitude, relativistically fast electron plasma waves, and complex emission spectra. At intensities of 10^{18}Wcm^{-2} and above the laser-induced relativistic electron mass increase is a dominant factor in determining the instability characteristics ($I_L\lambda^2_L$ = $1.37\times10^{18}q^2$Wcm$^{-2}\mu$m^2, q=eA/mc^2 and A is the vector potential of the laser pulse). The variable intensity across short pulses provides an inhomogeneous environment and a localisation of the resonance. A stability analysis is carried out for the intensity regime up to 10^{20}Wcm^{-2} and the linear and non-linear space-time evolution studied by numerically evolving the full 1d relativistic fluid equations (without use of enveloping or quasistatic approximations) .

ANALYTIC AND COMPUTATIONAL MODEL

Consider direct forward scattering of a linearly polarised laser pulse from an underdense plasma modelled by the 1d covariant fluid equations. The vector potential a is given by

$$\ddot{a} - a'' + \frac{\omega_{p0}^2}{\gamma}\frac{n}{n_0}a = 0$$

where dots are time derivatives, primes space derivatives in the propagation direction (x), n_0 is the ambient electron (ion) density assumed constant, n is the electron density, ω_{p0} is the plasma frequency and γ is the relativistic mass increase. Times are normalised to ω_o^{-1}, lengths to c/ω_0, densities to the laser critical density n_c, and a=eA/mc^2 where A is the vector potential. The electrostatic response is described by

$$\dot{p}_x = (\phi - \gamma)'$$

$$\dot{n} + (np_x/\gamma)' = 0$$

$$\phi'' = n - n_0$$

where $\gamma = (1 + p_x^2 + a^2)^{1/2}$, p_x the electron fluid momentum and ϕ is the potential. Kinetic pressure is negligible here.

THE SRFS/RMI HYBRID INSTABILITY

A stability analysis is performed in the laser pulse group velocity frame, Lorentz transformed from the laboratory frame. Linearly polarised light, frequency and wavenumber (ω_0,k_0), couple an infinite hierarchy of fluctuations at ($l\omega_0 \pm \omega$, $lk_0 \pm k$) where l is an integer. At low intensities, SRFS is well-understood as a four wave process coupling Stokes and anti-Stokes lines (l=1) with a plasma wave at (ω, k) while the weaker RMI process couples Stokes and anti-Stokes lines directly through modulations in the relativistic mass increase. The instabilities are spectrally distinct at low intensities but merge to form a hybrid when q >1[1]. RMI acts to reduce Raman growth. Mode coupling is determined by the coupling parameter $\lambda = q^2\,\omega_{pr}^2/4\,\gamma_a^2$ where $\gamma_a=(1+q^2/2)^{1/2}$ is the relativistic mass increase due to the laser driver. This reduces the relativistic plasma frequency, ω_{pr} and saturates the electron quiver velocity q/γ_a when q>>1. λ maximises when q = 2. At low intensities, q < 1, growth is determined by the quiver velocity $q/\gamma_a \approx q$; when q > 1, growth is determined by intensity dependence of the relativistic plasma frequency ω_{pr}. The question arises as to how many modes of the infinite hierarchy are active in determining the growth characteristics of the SRFS/RMI hybrid. Up to q=1 the instability is well described as a four wave hybrid while at ultrahigh intensities, q>1, a six wave description is necessary. The six modes are the laser photon (ω_0,k_0), the electromagnetic Stokes and anti-Stokes lines at ($\omega_0 \pm\omega$,$k_0\pm$k) and three electrostatic modes (ω,k), ($2\omega_0\pm\omega$,$2k_0\pm$k). Higher order couplings are prevented not just by the relativistic saturation of the coupling parameter but also the near exact destructive interference of SRFS and RMI contributions. The net effect is that, when q>1, the instability is in a strongly coupled regime where the peak growth rate is given by

$$\nu = 2^{1/4}\sin(\pi/8)\omega_{pr}^2 \approx 0.455\omega_{pr}^2$$

and the frequency is locked at $\omega=2^{1/4}\cos(\pi/8)\omega_{pr}\approx1.1\omega_{pr.}$

Figure 1 plots the peak growth rates for the exact (or six-wave) solution and compares these with the four wave SRFS (RMI contributions neglected) and the four-wave SRFS/RMI hybrid values. The plotted values are as measured in the laboratory frame but assuming a real wavenumber in the pulse frame; these are a factor ω_{pr} greater than when the wavenumber is assumed real in the laboratory frame). A one-tenth critical density is assumed in this figure.

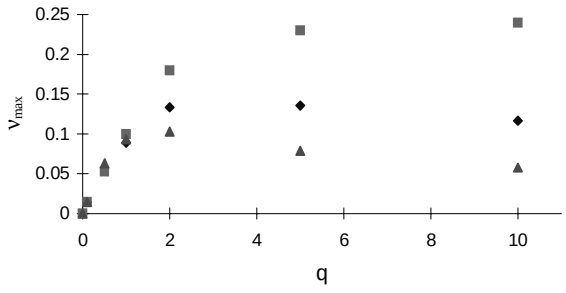

Figure 1: Comparison of maximum growth rates for 4-wave SRFS (squares), 4-wave SRFS/RMI hybrid (diamonds) and 6-wave SRFS/RMI hybrid (triangles) over range of laser intensity 0<q<10 (i.e.(0<I<10^{20}Wcm^{-2})

SIMULATIONS

The linear and non-linear space-time characteristics are determined by numerically evolving the above equations. The full spectral and mode-coupling information is retained. No electromagnetic (em) nor electrostatic (es) source waves were included except for those generated by the pulse itself; the ponderomotive effect of the pulse leading edge has been shown to be a dominant source[3]. The simulations were run to saturation of the growth in the relativistically fast electron plasma waves. Table-top pulses were used to confirm the linear instability characteristics. For moderate intensities (q≤1) the space-time evolution of the SRFS/RMI growth shows the anticipated regimes. A convective gain regime immediately behind the leading edge in which any point has experienced a

full complement of sources from the leading edge. Behind this is a space-time growth regime which includes the point, convecting back from the pulse leading edge, having maximum growth. The observed growth agrees well with the predicted rate for the hybrid. Finally, a region which sees no information from the leading edge and hence shows no growth. These observations are in agreement with ref[3] when allowance is made for em group velocities which are not assumed to be approximated by *c*. An example of the spectral output when q=0.5 is shown in Figure 2 for a 200*fs* table top pulse. This shows 'clean' em and es spectra for SRFS at a time shortly before saturation. The em spectrum shows the Stokes and anti-Stokes cascade with separation of ω_{pr} between successive spectral peaks. The relativity is manifest in relativistic reduction of the plasma frequency. The es spectra shows this same cascade mapped onto the fast oscillations around $2k_0$ due to the linear polarisation. The three leftmost peaks in the es spectra are the SRFS-excited plasma wave together with two harmonics which constitute the large amplitude non-linear plasma wave. When q>1, the effects of the leading edge in generating immediate large amplitude plasma waves by wake-field action prevented any useful observation of a linear growth regime.

Using realistic Gaussian-like pulses gives rise, for q < 1, to a space-time evolution similar to the table-top pulses except that the growth is much slower than would be anticipated on the basis of an average *q* for the pulse. When *q* > 1 the space-time evolution is quite distinct. The instability now occurs in an inhomogeneous environment due to the large *q* variations across the pulse. Rapid growth is observed in the leading edge of the pulse where *q*=2 which is the region of maximum growth. Growth convectively saturates around this location with the large amplitude plasma convecting back through the pulse. The variable *q* implies a range of ω_{pr} and hence a spectrum of unstable plasma waves; the em spectrum produced by the cascade process is smeared out without the structure seen in the low intensity case.

Figure 3 illustrates for a peak intensity q=5 the spatial structure

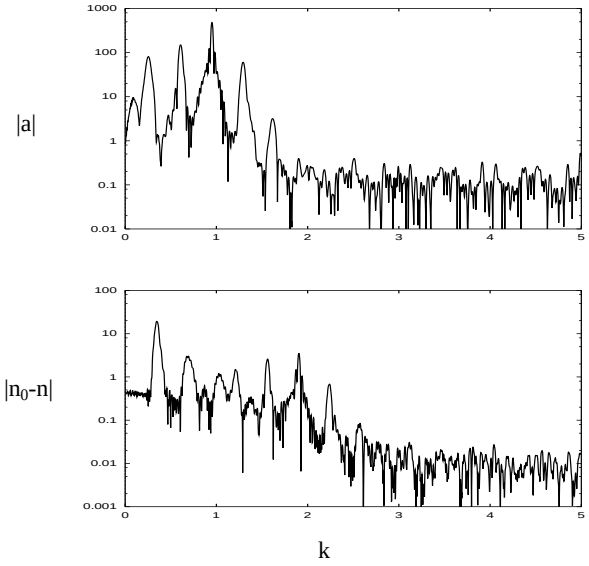

Figure 2: Wavenumber spectra of vector potential and density fluctuations at t=294fs
[$I \approx 3\times10^{17}$Wcm^{-2}, τ_p=200fs, n=0.1n_c]

of the pulse vector potential, the density fluctuations, the momentum and the relativistic factor when the plasma wave has saturated. The density shows the structure expected of a relativistically fast and relativistically intense plasma wave with narrow density peaks more than a factor of 10 above the mean density connected by longer homogeneous plasma regions whose density is one half the mean density. The electric field has the familiar sawtooth shape with peak fields of about 1.5TeV/m. The main features are accurately described by the cold plasma theory of Akhiezar and Polovin[5] provided one uses the adjusted plasma frequency ω_{pr}. The leading edge of the em pulse is strongly corrupted with the remainder now propagating in what is essentially homogeneous plasma with periodic overdense density peaks comoving with the pulse.

REFERENCES

1) C J McKinstrie and R Bingham

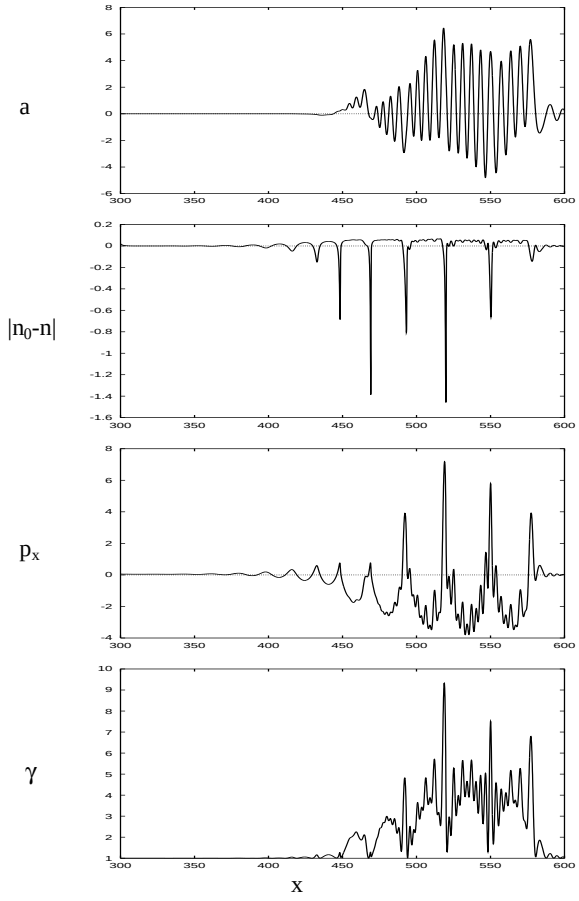

Figure 3: Spatial plots at saturation
[$I=2.5\times10^{19}$Wcm^{-2}, τ_p=100fs, n=0.1n_c]

Physics of Fluids B, 4 2626 ,(1992)

2) S Guerin, G Laval, P Mora, J C Adam, A Heron
Physics of Plasmas, 2 2807, (1995)

3) W B Mori, C D Decker, D E Hinkel, T Katsouleas
Phys. Rev. Lett.,72 1482, (1994) ;
C D Decker, W B Mori, T Katsouleas, D E Hinkel
Physics of Plasmas, 3 1360, (1996)

4) H C Barr, T J M Boyd, F I Gorden, S J Berwick
Laser and Particle Beams, 13 525, (1995)

5) A I Akhiezar and R V Polovin
Soviet Physics JETP, 3 696, (1956)

IGNITION OF AN X-RAY DRIVEN INERTIAL CONFINEMENT FUSION TARGET

Abdeslem Djaoui

Rutherford Appleton Laboratory, Chilton, Didcot, Oxon, OX11 0QX,UK. Email A.Djaoui@RL.AC.UK

INTRODUCTION

Interest in Inertial Confinement Fusion (ICF) has increased since the 1993 declassification of ICF research in the US and the publication of some details of an indirectly driven target[1,2,3]. This target is referred to as the PT or "point design target" and consists of a capsule containing 80 μm spherical shell of solid deuterium-tritium (DT) with an inside radius of 0.87 mm which is filled with DT gas and surrounded by 160 μm of a doped CH ablator (see Fig 1). With a maximum laser power of 500 TW, radiation temperatures of around 300 eV are expected inside a high-Z hohlraum[2]. It is estimated that 1-2 MJ of frequency tripled Nd:glass laser energy is sufficient for the demonstration of ignition and nuclear burn propagation in such capsule. Both Lawrence Livermore (LLNL)[1,2] and Los Alamos (LANL)[3] Laboratories have studied the PT target. Their one dimensional calculations yield 14-16 MJ with radiation temperature drives which peak at 300 eV. We have also performed simulations of the PT target using the one dimensional radiation hydrodynamic code MEDX[4,5] and we present here a summary of our findings. In order to achieve ignition, it was necessary to use a peak radiation drive temperature which about 3% higher. Severe requirements are also imposed on the timing of shocks through the DT fuel and consequently on the shape of the radiation drive.

OPTIMISED DRIVE CONDITIONS

An optimised radiation drive for the PT target is shown in Fig 1 together with a radius-time history of the computational cells. Since the x-ray flux is proportional to T_r^4, most of input energy is contained in the constant part (at 310 ev) and is delivered in about 2 ns at times greater than 15 ns. The insert shows the situation near the time of maximum compression as well as the rate of thermonuclear neutron production. This simulation of the PT target yields 16 MJ. A maximum implosion velocity of 4.17×10^7 cm/s, a maximum $\rho r = 2.87$ g/cm^2 and maximum density of 1500 g/cc are achieved. 1.2 MJ of nuclear energy is produced up to the time of maximum compression. Another 12 MJ is generated in only 20 ps following the time of maximum compression. The radiation drive is switched off at 17 ns by which time the capsule absorbs 190 kJ of incident x-ray energy of which 40 kJ is re-radiated, 70 kJ is transformed into internal thermal energy and 80 kJ into kinetic energy of the plasma. The net absorbed x-ray flux of 150 kJ is the same as in the LLNL calculation[1].

At early times (less than 15 ns), although the fraction of energy in the drive is small, precise shaping of the pulse is critical in order to achieve near isentropic compression. The radiation drive in Fig 1 generates four steps of pressure at the CH/solid DT interface as shown in figure 2 (dashed curve). An optimum pressure pulse which ignites the DT shell (and gas) is also shown in Fig. 2 (continuous thin curve). The steps in the radiation drive which result in the corresponding pressure steps are shown with arrows. The first radiation step at about 85 eV launches the 1 Mbar shock which takes 9 ns to travel through the CH ablator. The second step at about 125 eV is responsible for the 4 Mbars steps. As the strength of the shocks increases and the ablator is depleted the x-rays are deposited nearer to the CH/DT interface and subsequent shocks take less time to emerge at the interface. The shocks are also weakened when travelling from the absorption region to the interface. Just before the end of the drive more than 90 percent of the doped CH is ablated away and maximum absorption of the incoming

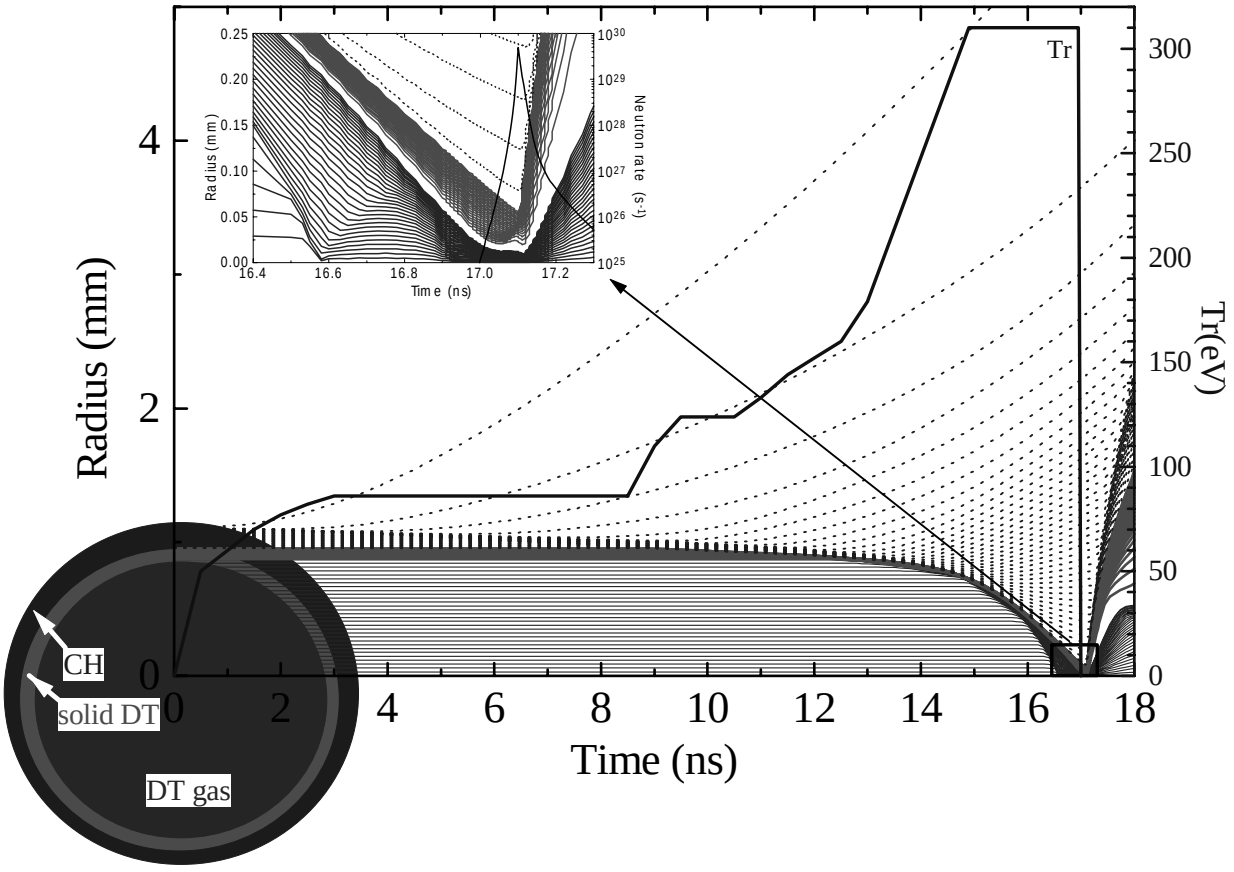

Fig. 1: Diagram of the PT target and radius-time (r-t) history of computational cell boundaries of the same target driven by the radiation pulse shown. The insert shows the r-t plot near the time of peak compression for clarity, as well as the rate of thermonuclear neutron production.

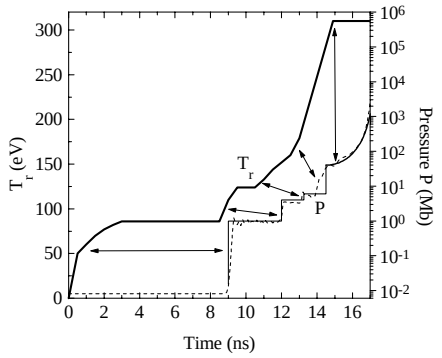

Fig 2: Radiation drive Tr (continuous thick curve) and resulting pressure P (dotted curve) at the CH/solid DT interface. The optimum driving pressure pulse for the solid DT shell and gas is also shown (continuous thin curve)

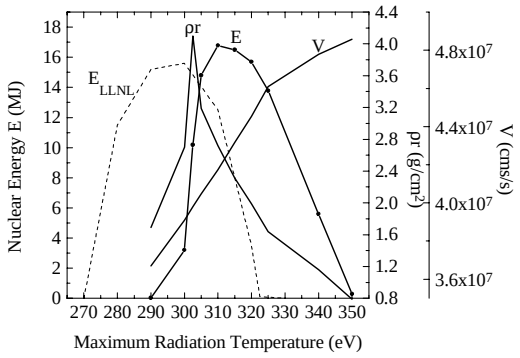

Fig 3: Variation of nuclear energy yield with maximum drive temperature from our calculations (E) and from the Lawrence Livermore National Laboratory's calculations (E_{LLNL}). The maximum fuel ρr and the maximum implosion velocity V are also shown.

x-rays occurs in the inner cell of CH (adjacent to DT). At this time, the pressure at the interface is directly related to the incoming x-ray flux at the maximum drive temperature.

SHOCK TIMING AND PULSE SHAPING

The role of the CH ablator is to convert the radiation drive into a pressure pulse at the CH/solid DT shell boundary. The implosion of the PT target can therefore be divided into two separate problems. The implosion of the DT shell and gas using a pressure pulse and the design of a radiation drive which when applied to the CH ablator reproduces closely such a pulse at the CH/DT interface. This separation is valid since energy exchanges at the CH/DT interface are dominated by PdV work of the pressure pulse (During the implosion, heat conduction and radiative energy transfer through the interface are much smaller and can be ignored for the purpose of this analysis). This separation is also beneficial since the simulation of each phase separately is much less demanding on computer time than the full simulation of the PT target driven by a radiation pulse. An optimum pressure pulse which ignites the DT shell and gas is shown in Fig.2.

The effect of shock timing on burn can be studied by varying the time of launch of the different pressure steps on the solid DT shell. We assume that the different pressure steps in Fig 2 can be generated and changed independently for the purpose of this analysis. Times in this section are measured with respect to the time of launch of the first step at 1Mbar (9ns in Fig 2). The yield increases from 2.6 to 10.1 MJ when the timing of the second step at 4 Mbars (with respect to the first step) is changed from 2.7 ns to 2.9 ns. The maximum ρr shows a peak at 2.8 ns while the maximum implosion velocity increases as the launch time increases. A high yield therefore requires that the second step at 4 Mbars must be launched at least 2.8 ns after the first. For separations times of 2.5 ns or less, the target fails to ignite as a result of smaller implosion velocities and compressions.

The timing of the third step is not important. Changing the launch time by +/- 500 ps has little effect on the yield. The third shock is merely used to reduce the entropy increase generated by the final shocks. A calculation without this third step resulted in 30 percent decrease in yield.

The yield increases from 2.4 MJ to 9.9 MJ as the time of the 4th step at 40 Mbars is reduced from 5.8 ns to 5.6 ns. A high yield therefore requires that the fourth step be launched no more than 5.7 ns after the first step. For times greater than 5.8 ns adequate implosion velocities (and compressions) are not achieved. As the time of launch is reduced to 5 ns a small increase in the entropy of the fuel is obtained but this is compensated by a higher implosion velocity. For ignition to occur, the steps of a pressure pulse such as the one in Fig. 2 must be timed no more than 100 to 200 ps around their optimum values.

The PT target can tolerate moderate variations of the maximum temperature. The yield as a function of maximum drive temperature is shown in Fig. 3. Our results (E) are shifted to higher temperatures compared to the LLNL results[2] (E_{LLNL}). For temperatures greater than 340 eV, very high implosion velocities are obtained but the fuel is also raised to high entropies. For temperatures less than 300 eV, our calculation shows it is not possible to achieve adequate implosion velocities.

CONCLUSION

Using the 1D radiation hydrodynamic code MEDX, we have shown that the indirectly driven PT target will ignite and yield 16 MJ if adequate pulse shaping is achieved in the radiation drive. Our calculation shows that in order to achieve ignition and adequate burn, a maximum radiation temperature of 310 eV is necessary. This is 10 eV higher than the maximum temperature used for the LLNL calculation but is still within the temperature range that is expected to be achieved on the National Ignition Facility (NIF). The requirement to create a small hot spot surrounded by a cold compressed fuel shell restricts this maximum temperature to a widow of 30 to 40 eV width around 310 eV (300 eV for LLNL). Outside this window and for lower temperatures, the implosion velocities achieved are too small while for higher temperatures the fuel is raised to very high entropies which results in low compression.

ACKNOWLEDGMENT

The group opacity tables for these calculations were generated by Professor Rose using the IMP code[6].

REFERENCES

1) S.W. Haan, *et al*
Phys. Plasmas, 2, 2480 (1995)

2) J. Lindl
Phys. Plasmas, 2, 3933 (1995)

3) W. J. Krauser, *et al*
Phys. Plasmas 3, 2084 (1996)

4) A. Djaoui
J. Quant. Spectros. Radiat. Transfer 54, 143 (1995)

5) A. Djaoui
Phys. Plasmas, 3, 4677 (1996)

6) S. J. Rose
J. Phys. B: Atom. Mol. Opt. Phys. 25, 1667 (1992)

R-MATRIX-FLOQUET THEORY OF MULTIPHOTON PROCESSES

D H Glass[1], P G Burke[1] and C J Noble[2]

1) Department of Applied Mathematics and Theoretical Physics, The Queen's University of Belfast, Belfast B77 1NN, N Ireland

2) Department for Computation and Information, CLRC Daresbury Laboratory, Warrington WA4 4AD

INTRODUCTION

The *R*-matrix-Floquet theory of multiphoton processes was first introduced by Burke, Francken and Joachain[1] to describe the interaction of a linearly polarized, monochromatic, monomode and spatially homogeneous laser field with a general atom or atomic ion. The theory is non-perturbative and is applicable to both multiphoton ionisation of atoms or ions and to laser-assisted electron-atom scattering enabling electron-electron correlation effects to be treated accurately.

During the last few years a general computer program package has been developed which enables multiphoton ionisation rates for general atoms and ions and laser-assisted electron-atom scattering cross sections to be calculated in situations where relativistic effects can be neglected. This program package has been used with considerable success to obtain multiphoton ionisation and detachment rates for a number of atoms and negative ions. In addition, the program package has recently been extended to treat laser-assisted electron-proton scattering[2] multiphoton ionisation involving two incommensurate frequencies[3] and harmonic generation[4].

THEORY

The theory takes advantage of the fact that in the R-matrix method[5] configuration space is divided into internal and external regions, in each of which the most appropriate form of the laser-atom interaction Hamiltonian is adopted. In the internal region electron exchange and electron-electron correlation effects involving all electrons are included by adopting an antisymmetrised configuration interaction expansion of the total wave function. In the external region exchange between an ejected electron and the remaining electrons in the residual atom or ion is neglected since the ejected electron is considered to lie in a different region of configuration space.

A Floquet-Fourier expansion of the wavefunction is used in both regions to transform from the solution of the time-dependent Schrödinger equation to the solution of a time-independent problem. The solution in the internal region yields the *R*-matrix which is then used to match the internal and external region wavefunctions. Asymptotically the solutions are matched to outgoing wave 'Siegert' boundary conditions. Finally, an iterative procedure in the complex energy plane gives the quasi-energy, $E=E_R - i\Gamma/2$ where E_R is the energy and Γ the total ionisation rate.

Recently a new approach has been proposed for the solution in the internal region[6]. This replaces the diagonalisation of a large Hamiltonian matrix by the solution of a system of linear equations. As larger systems are treated the computer time and memory requirements of the diagonalisation procedure become prohibitively expensive. The present implementation of the linear equations takes advantage of the sparsity and repetitive nature of the Hamiltonian and thus reduces the memory requirements substantially. The other main advantage of this approach is that it is much more accessible to parallelisation.

Other developments include the introduction of a new external region program package which incorporates 'dressed' channel momenta in the asymptotic expansion in the external region. These channel momenta arise because of the truncation in the Floquet expansion and so it is expected that their inclusion will enable convergence to be obtained with fewer terms of the expansion retained. This will be of great significance for treating larger physical systems and higher field strengths where many terms in the Floquet expansion are required.

RECENT RESULTS

Recently harmonic generation has been developed within the R-matrix-Floquet framework[4]. The *R*-matrix-Floquet package of programs, as described above, is used to calculate the harmonic components of the wavefunction and from these the electric dipole moment can be obtained, which in turn enables the harmonic generation rate to be calculated. This has been applied[7] to Mg where third harmonic generation was studied in the vicinity of a three-photon resonance with the $3s3p\,^1P^o$ autoionising state at intensities of up to 10^{11} Wcm^{-2} . Fig. 1 illustrates that the third harmonic generation rate is enhanced by several orders of magnitude near the autoionising resonance over a range of intensities. It is also clear that the peak position of the spectrum moves away from $\Delta = 0$ as the field intensity decreases. The distinctive minimum in the spectrum at $10^{10}Wcm^{-2}$ was found to exist over a range of field intensities.

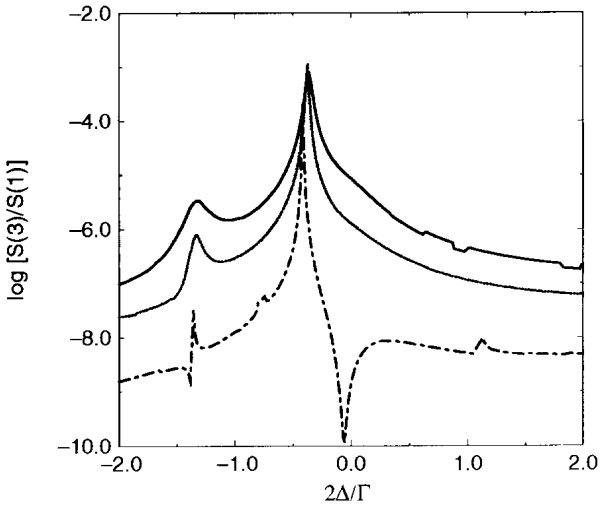

Fig. 1. The third harmonic generation spectrum against the scaled detuning, Δ for three intensities $10^{11}Wcm^{-2}$ (solid curve), $5x10^{10}Wcm^{-2}$ (dotted line) and $10^{10}Wcm^{-2}$ (dashed line).

T'hree-photon ionisation of He has also been considered at frequencies where double resonances with a bound state and autoionising states are important[6]. A three-state approximation *(1s,2s,2p)* was used to describe the He^+ target and found to give field-free energies and widths of $^1P^o$ autoionising states in good agreement with recent calculations such as those of Brage et al[8]. In this approximation it is found that the three-photon ionisation from the $1S^{21}S^e$ ground state in the neighbourhood of the (2s3p - 2p3s)$^1P^o$ autoionising state is almost resonant with the single-photon excitation of the $ls2p^1P^o$ bound state. A study of the influence of the series of $^1P^o$ and $^1F^o$ autoionising resonances converging to the n = 2 threshold on the total ionisation rate from the $ls2p^1P^o$ bound state and $1s^{21}S^e$ ground state was carried out, with a large enhancement found in the neighbourhood of the double resonance. Fig. 2 illustrates that an adiabatic transfer of population from the $1s^{21}S^e$, ground state to$1s2p^1P^0$ bound state via the $(2s3p\text{-}2p3s)^1P^o$ autoionising state

is possible at an intensity of $5x10^{12}Wcm^{-2}$. This arises due to the interaction of all three states in the frequency range near the double resonance.

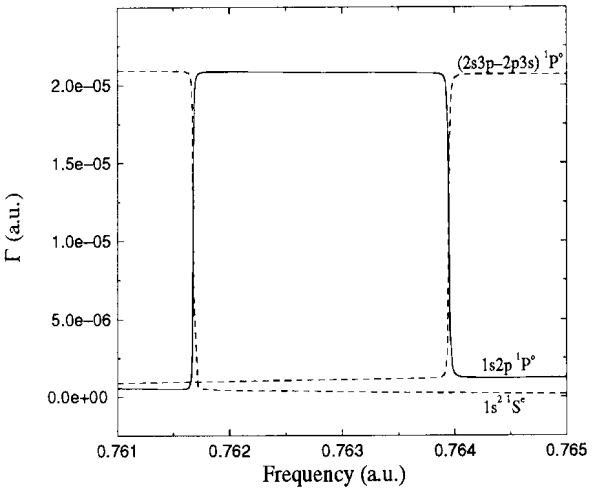

Fig. 2. The solid line indicates an adiabatic transition from the ground

Laser-induced continuum structure (LICS) is the process whereby atomic states become embedded in the continuum due to the dressing of an intense laser field. Laser-induced degenerate states (LIDS) occur when, for a particular laser frequency and intensity, two laser dressed atomic states become degenerate. Such LIDS were found[9] between the $3s3p^64p^1P^o$ autoionising state and the ground state of Ar connected by a three-photon transition at a laser frequency of approximately 0.337975 *a.u.* and an intensity of approximately $1.54x10^{14}Wcm^{-2}$. Fig. 3 illustrates the trajectory of the states in the neighbourhood of the degeneracy. At a frequency just below that of the degeneracy the states interact strongly, while at a higher frequency there is a complete reversal of roles as the intensity increases through its critical value. A single-photon model was used to interpret the results and was found to predict another degeneracy at a higher frequency and intensity.

The results in this article indicate the ability of the *R*-matrix Floquet approach to represent accurately the physics of complex systems in a non-perturbative manner, although the computational requirements are large. Future work, such as the parallelisation of our codes, should enable calculations at higher intensities to be carried out and higher orders to be treated in harmonic generation. These developments will enable calculations to be made which are of direct relevance to the CLF research at RAL.

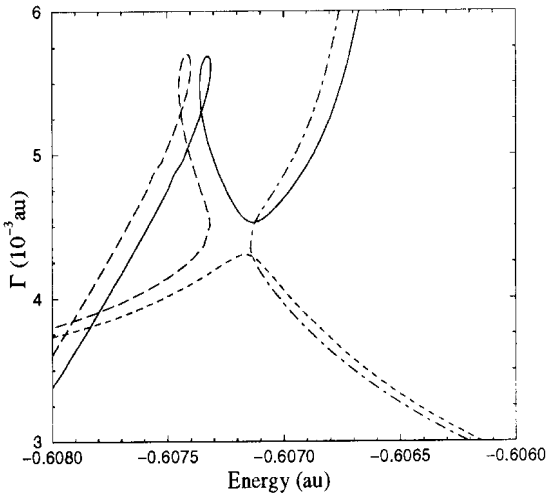

Fig. 3. The trajectory of the states as a function of intensity. The solid (long-dashed) curve represents the trajectory that starts from the autoionising state and the short-dashed (dot-dashed) curve the trajectory that starts from the ground state for a frequency just below (above) that of the degeneracy.

REFERENCES

1) P G Burke, P Francken and C J Joachain
J. Phys. B: At. Mol. Opt. Phys. 24, 761, (1991)

2) M Dörr, M Terao-Dunseath, P G Burke, C J Joachain, C J Noble and J Purvis
J. Phys. B: At. Mol. Opt. Phys. 28, 3545, (1995)

3) H W van der Hart
J.Phys. B: At. Mol. Opt. Phys. 29, 2217, (1996)

4) R Gcbarowski, P G Burke, K T Taylor, M Dörr, M Bensaid and C J Joachain
J. Phys. B: At. Mol. Opt. Phys. 30, 1837, (1997)

5) P G Burke and K A Berrington
Atomic and Molecular Processes: An *R*-matrix Approach, (Institute of Physics, Bristol and Philadelphia) (1993)

6) D H Glass, P G Burke, H W van der Hart and C J Noble
J. Phys. B: At. Mol. Opt. Phys. Accepted for publication, (1997)

7) R Gebarowski, K T Taylor and P G Burke
J. Phys. B: At. Mol. Opt. Phys. 30, 2505, (1997)

8) T Brage, C Froese Fischer and G Miecznik
J. Phys. B: At. Mol. Opt. Phys. 25, 5289, (1992)

9) A Cyr, O Latinne and P G Burke
J.Phys. B: At. Mol. Opt. Phys. 30, 659, (1997)

EFFECT OF COULOMB EXPLOSION ION HEATING ON GAIN IN OFI NITROGEN

M.J. Grout and G.J. Pert

Department of Physics, University of York, York YO1 5DD, e-mail mjg102@york.ac.uk

INTRODUCTION

Optical-field ionisation has been suggested as a mechanism for producing a cold electron plasma suitable for recombination X-ray lasers. Simulations using two models have been used to calculate the electron temperature and to investigate the possibility of gain for different targets. Nitrogen mixed with a large concentration of hydrogen at ion temperature of 0.025eV gave gains up to 155cm^{-1} at 247Å[1)], and is therefore an interesting target to pursue. However nitrogen is diatomic and will suffer a Coulomb explosion during ionisation which acts to heat the nitrogen ions. Calculations showed that the linewidth of the lasing transition is Doppler dominated and so the heating of ions will broaden the linewidth and decrease gain. This report will investigate the scale of ion heating, utilising a pre-pulse as a technique to limit ion heating and the resulting effect on gain in OFI nitrogen.

COMPUTATIONAL MODELS

Models of OFI and hydrodynamics with atomic kinetics are used in this work and have been described in detail elsewhere[1,2)]. The laser pulse is simulated by a numerical code and calculates tunneling ionisation with above-threshold ionisation and inverse bremsstrahlung electron heating mechanisms, giving electron energies at the spatial centre of the pulse. A 1D Lagrangian hydrodynamics model is used as a postprocessor and includes flux limited thermal conduction and electron-ion equilibration. The atomic physics is treated by a time-dependent COLRAD model which includes three-body recombination. Gain coefficients may be calculated for any transition. In both codes a simple time-dependent Coulomb explosion ion heating term has been added.

RESULTS AND CONCLUSIONS

A gain optimised mixture assuming room temperature ions of nitrogen ion density of 3x10^{17} per cc and hydrogen density of 3.3x10^{18} per cc has been identified[1)]. Simulations used a single pulse of rise-time 100fs with a FWHM time of 100fs and peak intensity of 3x10^{16} Wcm^{-2}. However when Coulomb explosion heating was included the ions were heated to a temperature of 27eV due to the rapid ionisation on the rise of the pulse leading to large inter-ion forces before the ions could separate significantly. The calculated gain was reduced to 19cm^{-1} which is unlikely to give a saturated output.

The Coulomb explosion heating may be controlled by a pre-pulse, ionising nitrogen to just the first ionisation stage. If sufficient time is allowed for ion separation, little further ion heating will result when the main pulse strips the target to the closed shell configuration.

A 1% intensity pre-pulse was used and the pre- to main pulse separation varied. The variation of peak gain is shown in figure 1. Gains up to three times the single pulse value were obtained. The temporal development of electron and ion temperatures and effective charge of 2.8ps separated pulses is shown in figure 2. This shows the effectiveness of a pre-pulse to limit the heating. An ion temperature of ~3eV is produced at the end of the main pulse. It remains almost unaffected by further Coulomb explosion heating due to electron-ion thermalisation.

In conclusion a pre-pulse several picoseconds before the main pulse and hydrogen doping are essential to limit Coulomb explosion heating and produce high gain in OFI nitrogen targets.

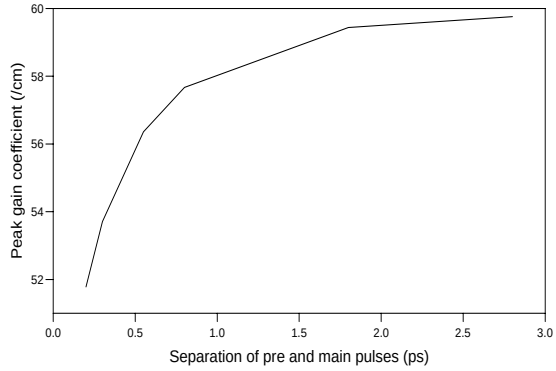

Figure 1. Dependence of peak gain coefficient after main pulse on separation time of pre and main pulses. For gain optimised nitrogen hydrogen mixture with 1% pre-pulse.

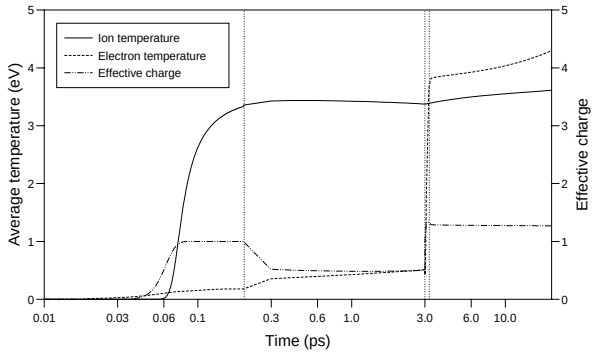

Figure 2. Graph of temporal variation of electron (solid) and ion (dashed line) temperatures with effective charge (double dot, dashed line) for double pulsed ionised target. End of pre-pulsed (0.2 ps), start of main pulse (3.0 ps) and end of main pulse (3.2 ps) shown by vertical dotted lines.

REFERENCES

1) M.J. Grout, K.A. Janulewicz, S.B. Healy and G.J. Pert, Optics Communications, in press.

2) K.A. Janulewicz, M.J. Grout and G.J. Pert, J. Phys. B 29, 901 (1996).

1D PIC SIMULATIONS OF FAST ELECTRON TRANSPORT

S Guerin, A R Bell, J R Davies

Blackett Laboratory, Imperial College, Prince Consort Road, London SW7 2BZ, UK

Now that laser irradiances up to $I\lambda^2=10^{19}Wcm^{-2}\mu m^2$ can be reached, their interaction with solid targets can reveal new phenomena because of the relativistic motion of the electrons in this regime. The fast electrons that are created at the vacuum-plasma interface can be used as a source of X-ray radiation[1]. They are also supposed to play a crucial role in the proposed fast ignitor fusion scheme[2].

From a simple theoretical model we have shown that the fast electron penetration depends on the electrical conductivity of the target by the space charge effect[3].

Fast electron transport can be treated with Fokker-Planck or multi-group diffusion codes but characteristics about fast electron behaviour can also be deduced from electromagnetic particle-in-cell codes. Recently such a PIC code with the addition of a Monte-Carlo operator has taken into account the collisions and their effects during the interaction of ultra-intense laser pulses with solid targets[4]. In our work a one dimension electrostatic PIC code is used to study the fast electron transport in the cold plasma and verify the predictions of the previous theoretical model. This code differs from usual electrostatic PIC codes because it includes two populations of electrons: the fast one created by the laser and the cold one from the target. They are treated in different manners. The laser is only considered as a source of fast electrons and plays no other role in the simulation. It is considered to be switched off as the simulation starts. The energetic electrons are generated at initial time as a mono-energetic beam with a given density profile in a small region (the heated region) at the edge of the target. We focus on the penetration of this beam in the cold plasma. The background conductivity has been included in the cold electron motion. Ions are stationary. The target has a uniform density and is neutral at the initial time. The electron momentum has only one component.

Numerical results show that the fast electron distribution is sensitive to the initial distribution of energy (density profile and temperature of the fast electrons) and also to the background conductivity. Generally fast electrons have a temperature of 200keV and the cold plasma of 100eV.

We consider the case where all the electrons in the heated region belong to the beam. Because of the steep gradient for the fast electron density profile a strong electric field is generated at the hot-cold plasma interface. The fast electrons then are bounced back and forth in the heated region. Therefore the initial mono-energetic distribution rapidly becomes Maxwellian as shown in Fig. 1 due to the excitation of oscillations. The resulting width of the fast electron distribution depends on the initial energy given to the fast electron and also on the conductivity of the cold plasma. For thin targets the fast electrons go through all the target and once in the vacuum on the other side they are repelled back by the electrostatic field.

As the conductivity decreases the fast electrons have greater difficulty to penetrate in the cold plasma. They need a higher energy and we observed the propagation of bunches of fast particles. Their penetration decreases with decreasing conductivity. As the fast electron penetration proceeds we observe the cooling down of the Maxwellian distribution, but the time integrated distribution of the energetic electrons gives a Maxwellian which corresponds to what has been observed in experiments.

In the case of a smooth gradient in the initial fast electron distribution, only a steady electric field is generated and the distribution does not become Maxwellian. Oscillations are not excited and the beam of fast electrons steadily slows down as it penetrates the target.

As improvements, the code will soon contain the three components of momentum and collisions will be included as small angle scattering.

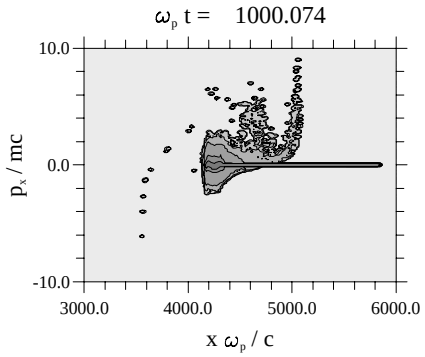

Fig. 1. Momentum as a function of the position at $\omega_p t$=1000. The initial fast electron distribution is a mono-energetic beam located at the left edge of the plasma slab. The thickness of the plasma layer is 10 microns of Al.

ACKNOWLEDGMENTS:

This work is supported by SILASI European Network ERB 4061 PL 95-0765.

REFERENCES

1) RL Carman, DW Forslund and JM Kindel, Physical Review Letters 46, 29 (1981).

2) M Tabak , J Hammer, ME Glinsky, WL Kruer, J Woodworth, EM Campbell, MD Perry and RJ Mason, Physics of Plasmas 1, 1626 (1994).

3) AR Bell, JR Davies, S Guerin and H Ruhl, Plasma Physics and Controlled Fusion 39, 653 (1997).

4) WS Lawson, PW Rambo, and DJ Larson, Physics of Plasmas 4, 788 (1997).

ENHANCEMENT OF PONDEROMOTIVELY GENERATED WAKEFIELDS IN 1D

R J Kingham [1] and A R Bell [1]

1) Plasma Physics Group, Blackett Laboratory, Imperial College, London, SW7 2BZ. Email rj.kingham@ic.ac.uk

INTRODUCTION

Linear theory [1] of ponderomotively excited wakefields, in 1D, relates the wake amplitude to the Fourier transform of the pulse intensity profile at wavenumber $k=k_p$. The "standard" LWFA uses a short "matched" pulse of length $L_m \approx \lambda_p/2$. The intensity spectrum of a matched pulse has a large value at $k=k_p$ owing to the wide bandwidth of such a pulse. Consequently, matched pulses can excite wakefields of wave breaking amplitude at sufficient intensities; $I>10^{18}$ W cm^{-2}. Long smooth pulses (e.g. Gaussian) have narrow bandwidths so excite vanishingly small amplitude wakefields, even at high intensity, according to linear theory.

We present work on ponderomotive wakefield excitation by long smooth laser pulses. Using a nonlinear, relativistic envelope equation, we determine the amplitudes of wakefields generated by smooth laser pulses much longer than $\lambda_p/2$. We find that such wakefields are significantly larger than wakes predicted by linear theory, at relativistic pulse intensities. Enhancement occurs because the pulse bandwidth experienced by the electrons during their interaction with the laser pulse is increased by nonlinearities in the envelope equations. Wakefield enhancement for long pulses is relevant to the seeding of beam breakup in the "self-modulated" LWFA [2]. Enhanced wakefields should be large enough to act as the dominant seeding source for RFS induced beam breakup under suitable experimental conditions. This avoids having to rely upon other, noisy seeding mechanisms, such as RBS and ionization seeding, which are inherently unpredictable.

MODEL

We use the following envelope equation (cast in the pulse group velocity frame) to determine the wakefield $\phi(\zeta,\tau)$ generated by a laser pulse with a vector potential envelope $a(\zeta,\tau)$,

$$\frac{\partial^2\phi}{\partial\zeta^2} = -\gamma_g^2\left[\frac{(1-\phi)\beta_g}{\left\{(1-\phi)^2 - \left(1+2\alpha|a|^2\right)/\gamma_g^2\right\}^{\frac{1}{2}}} - 1\right] \quad . \qquad (1)$$

$\phi(\zeta,\tau)$ is the scalar potential of the plasma, $\beta_g \equiv v_g/c$ is the normalised group velocity of the laser pulse (given by the usual dispersion relation), $\gamma_g^2 = (1-\beta_g^2)^{-1}$ is the relativistic gamma factor associated with the laser pulse group velocity and $\alpha = 1$ or 2, a parameter that specifies linear or circular polarization. The laser pulse frame coordinates ζ, τ are related to the laboratory coordinates z, t by $\zeta = z - v_g t$, $\tau = t$. Equation 1 represents the cold, collisionless, relativistic, undamped response of an electron-fluid to a laser pulse. Ions are assumed immobile and the quasistatic approximation [3] has been used. Not shown here is the nonlinear wave equation for $a(\zeta,\tau)$ which can be used (with eqn. 1) to determine self consistent propagation and wakefield excitation. We use the following normalisations in the above equation and throughout this report: $\zeta\,\omega_p/c \rightarrow \zeta$, $\tau\,\omega_p \rightarrow \tau$, $\omega/\omega_p \rightarrow \omega$, $v/c \rightarrow \beta$, $\phi\, e/(m_e c^2) \equiv \phi/\phi_{cwb} \rightarrow \phi$ and $a\, e/(m_e c) \equiv v_{osc}/2c \rightarrow a$, where ϕ_{cwb} is the cold wave breaking potential and v_{osc} the electron quiver velocity. The full vector potential, **A** and the complex vector potential envelope, $a(\zeta,\tau)$, are related via

$$\mathbf{A}(\zeta,\tau) = a(\zeta,\tau)\exp\left\{ik_o\left[\zeta - \left(\beta_p - \beta_g\right)\tau\right]\right\}\mathbf{b} + \text{c.c.} \qquad (2)$$

In equation 2 the vector **b** is either **x** or **x**+i**y** for linearly or circularly polarized light respectively (**x** and **y** are unit vectors) and $\beta_p = \omega_o/k_o$ is the laser phase velocity (ω_o, k_o are the laser frequency and wavenumber). Equations similar to 1 are considered by Sprangle *et al* [3], Dalla & Lontano [4], Teychenné & Bonnaud [5] and others for high-intensity *short pulse*, wakefield excitation and wave breaking.

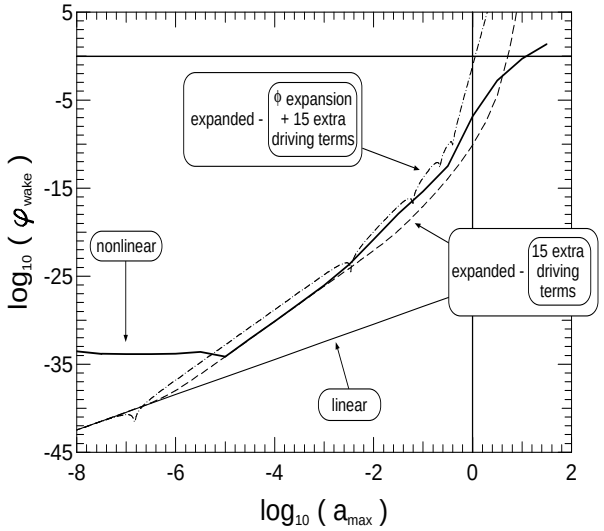

Figure 1: Peak-to-peak wake amplitude against pulse height for a Gaussian pulse of width $\sigma_g = 16$. Shown are the numerically determined amplitude (thick solid curve), the linear prediction (thin solid curve) and the "expanded equation" prediction (dashed curve) with 16 driving terms. The dotted-dashed curve corresponds to a second type of linear prediction not covered here.

RESULTS

Equation 2 was integrated numerically over the computational domain $\zeta_{max} \geq \zeta \geq -\zeta_{max}$ using the boundary conditions $\phi(\zeta_{max})=0$ and $[\partial\phi/\partial\zeta]_{\zeta max}=0$ (i.e. the plasma is undisturbed ahead of the pulse) for a Gaussian laser profile $a(\zeta) = a_{max}\exp(-\zeta^2/2\sigma_g^2)$ centred at $\zeta=0$. ϕ_{wake}, the peak-to-peak wake amplitude left behind the pulse was measured. A value of $\omega_o/\omega_p = 8.2$ ($v_g = 0.99c$) was used, corresponding to a $\lambda = 1.0\mu$m laser and an electron density of $n_e = 1.5\times10^{19}$cm^{-3}. ζ_{max} was set to 1050 and 2^{16} grid points were used. Figure 1 shows curves of ϕ_{wake} against pulse height, for a Gaussian pulse of width $\sigma_g=16$ ($L \approx 5\lambda_p$). The numerically determined wake amplitude (thick solid curves) is markedly higher than the linear theory prediction (thin solid curve) obtained using equation 4 (with $\phi_{wake} = 2\phi_o$) especially at relativistic intensities. For instance at $a_{max}=1$ (i.e. $I = 6\times10^{18}$ W cm^{-2}) the numerically determined wakefield has an amplitude of 10^{-7} rather than 10^{-27} as predicted by linear theory. These values of ϕ_{wake} represent the amplitudes of wakefields generated at t=0 (i.e. before instabilities and propagation effects change the pulse shape from Gaussian). Such wakes would serve as the seed for self-modulation of intense pulses. Notice that the curve obtained numerically (thick solid) flattens out and oscillates randomly for low pulse

heights. This effect is not physical, but rather computational; i.e. due to machine accuracy and rounding errors.

ENHANCEMENT MECHANISM

As it stands equation 1 is difficult to analyse so we expand the square root term in the denominator. The expression $\{(1-\phi)^2 - (1+2\alpha|a|^2)/\gamma_g^2\}$ can rearranged to read $\beta_g^2[1+\varepsilon]$ where $\varepsilon=[\phi^2-2\phi-2\alpha|a|^2/\gamma_g^2]/\beta_g^2$ is a small expansion parameter. After a binomial expansion in ε equation 1 reads

$$\frac{\partial^2\phi}{\partial\zeta^2} + k_p^2\phi = -k_p^2|a|^2 + \left\{-\frac{3}{2}k_p^4\frac{|a|^4}{\gamma_g^2} - \frac{5}{2}k_p^6\frac{|a|^6}{\gamma_g^4} - \ldots\right\} + \qquad (3)$$

$$\phi\left\{k_p^4|a|^2\left(\beta_g^2-3\right) - 3k_p^4\frac{|a|^4}{\gamma_g^2} + \ldots\right\} + \phi^2\left\{\frac{3}{2}\frac{k_p^4}{\gamma_g^2} + \ldots\right\} + \ldots$$

where $k_p=1/\beta_g$ has been used. The linear equation can easily be obtained from equation 3 by only retaining terms of order δ (where ϕ , $|a|^2 \sim \delta$) and is given by $\partial^2\phi/\partial\zeta^2 + k_p^2\phi = -k_p^2|a(\zeta)|^2$. This is the equation for harmonic motion driven by the ponderomotive potential. The solution of the linear equation reduces to $\phi(\zeta) = \phi_o \sin(k_p\zeta+\theta)$ in the limit as $\zeta \rightarrow -\infty$. The wakefield amplitude is given by

$$\phi_o = \left| \Im\left\{ \left|a(\zeta)\right|^2 \right\}_{k=k_p} \right| \quad , \qquad (4)$$

where $\Im\{|a(\zeta)|^2\}_{k=kp}$ is the Fourier transform of the driving term evaluated at wavenumber $k=k_p$. A comparison of the expanded nonlinear equation (equation 3) and the linear equation highlights where the enhanced wake amplitude comes from. If the terms in ϕ, ϕ^2, etc. on the right hand side of equation 3 are ignored, the expanded nonlinear equation looks like the linear equation but with extra driving terms. We obtain a better prediction for the wake amplitude by including the extra driving terms, $-3/2\ k_p^4|a|^4/\gamma_g^2 - 5/2\ k_p^6|a|^6/\gamma_g^4 - \ldots$ which involve higher orders of intensity ($I \propto |a|^2$). This is shown in figure 1 for a Gaussian pulse of width $\sigma_g=16$. To understand wake enhancement for long smooth pulses consider the spectra of the pulse intensity profile ($\Im\{|a|^2\}$) and of higher powers of the pulse intensity profile ($\Im\{|a|^{2m}\}$, m=2,3,…). At low pulse intensities $\Im\{I(\zeta)\}_{k=kp} >> \Im\{I(\zeta)^m\}_{k=kp}$ (for m>1) and the extra driving terms (which have narrower "bandwidths" than the linear driving term) are negligible. But at a sufficient pulse intensity the driving term in $I(\zeta)^2$ starts to dominate having the largest spectral amplitude at $k=k_p$ (despite a narrower bandwidth than the term in $I(\zeta)$). This is demonstrated in figure 1 where an $(a_{max})^4$ scaling (rather than the usual $(a_{max})^2$ scaling) can clearly be seen for both the improved prediction and the numerically determined wake amplitude, in the range $-5 < \log(a_{max}) < -3$. Raising the pulse intensity further sees the third, then fourth, then fifth order, etc. driving terms dominate in succession. So we attribute wake enhancement to an effective increase in the pulse bandwidth experienced by the electrons during their interaction with the laser pulse. This bandwidth increase arises from nonlinearities in the envelope equations. Note that even though the calculations presented here are for Gaussian shaped pulses, wake enhancement can occur for other profiles. The equations presented in this section are valid for arbitrary profiles with the details of wakefield enhancement depending upon the Fourier spectra of $|a|^{2n}$.

SEEDING PULSE MODULATION

Recent LWFA experiments using intense long pulses ($L >> \lambda_p$) have detected electrons accelerated up to 44 MeV [6]. Such high energies are attributed to "self-modulation" of the long pulse into beamlets spaced at λ_p. The proposed mechanisms for pulse modulation include *pure* Raman forward scattering (RFS) [7] and an instability resulting from the coupling of RFS and self-focusing [2]. A seed plasma wave is required in either case. Various seeding mechanisms have previously been compared by other authors [7,8]. They argue that the ponderomotive wake from a long smooth pulse is too small to seed: too many e-foldings of RFS growth are needed to modulate the pulse. Raman back scattering and/or ionization induced pulse front steepening are normally considered to be more effective seeding mechanisms. The problem with these seeding mechanisms which grow from noise is that they are unpredictable and uncontrollable. Under suitable experimental conditions, enhanced wakes should be large enough to act as the dominant seeding mechanism. Ionization induced seeding cannot occur if the plasma is pre-ionized. RBS can be suppressed by Landau damping while still permitting RFS at a suitable electron temperature; $100 >> T_e > 1$ KeV when $n_e=1.6\times10^{19}$ cm^{-3} and $\lambda_o=1\mu$m . Wake enhancement greatly reduces the number of e-foldings of forward Raman (or coupled RFS self-focusing) growth required for complete modulation of the seeded pulse. For a Gaussian pulse of length $L=5\lambda_p=10L_m$ and intensity $I=6\times10^{19}$ W cm^{-2} ($\sigma_g=16$, $a_{max}=4$), the wake amplitude is $10^{-2}\phi_{cwb}$ rather than $10^{-26}\phi_{cwb}$ as predicted by linear theory (see Figure 1). This enhanced wake can be used to seed RFS induced beam breakup in a second trailing pulse. Just 5 rather than 62 e-foldings of the instability are needed before a wakefield of wave breaking amplitude is produced. A single long intense pulse should be able to seed the rear portion of itself too. This is because the excited plasma wave attains a significant fraction of its final amplitude by the rear of the pulse.

REFERENCES

1) L M Gorbunov and V I Kirsanov
Sov. Phys. JETP, 66 290, (1987)

2) J Krall, A Ting, E Esarey and P Sprangle
Phys. Rev. E, 48 (3) 2157, (1993)

3) P Sprangle, E Esarey and A Ting
Phys. Rev. A, 41 4463, (1990)

4) S Dalla, and M Lontano
Physics. Lett. A, 173 (6) 456, (1993)

5) D Teychenné and G Bonnaud
Phys. Rev. E, 48 (5) 3248, (1993)

6) A Modena *et al*
Nature, 377 606, (1995)

7) C D Decker *et al*
Phys. Plasmas, 3 (4) 1360, (1996)

8) D L Fisher and T Tajima
Phys. Rev. E, 53 (2) 1844, (1996)

OPTIMISATION OF DOUBLE DRIVE PULSE PUMPING IN NE-LIKE GE X-RAY LASERS

J.Y. Lin[1)], G.J. Tallents[1)], A. Demir[1)], S.B. Healy[2)], and G.J. Pert[2)]

1) Department of Physics, University of Essex, Colchester CO4 3SQ, UK. Email jlin@essex.ac.uk
2) Department of Physics, York University, York, YO1 5DD, UK

INTRODUCTION

In this report, optimum double short pulse irradiation conditions and the processes producing high x-ray laser output are investigated using the EHYBRID[1)] fluid and atomic physics code coupled to a 3D raytracing post-processor code[2)]. These codes have produced good agreements with recent experimental x-ray laser output[3,4)]. We will show that the enhancement of x-ray laser output is determined by the level of the prepulse and the time interval between the prepulse and main pulse. A critical irradiance of the main pulse needed to enable the prepulse techniques to enhance the output was found by varying the intensity of the main driving pulse irradiance. We show in this report that a prepulse in a collisionally-pumped x-ray laser can reduce the peak gain coefficient, but usually broadens the spatial gain region because more driving laser energy is absorbed by the laser produced pre-plasma. The prepulse also causes shallow electron density gradients and less x-ray refraction which improve the ability of the x-ray laser beam to remain in the gain medium and leads to higher x-ray laser output. An optimum pulse configuration is found as a compromise between the peak gain value, gain width, and the electron density gradients.

RESULTS AND DISCUSSIONS

The results presented in this paper refer to Ge slab targets of 1.8cm length, 100μm width, and an effectively massive 1μm thickness. The target is assumed irradiated by a 1.053μm optical laser of pulse duration 100ps. The shape of the optical short pulse is assumed to be Gaussian. The driving pulse configurations considered here consist of double pulses with pulse intervals of 800ps, 2ns, 3ns or 4ns between the pulses. The peak irradiance of the main (2nd) pulse is usually fixed at 4.75×10^{13} W/cm^2 which means that the energy delivered by the main pulse to the target is ~85J. The intensity variation of the prepulse (1st pulse) is adjusted in the range from 1% to 100% with respect to the main pulse.

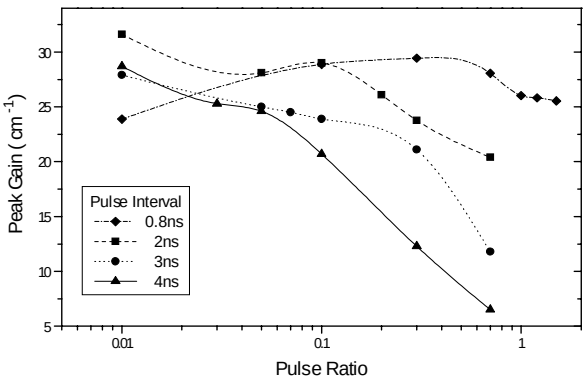

Figure 1. Variation of the peak gain coefficient with pulse ratio for various pulse intervals.

With a 2 - 4 ns delay between prepulse and main pulse, the peak gain coefficient of the double pulse configurations reduces with increasing energy level of the prepulse as shown in Fig.1. A larger volume of pre-plasma is generated by a more intense prepulse which results in a larger volume of plasma heated by the following main drive pulse and a broader gain region (Fig.2). Although a broader gain region is preferred during the amplification, a larger pre-formed plasma causes the peak gain coefficient to decrease due to a reduced electron temperature as the main pulse irradiance (assumed constant) does not have enough energy to heat the larger volume of pre-formed plasma. However, with shorter pulse intervals (0.8ns), the peak gain coefficient increases with increasing prepulse level (see Fig.1) because the pre-plasma has not fully expanded within the shorter time interval and thus the electron temperature increases. If the prepulse level continues to increase, more plasma is formed and it expands faster and further and therefore the peak gain falls because of the reduction of the electron temperature. A lower (< 10%) prepulse level is optimum for producing gain with longer pulse intervals. Double pulses with longer pulse interval generally have lower peak gain because with the longer expansion time, the initial pre-formed plasma is cooler.

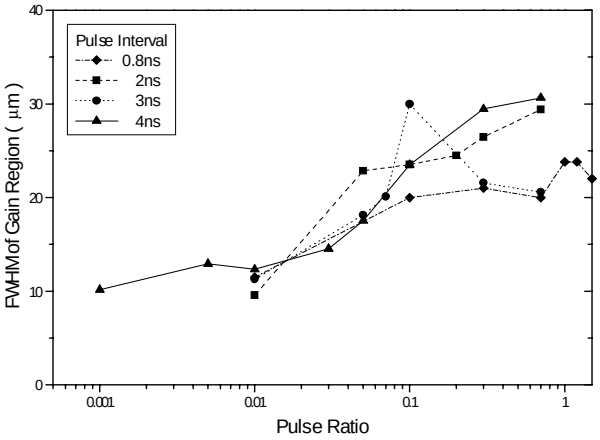

Figure 2. The spatial width of the gain region (FWHM) as a function of pulse ratio for various pulse intervals.

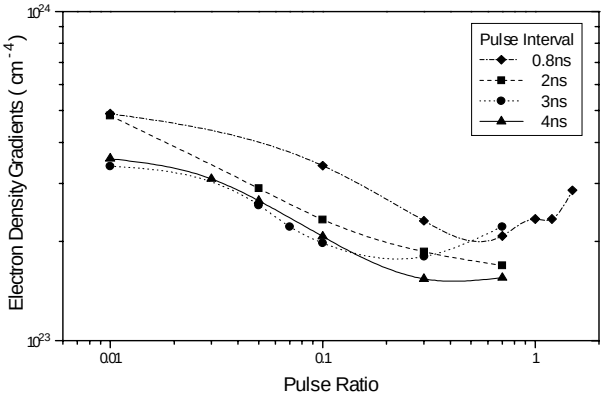

Figure 3. Variation of electron density gradients at the position of peak gain with pulse ratio for various pulse intervals.

Refraction effects determine the effective gain region which can be sampled by the amplifying x-ray laser beams. Fig.3 shows the electron density gradients at peak gain for the various pulse configurations. It is apparent that the electron density gradient is reduced with increases of the prepulse level as more free electrons are produced with a larger prepulse. With longer delay time between prepulse and the main pulse (2 ~ 4ns), the electrons produced by the two pulses overlap and form a flat density profile. In contrast, if the prepulse level is too low, the electron density profile is only smoothed in the low density region (< 10^{20} cm^{-3}), where there is little or no gain. Therefore the higher prepulse level produces less refraction and better

amplification. It can also be seen from figure 3 that the electron density gradients are not further reduced for pulse intervals longer than 3ns (compare the 3 and 4 ns pulse interval curves). The pre-form plasma simply expands further away the target surface with a longer pulse interval. This means that the pulse interval is too long, and the advantage of using a pre-pulse disappear because the peak gain coefficients reduce rapidly (see Fig.1).

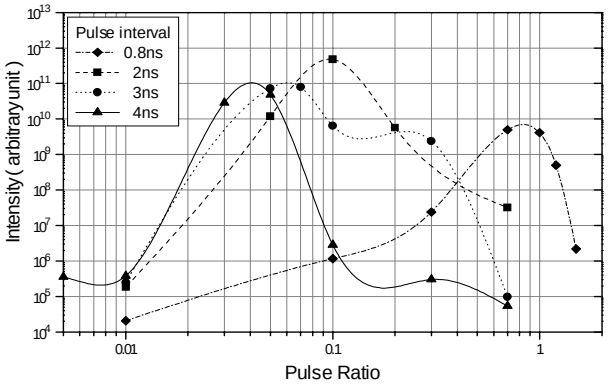

Figure 4. Variation of the output intensity with pulse ratio for various pulse intervals.

To obtain the maximum laser output, refraction effects have to be minimized and the gain coefficient and the width of gain region maximized. A compromise between the gain and refraction effects determines the final x-ray laser output. Fig.4 shows the laser output with various pulse irradiance as a function of pulse ratio (pre-pulse/main pulse). It is found that the laser output peaks at lower pulse ratios when the time delay between prepulse and main pulse is longer. This is due to the peak gain dropping faster with pulse ratio in the long pulse interval case. A double pulse with 2ns time delay at pulse ratio 0.1 gives the maximum output (Fig.4) because of the relative high peak gain (Fig.1) and low electron density gradients (Fig.3).

In order to enhance the efficiency of x-ray lasers, the minimum irradiance required with the main driving pulse for x-ray laser gain has been investigated. With the pulse interval fixed at 4ns, the x-ray laser output for different irradiances of the main pulse are simulated (Fig.5). It is apparent that when the main pulse intensity is higher than 4×10^{13} W/cm^2, the prepulse is able to provide several orders of magnitude more intense x-ray laser output than a single pulse irradiance (at 4×10^{13} W/cm^2). In contrast, if the main pulse intensity is reduced to 2 or 3×10^{13} W/cm^2, the advantage of using a prepulse disappears. The intensity of the main pulse is then too low to heat the whole pre-plasma to reach the required temperature and thus the gain coefficient reduces. The x-ray laser output is reduced even though the electron density gradient is relatively smoother than that for single pulse irradiation.

CONCLUSION

Simulations have shown how a prepulse which precedes the main pulse by few ns can modify a laser produced plasma medium during the main pulse and produce more x-ray laser output. Higher prepulse levels produce lower peak gain coefficients, but broader gain regions. An optimal prepulse level is found because a larger prepulse gives lower electron density gradients which allow the laser beam to propagate better in the gain region. The simulations have shown that the maximum output of the double pulse configuration is reached at lower pulse ratio as the pulse interval is increased. The results from a 3D raytracing code suggests that the optimal double pulse configuration is the double pulses separated by 2ns at pulse ratio ~ 0.1 because of the relative low electron density gradients and high gain coefficient.

The simulations predict that the threshold irradiance of the main pulse for prepulse effects to show orders of magnitude enhancement of output is around $3 \sim 4\times10^{13}$ W/cm^2 for Ne-like Ge. This may explain why some experiments[5] can not find an apparent optimum driving pulse ratio. The intensity of the main drive pulse in these cases may be close to or under the relevant threshold value.

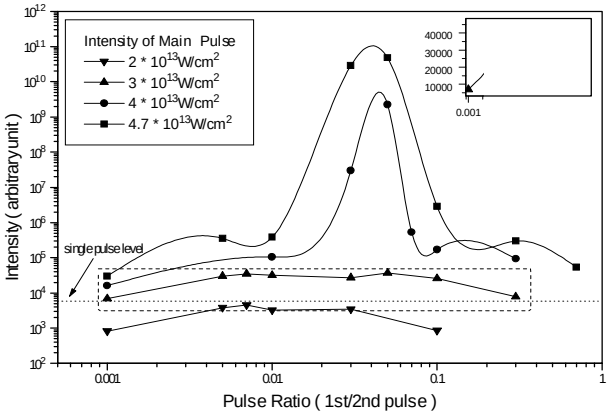

Figure 5. Ge x-ray laser output for various peak irradiance of the main pulse as a function of pulse ratio. The inset shows a linear plot of the x-ray laser output for a peak irradiance close to the threshold for lasing of 3×10^{13} W/cm^2 as a function of pulse ratio.

REFERENCES

1) P B Holden, S B Healy, M T M Lightbody, G J Pert, J A Plowes, A E Kingston, E Robertson, C L S Lewis and D Neely
J. Phys. B 27, 341, (1994)

2) J A Plowes, G J Pert, S B Healy and D T Toft
Optical and Quantum Electronics 28, 219, (1996).

3) A Behjat, J Y Lin, G J Tallents, A Demir, M. Kurkcuoglu, C L S Lewis, A G MacPhee, S P McCabe, P J Warwick, D Neely, E Wolfrum, S B Healy and G J Pert
Optics Comm.135, 49, (1997).

4) J A Plowes, G J Pert and P B Holden
Optics Comm. 116, 260, (1995).

5) A G MacPhee, C L S Lewis, P J Warwick, I Weaver, A Demir, M Holden, J Krishnan, G J Tallents, P Goedkindt, P Jaegle, G Jamelot, A Klisnick, M Nantel, B Rus and Ph Zeitoun
Optics Comm. 133, 525, (1997).

A PRELIMINARY COMPUTATIONAL STUDY OF THE NI-LIKE GADOLINIUM X-RAY LASER

S. McCabe and G. J. Pert.

Department of Physics, University of York, York YO1 5DD, e-mail spm4@york.ac.uk

INTRODUCTION

The desire for shorter lasing wavelengths, and interest in laser operation in the water window near 4 nm, has precipitated experimental interest in higher Z target materials for laser produced plasma sources. As a consequence of this, focus has shifted from Ne-like to Ni-like collisionally pumped lasing schemes. In recent years computational models of the physics of Ne-like systems have improved in parallel with increasing experimental efficiency. The physics of these lasers is now well understood and agreement between model and experiment is such that the model can be considered robust. Significant success has been achieved in York using the hydrodynamic / atomic physics code EHYBRID to model the characteristics of the Germanium Ne-like laser over a wide parameter space. This code has been modified to treat the 4d-4p Ni-like transitions using data for the element Gadolinium. In this article we present some simulation results with reference to recent experiment and in comparison to complimentary Ne-like Germanium simulations.

THE COMPUTATIONAL MODEL

The primary code used in this study is the 1.5-D hydrodynamics / atomic physics code EHYBRID[1]. The output from EHYBRID is post-processed using a 3-D raytracing code RAYTRACE[2] for comparison with experimental data. RAYTRACE models saturation and the effect of X-ray refraction in the transverse electron density gradients of the plasma. The non-LTE behaviour of the ionisation distribution has been studied in isolation from the hydrodynamic problem to elucidate the differences between the Ne-like and Ni-like schemes.

RESULTS

Initial studies with EHYBRID for various pumping schemes were not promising. Ni-like simulations predicted lower gains (<10), and narrower gain regions (5μm) than equivalent Ne-like simulations. Output powers calculated with the RAYTRACE code were low (<1kW). In contrast experimentally achieved output powers, using pre-pulse techniques, were similar to those of Ne-like schemes. To understand why the simulations were at variance with experiment we needed to investigate more thoroughly the differences between Ne-like and Ni-like schemes as predicted by EHYBRID.

The non-LTE response of the two schemes was studied using the atomic physics only single cell code. The response to a pump pulse, temporally similar to the experiment, was studied over a wide range of material densities. A plot of the peak gain as a function of material density (see figure 1) effectively illustrates the differences between Ni-like and Ne-like lasers. The density region of operation of Ne-like Germanium is much broader than Ni-like Gadolinium and the predicted gains are higher. In addition the lifetime of the gain is longer for the Ne-like scheme. This suggests that Ne-like lasing will be observed over a much wider parameter space than Ni-like lasing.

An interesting result from this study is the low gains predicted over a wide range of density for Gd. Further study shows that the gain does not scale as favourably with increasing energy as Ge. We gain further insight into this from the ionisation balance of Gd and Ge as a function of time under identical drive conditions. This non-LTE single cell simulation used the optimum operation density (7.9×10^{-2} gm/cc) for Gd obtained from earlier simulations (see figure 1). The average ionisation and the proportion of ions in the lasing stage are plotted in figure 2.

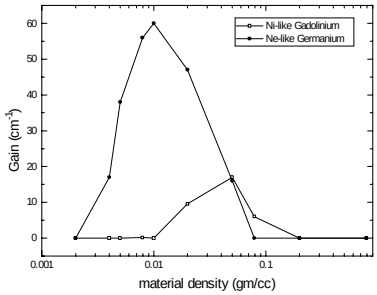

Figure 1. Peak gain vs. material density

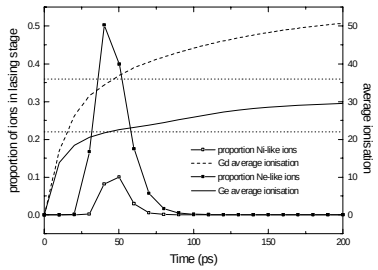

Figure 2. Ionisation balance study for Ne-like Ge and Ni-like Gd at a material density of 7.9×10^{-2} gm/cm^3 (1% solid density)

Clearly Gd ionises far more rapidly than Ge and the Ni-like ionisation stage in Gd is not as stable as the Ne-like stage in Ge. The peak fraction of ions in the lasing stage for Gd is a factor of 5 smaller than Ne-like Ge. This will significantly limit the gain.

After minor modifications to the EHYBRID input data better agreement was achieved between simulation and experiment. These simulations indicate that despite the very rapid over-ionisation of the Ni-like plasma it is possible to maintain output for at least 50ps at output powers of 10^6 Watts from a 2 cm target using the pre-pulse technique with 30-50% level pre-pulses. The short lifetime of Ni-like lasing suggests that the scheme will operate more favourably for shorter pulse durations. Simulations using 2ps CPA pulses on single 800ps pulses have yielded output powers of 10^6 Watts with >3 ps duration for 1cm targets.

Further work is needed to fully understand the limitations imposed by the overionisation problem. Other schemes for generating shorter wavelength lasers such as inner shell ionisation may prove more useful in the long term [3].

REFERENCES

1) P.B. Holden et al, J. Phys. B., 27, 341, 1994.

2) J.A. Plowes et al, Ph.D. thesis, University of York, 1995.

3) S. B. Healy et al, submitted to Optics Comm.

HARMONIC AND SUBHARMONIC GENERATION

D C McDonald [1] , R A Cairns [1] , H Ruhl [2]

1) School of Mathematical and Computational Sciences, University of St Andrews, St Andrews, Fife KY16 9SS, UK
2) Institut für Angewandte Physik, Technische Hochschule Darmstadt, D-64289 Darmstadt, Germany.

INTRODUCTION

We have previously developed a model to study the interaction of an intense laser beam with a solid density plasma and have used it to analyse absorption and second harmonic emission[1]. The calculation assumes a step function density profile, so the theory is relevant to very short pulses where there is no time for the target to expand and form an underdense corona. The results of this model have been shown to be in reasonable agreement with those of Vlasov simulations.

This theory is based on an iterative approach, where the linear response of the plasma is first calculated, then used to calculate the second harmonic emission. Although a method of this sort is suitable for estimating harmonic emission, it is a familiar feature of driven nonlinear systems that they exhibit a more complicated response than just production of harmonics of the driving force. It is quite usual for there to be a subharmonic response, or a chaotic response.

Here we will outline an extension to the theory which allows us to construct a tractable equation approximating the temporal response of the plasma to the incident wave. With this equation we anticipate being able to investigate the behaviour of the plasma over a range of parameters. Although this investigation is at an early stage, we have already seen a period doubling, producing half harmonic contributions to the Fourier spectrum.

In laser plasma interaction theory, the explanation for a plasma response at a lower frequency than the driving frequency has generally been sought in terms of parametric coupling to lower frequency wave modes. However, we shall demonstrate that such a response can arise in the strongly nonlinear regime in a way which is not attributable to weak wave-wave couplings.

THE MODEL

The method of Ref. 1 involves solving the Vlasov equation be the standard method of integration along the particle orbits, assuming that the initial electron distribution function is Maxwellian. This produces a formal solution which is expanded to second order in the field amplitudes, used to calculate the current and charge densities, then substituted into Maxwell's equations to give nonlinear equations for the current and field components. The usual boost transformation is used to transform an obliquely incident wave in the laboratory frame into normal incidence in a plasma with a flow velocity. The equation which concerns us takes the form

$$(\partial_x^2 - \frac{1}{c^2}\partial_t^2)A_y = \frac{\omega_p^2 \bar{\gamma}}{\sqrt{2\pi} v_{th} c^2}\int_{-\infty}^{\infty} dp_x \exp(-\frac{p_x^2}{2m^2 v_{th}^2}) \times \int_0^t d\tau [\frac{1}{m\bar{\gamma}^3}\partial_\tau A_y + \frac{p_x}{m^2 v_{th}^2}(\bar{\beta}c - \frac{eA_y(t)}{m\bar{\gamma}^3}) \times (E_L + \frac{eA_y \partial_x A_y}{m\bar{\gamma}^3})] \quad (1)$$

Here, A_y is the component of vector potential parallel to the surface and in the plane of incidence in the laboratory frame and $\bar{\gamma} = (1-\bar{\beta}^2)^{1/2}$, $\bar{\beta} = \sin\theta$ with θ the angle of incidence in the lab frame. The quantity E_L in (1) is an electric field, normal to the surface of the plasma. From our more exact calculations we find that the term in (1) involving this field is generally small compared to the other terms, so we neglect it.

The final integral in (1) involves an integration of the variables along particle orbits. We assume that these are simply straight line orbits with specular reflection at the boundary . To obtain a further simplification we use the fact that both the analytic model and Vlasov simulations indicate that the variation normal to the surface is well approximated by an exponential decay. Assuming this variation allows us to reduce (1) to an equation for the time variation of the potential, of the form

$$\frac{d^2 A_y}{dt^2} + \omega_0^2 A_y = B\cos(\omega t) + \int_0^t F(t-t') \times A_y(t')^2 dt' \quad (2)$$

The integral term in (2) comes from the orbit integral in (1). Physically it represents the fact that the response has a memory over the a time of the order of the time it takes for a typical particle to enter the skin layer, bounce off the plasma boundary and leave the skin layer again. The term proportional to B in (2) is a driving term, at the laser frequency, which will be related to the incoming wave intensity.

RESULTS

The analysis of the properties of (2) is at an early stage, so we will restrict ourselves here to some general comments. Since the equation contains a quadratic nonlinearity, there is secular growth of a zero frequency component of A_y . In the more detailed theory this appears as a ponderomotive force which is balanced by a steady electric field. However, our main object in simplifying the system to equation (2) is so that we may examine the oscillatory response. We have not yet done a systematic study, but we have already found that a period doubled response is possible. The response repeats itself every two cycles of the driving force, giving it a Fourier spectrum which includes half harmonics. Period doubling is a well known feature of many nonlinear systems, in which transition to chaos often occurs through a series of period doubling bifurcations. It has, however, received little attention in the laser-plasma literature, where theory has mostly dealt with wave-wave interactions in explaining the spectrum of the plasma response.

ACKNOWLEDGEMENT

This work was partly supported by the SILASI collaboration, funded by the European Commission, and partly by EPSRC Grant GR/K58937.

REFERENCE

1) H Ruhl and R A Cairns
Phys. Plasmas, to be published.

EFFECT OF LARGE VELOCITY GRADIENTS ON X-RAY LINESHAPES

P K Patel[1], O Renner[2], S J Rose[3], J S Wark[1]

1) Department of Physics, Clarendon Laboratory, University of Oxford, OX1 3PU, UK. Email p.patel1@physics.ox.ac.uk
2) Institute of Physics, Czech Academy of Sciences, 18040 Prague, Czech Republic
3) Rutherford Appleton Laboratory, Chilton, Didcot, Oxon, OX11 0QX

INTRODUCTION

The high expansion velocities often attained over the small spatial dimensions of a laser-produced plasma may result in gradients in the velocity of over $10^9 s^{-1}$. Such large velocity gradients have a significant role to play in the radiation transport process, particularly for optically thick lines where re-absorption within the plasma is of importance. In this paper we highlight the influence of the velocity gradient on the emission profiles of optically thick lines.[1] In particular we examine the characteristics of the Al XIII Ly-α resonance line emitted from a cylindrical expanding plasma.

COMPUTED PROFILES

The line profile is computed by a multi-frequency ray-tracing routine which has been incorporated into the laser-plasma simulation code, MED103:[2,3] The ionisation balance is determined by a time-dependent non-LTE average-atom calculation. The coupling of the radiation field to the atomic rate equations is carried out for the transitions of interest, the hydrogen-like *np*-1*s* series, using escape factors.[4] Remaining bound-bound transitions are assumed to be optically thin. This approximation is justified in our case since the plasma is highly ionised, with almost all of the ions in the fully-stripped or hydrogen-like stages.

We compute the emergent intensity along a specific ray through the plasma by constructing a discrete frequency grid to cover the lines of interest and a discrete spatial grid with the values of the plasma density, velocity, ion temperature and bound state population distributions specified at each point. We calculate the emission intensity at each frequency and each spatial point and then transport it through the intervening plasma along the ray. The absorption is calculated in the local fluid frame of the plasma at the Doppler-shifted frequency of the radiation. The opacity term includes contributions from line absorption and photoionization.

The results presented in the remainder of the paper are taken from the simulation of a 50μm diameter aluminium wire uniformly irradiated at $4x10^{14}Wcm^{-2}$ by 0.53μm light in a 1ns FWHM pluse. We examine the emission characteristics of the Al XIII Ly-α line which is a well-resolved doublet - with the two components, ($2p_{3/2}$-1*s* and $2p_{1/2}$-1*s*), separated by 5.4mÅ.

Figure 1 plots the emergent line intensity at the time of the peak of the pulse for a ray in the radial direction, i.e. passing through the centre of the wire perpendicular to the cylinder axis. Over a radial distance of 100μm from the ablation surface the electron density falls sharply from $1x10^{22}$ to $6x10^{20}cm^{-3}$, the ion temperature is fairly constant at 500eV, and the velocity increases almost linearly from 0 to $6x10^7cms^{-1}$. The solid line represents the emergent lineshape under these conditions. To illustrate the influence of the velocity gradient we have also plotted the lineshapes resulting from setting the velocities to half their actual value or to zero in the line transfer portion of the calculation. We clearly observe gross variations in the peak, width, position, and overall shape of the profile. For the static case we see the familiar result of almost complete absorption at the line centres with emission restricted to the wings. However, in the presence of a large velocity gradient all points of the plasma are receeding from each other and therefore a photon, wherever it originates, and in whichever direction it propagates, is continually red-shifted in the local fluid frame of the plasma. This results in a reduction in the opacity of the red wing and an increase in the opacity of the blue wing. In the case of the Al Ly-α doublet the macroscopic Doppler shift, 14mÅ at $6x10^7cms^{-1}$, is larger than the separation of the components. The expected result is that photons emitted in the shorter wavelength $2p_{3/2}$-1*s* component (the stronger line according to the statistical weights of the upper levels) may experience a red shift as they propagate through the plasma which is sufficient to bring them into the absorption profile of the longer wavelength line. Since the converse case cannot arise we should expect a preferential trapping of the shorter wavelength component. Indeed, the code predicts that the overall emission profile is actually dominated by the weaker component.

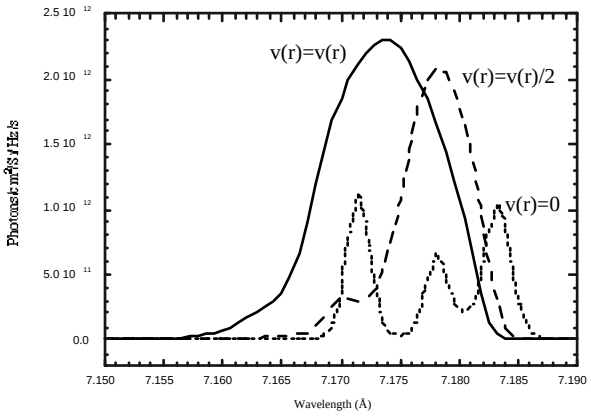

Fig. 1 Al Ly-α line profile for three different velocity profiles

EXPERIMENT

Experimental verification of the lineshape requires spectra of extremely high resolution. Such spectra were obtained with the aid of a vertical dispersion variant of the double-crystal spectrometer[5] in an experiment performed at the Trident Laser Facility at Los Alamos. The spectrometer provided a spectral resolution of 6400 with a 1D spatial resolution of 9μm. In order to approximate a uniform surface irradiance two beams were focused so as to overfill the 50μm Al wire from opposing directions. The laser parameters were as described for the simulation. The time-integrated emission was recorded onto DEF film.

In Figure 2 we give a comparison between theory and experiment. The theoretical profile is the time-integrated emission, constructed by summing together the emission calculated at discrete time intervals throughout the simulation. There is extremely good agreement between the normalised lineshapes, especially in the blue wing of the doublet which is the more sensitive to changes in the velocity profile. The actual peak intensities are also found to agree to better than a factor of two. We do observe some discrepancy in the red wing, the source of which is as yet unresolved. The overall agreement does, however, confirm the paramount importance of the velocity field in determining the doublet lineshape through its

part in bringing about an interaction between the two components.

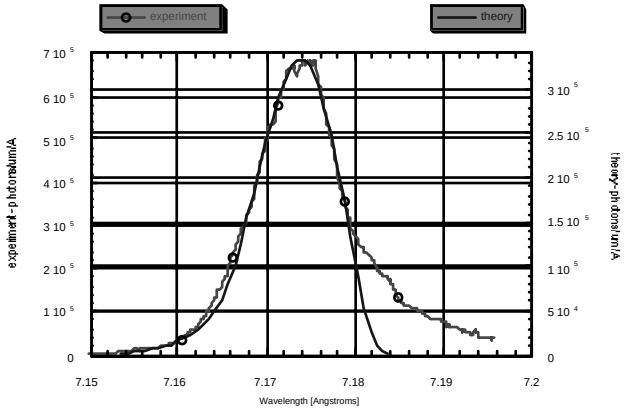

Fig. 2 Comparison of simulated and experimental Al Ly-α lineshapes

The author would like to acknowledge funding from EPSRC and the Rutherford Appleton Laboratory.

REFERENCES

1) J. S. Wark, A. Djaoui, S. J. Rose, H. He, O. Renner, T. Missalla and E. Foerster
Phys. Rev. Lett. 72 (12) 1826, (1994)

2) A. Djaoui and S. J. Rose
J.Phys. B. 25 2745, (1992)

3) P. K. Patel, J. S. Wark, D. J. Heading, A. Djaoui, S. J. Rose, O. Renner and A. Hauer
JQSRT. 57 (5) 683, (1997)

4) A. I. Shestakov and D. C. Eder
JQSRT. 42 (6) 483, (1989)

5) O. Renner, M. Kopecky, J. S. Wark, H. He and E. Forster
Rev. Sci. Instrum. 66 (5) 3234, (1995).

THE ELECTRON DISTRIBUTION FUNCTION AFTER IONISATION BY LIGHT OF ARBITRARY POLARISATION

G J Pert

Department of Physics, University of York, Heslington , York, YO1 5DD

The electron energy on release is calculated within the classical picture very simply by assuming that immediately after ionisation the electron is at rest. As a result its total (zero) velocity can be imagined to be comprised of two components: the thermal velocity and the instantaneous quiver velocity. Assuming that the field changes sufficiently slowly the quiver velocity will change adiabatically without introducing further changes in the thermal component. Once ionised the electron thermal velocity can be considered independent of the quiver apart from any change introduced by electron-ion collisions, i.e. inverse bremsstrahlung heating. The ATI thermal velocity is determined by the instantaneous quiver velocity at the instant of release such that the total velocity is zero, and is therefore the negative of the instantaneous quiver velocity at release. Assuming the field is not relativistic so that magnetic field effects are small, its direction is in the plane of the electric field as determined by the polarisation. The electron energy distribution function reflects the ionisation probability distribution over the electric field cycle. Clearly this approximation makes two important assumptions, firstly that the electron is initially at rest, and secondly that the electron does not make a second interaction with the ion. Both these conditions are much less significant when the field is not linearly polarised. Comparison with experimental data indicates that even for linear polarisation the overall error introduced by these effects is small.

Within the tunnelling regime, when the classical picture is appropriate, the ionisation probability is determined by the instantaneous field ionisation rate. The corresponding value was given by Peremelov and Popov:

$$\delta P = P_0 \left(\frac{E_0}{E}\right)^{\left(2n^* - |m| - 1\right)} \exp\left[\alpha\left(1 - \frac{E_0}{E}\right)\right] \delta t \qquad (1)$$

where δP is the probability of ionisation in time δt at an instantaneous field E when the d.c. ionisation probability per unit time is P_0 in an electric field E_0 and n^* is the effective principal quantum number of the state and m the magnetic quantum number: the constant $\alpha = \frac{2}{3}\left(\frac{\varepsilon_i}{\varepsilon_h}\right)^{3/2} \frac{E_{at}}{E_0}$. The field ionisation rate for a state (n^*, l, m) is given by:

$$P_0 = \frac{\omega_{at}}{2} \cdot C_{n^*}^2 \cdot \frac{\varepsilon_i}{\varepsilon_h} \cdot \frac{(2l+1)(l+|m|)!}{2^{|m|}\,(|m|)!\,(l-|m|)!} \cdot \left[2\left(\frac{\varepsilon_i}{\varepsilon_h}\right)^{3/2} \frac{E_{at}}{E_0}\right]^{\left(2n^* - |m| - 1\right)} \cdot \exp\left\{-\frac{2}{3}\left(\frac{\varepsilon_i}{\varepsilon_h}\right)^{3/2} \frac{E_{at}}{E_0}\right\} \qquad (2)$$

where ε_i and ε_h are the ionisation energies of the ion and hydrogen respectively, and ω_{at} and E_{at} are the atomic units of frequency and electric field. The constant $C_{n^*} \approx \left(2e/n^*\right)^{n^*} \left(2\pi n^*\right)^{-1/2}$ is given by Ammosov, Delone and Krainov. For an ion of charge state (Z-1) the effective quantum number $n^* = Z\sqrt{(\varepsilon_h/\varepsilon_i)}$. The tunnel approximation is valid provided the Keldysh parameter $\gamma = \omega\sqrt{(2m\varepsilon_i)} / eE_0$ is sufficiently small typically less than 1, or equivalently that the quiver energy, ε_0, is greater than the ionisation energy, ε_i. For convenience we identify the exponential factor

$$\alpha = \left\{\frac{2}{3}\left(\frac{\varepsilon_i}{\varepsilon_h}\right)^{3/2} \frac{E_{at}}{E_0}\right\}.$$

We consider an oscillating field of arbitrary elliptical polarisation. The polarisation parameter $[\phi \in (0,1)]$ is the fraction of the intensity in one polarisation, say x, the two polarisations being $\pi/2$ out of phase, so that $E_x \sim \cos(\omega t)$ and $E_y \sim \sin(\omega t)$. The total electric field varies as: $E = E_0\sqrt{\left[\tfrac{1}{2} + \left(\phi - \tfrac{1}{2}\right)\cos(2\omega t)\right]}$ at time t, where $E_0 = \sqrt{(8\pi I/c)}$ is the effective peak field determined by the intensity I and ω the angular frequency. The corresponding thermal energy after ionisation at time t is $\varepsilon = \varepsilon_0\left[\tfrac{1}{2} - \left(\phi - \tfrac{1}{2}\right)\cos(2\omega t)\right]$, where ε_0 is the peak quiver energy $e^2E_0^2/(2m\omega^2)$. Hence the probability of ionisation in a time δt averaged over many cycles with an energy $(\varepsilon, \delta\varepsilon)$ is

$$p(\varepsilon)\,\delta\varepsilon = \frac{(P_0\,\delta t)\left(\frac{\varepsilon_0}{\varepsilon_0 - \varepsilon}\right)^{\left(n^* - \frac{1}{2}|m| - \frac{1}{2}\right)} \exp\left[\alpha\left(1 - \sqrt{\frac{\varepsilon_0}{\varepsilon_0 - \varepsilon}}\right)\right]}{\pi\sqrt{\left[\left(\phi - \tfrac{1}{2}\right)^2 - \left(\tfrac{1}{2} - \varepsilon/\varepsilon_0\right)^2\right]}} \frac{\delta\varepsilon}{\varepsilon_0} \qquad (3)$$

since $E/E_0 = \sqrt{[\tfrac{1}{2} + (\phi - \tfrac{1}{2})\cos(2\omega t)} = \sqrt{[1 - \varepsilon/\varepsilon_0]}$.

Some points may be immediately made with reference to this equation:

1. The distribution is identical for ϕ and $(1-\phi)$. The electric field has a minimum value $E_{min} = E_0\sqrt{\{\mathrm{Min}[\phi,(1-\phi)]\}}$ and maximum $E_{max} = E_0\sqrt{\{\mathrm{Max}[\phi,(1-\phi)]\}}$. Electron energies are therefore only allowed in the range $\varepsilon_{min} \le \varepsilon \le \varepsilon_{max}$, where $\varepsilon_{min} = \varepsilon_0\,\mathrm{Min}[\phi,(1-\phi)]$ and $\varepsilon_{max} = \varepsilon_0\,\mathrm{Max}[\phi,(1-\phi)]$.

2. No general analytic expressions are available for the average ionisation rate or mean 'thermal' energy. However if $\alpha|\phi - \tfrac{1}{2}| \gg 1/2\sqrt{2}$, the ionisation is much stronger near the field maximum and we may use the method of steepest descent to obtain useful approximations. In this limit the general result (3) approximates to:

$$p(\varepsilon)\delta\varepsilon = \begin{cases} \dfrac{(P_0\delta t)\left(\dfrac{\varepsilon_0}{\varepsilon_{max}}\right)^{\left(n^*-\frac{1}{2}|m|-\frac{1}{2}\right)} \exp\left[\alpha\left(1-\sqrt{\dfrac{\varepsilon_0}{\varepsilon_{max}}}\right)\right] \exp\left[-\dfrac{\alpha\varepsilon_0^{1/2}(\varepsilon-\varepsilon_{min})}{2\varepsilon_{max}^{3/2}}\right]}{\pi\sqrt{\dfrac{2\left|\phi-\frac{1}{2}\right|(\varepsilon-\varepsilon_{min})}{\varepsilon_0}}} \dfrac{\delta\varepsilon}{\varepsilon_0} & \text{if } \varepsilon_{max} > \varepsilon > \varepsilon_{min} \\ 0 & \text{otherwise} \end{cases} \quad (4)$$

giving a displaced one dimensional Maxwellian. The total probability of ionisation:

$$\bar{p} = (P_0\delta t)\sqrt{\frac{1}{\pi\alpha\left|\phi-\frac{1}{2}\right|}}\left[\frac{\varepsilon_0}{\varepsilon_{max}}\right]^{\left(n^*-\frac{1}{2}|m|-\frac{5}{4}\right)} \exp\left[\alpha\left(1-\sqrt{\frac{\varepsilon_0}{\varepsilon_{max}}}\right)\right]$$

and the mean thermal energy

$$\bar{\varepsilon} = \varepsilon_{min} + \frac{1}{\alpha}\sqrt{\frac{\varepsilon_{max}}{\varepsilon_0}}\,\varepsilon_{max}. \quad (6)$$

3. For circular polarisation ϕ=½ all electrons are released with the same energy ½ε_0:

$$p(\varepsilon)\,\delta\varepsilon = (P_0\ \delta t)\,2^{\left(n^*-\frac{1}{2}|m|-\frac{1}{2}\right)} \exp\left[\alpha\left(1-\sqrt{2}\right)\right]\delta\left(\frac{\varepsilon}{\varepsilon_0}-\frac{1}{2}\right)\frac{\delta\varepsilon}{\varepsilon_0} \quad (7)$$

4. For linear polarisation ϕ=0, ε_{min} = 0 and ε_{max} = ε_0, and

$$p(\varepsilon)\,\delta\varepsilon = \frac{(P_0\ \delta t)\left(\dfrac{\varepsilon_0}{\varepsilon_0-\varepsilon}\right)^{\left(n^*-\frac{1}{2}|m|-\frac{1}{2}\right)} \exp\left[\alpha\left(1-\sqrt{\dfrac{\varepsilon_0}{\varepsilon_0-\varepsilon}}\right)\right]}{\pi\sqrt{\left(\dfrac{\varepsilon}{\varepsilon_0}\right)}}\frac{\delta\varepsilon}{\varepsilon_0} \quad (8)$$

The total probability in time δt is then

$$\bar{p} = \frac{2}{\pi}(P_0\delta t)e^{\alpha}\frac{d^{\left[2n^*-|m|-2\right]}}{d\alpha^{\left[2n^*-|m|-2\right]}}K_0(\alpha) \quad (9)$$

where $K_0(\alpha)$ is the modified Bessel function of order 0. In the particular case n^*=1 and m=0 this equation simplifies to

$$\bar{p} = \frac{2}{\pi}(P_0\delta t)e^{\alpha}\,K_0(\alpha) \quad (10)$$

and the average energy is:

$$\bar{\varepsilon} = \varepsilon_0\left[1+\alpha\left\{Ki_1(\alpha)-K_1(\alpha)\right\}/K_0(\alpha)\right] \quad (11)$$

where $K_1(\alpha)$ is the modified Bessel function of order 1 and $Ki_1(\alpha)$ the integral of $K_0(\alpha)$.

5. For linear polarisation, ϕ=0, and fields near threshold, E ~ E_0, the distribution is a one-dimensional Maxwellian. In this case α is large and we obtain either from (4) or (6), or directly by the method of steepest descent from (3):

$$p(\varepsilon)\delta\varepsilon = \frac{(P_0\ \delta t)\exp\left[-\dfrac{\alpha\varepsilon}{2\varepsilon_0}\right]}{\pi\sqrt{\left[\dfrac{\varepsilon}{\varepsilon_0}\right]}}\frac{\delta\varepsilon}{\varepsilon_0} \quad (12)$$

with a total probability $\bar{p}$ = $\sqrt{(2/\pi\alpha)}$ ($P_0\delta$t) and mean energy $\bar{\varepsilon}$ = ε_0 / α. These latter results have been obtained previously by many workers.

When α is not too large (~5) the asymptotic form is no longer valid and the additional term in the denominator (ε_{max}-ε) plays a role. The probability then shows a further maximum near the field minimum.

In practice the electron distribution is modified by successive ionisation, which occur as the rising edge of the laser pulse passes through the threshold intensity. Each ionisation stage will produce a distribution of the above form integrated over the rise of the pulse. In the case of circular polarisation additional fine structure is imposed on the distribution by the finite rise of the laser pulse, but this is rapidly lost by the effect of collisions. Electron collisions with both ions and other electrons will lead to both isotropisation and thermalisation at rates governed by the appropriate collision frequencies.

REFERENCES

1) N H Burnett and P B Corkum
J Opt Soc Am B 6, 1195 (1989)

2) A M Perelomov, V S Popov and V M Terent'ev
Sov Phys J E T P 23, 924 (1966)

3) M V Ammosov, N B Delone and V P Krainov
Sov Phys J E T P 64, 1191 (1987)

4) L V Keldysh
Sov Phys J E T P 20, 1307, (1965)

5) N B Delone and V P Krainov
J Opt Soc Am B 8, 1207, (1991).

DENSITY WELL WAVEGUIDING FOR X-RAY LASERS

P A Simms and G J Pert

Department of Physics, University of York, Heslington, York, YO1 5DD, e-mail pas103@york.ac.uk

INTRODUCTION

A major problem with x-ray lasers is a limited gain region due to refractive losses caused by high electron density gradients. Losses in the radial direction (parallel to the driving pulse) have been successfully reduced by a number of techniques including target curvature, double targets, double pulses and pre-pulses.[1] As refraction in this direction can now be compensated for, lowering the refractive losses in the transverse direction (perpendicular to both driving and output beams) becomes important and is addressed in this work.

The method being considered is to produce a well in the density profile in this direction, thus trapping the x-ray beam and waveguiding it through the gain region. The basic configuration required to produce such wells is to use a loosely focused, low intensity initial pulse to produce a cool, highly ionised plasma with a Gaussian density profile. The well is formed by applying a tightly focused, high intensity second pulse to the target. This rapidly heats the plasma in the centre of the target, which increases the pressure thus forcing the material outwards to form the sides of the well.

COMPUTATIONAL MODELS

Three computer codes are required for these simulations. Density and temperature profiles of the plasma which show the well formation are produced by POLLUX, a 2-d hydrocode. Atomic data of the system is produced by EHYBRID,[2] a 1.5-d hydrodynamic/atomic code. EHYBRID produces on axial values for gain, saturation intensity, linewidths, density, temperature and spontaneous emission rates. A 3-d RAYTRACE [3] code is used as a post-processor. It has been modified in order to interpolate the atomic data supplied by EHYBRID onto the density profile produced by POLLUX. This gives the characteristics of the output beam, including intensity, power, near and far field patterns.

RESULTS

Although encouraging results have been obtained using the basic two pulse configuration described above, significantly better results were obtained with an additional 10% prepulse. Extending the system to include a high intensity 2 picosecond pulse on the fall of the main pulse further improved the output intensity. Table 1 gives the best driving pulse configuration found. All driving pulses used were Nd:YAG, of wavelength 1.06μm. Second harmonic green light was investigated but no improvement was found. A Ne-like germanium slab target, of length 4.5 cm and width 100μm was considered. This had a curvature of 8mrad for the J=0→1 196Å line, and 2mrad for the J=0→1 132Å line. This target curvature in conjunction with multiple pulses fully compensated the radial refraction. Simulations suggested that using a 3 pulse configuration (first 3 pulses in table 1) gives the tightest output beam, but the 2ps pulse increases the output power by a factor ≈ 4. The time between the first 2 pulses was not critical although it appears important that the pre-pulse has an intensity 10% of the second pulse. The density well profile is short lived ≈ 25ps. It has not sufficiently formed before 6.075ns and becomes too wide after 6.1ns (results given are at 6.08ns). The timing of the 2ps pulse is thus crucial as the best results are produced a few picoseconds afterwards. Travelling wave excitation is required due to short duration of the well. Using 4 pulses gives an output intensity of ≈ 1.5×10^{12} W/cm^2, and power ≈ 3.5 MW for the 196Å line and intensity ≈ 8.3×10^{11} W/cm^2 and power ≈ 1.1 MW for the 132Å line. Figures 1&2 show the near and far field intensity profiles, respectively for the 196Å case.

Time On (ns)	FWHM (ps)	Intensity (Wcm^{-2})	Beam Focus FWHM(μm)
0	100	$1.0*10^{12}$	100
5	100	$1.0*10^{13}$	100
6	100	$5.0*10^{13}$	25
6.075	2	$1.0*10^{15}$	25

Table 1 Parameters of driving pulses

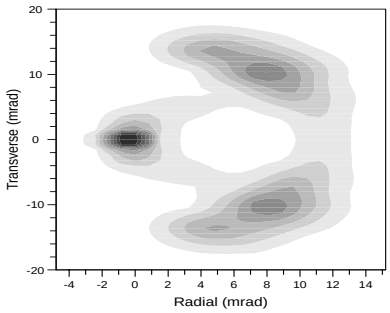

Figure 1 Far field profile

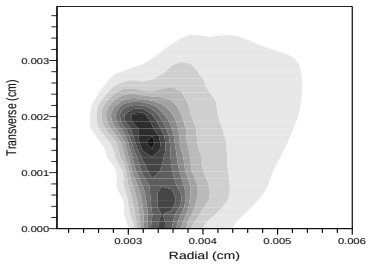

Figure 2 Near field profile

CONCLUSION

Simulations show that transverse refractive losses can be compensated for by waveguiding the output beam in a density well produced by a tightly focused, high intensity driving pulse incident on a cool, wide, highly ionised preformed plasma. Beam quality was best when using a 3 pulse configuration, but the output power was increased by employing a 2ps pulse directly before output. Density wells produced well collimated and highly saturated output beams both for the 196Å and 132Å lasing lines which were both extremely bright.

REFERENCES

1) G J Pert, S B Healy, J A Plowes and P A Simms
Inst. Phys. Conf. Ser. No. **151,** (Lund, Sweden) 260, (1996)
2) P B Holden, S B Healy, M T M Lightbody, G J Pert, J A Plowes, A E Kingston, E Robertson, C L S Lewis and D Neely
J. Phys. B **27** 341, (1994)
3) J A Plowes
PhD Thesis, University of York, (1995)

LASER-DRIVEN HELIUM INVESTIGATED USING A CRAY T3D

K T Taylor, J S Parker, D Dundas, E Smyth and S Vivirito

School of Mathematics and Physics, The Queen's University of Belfast, BT7 1NN, UK.
Email: k.taylor@qub.ac.uk

INTRODUCTION

For some years it has been possible to calculate High Harmonic Generation (HHG) for a single active atomic electron, in particular for linearly-polarized laser light where a 2-dimensional, time-dependent Schrödinger equation (TDSE) must be solved. The extra acceleration gained by the electron in being driven to and fro across the quasi-static nucleus gives rise here to HHG. But a multi-electron atom has, in the repulsive forces between its electrons, additional instances of Coulombic interaction. What features appear in HHG, for instance, as a consequence of these electron-electron (e-e) interactions?

THE CALCULATION

Helium is the simplest multi-electron atom, but nevertheless requires the solution of a 5-dimensional TDSE. For the past decade supercomputers have slowly been approaching the performance necessary but the challenge remained unaddressable until the advent of the Cray T3D. The code we have developed handles the three angular variables by a basis-set expansion over partial-waves and the radial variables are represented over a finite-difference mesh. Because the HHG spectrum for an atom extends over such a large dynamic range (typically 10 orders of magnitude) the resulting coupled partial-difference equations must be solved to a much greater level of accuracy (about 10 decimal places) than is typically required in engineering applications.

HIGH HARMONIC GENERATION

In Figure 1 we present results from the T3D for single-atom HHG by He for a variety of peak intensities. 128 partial waves were retained for the lowest two intensities, and 256 for the others. At the lowest few intensities the spectra display a sharp fall to a plateau region before individual harmonics vanish.

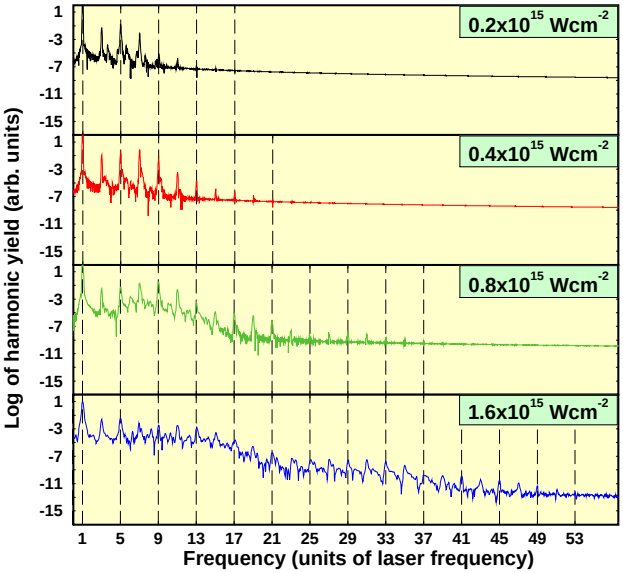

Figure 1: Single-atom harmonic response of He for a selection of increasing peak intensities of 248nm laser radiation. In each case the pulse rises linearly to peak intensity over 2 cycles.

This is characteristic of a one-electron atom and at these peak intensities only the outer electron of He is responding to the laser. However at higher intensities (bottom two frames of Figure 1) not only does the harmonic train lengthen substantially but a second plateau region emerges. Since the inner electron of the atom is certainly responding to the laser-field at these higher intensities, we conjecture that this secondary plateau is due to a co-operative effect mediated by the e-e interaction.

WAVEFUNCTION VISUALISATION

To gain more insight into the underlying dynamics, we have developed several visualisations that allow the time-evolution of the 5-dimensional helium wavefunction to be followed. In practice this amounts to taking a 2-dimensional cut, with the other dimensions essentially averaged over. Post-processing and subsequent visualisation display are carried out on local graphical workstations to which T3D generated data (typically several Gb per pulse) are downloaded from Edinburgh.

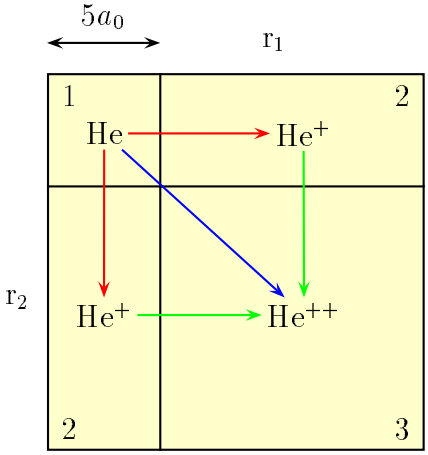

Figure 2: Schematic diagram of the radial plots showing the ionization pathways.

The first visualisation we consider is a radial plot of the probability density. Such plots are produced by integrating the probability density over all angular variables, and three distinct regions can be labelled (see Figure 2). Migration of electron flux between these regions identifies ionization pathways. Region 1, extending to about 5 Bohr (a_0) from the nucleus in both radial co-ordinates encompasses the innermost part of the two-electron wavefunction. Ground state He lies almost entirely within this region. Region 2, where one radial co-ordinate is large and the other small, is where singly-excited and singly-ionized states of He are mostly to be found, while region 3, where both radial co-ordinates are large, contains most wavefunction of doubly-excited and doubly-ionized states. Thus a movement of electron flux from region 1 to region 2 corresponds to single-electron excitation and ionization of the atom; from region 1 directly to region 3 corresponds to simultaneous-double-electron excitation and ionization. Finally, movement from region 2 to region 3 indicates both second electron excitation and second electron ionization of already singly-excited or singly-ionized He.

Figure 3 displays radial plots of the probability density at four time-instants during a pulse rising to a maximum intensity of 2×10^{15} Wcm^{-2}. In Figure 3(a), at an instant during the initial ramp on, single-electron excitation and ionization is indicated by a population in region 2. In (b) where the field has ramped on fully a packet entering region 3 directly from region 1 indicates the onset of simultaneous-double-electron ionization and excitation. In (c) where the field is passing through a maximum, we see that in addition to simultaneous-double-

electron ionization and excitation, sequential-double-electron ionization and excitation is indicated by wavefronts passing from region 2 to region 3. In (d), shortly after the field has passed through a maximum, another burst of population moving from region 1 to region 3 indicates further simultaneous-double-electron ionization and excitation. A subsequent burst occurs every half-cycle and sequential-double-electron ionization and ionization continues to occur. Other visualisations yielding angular information on electron dynamics have either been produced or are in course of development.

THE HYDROGEN MOLECULE

Another system isoelectronic with the helium atom, and accessible to experiment, is the hydrogen molecule H_2. A diatomic molecule brings in extra degrees of freedom but in fact the rotational motion is sufficiently slow in H_2 to be quasi-static over a time-scale of a hundred femto-seconds. The electrons absorb energy and angular momentum from the laser and, being light, quickly move from one side of the molecule to the other as the laser field oscillates. In consequence the nuclei find themselves less effectively screened by electronic charge and the molecule begins to dissociate. A quantitative description of the competition and interplay between the electronic dynamics and the dissociating nuclei is badly needed but probably requires the power of the T3D's successor.

REFERENCES

1) J Parker, K T Taylor, C W Clark and S Blodgett-Ford J. Phys. B.:At. Molec. Opt. Phys., **29** L33, (1996)

2) K T Taylor, J S Parker, D Dundas, E Smyth and S Vivirito in 'Multiphoton Processes 1996' the Proceedings of ICOMPVII, Ed. P Lambropolous and H Walther, IOP Publishing, Bristol and Philadelphia, 1997

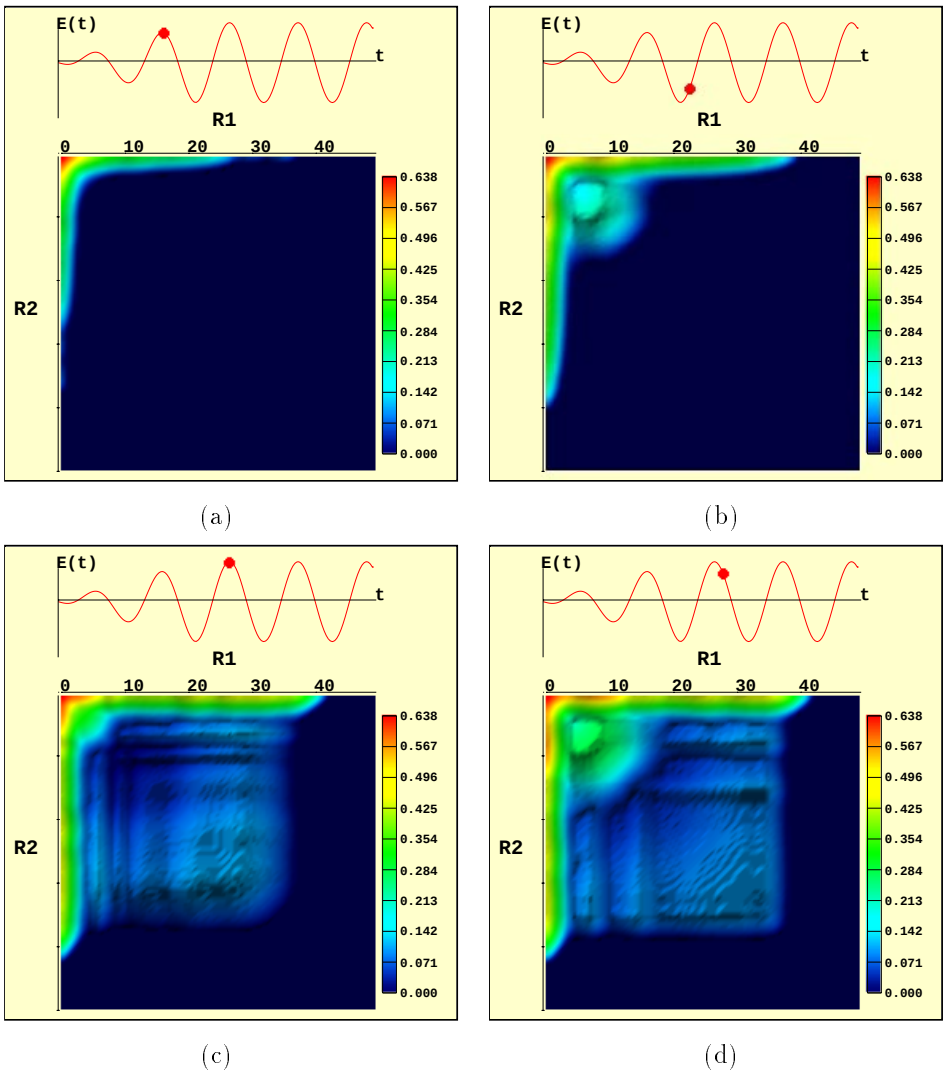

Figure 3: Radial plots at various instants during a 248nm pulse which linearly ramps up over two optical cycles to an intensity of 2×10^{15} Wcm^{-2}.

SIMPLE ANALYTIC MODEL ILLUSTRATING EFFECT OF TRAVELLING WAVE VELOCITY ON TRANSIENT PUMPED X-RAY LASER OUTPUT

P.J. Warwick and C.L.S. Lewis

School of Mathematics and Physics, Queen's University of Belfast, Belfast, BT7 1NN

INTRODUCTION

In a recent experiment [1)], described separately in these proceedings, a few ps duration laser pulse was used to generate a high gain X-ray laser. Because of the transient nature of the gain it was necessary to use travelling wave (TW) irradiation of the target. A preformed plasma was heated at different times along the length of the target, the plasma wave travelling at the same speed as the XUV photons in an optimum configuration, so that they continually experience gain as they traverse the entire target. The optimum TW velocity is thus the speed of light, c. If however, due to experimental uncertainties the TW velocity was not set exactly equal to c, how sensitive would the output be to variations of this parameter? Also, what differences might we expect between the output from the end of the target favoured by the TW (the forward end) and that from the end disadvantaged by the TW (the backward end)?

In order to facilitate an understanding of how the observed X-ray laser intensity varies as a function of TW velocity, gain duration and target length a simple analytic model was developed. This model makes a number of assumptions, foremost amongst them being that the plasma medium remains optically thin to the laser radiation for a short time on either side of the gain period. This allows stimulated photons that were generated during the inversion to propagate to the end of the target even if the inversion is subsequently destroyed. Simulations show that while the exceptionally high gain lasts only a few ps, lower positive gain still exists for tens of ps. Thus the assumption of no absorption is valid at least for the case where the TW velocity is > c, and rays in the model never travel through plasma that has not already undergone a period of gain through pumping by the short pulse. Before arrival of the short pulse the simulations also show that the gain is very low and generally positive, although a brief period of absorption may occur. This negative gain is negligible in comparison to the peak positive gain however.

We define units such that the speed of light, c = 1. Then "time" is expressed in terms of the "distance" light would have travelled in that time. For an amplifier of length L cm, assume that the gain duration is αL with $0 < \alpha \leq 1$, i.e. that the gain duration is less than the target transit time. Also assume that the gain is constant at g cm^{-1} during this time and that before and after this time g ~ 0. Assume that pumping of the amplifier is of TW nature where the effective velocity of the "pumped region" along the amplifier is $V_{tw} = fc$ where $0 < f \leq \infty$. An ideal TW will ensure V_{tw} is equal to the phase velocity of the amplifying XRL beam within the plasma medium, thus to a good approximation we require f = 1 for the most efficient case.

Figure 1 illustrates the system schematically. x is distance along the target and photons can be considered to travel at 45° to the x-axis, forward photons travelling to the right and backward ones to the left. The gain zone is the shaded area (both light and dark shading) of space-time where the gain is turned "on" and rays amplify as long as they remain within it. Because V_{tw} is greater than c in the diagram, the TW reaches a distance L before a time L has elapsed, and the gain zone does not have a slope of 45° as it would if the V_{tw} were c. For a V_{tw} approaching infinity the gain zone has no gradient and all lengths are pumped simultaneously. Similarly, for V_{tw} less than c the gain zone gradient becomes greater than one. X_0 is the x coordinate from which a ray can originate (within the gain zone) and travel the maximum distance possible while reaching the end of the target still within the gain zone i.e. for forward travelling rays reaching the end of the target while still in the gain zone, the minimum value of their starting x coordinates is X_0.

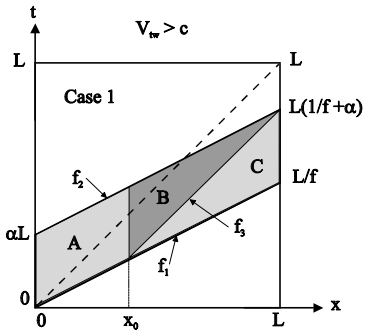

Figure 1 Schematic representation of the model system for case 1, where $V_{tw} > 0$ and $X_0 > 0$ (see text for explanation)

FORWARD DIRECTION

Consider first rays travelling in the forward direction for $\infty \geq f \geq 1$ and $X_0 > 0$, as shown in Figure 1. In this case

$$f_1 = x/f$$
$$f_2 = x/f + \alpha L \qquad (1)$$
$$f_3 = x - L(1-1/f - \alpha)$$

X_0 is the x coordinate of the intersection of f_1 and f_3, thus for $f \geq 1$

$$X_o = L\left(1 - \frac{\alpha f}{f-1}\right) \qquad \text{for } f \geq \frac{1}{1-\alpha}$$
$$X_o = 0 \qquad \text{for } \frac{1}{1-\alpha} \geq f \geq 1 \qquad (2)$$

In order to calculate the total intensity emitted from the gain zone we will add the contributions from rays emitted in regions A, B and C in Figure 1. However for $1/(1-\alpha) \geq f \geq 1$ these regions must be redefined in order to treat the integration physically. Similarly for f < 1 there are two subsets of parameter space whose mathematical treatments are different. There are thus four distinct cases to be considered for rays travelling in the forward direction.

Case I: $f \geq \frac{1}{1-\alpha}$

This scenario is illustrated in Figure 1, with f_1, f_2 and f_3 given by (1). The amplifying path length for a ray leaving from (x,t) within regions A or B is given by

$$l_A(x,t) = l_B(x,t) = \left(\frac{f}{f-1}\right)\left(\frac{x}{f} - t + \alpha L\right) \qquad (3)$$

The amplifying path length for a ray leaving from (x,t) within region C is

$$l_C(x,t) = L - x \qquad (4)$$

The total output is $I_{tot} = I_A + I_B + I_C$, therefore, since $e^{gl} >> 1$ for situations of interest

$$I_{tot} = \varepsilon A \int_0^{X_0}\int_{f_1}^{f_2} e^{gl_A} dtdx + \int_{X_0}^{L}\int_{f_3}^{f_2} e^{gl_B} dtdx + \int_{X_0}^{L}\int_{f_1}^{f_3} e^{gl_C} dtdx \quad (5)$$

where A is the cross sectional area of the gain zone volume and ε represents the emissivity and we shall let εA = 1. This approach is strictly valid only in the small signal gain regime where there are no saturation effects, and also takes no account of refraction of rays within the plasma. This expression may be solved to give

$$I_{tot} = \left(e^{\frac{gf\alpha L}{f-1}} - 1 \right) \left[\left(\frac{f-1}{gf} \right) \left(\frac{2}{g} + L \right) - \frac{\alpha L}{g} \right] - \frac{2\alpha L}{g}$$

valid for $\infty \geq f \geq \frac{1}{1-\alpha}$ (6)

Similar logic gives for case II: $\frac{1}{1-\alpha} \geq f \geq 1$

$$I_{tot} = \left(e^{gL} - 1 \right) \left[\left(\frac{f-1}{gf} \right) \left(\frac{2}{g} - L \right) + \frac{\alpha L}{g} \right] - \frac{2L(f-1)}{gf} \quad (7)$$

for case III: $\frac{1}{1+\alpha} \geq f > 0$

$$I_{tot} = \left(e^{\frac{gf\alpha L}{f-1}} - 1 \right) \frac{2(1-f)}{fg^2} + \frac{L}{g}\left(\frac{1}{f} - 1 - \alpha \right) e^{\frac{gf\alpha L}{1-f}} + \frac{L}{g}\left(1 - \alpha - \frac{1}{f} \right) \quad (8)$$

and for case IV: $1 \geq f \geq \frac{1}{1+\alpha}$

$$I_{tot} = \left(e^{gL} - 1 \right) \left[\frac{2(1-f)}{fg^2} + \frac{L}{g}\left(1 - \frac{1}{f} + \alpha \right) \right] - \frac{2L(1-f)}{gf} \quad (9)$$

BACKWARD DIRECTION

A similar treatment yields the total output from the back end. In this case f > 1 and f < 1 have the same treatment. Now for ∞ > f ≥ 0

$$I_{back} = \left(e^{\frac{gf\alpha L}{f+1}} - 1 \right) \left(\frac{2(f+1)}{fg^2} + \frac{L}{g}\left(1 - \alpha + \frac{1}{f} \right) \right) - \frac{2\alpha L}{g} \quad (10)$$

When $f \to \infty$ the output from the forward end must equal the output from the back end as the entire target is pumped simultaneously. When this happens equations (6) and (10) collapse down to the same expression as expected.

MODEL PREDICTIONS

By simply entering the target length, gain coefficient, gain duration and V_{tw} in the form of f, the model produces output intensities in arbitrary units from both the front and back of the target. Figure 2 shows how the output from the forward end varies with f for g = 35 cm^{-1}, L = 0.5 cm, and α = 0.6 (10 ps). Although the mathematics consists of four different cases for different values of f, the overall function is continuous across the boundaries between the different cases.

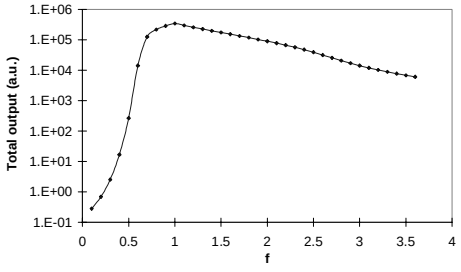

Figure 2 Model prediction for output from the forward end as a function of f for g = 35 cm^{-1}, L = 0.5 cm, and α = 0.6 (10 ps).

Figure 3 plots an example of the output from the forward end as a function of α and f for a gain coefficient of 35 cm^{-1} and a length of 0.5 cm. The different shadings represent contours of equal output. It is evident that for short gain durations the output is highly sensitive to the V_{tw}. However as the gain duration becomes longer the TW becomes less necessary, there being a plateau region at longer durations where the output is within an order of magnitude over a wide range of f. The system is also much more tolerant of f > 1 than it is of f < 1, output dropping rapidly as f decreases when it is less than 1. Thus f = 3 will have a larger output than f = 0.3

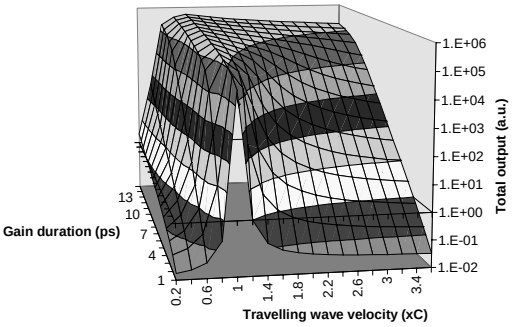

Figure 3 Model predictions for the output from the forward end of a 5 mm target with a gain coefficient of 35 cm^{-1}

Figure 4 plots predicted output from the back end of the target under the same conditions.

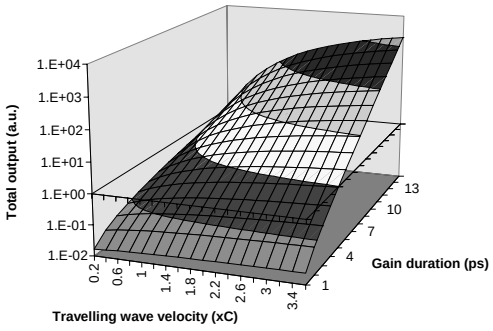

Figure 4 Model predictions for the output from the back end of a 5 mm target under a gain coefficient of 35 cm^{-1}

Output increases monotonically with both f and gain duration. As either one of these parameters becomes very large the output from the forward and the back end will become the same.

SUMMARY

We have developed a simple model capable of estimating the sensitivity of X-ray laser output to TW velocity when the expected gain duration is very short. It can also give a good idea of the expected ratio between the forward and backward outputs.

The model helps to explain why we could not distinguish between the output signals from the data sets for the Ti X-ray laser [1)] with and without the TW grating in place. Since the CPA drive pulse was longer than desired (~ 7 ps) the gain duration will also have been relatively long. If the duration were 15 ps, then the expected decrease in signal level on removal of the TW grating (f=1.0 → f=2.7) is only a factor of 2.6, which is significantly less than the shot to shot scatter in the data.

REFERENCE

1) P.J. Warwick, A. Behjat, A. Demir, M.P. Kalachnikov, C.L.S. Lewis, D. Neely, P.V. Nickles, M. Schnurer, G.J. Tallents, E. Wolfrum, J. Zhang
These proceedings

PRODUCTION AND CHARACTERISATION OF AMORPHIC DIAMOND FILMS PRODUCED BY PULSED LASER ABLATION OF GRAPHITE

M. N.R. Ashfold,[1)] S. E. Johnson,[1)] R. J. Lade[1)], K. N. Rosser[1)], N. A. Fox[2)], W. N. Wang[2)]

1) School of Chemistry, University of Bristol, Bristol BS8 1TS
2) H.H. Wills Physics Laboratory, Tyndall Avenue, University of Bristol, Bristol BS8 1TL

INTRODUCTION

Pulsed laser deposition (PLD) is finding ever increased application as a route to producing thin films of a variety of materials, with controlled composition and properties. In early studies of the PLD of high density graphite under vacuum conditions, Davanloo *et al*.[1] identified two generic forms of hydrogen free carbon films. These have been termed amorphic carbon (a-C) and amorphic diamond (a-D), respectively; the structure and properties of these materials appear to be determined primarily by the kinetic energies with which the ablated carbon particles impact upon the target substrate. More recent work by this same group, using laser intensities in excess of 10^{11} W cm^{-2} together with an ancillary high current discharge within the small volume defined by the laser focus, have succeeded in depositing hydrogen free carbon films at ambient temperatures and at growth rates of ~ 0.5 μ m hr^{-1}, over areas of ~100 cm^2 with hardness (>80 GPa) approaching that of natural diamond. Davanloo *et al.*[2] favour the term nanophase (rather than amorphic) diamond for such material, which they argue to be a unique product of the energetic condensation of multiply charged carbon ions produced in the laser plasma. The combination of hardness, adherence, infrared transparency and comparatively low residual compressive stress exhibited by these films has encouraged the view that they should find considerable application as abrasion and corrosion resistant coatings for infrared optical materials.

The electron emission properties of carbon films are also of great contemporary interest, particularly the so called negative electron affinity (NEA) exhibited by hydrogen terminated diamond surfaces such as those grown in typical chemical vapour deposition (CVD) processes.[3-7] For such materials the conduction band minimum lies close to, or even below, the vacuum level, so even small bias voltages can lead to efficient electron emission. Okano *et al.* [8] have reported electron emission from nitrogen doped polycrystalline CVD diamond films at bias field strengths, E, as low as 0.5 V μ m^{-1}. Field induced electron emission has also been observed from individual Si or Mo tips coated with synthetic high pressure diamond particles.[9] All these varieties of diamond based films are attracting considerable interest as possible cold cathode materials for use in diodes and field emission display devices.[10]

Here we report use of a high powered excimer laser operating at 193 nm (ArF) to prepare a-D films by PLD from a high density graphite target.[11] Both continuous and patterned films have been prepared in this way; the latter using TEM grids to mask selected portions of the substrate. The resulting films have been characterised by optical and scanning electron microscopy, and by Fourier transform infrared (FTIR), laser Raman and Auger spectroscopy, and their electron emission properties investigated under vacuum by repeated cycling of an applied bias voltage. Using sample–probe separations in the range 10–50 μ m, we establish that these a-D films show a turn on voltage of ~20 V μ m^{-1} and emission current densities of the order of a few A cm^{-2} at bias voltages ~1 kV. In passing, we note two other recent, related studies of field emission from amorphous tetrahedrally bonded diamond like carbon films (both with and without added nitrogen) grown by PLD methods.[12,13]

EXPERIMENTAL

a-D films were produced on single crystal (100) silicon, on quartz and on NaCl substrates by ablation of a high density (2.09-2.23 g cm^{-3}), Ultra F (99.9995%) graphite rod (Johnson Matthey) in vacuum, using the 193 nm output of a Compex 205 excimer laser (Lambda-Physik) operating on ArF at a repetition rate of 10 Hz. The laser output was steered using two mirrors, irised to a spot 15 mm in diameter, then focused using a 20 cm f.l. plano-convex fused lens through an entrance window onto the target graphite rod. The rod, which is first polished with fine emery cloth and cleaned in a jet of compressed air, is mounted vertically, and rotated and translated during an ablation run using a screw thread mechanism and a 1.8^o, four phase stepper motor operating at half step mode, giving an angular frequency of 1.0 revs. min^{-1}. The energy incident on the rod was typically 300 mJ pulse^{-1} in a focal spot size of 0.5 mm^2 which, given the laser pulse duration (*ca*. 20 ns), equates to a power density at the target approaching 10^{10} W cm^{-2}. The focal volume, and the ablated material (which appears as a divergent conical plume concentrated around the normal to the surface at this spot) are both clearly visible as a result of the accompanying optical emission. The former appears as an intense blue-white spot, but the emission becomes progressively redder as the plume expands towards the target. The ablated material deposits on a suitably positioned substrate (typical area ~1 cm^2) mounted behind a mask on a rotatable carousel. The substrates are cleaned successively with 2% ammonium bifluoride solution, deionised water, then *iso*-propanol, prior to use. The target–substrate distance is adjustable in the range 2–5 cm. The vacuum chamber, which has been fully described elsewhere,[11] is equipped with Pirani and Penning gauges, a port for viewing the ablation process and three additional (spare) flanges, and is maintained at ~ 10^{-6} Torr using an Edwards 100 mm Cryo-Diffstak diffusion pump in series with a two stage rotary pump.

Field emission tests were carried out in an evacuated glass bell jar. The sample under test is mounted on an insulated and translatable glass support and biased relative to a (fixed) cylindrical anode probe of 3 mm diameter. The surface–probe separation is user adjustable via a micrometer, and I–V curves measured by ramping the bias voltage up and down between 0 and ~1.5 kV (typically in 20 V steps) whilst measuring any emission current with a multimeter. The emission measurements were fully automated, with a PC controlling both the power supply and data logging (both I and V).

RESULTS AND DISCUSSION

Fig. 1 shows an SEM image of a 95±5 nm thick a-D film on Si(100) produced by PLD of a high density graphite rod for 20 mins. using an ArF laser delivering 250 mJ pulses at a repetition rate of 10 Hz. This shows the film to be generally nanophase, uniform and smooth, but also reveals the presence of occasional larger, randomly distributed sputtered particles that seemingly are endemic in such films.[2,13] Analysis of cross-sectional images such as fig. 1 enables investigation of the way the film deposition rate varies with laser pulse energy and with the time duration of the PLD process.[11]

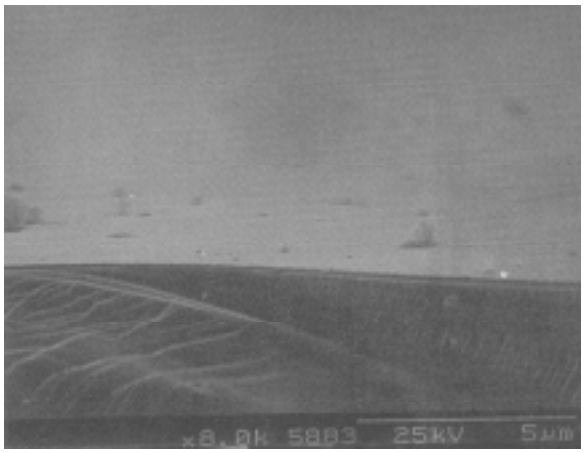

Fig. 1 SEM image of a 95 ± 5 nm thick a-D film on Si(100) formed by PLD of a high density graphite rod for 20 mins using an ArF laser delivering 250 mJ pulses at 10 Hz repetition rate.

As in any ablation process, we find there to be a threshold fluence below which no ablation occurs; thereafter the deposition rate increases with incident fluence but ultimately starts to plateau at the highest available pulse energies. Complementary experiments conducted at constant incident fluence show the deposition rate to be essentially constant with time.[11] It is worth mentioning, however, that attempts to deposit a-D films thicker than ~150 nm using yet longer deposition times were unsuccessful; such films were found to delaminate, presumably because of the accumulated compressive stress within the film. The as grown a-D films show a characteristic broad, asymmetric Raman profile when excited using a 632.8 nm He-Ne laser, peaking around 1495 cm^{-1}.[11]

The main thrust of these experiments concerns the electron emission properties of such a-D films. I–V curves were measured for several different samples, at a number of sample-probe separations in the range 10–50 μm. For any given sample, the voltage was first ramped from zero up to ~1.5 kV in 20 V steps and then stepped back to zero; this up-down cycle was then repeated several times. For all films investigated, the emission current measured on the 'down' leg was found to be consistently larger (for a given bias voltage), by some 25%, presumably as a result of some surface conditioning. Fig. 2a shows a representative set of results for a 150 nm thick a-D film on silicon. These curves were each measured whilst the bias voltage was being ramped down, using 10, 20 and 30 μm sample-probe separations, respectively. Surface conditioning also affects the emission current observed on subsequent cycles. For any given sample-probe separation the emission current (for a given applied voltage) was found to vary by as much as 25% from one run to the next; this variation can manifest itself as an increase or decrease in emission efficiency, depending on the particular sample under investigation. The emission stability was investigated briefly. In all cases the emission current was found to drop, typically by a factor of two, within ~2 minutes but thereafter to decline much less steeply. The turn on voltage is observed to scale with the sample-probe separation, having a value ~20 V μm^{-1}. Such field emission data are traditionally analysed in terms of the Fowler-Nordheim theory describing emission via barrier tunnelling. The Fowler-Nordheim equation can be written in the form[7]

$$I = k\left(\frac{\beta V}{d}\right)^2 \exp\left(\frac{-6530 d \phi^{3/2}}{\beta V}\right) \qquad (1)$$

where k is a constant related to the emission area, V is the applied bias voltage (in V), d (μm) is the sample-probe separation, ϕ (eV) is the barrier height, and β is the geometric field enhancement factor.

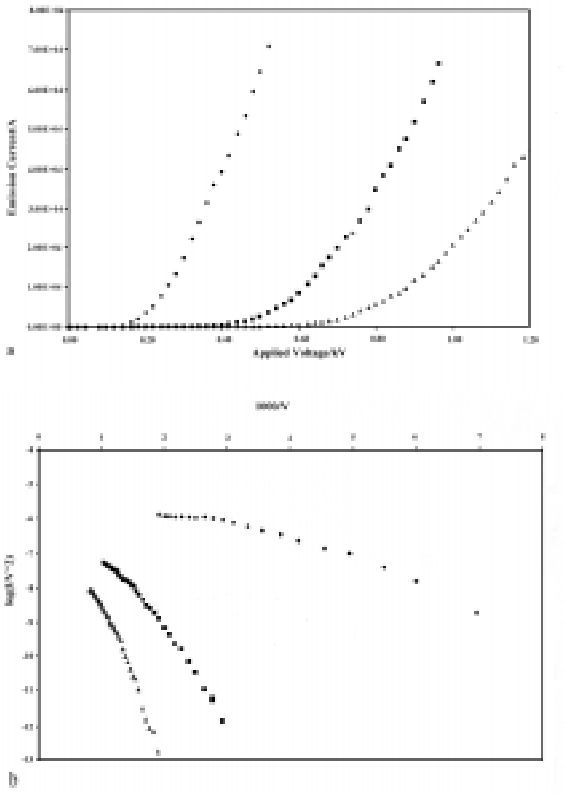

Fig. 2 (a) I–V curves for a 150 nm thick a-D film on Si(100), obtained using 10 (♦), 20 (■) and 30 μm (Δ) sample-probe separations. (b) Fowler-Nordheim plots of the data shown in (a).

Fig. 2b shows plots of $\log_{10}(I/V^2)$ versus V^{-1} for the three I–V data sets displayed in fig. 2a. None is strictly linear, but the best-fit straight line for each provides some indication of the size of $\phi/\beta^{2/3}$, and thus an effective barrier height. The resulting values are ~0.05, 0.10 and 0.12 eV when using nominal sample-probe separations of 10, 20 and 30 μm, respectively. Quantifying ϕ, the work function of the deposited a-D films, requires a value for β. In the absence of other information, β is often assumed to be unity[7] – the value appropriate for a uniformly flat film. Such an approximation is likely to be least valid for small d (*e.g.* 10 μm) given the occasional lumps embedded in the surface (recall fig. 1). This may explain the low value of $\phi/\beta^{2/3}$ deduced using the smallest sample-probe separation, and suggests that $\phi \geq 0.1$ eV. SEM images of the a-D films after field emission testing allow an estimate of the emission current density, since the conditioned surface shows a markedly different morphology and response to electron irradiation. Thus we have established that the measured emission current emanates from an area of ~3×10^4 μm^2 and that the emission current density can thus be as high as ~ 2–5 A cm^{-2} at bias voltages ~ 1 kV.

In conclusion, we have demonstrated that hydrogen free a-D films produced by 193 nm PLD of an ultrapure graphite target represent another class of carbon film meriting serious consideration as a cold cathode material. We are now

conducting analogous experiments on carbon films ablated from other carbon rich target materials, whilst planned studies will address the possibility doping the growing a-D films *in situ* and thereby altering their electrical properties.

REFERENCES

1) F. Davanloo, E.M. Juengerman, D.R. Jander, T.J. Lee and C.B. Collins
Journal of Applied Physics 67 2081 (1990).

2) F. Davanloo, J.H. You and C.B. Collins
Journal of Materials Research 10 2548 (1995) and refs. therein

3) C. Wang, A. Garcia, D.C. Ingram, M. Lake, M.E. Kordesch
Electronics Letters, 27 1459 (1991)

4) J. van der Weide, Z. Zhang, P.K. Baumann, M.G. Wensell, J. Bernholc and R.J. Nemanich
Physical Review B. 50 5803 (1994)

5) T. Asano, Y. Oobuchi and S. Katsumata
Journal of Vacuum Science and Technology B. 13 431 (1995)

6) I.L. Krainsky, V.M. Asnin, G.T. Mearini and J.A. Dayton
Physical Review B. 53 R7650 (1996)

7) S.P. Bozeman, P.K. Baumann, B.L. Ward, M.J. Powers, J.J. Cuomo, R.J. Nemanich and D.L. Dreifus
Diamond and Related Materials 5 802 (1996)

8) K. Okano, S. Koizumi, S.R.P. Silva and G.A.J. Amaratunga
Nature 381 140 (1996) and references therein

9) V.V. Zhirnov, W.B. Choi, J.J. Cuomo and J.J. Hren
Applied Surface Science 94 123 (1996) and references therein

10) See, e.g., R.J. Nemanich, P.K. Baumann and J. van der Weide
in 'Applications of Diamond Films and Related Materials': Third International Conference, 1995 (eds. A. Feldman et al.).

11) S.E. Johnson, M.N.R. Ashfold, M.P. Knapper, R.J. Lade, K.N. Rosser, N.A. Fox and W.N. Wang
Diamond and Related Materials 6 569 (1997)

12) A.A. Talin, T.E. Felter, T.A. Friedmann, J.P. Sullivan and M.P. Siegal
J of Vacuum Science and Technology A. 14 1719 (1996)

13) C. Park, H. Park, Y.-K. Hong, J.S. Kim and J.K. Kim
Applied Surface Science 111 140 (1997)

14) M.C. Polo, J. Cifre, G. Sanchez, R. Aguiar, M. Varela and J. Esteve
Diamond and Related Materials 4 780 (1995)

LASER SPECTROSCOPY OF AMIDE AND AMINO ACID WATER CLUSTERS

J. A. Dickinson, M. R. Hockridge, E. Robertson, and J. P. Simons

Physical and Theoretical Chemistry Laboratory, Oxford OX1 3QZ

INTRODUCTION

The low temperature environment of a free jet expansion or a molecular beam provides an excellent 'laboratory' for probing the conformational structures of flexible organic molecules attached to an optical chromophore. The rotational band contours of their laser induced fluorescence (LIF) or resonantly enhanced two photon ionisation (R2PI) spectra are sensitive to conformationally induced changes in not only the rotational constants and the inertial axes, but, more interestingly, in the alignment of the electronic transition moment, TM, in the molecular frame.[1-3)]

Many of the molecules under current investigation, by our group, provide models for simple biological molecules. They each possess an aromatic chromophore, a flexible side chain with a polar (or non polar) terminal group, e.g. an amide, carboxylic acid, alkyl, amino or hydroxy group. The amino acids phenylalanine and tyrosine and the amine neurotransmitter dopamine, for example, are all variants on this theme. Understanding their conformational preferences is important in helping to understand the structures and properties of larger biosystems, in particular, the role of intra and intermolecular hydrogen bonding.

We have probed the conformational properties of phenylethyl alcohol, formanilide and their complexes with water at both low (vibronic) and high ($0.08cm^{-1}$) resolution. At low resolution we have been able to 'count' the number of band origins. With higher resolution it has been possible to assign these origins to conformers and, most interestingly, to investigate the influence of both inter and intra molecular interactions on the conformational preferences and photophysical properties.

EXPERIMENTAL

The experimental apparatus consisted of a Nd:YAG laser (Spectron SL805; 1.1 W/355 nm, 10 Hz) used to pump a grating tuned dye laser (Lambda Physik FL2002, 15 mW/530 nm, 10 Hz), the doubled output of which serves as pump and photoionisation laser in a one-colour R2PI experiment, and pump laser only in a two-colour R2PI. A second Nd:YAG laser (Spectra-Physics GCR-11; 1.5 W/532 nm, 10 Hz) pumps a dye laser (Spectra Physics PDL-3, 11 mW/585 nm) which is frequency doubled and used as the photoionisation laser in the 2-colour R2PI experiment. The doubled dye laser outputs are combined co-linearly and directed into the interaction region of a differentially pumped time-of-flight mass spectrometer (R. M. Jordan, Co.),4 at right angles to the expansion axis of a pulsed molecular beam (General Valve, Series 9, 800 mm orifice). Rotational band contours were obtained by narrowing the bandwidth of the FL2002 pump laser using an intracavity etalon. The sample was heated (T=120-140 ^{o}C) and entrained in helium, total pressure 3-4 bar. Water solvent incorporated into the carrier gas by bubbling helium through a room temperature water sample and combining this flow with the main carrier using a needle valve. Mass-resolved photoionisation (MS-R2PI) signals are sampled by a digitising oscilloscope (Tektronix TDS 520) and recorded as a function of pump laser wavelength.

RESULTS AND INTERPRETATION

PHENYLETHYL ALCOHOL

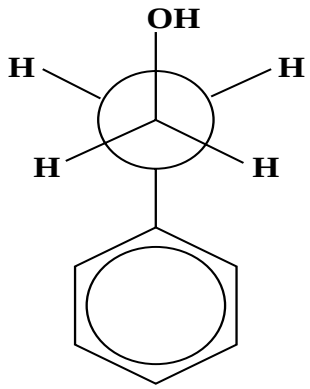

Fig.1 Phenylethyl alcohol, Newman projection along the C_α-C_β bond.

Phenylethyl alcohol, figure 1, can be considered as an analogue of the amino acids phenylalanine and tyrosine and of the aromatic neurotransmitter phenylethylamine. *Ab initio* calculations at the HF/6-31G* and *CIS*/6-31G*levels of theory predict the existence of 2 *anti* and 3 *gauche* conformations differing only in the orientation of terminal hydroxyl group, (the terms *anti* and *gauche* refer to the orientation of the Ca-Cb bond). These calculations yield both the ground and excited state rotational constants as well at the alignment of the optical transition moment (TM) for each of the five conformers. They predict that the orientation of the terminal hydroxyl group in the *gauche* conformers, where it has an opportunity to hydrogen bond to the benzene ring, will have a significant effect on the alignment of the TM in the molecular frame.

Low resolution MS-R2PI and LIF spectra of phenylethyl alcohol are shown in figure 2. Five band origins, A-D, have been observed. Bands A, B, D and E are assigned as conformer band origins of the monomer. Band C appears in both the monomer and 1:1 water complex mass channel, however, it is assigned to an overlapping feature on the basis of two colour etalon scans.

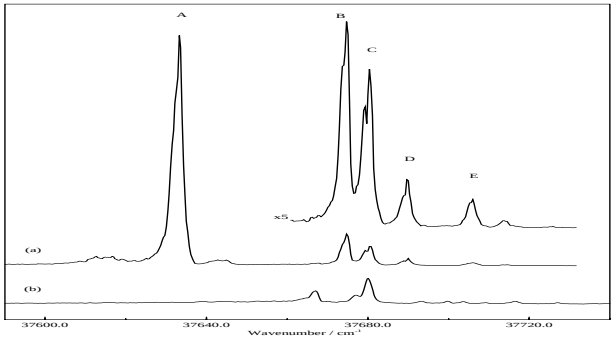

Fig. 2 MS-R2PI spectrum of 2-phenylethyl alcohol in the region of the $S_1 \leftarrow S_0$ band origins: (a) gating the monomer mass channel (m/z=122); (b) gating the 1:1 water complex mass channel (m/z=140).

Rotational band contours (not shown due to the lack of space) were measured by LIF and MS-R2PI for the five band origins. The contour of band A is predominantly b-type and the K sub band spacing is consistent with a *gauche* conformer. In contrast the band contour of band B is strongly a-type, however, the K sub band spacing is almost unchanged from that of band A.

Band D is predominantly b-type and exhibits K sub band spacing consistent with an *anti* conformation. Band E is too weak to obtain a clearly resolved band contour, however, the K sub band structure present is what would be expected for a *gauche* conformer. Two colour MS-R2PI etalon scans of the remaining band, C, taken in the monomer and the 1:1 water complex mass channel, are shown in figure 3.

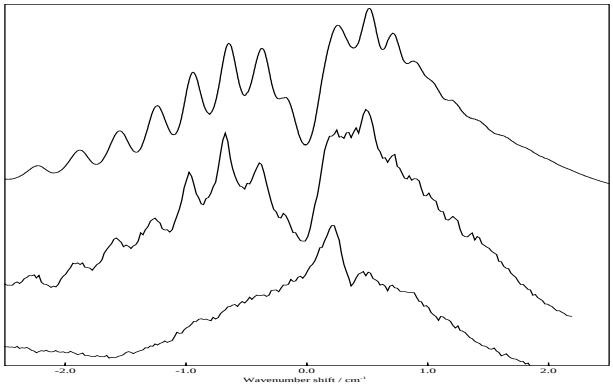

Fig. 3 Partially resolved rotational band contours of 2-phenylethyl alcohol: Band C. Upper trace: Best fit simulation. Centre trace: R2PI trace recorded in the monomer mass channel. Lower trace: R2PI spectra recorded in the 1:1 water complex mass channel

Clearly the two band contours obtained in the two mass channels are very different confirming the assignment of band C to an overlapping feature. The band contour appearing in the monomer mass channel closely matches that of Band D and is consistent with an *anti* conformer.

The one and two colour MS-R2PI experiments have revealed the existence of two *anti* and three *gauche* conformers stabilised in the jet expansion. It is not possible to distinguish the differing *anti* conformers on the basis of the K sub band spacing alone because the different orientations of the light hydrogen atom in the terminal hydroxyl group has very little effect on the rotational constants. These origin bands can only be assigned on the basis of their relative intensities and frequencies.

In contrast the *gauche* conformers are predicted and observed to exhibit significantly different alignments of their TM's in the molecular frame. Comparison of the ab inito data with the experimental has allowed definite assignments to be made.

FORMANILIDE

Formanilide, the simplest aromatic amide provides a simple peptide analogue. It can exist in two forms, *cis* and *trans*, see figure 4. *Ab initio* MO calculations have been carried out on both the ground and first singlet excited states of these two conformers. They predict that the *trans* conformer is planar in both the ground and first excited states, whereas the *cis* conformer is non planar (t_{S0}=42°) in the ground state and undergoes a geometry change, towards planarity, on excitation (t_{S1}=6°).

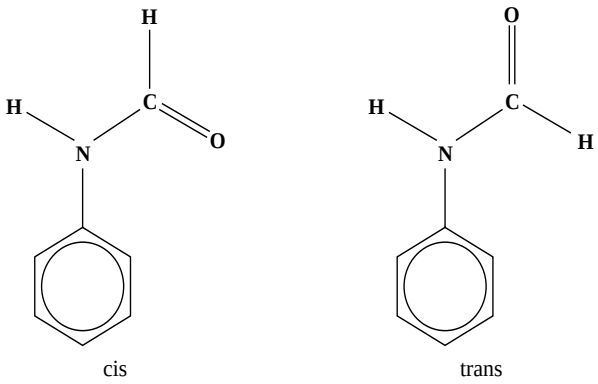

Fig. 4 The *cis* and *trans* conformers of formanilide.

The low resolution MS-R2PI spectrum taken in the monomer mass channel is shown in figure 5. There are two band origin regions, A and B. Region A, around 36000cm^{-1}, exhibits a single strong feature at 36017cm^{-1}. Additional origins at -300 and +90 cm^{-1} appear upon addition of water to the helium carrier gas. The cluster ion associated with the band at -300 cm^{-1} exhibits extensive fragmentation into the monomer mass channel. In contrast the band at +90 cm^{-1} appears only in the 1:1 water complex mass channel and shows no evidence of fragmentation.

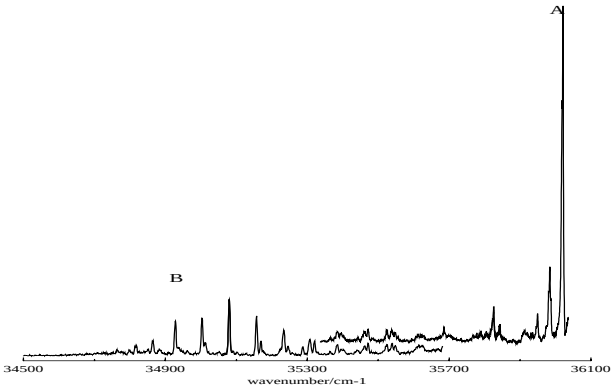

Fig. 5 Low resolution spectra of the two band origin regions of formanilide.

The rotational band contour of the monomer origin in region A is shown in the lower traces of figure 6. The *ab initio* calculations of both the ground and first excited states allow a purely '*ab initio*' simulation of the band contour of both conformers to be generated. These '*ab initio*' simulations are shown in the upper traces of figure 6. Clearly the simulation based on the *cis* conformer gives the best agreement with the experimental band.

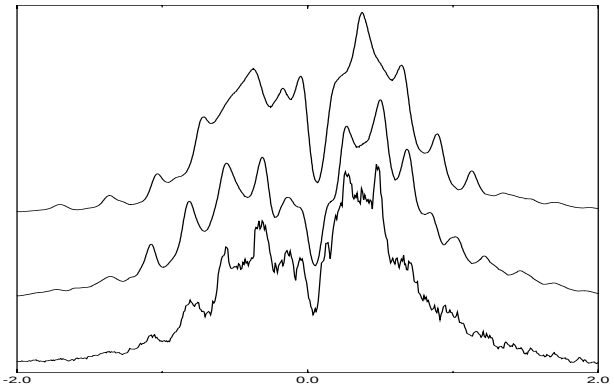

Fig. 6 Partially resolved rotational band contour of the main band in region A. Lower trace: experimental LIF spectrum. Centre trace: *ab initio* simulation based on the *cis* conformation. Upper trace: *ab initio* simulation based on the *trans* conformation.

Hole burning spectra of the two water complex band origins are shown in figure 7. They show that the two bands are indeed due to different species in the jet expansion. Frustratingly, high resolution one and two colour etalon scans of these two band origins do not exhibit resolved rotational structure. A variety of possible reasons can be proposed for this

- Binding of the water molecule in a position that results in small rotational constants
- Line broadening due to a greatly reduced excited state lifetime
- Line broadening due to tunnelling or non rigid motion of the complex

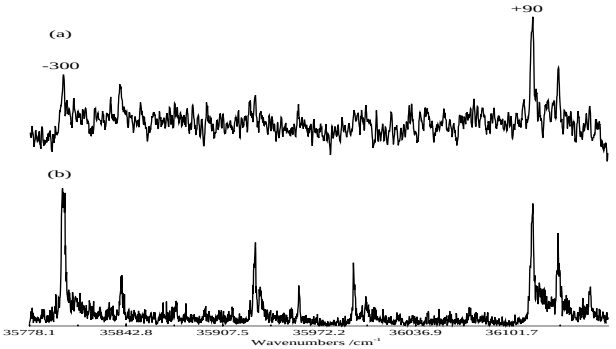

Fig. 7: Hole burning spectra of the -300cm^{-1} and +90cm^{-1} 1:1 formanilide:water cluster band origins. (a) Burn laser centered on band A. (b) No burn laser.

Region B, which exhibits a low frequency progression was first observed by Manea et al[4]. The progression was attributed to an out of plane torsional motion of the amide group in the non planar *trans* conformer. The *ab initio* calculations of the excited state of this conformer predict the existence of a torsional mode at 70 cm^{-1}, within 10% of that observed in the spectrum, confirming the assignment of this band. Attempts to observe this progression in LIF experiments or to observe two colour signal enhancements in the MS-R2PI experiments have not been successful. The reasons for this are not clear at present but may be due to rapid non-radiative decay of the S_1 electronic state in this conformer.

ACKNOWLEDGEMENTS

We acknowledge grant support from EPSRC and BBSRC and the award of a CASE studentship to J.A.D in collaboration with the Central Laser Facility (CLF) at the Rutherford Appleton Laboratory (RAL). We thank the EPRSC Laser Support Facility for the loan of laser systems critical for the two colour experiments.

REFERENCES

1) J. A. Dickinson, P. W. Joireman, R. W. Randall,
E. G. Robertson and J. P. Simons
J. Phys. Chem. 105 6075, (1997)

2) J. A. Dickinson, P. W. Joireman, R. T. Kromer,
E. G. Robertson and J. P. Simons
J. Chem. Soc. Faraday *Trans*. 93 1467, (1997)

3) J. A. Dickinson, M. R. Hockridge, R. T. Kromer,
E. G. Robertson , J. P. Simons, J. McCombie and M. Walker
J. Am. Chem. Soc., submitted.

4) V. P. Manea, K. J. Wilson and J. R. Cable
J. Am. Chem. Soc. 119 2033, (1997)

STUDIES OF ATMOSPHERIC AEROSOL MATERIAL BY SURFACE SECOND HARMONIC GENERATION - A PRELIMINARY REPORT

J. G. Frey and A. G. Howard

Department of Chemistry, University of Southampton, Southampton SO17 1BJ

INTRODUCTION

The importance of heterogeneous chemistry to atmospheric processes has been highlighted by the Antarctic ozone hole and atmospheric changes induced by volcanic activity. The processing of material on solid acid crystals (nitric and sulphuric acid water mixtures) has been shown to play a major role in the conversion of halogen materials to a form active in ozone depletion. Similar chemistry has been observed on related liquid drops.

The sticking probabilities and reaction rates on these 'ice' and water surfaces depend strongly on the acid and water concentrations. The Surface Second Harmonic Generation (SHG) studies we are carrying out at Southampton investigate the nature of the acid surface under ambient conditions. We have observed a dependence of the SHG signal on the acid concentration, signals which also show a significant temperature dependence in the 290-340 K range. The results indicate a change in the surface structure as the acid concentration is varied, with the 1:1 Sulphuric acid:water complex being involved.

Our current experiments using a nanosecond laser system are hampered by the need to use high pulse energies and to focus very close to the surface. While this does not seem to be a problem for pure water, for the higher acid concentrations it causes excessive breakdown. The higher peak power and lower average power obtained from the Ti:Sapphire laser will enable us to observe SHG signals under much milder conditions.

EXPERIMENTAL PROGRAMME

SULPHURIC ACID/WATER MIXTURES (LIQUID)

The SHG signals (intensity and polarisation) will be recorded from the surface of H2SO4 (aq) as a function of acid concentration and temperature. The use of the Ti:Sapphire laser enabled us to resolve many of the experimental difficulties encountered with the nsec systems and produce definitive data on the change in surface response with concentration of the acid.

NACL SOLUTIONS

The effect on the water/air interface as the concentration of NaCl was varied over a wide range was studied. This mimics the changes that occur when a salt water droplet evaporates.

ADVANTAGES OF THE TI:SAPPHIRE LASER SYSTEM FOR SHG STUDIES

- Power levels of Ti-Sapphire picosecond laser have many times the stability of the YAG pumped die laser output powers. This results in signal levels which can be attributed to surface phenomena rather than fluctuations in laser input power.
- The low mean power of the pico-second laser, allows the focus to be moved to the interface. This would, in theory, give a more repeatable experiment and enables experiments on different samples to be compared.
- Problems caused by ionisation of surface molecules can be eliminated since the peak power is relatively low. Since ionisation is the main problem preventing focusing at the interface. By being able to focus at the interface, a well defined position giving the maximum SHG signal, we can avoid errors introduced by the movement of the interface due to for example evaporation.

All these factors mean that we can obtain data at RAL that will link together the various sets of results we have obtained at Southampton and so provide a more detailed description of the surface of sulphuric acid water mixtures.

COMPARISON WITH OUR PREVIOUS EXPERIMENTS AT RAL

On two previous occasions we have used the Ti:Sapphire laser to investigate surface SHG. On the last occasion we obtained less than satisfactory signals. This was partly due to difficulties in the single photon counting detection and problems in maintaining alignment of the optical system, something we know from our work at Southampton that is critical.

In order to overcome these problems and enable us to look at the water and acid surfaces we made the following changes to the previous experiment.

(a) The single photon counting PMT will be obtained specially for this experiment and checked and optimised with the photon counter in Southampton.

(b) The separation of the harmonic radiation will used filters and a simple monochromator that we have in my group, rather than use the one used previously at RAL which is designed for an array detector.

(c) We had intended to frequency double the output from the Ti:sapphire laser into the visible so that we can use better optics that we have in Southampton. However the practical difficulties of running the laser at the long wavelength end of its current range prevented us from using the visible wavelengths. We did employ a much improved a rigid optical system and this went some way to achieving the required stability and reproducibility

RESULTS

The signal level from the pure water surface was highly reproducible, but about a factor of 2 less than we had expected. This was sufficient for the main experimental programme but did mean that the data collection times were longer than we had originally anticipated. The special photon counting tube with built in discriminator and amplifier worked very well and provided us with low background levels and reliable operation.

SULPHURIC ACID MIXTURES

The main results obtained for a range of acid concentrations are presented in Figure 1. The results confirm what we had suspected from the Southampton experiments and now allow us to normalise all the signals to a common reliable set. We are at present analysing the polarisation dependencies determined at Southampton having normalised the intensities to those obtained at RAL.

Or initial conclusions are that there is a very significant change in the surface structure at a bulk concentration of about 1:1 sulphuric acid: water (by moles). The exact transition point depends on the temperature, but the values of the SHG signal on either side of the transition are much less sensitive to temperature. The model we are working on to explain these results involves a change in the hydrogen bonding network from initially largely acid SO_4 tetrahedra bonded edge sharing, to a network that involves alternate SO_4 and H_2O species.

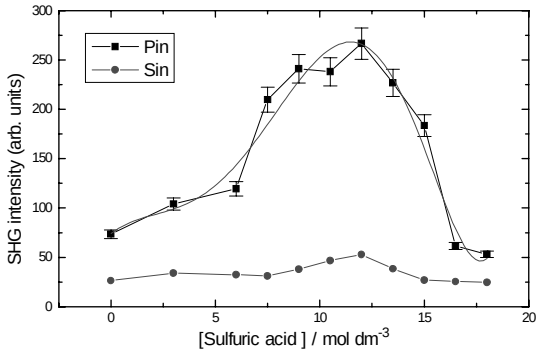

NACL SOLUTIONS

The initial studies on NaCl solutions show that while the overall SHG intensity stays relatively constant over a wide range of [NaCl], there are significant changes to the details of the signal, Figure 2. These changes suggest sometime reorientation of the surface hydrogen bonds for larger [NaCl] and this may indicate a change in the sticking and absorption properties of the surface.

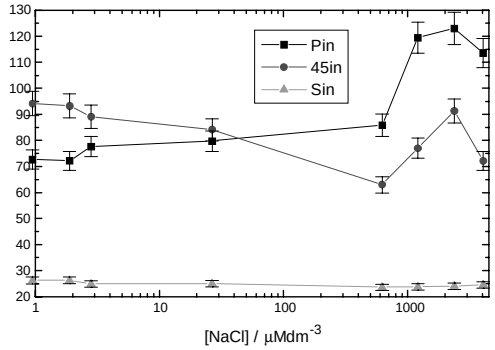

CONCLUSIONS

The experiments on Sulphuric acid were very successful. They have allowed us to link much of the disparate data we have collected previously. A publication is being prepared. The work on NaCl solutions is very suggestive and will now be followed up at Southampton.

FUTURE EXPERIMENTS

The use of the different laser systems at RAL and Southampton has been very constructive. We hope to continue using the various ps/fs laser systems at RAL in the future to look at the adsorption of species from the gas phase on to the solution surface.

RATE COEFFICIENT FOR THE REACTION OF OH WITH METHYLAMINE (CH_3NH_2)

M R Heal , B Müller

Department of Chemistry, University of Edinburgh, West Mains Road, Edinburgh, EH9 3JJ, UK. Email m.heal@ed.ac.uk

INTRODUCTION

The amine compounds R-NH_x (in particular methylamine, CH_3NH_2) are emitted to the atmosphere in increasingly large quantities from intensive livestock farming, and also by marine phytoplankton. The compounds are basic, and their subsequent oxidation chemistry has direct environmental impact through neutralisation of atmospheric acidity, formation of aerosol cloud condensation nuclei (particularly in association with oxidation products of S-containing compounds in the marine environment), and as a possible source of atmospheric N_2O and HCN [1]. Current assessments of the oxidation of CH_3NH_2 with OH (reaction 1) rely on only one previous determination of the rate coefficient by Atkinson and Perry in 1977 [2].

$$CH_3NH_2 + OH \rightarrow \text{products} \qquad (1)$$

The value of $k_1 = 2.2 \times 10^{-11}$ cm^3 molecules^{-1} s^{-1} at 298 K obtained by these workers indicates that atmospheric gas-phase removal is fast.

The LSF fluoride excimer laser has been used in conjunction with a tuneable YAG pumped dye laser loan facility at Edinburgh to undertake a very preliminary investigation of the rate coefficient for reaction 1 using the technique of pulsed laser photolysis-laser induced fluorescence.

EXPERIMENTAL

A standard pulsed laser photolysis-laser induced fluorescence experimental procedure was followed. The LSF Lambda Physik COMPEX excimer laser, operating at 10 Hz and 248 nm output (KrF), provided a source of OH *via* the photolysis of H_2O_2 (and occasionally HNO_3). A low photolysis fluence of ~30 mJ cm^{-2} was maintained in order to minimise secondary radical reactions and accumulated depletion of H_2O_2 precursor. Laser output to probe OH A $^2\Sigma^+$ (v'=1) ← X $^2\Pi$ (v''=0) rovibronic transitions in the wavelength region 282 nm was provided by a frequency-doubled Continuum Surelite YAG laser pumped ND6000 dye laser with Rhodamine 6G. Photolysis and probe laser beams were directed counter-parallel through a standard metal LIF cell sealed with quartz windows. Off-resonance OH fluorescence from the (v'=0) → (v''=0) electronic transition at 308 nm was collected by an EMI 9813 photomultiplier tube at right angles to the point of laser beam intersection. The resultant signal was integrated by a Stanford SRS 250 boxcar integrator before output to a chart recorder. Methylamine (Aldrich 98+% purity) was pre-diluted in N_2 buffer. To offset reduced fluorescence signal resulting from efficient quenching of electronically excited OH, preliminary experiments were carried out with relatively low total pressure of < 3 Torr. An OH decay trace was built up by randomly varying the delay between photolysis and probe lasers during a single experiment using external triggering from a multichannel pulse generator. OH fluorescence was measured at λ_{ex} = 281.9 nm ($Q_1$1+$R_2$3 transitions) and experimental conditions were arranged so that OH removal followed pseudo first order kinetics.

RESULTS AND DISCUSSION

LIF rotational spectra of the OH A $^2\Sigma^+$ (v'=1) ← X $^2\Pi$ (v''=0) band in the region 279-284 nm were recorded to confirm the production of OH and to permit spectral assignment using the values of Dieke and Crosswhite [3] (Figure 1).

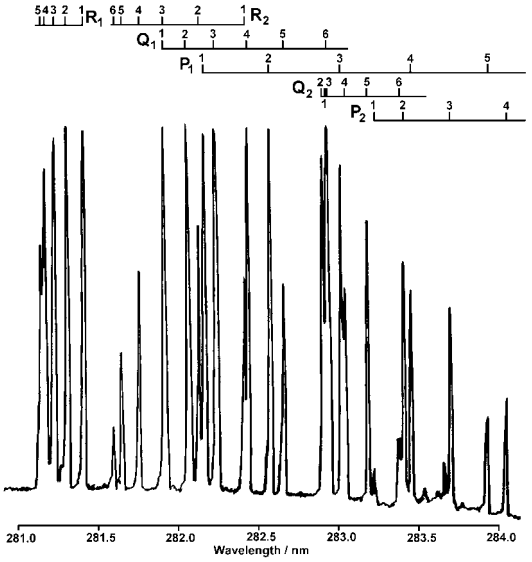

Fig. 1: OH A $^2\Sigma^+$ (v'=1) ← X $^2\Pi$ (v''=0) LIF spectrum.

Unfortunately, owing to a variety of external factors the amount and quality of kinetic data that were ultimately obtained during the loan period were restricted. One particular problem was possible loss of methylamine to the walls of tubing and cell which limits the accuracy in the value of CH_3NH_2 partial pressure required to calculate the bimolecular rate coefficient. A further intrinsic problem is the rapid competing reaction of OH with undissociated H_2O_2 precursor ($k_{H2O2} = 1.7 \times 10^{-12}$ cm^3 molecules^{-1} s^{-1} [4]).

Figure 2 illustrates an example first-order semi-logarithmic plot obtained with a CH_3NH_2 partial pressure of ~ 20 mTorr (6.6 x 10^{14} molecules cm^{-3}). The value of the pseudo first order coefficient, k', obtained from a least squares fit to the data is 7.9 x 10^3 s^{-1}.

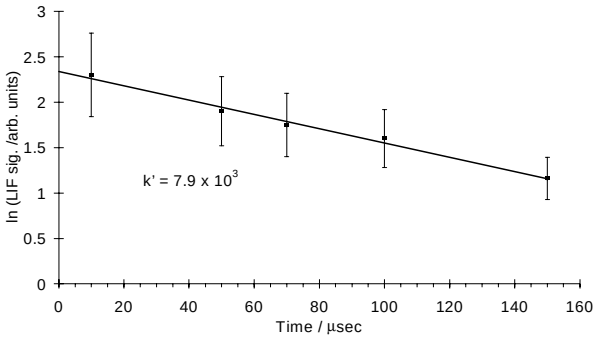

Fig 2: Semi-logarithmic plot of OH LIF decay with [CH_3NH_2] = 6.6 x 10^{14} molecules cm^{-3}.

Unfortunately, satisfactory OH decays were obtained for only two different pressure conditions, for problems highlighted above, so a standard bimolecular plot of the data is not appropriate. Decay traces were analysed assuming reaction with CH_3NH_2 and H_2O_2 were the predominant removal processes. (Diffusional losses are minimal on this timescale at this pressure). For the k_{H2O2} rate coefficient given above and an H_2O_2 concentration of ~ 5 x 10^{14} molecules cm^{-3}, the correction to the observed k′ to allow for H_2O_2 + OH reaction is 9 x 10^2 s^{-1}. The results are summarised in Table 1.

k'_{obs} / s^{-1}	$k'_{corr.}$ / s^{-1}	$[CH_3NH_2]$ / molecs. cm^{-3}	k_1 / cm^3 molecs.$^{-1}$ s^{-1}
7.8 x 10^3	6.9 x 10^3	1.2 x 10^{15}	0.6 x 10^{-11}
7.9 x 10^3	7.0 x 10^3	6.6 x 10^{14}	1.1 x 10^{-11}
		AVERAGE:	**0.9 x 10^{-11}**

Table 1: Bimolecular rate coefficient for reaction of CH_3NH_2 with OH at 290 K.

It must be stressed that these present results are entirely preliminary and are clearly subject to unacceptably high ranges of error and/or lack of precision. Further validation, more data and increased experimental precision are clearly essential.

The value of k_1 ~ 1 x 10^{-11} cm^3 molecules^{-1} s^{-1} presented here can be compared with only the one previous determination by Atkinson and Perry of k_1 = 2.2 x 10^{-11} cm^3 molecules^{-1} s^{-1} measured at 50 Torr total pressure [2]. It is not possible to comment meaningfully at present on the difference between these values, given the considerable uncertainties associated with our measurements. Nevertheless we have confirmed that reaction 1 must occur on a fairly rapid timescale in the troposphere (atmospheric lifetime of hours to a few days) with a rate coefficient towards the upper end of values for other important atmospheric VOC (e.g, k_{OH} (dimethylsulphide) = 5 x 10^{-12} cm^3 molecules^{-1} s^{-1}). However, it should also be noted that the fairly high solubility of CH_3NH_2 (Henry's Law constant H ~ 140 M atm^{-1} [5]) coupled with its strong basicity in aqueous solution (pK_b = 3.34 [1]) suggest that partitioning into, and removal *via*, the tropospheric aqueous phase (cloud droplets, rain) will also be important atmospheric processes for methylamine.

We would clearly wish to undertake further investigation into this reaction. The rate coefficient needs to be determined as a function of temperature and pressure. In particular, the reaction must be studied at atmospheric conditions since adduct formation is possible, and in the presence of oxygen there is likely to be some regeneration of OH *via* reaction intermediates. Such kinetic data will provide further insight into the oxidation mechanism. Experiments should also include higher substituted amines for which, like monomethylamine, atmospheric oxidation is very poorly characterised.

REFERENCES

1) G. W. Stead and P. J. Crutzen
J. Atmos. Chem., 22 319-46, (1995)

2) R. Atkinson and R. A. Perry
J. Chem. Phys., 66 1578-81, (1977)

3) G. H. Dieke and H. M. Crosswhite
J. Quant. Spectrosc. Radiat. Transfer, 2 97-199, (1962)

4) R. Atkinson, D. L. Baulch, R. A. Cox, R. F. Hampson, J. A. Kerr and J. Troe
J. Phys. Chem. Ref. Data, 21 1125-1568, (1992)

5) P. Saxena and L. M. Hildemann
J. Atmos. Chem., 24 57-109, (1996)

NEAR INFRARED FEMTOSECOND PHOTOIONISATION OF LARGE MOLECULES

A. Hollingsworth [1], R.J.J. Maier [1], P.R.R. Langridge-Smith [1], A.J. Langley [2], P.F. Taday [2]

1) Department of Chemistry, University of Edinburgh, King's Buildings, West Mains Road, Edinburgh, EH9 3JJ
2) Rutherford Appleton Laboratory, Chilton, Didcot, Oxon, OX11 0QX

INTRODUCTION

Lasers are now routinely used for molecular photoionisation, in various forms of optical spectroscopy and mass spectrometry. The use of ultrafast lasers for photoionisation is attracting increased attention. In the case of sub-picosecond laser ionisation the mechanism of photoionisation is not necessarily obvious. Several possibilities exist, such as multiphoton ionisation, tunnelling ionisation and barrier suppression [1].

The majority of previous femtosecond laser ionisation studies have been carried out on atomic, diatomic or small polyatomic systems. Ledingham and Singhal have recently reviewed work in the field of ultrafast laser mass spectrometry [2]. One problem in extending studies to much larger molecules is their involatility and/or thermal lability. This problem can be circumvented by the use of laser desorption for sample introduction into the gas-phase. The only previous reported work using this approach is that of Weinkauf *et al* [3] and Aicher *et al* [4] who carried out comparative measurements of nanosecond versus femtosecond laser photoionisation for several amino acids and peptides. In their studies laser wavelengths in the UV, near 255 nm, were employed and the shortest pulse duration was 500 fs.

Presented here are preliminary results on the femto- and picosecond photoionisation of a group of metalloporphyrins and some other biologically important molecules such as amino acids and chlorophyll-*a*. These studies were carried out using near infrared laser radiation at 750 nm using pulse lengths as short as 50 fs.

EXPERIMENTAL

A nanosecond pulsed infrared CO_2 laser (λ=10.6 μm) was used for volatilisation of intact neutrals. Ionisation was carried out using a chirped pulse amplified femtosecond laser system (λ=750 nm, Δt≈50 fs). The near infrared wavelength used is much longer than those commonly employed in near-resonant nanosecond photoionisation studies.

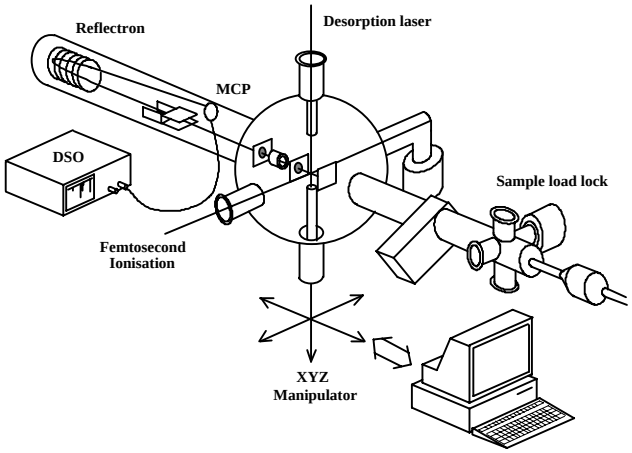

Fig.1 Schematic diagram of apparatus

Picosecond (Δt ≈2 ps) and nanosecond (Δt ≈3 ns) pulses at 750 nm were generated on the same system and used for comparative photoionisation measurements. Product photoions were mass analysed using a reflectron time of flight mass spectrometer. Time-of-arrival waveforms were acquired using a 500MS/s digital storage oscilloscope.

RESULTS

Metalloporphyrins are macrocyclic compounds that are of importance in geology and biochemistry. Figure 2 shows the mass spectrum obtained following photoionisation of copper octaethylporphyrin (CuOEP) using 750 nm laser radiation with

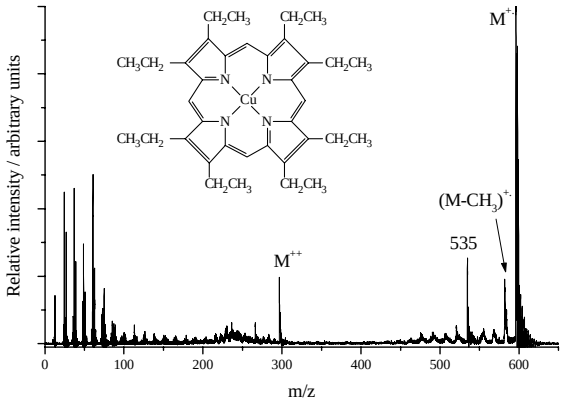

Fig. 2 Mass spectrum for CuOEP; λ=750 nm, 50 fs pulse length

50 fs pulse duration. The mass spectra obtained for nickel octaethylporphyrin (NiOEP) using photoionisation at the same wavelength with femto-, pico-, and nanosecond laser pulse lengths are shown in Figure 3.

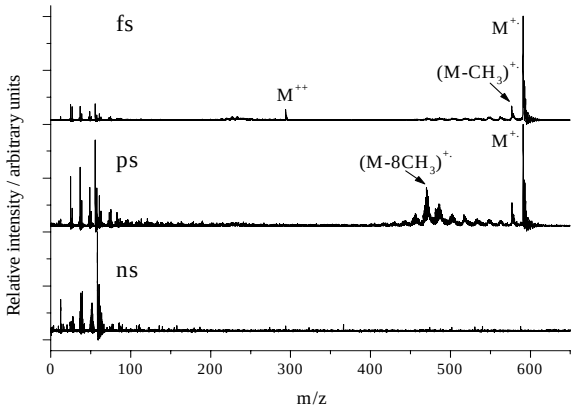

Fig. 3 Mass spectra for NiOEP using ns, ps, and fs pulse lengths

A remarkably strong molecular ion signal is observed in the femtosecond photoionisation mass spectra for both nickel and copper octaethylporphyrin at this laser wavelength. Indeed the molecular ion signals are the base peaks in the spectra for both molecules. Fragmentation, due to successive methyl group loss, is markedly more prominent with increasing laser pulse duration, as can be seen from the picosecond mass spectrum for NiOEP. No significant parent ion signal was observed at 750 nm using pulses of nanosecond duration. The peak at m/z=535 in the spectrum of CuOEP is due to the free base OEP itself, present as an impurity in the sample.

Surprisingly, the femtosecond photoionisation mass spectra of both CuOEP and NiOEP also exhibit peaks due to the doubly charged molecular ions, present at half the mass-to-charge ratio of the corresponding singly charged molecular ion. Also present are doubly charged fragment ions. Interestingly, fragmentation

of the doubly charged molecular ions is more extensive than that observed for the singly charged molecular ions. Similar behaviour has been previously observed in electron impact mass spectra of metallo octaethylporphyrins [5].

The highest laser power density that has been employed in these studies ($10^{12\text{-}13}$ Wcm^{-2}) is in the regime where a tunnelling ionisation mechanism might be operative. The characteristic fragmentation pattern of successive methyl group loss observed in the mass spectra resembles that seen in previous nanosecond photoionisation studies at UV wavelengths [6]. Moreover, the high parent ion yield at this relatively long wavelength is suggestive of a multiphoton ionisation process, perhaps near resonantly enhanced at the two-photon level.

As well as these metallo OEP's other biologically important molecules were also examined. Figure 4 shows the femtosecond photoionisation mass spectrum obtained for chlorophyll-*a*. This compound is a porphyrin found widely in natural systems and is the principal photoreceptor in plant material.

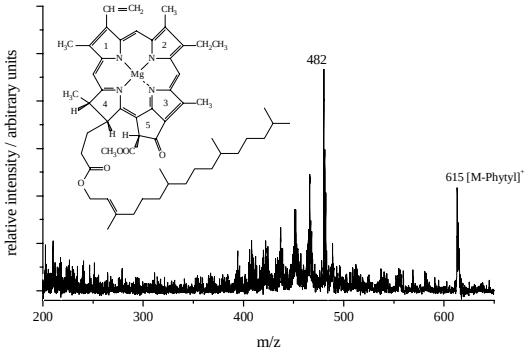

Fig.4 Femtosecond laser mass spectrum of chlorophyll-*a*

No parent ion signal is observed in the spectrum. The peak at m/z=615 is a fragment corresponding to loss of the long phytyl hydrocarbon side-chain. The base peak in the spectrum, at m/z=482, corresponds to further loss of the [CH_3OOC] group from ring 5. Also studied were various amino acids. Figure 5 shows the femtosecond mass spectrum obtained for glycine. This molecule does not contain a UV chromophore and hence is not easily ionised using near-resonant nanosecond photoionisation.

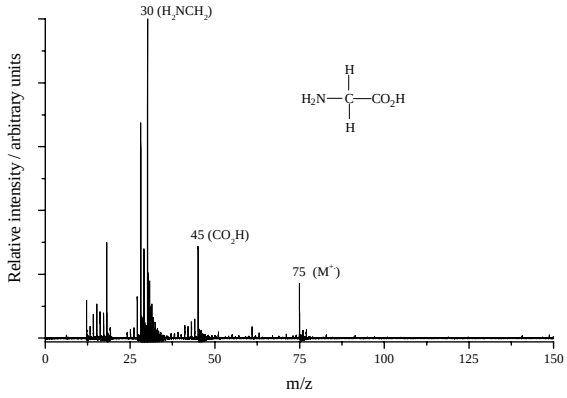

Fig.5 Femtosecond laser mass spectrum of glycine

The mass spectrum exhibits a clear peak due to the molecular ion, at m/z=75, as well as two prominent peaks at m/z=30 and 45 corresponding to the fragment ions resulting from cleavage of the C-C bond.

Figure 6 shows the femtosecond mass spectrum obtained for an aromatic amino acid, tryptophan. The mass spectrum for this molecule again exhibits a clear molecular ion peak, at m/z=204, together with an intense peak at m/z= 130 due to the characteristic dehydroindole fragment ion.

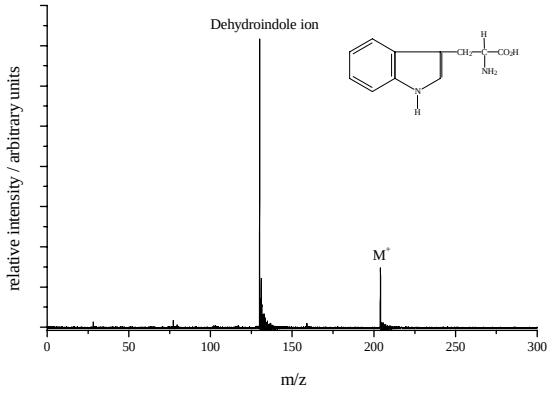

Fig.6 Femtosecond laser mass spectrum of tryptophan

CONCLUSIONS AND FUTURE WORK

These initial studies have demonstrated the feasibility of using near infrared femtosecond laser radiation for photoionisation of large polyatomic molecules. Further work is required in order to conclusively identify the ionisation mechanisms in operation at these laser fluences and wavelength. Detailed laser power dependence studies might enable the order of the ionisation processes, *i.e.* the number of photons required for ionisation, to be identified. An order significantly exceeding that expected for resonant ionisation would be suggestive of a tunnelling or barrier suppression ionisation mechanism.

It would also be of interest to extend these measurements into the UV using the second and higher harmonic output from the femtosecond laser system. Preliminary femtosecond photoionisation studies of metallo OEP's have been carried out at 375nm but the pulse energy available was extremely low. The recent upgrade to the system should make such future studies considerably easier.

REFERENCES

1) M J DeWitt, R J Levis
Journal of Chemical Physics, 102 8670, 1995

2) K W D Ledingham, R P Singhal
International Journal of Mass Spectrometry and Ion Processes, in press

3) R Weinrauf, P Aicher, G Wesley, J Grotemeyer, E W Schlag
Journal of Physical Chemistry, 98 8381, 1994

4) K P Aicher, U Willhelm, J Grotemeyer
Journal of the American Society of Mass Spectrometry, 6 1059, 1995

5) K D Stanley, R L Delavega, J M E Quirke, B D Beaton, R A Yost
Chemical Geology, 91 (2) 169, 1991

6) M J Dale, K F Costello, A C Jones, P R R Langridge-Smith
Journal of Mass Spectrometry, 31 590, 1996

RATE COEFFICIENTS FOR THE VIBRATIONAL SELF-RELAXATION OF NO($X^2\Pi$, v = 3) AT TEMPERATURES DOWN TO 7 K

P.L. James, I.R. Sims and I.W.M. Smith

School of Chemistry, The University of Birmingham, Edgbaston, Birmingham B15 2TT, UK. Email i.r.sims@bham.ac.uk

INTRODUCTION

The collisionally-induced relaxation of NO from excited vibrational levels of its $X^2\Pi$ electronic ground state has been a subject of interest for many years.[1)] With most *molecular* collision partners, the dominant relaxation mechanism is single quantum vibrational-vibrational (V-V) energy exchange. This is also true for *self-relaxation* of NO vibrational levels above v = 1,[2-7)] when the V-V process can be represented by the equation:

$$NO(v) + NO(v = 0) \rightarrow NO(v - 1) + NO(v = 1) \quad (1)$$

When relaxation is dominated by V-V energy exchange, NO appears to behave as a 'normal', non-hydride, diatomic molecule; that is, there is no clear evidence that its rate of relaxation is affected by the fact that the electronic ground state is $^2\Pi$ rather than $^1\Sigma$. Thus the rates of processes represented by equ (1) are similar to those for self-relaxation of CO from high vibrational levels.[8,9)]

The situation is different for self-relaxation of NO(v = 1) which must occur by vibrational-translational (V-T) energy transfer. At room temperature, this process

$$NO(v = 1) + NO(v = 0) \rightarrow 2\ NO(v = 0) \quad (2)$$

is much faster[10-13)] than the corresponding processes for CO(v = 1).[14)] At 300 K, the rate constant for (2) is $k(v = 1) = 7.7 \times 10^{-14}$ cm^3 molecule^{-1} s^{-1},[10-13)] a result which compares with $k(v = 1) < 10^{-20}$ cm^3 molecule^{-1} s^{-1} for the corresponding self-relaxation process in CO.[14)] Moreover, the temperature dependence of k(v = 1) is quite different in the two cases. For CO, the rate constant for self-relaxation above room temperature shows a strong positive dependence on temperature, approximately in accord with the predictions of SSH (Schwartz, Slawsky and Herzfeld) theory,[15)] whereas for NO the variation of k(v = 1) shows a shallow minimum at around room temperature.[11)]

The unusually rapid V-T relaxation of NO(v = 1) has attracted considerable theoretical attention. The early experimental observations led to the proposal by Nikitin[16)] that V-T relaxation occurs by an electronically non-adiabatic mechanism. That is, during collisions, the system undergoes a transition between different vibronic states at geometries where the energy splitting between different electronic potential energy surfaces matches the separation of the (v = 1) and (v = 0) vibrational levels. An alternative possibility in the case of NO-NO collisions is that relaxation is facilitated by the nature of the lowest potential energy surface. It is known that NO can form $(NO)_2$ dimers which are held together by a bond that is weak (D_0 = 8.5 kJ mol^{-1} ≡ 710 cm^{-1}),[17)] but which is stronger and more directional than van der Waals attraction, and it has been suggested[17-19)] that this attraction, like that between species that can form hydrogen bonds, might accelerate energy transfer.

Weak intermolecular attractions are likely to exert their greatest effect on collisional processes at low temperatures, when the average kinetic energy is much less than the well-depth on the intermolecular potential. The lowest temperature at which self-relaxation in NO had been investigated before the present work was 77 K, in the experiments performed in cryogenically cooled cells on the relaxation of NO(v = 2) and NO(v = 3) by Islam et al..[6)] Earlier, Stephenson[10)] had measured the rate of self-relaxation of NO(v = 1) at 100 K. In the present paper, rate constants for vibrational self-relaxation of NO(v = 3) are reported at temperatures down to 7 K. These data have been obtained by implementing the IRUVDR (Infrared-Ultraviolet Double Resonance) technique in a CRESU (Cinétique de Réaction en Ecoulement Supersonique Uniforme) apparatus.[20,21)] We have previously reported the results of such experiments yielding total and state-to-state rate coefficients for *rotational* energy transfer in collisions between NO and He at temperatures down to 15 K.[21)]

EXPERIMENTAL METHOD

Our experiments make use of a CRESU apparatus which has recently been established in Birmingham, and, in other respects, they are similar to those that have been performed previously in our laboratory to measure total and state-to-state rate coefficients for rotational energy transfer in collisions between NO and He. [6,21)] The six nozzles used in the present work were characterised by impact-pressure measurements which yielded temperatures of 85, 52, 45, 27, 15 and 7 K. In some cases, these temperatures were confirmed by recording LIF spectra of NO at a time delay of 5 μs which was long enough to allow complete equilibration of the rotational state distribution but short enough for vibrational relaxation to be prevented. To achieve 7 K, the gas reservoir and the nozzle itself were cooled by liquid N_2.

The IR-pump laser in our experiments causes initial excitation to a single rotational level in the v = 3 vibrational level of the lower spin-orbit component (Ω = 1/2) of the $^2\Pi$ electronic ground state of NO. Our previous experiments[21)] and those of Islam et al.[6)] on rotational energy transfer demonstrated that, as a result of collisions between NO and the carrier gas, rotational and spin-orbit relaxation would be complete within ca. 2 μs in all the gas flows used in the present work. On the other hand, helium, argon and nitrogen are all inefficient at inducing vibrational relaxation.[10)] Consequently, the rate coefficient for self-relaxation of NO(v = 3) at each temperature could be determined by performing a series of experiments on gas flows which contained different concentrations of NO. For each gas mixture (the mole fraction of NO was, in all cases, < 2%), the first-order decay of LIF signal from NO(v = 3) was measured as the time delay between the IR-pump laser and the UV-probe laser was varied systematically. In the case of experiments at 7 K, the amount of NO included in the gas mixture was limited to 0.1% by the requirement not to exceed the vapour pressure of NO at 77 K (81 mTorr) in the liquid N_2 cooled reservoir prior to expansion through the Laval nozzle.

RESULTS

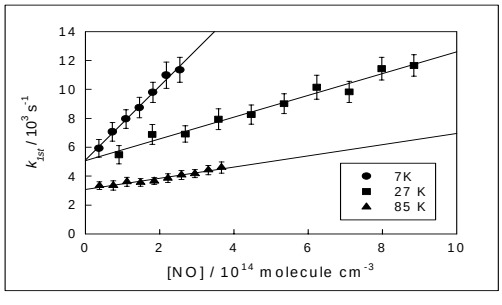

Figure 1 Variation of first-order rate coefficients, k_{1st}, for self-relaxation of NO(v = 3) with concentration of NO, [NO], at 7 K, 27 K and 85 K.

A non-linear least-squares algorithm was employed to fit each trace of LIF intensity *versus* time delay to a single exponential decay, yielding pseudo-first-order rate coefficients, k_{1st}, for vibrational relaxation. Fitting was started after a delay of 5 μs to ensure complete rotational and spin-orbit relaxation, and the baseline was fixed using points recorded with 'negative' time delays (probe before pump), necessitated by the restricted scan times arising in some cases from the finite duration of the uniform supersonic flow. The set of first-order rate coefficients obtained at a given temperature was then plotted against the concentration of NO present in the flowing gas mixture as shown in Fig 1. The gradients of the lines gave second-order rate coefficients (k) for self-relaxation of NO(v = 3). The intercepts obtained from these plots were consistent with the rate estimated for diffusion out of the volume illuminated by both the pump and the probe lasers. The linear dependence of k_{1st} *versus* [NO] in all cases demonstrates the absence of any stable $(NO)_2$ dimer formation under these conditions.

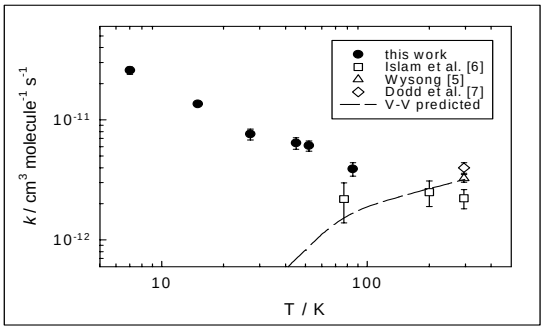

Figure 2 Variation of rate coefficients for self-relaxation of NO(v = 3) with temperature presented on a log-log plot, showing results from the present work, and for comparison, results from Islam et al.,[6] Wysong[5] and Dodd et al..[7] The dashed line is a prediction of the rate coefficient based solely on (V-V) exchange, as described in the text.

DISCUSSION

The rate coefficients for vibrational self-relaxation of NO(v = 3) which have been obtained in the present work at very low temperatures are compared in Fig 2 with those from previous studies conducted at and above 77 K. Where they overlap with the result of Islam et al.[6] at 77 K, the present results are ca. 80% higher. The reason for this discrepancy is unknown, although we note that the rate coefficient measured at 295 K by Islam et al. is also somewhat lower than other recently measured values.[5,7]

Below 77 K, where the present results are quite unique, the rate coefficients for vibrational self-relaxation of NO(v = 3) are large and show a strong negative temperature dependence. The relatively rapid self-relaxation of NO(v > 1) at T ≥ 77 K has been ascribed to near-resonant V-V energy exchange.[5,6] However, because of vibrational anharmonicity, this process, which is represented by equ (1) with v = 3, is endothermic by 55.9 cm^{-1}, which corresponds to a value of $\Delta E / k_B$ (where k_B is the Boltzmann constant) of 80 K. Consequently, the rate of V-V energy exchange between NO(v = 3) and NO(v = 0) must decrease sharply through the temperature range covered by our experiments. The dashed line in Fig 2 is a rough estimate of its rate constant, based on the assumption that the rate constant for the reverse exothermic process, i.e. V-V energy exchange between NO(v = 2) and NO(v = 1), is invariant with temperature and equal to the average of the values determined at room temperature by Wysong,[5] Islam et al.[6] and Dodd et al..[7] It is clear that V-V energy exchange cannot be responsible for the rapid, and rapidly accelerating, rate of self-relaxation of NO(v = 3) which we observe as the temperature is lowered towards 0 K.

If V-V energy exchange is excluded, then the observed rates of relaxation must correspond to those for V-T energy transfer and it seems certain that the rapidity of this process must be associated with the relatively strong attractive forces which lead to formation of $(NO)_2$ dimers at low temperatures.[17] At 7 K, the lowest temperature of our experiments, D_0 / k_BT is equal to ca. 150,[17] and it seems likely that transient collision complexes can form in collisions between NO(v = 3) and NO(v = 0), with lifetimes with respect to re-dissociation that are long enough for intramolecular vibrational relaxation, and hence vibrational predissociation**,** to occur. This mechanism for facile, collisionally-induced, vibrational relaxation has previously been invoked[22,23] to explain the rapid rates found for relaxation of one radical species by another (e.g. NO(v = 1) by radical atoms[24] and OH(v = 1) by NO and NO_2).[25] Unfortunately, and contrary to the situation for radical-radical systems,[22,23] there have been no measurements of the pressure-dependent rates of association of two NO molecules to form $(NO)_2$. It is therefore impossible to compare the present results with rate coefficients for association to the dimer in the limit of high pressure.

The phenomenon of vibrational predissociation of $(NO)_2$ dimers has been investigated in a series of elegant experiments by Casassa et al..[17] They created dimers in free jet expansions of NO and excited them to various vibrationally excited states using tuneable infrared radiation. The rates of vibrational predissociation were found to depend quite strongly on which vibration was excited. Thus, the dimer with one quantum in the *symmetric* NO stretch mode was found to have a mean lifetime of 880 ps, whereas for the dimer with one quantum in the *anti-symmetric* NO stretch vibration the lifetime with respect to vibrational predissociation is only 39 ps.[17(c)] It is not clear which value provides the better estimate of the rate of intramolecular energy transfer in $(NO)_2$ complexes formed at low temperatures from association of NO(v = 3) with NO(v = 0).

Casassa et al.[17(c),17(d)] have discussed the mechanism for vibrational predissociation of $(NO)_2$ dimers in some detail. They pointed out that eight electronic potential energy surfaces, four singlets and four triplets, correlate with $NO(X^2\Pi_\Omega)$ + $NO(X^2\Pi_\Omega)$ and they discussed whether the mechanism for dissociation of a dimer which is excited vibrationally in one or both of the monomer units involves intramolecular vibrational energy transfer within the ^{1}A' electronic ground state or an electronically non-adiabatic mechanism in which the dimer dissociates via an electronically excited state. Unfortunately, although the electronic and geometric structure of the $(NO)_2$ ^{1}A' ground state are well-characterised, little is known about the excited states.

Since the spin-orbit splitting in the electronic ground state of NO is 121 cm^{-1}, corresponding to $(\Delta E_{s\text{-}o} / k_B)$ = 174 K, in our experiments at temperatures ≤ 85 K only the lower Ω = 1/2 spin-orbit component is appreciably populated, reducing to two (one singlet and one triplet) the number of surfaces which can be accessed adiabatically. If one assumes that only one quarter of NO + NO collisions occur on the ^{1}A' potential energy surface and that only these collisions cause vibrational relaxation, then our values of k_{relax} correspond to thermally averaged cross-sections for relaxation on this surface of 33 $Å^2$ at 15 K and 103 $Å^2$ at 7 K.

The cross-sections, $\langle S \rangle_{LJ}$, for capture on an orientation-averaged Lennard-Jones potential, according to a simple two-body model, are given by $\langle S \rangle_{LJ} = \pi\sigma_{LJ}^2\,\Omega^{(2,2)*}$, where $\Omega^{(2,2)*}$ is the collision integral.[26] With values of the Lennard-Jones parameters of σ_{LJ} = 3.49 Å and ε_{LJ} / k_B = 117 K, the values of

$\langle S \rangle_{LJ}$ are ca. 200 Å^2 at 15 K and 260 Å^2 at 7 K. It therefore appears that, even at the lowest temperatures of our experiments, vibrational relaxation may not occur in every collision on the lowest $(NO)_2$ potential in which capture occurs, but that re-dissociation of the complexes to NO(v = 3) + NO(v =0) prior to vibrational predissociation may occur in a fraction of these collisions.

SUMMARY

Implementing an IR-UV double resonance technique within the extremely cold environment provided by expansion through a Laval nozzle in a CRESU apparatus, rate coefficients have been measured for the vibrational relaxation of NO(v = 3) in collisions with NO(v = 0) at six temperatures between 85 and 7 K. The rate coefficients show a marked negative dependence on temperature, reaching a value at 7 K which suggests a collisional deactivation efficiency approaching unity. It is pointed out that the observed relaxation must be the result of V-T energy transfer, since V-V energy exchange is too endothermic to occur at the rates which are observed experimentally at the lowest temperatures. It is further proposed that V-T energy transfer is facilitated by the transient formation of $(NO)_2$ complexes which last long enough for vibrational predissociation within the complexes to compete with re-dissociation to NO(v = 3) + NO(v = 0).

ACKNOWLEDGEMENTS

We express our thanks to Delphine Chastaing for assistance with some of the experimental work reported here. We are grateful to EPSRC for a research grant to construct the CRESU apparatus and for a studentship (PLJ). The IR-pump laser system was obtained on loan from the EPSRC Laser Loan Pool at the Rutherford-Appleton laboratory, for which we express thanks. We are also very grateful to Dr Bertrand Rowe, Dr André Canosa and their colleagues at Rennes for valuable advice and discussions, as well as the loan of some of the Laval nozzles used in this work. Finally, we thank Stuart Arkless and Steve West for their skilled technical assistance.

REFERENCES

1) (a) H.J.Bauer, H.O. Kneser and E. Sitting
J. Chem. Phys. 30 (1959) 1119;
(b) F. Robben
J. Chem. Phys. 31 (1959) 420
(c) N. Basco, A.B. Callear and R.G.W. Norrish
Proc. Roy. Soc. A260 (1960) 459.

2) H. Horiguchi and S. Tsuchiya
Jpn. J. Appl. Phys. 18 (1979) 1207.

3) R.G. Macdonald and F.C. Sopchyshyn
Chem. Phys. 94 (1985) 455.

4) (a) X. Yang, E.H. Kim and A.M. Wodtke
J. Chem. Phys. 93 (1990) 4483;
(b) X. Yang, E.H. Kim and A.M. Wodtke
J. Chem. Phys. 96 (1992) 5111
(c) X. Yang, J.M. Price, J.A. Mack, C.G. Morgan,
C.A. Rogaski, D. McGuire, E.H. Kim and A.M. Wodtke
J. Phys. Chem. 97 (1993) 3944.

5) (a) I.J. Wysong
Chem. Phys. Lett. 227 (1994) 69
(b) I.J. Wysong
J. Chem. Phys. 101 (1994) 2800.

6) (a) M.J. Frost, M. Islam and I.W.M. Smith
Can. J. Chem. 72 (1994) 606
(b) M. Islam, I.W.M. Smith and J.W. Wiebrecht
J. Phys. Chem. 98 (1994) 9285.

7) J.A. Dodd, S.M. Singleton, S.M. Miller, P.S. Armstrong and W.A.M. Blumberg
Chem. Phys. Lett. 260 (1996) 103.

8) G. Hancock and I.W.M. Smith
Appl. Opt. 10 (1971) 1827.

9) (a) I.W.M. Smith and C. Wittig
J. Chem. Soc. Faraday Trans. 2 69 (1973) 939
(b) H.T. Powell
J. Chem. Phys. 59 (1973) 4937.

10) (a) J.C. Stephenson
J. Chem. Phys. 59 (1973) 1523
(b) J.C. Stephenson
J. Chem. Phys. 60 (1974) 4289.

11) M.R. Dasilva, M.H. Vasconcelos, F. Lepoutre and M.Y. Perrin
Chem. Phys. Lett. 91 (1982) 135.

12) M. Koshi, K. Koseki and H. Matsui
Ber. Bunsenges. Phys. Chem. 89 (1985) 309.

13) L. Doyennette and M. Margottin-Maclou
J. Chem. Phys. 84 (1986) 6668.

14) (a) R.C. Millikan and D.R. White
J. Chem. Phys. 39 (1963) 3209
(b) D.J. Miller and R.C. Millikan
J. Chem. Phys. 53 (1970) 3384.

15) (a) R.N. Schwartz, Z.I. Slawsky and K.F. Herzfeld
J. Chem. Phys. 20 (1952) 1591
(b) K.F. Herzfeld and T.A. Litovitz
Absorption and Dispersion of Ultrasonic Waves (Academic, New York, 1959).

16) (a) E.E. Nikitin
Optika i Spectroskopiya 9 (1960) 8
(b) E.E. Nikitin
Optika i Spectroskopiya 11 (1960) 452
(c) E.E. Nikitin and S.Ya. Umanski, Faraday Discuss. Chem. Soc. 53 (1972) 1.

17) (a) M.P. Casassa, J.C. Stephenson and D.S. King
J. Chem. Phys. 85 (1986) 2333
(b) M.P. Casassa, J.C. Stephenson and D.S. King, Faraday Discuss. Chem. Soc. 82 (1986) 251
(c) M.P. Casassa, J.C. Stephenson and D.S. King
J. Chem. Phys. 89 (1988) 1966
(d) J.R. Hetzler, M.P. Casassa and D.S. King
J. Phys. Chem. 95 (1991) 8086.

18) R.J. Gordon
J. Chem. Phys. 74 (1981) 1676.

19) H.K. Shin
J. Chem. Phys. 87 (1987) 993.

20) I.R. Sims, J.-L. Queffelec, A. Defrance, C. Rebrion-Rowe, D. Travers, P. Bocherel, B.R. Rowe and I.W.M. Smith
J. Chem. Phys. 100 (1994) 4229.

21) P.L. James, I.R. Sims and I.W.M. Smith
Accompanying article (1997).

22) M.J. Howard and I.W.M. Smith
Prog. Reac. Kinet., 12 (1983) 55.

23) I.W.M. Smith
J. Chem. Soc. Faraday Trans., in press (1997).

24) (a) R.P. Fernando and I.W.M. Smith
Chem. Phys. Letters, 66 (1979) 218
(b) R.P. Fernando and I.W.M. Smith
J. Chem. Soc. Faraday Trans., 77 (1981) 459.

25) I.W.M. Smith and M.D. Williams
J. Chem. Soc. Faraday Trans., 81 (1985) 1849.

26) J.O. Hirschfelder, C.F. Curtiss and R.B. Bird
The Molecular Theory of Gases and Liquids (Wiley, New York, 1954).

TOTAL AND STATE-TO-STATE RATE COEFFICIENTS FOR ROTATIONAL ENERGY TRANSFER IN COLLISIONS BETWEEN NO($X^2\Pi$) AND HELIUM AT TEMPERATURES DOWN TO 15 K

P.L. James, I.R. Sims and I.W.M. Smith

School of Chemistry, The University of Birmingham, Edgbaston, Birmingham B15 2TT, UK. Email i.r.sims@bham.ac.uk

INTRODUCTION

Over the past four years, as the result of a collaboration between our group and that of Rowe at the University of Rennes, rate constants have been measured for a number of elementary reactions between neutral species at temperatures down to 13 K, using the PLP-LIF (pulsed-laser photolysis – laser-induced fluorescence) technique, implemented in gas mixtures which have been cooled drastically by expansion through a Laval nozzle in the CRESU (Cinétique de Réaction en Ecoulement Supersonique Uniforme) apparatus at the University of Rennes.[1-4)] The expansion creates a supersonic flow of relatively dense gas in which there are frequent collisions so that thermal equilibrium is maintained. Recently a CRESU apparatus has been established at the University of Birmingham and here we report its first application, to the measurement of rates of rotational energy transfer in collisions between NO and He. Measurements on NO have become a major testing ground for models and theoretical treatments of rotational energy transfer. Previous measurements fall into two main categories: (i) infrared-ultraviolet double resonance experiments performed under thermally equilibrated conditions,[5-8)] like those reported in the present paper; and (ii) crossed molecular beam experiments which provided cross-sections for energy transfer, generally out of the lowest rovibrational level, at a defined collision energy.[9-12)] Alexander and co-workers[13,14)] have been particularly active in performing high quality quantum scattering calculations on *ab initio* potential energy surfaces, especially for NO-He collisions.

The present experiments are the first direct measurements on the rates of rotational energy transfer that have been carried out at temperatures below 80 K, the temperature achieved by Islam et al.[7,8)] in cryogenically cooled cells. Of course, rate constants for rotational energy transfer are closely related to those for collisional broadening and, using a 'collisional cooling' technique, Willey et al. have measured line-broadening for spectroscopic transitions in a number of gases, including NO diluted in He,[15)] at temperatures down to 1.7 K.

There are at least two reasons for interest in the rates of rotational energy transfer at ultra-low temperatures. First, such measurements will provide particularly demanding tests of theory at collision energies less than the typical well-depth in the intermolecular potential between closed shell species and comparable to the spacing between neighbouring rotational levels even at low levels of excitation. Second, such rates are required for the interpretation of astrophysical observations. In particular, the temperatures in interstellar clouds are inferred from the intensities of lines in the rotational spectra of observed molecules and proper analysis must include rates of collisional transfer between specific rotational levels at the very low temperatures in these regions of the interstellar medium.[16)]

EXPERIMENTAL METHOD

The method employed in our experiments is similar in principle, but different in detail, to that employed by Islam et al..[7,8)] Pulses of tuneable infrared radiation at *ca*. 1.8 μm were provided by difference frequency mixing the output of an injection-seeded Nd:YAG laser and a Nd:YAG-pumped dye laser (Continuum) in a $LiNbO_3$ crystal. Typically, pulse energies of 5 mJ and spectral bandwidths of 0.1 cm^{-1} were achieved, though it is estimated that only *ca*. 1–2 mJ reached the experiment. The population in the v = 3 level of the $X^2\Pi_{1/2}$ state was observed by exciting LIF in the (0,3) band of the ($A^2\Sigma^+$— $X^2\Pi$) system using the frequency-doubled output of a second Nd:YAG-pumped dye laser (LAS LDL205). As in the previous experiments in Rennes, the two laser beams were combined and co-propagated through the gas reservoir and nozzle in the CRESU apparatus and out along the axis of the supersonic flow. The four nozzles used in the present work were characterised by impact-pressure measurements which yielded temperatures of 149, 63, 27 and 15 K.

Two kinds of experiments were performed on collisional energy transfer. In the first, *total* rates of relaxation from a particular selected level were measured by fixing the UV-probe laser to a line from the level (v = 3, Ω = 1/2, J), which was being directly populated by the IR-pump laser and the time delay between the two laser pulses was varied systematically as the LIF intensity was recorded. In the second, the time delay was fixed at 30 ns, corresponding to a short fraction of the time between collisions and the frequency of the UV-probe laser was scanned, yielding LIF spectra from which relative populations in individual states could be calculated and hence *state-to-state* rate coefficients for energy transfer in collisions between NO and He deduced.

RESULTS AND DISCUSSION

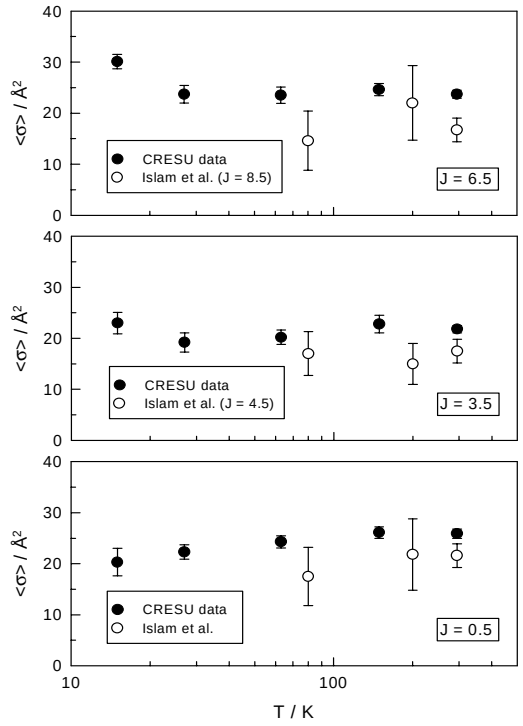

Figure 1 Cross sections for relaxation of NO ($X^2\Pi$; Ω = 1/2; v = 3; J = 0.5, 3.5 or 6.5) in collisions with He at 15, 27, 63, 149 and 295 K, measured in the CRESU apparatus (●). The data of Islam et al. [7, 8] for J = 0.5, 4.5 and 8.5 are indicated for comparison (○).

Thermally averaged cross-sections for the relaxation of NO by He from selected rotational levels in the $X^2\Pi_{1/2}$, v = 3 vibronic level derived from the present work are compared in Fig 1 with those measured for rotational energy transfer by Islam et al.,[7,8)] and in Fig 2 with the values at temperatures below 5 K derived by Willey et al.[15)] from pressure-broadening parameters for

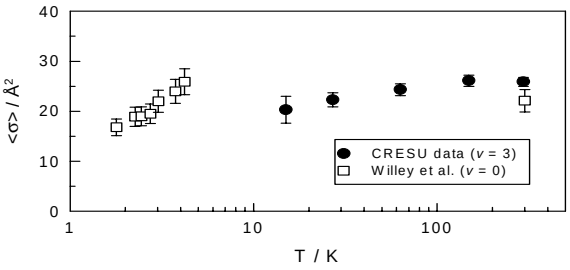

Figure 2 Comparison of cross sections for overall relaxation of NO ($X^2\Pi$; Ω = 1/2; v = 3; J = 0.5) in collisions with He, measured in the CRESU apparatus (●), with those of Willey et al. [15] for NO ($X^2\Pi$; Ω = 1/2; v = 0; J = 0.5) measured in their collisional cooling apparatus ( ).

lines from the $X^2\Pi_{1/2}$, v = 0, J = 0.5 state. The agreement with the data of Islam et al. is good and the results demonstrate the invariance in the thermally averaged cross-sections for relaxation from specific rotational levels of NO($X^2\Pi$) in collisions with He down to 15 K. Our results are also similar to those deduced by Willey et al.[15] at the higher end of the temperature range covered in their experiments (1.8 - 4.2 K).

On the naive basis in which rotational energy transfer occurs as a result of impulsive collisions between 'hard' species, it surprising that the total cross-section for energy transfer does not decrease at low temperatures. As the temperature is lowered, the decrease in (average) collision energy should reduce the torques on the molecule during 'hard' collisions. Hence, in an increasing fraction of collisions, the torque might be insufficient to change the rotational state of the molecule, resulting in a decrease in the effective cross section for J-changing collisions. Two effects, both connected to the existence of an attractive well on the intermolecular potential might counteract this effect at very low temperatures and hence explain the lack of any reduction in the cross-section for overall rotational energy transfer, at least until the lowest temperatures of the experiments of Willey et al..[15] First, the long-range intermolecular attraction could increase the rate of 'capture' and hence the cross-section for collisions with the repulsive 'core'. If this is so, the 'extra' collisions will have large impact parameters and be especially effective in transferring rotational energy. Second, rotational energy transfer may be facilitated through the effects of long-lived resonances.

As well as the rate constants for total relaxation from specific rotational levels, we have measured state-to-state rate coefficients for transfer from J = 0.5, 3.5 and 6.5 at 149, 63, 27 and 15 K. In these experiments, pairs of LIF spectra were recorded with delays of 30 ns and 5 μs set between the IR-pump and UV-probe laser pulses. The shorter delay corresponds to a collisional probability of ≤ 0.1 at each temperature, whilst the longer delay allows for complete rotational and spin-orbit equilibration. The intensities of individual lines of the (0,3) band in the ($A^2\Sigma^+$— $X^2\Pi_{1/2}$) sub-band were compared at these two delays.

The state-to-state rate coefficients obtained from analysis of experiments at 15 and 63 K for J = 0.5, 3.5 and 6.5 are displayed in Figs. 3 and 4. The variation of $k_{J',J}$ with $|\Delta J|$ shows the familiar form in which the rate coefficients decrease with increasing $|\Delta J|$ with a steeper fall-off for positive ΔJ (= J'-J) than negative ΔJ on account of the endothermicity of the former processes. This effect is more marked the higher the value of J as the energy gaps between successive rotational levels increase. In addition, we note that the rate coefficients fall-off more steeply with ΔJ the lower the temperature. Although the cross-section for total removal from an initially prepared state is invariant with temperature, the state-to-state

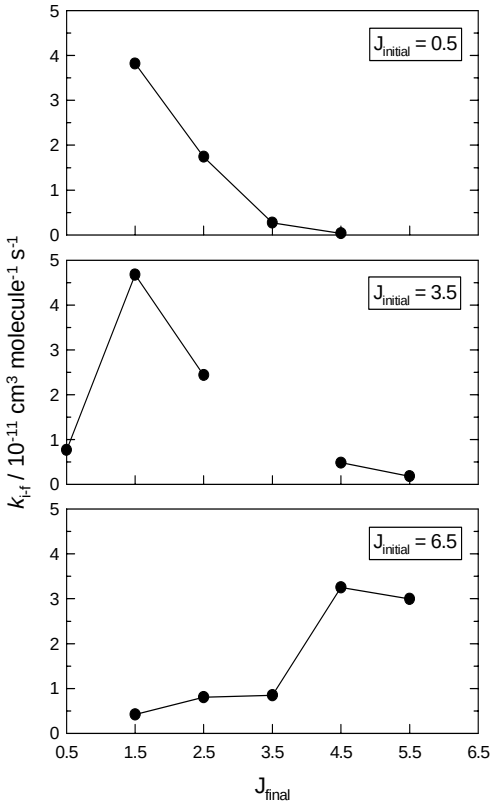

Figure 3 State-to-state rate coefficients for transfer of NO ($X^2\Pi$; Ω = 1/2; v = 3; J = 0.5, 3.5 or 6.5) to ($X^2\Pi$; Ω = 1/2; v = 3; J_{final}) in collisions with He at 15K, measured in the CRESU apparatus.

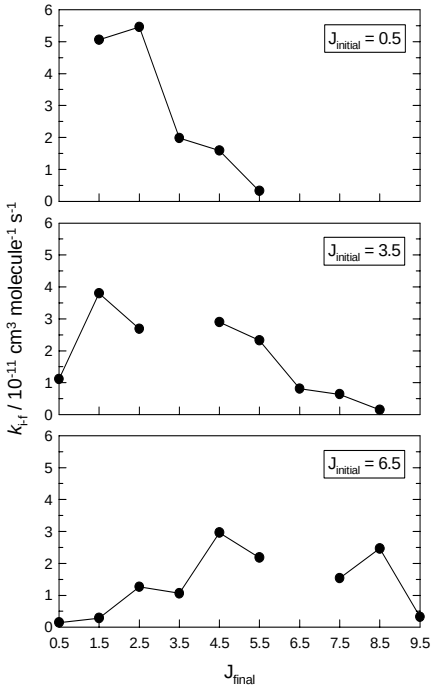

Figure 4 State-to-state rate coefficients for transfer of NO ($X^2\Pi$; Ω = 1/2; v = 3; J = 0.5, 3.5 or 6.5) to ($X^2\Pi$; Ω = 1/2; v = 3; J_{final}) in collisions with He at 63 K, measured in the CRESU apparatus.

cross-sections change with temperature, those for lower ΔJ increasing as the temperature is lowered whilst those for higher ΔJ decrease.

Finally, we note that, in our results, there is a clear preference for *even* ΔJ transfers over *odd* ΔJ transfers, as has been observed in the results of experiments at defined collision energy.[9-12] This propensity in the state-to-state rate coefficients is predicted by theory whenever the diatomic molecule in which energy transfer is being observed is 'nearly homonuclear'. Using semi-classical scattering theory, McCurdy and Miller[17] ascribed this effect to interferences which arise between trajectories scattered from similar parts of the two 'ends' of the intermolecular potential. Yang and Alexander[14] have calculated state-to-state integral and differential cross-sections using full close coupling and coupled states methods and potential energy surfaces computed by the coupled electron pair approximation. They point out that the 'even' terms in the intermolecular potential, which would be the only ones present for a homonuclear molecule, couple *e/f* conserving transitions with even ΔJ and *e/f* changing transitions with odd ΔJ, whilst the reverse is true for the additional 'odd' terms which are present in the intermolecular potential in the case of a heteronuclear molecule. The preference for even J is then equivalent to a preference for *e/f* conservation.

Further details of the results on state-to-state rotational energy transfer will be given in a future publication which will include the results of experiments on energy transfer induced by collisions with partners other than helium. The extension of the quantum scattering calculations to the regime of collision energies appropriate to our low temperature experiments is desirable.

We are grateful to EPSRC for a substantial research grant to construct the CRESU apparatus and a studentship to one of us (PLJ) The Continuum laser system providing the IR-pump beam was obtained on loan from the EPSRC Laser Loan Pool at the Rutherford-Appleton laboratory, for which we express our thanks. We are also very grateful to Dr Bertrand Rowe and his colleagues at Rennes for valuable advice and discussion and to Stuart Arkless, Mark Cheshire and Steve West for their skilled technical work.

REFERENCES

1) (a) I.R. Sims, J.-L. Queffelec, A. Defrance, C. Rebrion-Rowe, D. Travers, B.R. Rowe and I.W.M. Smith J. Chem. Phys. 97 8798 (1992)
(b) I.R. Sims, J.-L. Queffelec, A. Defrance, C. Rebrion-Rowe, D. Travers, P. Bocherel, B.R. Rowe and I.W.M. Smith J. Chem. Phys. 100 (1994) 4229.

2) I.R. Sims and I.W.M. Smith Annu. Rev. Phys. Chem. 46 109 (1995).

3) L.B. Herbert, I.R. Sims, I.W.M. Smith, D.W.A. Stewart, A.C. Symonds, A. Canosa and B.R. Rowe J. Phys. Chem. 100 14928 (1996)

4) R.A. Brownsword, A. Canosa, B.R. Rowe, I.R. Sims, I.W.M. Smith, D.W.A. Stewart, A.C. Symonds and D. Travers J. Chem. Phys. in press (1997).

5) P. Esherick and R.J.M. Anderson Chem. Phys. Lett. 70 621 (1980).

6) (a) Aa.S. Sudbo and M.M.T. Loy Chem. Phys. Lett. 82 135 (1981);
(b) Aa.S. Sudbo and M.M.T. Loy J. Chem. Phys. 76 3646 (1982).

7) (a) M.J. Frost, M. Islam and I.W.M. Smith Can. J. Chem. 72 606 (1994)
(b) M. Islam, I.W.M. Smith and J.W. Wiebrecht J. Phys. Chem. 98 9285 (1994).

8) M. Islam, I.W.M. Smith and J.W. Wiebrecht J. Chem. Phys. 103 9676 (1995).

9) (a) P. Andresen, H. Joswig, H. Pauly and R. Schinke J. Chem. Phys. 77 2204 (1982)
(b) H. Joswig, P. Andresen, and R. Schinke J. Chem. Phys. 85 1904 (1986).

10) S.D. Jons, J.E. Shirley, M.T. Vonk, C.F. Giese and W.R Gentry J. Chem. Phys. 97 7831 (1992).

11) L.S. Bontuyan, A.G. Suits, P.L. Houston and B.J. Whitaker J. Phys. Chem. 97 6342 (1993).

12) H. Meyer J. Chem. Phys. 102 3151 (1995).

13) (a) T. Orlikowski and M.H. Alexander J. Chem. Phys. 79 6006 (1983);
(b) T. Orlikowski and M.H. Alexander J. Chem. Phys. 80 4133 (1984);
(c) M.H. Alexander J. Chem. Phys. 99 7725 (1993).

14) M. Yang and M.H. Alexander J. Chem. Phys. 103 6973 (1995).

15) D.R. Willey, D.N. Bittner and F.C. De Lucia Mol. Phys. 67 455 (1989).

16) E. Roueff in *Molecular Astrophysics – A Volume Honouring Alexander Dalgarno,* ed. T.W. Hartquist (Cambridge University Press, Cambridge) p. 232 (1990).

17) C.W. McCurdy and W.H. Miller J. Chem. Phys. 67 463 (1977).

THE 355 NM PHOTODISSOCIATION DYNAMICS OF JET-COOLED METHYL THIONITRITE

G.R.Kennedy, C.Ning and J.Pfab

Department of Chemistry, Heriot-Watt University, Edinburgh, EH 14 4AS

INTRODUCTION

The photodissociation dynamics of methyl nitrite (CH_3ONO) in the near-UV have been studied extensively over the past fifteen years,[1] but the sulfur analogue, methyl thionitrite (CH_3 SNO), has received much less attention. The near-UV electronic absorption spectrum of methyl thionitrite exhibits a medium strong, broad and continuous $S_2 \leftarrow S_0$ band, centred on 340 nm in addition to a very weak $S_1 \leftarrow S_0$ band in the visible around 560 nm. The nature of the $S_2 \leftarrow S_0$ electronic transitions in alkyl thionitrites has not yet been established firmly by experiments. Previous laser photodissociation-LIF probe experiments with alkyl thionitrites at 300 K[2] have shown that photodissociation from the S_2 potential energy surface generates rotationally hot NO with an inverted rotational state distribution but little vibrational excitation, consistent with prompt dissociation from a repulsive PES. The work reported here was carried out with the loan laser and was one of a range of similar measurements aimed to provide information on the vector correlation between the electronic transition dipole moment μ of the parent molecule and the angular momentum vector **J** of the NO photofragment. Measurements of the (μ,**J**) correlation, that is the rotational alignment $A_0^{(2)}$ of the NO by polarised laser-induced fluorescence (LIF) can provide information on the lifetime of the excited state and on the symmetry of the parent electronic transition.

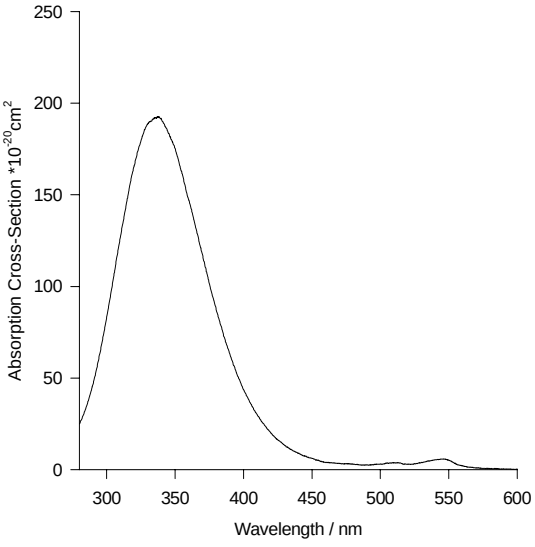

Fig.1 Electronic absorption spectrum of methyl thionitrite

EXPERIMENTAL

The experimental set-up used for the alignment measurements employed a conventional pump-probe arrangement and is shown in figure 2. The gas sample consisted of 3% methyl thionitrite in helium and was jet-cooled by expansion from close to atmospheric pressure into the evacuated anodised aluminium chamber by means of a pulsed solenoid valve with a nozzle diameter of 0.5 mm. The pulsed supersonic jet was intersected by the two counter-propagating laser beams at a distance of 8 mm below the nozzle. The third harmonic of the loaned Spectron SL805G-10 Nd:YAG laser provided the 355 nm photolysis beam. The probe beam was derived from the frequency-doubled output of a Nd:YAG pumped Lumonics HD-500 laser which was operated with Coumarin 47 dye in methanol.

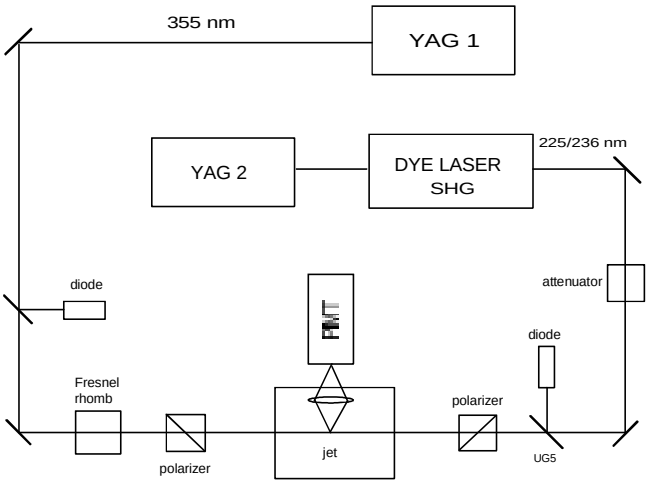

Fig.2 Experimental set-up used for the alignment measurements

A delay of about 20 ns was used between the dissociation and the probe pulses. The lasers and the pulsed nozzle were operated at a repetition rate of 10 Hz with the synchronisation and delays controlled by a digital pulse generator. The laser-induced fluorescence (LIF) was observed at right angles to the colinearly aligned laser beams and perpendicularly to the jet-axis. LIF spectra of the NO photofragment were recorded through the range 225.9 to 225.0 nm for probing NO in the v"=0 state and from 237 to 233 nm when probing NO in the v"=1 state. The polarisation of the photolysis beam was altered using a Fresnel rhomb. The polarisation of both laser beams was further defined by calcite polarisers. The effect of changing the polarisation from vertical to horizontal with respect to the experimental plane defined by the laser beams and the observation axis, on the relative intensities of signals in the LIF spectrum was used to determine the alignment parameter $A_0^{(2)}$ by means of Dixon's formulae.[3]

RESULTS AND DISCUSSION

The alignment parameter, $A_0^{(2)}$, was determined for both NO (v"=0) and NO (v"=1) photofragments as shown in figures 3 and 4.

The values measured reach a high-J limit of -0.30 in both cases, close to the theoretical maximum for a planar dissociation of -0.4. The negative values obtained confirm that the broad band in the near-UV absorption spectrum of methyl thionitrite results from an electronic transition with a transition dipole moment in the plane of the parent molecule. The medium strong near-UV bands of methyl and other thioalkyl nitrites can therefore be assigned unambiguously to an electronic transition of $\pi^* \leftarrow \pi$ character.

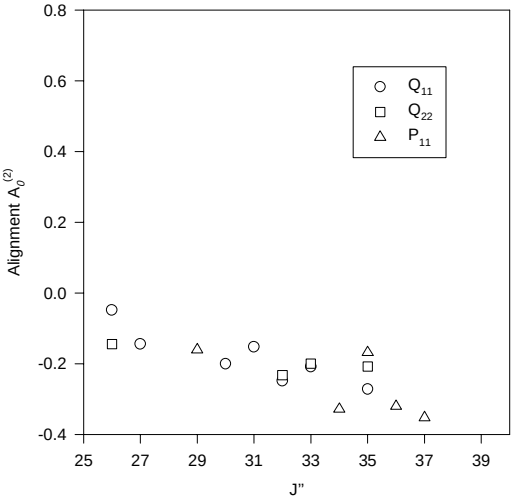

Fig.3 Alignment of the NO (v''=0) photofragment from the 355 nm photolysis of jet-cooled methyl thionitrite

Previous work on the 355 nm photodissociation of jet-cooled CH_3SNO by Giovanacci *et al.* has employed two-photon LIF for probing the nascent NO (v=0 and 1).[4] The shape of the rotational population distributions was found to be close to Gaussian, the vibrational state distributions showed a strong preference for formation of NO(v=0) in line with photodissociation occurring from a steeply repulsive potential surface. Other dynamical features known from our previous work are a distinct preference for the A" lambda doublet component and a weak preference for the F_1 spin-orbit component.

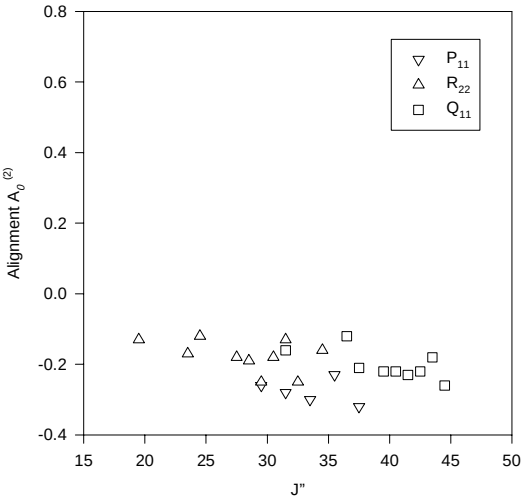

Fig.4 Alignment of the NO (v''=1) photofragment from the 355 nm photolysis of jet-cooled methyl thionitrite

The broad dissociation continuum in the near-UV absorption spectrum of methyl thionitrite indicates that the transition involved takes the molecule to an S_2 state with a repulsive potential and with a dissociation lifetime considerably shorter than 100 fs. The closeness of our high-J values for the alignment parameter to the theoretical limit of -0.4 confirms that the dissociation is on a timescale shorter than a rotational period, with little deviation from planarity in the excited state.

The same series of alignment measurements of the NO(v=0 and 1) photofragment were also carried out for the 355 nm photodissociation of jet-cooled t-butyl thionitrite. The results obtained are in excellent agreement with those for methyl thionitrite and will be reported in detail elsewhere.[5]

CONCLUSIONS

We have shown through measurements of the alignment of NO(v=1 and 2) by polarised laser-induced fluorescence that the near-UV absorption bands of methyl and t-butyl thionitrites are due to a $\pi^* \leftarrow \pi$ transition, and that dissociation to NO and an alkylthio radical occurs promptly from a steeply repulsive potential surface.

The same technique has also been applied to the 355 nm photodissociation of methyl nitrite and several other alkyl nitrites, where the NO is formed by dissociation from a longer lived excited state. Here the measured alignment values are positive, in line with the perpendicular direction of the transition moment characteristic of the n,π^* character of the $S_1 \leftarrow S_0$ transition involved in the well known near-UV absorption bands of alkyl nitrites.

REFERENCES

1) H.Reisler, M.Noble and C.Wittig
in Molecular Photodissociation Dynamics, ed. M.N.R.Ashfold and J.E. Baggot (Royal Society of Chemistry, London,1987), ch.4

2) M.R.S. McCoustra and J.Pfab
Chem.Phys.Lett., 137 355 (1987)

3) R.N. Dixon
J.Chem.Phys., 85 1866 (1986)

4) P.A. Giovanacci, M.R.S. McCoustra and J. Pfab, in preparation.

5) G.R. Kennedy, C. Ning and J. Pfab, Chem. Phys. Lett., in preparation.

BRANCHING RATIOS AND DYNAMICS FOR THE PHOTODISSOCIATION OF HI

S.R. Langford, P.M. Regan, L.J. Rogers, M.N.R. Ashfold and A.J. Orr-Ewing

School of Chemistry, University of Bristol, Bristol BS8 1TS, UK. Email A.Orr-Ewing@Bristol.AC.UK

The photodissociation of HI and HBr is widely used in studies of reaction dynamics as a source of translationally hot hydrogen atoms. In particular, highly detailed studies of the benchmark bimolecular reaction of H + $H_2 \rightarrow H_2$+ H and its isotopic analogues at a number of collision energies have relied on the photolysis of HI at a variety of UV wavelengths to initiate reaction.[1),2)] To interpret the new generation of photoinitiated reaction studies that have, in recent years, provided quantum-state specific differential cross sections,[3)] an accurate understanding is required of the branching ratios and anisotropy parameters for the competing processes (X=Br or I):

$$HX + h\nu \rightarrow H + X(^2P_{3/2}) \quad (1)$$

$$HX + h\nu \rightarrow H + X^*(^2P_{1/2}) \quad (2)$$

The translational energy of the H atoms produced by channels (1) and (2) differ because of the different electronic energies of the halogen cofragment, and hence the branching ratio between the two channels affects the distribution of centre-of-mass frame collision energies for photoinitiated reactions. Interpretation of the speed distribution of reaction products to extract differential cross sections is helped by precise knowledge of the anisotropy parameter, β, for the photodissociation.[4)] Previous studies of the photodissociation dynamics of HI and HBr have measured branching ratios at a few specific wavelengths, generally corresponding to the wavelengths of standard excimer lasers or of Nd:YAG laser harmonics. Theoretical studies[5)] have successfully modelled the (limited) experimental data, but no careful systematic study of the variation of the branching ratios and anisotropies has been reported to date. Such a detailed study is required because of the complexity of four optically accessible repulsive states of HI and HBr lying close in energy and having comparable transition strengths for excitation from the ground state: these states are shown schematically in figure 1. To complicate matters further,

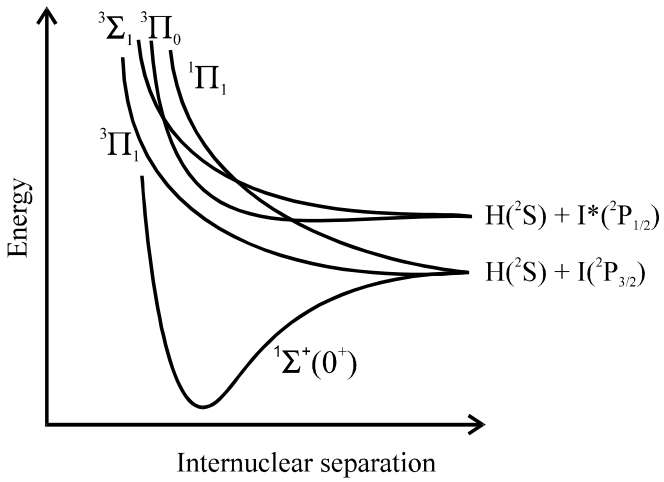

Fig 1. Potential curves for HI

the repulsive states correlating with the two asymptotic channels to X and X^* cross in the Franck-Condon region and hence a wavepacket excited on a single surface can evolve with time on two or more repulsive potentials. The previous investigations of H-atom translational energy release suffered in all cases from incomplete separation of the two channels in the detection process: for example, Doppler profiles of the H atoms are a composite of the two channels,[6)] and even ion-imaging methods do not separate completely signal from the two channels because of the modest translational energy resolution of the reported results.[7)]

Photodissociation anisotropy parameters are determined by the change in the quantum number Ω upon excitation from the ground $^1\Sigma^+$ (0^+) electronic state to the upper, repulsive electronic states. For prompt dissociation, for $\Delta\Omega = 0$ (a parallel transition) a value of $\beta = +2$ is expected, whereas for $\Delta\Omega = \pm 1$ (a perpendicular transition), $\beta = -1$. The $\Omega = 0$ states of HI correlate with electronically excited $I^*(^2P_{1/2})$ whereas $\Omega = 1$ states can correlate with either ground state products via channel (1) or can fragment via channel (2). Detailed considerations of the electronic correlations give the potential curves shown in fig. 1. The β values for channels (1) and (2) can, however, deviate from the expected limiting cases for these channels if curve crossings in the Franck-Condon region affect significantly the evolution of the separating atoms.

We have the facility to study the photodissociation of HI and HBr using two state-of-the-art experimental techniques, photofragment ion imaging and hydrogen atom photofragment translation spectroscopy (PTS). Ion imaging has been used previously to study the photodissociation of HI and HBr but the superior resolution of the H-atom PTS method permits a complete separation of the two channels at the detector and hence should provide more accurate branching ratios. The ion-imaging method, however, has the advantage of yielding accurate anisotropy parameters for the two channels. The imaging measurements also serve as a check of the H-atom PTS results to ensure the absence of any potential systematic errors. Detailed descriptions of the H-atom PTS[8)] and ion-imaging[9)] experimental methods have been given elsewhere and will not be repeated here. The addition of a tunable laser capable of generating UV light in the wavelength range of 300 - 240 nm, however, enabled us to perform photodissociation experiments at a variety of wavelengths systematically stepped across the range of absorption of the hydrogen halide. A second laser then tagged the H atoms for detection, either by 2+1 multiphoton ionisation at 243 nm or by excitation to a high-lying Rydberg state. HBr (Linde gases, 99.8%) was diluted in argon and used without further purification. HI was synthesized by refluxing I_2 with tetrahydronaphthalene and required substantial further purification using traps cooled by a dry-ice/acetone slush to remove organic impurities. The HI was diluted in argon prior to use.

The relative advantages and disadvantages of the two detection methods are illustrated by the data shown in the figures below. Figure 2 shows a (symmetrised) ion image for HI photolysed at 243 nm with the I and I^* channels preferentially giving H atoms recoiling perpendicular and parallel to the photolysis laser polarization (which is vertical in the figure). In figure 3, we show the results of an H-atom PTS experiment for photolysis of HI at 258 nm. The separation of the H atoms from the two channels is markedly superior because of the higher kinetic energy resolution of the PTS method, but to obtain accurate anisotropy parameters requires repetition of the experiment for a number of angles between the polarization of the photolysis laser and the detection axis of the time-of-flight apparatus. The ion images can be fitted directly to yield anisotropy parameters.

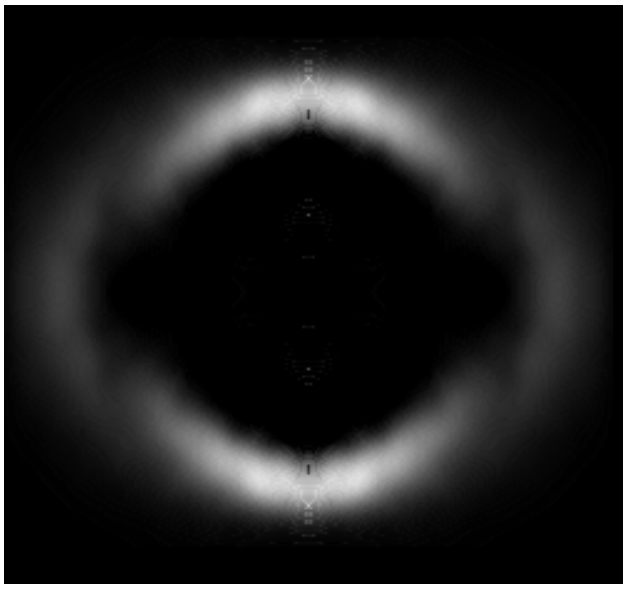

Fig. 2 Ion image of H atoms from the 243-nm photolysis of HI

To obtain branching ratios from the H-atom PTS experiment, we set the polarization angle at 54.7° so that the effects of photofragment anisotropy are eliminated. Careful modelling of the experimental conditions via Monte Carlo simulations, however, shows that the measured branching ratios will be very sensitive to the polarization angle: this angle must be precisely set to 54.7° to avoid significant systematic errors.

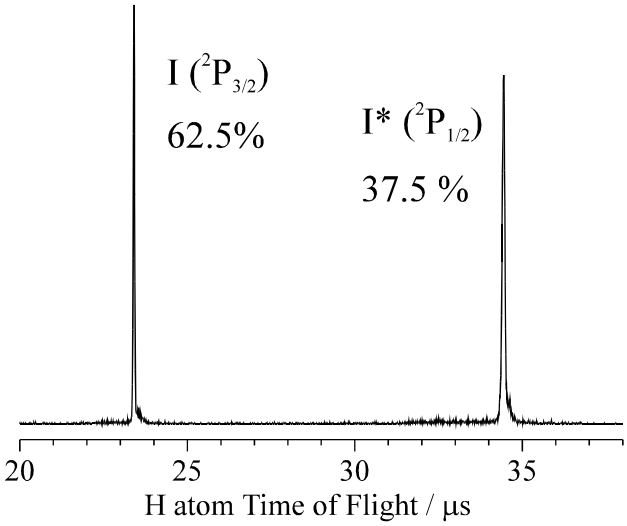

Fig. 3 H-atom photofragment translational spectrum for the 258-nm photolysis of HI.

Experimental values of the branching ratios for HI photolysis are summarised in table 1 for selected photolysis laser wavelengths.

Equivalent data sets have now been accumulated for the UV photodissociation of HBr. The poorer resolution of the ion-imaging experiment makes separation of the two channels much harder than for HI photolysis because of the smaller spin-orbit energy gap for Br compared to I.

Detailed comparisons of our measurements with theoretical calculations are currently being performed to understand the photochemistry and role of electronic curve crossings for these hydrogen halides. For HI, *ab initio* potential curves are available in the literature and we constructed diabatic potentials from these *ab initio* results. Adiabatic potentials were then derived using calculated couplings between the repulsive potentials. The program BCONT[10] is now being used to obtain calculated absorption spectra for excitation to the individual repulsive potentials. Calculations of the effects of the crossings between potentials on the I / I* branching ratios are underway and the results will be compared with our experimental data.

Wavelength / nm	% I	% I*
243.6	38.7	61.3
258	37.5	62.5
266	44.2	55.8
283	65.9	34.1
303	94.4	5.6

Table 1: I and I* percentages for HI photodissociation at different photolysis laser wavelengths

REFERENCES

1) E Wrede, L Schnieder, K H Welge, F J Aoiz, L Banares, V J Herrero, B Martinez-Haya and V Saez Rabanos
Journal of Chemical Physics 106 7862 (1997).

2) H Xu, N E Shafer-Ray, F Merkt, D J Hughes, M Springer, R P Tuckett and R N Zare
Journal of Chemical Physics 103 5157 (1995).

3) N E Shafer, A J Orr-Ewing, W R Simpson, H Xu and R N Zare
Chemical Physics Letters 212 155 (1993).

4) W R Simpson, T P Rakitzis, S A Kandel, A J Orr-Ewing and R N Zare
Journal of Chemical Physics 103 7313 (1995).

5) I Levi and M Shapiro
Journal of Chemical Physics 89 2900 (1988).

6) R Schmiedl, H Dugan, W Meier and K H Welge
Zeitschrift fur Physik A 304, 137 (1982).

7) T N Kitsopoulos, M A Buntine, D P Baldwin, R N Zare and D W Chandler
Proceedings of the SPIE 1858 2 (1993).

8) M N R Ashfold, D H Mordaunt and S H S Wilson
Comments in Atomic and Molecular Physics 32 187 (1996).

9) L J Rogers, M N R Ashfold, Y Matsumi, M Kawasaki and B J Whitaker
Chemical Physics Letters 258, 159 (1996).

10) R J LeRoy
Computer Physics Communications 52, 383 (1989).

ULTRAFAST SPECTROSCOPY OF AZOBENZENE

I K Lednev [1)] , T-Q Ye [1)] , P Matousek [2)] , M Towrie [2)] , S Umapathy [3)] , R E Hester [1)] , J N Moore [1)]

1) Department of Chemistry, The University of York, Heslington, York, YO1 5DD, UK. Email jnm2@york.ac.uk
2) Lasers for Science Facility, Rutherford Appleton Laboratory, Chilton, Didcot, Oxon, OX11 0QX
3) Department of Inorganic and Physical Chemistry, Indian Institute of Science, Bangalore 560 012, India

INTRODUCTION

Photoisomerisation is a fundamental reaction class which has wide importance in pure and applied chemistry, and in nature. The classic example of a photoisomerisation reaction is provided by stilbene, for which the mechanism and dynamics have been elucidated since the development of ultrafast spectroscopic techniques.[1] These studies have been extensive, including our own past work at RAL on mode-specific vibrational excitation and relaxation as studied by time-resolved resonance Raman spectroscopy.[2] Another textbook example of photoisomerisation is provided by azobenzene, for which only very early attempts at direct study by time-resolved spectroscopy had been reported [3] prior to our recent work in York,[4] in stark contrast with the large number of studies reported for the isosteric stilbene molecule. In the past, the mechanism of azobenzene photoisomerisation and its wavelength dependence have been debated almost exclusively on the basis of steady-state studies, with an in-plane inversion mechanism proposed for isomerisation from the $S_1(n\pi^*)$ state and an additional rotation mechanism, similar to that for stilbene, proposed for isomerisation from the $S_2(\pi\pi^*)$ state.[5]

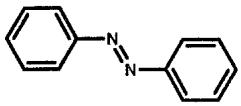

In York, we have used femtosecond time-resolved UV-visible absorption (TRVIS) spectroscopy [6] to observe the photochemistry of trans-azobenzene directly for the first time.[4] On UV excitation to the $S_2(\pi\pi^*)$ excited state, the first-formed species was identified by a band at ca. 390 nm which decayed in ca. 900 fs. A second component in the decay, prominent at shorter wavelengths, was similar to that of ca. 15 ps observed for the recovery of the bleach of the ground-state UV absorption band. Drawing on the results of steady-state experiments and ab initio calculations [7] reported in the literature, our interpretation of these results is that rotation on the S_2 potential energy surface occurs in ca. 900 fs to form a 'bottleneck' state (S_2^{Φ} or S_1^{Φ}) which is relatively long lived, and which results in the relatively long time of ca. 15 ps for ground-state recovery (Fig. 1).

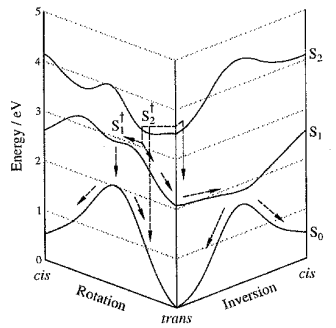

Fig. 1 Proposed mechanism for azobenzene photoisomerisation.[4,7]

Following these initial experiments, we wished to extend our studies of trans-azobenzene to visible excitation to the $S_1(n\pi^*)$ excited state. The excitation wavelengths required (400-500 nm) are not readily available using our amplified dye laser apparatus in York, and so these studies have been carried out at RAL. The aim was to pump the molecule into the S_1 state and to use ultrafast TRVIS spectroscopy to study the photochemistry.

EXPERIMENTAL

The OPA system in the LSF Ultrafast Spectroscopy Laboratory was used at a repetition rate of 40 kHz and provided both pump (ca. 25-600 nJ) and probe (ca. 6-90 nJ) pulses (ca. 600 fs instrument response function) at various wavelengths. The beams were overlapped in a 0.5-mm path length cell through which a solution of trans-azobenzene in n-hexane was flowed. The pump beam was chopped at ca. 2 kHz, and the probe beam was sampled by two photodiodes, detecting both sample and reference signals. The data were collected, by lock-in amplifier, as kinetic traces at single probe wavelengths.

RESULTS AND DISCUSSION

Our initial experiments at RAL were essentially a repeat of our earlier studies at York: trans-azobenzene was excited at 260-280 nm, into the $S_2(\pi\pi^*)$ state (Fig. 2), and the TRVIS kinetics were probed at 390, 420, and 490-700 nm. The time resolution at RAL was inferior to that at York, and this precluded a detailed analysis of the fast component observed at ca. 390 nm. Nevertheless, the observed kinetics could be fitted by a dual exponential decay with lifetimes of ca. 900 fs and 10 ps; these results essentially confirmed the earlier work at York, within the constraints of the RAL apparatus at the time of our visit.

The principal aim of the visit was to study the photochemistry of trans-azobenzene on excitation to the $S_1(n\pi^*)$ state. On pumping at 503 nm, at low excess energy above the S_1 origin (Fig. 2), excited-state absorption was observed at 390-420 nm. These probe wavelengths comprised the rather limited range

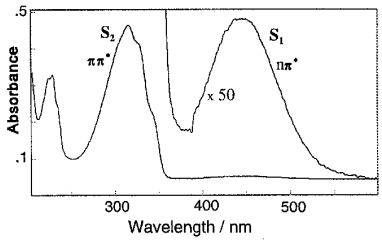

Fig. 2 Ground-state UV-visible absorption spectrum of trans-azobenzene in n-hexane.

that was available under these particular experimental conditions. The 'spectrum' obtained across this limited range, scaled for changes in alignment and energy which occurred as the laser system was tuned, is shown in Fig. 3.

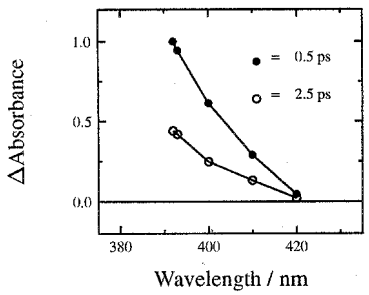

Fig. 3 Scaled TRVIS spectrum of trans-azobenzene. Pump 503 nm.

All of the TRVIS kinetics obtained within this limited probe range showed a single exponential decay of ca. 2.5 ± 0.2 ps, as shown in Fig. 4. This figure also serves to illustrate the high signal-to-noise ratio obtained, and also the excellent fit of these data on 503-nm pumping to a single exponential decay. The transient absorption at 390-420 nm and the lifetime of ca. 2.5 ps may be assigned to the $S_1(n\pi^*)$ state of trans-azobenzene.

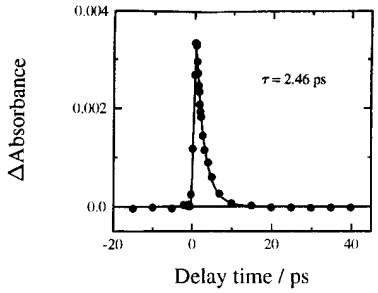

Fig. 4 TRVIS kinetics of trans-azobenzene. Pump 503 nm. Probe 392 nm.

Experiments were also carried out with excitation at 390-420 nm, at high excess energy above the S_1 origin (Fig. 2). Transient absorption was observed throughout the range 370-600 nm, using the much wider probe wavelength range available with these experimental conditions. The significantly different experimental arrangements resulting from tuning the OPA system required the TRVIS data to be scaled; the resulting 'spectrum' comprised a strong peak at ca. 400 nm and a weaker peak at ca. 520 nm, the latter shown in Fig. 5.

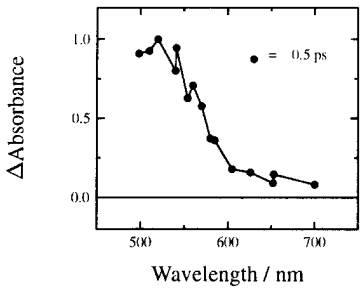

Fig. 5 Scaled TRVIS spectrum of trans-azobenzene. Pump 420 nm.

The TRVIS kinetics obtained on excitation at ca. 400 nm were different from those obtained on excitation at ca. 500 nm or at ca. 300 nm. They did not fit to a single exponential decay, but did fit reasonably well to a dual exponential decay: a fit with components of ca. 0.6 and 2.4 ps is illustrated in Fig. 6, with the decay on pumping at 503 nm also shown for comparison, but fits of similar quality could be obtained with different combinations of lifetimes and amplitudes.

This second, faster component observed on excitation at ca. 400 nm may arise from rotation on the S_1 surface at these high excess energies, but is not interpretable from the current set of data. We plan further work to address this question.

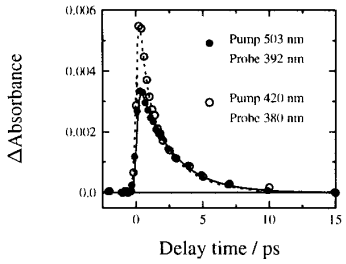

Fig. 6 Scaled TRVIS kinetics of trans-azobenzene.

CONCLUSION

Ultrafast TRVIS studies have established that the lifetime of the S_1 ($n\pi^*$) state of trans-azobenzene is 2.5 ps. An additional decay component has been observed when pumping trans-azobenzene to high excess energies above the S_1 origin; the interpretation of this effect requires further experiments. A paper on this work shortly will be submitted for publication.[8]

ACKNOWLEDGEMENTS

We acknowledge the assistance of G Gaborel (RAL) and L C Abbott (York).

REFERENCES

1) D H Waldeck,
Chem. Rev., 91, 415 (1991).

2) R E Hester, P Matousek, J N Moore, A W Parker, W T Toner and M Towrie,
Chem. Phys. Lett., 208, 471 (1993); P Matousek, A W Parker, W T Toner, M Towrie, D L A de Faria, R E Hester and J N Moore, Chem. Phys. Lett., 237, 373 (1995).

3) W S Struve
Chem. Phys. Lett., 46, 15 (1977); C G Morgante and W S Struve, Chem. Phys. Lett., 68, 267 (1979).

4) I K Lednev, T-Q Ye, R E Hester and J N Moore
J. Phys. Chem., 100, 13338 (1996).

5) H Rau
'Photochromism. Molecules and Systems', eds. H Durr and H Bouas-Laurent (Elsevier, Amsterdam, 1990), Chapt 4, p 165.

6) T-Q Ye, C J Arnold, D I Pattison, C L Anderton, D Dukic, R N Perutz, R E Hester and J N Moore
Appl. Spectrosc., 50, 597 (1996).

7) S Monti, G Orlandi and P Palmieri
Chem. Phys., 71, 87 (1982).

8) I K Lednev, T-Q Ye, P Matousek, M Towrie, S Umapathy, R E Hester and J N Moore
Chem. Phys. Lett., to be submitted.

A STUDY OF S_1 *CIS*-STILBENE USING PS-TR^3 SPECTROSCOPY

P.Matousek[1)], G.Gaborel[1)], A.W.Parker[1)], D.Phillips[2)], G.D.Scholes[2)], W.T.Toner[3)], M.Towrie[1)]

1) Rutherford Appleton Laboratory, Oxfordshire OX11 0QX
2) Department of Chemistry, Imperial College, London SW7 2AY
Clarendon Laboratory, Oxford University, Oxford OX1 3PU

INTRODUCTION

Stilbene plays an important role as a model system for isomerisation dynamics. Its two isomers, *trans* and *cis*, undergo fast isomerisation in solution following photoexcitation to the first excited electronic state. For S_1 *trans*-stilbene, the process is hindered by a barrier and occurs on ~ 100 ps timescale. In contrast, S_1 *cis*-stilbene isomerisation is near barrierless and proceeds on ~ 1 ps timescale competing with vibrational relaxation[1,2,3)].

The successful modelling of reaction dynamics requires greater knowledge of the molecular structure of the S_1 *cis*-stilbene[1,4),] Such information can be obtained from picosecond time-resolved resonance Raman spectroscopy (TR^3). To date the detection of S_1 *cis*-stilbene by TR^3 has been hindered by the short lifetime of the excited state (~ 1 ps) and required pump (260 - 290 nm) and probe (630 - 670 nm) wavelengths which have been difficult to access. Here we present the first TR^3 spectrum of S_1 *cis*-stilbene.

EXPERIMENTAL

The experiments were carried out using a TR^3 apparatus based on optical parametric amplifiers (OPAs)[5)], also described in this report elsewhere. The system provides synchronised, independently tunable pump and probe pulses of high spectral brightness. Typical pump and probe pulse energies at the sample were ~ 0.4 - 2 μJ. *Cis*-stilbene (97 % purity) was obtained from Aldrich and used without further purification. Solutions were prepared at concentration 1x10^{-3} mol.dm^{-3} in spectroscopic grade solvents. Laser pulses were focused to a spotsize of around 100 μm. TR^3 spectra could be measured down to a limit of ~ 200 cm^{-1}. The position and bandwidth of Raman bands have been determined with accuracy of ± 5 cm^{-1} and ± 15 cm^{-1}, respectively.

RESULTS

The TR^3 spectrum shown in figure 1a was obtained following photoexcitation of *cis*-stilbene at 267 nm in *n*-hexane and probing at 630 nm near the centre of the broad S_1 transient absorption band. The most notable features are the Raman bands at lower frequency. The bands were fit[6)] to Gaussian functions whereas the S_1 *trans* isomer bands fit better to Lorentzian profile. The bands in the region 243, 475 and 742 cm^{-1} have internal structure and were fit to pairs of bands. TR^3 spectrum of *trans*-stilbene in *n*-hexane obtained under similar conditions is shown for comparison in figure 1b.

Ps-TR^3 spectra of *cis*-stilbene were also taken (i) in acetonitrile and cyclohexane, (ii) at longer probe wavelength (670 nm) and (iii) at longer pump wavelengths (273 and 305 nm). No gross change in the spectral profile was detected within the accuracy of the experiment in any of these measurements.

Estimate from the TR^3 spectrum of the S_1 *cis*-stilbene lifetime in *n*-hexane yielded a value 1 ± 0.5 ps. Comparison of spectra between time delays 0 ps and 1.5 ps did not show any gross changes in the spectral profile within the accuracy of the experiment. The lifetime in cyclohexane was longer than that in *n*-hexane. The transient spectrum obtained in acetonitrile had lifetime significantly shorter than that in *n*-hexane. No gross changes were observed in the spectral profile measured in different solvents.

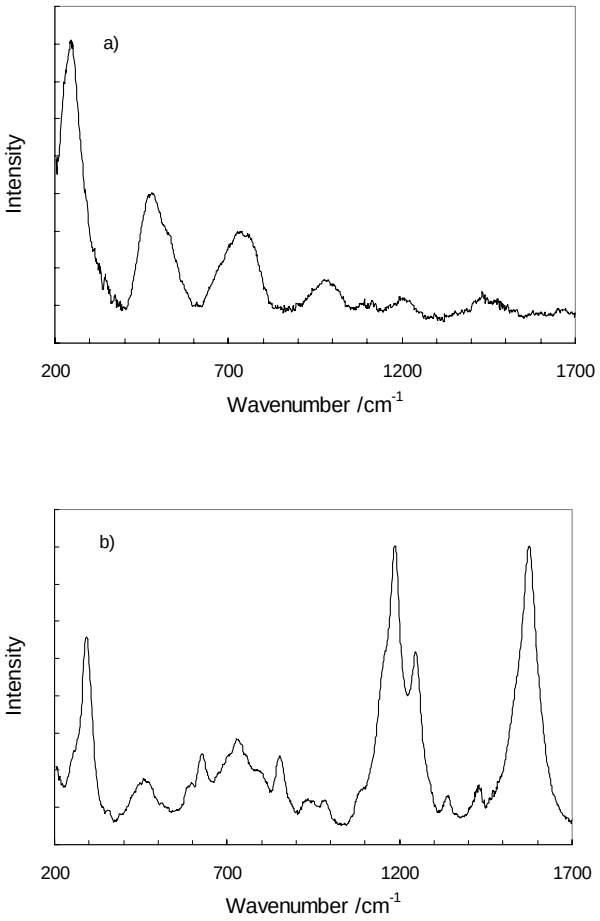

Figure 1 (a) ps-TR^3 spectrum of S_1 *cis*-stilbene in *n*-hexane obtained at time delay 0 ps and pump and probe wavelengths 267 and 630 nm, respectively. (b) ps-TR^3 spectrum of S_1 *tran*-stilbene obtained under the same conditions at time delay 20 ps. Solvent spectra and in the case of *cis*-stilbene weak residual *trans*-stilbene spectrum have been subtracted.

DISCUSSION

The observed ps-TR^3 spectrum is attributed to the S_1 state of *cis*-stilbene on the following basis: (i) The spectrum was obtained at probe wavelengths (630 and 670 nm) that fall directly under an intense S_1 - S_n absorption band of S_1 *cis*-stilbene where no other product of isomerisation contributes[7)] (ii) The estimated lifetime of ~ 1 ps is consistent with the lifetime of S_1 *cis*-stilbene[8)] and lifetime dependencies in other solvents are consistent with S_1 *cis*-stilbene lifetimes (0.38 ps in acetonitrile[8)] and 1.8 ps in cyclohexane[9)]). (iii) Pump and probe power dependence measurement did not reveal the presence of any nonlinear processes in either pump or probe energy giving rise to the observed signals. Saturation of the signal with pump pulse energy above ~ 1 μJ is consistent with the saturation of the ground state population above this level. The observed threshold level is in good agreement with the calculated saturation energy ~ 1.4 μJ (saturation fluence 18 mJ/cm^2) estimated from the ground state extinction coefficient[10)] (ε ~ 10,000 dm^3/(mol.cm)).

The positions and relative intensities of the observed bands strongly suggest that the spectrum is dominated by an intense overtone progression, up to the 5th order, originating from the 243 cm^{-1} fundamental.

Activity in the low-frequency region of S_1 *cis*-stilbene was recently reported by Szarka and co-workers who used the femtosecond transient absorption technique[4]. Wavepacket motion was detected on the excited state potential surface and was associated with the phenyl torsion mode. Its dephasing time was estimated to be ~ 100 fs which is in good agreement with typical bandwidths observed in our measurements (~ 100 cm^{-1}) and is consistent with the presence of a fast isomerisation channel in the S_1 state. The frequency of the vibrational spacing which gives rise to the oscillations in the pump-probe signal fit to ~ 110 cm^{-1} (measured in *n*-hexane) is lower than the current detection limit of our apparatus (200 cm^{-1}). Similarly, the time resolution of Szarka *et al* gave a cut-off of ~ 220 cm^{-1} precluding measurements in the 243 cm^{-1} region. Despite that, we can conclude that the mode corresponding to the reported 110 cm^{-1} motion must exhibit much lower displacement between S_1 and S_n states than that of the 243 cm^{-1} mode otherwise it would be resolved in our spectra as the 2nd order overtone (330 cm^{-1}).

The internal structure of Raman bands in our spectra may originate from Fermi resonance enhancing fundamental bands in the vicinity of the intense overtone progression.

The absence of intense high-frequency Raman bands in our spectra is ascribed to lower displacement possessed by these modes relative to that of the 243 cm^{-1} band. This is consistent with previous time-resolved absorption experiments showing that the majority of energy placed in high-frequency Franck-Condon active modes by the pump excitation pulse remains locked in those modes until long after the isomerization is completed. These modes have been identified as having only a spectator role in the reaction[7,11]. Such modes would be expected to have only moderate displacements and consequently much lower Raman intensity relative to that of the 243 cm^{-1} mode.

CONCLUSION

The ps-TR^3 spectrum of S_1 *cis*-stilbene in *n*-hexane was obtained when probing under an S_1 transient absorption band. The spectrum is notable for having intense low-frequency bands and these are assigned to a high-order overtone progression originating from the 243 cm^{-1} fundamental. This implies a large geometry change in the resonant state S_n corresponding to the nuclear coordinate involving the 243 cm^{-1} mode. The S_1 *cis*-stilbene spectra observed in different solvents did not reveal any gross changes within the spectral profile and the observed lifetime changes were consistent with previously reported S_1 lifetimes. It is hoped that the TR^3 spectra of S_1 *cis*-stilbene will provide structural information which will help to further understanding of reaction dynamics[1,4].

Further details on this work can be found in Ref[12].

ACKNOWLEDGEMENTS

We should like to thank I.R.Gould and S.M.Tavender for contribution to this work and to D.L.Phillips, T.L.Gustafson, R.E.Hester and K.Iwata for valuable comments in the preparation of this article. This work was supported by EPSRC. GDS gratefully acknowledges support of the Ramsay Memorial Fellowship Trust.

REFERENCES

1) D C Todd, G R Fleming
J Chem Phys, 97 8915 (1992).

2) R J Sension, S T Repinec, R M Hochstrasser
J Chem Phys, 93 9185 (1990)

3) D Raftery, R J Sension, R M Hochstrasser
The Barrier Crossing Problem, eds G R Fleming and P Hanggi (World Sciencific, Singapore, 1993).

4) A Z Szarka, N Pugliano, D K Palit, R M Hochstrasser
Chem Phys Lets, 240 25 (1995)

5) M Towrie, P Matousek, A W Parker, W Shaikh
Meas Sci Technol to be published.

6) P Matousek, A W Parker, M Towrie
Raman Analysis Rutherford Appleton Laboratory Report RAL-95-028, 1 (1995).

7) R J Sension, S T Repinec, A Z Szarka, R M Hochstrasser
J Chem Phys, 98 6291 (1993).

8) L Nikowa, D Schwarzer, J Troe
J Chem Phys, 97 4827 (1992)

9) J K Rise, A P Baronavski
J Phys Chem, 96, 3359 (1992).

10) H-H Perkampus
UV-VIS Atlas of Organic Compounds, 2nd Ed (VCH Verlagsgesellschaft, Weinheim, 1992).

11) R J Sension, A Z Szarka, R M Hochstrasser
J Chem Phys, 97 5239 (1992).

12) P Matousek, A W Parker, D Phillips, G D Scholes, W T Toner, M Towrie
Chem Phys Letts submitted.

A TR^3 STUDY OF THE NITRATE RADICAL WITH ORGANIC MOLECULES IN SOLUTION

D J McGarvey[1)], L Mulroy[1)], A B Robertson[1)], T G Truscott[1)], A W Parker[2)], S Tavender[2)], M King[3)], P. Biggs[3)], C Canosa-mas[3)], R P Wayne[3)]

1) Department of Chemistry, University of Keele
2) Lasers *for* Science Facility, Rutherford Appleton Laboratory
3) Physical and Theoretical Chemistry Laboratory, University of Oxford

INTRODUCTION

The nitrate radical (NO_3•) is an important oxidant in the troposphere at night, able to react with air pollutants and biogenic emissions. The majority of NO_3• present in the atmosphere is formed by the reaction of the nitrogen dioxide radical (NO_2•) with ozone (O_3), shown in equation 1. During the day NO_3• is rapidly photolysed and the hydroxyl radical is the important oxidising species.

$$NO_2\bullet + O_3 \rightarrow NO_3\bullet + O_2 \qquad (1)$$

The reactions of NO_3• with organic compounds are of interest as they can lead to the formation of nitric acid and peroxyacylnitrates, producing photochemical smog. The reactions which can occur include hydrogen abstraction, which leads to the formation of nitric acid, addition across double bonds and, in solution, electron transfer can occur producing the nitrate ion.

The geometric and electronic structure of NO_3• are of interest due to their influence on the reactivity of the radical. However, these have not been unequivocally established with experimental and theoretical studies indicating a structure of either C_{2v} or D_{3h} symmetry.

In the work reported here time resolved resonance Raman spectroscopy has been used to study the vibrational spectrum of this radical and to investigate its reactions with aromatic hydrocarbons.

EXPERIMENTAL

The ns-TR^3 experiments were performed at the Lasers for Science Facility using the experimental set up described previously[1)]. Probe wavelengths of 590 nm and 630 nm were produced from a Nd:YAG (3rd harmonic, 355 nm) pumped OPO laser and the pump wavelength of 355 nm obtained using an excimer pumped dye laser. The 670 nm probe wavelength was produced using an excimer pumped dye laser with the 355 nm pump wavelength from the 3rd harmonic of the Nd:YAG. Spectra were obtained at pump probe time delays varying from 0 - 1000 ns. The solutions of ceric ammonium nitrate (Fluka) in acetonitrile (BDH) were 5 x 10^{-5} mol dm $^{-3}$. Naphthalene and biphenyl (Aldrich, recrystallised in methanol) were used at concentrations of 10^{-2} - 10^{-3} mol dm $^{-3}$. The sample solution was flowed in a quartz capillary tube.

The transient shown in figure 1 was produced by 355 nm ns-laser flash photolysis using the experimental set up described peviously[1)]. The solutions of ceric ammonium nitrate (Fluka) in acetonitrile (Aldrich) were 2 x 10^{-4} mol dm $^{-3}$.

RESULTS AND DISCUSSION

NO_3• is generated by laser excitation of ceric ammonium nitrate (CAN) in acetonitrile. The three probe wavelengths for the Raman experiments were selected to coincide with the three vibrational bands of NO_3• shown in figure 1. The TR^3 spectra are shown in figures 2 and 3. This is the first vibrational spectrum obtained for NO_3• in solution. The relative band intensities in the spectra remain constant at different time delays indicating only one species is present. However, the spectra show a variation in band intensity with probe wavelength. A list of bands positions and vibrational assignments are given in table 1. The vibrational bands of NO_3• have been assigned previously in laser induced fluorescence and gas phase infrared studies[2)]. The broad noisy bands at 1430 cm^{-1} and 2040 cm^{-1} are unassigned and are thought to be due to poorly subtracted solvent bands. There is also a possible band at 340-370 cm^{-1} which is not shown as it is hidden by the acetonitrile band at 380 cm^{-1}.

Shift/cm^{-1}	Vibrational assignments	
	C_{2v}	D_{3h}
1050	ν_1, sym stretch, a_1	ν_1, sym stretch, a_1
1508	ν_2, N-O stretch, a_1	ν_3, stretch, e'
1518	2 ν_3, a_1	2 ν_2 out plane bend, a_1
760	ν_3, in plane bend, a_1	
813	ν_6, asym bend, b_2	
1805	$\nu_3 + \nu_6$, b_2	
2116	2 ν_1, a_1	2 ν_1, a_1

Table 1. List of band positions and proposed vibrational assignments

The assignments show that with the exception of the bands at 760 cm^{-1}, 813 cm^{-1} and the combination band at 1805 cm-1 assignments can be made in terms of both the C_{2v} and D_{3h} structures. There are bands predicted at 360 cm^{-1} for both structures and at 2008 cm^{-1} for C_{2v}. However, these are not observed due to overlapping solvent bands and poor signal to noise ratios.

The bands at 1508 cm^{-1} and 1518 cm^{-1} appear as a doublet for both 670 nm and 630 nm probe wavelengths. The bands are of equal intensity with the background slightly distorting their height. This feature cannot be seen for the 590 nm probe due to the poor signal to noise ratio. Both structures are predicted to have a band in this region, the ν_2 N-O stretch for the C_{2v} structure [2)] or a ν_3 degenerate stretch for D_{3h}.[3,4)] . Therefore, the doublet may indicate that both structures are present. Alternatively, the 1518 cm^{-1} band may be assigned as a first overtone for both structures (2 ν_3 for C_{2v} or 2 ν_2 for D_{3h}). The proximity of this to the fundamental band at 1508 cm^{-1} (accidental degeneracy) may allow Fermi resonance to occur. The overtone gaining intensity at the expense of the fundamental. This will only occur for the C_{2v} structure where the fundamental and overtone vibrations involved are of the same symmetry.

Assuming Fermi resonance explains the doublet feature then it may be concluded that in solution NO_3• has a C_{2v} symmetry. The doublet may also be interpreted as indicating that both species are present in equilibrium[5)] . However, this seems unlikely since other bands that can be assigned to both structures, are not split.

Addition of naphthalene and biphenyl to the CAN solution in acetonitrile is seen to quench the NO_3• with the concurrent formation of another species, shown for naphthalene in figure 4. These species are assigned as the radical cations following the assignments of Shida [6)] and Hug [7)] for the naphthalene radical cation. The assignments of Hamaguchi [8)] were used to identify the biphenyl radical cation.

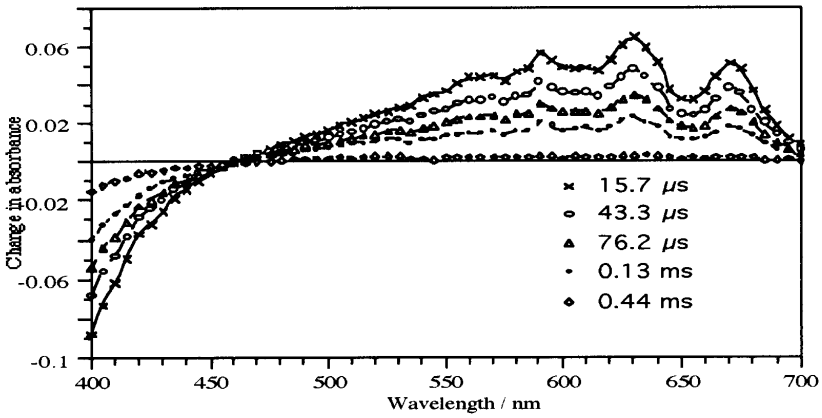

Figure 1. Transient absorption spectra of NO_3• in acetonitrile produced following 355 nm laser excitation of CAN (2 x 10^{-4} mol dm^{-3}).

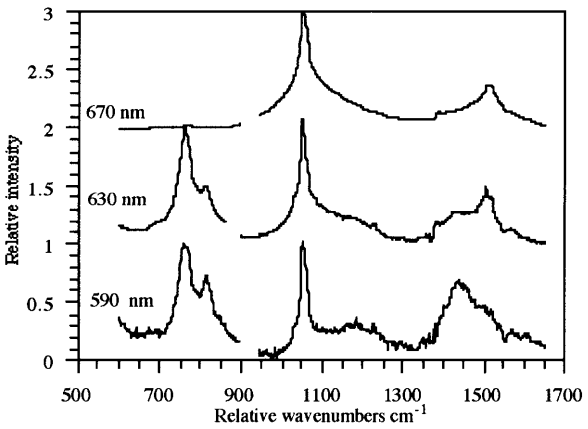

Figure 2. TR^3 spectra of NO_3• in acetonitrile with a time delay of 50 ns, between 500 - 1700 cm^{-1}.

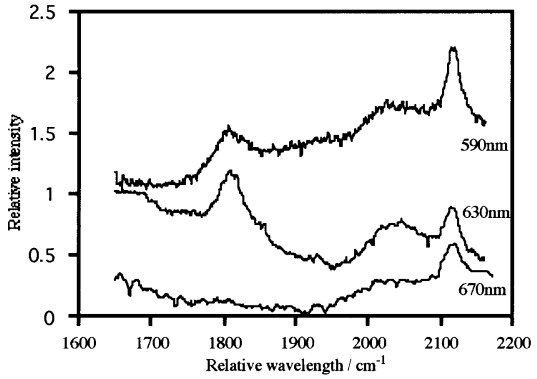

Figure 3. TR^3 spectra of NO_3• in acetonitrile with a time delay of 50ns, between 1600 - 2200 cm^{-1}.

CONCLUSION

We have obtained the first resonance Raman spectra of NO_3• in solution. The spectra can be interpreted to indicate that NO_3• has a C_{2v} structure or, less likely, that both C_{2v} and D_{3h} species are present.

The NO_3• reacts with naphthalene and biphenyl via electron transfer.

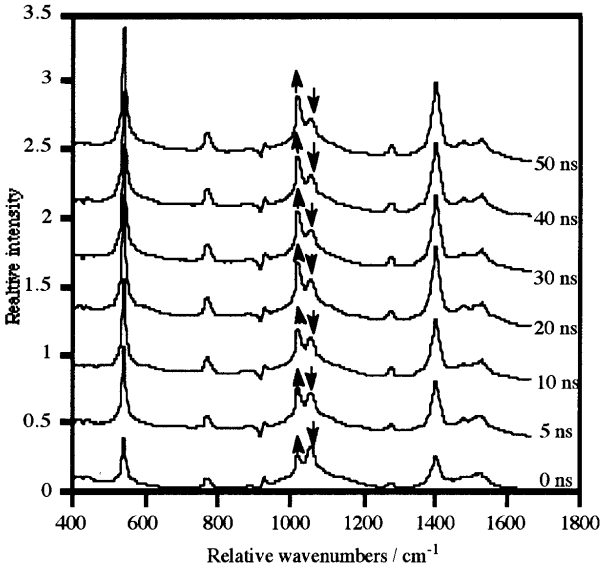

Figure 4. TR^3 spectra showing the naphthalene radical cation growing in with the concurrent decay of the NO_3 in acetonitrile using a 670nm probe wavelength.

REFERENCES

1) D J McGarvey et al
J. Am. Chem. Soc.,118 1756 (1996)

2) R P Wayne et al
Atmospheric environment, 25 1, (1991)

3) R Atkinson, S M Aschmann and J N Pitts
J. Phys. Chem., 92 3454, (1988)

4) R R Friedl and S P Sander
J. Phys. Chem., 91 2721 (1987)

5) J F Stanton, J Gauss and R J Bartlett
J. Chem. Phys., 94 4084 (1991)

6) H Kawashima T Kato and T Shida
Chem. Phys. Letts., 165 5554 (1990)

7) S J Sheng and G Hug
Chem. Phys. Letts., 57 168 (1978)

8) Y Sasaki and H O Hamaguchi
Spectrochimica Acta 50 1475 (1994)

STATE-SPECIFIC COLLISIONAL ENERGY TRANSFER IN ELECTRONICALLY EXCITED CH RADICALS

C. J. Randall and K. G. McKendrick

Department of Chemistry, The University of Edinburgh, Edinburgh EH9 3JJ, UK.
E-mail <K.McKendrick@ed.ac.uk>

INTRODUCTION

Inter-electronic state collisional quenching is a potentially important process whenever electronically excited molecules are produced under conditions where the number density makes the rate of collisions competitive with the radiative rate. Typical environments of this type would include those prevailing in combustion, regions of the atmosphere, plasmas, discharges, certain laser gain media, etc.

The proper understanding and modelling of such systems requires not only a knowledge of the total collisional removal rates of the excited species, which have historically been quite extensively examined, but also of the detailed branching over the possible product levels. These measurements are, in general, significantly more challenging and correspondingly far fewer have been performed.

In particular, in this report we examine collisional transfer between specific electronically excited states of the CH radical:

$$CH(B^2\Sigma^-, v, J) + Q \rightarrow CH(A^2\Delta, v', J') + Q \qquad (1)$$

where Q represents a collision partner, typically a small, closed-shell gas phase molecule.

The CH radical has been selected as the target of these investigations for several different reasons. It is a species of real practical interest in combustion, and is also abundant in more exotic astrophysical environments such as interstellar clouds and comet tails. State-resolved measurements are assisted by the relatively wide spacings between rovibrational levels which are characteristic of a hydride. There is some evidence for collision-induced transfer specifically between the CH B and A states from measurements in high[1)] and relatively low[2)] pressure flames, although inevitably the identity of the collision partner is unclear in these complex systems. From a theoretical perspective, the restricted number of open channels and the relatively small numbers of electrons make CH collisions with simple partners a viable prospect for rigorous treatments of the intermolecular potentials and of the inelastic scattering.

EXPERIMENTAL

Experiments were carried out in a custom-built stainless steel vacuum chamber. Ground state CH($X^2\Pi$) radicals were generated by laser photolysis of bromoform ($CHBr_3$) at a typical partial pressure of a few mTorr. The quencher was admitted into the chamber independently, with partially throttled pumps used to maintain steady total pressures of up to 100 Torr.

The photolysis source was an excimer laser (Lambda Physik COMPex 205, provided from the Loan Pool of the Lasers for Science Facility at CLF) operating at the ArF wavelength of 193 nm. Typical pulse energies entering the chamber were 30 mJ, which were kept constant during experimental runs using the manufacturer's in-built feedback system.

An independent, tunable Nd:YAG laser-pumped dye laser system was used to state-specifically excite CH on the $B^2\Sigma^-$-$X^2\Pi$ (0,0) transition. The necessary wavelengths around 390 nm were generated by frequency mixing the dye fundamental beam with the residual Nd:YAG fundamental. The photolysis and pump beams counterpropagated through the chamber. Fluorescence was collected perpendicular to the common laser beam axis by a system of lenses. An interference filter appropriate to the particular measurement (see below) was used to isolate the desired CH emission band(s) and discriminate against scattered laser light. The transmitted signals were detected by a fast photomultiplier tube (EMI 9789QB), preamplified (Stanford SR240) and captured by a transient digitiser (DSP 2001A, 100 MHz) incorporated in a CAMAC (IEEE-583) modular data acquisition system. Various other experimental parameters, including the timing of the firing of the lasers, were also controlled electronically through appropriate CAMAC modules. The pump pulse was typically delayed by ~5 μs from the photolysis pulse to separate the desired signal from the fluorescence emitted by electronically excited CH formed directly in the photolysis of $CHBr_3$.

RESULTS AND ANALYSIS

A typical laser-induced fluorescence (LIF) excitation spectrum in the 390 nm region is shown in Fig.1. The lines are readily assigned to R-branch transitions in the well-characterised CH $B^2\Sigma^-$- $X^2\Pi$ (0,0) band.[3)] We were therefore able to prepare unique initial rovibronic levels for inelastic collisional experiments by appropriate choices of pump laser wavelength.

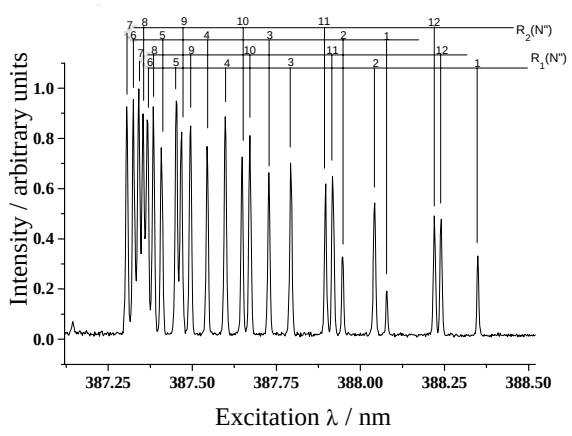

Fig. 1 LIF excitation spectrum of the CH B-X (0,0) R-branch region.

The remainder of the experiments to date involved temporally resolving the fluorescence emissions in either one of two spectral windows.

Most straightforwardly, an interference filter centred at 390 nm with a bandwidth of 10 nm isolated the directly returning B-X (0,0) emission. Neglecting the effects of a finite pump laser pulse length or of multiple collisions, this signal is expected to be a simple single-exponential with a decay constant which is the sum of the radiative rate and any collisional removal from the $B^2\Sigma^-$ v=0 level.

A similar filter centred at 430 nm was selected to transmit any emission on the $A^2\Delta$-$X^2\Pi$ Δv =0 diagonal bands[3)] which can only result from collisional transfer of population from the initially prepared B state. However, the B-X (0,1) band is accidentally nearly resonant with the A-X diagonal bands, so there is also a directly returning contribution to this signal with a time-dependence identical to the B-X (0,0) emission. At least in principle, this contribution can therefore be subtracted to reveal the residual A-X waveform. A kinetic analysis indicates that this collisionally produced signal should be a difference of exponentials

$$I(t) = a\,(e^{-k_1 t} - e^{-k_2 t}) \qquad (2)$$

where a is an arbitrary scaling constant, and k_1 and k_2 are total removal rates for the B and the A states: as formulated, whichever is the faster rate is associated with k_2 and the slower with k_1. Because the B-X decay rate can be obtained from the B-X(0,0) profile, it is possible to unambiguously identify in practice which decay rate is which.

Quenching by the $CHBr_3$ Precursor

As a first test of our methods, we examined the collisional behaviour of CH $B^2\Sigma^-$ with the precursor molecule, $CHBr_3$. We were restricted to the range of pressures of 0-60 mTorr of pure $CHBr_3$ by a combination of the rapid reactivity of CH(X) with bromoform and rapid formation of sooty deposits on the windows at higher pressures. Typical fluorescence profiles in the two wavelength intervals are shown in Figs. 2 and 3, respectively. In Fig. 3 the decomposition of the observed signal into B-X(0,1) and A-X (Δv=0) contributions is indicated. This is, as far as we are aware, the first demonstration of specific CH B-A collisional transfer by a single, well-defined quencher molecule.

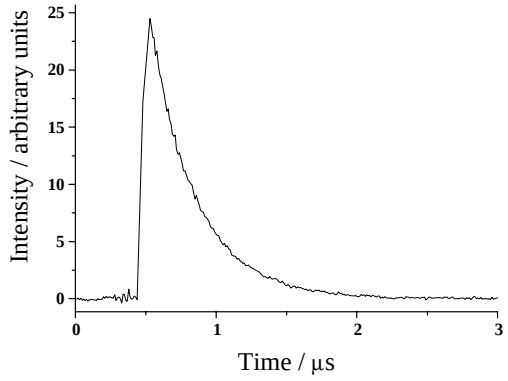

Fig. 2 CH B-X (0,0) fluorescence decay profile. 30 mTorr $CHBr_3$.

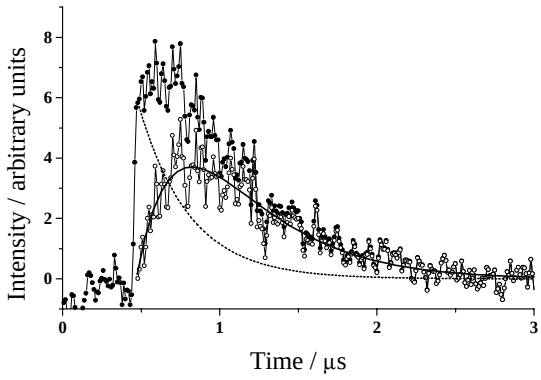

Fig. 3 Observed CH fluorescence profile at 430 nm (filled points). Subtracted B-X (0,1) contribution (dashed line). Residual A-X collisionally produced emission (open points). Conditions as Fig. 2.

Satisfactory kinetic fits to both profiles were obtained at a series of pressures, yielding the decay constants plotted in Fig. 4. The slopes of the lines yield bimolecular total quenching rate constants of $(52 \pm 6) \times 10^{-11}$ and $(41 \pm 2) \times 10^{-11}$ cm^3 molecule^{-1} s^{-1} for the CH B and A states, respectively, by $CHBr_3$. These relatively large values agree reasonably well with literature values obtained by different methods.[4] The zero pressure intercepts are also consistent with accepted radiative lifetimes for these states.[5]

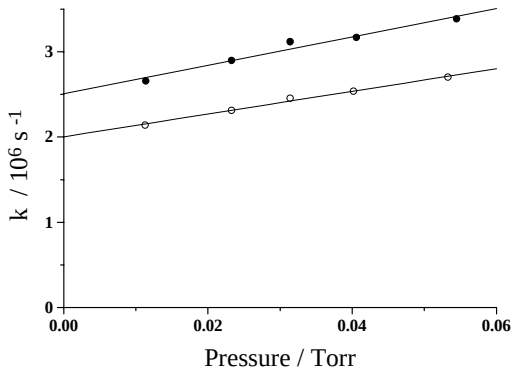

Fig. 4 Variation of first order rate coefficients with pressure of $CHBr_3$. CH B state (filled symbols) and A state (open symbols).

Quenching by Other Molecules

In the remaining time available during the loan period, we also provisionally examined the ability of CH_4 and Ar to collisionally couple the CH B and A states.

Sequences of fluorescence decay profiles at 390 and 430 nm were recorded for CH_4 pressures in the range 0-1 Torr. The behaviour was qualitatively similar to that described above for $CHBr_3$, except that signal-to-noise ratios were generally poorer, particularly for the A-X data. We believe this to be the result of a less favourable ratio of the specific CH B-A quenching rate constant to the CH X state reactive rate constant for CH_4.

The total quenching rate constants of both CH B and A states by Ar are known to be much smaller than those for either $CHBr_3$ or CH_4.[4] We were able to add relatively large pressures of Ar (up to 100 Torr) and still record strong B-X (0,0) fluorescence decays with only subtly varying time dependences. Very interestingly, however, increasing Ar pressures simultaneously promoted strong CH A-X signals in the 430 nm region. These combined results suggest that Ar is relatively efficient at inducing CH B-A transfer, but not at removing either state. At the higher pressures of these experiments, the simple kinetic analysis above is inadequate, because the rate of reverse A-B transfer must be significant for B-X (0,0) signals to persist to long times. This reversibility is in itself interesting, because it suggests that the B, v=0 level is collisionally coupled to the relatively isoenergetic A, v′=1 level, and not to the lower-lying A, v′=0 level. We hope to pursue these aspects in future work.

REFERENCES

1) N L Garland and D R Crosley
Applied Optics 24, 4229 (1985)
2) K J Rensberger, M J Dyer and R A Copeland
Applied Optics 27, 3679 (1988)
3) P F Bernath, C R Brazier, T Olsen, R Hailey, W T M L Fernando, C Woods and J L Hardwick
Journal of Molecular Spectroscopy 147, 16 (1991)
4) C Chen, Y Shang, S Yu and X Ma
Journal of Chemical Physics 101, 5727 (1994)
5) S Couris, N Anastasopoulou and C Fotakis
Chemical Physics Letters 223, 561 (1994)

OBSERVATION OF MODE-SPECIFIC REORGANISATION DYNAMICS ACCOMPANYING CHARGE TRANSFER IN CYANOTERPHENYL

G.D. Scholes [1] , P. Matousek [2] , M. Towrie [2] , D. Phillips [1] , A.W. Parker [2]

1) Department of Chemistry, Imperial College, London SW7 2AY, UK
2) Rutherford Appleton Laboratory, Chilton, Didcot, Oxon, OX11 0QX, UK.

INTRODUCTION

The role of solvent effects during chemical reactions has been the subject of a wide range of investigations. Ultrafast spectroscopy can provide detailed information on the dynamic coupling between molecule and solvent by interrogating the ensemble with excitation pulses which are shorter than the period of many intramolecular and almost all intermolecular nuclear motions. In the present work we investigate intramolecular and solvent relaxation in a charge transfer reaction. We employ a variety of the pump-probe techniques (with picosecond time resolution) in which we probe the resonantly-enhanced vibrational spectrum of an excited singlet state by time-resolved resonance Raman (TR^3) spectroscopy. This method enables us to examine directly high frequency intramolecular modes which would be obscured in a time-domain experiment owing to the limits of time resolution in ultrafast measurements.

A huge range of photoinduced intramolecular charge transfer reactions have been studied, by a wide variety of techniques. In some systems a full electron is transferred from the donor to the acceptor part of a bichromophore, in other systems only partial charge is transferred. In solvents for which the intermolecular reorganisation rate is much less than the rate of charge transfer, a frequency shift of the observed emission spectrum (a dynamic Stokes' shift) is observed. This can be interpreted in terms of the relaxation of the polar/polarisable solvent to accommodate the change in dipole moment of the solute molecule and is therefore often associated with the longitudinal relaxation time of the solvent. Theories for the rates of electron transfer and these subsequent relaxation dynamics have been developed and have been examined using methods such as time-resolved fluorescence, transient absorption and echo peak shifts. Clearly, to observe this diffusive dielectric relaxation of the solvent there must be a separation of time-scales between the charge separation and the relatively slow solvent reorganisation. In the present work we shall take this a step further and examine the mode-specific dynamics of the *intramolecular* component of the reorgansiation accompanying a dynamic Stokes' shift for the molecules 4'-*n*-pentyl-4-cyanoterphenyl (cyanoterphenyl, CTP) and *p*-terphenyl (TP) using a combination of transient absorption and TR^3 spectroscopies with picosecond time resolution.

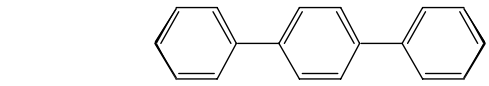

TP

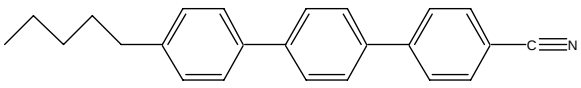

CTP

EXPERIMENTAL

The transient absorption measurements were carried out using two independently tuneable and synchronised 150 fs pulses generated using a 40 kHz regenerative amplifier system as described in detail previously. The frequency-tripled Ti:sapphire output (277 nm) was used as a pump pulse. A white light continuum (*ca.* 500-750 nm) generated in a sapphire crystal was used as the probe. The signal was focused into an optical fibre and dispersed across a CCD camera.

A modified configuration was used for the TR^3 measurements in which the regenerative amplifier was operating at a repetition rate of 1 kHz and the femtosecond pulse was spectrally filtered to 20 cm^{-1} inside the stretcher. The frequency-doubled output of the regenerative amplifier was used to pump two optical parametric amplifiers (OPAs), providing pump and probe pulses with typical energies at the sample of 0.1 - 2 μJ. Pump and probe pulses (parallel polarisation) were focused separately and combined using a dichroic mirror (spot size *ca.* 200 μm at sample). The sample was flowed in a jet (550 μm diameter). The TR3 signal was detected at right angles to both the direction of flow of the jet and the pump and probe beams using a single stage spectrometer and a liquid nitrogen cooled CCD camera (Princeton Instruments). Scattered light was rejected using a holographic filter and a low-fluorescence cut-off filter.

RESULTS AND DISCUSSION

The transient absorption data (Figure 1) reveal that the S_1 state of CTP is strongly solvent-dependent, in contrast to TP, owing to the electron-withdrawing CN substituent. Hence, in polar solvents with long enough dielectric relaxation times we observe a dynamic Stokes' shift of the first excited singlet state of CTP as it is stabilized by reorientation of the solvent. Concomitant with this, we observe solvent-dependent changes in the TR^3 spectra of CTP (Fig. 2 and 3), again absent from TP. It thus seems that CTP is an archetype for studying intramolecular reorganisation accompanying the dynamic dielectric stabilisation (intermolecular reorganisation) about an excited charge transfer state.

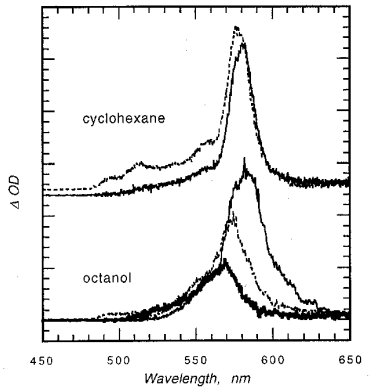

Fig. 1 Transient absorption spectra of CTP (2ps to 200ps delays) in cyclohexane (upper trace) and octanol (bottom trace).

The frequency of the C≡N stretch has been observed previously to be sensitive as an indication of the charge transfer character for the molecular 4-dimethylaminobenzonitrile. It was reported by Hashimoto and Hamaguchi[1)] that this frequency shifted from 2216 to 2096 cm^{-1} on going from the ground state to the twisted intramolecular charge transfer state in butanol solvent using transient infrared spectroscopy. Moreover, Mitambo and Loppnow[2)] have reported a similar observation for Raman

frequencies of such an electron-withdrawing group in a related molecule in the ground state. Similarly, for the S_1 state of CTP we find there to be a solvent-dependence of the C≡N stretch frequency. The dynamics of this Raman frequency shift could not be resolved in any of the solvents studied. If the frequency of this band does indeed signal the change in electron density on the C≡N group and hence the charge transfer, then the fast dynamics of the shift (< 1 ps in all solvents studies) suggests that there is a definite separation of time-scales between a fast charge transfer and the subsequent solvent reorganisation which we observe as the dynamic Stokes' shift.

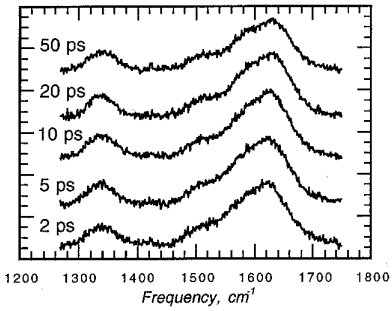

Fig. 2 TR^3 spectra of CTP in butanol.

For the S_1 state of CTP we observe also solvent-dependent band shifts in the 1200 to 1800 cm^{-1} region. Moreover, we are able to resolve the dynamics of these shifts for some of the solvents. The bands observed at 1300 to 1500 cm^{-1} do not exhibit any frequency shifts. However, the dynamics of the 1612 cm^{-1} band may be compared with the Stokes' shift using a normalized spectral correlation function, $C(t)$, defined as

$$C(t) = \frac{\nu(t) - \nu(0)}{\nu(\infty) - \nu(0)} \qquad (1)$$

where ν is the frequency of the transient absorption maximum or Raman band.

From the results of such an analysis for CTP in octanol, it is evident that the time scale of the Raman shift is shorter than that of the Stokes' shift. By fitting the correlation function data to a single exponential decay we retrieve time constants of 18 ps versus 27 ps for the Raman shift and the Stokes' shift respectively. Our preliminary study of the TR^3 dynamics of CTP in butanol have yielded a time constant of *ca.* 9 ps for the dynamics of this Raman band.

Iwata and Hamaguchi[3)] and others[4)] have reported recently a shift for the 1570 cm^{-1} band of *trans*-stilbene which they were able to ascribe to vibrational cooling. This effect was not dependent on solvent dielectric constant, in contrast to our observation, but was connected to the cooling of a "hot" molecule created by excess excitation energy or by chemical reaction. The frequency-shifts that we observe may be analogous to those reported by Iwata and Hamaguchi, but are connected with the charge transfer reaction. In polar solvents, for which we observe evidence for a charge separation in the S_1 state in the transient absorption measurements, the rate of the shift depends upon the solvent polarity and, in turn, the rate of the Stokes' shift of S_1. We suggest two possible explanations: (i) rather than being dissipated by thermalisation into the bulk solvent, the excess energy is actively funnelled into the (reorganising) solvent; (ii) the frequency of the low frequency mode changes owing to intramolecular reorganisation. The overall implication for the charge separation in the CTP S_1 state is that the high frequency intramolecular reorganisation is fast (*cf.* the CN stretch), whilst the reorganisation involving low frequency modes (i.e. the classical coordinate) is slow.

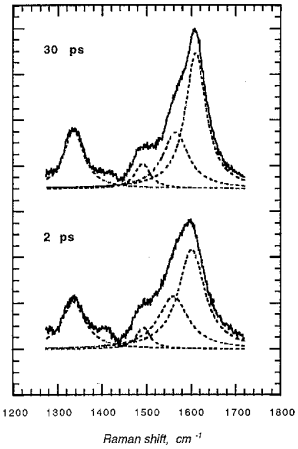

Fig. 3 Fitted TR^3 spectra of CTP in octanol.

Mode-specific reorganisation energies have been estimated previously for charge transfer states using ground state resonance Raman spectroscopy. We observe two modes of CTP which probe intramolecular reorganisation via a change in the frequency of the excited state mode. Moreover, we observe directly the dynamics of the intramolecular component of the reorganisation for each of these modes.

The observation reported in the present work suggest that we are able to elucidate qualitatively two-dimensional diagrams which portray the mode-specific dynamics of the charge transfer reaction for CTP in the spirit of the Sumi-Marcus picture. We postulate that for the 1612 cm^{-1} mode, case (a), the reaction is initiated by fluctuations in the outer-sphere coordinate and then proceeds along the intramolecular coordinate also. Finally, the product is trapped by motion mainly along the solvent coordinate. On the other hand, the picture for the CN stretch coordinate probably involves a fast intramolecular reorganisation contribution, presumably because the displacement along this coordinate is quite large. Stabilisation of the product state along the solvent reorganisation coordinate ensues. A more detailed test of these proposed reaction pathways will be possible from the analysis of better kinetic data than we have obtained so far.

REFERENCES

1) M. Hashimoto and H. Hamaguchi
J. Phys. Chem. 99, 7875 (1995).

2) M.M. Mitambo and G.R. Loppnow
Chem. Phys. Lett. 261, 691 (1996).

3) K. Iwata and H. Hamaguchi
J. Phys. Chem. A 101, 632 (1997).

4) W.L. Weaver, L.A. Huston, K. Iwata and T.L. Gustafson
J. Phys. Chem. 96, 8956 (1992).

REMPI STUDIES OF ADSORBED ALKYL NITRITES

C.J.S.M. Simpson[1)], P.T. Griffiths[1)], M. Towrie[2)]

1) Department of Physical and Theoretical Chemistry, Oxford University
2) Rutherford Appleton Laboratory

INTRODUCTION

Our work at the Lasers for Science Facility has concentrated on detailed studies of the dynamics of the photolysis of adsorbed alkyl nitrites. In order to understand the dynamics of the photochemical processes occurring on dielectric surfaces, we consider that it is most fruitful to compare processes in the gas phase with those of adsorbed molecules. By comparing the (v,J) state of the desorbed products with gas phase data,. the role of the surface and surrounding molecules can be inferred.

This year has seen the extension of our previous experiments on the photolysis of adsorbed alkyl nitrites through the use of the LSF's new tunable optical parametric oscillator source as a photolysis laser. As before, we have used the frequency doubled dye laser for detection of the products of the reaction but have greatly increased the sensitivity of detection by using a new detection scheme. These two developments have yielded many new results.

Alkyl nitrites were chosen for study since they have been extensively studied in the gas phase[1)]. Their absorption spectrum is structured in the region 300-400 nm, corresponding to an ($\pi^* \leftarrow n$) transition with simultaneous excitation of the ν_3, N=O stretching mode. The electronically excited nitrites dissociate promptly to yield NO and alkoxy radicals via a vibrational predissociation mechanism in which one quantum of the N=O stretching vibration is lost. The NO is born highly rotationally excited with a Gaussian distribution of rotational states and with kinetic energies of around 4000cm^{-1} [2,3)].

Dissociation occurs from an approximately planar state of A" symmetry and the rapid dissociation preserves the stereochemistry of the parent molecule in the product NO [2)]. The spectroscopy of NO can be used to study these effects. In particular, the unpaired electron of the product carries a great deal of information: in the high-J limit of NO, the pπ orbital in which this electron is found takes one of two orientations with respect to the plane of rotation of the molecule. These have different symmetries and are known as the Π_8 or Π(A") and the Π_∞ or Π(A') lambda-doublets[1)]. Gas phase experiments have shown a preference for the Π_8 lambda-doublet indicating that the NO retains the A" symmetry of the excited state. The NO product is also found to be to be aligned, with the J vector of the NO product preferentially oriented along the transition dipole of the molecule.

In our previous work[4,5)] we have shown that NO is desorbed in two classes, with about half of the desorbed molecules falling into each class: the first is found over a narrow range of velocities from 2000 to 1000 ms^{-1} and has a Gaussian rotational distribution. We consider that these molecules are desorbed having suffered no collisions with neighbouring molecules or with the dielectric surface. The second class displays a much lower degree of rotational and translational excitation, having a Boltzmann distribution of rotational states with T_{rot}=370 +/- 20 K and a mean velocity of 500 ms^{-1}. This class is desorbed following collisions which deactivate the rotational and translational, but not vibrational, degrees of freedom. In the past year we have used resonance-enhanced multi-photon ionisation (REMPI) spectroscopy to extend the analysis of the NO product to include the study of the spin-orbit components, the lambda doublet population and the effect of photolysis laser polarisation which acts as a probe of the alignment of the product NO.

Recently, gas phase studies have been extended by the application of photofragment yield (PHOFRY) spectroscopy[6,7)]. In this technique, the yield of a (v,J) state of the NO product is monitored as a function of the photolysis laser wavelength. These individual spectra are then summed to give a total PHOFRY spectrum. This is analogous to the absorption spectrum of the parent molecule, provided that all the absorbing molecules dissociate. After a major experimental effort, we have now recorded the PHOFRY spectrum of adsorbed nitrites.

EXPERIMENTAL

In these experiments we choose to work with thin layers of adsorbed nitrites. As before, we chose iso- and tert-butyl nitrites for study.

We have made a significant advance through the use of a (1+1') REMPI detection scheme. In the (1+1') REMPI technique, the frequency-doubled output of an excimer-pumped dye laser system is employed for the resonant excitation step, in this case the $A^2\Sigma^+ \leftarrow X^2\Pi$ transition. A portion of the 308 nm beam which pumps the dye laser ionizes the electronically excited NO. The ionisation beam is optically delayed by around 15 ns for maximum enhancement of the REMPI signal. This results in a 20-fold increase in sensitivity of our detection apparatus over the (1+1) scheme used previously[8)].

The extremely sensitive detection system means that we are able to use very low desorption laser fluences of <0.05 mJ cm^{-2}. These fluences preclude thermal effects in the adsorbate layer and desorb only a very few molecules per shot so that the surface coverage changes very little during the course of an experiment. For these experiments we used the frequency doubled output of the newly installed OPO laser as a photolysis source. While the OPO source gave a much poorer beam profile the low fluences avoided significant desorption from hot spots within the beam. The OPO has the advantages that it is tunable, allowing us to conduct our PHOFRY experiments, and is polarized.

RESULTS

1. Lambda-doublet populations

The analysis of the experiments on both iso- and tert-butyl nitrite shows that there is preferential population of the Π_8 lambda-doublet of NO. Since the lambda-doublets are only well-defined with respect to the plane of rotation of the molecule in the high-J limit, the analysis was confined to the molecules desorbed with Gaussian rotational distributions at velocities of 2000 ms^{-1}. In the case of tert-butyl nitrite, the ratio of Π_8 to Π_∞ was found to be 1.9 +/- 0.2. This is very close to the gas phase value of 2.0 found by Huber and co-workers[9]. The results are shown in Figure 1.

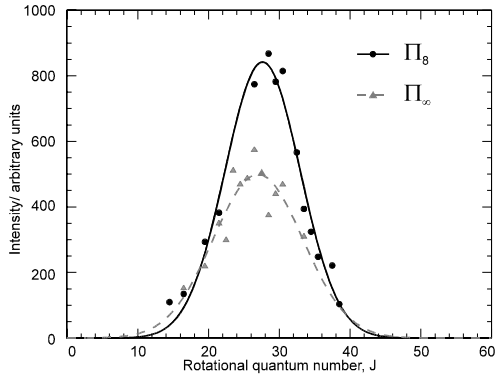

Fig. 1 The relative population of the lambda doublets of NO desorbed from tert-butyl nitrite

2. Spin-orbit components

The ratio of population of the two spin-orbit components of NO desorbed from tert-butyl nitrite is found to vary with the class of molecule: for molecules desorbed with a Gaussian distribution, the ratio $^2\Pi_{1/2}$ to $^2\Pi_{3/2}$ is found to be 1.7 +/- 0.3, while for Boltzmann distributions the ratio is 2.3 +/- 0.5. The variation is shown in Figure 2.

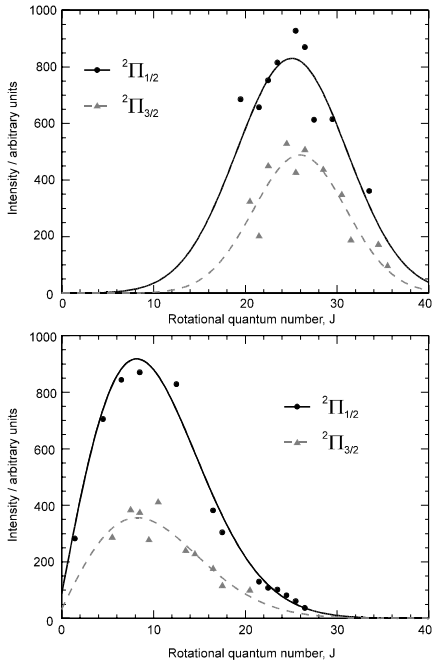

Fig. 2 The variation in population of the two spin-orbit states of NO with class of desorbed molecule. Top panel: Gaussian distribution; lower panel: Boltzmann distribution

3. PHOFRY experiments

The spectrum of adsorbed iso-butyl nitrite was measured over the range 300-400 nm. Individual PHOFRY spectra were recorded for NO(v=0,1,2 and 3) desorbed with J=9.5 to 15.5 and velocities of 500 ms^{-1}. The individual spectra are summed to give the total PHOFRY spectrum, shown in Figure 3, the gas phase spectrum is also shown for comparison. Within the experimental error, there is no significant shift in the peak positions or in their intensites.

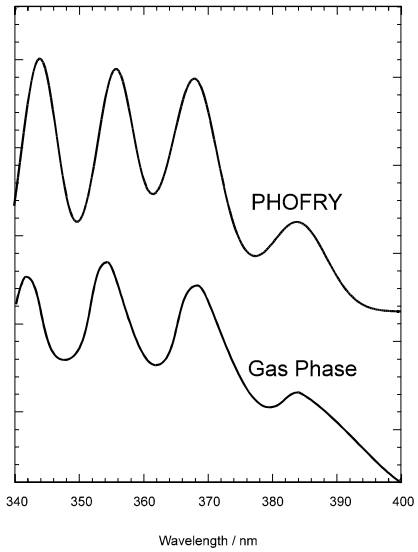

Fig. 3 PHOFRY spectra of adsorbed iso-butyl nitrite. The gas-phase spectrum is shown for comparison

3. Polarisation experiments

Spectra were recorded as a function of the polarisation of the photolysis laser for NO(v=2) desorbed from iso-butyl nitrite with a velocity of 2000 ms^{-1}. The intensity of the Q-branch transitions relative to those of the P- and R- branches was found to depend on the polarisation of the photolysis laser, E(phot), relative to that of the REMPI laser, E(rempi). When E(phot) is parallel to E(rempi), an enhancement of the Q-branch transitions is seen over the P- and R-branches, as shown in Figure 4. When perpendicular there is the opposite enhancement. There was no effect of the polarisation of the photolysis laser on the spectra of NO desorbed with a Boltzmann distribution of NO.

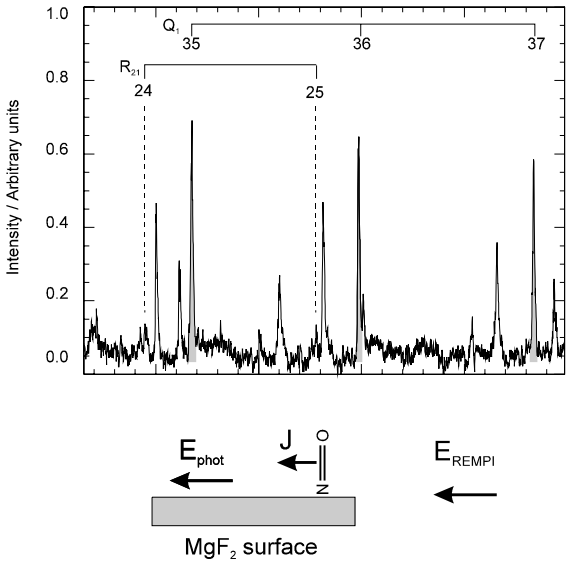

Fig. 4 The effect of photolysis laser polarisation. Our spectra show that NO is born cartwheeling away from the surface for this polarisation

DISCUSSION

We employ dielectric surfaces and low desorption laser fluences in order to avoid surface-assisted processes seen on metallic and semi-conductor surfaces and to concentrate on the photochemistry of the adsorbed molecules. By studying the different degrees of freedom of the desorbed NO, we sample the whole range of intermolecular interactions between molecules. We find that vibration is almost immune to relaxation, while the degree of rotational excitation depends on the velocity of the desorbed NO. Our previous work lead us to suggest that the high velocity NO is desorbed without collisions with neighbouring molecules. We have gone on to test this suggestion with more sensitive probes of the relaxation processes which may occur at the surface.

We have observed that the population ratio of the two $^2\Pi$ states of NO is velocity-dependent, and that at high velocities is close to gas phase values observed by Huber and co-workers. At lower velocities there is an increase in population of the lower $^2\Pi_{1/2}$ state, probably as a result of collisions with the surrounding molecules. Analysis of the lambda-doublet states for NO desorbed with high velocity indicate preferential population of the Π_8 state.

We also observe alignment of the desorbed NO, and find that the angular momentum vector of the desorbed NO is parallel to the polarisation of the photolysis laser. Since this effect depends principally on the photolysis laser we conclude that the aligned NO is desorbed without colliding with surrounding molecules. We conclude that there is no significant relaxation of this class of NO and that for this photolysis laser polarisation the NO molecules leave the surface with a cartwheeling motion relative to the plane of the surface.

REFERENCES

1) H. Reisler, M. Noble and C. Wittig
in Molecular Photodissociation Dynamics, eds. M.N.R. Ashfold and J.E. Baggot (Royal Society of Chemistry, London, 1987) p. 162.

2) U. Bruhlmann, M. Dubs and J.R. Huber
J. Chem. Phys. 86 1249 (1987)

3) B.A. Keller, P. Felder and J.R. Huber
Chem. Phys. Letters, 124 135 (1986).

4) C.J.S.M. Simpson, P.T. Griffiths and M. Towrie
Chem. Phys. Letters, 234 203 (1995).

5) Simpson, P.T. Griffiths, H.L. Wallaart and M. Towrie
Chem. Phys. Letters, 263 19 (1996).

6) J.T. Brandon, S.A. Reid, D.C. Robie and H. Reisler
J. Chem. Phys., 97 5246 (1992).

7) E. Kades, M. Rosslein and J.R. Huber
Chem. Phys. Letters, 209 275 (1993).

8) A.E. Wiskerke, C.A. Taatjes, A.W. Kleyn,
R.J.W.E. Lahaye, S. Stolte, B.K. Bronnikov and B.E. Hayden
Chem. Phys. Letters 216 93 (1993).

9) Kades, M. Rosslein, U. Bruhlmann and J.R. Huber
J. Phys. Chem., 97 989 (1993).

TRIPLET 1-NITRONAPHTHALENE: COMPETITIVE ENERGY AND ELECTRON TRANSFER REACTIONS WITH *TRANS*-STILBENE

S.M. Tavender[1)] , T.Fournier[1)], G.D. Scholes[2)], I.R. Gould[2)], D. Phillips[2)], A.W. Parker[1)]

1) Rutherford Appleton Laboratory, Chilton, Didcot, Oxfordshire., OX11 OQX , UK
2) Department of Chemistry, Imperial College of Science Technology and Medicine, London, SW7 2AY, UK

INTRODUCTION

Most aromatic nitro-molecules are known to be non-fluorescent and their excited states and photochemistry have been the subject of many studies[1-3)]. Triplet 1-nitronaphthalene (1NN) is known to be formed quickly and with a high yield. However, the nature of this state is not clear from the literature; whilst some authors propose π-π* state[4)], others and n-π^* state[5)], some even suggest that the lowest energy state switches from n-π* to π-π* with an increase of solvent polarity[3)].

Previously we reported the time resolved resonance Raman spectra of triplet 1-nitronaphthalene (1NN) and its reaction with trans-stilbene (tS) in solvents of different polarities[6)]. In polar solution, ^{3}1NN acts as an electron acceptor whereas in non-polar solution only energy transfer to tS is observed. Moreover, at high concentrations of tS, the radical cation tS^+ reacts with ground-state tS to form a dimer radical cation $(tS_2)^{+\bullet}$. We now present transient absorption data and *ab initio* calculations to determine the nature and the geometry of this state in environments of different polarity. Differences between the Raman spectra of the monomeric and the dimeric radical cations are reported in the 1500-1650 cm^{-1} region. The switch from energy to electron transfer when going from non-polar to polar solutions is discussed in terms of the Marcus-Hush theory of electron transfer.

RESULTS

The equilibrium ground state geometry of 1NN was determined using an *ab initio* RHF wavefunction with a 6-31G(d,p) basis set and analytical gradients[7)]. Harmonic frequencies were calculated analytically and were found to be in good agreement with the observed Raman frequencies. Equilibrium geometries and harmonic frequencies of the first two excited triplet states were determined using the configuration interaction singles (CIS) method. The calculated structures indicate that the main difference between ground and first triplet state is the change in angle between the C-NO_2 plane and the aromatic plane; 45^o and 37^o in the ground and first triplet state respectively. In each case, atomic charges on the NO_2 moiety were calculated to be *ca.* +0.5 (N) and -0.5 (both O) from a Mulliken population analysis. However, the second triplet state is characterised by a strong change in electron density on the atoms of the nitro group, now roughly 0 (N) and -0.2 (both O), accompanied by an important geometrical change in the NO_2 arrangement: whilst one C-N-O plane is almost perpendicular to the aromatic plane (with the oxygen atom above it), the other C-N-O makes a 48^o angle with the aromatic plane (with the oxygen below it).

The calculations show that the lowest triplet state is of π-π^* nature and the second triplet state, estimated to lie less than 0.1 eV above the former in the gas phase, is of n-π^* type. However, the n-π^* (T_2) state has a lower dipole moment (2.9 D) than the π-π^* (T_1) state (4.9D). Hence, T_2 would not be expected to be stabilised relative to T_1 in a polar solvent. This is consistent with the TR^3 data, where there was little difference in the Raman spectra in non-polar and polar solvents (Fig 1) and the observed frequencies for the lowest triplet state were well in agreement with the calculated ones.

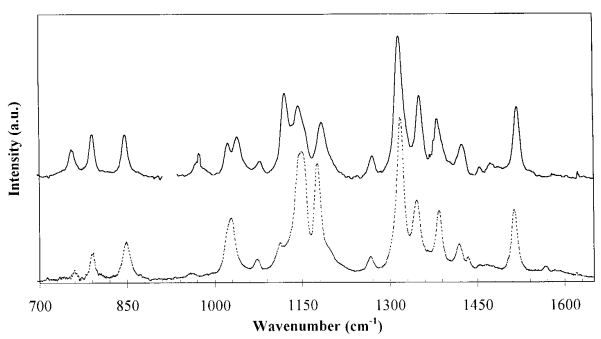

Fig. 1 TR^3 spectra of triplet 1NN in CCl_4 (┈) and MeCN (—).

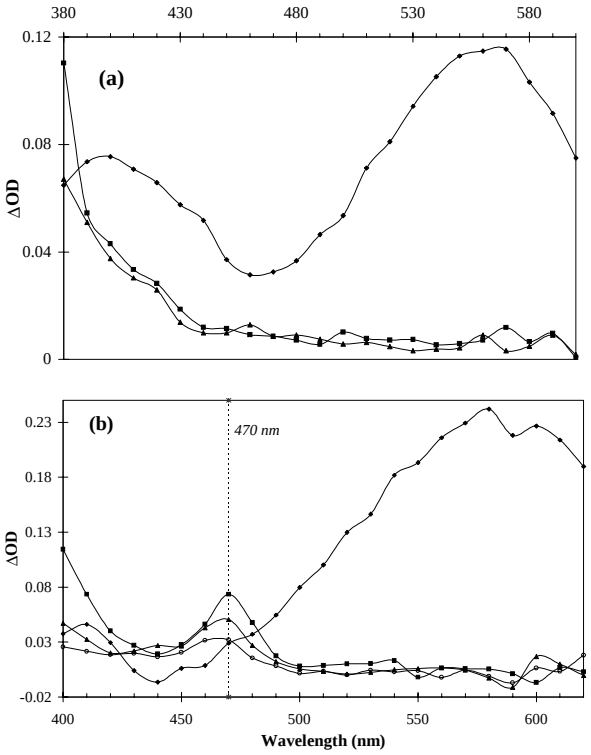

Fig. 2 Differential absorption spectra of 1NN (1 mM) + tS (10 mM) (a) in CCl4 at time delays ◆ 200 ns, ■ 540 ns and ▲ 2ms. (b) in MeCN at time delays ◆ 180 ns, ■ 380 ns, ▲ 1.18 ms and ○ 2.58 ms. Pump 355 nm.

Reactions with trans-stilbene

By exciting 1NN and tS solutions in carbon tetrachloride ($CC1_4$) and acetonitrile (MeCN) with a 355 nm laser pulse (3rd harmonic of a Continuum 8000 Nd:YAG), we obtained the triplet 1NN species, characterised[8)] by a main absorption band at 540 nm ($CC1_4$) or 580 nm (MeCN) (Fig 2). We then observe a quenching of this species and the rise of absorption bands peaking below 380 nm ($CC1_4$) and at 470 nm (MeCN). In MeCN and with high tS concentrations we can identify the formation of the dimer radical cation of tS by a shift towards 465 nm. These absorptions are characteristic of the triplet excited state of tS[9)], its radical cation[10)], $tS^{+\bullet}$, and a dimeric species formed by reaction of $tS^{+\bullet}$ with ground state tS[10)], $(tS)_2^{+\bullet}$, respectively. The absence of tS^+ in non-polar solution was confirmed by a TR^3 experiment performed with a probe laser beam at 480 nm (Continuum Sunlite^{TM} OPO). However, in MeCN, the radical cation $tS^{+\bullet}$ is characterised in the 1500-1650 cm^{-1} region by two bands at 1570 and 1607 cm^{-1} (Fig 3) as well as a shoulder at *ca* 1590 cm^{-1}, whereas the shoulder is absent from the vibrational spectrum of $(tS)_2^{+\bullet}$ and also the

band at 1607 cm^{-1} is more intense relative to the band at 1570 cm^{-1} for the $tS^{+\bullet}$. These observations are consistent with calculations of the vibrational frequencies of the ions of various stilbenes[11] and a recent Raman study of tS monomeric and dimeric cations produced by UV irradiation in boric acid matrices[12].

DISCUSSION

Using Marcus-Hush theory[13,14], the rate of electron transfer can be written as in equation (1)

$$k_{ET} \approx \frac{2\pi}{\hbar}|V|^2(\mathrm{FCWD}) \qquad (1)$$

with

$$(\mathrm{FCWD}) \approx (4\pi\lambda_s k_B T)^{-\frac{1}{2}} \exp\left(-\Delta G^{\ddagger} / k_B T\right) \qquad (2)$$

where

$$\Delta G^{\ddagger} \approx \left(\Delta G + \lambda_s\right)^2 / 4\lambda_s - V \qquad (3)$$

with V on the order of 0.02 eV is generally negligible.

The free energy (ΔG) of the electron transfer reaction may be estimated using the theory of Rehm-Weller[15] by equation 4.

$$\Delta G \approx E^{ox}_{\frac{1}{2}}(\mathrm{D}) - E^{red}_{\frac{1}{2}}(\mathrm{A}) - E_T + \frac{e^2}{4\pi\varepsilon_0}\left\{\frac{1}{2r_+}\left(\frac{1}{\varepsilon}-\frac{1}{\varepsilon'}\right)+\frac{1}{2r_-}\left(\frac{1}{\varepsilon}-\frac{1}{\varepsilon''}\right)\right\} - \frac{e^2}{4\pi\varepsilon R} \qquad (4)$$

and the solvent reorganisation energy may be approximated by equation 5

$$\lambda_s \approx \frac{e^2}{4\pi\varepsilon_0}\left(\frac{1}{2r_+}+\frac{1}{2r_-}-\frac{1}{R}\right)\left(\frac{1}{n^2}-\frac{1}{\varepsilon}\right) \qquad (5)$$

where $E_{½}^{red}$(A) is the halfwave potential for reduction of the electron accceptor (measured in solvent with dielectric constant ε'), $E_{½}^{ox}$(D) the halfwave potential for oxidation of the donor (measured in solvent with dielectric constant ε"), E_T is the energy of the triplet. The solvent has refractive index n and dielectric constant ε, r_+ and r_- denote the radii of cation and anion respectively and R is their separation. Hence we can show that the experimental observations can be explained simply[16].

We emphasise that the above equations are very approximate, but can serve as a useful guide to the relative probabilities of electron transfer reactions. In the present work we use them as follows: If the free energy of the reaction from equation 4 is positive, then the electron transfer reaction will probably not occur. If it is found to be negative, then we examine the activation barrier for the reaction via equation 3.

To examine the thermodynamic factors for the electron transfer reaction between 1NN and tS, we use the following values for the parameters in eqs 2-4: $E_{½}^{red}$(1NN) = -0.97 V (vs SCE in dimethylformamide[17]), $E_{½}^{ox}$(tS) = +1.43 V (vs SCE in MeCN[17]), E_T(1NN) = 2.39 eV, r_+(tS) = 4 Å, r_-(1NN) = 3 Å and R = 5 Å for 1NN and tS, and ε = 36, n = 1.36 for MeCN, ε = 2.2, n = 1.46 for CCl_4, ε = 9.0, n = 1.42 for DCM, and ε = 37 for DMF. Consequently it is found that approximate free energies for the reaction in various solvents are 0.50 eV (CCl_4), 0.04 eV (DCM) and -0.07 eV (MeCN). Thus it is expected that the electron transfer reaction is possible only in quite polar solvent (MeCN), with an activation barrier determined by $\Delta G^{\ddagger}$ = 0.14 - V eV. This is consistent with our experimental observations.

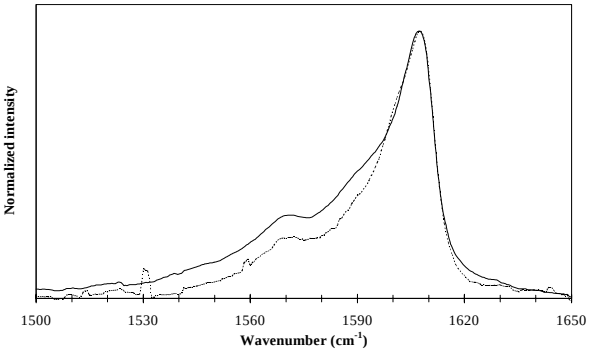

Fig. 3 Normalised TR^3 spectra of 1NN (2mM) + tS (3mM) in MeCN at time delays 50 ns (—) and 1 μs (---). Pump 360 nm, probe 480 nm.

CONCLUSION

Ab initio calculations of the first triplet excited state of 1NN in various solvents have shown the nature of this state in environments of different polarities which have agreed with our experimental data. We have studied the quenching of ^{3}1NN by tS in various solvents. By recording the resonance Raman spectra of solutions containing various amount of tS we have been able to demonstrate some subtle differences in the vibrational spectra of the monomeric and dimeric radical cation species of tS in solution. Moreover, by comparing the reactions occurring in solvents of different polarities it was found that energy and electron transfer reactions compete, with their relative probabilities determined primarily by the thermodynamics of the electron transfer, in accordance with Marcus-Hush theory.

ACKNOWLEGEMENTS

This work was supported by the Engineering and Physical Science Research Council (Grant GR/K20989). Grants from the EEC Human Capital and Mobility Programme (Grant ERBCHBICT941642 supporting T. F.) and the Ramsay Memorial Trust (supporting G. D. S.) are also gratefully acknowledged. Dr Andrew Clayton is gratefully acknowledged for discussions concerning electron transfer.

REFERENCES

1) O Khalil, H Bach , S McGlynn
J. Mol. Spec. 35 455 (1970)
2) H Ohtani, T Kobayashi, K Suzuki, S Nagakura
Bull. Chem. Soc. Jpn. 43 (1980)
3) Y Shioya, M Yagi, J Higuchi
Chem. Phys. Lett. 154 25 (1989)
4) R Rusakowicz, A Testa
Spectrochim. Acta A 27A 787 (1971)
5) J Bolton, N Mataga, G McLendon, Eds,
Advances in Chemistry Series 22 Am Chem Soc (1991)
6) T Fournier , G Scholes, D Phillips, S Tavender,A W Parker
CLF Ann Rep 123 (1996)
7) M. J. Frisch *et al*,
Gaussian 94, Rev C.2, Gaussian, Inc., Pittsburgh PA, (1995)
8) C Capellos, G Porter
J. Chem. Soc., Farad Trans. 2 (70) 1159 (1974)
9) H Görner, D Schulte-Frohlinde
J. Phys. Chem., 85 1835 (1981)
10) R Akaba, H Sakuragi, K Tokumaru,Y Yoshida, S Tagwa
Bull. Chem. Soc. Jpn. 66 1852 (1993)
11) S Schneider, C Scharnagl, R Bug, G Baranovic, Z Meic
J. Phys. Chem. 96 9748 (1992)
12) Y Kuriyama, S Oishi
Chem. Lett., 149 (1995)
13) R Marcus
Ann. Rev. Phys. Chem. 15 155 (1964)
14) N Hush
Electrochim. Acta 13 1005 (1968)
15) D Rehm, A Weller
Isr. J. Chem., 8 259 (1970)
16) T Fournier, S Tavender, A Parker, G Scholes, D Phillips
Accepted for publication in J. Phys. Chem.
17) L Meites, P Zuman,
CRC handbook series in Organic Photochem Vol I-IV: CRC press, Inc., Boca Raton, Florida, USA (1977-82)

SECOND HARMONIC STUDIES OF SI GROWTH ON SI(001) SURFACES DURING GAS SOURCE MOLECULAR BEAM EPITAXY

A.G.Taylor[2], A.K.Lees[1] and J.Zhang[1]

1) IRC for Semiconductor Materials, Imperial College of Science Technology and Medicine, Blackett Laboratory, Prince Consort Road, London SW7 2BY.

2) Department of Chemistry and IRC for Semiconductor Materials, Imperial College of Science Technology and Medicine, London SW7 2AY. email a.g.taylor@ic.ac.uk.

INTRODUCTION

The use of surface second harmonic generation(SHG) to probe interfaces has been growing steadily. In particular studies on centrosymmetric semiconductor materials, primarily crystalline Si, have been numerous[1-9]. This, in part, derives from the search for alternative surface diagnostics to assist in the evaluation of semiconductor film growth. Many electronic materials are grown by chemical vapour deposition(CVD) at or near ambient pressures. In these pressure regimes the more traditional electron beam based surface diagnostics cannot be used.

In this article we present some preliminary studies of SHG measurements recorded during actual semiconductor growth. This represents the first time that SHG has been reported for a growing Si surface. The measurements were carried out in a UHV gas source molecular beam epitaxy(GSMBE) reactor. This enabled simultaneous measurements of SHG and reflection high energy electron diffraction(RHEED) patterns. We were therefore able to monitor the state of our surface and define the crystallographic orientation.

EXPERIMENTAL

The fundamental output of a Spectron SL805G Nd:YAG laser was steered into the reaction chamber by use of high energy mirrors such that the angle of incidence between the laser beam and the surface normal was 70°. It was necessary to use a long pass filter immediately prior to the reactor to remove any coaxial flash lamp radiation and any SHG generated by the optical chain. The polarisation state used was exclusively p polarisation with respect to the Si surface. The reflected near infrared radiation was filtered out from any second harmonic radiation by the use of a number of short pass filters and an interference filter chosen to accept only 532nm light. The polarisation state of the second harmonic signal collected was selected to be p polarised also. The SH signal was detected by a photomultiplier tube and processed with a boxcar averager assembly. The incident laser power was of the order 60mJ/cm^2 in a 5-7ns pulse.

The GSMBE system has been described in detail elsewhere[10] and is capable of growing high quality Si epilayers. The Si(001) wafers used here were misoriented 6° towards the [110] direction. They were prepared by a standard HF etch procedure, introduced into a load lock, outgassed and transferred into the reactor chamber. Before use a 1000Å Si buffer layer was grown and the wafer annealed to ~900°C to smooth the surface. At regular intervals the RHEED diffraction pattern was monitored to check the state of the surface.

RESULTS

The surface SHG signal was recorded as a function of temperature during a short film growth cycle. Figure 1 shows the SHG signal as a function of time. Initially the SHG from the wafer was recorded under UHV background pressures. At 180 seconds the wafer was exposed to disilane gas at a pressure of 1.5 x 10^{-4} mbar . The total exposure time was 240 seconds. The disilane source was closed and the chamber pressure rapidly returned to UHV conditions. As can be seen from the figure, exposure of the surface to disilane led to a drop in the SH signal. The SHG level was relatively constant after 60 seconds exposure. During the whole exposure time the semiconductor film was growing at a rate of a few monolayers per minute. Thus for an exposure time of 240 seconds some 15 monolayers of Si were deposited.

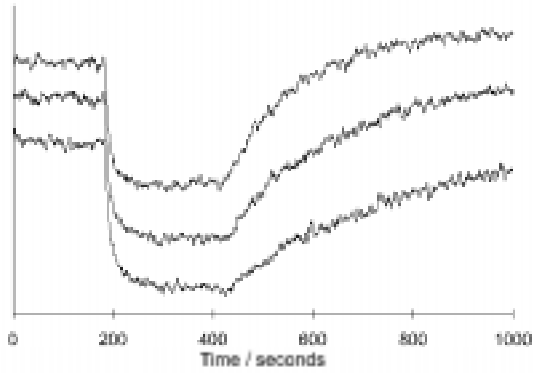

Figure 1. A plot of the square root of the measured SHG intensity versus time. The top graph was recorded at 470°C, the middle graph at 455°C and the bottom graph at 445°C. The graphs have been offset vertically for clarity.

Upon interruption of the disilane supply the SHG signal intensity recovered to its initial position. As can be seen from the figure the recovery rate shows a marked temperature dependence.

In order to test if the alignment of the wafer with respect to the incident electric vector of the light source an additional experiment was carried out.

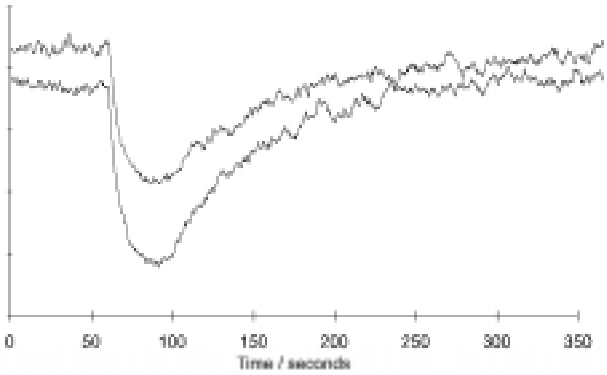

Figure 2. A plot of the square root of the measured SHG intensity versus time This was recorded for a 30 second exposure to disilane at 500°C. The upper graph was recorded when the incident electric vector was perpendicular to the surface step edges, whilst the lower graph has the incident electric vector parallel to the step edge. The graphs are offset for clarity.

There is clearly a difference in the data recorded for each case. In particular the gradients of the data subsequent to exposure are different, as is the initial magnitude of the change in SHG on exposure. Under these conditions a steady state SHG signal

during growth was not reached due to the shorter exposure time.

DISCUSSION

In a number of studies by Höfer and co-workers[3-5] the associative desorption of molecular hydrogen from Si(001) surfaces has been reported. These authors state that the SHG intensity depends in a linear fashion on the surface hydride coverage at low exposures, in that, the SHG intensity falls as hydride coverage increases. The surface non-linear susceptibility, which is measured by the square root of the collected SHG intensity, was found to be linear only in the range 0-0.15 of a monolayer. This study was based on SHG data obtained from surfaces exposed to hydrogen and calibrated with temperature programmed desorption methods(TPD). The most widely held view of the Si(001) surface in the presence of surface hydride is that the localised Si dimers can accommodate either one hydrogen atom each and maintain a dimer reconstruction or, at higher coverages exist in a dihydride surface phase. In each case bonding reduces the number of electrons directly involved in Si-Si bonds. In line with the above work, exposure of Si to disilane gives rise to a drop in the surface non-linear susceptibility. This is because during growth the concentration of surface hydrogen is increased. The length of exposure reported in Fig 1 shows that after a 60 second exposure, the surface non-linear susceptibility no longer changes. This must suggest that no additional surface hydride concentration can build up and that the growing surface is saturated with hydrogen. The non-linearity does not change despite the fact that the surface is growing. For shorter exposure time and higher temperatures, such as in Figure 2, the surface does not become saturated with hydrogen.

Interruption of growth leads to hydrogen desorption. The change in the SHG signal at high coverage is most definitely not first order in hydride coverage, whilst at later times and lower coverage it may be possible to fit a linear plot to the data. Clearly as the temperature dependence of the data suggests the process is not barrier less.

The data of Figure 2 demonstrate unequivocally that great care should be taken in extracting SHG data from Si surfaces. These experiments show that the shape of the SHG versus time curve is dependent on exactly which experimental geometry is chosen. The effect of step edges on SHG from Si has been examined by van Driel and co-workers[7] and they found that for static systems with stepped surfaces the overall non-linearity was strongly affected by the number of steps. They suggest that the overall susceptibility is a combination of both surface and step effects. We have demonstrated that there is an effect of the step edges on the observed form of the SHG versus hydride dependence, particularly at high coverages. In our cases the wafers were chosen to be 6° misorientated to provide highly stepped surfaces. The detailed effect of misorientaion on the SHG signal will be the subject of further studies.

CONCLUSIONS

We have demonstrated that *in-situ* SHG measurements can be made of growing Si surfaces in a GSMBE reactor, and have reported the first ever SHG data from a growing Si surface. The fact that no change in SHG intensity was observed during growth confirms that the surface hydride concentration does not change during growth, at least within the signal to noise ratio of our experiment. The surface non-linearity was found to change in the presence of disilane chemisorption as can be expected. Care must be taken in interpreting SHG data at high coverages and the role of surface steps in altering the surface non-linearity is not yet clear.

ACKNOWLEDGEMENTS

We would like to thank the LSF for the loan of experimental equipment and Prof.B.A.Joyce at the IRC for Semiconductor materials for access to the GSMBE reactor. We would also like to thank the EPSRC for financial support for the ongoing Si project at the IRC and for the provision of a studentship for A.K.Lees and a fellowship for J.Zhang.

REFERENCES.

1) H.W.K. Tom, T.F.Heinz and Y.R.Shen
Phys.Rev.Letts., 51, 1983, (1983).

2) T.F.Heinz, M.M.T.Loy and W.A.Thompson
Phys. Rev. Letts., 54, 6 (1985).

3) U.Höfer, L.Li and T.F.Heinz
Phys Rev. B, 45, 9485, (1992).

4) P.Bratu, K.L.Kompa and U.Höfer
Chem.Phys.Letts., 251, 1, (1996).

5) W.Brenig, A.Gross, U.Höfer and R.Russ
Phys. Stat.Sol. A, 159, (1997),75.

6) J.A.Litwin, J.E.Sipe, and H.M. van Driel
Phys. Rev.B., 31, 5543 (1985),.

7) G.Lüpke, D.J.Bottomley, and H.M.van Driel
Phys.Rev.B, 47, 10389, (1993).

8) J.S.Power, S.Chandola, J.D.O'Mahony, P.Weightman and J.F.McGilp
Surface Science, 352-354, 337, (1996).

9) H.B.Jiang, Y.H.Liu, X.Z.Lu, W.C.Wangf, J.B.Zheng and Z.M.Zhang
Phys.Rev.B, 50, 14621, (1994).

10) Zhang, A. Marinopoulou, J.Hartung, E.C.Lightowlers, N.Anwar, G.Parry, M.H.Xie, S.M.Mokler, X.D.Wu and B.A.Joyce
J.Vac.Sci.Technol., A,12, 806, (1994).

PICOSECOND TIME RESOLVED RESONANCE RAMAN EXCITATION PROFILES AND ABSORPTION SPECTRA OF PHOTOEXCITED QUATERPHENYL IN SOLUTION

W T Toner [1)] , P Matousek [2)] , A W Parker [2)] and M Towrie [2)]

1) Clarendon Laboratory, Department of Physics, University of Oxford, Parks Road, Oxford OX1 3PU, UK
email W.T.Toner @RL.AC.UK
2) Rutherford Appleton Laboratory, Chilton, Didcot, Oxon, OX11 0QX, UK

In the first twenty picoseconds following the photoexcitation of molecules in solution, changes are observed in the frequencies, widths and intensities of Stokes resonance Raman bands[1,2,3,4] . The changes in frequency and width are similar to those induced by cooling the solvent bath but differ in the relative sizes of the frequency shift and bandwidth change[2)]. The changes in intensity could not be interpreted unambiguously in the absence of Raman excitation profiles but suggested the possible existence of short-lived conformers. The present work was undertaken to clarify these observations.

Resonance Raman and absorption spectra of S_1 quaterphenyl in solution were measured with ~ 1 ps resolution using a 40 kHz laser-OPA system[5)]. The pump wavelength was 277 nm, providing approximately 5000 cm^{-1} of excess photoexcitation energy. The spectrally filtered output of the OPA provided a transform-limited Raman probe tunable over a wide range of wavelengths. White light continuum was used for the transient absorption measurements.

All prominent bands in the transient absorbance shown in Fig. 1 shift to the blue between 2 and 50 ps by ~ 0.4% of the resonance energy (64 cm^{-1}) and reduce in width by ~10% (40 cm^{-1}). The evolution is smooth, with a 17 ps time constant, and the changes in width track the frequency shift. Cooling the bath at fixed time by 37 +/- 5 ^{0}C produces the same reduction in 0-0 bandwidth as does relaxation but cooling produces a small red-shift of the resonance frequency. The 766 cm^{-1} Raman band shifts to the blue by ~0.1% and reduces in width by ~ 5% between 0 and 50 ps. It exhibits the same difference between relaxation and cooling as shown by the electronic resonance.

The similarity of the electronic and Raman band changes indicates vibronic coupling. Much larger electronic shifts (due to solvation differences between ground and excited states) are seen on shorter timescales in many molecules but in some cases residual shifts persist to many picoseconds[6)]. We suggest that hitherto unresolved potential changes may also be responsible for the Raman shifts observed in the other cases referred to.

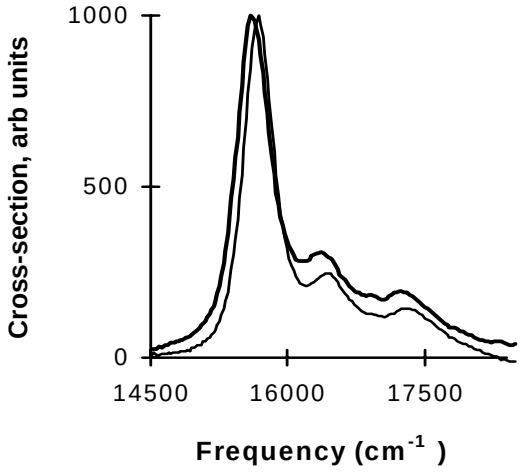

Fig. 1 Transient absorbance of S_1 quaterphenyl in THF at 2 ps (bold line) and 50 ps (light line). Room temperature.

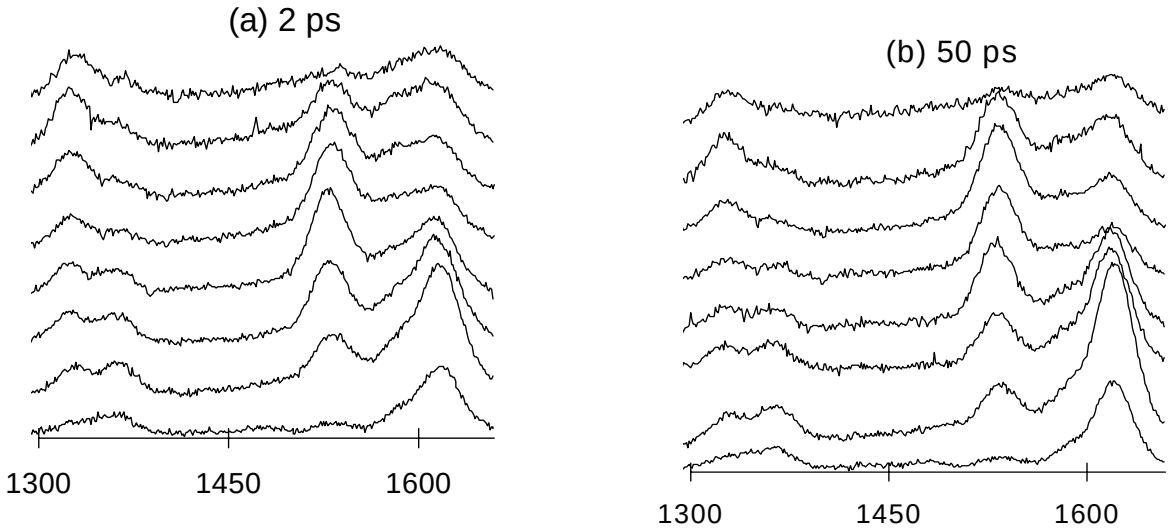

Fig. 2 Resonance Raman Spectra of S_1 quaterphenyl in THF at (a) 2 and (b) 50 ps after photoexcitation. Raman frequencies in cm^{-1}. Probe wavelengths (from top to bottom): 601, 606, 611, 621, 626, 631 and 641 nm.

Resonance Raman spectra of S_1 quaterphenyl are shown in Fig. 2. The sharp variation with probe wavelength is due to the small width of the transient absorption spectrum. The spectra also have a complex time dependence.

Ratios of Raman excitation profiles (REPs) computed from the data in Fig. 1 are compared with measured intensity ratios in Fig. 3, and Fig. 4 is a comparison of the 766 cm^{-1} intensity with the computed REP. Bands at 1624 and 766 cm^{-1} are identified as fundamentals and the 1532 cm^{-1} band as the first overtone of 766. This mode evidently has little anharmonicity. Franck-Condon displacement ratios deduced from this data show significant changes with time and temperature. The observed changes in resonance parameters and displacements fully account for the Stokes intensity changes.

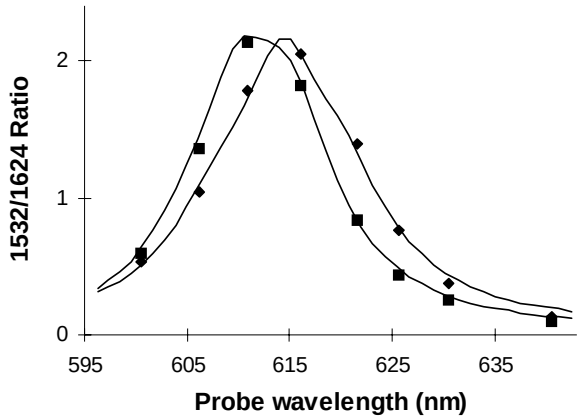

Fig.3 Ratio of intensities of 1532 and 1624 cm^{-1} bands at 2 ps (diamonds) and 50 ps (squares). Curves are REPs computed from data of Fig. 1 assuming 1532 band is overtone.

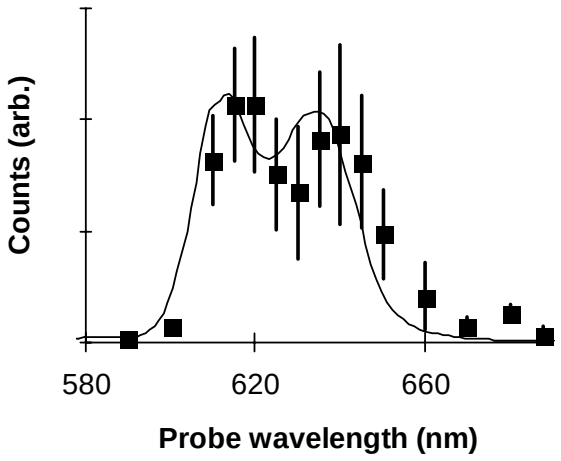

Fig. 4 Computed (line) and measured (points) excitation profile of 766 cm^{-1} Stokes band.

The time-dependence of the 766 cm^{-1} anti-Stokes intensity is shown in Fig 5. The initial transient is attributed to ultrafast energy transfer from v > 1 levels to other nearby modes. Since the REPs and Stokes data indicate that resonance and displacement changes should have < 10% effect on the anti-Stokes intensity at the 676.5 nm probe wavelength used, the subsequent slower decrease is taken as due to the decay of a residual hot population in v = 1. At 2 ps, the population excess corresponds to a temperature 175+/-100 ^{0}C above the bath, which is much larger than the 37 ^{0}C deduced from the bandwidth change. This mode has little anharmonicity and appears isolated; both factors may contribute to its slow decay. As few modes are likely to share such properties it is estimated that the total population energy is no more than a few times the ~ 60 cm^{-1} per molecule observed in this mode.

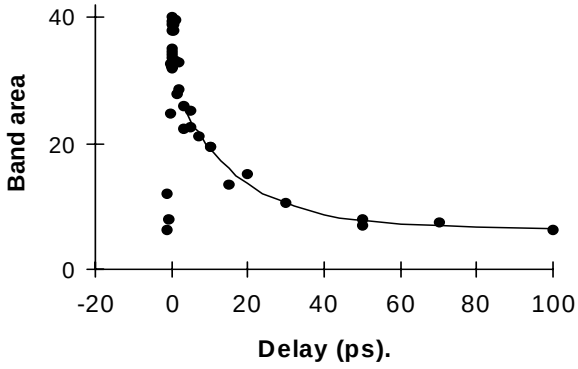

Fig. 5 Time dependence of 766 cm^{-1} anti-Stokes intensity. Curve is exp(t/17ps) plus constant.

CONCLUSION

The data show that changes in the frequency and width of the S_1 - S_n electronic resonance together with changes in Franck-Condon displacements fully account for the observed time and temperature dependence of the Stokes Raman band intensities. The similarity of the electronic and vibrational frequency and width changes suggests vibronic coupling in which electronic potential changes, perhaps due to solvent reorganisation, drive the vibrational changes. Relaxation and cooling are seen to differ. An excess v=1 population in the 766 cm^{-1} mode is seen to decay on the same 17 ps timescale. It is an open question whether this is causally related to the potential changes. A more complete account of this work has been submitted for publication[7].

REFERENCES

1) W.L.Weaver, L.A.Houston, K.Iwata and T.L. Gustafson J. Phys. Chem. **96,** 8956 (1992); K.Iwata and H.Hamaguchi, Chem. Phys. Lett. **196,** 462 (1992).

2) R.E.Hester, P.Matousek, J.N.Moore, A.W.Parker, W.T.Toner and M.Towrie
Chem. Phys. Lett. **208,** 471 (1993).

3) R.M.Butler, M.A.Lynn and T.L.Gustafson
J.Phys.Chem. **97,** 2609 (1993); D.L.Morris,Jr.and T.L.Gustafson, Appl. Phys. B**59,** 389 (1994); J. Phys. Chem. **98,** 6275 (1994).

4) M.Towrie, P.Matousek, A.W.Parker, W.T.Toner and R.E.Hester
Spectrochim. Acta **A51,** 2491(1995).

5) P.Matousek, A.W.Parker, P.F.Taday, W.T.Toner and M.Towrie
Opt. Comm. **127,** 307 (1996).

6) M.L. Hornig,, J.A.Gardecki, A.Papazyan, and M.Maroncelli J. Phys. Chem. **99**, 17311 (1995).

7) P.Matousek, A.W.Parker, M.Towrie and W.T.Toner (1997)

PHOTOPHYSICS OF CYANINE DYES ADSORBED ONTO SURFACES: SUB-NANOSECOND FLUORESCENCE LIFETIME MEASUREMENTS OF 3,3´-DIETHYLOXADICARBOCYANINE IODIDE AND PHOTOISOMER

L.F. Vieira Ferreira[1], A.S. Oliveira[1], K. Henbest[2], D.R. Worrall[3], F. Wilkinson[3]

1) Centro de Química-Física Molecular, Complexo I, IST, 1096 Lisboa Codex, Portugal
2) Central Laser Facility, Rutherford Appleton Laboratory, Didcot OX11 0QX, U.K.
3) Loughborough University, Loughborough, Leicestershire, LE11 3TU, U.K.

INTRODUCTION

3,3´-dDiethyloxadicarbocyanine iodide (DODCI) is commonly used as saturable absorber for mode-locking dye lasers and as a laser dye for pulsed operation, tuneable around 660 nm.

In recently published work [1] we described the behaviour of this dye when adsorbed onto a natural polymer, microcrystalline cellulose. In the range of concentration under study (from 0.005 to 25 μmol of dye per gram of cellulose) this dye exhibits sandwich type ground state dimers (H aggregates) and the degree of aggregation is dependent on the degree of hydration of the sample.

Both steady state and laser-excited fluorescence emission are dependent on the concentration of the dye on the surface of cellulose. For very low loadings of the dye only singlet excited monomers (M*) emit while for higher loadings a second emission band was observed superimposed on the normal monomer emission and peaking at about 655 nm. This emission was seen when high laser fluences were used (~ 40 mJ per pulse and per square centimetre) [1]. Similar effects were reported for 2,2'-carbocyanine iodide adsorbed onto the same substrate [2].

Previously reported solution studies [3] have shown that DODCI monomer M* and photoisomer N* fluorescence emissions were detected simultaneously from concentrated solutions of the dye in ethanol both with picosecond and microsecond laser pulses. When the energy content of the excitation pulse was reduced by calibrated neutral density filters, the N* fluorescence became weaker and the fluorescence spectra became more like M*.

Our recent report [1] shows this sharp new emission of the dye adsorbed onto microcrystalline cellulose for laser excitation and also a similar emission band (broader in this case) for the same samples obtained with a spectrophotometer.

The present study is a continuation of this work. Sub nanosecond lifetime measurements were performed for dry samples of DODCI adsorbed onto microcrystalline cellulose ranging from 0.02 to 10.0 micromoles of dye per gram of the substrate, to evaluate both M* and N* lifetimes.

EXPERIMENTAL

Ground-state absorption spectra and steady-state or laser induced fluorescence emission spectra of powdered samples were obtained using the methods and apparatus described in references [1,2] and references therein.

Sub-nanosecond lifetime measurements of DODCI adsorbed onto microcrystalline cellulose was made by the use of a fluorescence microscope described in detail in reference [4]. Dye laser excitation pulses were approximately 10 ps halfwidth. The excitation wavelength used in this work was 580 nm and the dye laser pulse repetition rate was 0.8 kHz. In some cases band pass filters were used to separate M* emission from the excited photoisomer and neutral density filters to reduce laser energy. Data was recorded every 250 ps after excitation using a 500 ps time gate.

RESULTS AND DISCUSSION

Steady-state fluorescence spectra of three dry samples exciting with a 450W Xenon lamp at 530 nm are presented in figure 1. Spectra were obtained with full lamp intensity and also with a reduction of the exciting light to 20% by the use of a neutral density filter.

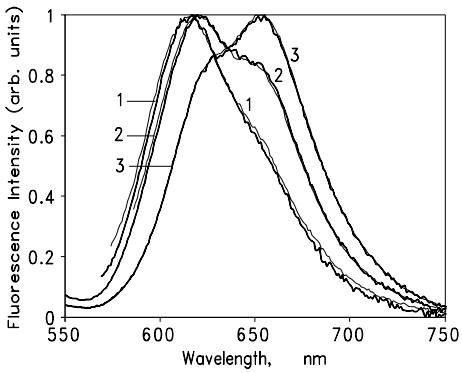

Figure 1 Steady-state emission spectra from dried samples of DODCI on microcrystalline cellulose, excited at 530 nm ----- full lamp ..... 20%. Sample concentration: (1) 0.05, (2) 0.30 and (3) 4.2 μmol g^{-1}.

The perfect superposition of the two spectra for each sample suggest that M and N are already formed in the ground state and that emission spectra reflect the relative ground-sate population independently of the number of photons used to excite the sample.

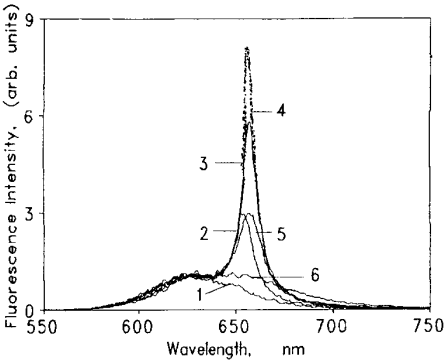

Figure 2 Laser induced fluorescence spectra for DODCI adsorbed onto microcrystalline cellulose, exciting at 532 nm and as a function of the dye concentration. Sample concentration is: (1) 0.02, (2) 0.05, (3) 0.10, (4) 0.30, (5) 1.0, (6) 4.2 μmol g^{-1}.

A powerful Nd:YAG pulsed laser was used (8ns excitation pulse width at 532 nm, ~ 40 mJ per pulse) and the obtained emission spectra are shown in figure 2. The photoisomer emission maximum peaks at ~ 655 nm (the same maximum as in figure 1, curve 3), but an intense peak instead of a broad

band exists now. This was interpreted as amplified spontaneous emission (ASE) acting to narrow the metastable photoisomer emission on cellulose [1]. Figure 3 shows some of the fluorescence decay curves obtained with a 10 ps laser excitation as a function of the sample concentration.

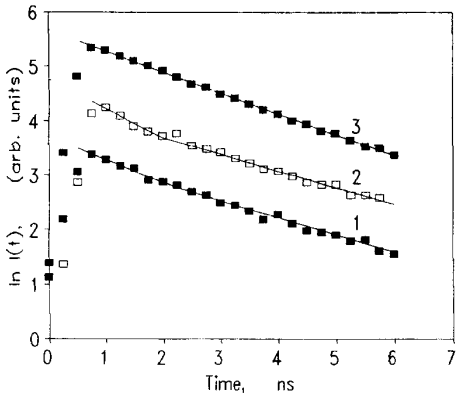

Figure 3 Fluorescence decay curves for DODCI adsorbed onto microcrystalline cellulose, exciting at 580nm and as a function of the dye concentration. Sample concentration is: (1) 0.02, (2) 0.30 and (3) 4.20 μmol g^{-1}.

In this system, a dichroic filter was used to separate laser excitation from fluorescence and the intensified CCD only detects $\lambda \geq 625$ nm. This obviously means that N* emission decay is amplified when compared with M* emission decay. At low loadings, two emissions were detected and as the concentration of DODCI increases, N* becomes predominant.

The decay curves presented in figure 3, together with data from Table 1, clearly show that the excited monomer lifetime is 1.6 ± 0.1 ns and that of the excited photoisomer is 2.7± 0.1 ns.

These values can be compared with τ_{N*}(ethanol) = 330 ps [3] and τ_{M*}(ethanol) = 1.25 ns [5] at room temperature.

Conc./ μmolg^{-1}	*0.02*	*0.05*	*0.10*	*0.30*	*0.50*	*1.0*	*4.2*	*10*
τ_{N*}/*ns*	2.70	2.78	2.73	2.77	2.75	2.65	2.63	2.67
τ_{M*}/*ns*	1.68	1.59	1.64	1.56	-	-	-	-

Table 1 Lifetimes of singlet monomer and photoisomer of DODCI adsorbed onto microcrystalline cellulose.

In conclusion, when cellulose matrix is swollen by the use of ethanol as solvent for sample preparation (see references [1,2] and references therein), DODCI stays entrapped between the polymer chains and nonradiative pathways for deactivation (internal conversion and trans-cis isomerization) are reduced, not only for M* but especially for N* which lives about one order of magnitude longer than in homogeneous media.

REFERENCES

1) A.S. Oliveira, L.F. Vieira Ferreira, D.R. Worrall, F.Wilkinson
Chem. Soc., Faraday Trans., **92** (1996) 4809.

2) L.F. Vieira Ferreira, A.S. Oliveira, D.R. Worrall, F.Wilkinson
J. Chem. Soc., Faraday Trans., **92** (1996) 1217.

3) E.G. Arthurs, D.J. Bradley, A.G. Roddie
Chem.Phys.Lett., **22** (1973) 230.

4) A.D. Scully, A.J. MacRobert, S. Botchway, P. O´Neill, A.W.Parker, R.B. Ostler, D. Phillips
J. Fluorescence, **6** (1996) 119.

5) D.N. Dempster, T. Morrow, R. Rankin, G.F. Thompson
J.Chem. Soc., Faraday Trans.2, **68** (1972) 1479.

CHARACTERISATION AND IMPLEMENTATION OF A LASER PLASMA SOURCE IN THE VUV

[1)]R.M. Allott, [1)]I.C.E. Turcu, [1)]N. Lisi, [1)]N. Spencer, [1)]W. Shaikh, [2)]A. Whybrew,
[3)]S. Wang, [3)]R. Donovan, [3)]K. Lawley, [4)]K. Ledingham, [5)]M. Folkard, [5)]K. Prise

1) Rutherford Appleton Laboratory, Chilton, Didcot, Oxon, OX110QX, UK
2) Clarendon Laboratory, University of Oxford, Oxford, OX13PU, UK
3) Department of Chemistry, University Edinburgh, King's Buildings, West Mains Road, Edinburgh, EH9 3JJ, UK
4) Department of Physics, University Glasgow, Glasgow, G12 8QQ, UK
5) Gray Laboratory Cancer Research Trust, Mount Vernon Hospital, Northwood, Middlesex, HA6 2JR, UK

INTRODUCTION

Leading edge research in molecular dynamics, photoelectron spectroscopy, surface interactions and radiobiology has pushed forward the requirement for intense, pulsed, tuneable sources of vacuum ultraviolet radiation. Presently, only synchrotron radiation sources (SRS) are sufficiently bright for these applications. A bright, continuously tuneable VUV beamline capable of delivering in excess of 10^{13} photons/sec/cm^2/1nm BW@100nm, 50Hz repetition rate (BW=$\Delta\lambda/\lambda$ is the bandwidth) to the sample, has been constructed on a plasma source generated by a high repetition rate, picosecond KrF excimer laser system [1]. This report details the progression of the beamline from initial concept to fully operational mode, a journey in which the beamline output is increased by over three orders of magnitude, utilising a combination of unique focusing optics and highly efficient coupling.

A full spatial, spectral and temporal characterisation of the beamline has been implemented. This involved measurement of the source size, the spectral output over the range 30 - 200nm (40 - 6eV) and the pulse duration.

THE LASER PLASMA SOURCE

The high repetition rate picosecond KrF laser system has been described in detail in the literature [1]. The system delivers 7ps pulses either as a single pulse or in a train of up to 16 pulses with energies of 30 mJ/pulse, at 248nm at repetition rates from 1-100 Hz. When combined with the high beam quality from the final excimer laser amplifier, focused intensities in excess of 10^{15} Wcm^{-2} are reached routinely. This high power density on target results in a plasma temperature $>10^6$ k, whilst the uv laser radiation ensures a plasma density of $1.8\text{x}10^{22}$ cm^{-3} The combination of high temperature and high density results in extremely bright continuum emission. Careful selection of focusing optics and target materials allows the plasma radiation to be optimised over different wavelength ranges.

THE VUV BEAMLINE

Having achieved the conditions for bright continuum emission in the range of interest (30-200nm) the next stage is to couple that radiation as efficiently as possible onto the sample. In addition to the laser system the VUV beamline consists of two other major parts, the target chamber and the vacuum spectrometer. The beamline is able to run in three modes of operation, (a) plasma in centre of chamber, no coupling to spectrometer (b) plasma radiation coupled into spectrometer via microchannel plate optics and (c) plasma formed at the slit of the spectrometer for maximum throughput. A schematic of the high throughput configuration is shown in figure 1.

The initial configuration yielded 10^{10} photons/cm^2/sec/1%BW @ 100nm and was the proof that indeed the source could provide useable photons in the VUV.

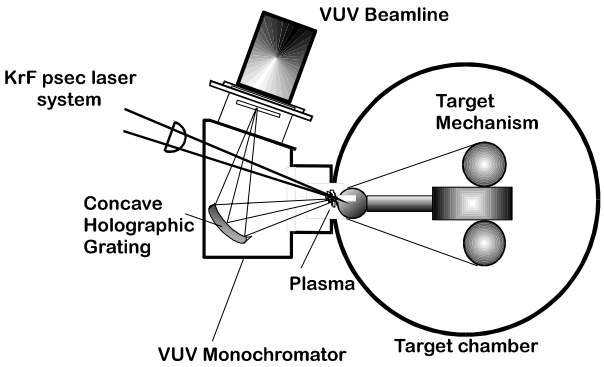

The VUV flux at the exposure station increases by an order of magnitude by configuring the source such that the radiation from the plasma is coupled into the entrance slit of the F4.5 VUV monochromator (Acton Research VM-502) via a microchannel plate (MCP) optic placed exactly half way between the slit and the source. This unique optic is based on reflection at grazing incidence and has the distinction of being achromatic. Careful positioning of the optic allows efficient coupling of the source to the slit whilst acting as a bandpass filter for the wavelength range of interest. The application of MCP optics to soft x-ray focusing can be found in the literature [2], however, it is believed that this is the first time such an optic has been used in the VUV. Dispersion of the radiation is achieved via a 1200 l/mm, F4.5 concave holographic grating. This is protected from any target debris by the MCP lens. Additionally, source debris is minimised by the combination of picosecond pulses on thin tape targets (25μm) [3], and by the addition of a buffer gas such as helium [4,5].

In the high throughput configuration, the tape target is positioned such that the plasma is formed exactly at the entrance slit. This allows the full solid angle of the spectrometer to be utilised without compromising the resolution provided that the source size is less than 250μm. In order to verify this, a pin hole camera was set up together with a narrow band filter (BW 10%) at 121nm. The image of the source at this wavelength was recorded on VUV sensitive film (Chinese) at a magnification of x6.3 The results indicate a diameter of 75μm at 121nm. As indicated in figure 1, the spectrometer had to be modified in order to allow the laser beam to enter through an opposing flange and strike the tape target.

The output of the beamline in a 1nm BW (250μm slit size) as a function of wavelength in the region 30-200nm is given in Figure 2.

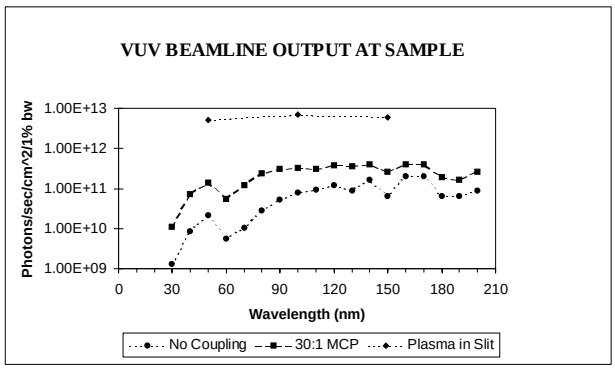

The high throughput configuration runs in atmospheric pressure helium in the wavelength range 60-200nm (E<22eV). This mode of operation relaxes the stringent vacuum requirements and provides a debris free source [4] whilst also providing spectral output at the sample which is free from higher orders. If wavelengths between 30-60nm are required the beamline can be switched to the MCP configuration.

One of the key features of the beamline is tuneability over a wide wavelength range due to the continuous spectral output of the plasma source. This has implications for molecular and photoelectron spectroscopy where a continuously tuneable source is desired. The continuous nature of the source is indicated by the densitometer trace given in figure 3. Here the exit slit was removed and a VUV sensitive film (Q-Plate) placed at the exit slit plane. The film was exposed to five shots from the laser. The large peak at 248nm is the scattered laser radiation and serves as a calibration point.

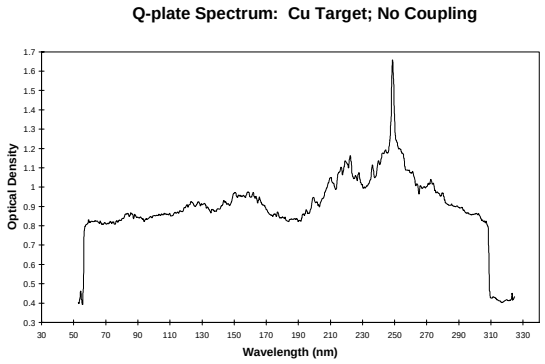

In order to complete the characterisation of the source, a fast VUV pin-diode (IRD) was used to measure the temporal width of the VUV radiation. The signal at 121 nm (defined by the narrow band interference filter) was limited by the temporal resolution of the diode ~1 ns, thus establishing an upper limit of 1ns for the pulse width. This measurement compliments earlier measurements of the pulse width in the XUV at 20 nm using an x-ray streak camera in which an upper bound of 700 ps was set [6].

APPLICATIONS OF THE VUV BEAMLINE

The vuv beamline has already been applied to the measurement of single photon ionisation spectra of large organic molecules (Ledingham et al, Glasgow University, UK), to the study of below threshold ionisation (ion pair production) (Donovan et al, Edinburgh University, UK) and to strand breakage in DNA samples (Folkard et al, Gray Laboratory, UK). In the case of the Glasgow experiment, the bandwidth of 1% was sufficient to resolve structure within the ionisation profile of the xylene molecule. The VUV photons have sufficient energy to cause ionisation with a single photon. This has the advantage over multiphoton techniques in that the parent molecule does not fragment during the interaction. A complete scan over the ionisation profile was performed with a 50 shot average at each point in under two minutes.

In order to study ion pair production, a reduction in the output bandwidth of the beamline to 0.1% was required. This was achieved by using a higher resolution spectrometer (1m focal length) in the same geometry i.e. plasma formed at the entrance slit plane. This configuration results in a reduction in photon flux at the sample by an order of magnitude. Using this configuration a preliminary study of ion pair production in methyl bromide and methyl iodide was successfully completed. Both experiments yielded exciting results and are presently being prepared for publication.

One of the goals in the field of radiation biophysics is to understand the radiobiological effects of ionising radiations in terms of the energy deposited at the molecular level. With this in mind the VUV beamline has been applied with great success to the study of single and double strand breakage in samples of DNA in the energy range 6-60eV. The beamline is particularly useful at ~10eV where previous experiments using different sources have suffered from low dose rates and in the region above 25eV where there is a severe lack of data. Initial experiments have proved very promising and an extension of the study to include hydrated DNA is planned for the near future. Using the high throughput configuration, it is possible to achieve the required dose in 1-2 minutes.

CONCLUSIONS

In conclusion, a high flux, continuously tuneable VUV beamline having an output in excess of 10^{13} photons/sec/cm^2/1%BW@100nm, 50 Hz at the sample has been constructed on a picosecond KrF laser plasma source. Characterisation of the spectral, spatial and temporal output of the beamline has been performed (emitting source size 75μm, pulsewidth <1ns at 121nm) and the output optimised in terms of focal intensity and target material.

The beamline has already been employed on a number of successful experiments spanning photochemistry and radiobiology. It is now fully operational and available for use by scientists from all disciplines requiring a compact useable source of VUV photons. In the future the goal is to significantly reduce the bandwidth whilst maintaining or surpassing the current photon flux to sample. Additionally, higher resolution measurements of the pulsewidth are planned which will allow an accurate measure of the source brightness.

REFERENCES

1) ICE Turcu, IN Ross and GJ Tallents
Appl. Phys. Lett 63 3046-8 (1993).

2) GW Fraser, AN Brunton, JE Lees, JF Pearson, R Willingale, DL Emberson, WB Feller, M Stedman and J Haycock
SPIE Vol. 2011 215-226 (1993).

3) ICE Turcu and IN Ross
Rev. Sci. Instrum 67 3245-7 (1996)

4) ICE Turcu, F O'Neill, GJ Tallents, T Hannon, D Batani, A Giulietti, CW Wharton, RA Meldrum
SPIE Vol. 1278 Excimer Lasers and Applications II (1990).

5) M Ginter and T Mcllrath
Appl. Optics 27 885 (1988).

6) O Meighan, A Gray, JP Mosnier, W Whitty, JT Costello, CLS Lewis, A MacPhee, R Allott, ICE Turcu, A Lumb
Appl. Phys. Lett 70, 1497-9 (1997).

LASER ANNEALING FOR HIGH INTENSITY FLAT SCREEN DISPLAYS

W.M. Cranton, E. Mastio, C.B. Thomas, R. Stevens and J.P.O. Evans

The Nottingham Trent University
Department of Electrical and Electronic Engineering

BACKGROUND

Thin film electroluminescent (TFEL) devices provide an effective solution to the global need for small area, high resolution, high intensity flat panel displays. In particular, the Displays Group at The Nottingham Trent University (NTU) have gained considerable headway in the development of emissive displays based on a novel configuration of the TFEL device structure which utilises the inherent waveguiding attributes of TFEL materials to produce laterally emitting thin film electroluminescent (LETFEL) devices. Under EPSRC Grant No GR/J45404, micro-mirror technology was demonstrated which facilitates the use of lateral emission combined with conventional surface emission for display applications, leading to a four-fold increase in the emitted intensity[1)]. In addition, the development of novel `barrier-layer' phosphor thin films has been shown to further improve the efficiency of LETFEL devices via modification of the internal electric field distribution[2)]. These improvements in TFEL efficiency have facilitated the development of high intensity fixed legend head mounted displays (HMDs) (Fig.1) based on the LETFEL technology, using the red/yellow/green emission of ZnS:Mn, which is the most efficient TFEL phosphor. Currently, luminances > 3000 fL have been demonstrated, which is the minimum requirement for effective sunlight readable HMD's. It would, however be of great advantage to further enhance the luminescent efficiency of these devices, particularly where highly attenuating optical systems may be necessary for a practical application. In addition, a major objective of future LETFEL development is to extend the technology to encompass full colour display applications, which also requires enhancements in device performance so that the low efficiency blue phosphors, such as ZnS:TmF may be effectively used.

Fig 1. LETFEL based HMD

The basic TFEL device structure consists of a phosphor thin film sandwiched between insulating layers. Upon application of a suitable ac drive voltage, electrons are field emitted from trapping states at the phosphor / insulator interface into the conduction band of the phosphor (typically ZnS:Mn). Under the action of the high applied field these electrons are accelerated, gaining sufficient energy to impact excite the luminescent centres which can relax radiatively to provide the useful visible emission. Critical to the luminescent efficiency of a LETFEL, and indeed any TFEL device, is a post deposition annealing treatment, which allows for the effective incorporation of luminescent dopant ions within the host lattice. Commercial TFEL devices, commonly used for large area flat panel displays, are typically subjected to a post deposition anneal at 500ºC for ~ 1 hour, which is the maximum practical temperature that may be employed due to the need for glass substrates. The LETFEL device, however, does not rely upon surface emission and may therefore be fabricated using substrates other than glass. Consequently, by using silicon substrates, we have been able to explore thermal annealing effects at temperatures > 500ºC, and in doing so have produced some interesting experimental results indicating both the beneficial and detrimental effects of thermal annealing upon LETFEL performance.

THERMAL ANNEALING

The luminescent properties of equivalent LETFEL devices as a function of annealing temperature are shown in Figure 2. Both photoluminescent (PL) and electroluminescent (EL) excitation were used to probe the effect of thermal annealing. From the PL results it is clear that the luminescent quality of the ZnS:Mn thin films is improving with increased temperature. This is indicative of improved incorporation of the luminescent Mn centres into the host lattice, which is the premise behind the standard TFEL annealing process. Under EL excitation, the films again show an improvement in luminescent properties as the temperature is raised from 400ºC to 500ºC, which is consistent with general TFEL results. However, at higher temperatures there is no significant improvement in EL luminance. Modelling this behaviour based on the electro-optic characteristics indicates that the effect is due to a reduction of the interface state density at the phosphor / dielectric interface [3)]. From a prior study of ZnS thin films on Si, this effect is consistent with an `improvement' of the interfacial layer due to the thermal annealing. For optimum EL performance, therefore, the ideal interface would be the as-grown *disturbed* structure, such that the density of electron traps remains high.

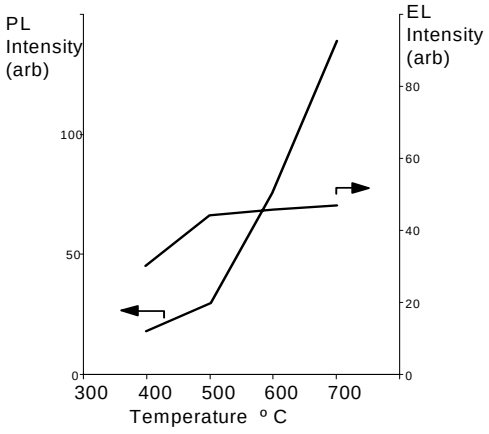

Fig. 2. PL and EL intensity of TFEL devices vs annealing temperature.

LASER-ANNEALING

Based on the results discussed above, it is proposed that the use of pulsed laser irradiation could provide a more effective means of heat treating the phosphor thin films of LETFEL devices. By use of suitable wavelengths, it is intended to optimise the process so that the majority of the energy is dissipated within the bulk of the ZnS thin films, with minimal effect upon the insulating layer (s). Investigations to date have been performed in collaboration with the LSF group using a pulsed KrF laser at 249nm. Wafers with varying thicknesses of thin film ZnS:Mn

phosphors have been used to investigate the effect of irradiation on luminescence. Initial experimentation is directed at defining the parameters to successfully anneal the phosphor thin films with no ablation. This has necessitated the construction of a pressure cell to house the target wafer during annealing, in an inert environment under a high pressure. The cell was designed by Tony Damerell at RAL and has been successfully utilised at pressures of 10bar, using Ar. For the initial experimentation the effect of energy density was investigated using the system shown schematically in Figure 3. With a focused beam spot of 3mm diameter, the energy density could be varied between $100mJcm^{-2}$ and $900mJcm^{-2}$. Single and multi shot irradiation was performed across the ZnS:Mn thin films and the irradiated area was then examined via photoluminescence using a pulsed N_2 laser for excitation, and a Minolta LS110 Luminance Meter for measurement. To facilitate the accurate positioning of the target wafer in the KrF beam, an XZ motion was constructed using two MicroControl stages with ± 10µm accuracy over 200mm total travel, capable of supporting 30kg. PC control of the stepper motor drives allows accurate positioning of specific target areas of the wafer.

PRELIMINARY RESULTS

Following 1.5 weeks experimentation with the LSF, the preliminary results are encouraging. Thin film structures investigated were ZnS:Mn/Si, ZnS:Mn/Y_2O_3/Si, and Y_2O_3/ZnS:Mn/Y_2O_3/Si. The results where a measurable effect on PL was produced are summarised in Table 1. The maximum improvement in PL occurred for thin films which had not been thermally annealed prior to laser irradiation, indicating that the potential exists to use pulsed laser irradiation as the primary means of activating the phosphor layer for thin film display devices. This is the rational behind the research, and will be further investigated when the experiments are repeated over larger areas using TITANIA. Of the 540 irradiations performed, improvement in PL was observed for 43. The remainder either showed no improvement, or suffered a degradation which was due to ablation at the thin film surface. In some cases, ablation was also evident on the films that showed an improvement in PL. This is a problem which needs to be addressed in the next batch of experiments. Furthermore, the effect on electroluminescence must be investigated, and will be a priority for the thin film structures to be irradiated using TITANIA in early July 97. With the facility to irradiate large areas (up to the full 4" wafer diameter), it will be possible to fabricate TFEL test devices within the irradiated regions. The early results of this work are thus encouraging, although the ablation effect must be addressed as part of the ongoing research. An experimental procedure has been established for irradiation with the KrF laser, and the parameters identified for successful annealing of the thin film phosphors will now be applied to the TITANIA experiments. Finally, we would like to acknowledge the support and guidance of all at the CLF who have been involved in this project, particularly Graeme Hirst, Edmund Turcu, Waseem Shaikh, Nick Spencer, and Noboyuki Takeyasu.

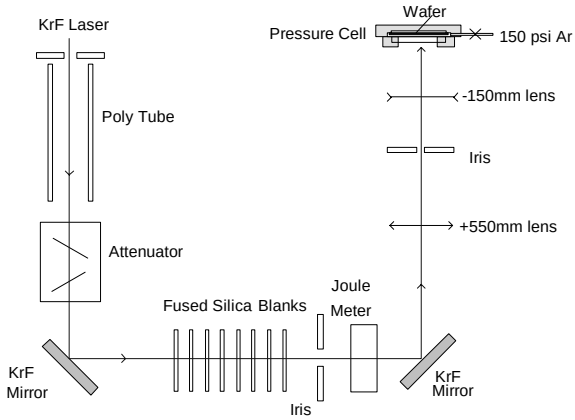

Fig. 3. Experimental system for KrF irradiation of TFEL wafers.

Wafer No. (Thin Film Structure)	Intensity in mJ/cm^2/shot.	Number of shots.	PL improvement factor.
NTU 141 (0.3µm Y_2O_3/ 0.8µm ZnS:Mn/0.3µm Y_2O_3). Thermal annealed at 500°C 1hour.	490 572 714	1 1 1	1.14 1.05 1.04
NTU 069 (0.3µm Y_2O_3/ 0.8µm ZnS:Mn/0.3µm Y_2O_3). Non thermal annealed.	264 360 460 570	10 10 5 10	1.58 1.69 1.77 1.73
NTU 067 (0.8µm ZnS:Mn on Si). Non thermal annealed.	124 256 370 470 570	5 2 2 2 2	1.72 2.28 2.20 2.21 1.97

Table 1. Summary of effect on PL luminescence of KrF irradiated TFEL structures on Si wafers.

REFERENCES

1) EPSRC Grant No. GR/J4504 Final Report, December 1995.

2) C.B. Thomas and W.M. Cranton
Appl. Phys. Lett., 63 (23), 3119, (1993).

3) W.M. Cranton, R. Stevens, C.B. Thomas, A.H. Abdullah, and M.R. Craven
IEE Colloquium on Materials for Displays, (1995).

VUV LASER RADIATION BY HIGH ORDER HARMONIC GENERATION

A C Flexen [1)], R J Donovan [1)], A J Langley [2)] and W Shaikh [2)]

1) Department of Chemistry, University of Edinburgh, West Mains Road, Edinburgh, EH9 3JJ. Email rjd04@holyrood.ed.ac.uk
2) Rutherford Appleton Laboratory, Chilton, Didcot, Oxon., OX11 0QX

INTRODUCTION

High-order harmonic generation has been developed in recent years to provide a source of coherent laser radiation with wavelengths extending into the XUV and soft X-ray regions of the electromagnetic spectrum (λ=7 nm has been observed) [1)]. This has been possible due to the development of lasers with ultrashort pulse lengths, on the picosecond and subpicosecond timescale [2)]. These sources are able to produce significantly higher peak intensities than conventional laser sources. Intensities developed are typically of the order 10^{14}-10^{18} W cm^{-2} which is necessary for efficient high-order harmonic generation (HG).

The high-order HG process is based on the nonlinear polarization response of atoms and molecules, to the strong electric field component of the applied radiation. Atoms in a strong field can emit radiation at energies exceeding the ionisation potential.

At laser intensities of the order 10^{14}-10^{18} W cm^{-2}, atoms or molecules may scatter incident radiation of input frequency ω yielding radiation at several frequencies equal to odd integer multiples of the fundamental radiation, $n\omega$, where $n \geq 3$. The most efficient and widely used nonlinear media are the inert gases given their stability, ease of handling and high polarizability. Harmonics are generated in the same direction as the applied fundamental beam and have similar pulse width characteristics. Harmonic orders with n as high as 10^2 have been generated using pulsed jets of inert gases [3)]. This approach may therefore provide a source of useable short wavelength radiation with picosecond or subpicosecond pulse widths [4,5)].

Results from our second experiment, using the Tsunami 50 fs laser system to generate high order harmonics, are presented here. The aim of this experiment was to generate and observe harmonics with wavelengths below the transmission cut-off of MgF_2 at 120 nm, i.e. to provide a windowless beam path from the interaction or generation region to the detector. To do this required the nonlinear medium used in the HG process to be introduced into the laser focus by a pulsed jet, in order to maintain a high vacuum in our differentially pumped system. The next stage of the experiment was to optimise the harmonic output and estimate the photon yield of each harmonic in order to test the suitability of the technique as a source of short wavelength, VUV radiation for photoionization experiments.

EXPERIMENTAL DETAILS

The experimental arrangement is shown on figure 1. Laser pulses of around 50 fs pulse length and 10 nJ energy were generated by a CW argon-ion pumped mode-locked titanium sapphire laser in an 82 MHz train. Pulses were amplified in an Nd:YAG pumped dye laser and yielded 750 nm radiation with pulse energy 100 μJ at a repetition rate of 10 Hz. This provided peak intensities, when focused, of the order 10^{14} W cm^{-2}. Laser radiation was directed and focused, using a 50 cm focal length lens, into a chamber containing a pulsed valve (nozzle diameter 600 μm). The focal point was estimated to be around 200-300 μm from the nozzle. Xenon and argon gases at backing pressures up to 6 atm were pulsed through the valve to form a jet of the nonlinear medium. Fundamental and generated radiation was directed onto a concave holographic grating housed in an evacuable monochromator. No windows were used in the beam path between generation region and grating.

Harmonic wavelengths were selected and directed to the exit window of the monochromator. The window was coated, on the vacuum side, with a thin layer of sodium salicylate. The compound, sodium salicylate fluoresces at 443 nm and has a high fluorescence quantum yield for a large range of wavelengths extending into the XUV region (from 3 nm to 400 nm). A UV-visible photomultiplier with a peak response around 440 nm (EMI 9664B) was placed at the exit window with a BG18 filter in front which gave 60% transmission at 443 nm and effectively zero transmission at 250 nm and 750 nm. The 443 nm fluorescence was detected by the PMT and the signal output to a Tektronix digital oscilloscope.

A high vacuum was maintained in the system by differentially pumping using a diffusion/rotary pump with cold trap removing the gas pulses and a turbo/rotary pump evacuating the monochromator, yielding a pressure in the system of <10^{-6} Torr. The jet was triggered from the synchronous Q-switch output of the Nd:YAG laser. An initial delay of 100 ms between successive pulses was generated followed by optimisation of the timing between the valve opening and the gas pulse reaching the laser focus. The optimum time delay was found to be 750 μs between these events. A backing pressure of around 6 atm was used in the jet.

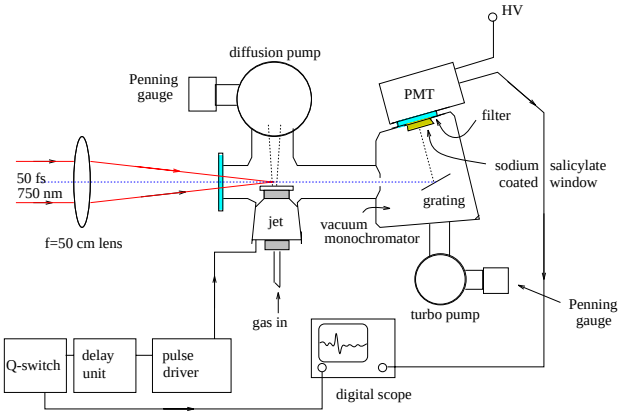

Figure1: The experimental set-up for harmonic generation in gasses

RESULTS

The main aim of the work was to generate and observe harmonic radiation with wavelengths below the transmission cut-off of magnesium fluoride. This was successful up to the 7th harmonic at 107 nm. Xenon and argon gases were used as nonlinear media with xenon found to be the more efficient. Table 1 shows the number of photons per pulse generated for each harmonic and the corresponding conversion efficiency relative to a 100 μJ pulse of 750 nm fundamental radiation.

Harmonic	λ/ nm	Number of photons	Conversion efficiency
3rd	250	$4x10^{11}$	$1x10^{-3}$
5th	150	$2x10^{9}$	$5.6x10^{-6}$
7th	107	$1.6x10^{6}$	$4.2x10^{-9}$

Table 1 Number of harmonic photons per pulse generated in Xe and corresponding conversion efficiency.

The values for conversion efficiency reported here compare well with the results from other work performed on quantifying

harmonic yields [6]. However, a number of assumptions were made in the calculations used to derive these values and therefore an uncertainty of 50% should be included. Comparison with our previous work [7], generating harmonics in a static cell, shows that a very large increase in yield has been obtained (a factor 10^3 increase for the 3rd and a factor 10^5 increase for the 5th harmonics. The large increase at the 5th harmonic is possibly due to the absence of a long path length, in the jet system, of Xe which absorbs around 150 nm).

The 3rd harmonic signal was optimised by varying the position of the laser focus in the direction of the atomic beam. In this way the gas density profile was mapped and the optimum distance from the nozzle output determined. It was found that the signal decayed exponentially to effectively zero over ca. 2 mm distance. A simple backing pressure versus intensity relationship was derived. The backing pressure of Xe was varied from 0.2 to 6 atm and an approximately linear dependence on 3rd harmonic signal was observed.

Photon yields and conversion efficiencies were calculated using data on the specification of the PMT and grating and by estimating the efficiency of the fluorescent screen. The results given in table 1 correspond to the estimated number of harmonic photons generated at the laser focus.

CONCLUSION

The feasibility of using a relatively simple experimental arrangement to generate high order harmonics with high conversion efficiency has been demonstrated. The large photon yields observed for harmonics *n*=5 and 7 is encouraging for future work, using the technique as a source of short wavelength, VUV or XUV laser radiation. With the experience of using a windowless vacuum system and pulsed jet, improvements to the generation region and detection system have been highlighted. The apparatus can then be adapted for using the VUV and XUV wavelengths produced as a source for photoionization experiments on molecular systems, introduced *via* a second pulsed jet for the purpose of jet cooling and maintaining a differentially pumped beam path.

REFERENCES

1) C.-G.Wahlstrom
Physica Scripta, 49 201, (1994)

2) G. Mourou and D. Umstadter
Phys. Fluids B, 4 2315, (1992)

3) K, Miyazaki, H. Sakai, G.U. Kim H.Takada
Phys. Rev. A, 49 548, (1994)

4) P. Balcou, P. Salieres, K.S. Budil, T.Ditmire, M.D. Perry and A. L'Huillier
Z. Phys. D, 34 107, (1995)

5) P. Erman, A. Karawajczyk, E. Rachlew, Kallne, E. Mevel, R. Zerne, A. L' and C.-G. Wahlstrom
Chem. Phys. Lett., 239 6, (1995)

6) T. Ditmire, J.K. Crane, H. Nguyen, L.B DaSilva and M.D. Perry
Phys. Rev. A, 51 R902, (1995)

7) A C Flexen, R J Donovan, R Maier, A J Langley and W Shaikh
CLF Rutherford Appleton Laboratory Annual Report 141, (1996)

IMAGING X-RAY FLUORESCENCE USING MICROCHANNEL PLATE X-RAY OPTICS

G.W. Fraser [1], A.N. Brunton [1], A.P. Martin [1] , A.D. Holland [1], A. Keay [1] , J. Hill [1], N.Nelms [1],
I.C.E. Turcu [2], R. Allott [2] and N. Lisi [2]

[1] X-ray Astronomy Group, Department of Physics and Astronomy, University of Leicester,
Leicester LE1 7RH. E-mail : gwf@star.le.ac.uk.
[2] Lasers *for* Science Facility, Rutherford Appleton Laboratory, Chilton,
Didcot, Oxon. OX11 OQX

INTRODUCTION

X-ray fluorescence (XRF) is a widely used materials analysis technique. In its simplest form, a sample is irradiated with primary X-rays and the area-averaged fluorescence spectrum is recorded. The composition of the sample is thus determined but no information is obtained on the spatial distribution of the elements. In certain applications (e.g. the mapping of low-Z contaminants (C,O,..) on silicon wafers in the semiconductor industry) this spatial information is of considerable interest. Imaging XRF generally relies on the (x,y) scanning of the sample past a tightly collimated X-ray beam [1]. Using single capillaries [2] or crystal optics [3] at synchrotron sources, 10 μm diameter probe beams have been produced. Alternatively, the sample may be imaged using coded aperture masks and an area detector [4]. These various methods provide good spatial resolution but require either complex equipment or the non-trivial deconvolution of the sample image from the shadowgram of the coded mask.

We have explored an alternative approach to imaging XRF which gives a direct image, is ideally suited to the mapping of low-Z elements and has no moving parts. We used a planar, square pore microchannel plate (MCP) [5] as an "X-ray relay lens", re-imaging fluorescent X-rays onto a 840 x 1024, 27 μm pixel, open-electrode CCD with high sub-keV quantum efficiency. The CCD was fabricated by EEV Ltd., under contract to Leicester University, for the EPIC instrument on the European Space Agency's XMM Observatory, due for launch in 1999. We describe here the results of a proof-of-concept experiment carried out using the pulsed, picosecond laser plasma X-ray source at the LSF in the period 3-14 February 1997.

EXPERIMENTAL PROCEDURE

The experimental arrangement is shown in Fig. 1. Laser light (λ = 2480 Å) enters the target chamber as a stream of 8 x 7 ps pulses, 12 ps apart. The energy in each pulse train is 10 mJ [6]. The beam was brought to a 10 μm diameter focus on a slowly moving Fe tape, producing L-shell (~ 1 keV) emission from highly ionised iron. These X-rays uniformly illuminated the sample at a distance from the tape of only 10 mm. Fluorescent X-rays are reimaged onto the CCD chip by equiangular reflection from the channels of the square-pore MCP. The 20 mm x 12 mm channel plate used in this experiment was provided by Nova Scientific Inc. [7] and had a channel length-to-diameter ratio of 30:1, well suited to the efficient focusing of sub-keV X-rays. Its small area, however, restricted the acceptance aperture for fluorescent X-rays. Since the laser plasma emits at all wavelengths from the infra-red to X-ray, it was important to ensure that only the desired fluorescent X-rays reached the CCD. In particular, a 1 μm polypropylene, 0.1 μm aluminium filter preceded the CCD input. To confine target debris, the target chamber was filled with He to a pressure of 10 Torr. The composite transmission of the helium, polypropylene and aluminium was ~30% at 0.5 keV and ~85% at 1 keV. The CCD detector (liquid nitrogen cooled to -100 _C) was in a separate, rotary-pumped enclosure separated from the target chamber by a gate valve.

The gate valve was opened for only a few seconds for each laser shot, in order to minimise the thermal problems caused by admitting helium to the vicinity of the CCD.

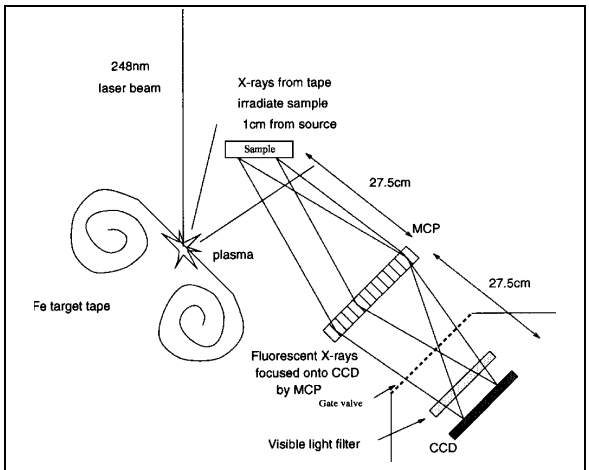

Fig.1 Experimental geometry.

RESULTS

Starting from the 10 mJ per laser pulse and folding in the various solid angle and efficiency factors, we estimated the number of photons per pixel per shot to be ~1.3. In order to obtain optimum CCD energy resolution, we require no more than a single X-ray per pixel per 16s CCD frame. Thus, a single laser shot was expected to provide images at full energy resolution. The laser was therefore operated in its slowest pulse rate of 6 Hz and its shutter operated manually.

A binary nickel/aluminium target was constructed as shown in Fig. 2. The relevant fluorescent X-ray energies are 1.49 keV (Al Kα), 0.85 keV (Ni Lα), 0.525 keV (O Kα) and 0.28 keV (C Kα), the last two lines originating in the plastic tape which secured the nickel and aluminium cylinders to their mount. It was found through trial and error that *three* laser pulses per CCD frame produced an acceptable count rate without significant levels of "pulse pile up". The CCD pulse height spectrum produced by co-adding eight individual frames is shown in Figure 3. Pulse-height-selected CCD images, corresponding to the same spectral data, are shown in Figures 4(a,b) ; the former image shows the spatial distribution of aluminium X-rays, the latter, of nickel X-rays. The cruxiform nature of the MCP point source focus [5] is readily apparent. Nevertheless, the locations of the Al and Ni sources are clearly resolved (compare the locations of the fiducial marks in Figures 4(a,b)) and we may claim that our concept of a novel imaging X-ray fluorescence spectrometer based on the laser plasma X-ray source, a square-pore MCP optic and an open-electrode CCD is thereby proven in practice.

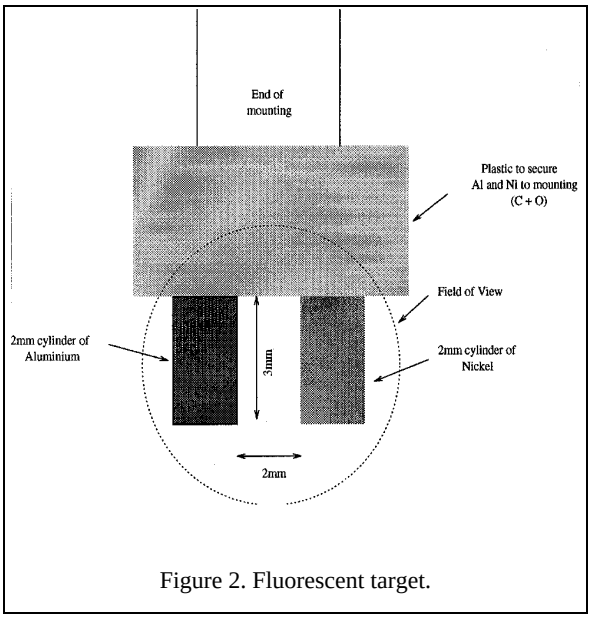

Figure 2. Fluorescent target.

FUTURE WORK

A number of improvements are possible in future runs. The use of a larger, higher quality MCP will increase both elemental sensitivity and spatial resolution. A thinner visible light filter will allow elements down to Boron to be imaged by the CCD. The use of a mylar tape will eliminate the high-energy continuum "tail" observed using the Fe tape. We hope to report on the development of the instrument concept in the near future.

ACKNOWLEDGEMENTS

APM and JH gratefully acknowledge the receipt of PPARC CASE studentships supported by Philips Photonics and EEV Ltd., respectively.

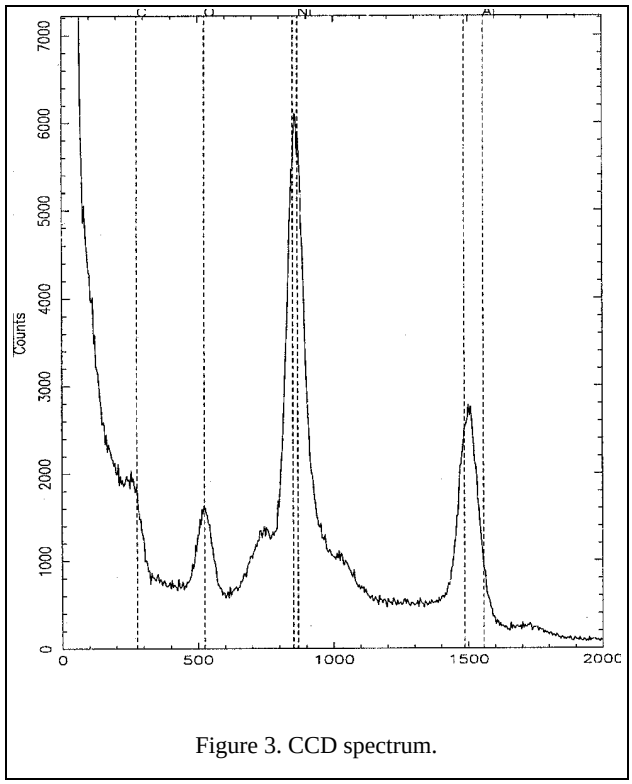

Figure 3. CCD spectrum.

REFERENCES

1) R.W. Morton and K.C. Witherspoon,
Adv.X-ray Analysis 36, 97 (1992).

2) L. Vicze, K. Janssens and F. Adams
Adv. X-ray Analysis 37, 553 (1994).

3) B. Veckhoff, K. Kanngiesser, J. Scheer and W. Swoboda,
Adv.X-ray Analysis 37, 523 (1994).

4) M. Bavdaz and N. Gurker,
X-ray Spectrometry 22, 65 (1993).

5) G.W. Fraser, A.N. Brunton, J.E. Lees and W.B. Feller
Nucl.Instr.Meth. A324, 404 (1993).

6) I.C.E. Turcu, I.N. Ross and G.J. Tallents
Appl.Phys.Lett. 63, 3046 (1993).

7) Nova Scientific Inc., 54 Main Street, Sturbridge MA 01566, USA.

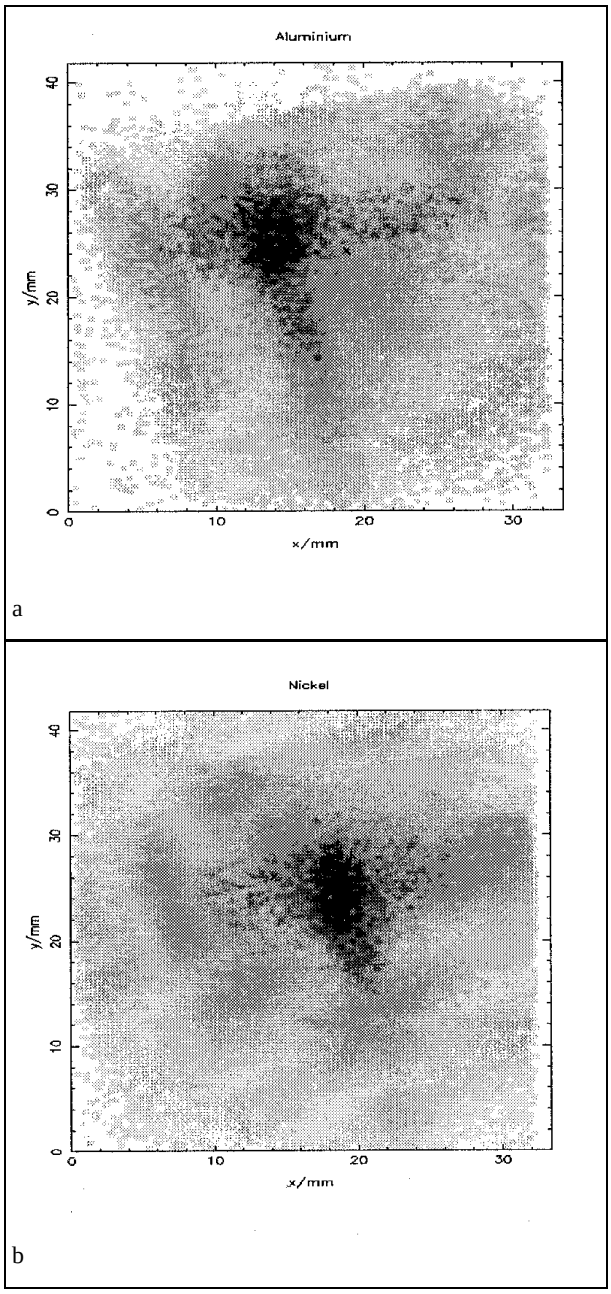

Figures 4(a,b) . Aluminium (top) and nickel (bottom) energy-resolved X-ray images.

CHARACTERISATION OF PERIODICALLY POLED PHOTOCONDUCTIVE MATERIALS AND INVESTIGATIONS OF NEW PHOTOREFRACTIVE MATERIALS

Malgosia Kaczmarek [1)], Peter Smith [2)], Graeme Ross [2)], Robert Eason [2)], Andrew Anderson [2)], Paul Brown [2)], Gero Maatz [2)]

1) Department of Physics, University of Exeter, Exeter EX4 4QL
2) Optoelectronics Research Centre, University of Southampton, Southampton SO17 1BJ

PROPERTIES OF RH:BATIO$_3$ CRYSTALS PROCESSED IN DIFFERENT CONDITIONS

In our investigations on novel, infrared-sensitive photorefractive materials we have concentrated on Rh:$BaTiO_3$ to determine both the optimum dopant concentration, and post-growth processing conditions to improve its performance in the infrared. Rhodium doped $BaTiO_3$ has interesting photorefractive properties, which enable us to observe high phase conjugate reflectivities [1] and signal amplification [2] both in the visible and the near-infrared. Firstly, we have studied the performance of Rh:$BaTiO_3$ grown with 400 ppm of rhodium added to the melt. The crystals came from the same boule and were then post-processed separately in different conditions. One sample was left as-grown, the second was annealed in air at 1000^{o}C, which effectively reduced the crystal, and the third sample was annealed in pure oxygen and then quenched to fix the oxygen concentration. Secondly, we have investigated crystals more heavily doped with rhodium: with 2400 ppm and 3200 ppm added to the melt.

We used the two-beam coupling technique to characterise the performance of these crystals at different wavelengths. The as-grown sample showed the strongest two beam coupling both in the visible and in the near-infrared (G=14.9cm^{-1}@514.5nm and 6.8cm^{-1}@1 mm). In the annealed in oxygen sample we observed finite coupling in the visible, but no effect above 750 nm. The annealed in air sample showed a negligible photorefractive effect (Table 1). The crystal was poled again to eliminate the possibility of spontaneous depoling. Two-beam coupling gain did not increase following the poling process. Therefore, one can speculate that annealing in air brought the crystal close to the compensation point and effectively prevented the formation of a photorefractive grating. This process also affected the crystal's absorption coefficient, decreasing its value. The results obtained in the annealed in air 400 ppm Rh:$BaTiO_3$ are very interesting and worth pursuing further for applications where the presence of photorefraction is undesirable.

	Coupling coefficient G [cm-1]	Absorption coefficient a [cm-1]
annealed in air	2.45	0.49
as-grown	14.9	1.32
annealed in oxygen	7.5	1.32

Table 1 The effect of processing conditions on beam coupling strength and absorption at 514.5 nm

The considerable gain was also achieved in the 400 ppm as-grown Rh:$BaTiO_3$ crystal at 1 mm, which is particularly promising for applications in the range close to the telecommunication wavelengths. Table 2 shows the results on beam coupling at 1.06 mm in various Rh:$BaTiO_3$ crystals and their absorption. It is worth noting that the relatively high beam coupling gain was measured both in the 400 ppm Rh:$BaTiO_3$ sample and in the original blue Rh:$BaTiO_3$ in spite of their low absorption at infrared wavelengths. It is likely that there may be some other impurity involved, which additionally to rhodium, is responsible for an efficient response in the infrared. The mass spectroscopy analysis detected the elements such as Mg, Al, Ca, Cr, Mn, Fe, Ni and Co, but all in extremely low concentrations, apart from cobalt. The concentration of rhodium was smaller than expected, suggesting a small segregation coefficient of 0.005-0.01.

	Absorption at 1.06 mm [cm^{-1}]	Coupling coefficient G [cm^{-1}]	References
original blue Rh:$BaTiO_3$	0.06	11.2	[2]
400 ppm Rh:$BaTiO_3$	0.05 (at 1 mm)	6.8	
2000 ppm Rh:$BaTiO_3$	0.15	23	[3]
3200 ppm Rh:$BaTiO_3$	0.13	9.35	[4]

TABLE 2 Infrared performance of Rh:$BaTiO_3$ crystals

We also investigated light induced change in absorption. Our earlier results from the original blue Rh:$BaTiO_3$ showed a strong light-induced transparency in the visible and the near-infrared and a finite light-induced transparency at 1.06 mm. However, in all three 400 ppm Rh:$BaTiO_3$ crystals we observed only small induced change in absorption in the visible, namely smaller than 0.1 cm^{-1}. This may suggest that the role of Rh^{4+} centres in charge transport is less pronounced than in the original blue Rh:$BaTiO_3$. Further work on characterising and modelling the parameters of photorefractive centres in Rh:$BaTiO_3$ is under way.

When investigating different samples of Rh:$BaTiO_3$, originating from different boules, it became apparent that their performance can be extremely sensitive to very fine changes in conditions of growth and processing, as well as to the exact position in the boule. This effect was particularly pronounced in 400 ppm crystals. The more heavily doped crystals (3200 ppm of rhodium added to the melt) were less sensitive to growth and annealing and showed more consistent absorption across their spectrum. Their relatively high absorption in the near-infrared (1.06 mm: 0.14 cm^{-1} for 2400 ppm and 0.3 cm^{-1} for 3200 ppm) is quite promising for achieving high two-beam coupling gain and extending their response to 1.3 mm.

REFERENCES

1) G.W. Ross, P. Hribek, R. W. Eason, M. H. Garrett, D. Rytz Optics Communications, 101, 60 (1993)

2) M. Kaczmarek, R. W. Eason

Optics Letters 20, 1850 (1995)

3) N. Huot, J. M. C. Jonathan, G. Pauliat, D. Rytz, G. Roosen Optics Communications, 135, 133 (1997)

4) A. Brignon, J.-P. Huignard, M. H. Garrett, I. Mnushkina, Conference on Lasers and Electro-optics, CLEO' 97, Baltimore, May 1997, paper CTuP7.

FEMTOSECOND LASER MASS SPECTROMETRY AS AN ULTRA-SENSITIVE ANALYTICAL TECHNIQUE

K W D Ledingham[1], R P Singhal[1], H S Kilic[1], T McCanny[1], D J Smith[1], W X Peng[1], C Kosmidis[2], A J Langley[3] and P F Taday[3]

Department of Physics & Astronomy, University of Glasgow, Glasgow G12 8QQ, Scotland
Department of Physics, University of Ioannina, Ioannina, GR-45110 Greece.
Rutherford Appleton Laboratory, Chilton, Didcot, Oxon OX11 0QX

Over the past two years, the Glasgow group[1-5] has studied the ionisation and dissociation of small and medium mass molecules induced by short pulse lasers. Most experiments were carried out at the Lasers *for* Science Facility (LSF) and utilised laser pulse widths of 90 fs and wavelengths of 375 or 750 nm. These experiments have demonstrated the enormous advantages of using femtosecond lasers over the longer pulse nanosecond lasers used extensively in previous studies[6]. The main features which make femtosecond laser mass spectrometry (FLMS) both an ultra-sensitive and –selective analytical technique are:

a) In a femtosecond laser, the prevailing intensity levels are very high (I~10^{12} Wcm^{-2} or greater in our measurements). Consequently, the probability of multiphoton absorption by the molecule (~ I^n, n is the number of absorbed photons) is greatly enhanced resulting in an increased ionisation yield. This increases the sensitivity achieved in FLMS.

b) A large number of molecules of interest have intermediate dissociative states which may cause fragmentation during the multiphoton excitation. The dissociative lifetimes are typically tens of fs to ps or longer. In FLMS, the ionisation process is completed within the duration of the laser pulse with the result that the molecule has insufficient time to fragment to any significant extent. Thus, the parent ion yield is enhanced. This increases the specificity which FLMS can deliver. In ns REMPI there is often no parent ion peak and dissociation produces small mass fragments which cannot be used for analytical analysis.

c) Because of the enhanced probability of multiphoton absorption in FLMS, two or even three photon transitions are routinely saturated. Saturation requires that all molecules in the interaction region are ionised. Therefore, FLMS can provide uniform sensitivity of detection which, to a large extent, does away with the need to have standards for calibration. This greatly simplifies the analysis. The ion yield also becomes relatively insensitive to modest fluctuations in laser intensity.

In fig. 1 we present some results[5] for the molecule m-nitrotoluene (m-NT). This molecule has one of the simplest structures in the substituted nitro-aromatics which form an important group of explosive molecules. On irradiation by ns pulses, the nitro-aromatics are known to fragment readily and while they all give a large NO ion signal in the mass spectrum, it is impossible to achieve the desired level of specificity due to the lack of a parent mass ion peak. The figure compares mass spectra obtained for femtosecond and nanosecond laser pulses. Following our discussion above, it is evident that the presence of the parent mass ion peak helps enormously in identifying the molecule and also the ion yield is several orders of magnitude greater in FLMS. This provides increased sensitivity. From fig. 1, we also observe the increased yield of high mass fragment ions which further help in the identification of the parent molecule. The fragmentation of NT appears to happen predominantly from the ionic state. This is demonstrated in fig. 2 where the intensities of different fragment ion peaks as a function of laser pulse energy are plotted. All gradients are similar, indicating that the ionisation precedes fragmentation in this molecule. We have studied a large number of molecules and the general features of FLMS are maintained without exception

Recently, ps lasers have been used for analytical studies and generally produce bigger parent peaks than their ns counterparts. However, the superiority of fs lasers, in this context, is well demonstrated by the case of CO_2 which was

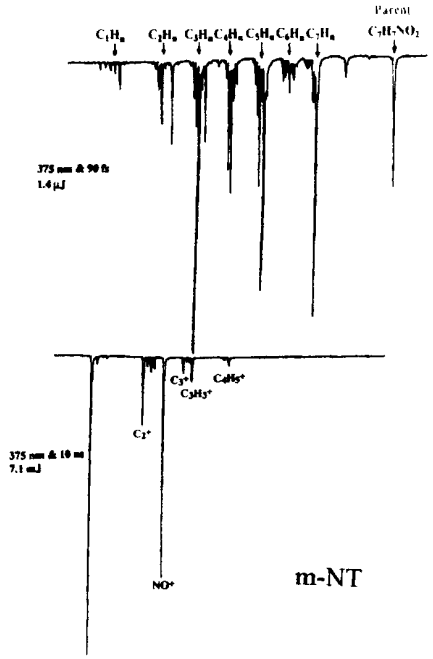

FIGURE 1 Mass spectrum of m-NT for fs and ns pulses

recently studied by He *et al.*[7] using 35 ps laser pulses at 532 nm. Even when the laser intensity was comparable or greater than for the 90 fs pulses used at RAL, the parent ion peak was barely observed. In fact, for the ps case the parent ion peak is

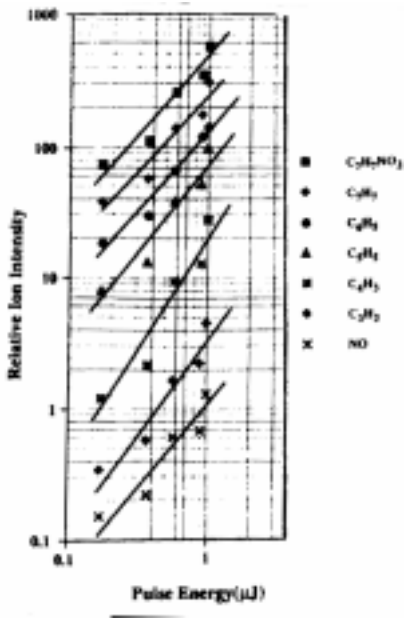

FIGURE 2 Pulse energy dependence of different m-NT fragment ions for 90 fs 375 nm laser pulses

reduced with increased laser intensity. We compare the ps and fs spectra in fig. 3.

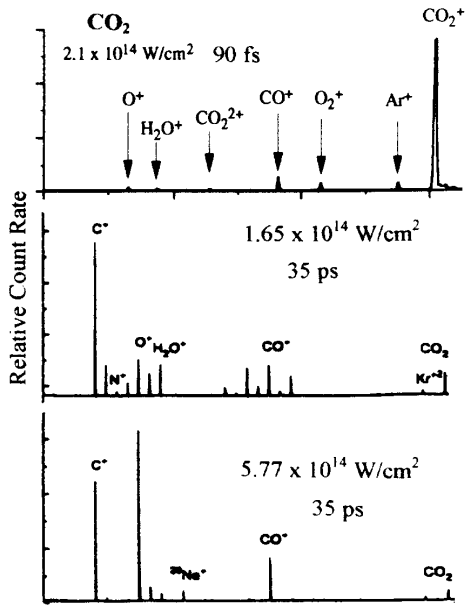

FIGURE 3 Comparison of 90 fs and 35 ps mass spectra of CO_2

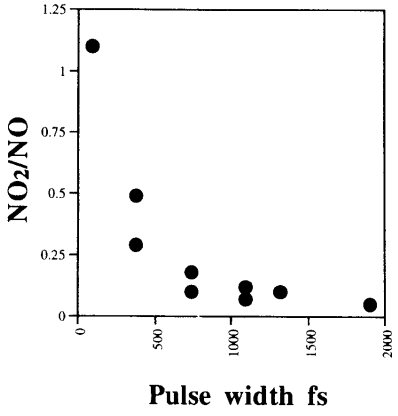

FIGURE 4 Ratio of NO_2 and NO ions as a function of pulse width for 750 nm laser wavelength

While a very powerful tool for analytical analysis, FLMS is likely to have a considerable impact in molecular fragmentation dynamic studies at a fundamental level. In fig. 4, we show the results[8] for the molecule NO_2 which, on bombardment with 750 nm photons, undergoes dissociation to NO and O with a time scale of a few hundred fs. For short pulse lasers, multiphoton ionisation (MPI) is also efficient, and the relative size of NO_2 and NO ion peaks in the mass spectrum represents the outcome of a competition between MPI and dissociation of NO_2. This ratio is seen to vary in a systematic fashion as the pulse width is increased. For the data shown in fig.4, the laser intensity was held constant maintaining a given MPI rate. For longer pulses, the molecule has more time to dissociate thus increasing the yield of NO ions.

Similar results have been obtained for the molecule benzaldehyde. We proposed to apply the rate equations model, which was developed by the Glasgow group, to understand this behaviour quantitatively and hope to extract dissociative life times for these molecules.

With the laser intensities up to 10^{15} Wcm^{-2} available at the LSF at different wavelengths, we hope to be able to study the competition between multiphoton ionisation and tunnel ionisation for a number of different light and medium mass molecules. In the analytical field we are intending to apply FLMS to the detection and sequencing of bio-molecules.

REFERENCES

1) K W D Ledingham, R P Singhal
Accepted for publication in Int. J. Mass Spectrom. Ion Proc. 1997

2) R P Singhal, H S Kilic, K W D Ledingham, C Kosmidis, T McCanny, A J Langley and W Shaikh
Chem Phys Lett 253 81, (1996)

3) K W D Ledingham, H S Kilic, C Kosmidis, R M Deas, A Marshall, T McCanny, R P Singhal and A J Langley
Rapid Commun Mass Spectrom 9 1522, (1995)

4) H S Kilic, KWD Ledingham, C Kosmidis, T McCanny, R P Singhal, A J Langley and W Shaikh
J Phys Chem A101 817, (1997)

5) C Kosmidis, K W D Ledingham, T McCanny, R P Singhal, A J Langley and W Shaikh
J Phys Chem A101 2264, (1997)

6) K W D Ledingham, R P Singhal, H S Kilic, T McCanny, D J Smith S Wong, C Kosmidis, A J Langley and W Shaikh
CLF, RAL Annual Report 1995-96, pp 165 and references therein.

7) C He and C H Becke
Surface & Interface Analysis 24 79, (1996)

8) R P Singhal, K W D Ledingham, H S Kilic, T McCanny, D J Smith, W X Peng, C Kosmidis and A J Langley
Submitted to Chem. Phys. Letters

RESEARCH & DEVELOPMENT OF LASER PLASMA X-RAY SOURCE PULSED DIODE OSCILLATOR

N.Lisi[1)], I.Ross[1)], I.C.E.Turcu[1)], R.Allott[1)], I.Y.Khrushchev[2)], I.H.White[2)], K.A.Williams[2)]

1) Rutherford Appleton Laboratory, Chilton, Didcot, Oxfordshire, OX11 0QX, UK
2) University of Bristol, Bristol, UK

The RAL laser plasma driven x-ray source is the brightest laboratory-sized plasma x-ray source in the world and generates 1W average power x-rays at 1nm wavelength [1)]

In the present configuration a seed pulse of 7ps duration and 0.2nJ is produced at the wavelength of 750nm. Successive amplification in two excimer (XeF or XeCl) pumped dye amplifier cells and frequency tripling yields a pulse of 100μJ energy at the wavelength of 248nm.

The pulse is then time multiplexed in a "pulse stacker" and a 16 pulse train is obtained. The signal is then amplified in two excimer (KrF) amplifiers to give the high intensities necessary for X-Ray generation.

The whole system runs at 100Hz which is limited by the repetition rate of the high energy excimer amplifiers.

The seed pulse is currently produced by a synchronously pumped dye laser in conjunction with a mode locked Nd:YAG.

In such a system the mode locked YAG emission is frequency doubled to give a train of 140ps pulses at 84MHz with the average power of 1W.

Both the longitudinal and transverse mode structure of the seed pulse are critical for x-ray production. The first being critical in the frequency tripling stage in order to obtain high conversion efficiency and the second being critical in the x-ray generation process itself.

The picosecond oscillator requirements are the following. Energy > 0.2nJ, Pulse duration ~ 10ps, repetition rate = 100Hz, wavelength = 750nm, bandwidth = 0.1nm.

The present system could be replaced in the near future by a diode laser, developed by Prof. Ian White and his team, now at the University of Bristol.

These devices consist of a quantum well AlGaAs diode lasers, for which the emission wavelength can be determined by appropriate design of the quantum wells structure.

The short pulse generation can be obtained in different operation modes such as Q-switching [2)], gain-switching [3)] and mode locking [4)]. Q-switching is the most appropriate high power scheme for low repetition rate. Mode-locking is appropriate for higher repetition rates.

In figure 1 we show a scheme of a multisection laser diode. The design for the Q-switched operation is provided by placing an absorber section between two gain sections. The reverse biased central section prevents laser oscillation until an enhanced gain condition is reached in the gain regions. The Bow-Tie laser geometry [5)] allows further enhancement in power and energy of the pulses generated.

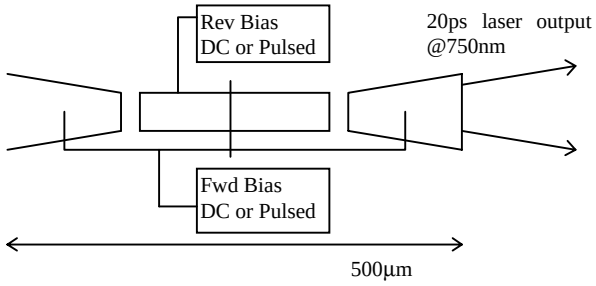

Fig.1. Bow-Tie Pulsed laser diode

The DC negative bias and the RF modulation signal are applied to the absorber using a bias-tee similarly to the experiment described in reference [2)]. The RF signal is pulsed and consists of 20-30ns bursts of 500MHz sine wave with a peak power of 30dBm. The scheme delivers externally triggered pulse trains 20ns in duration with the 2ns spacing between the optical pulses in train and therefore replaces the 'pulse-staker'.

The main challenge in developing the device is controlling the mode structure and the bandwidth while obtaining high energy and short pulse duration. The properties of the gain and of the absorption change considerably with varying the driving and bias conditions. Improved control of the temporal and spectral characteristics of the pulses generated can be achieved by using an external cavity or by introducing a two-cascade oscillator-amplifier scheme. Both approaches require high-quality AR coatings at the laser diode facet(s). The AR -coating facilities currently being installed at Bristol will allow for such schemes to be optimised.

Figure 2 and 3 show the spectrum and the oscilloscope trace measured for a Q-switched narrow-waveguide device.

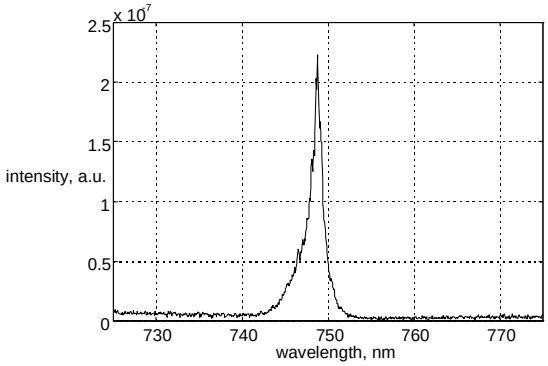

Fig.2. Spectrum of the Q-switched bow-tie laser diode output.

Pulses of 12ps duration with a central wavelength of 748nm have been generated. Two of the main targets, the wavelength and the pulse duration, have been achieved. The obtained pulse energy of 14pJ is sufficient for seeding into the system.

A feature of these devices is their astigmatism, which can be controlled with standard diode optics. Typically, the beam is diffraction limited along the transverse direction (orthogonal to the active layer) and close to the diffraction limited in the lateral direction (parallel to active layer). The lateral mode quality depends strongly on the construction geometry.

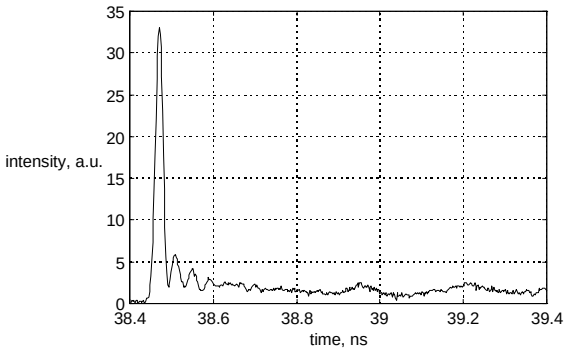

Fig.3. Oscilloscope trace of the Q-switched bow-tie laser diode output.

A Bow-Tie laser diode was successfully integrated in the present set-up of the laser plasma x-ray laboratory at the Rutherford during a short experimental period of one week. This device, shown in figure 1, had a pulsed RF signal applied to the absorber section. Problems of triggering, synchronisation, beam shaping and optical layout were solved. The main problem during the experiments was the feedback from the laser diode facet back to the dye amplifier resulted in the parasitic oscillation in the amplifier which prevented the observation of the signal amplification. A short-wavelength optical isolator now available in Bristol can be used to prevent such parasitic generation in future.

In conclusion there are good prospects of using pulsed picosecond diode lasers as oscillators for high power laser systems. They have great advantages in cost, maintenance and ease of use over many alternative systems.

REFERENCES

1) I.C.E.Turcu, I.N.Ross
Rev. Sci. Instrum. 67, (9) pp3245-3247 (1996)

2) P.P.Vasiliev, I.H.White, D.Burns, W.Sibbett
El.Lett. 29 (18) pp1593-1594, (1993)

3) D.Z.Tsang, J.N.Walpole
IEEE J.of QE 19 (2) pp145-156, (1983)

4) E.P.Ippen, D.J.Eilenberg, R.W.Dixon
Applied Phys.Lett. .37 (3) pp.267-269, (1980)

5) K.A.Williams, J.Sarma, I.H.White, R.V.Penty, I.Middlemast, T.Ryan, F.R.Laughton, J.S.Roberts
El.Lett. 30 (4) pp.320-321, (1994)

DETECTORS FOR THE LASER PLASMA SCANNING X-RAY MICROSCOPE

A.G. Michette[1], C.J. Buckley[1], I.C.E. Turcu[2], G.S. Dermody[1], N.I. Khaleque[1], S.J. Pfauntsch[1], N. Spencer[2] and W. Shaikh[2]

[1]Centre for X-ray Science, Department of Physics, King's College London, Strand, London WC2R 2LS
[2]Lasers *for* Science Facility, Rutherford Appleton Laboratory, Chilton, Didcot, Oxon OX11 0QX

INTRODUCTION

The scanning x-ray microscope (figure 1) is being developed and tested at King's College and is expected to be commissioned on the LSF x-ray source early in 1998. Since the 1980s all x-ray microscopes have been designed for use with synchrotron sources, apart from a prototype of the present system which has previously been tested.[1)] In addition to scanning the source rather than the specimen, which has several advantages,[2)] it is not possible to use a proportional counter detector as with synchrotron based microscopes, since the x-ray photons arrive in short pulses with peak count rates of up to about $10^{15}s^{-1}$ in the focal spot of the zone plate optic. Proportional counters can only count at up to $\sim 10^{6}s^{-1}$, and thus it is necessary to use a current measuring detector such as a photodiode or a modified electron multiplier. Both these types of detector have been tested on the LSF source; unfortunately, during these tests the source was not operating at full capability and the output was much lower than it might have been.

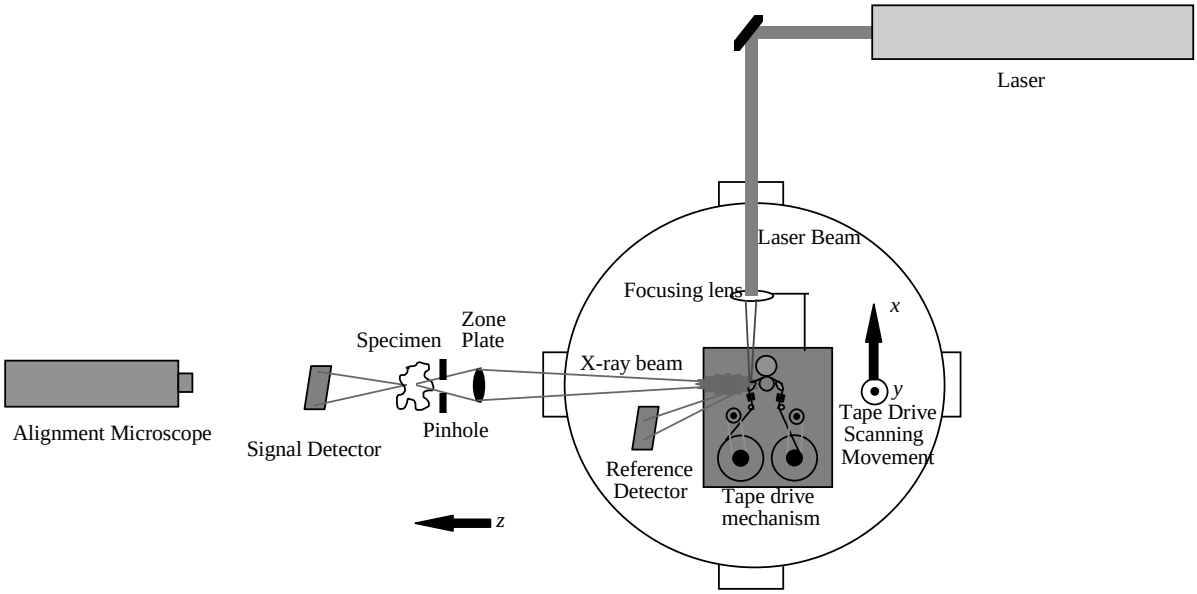

Figure 1. Schematic of the scanning x-ray microscope.

PHOTODIODE DETECTOR

Photodiodes are commonly used as detectors of laser-plasma x-rays, for example as the reference detector for the LSF source. The signal in the scanning x-ray microscope will be very much lower than the reference value, and so a more sensitive diode is required. That used was a UDT XUV-5, selected because it has a very thin dead layer and hence good quantum efficiency at the x-ray energies used in microscopy (a few hundred electron volts); unfortunately it is also susceptible to noise. This type of diode is normally used with a FET preamplifier and, e.g., an Amptek amplifier, but it turned out that the decay time of the resulting pulse was over three orders of magnitude too long for data acquisition via the available Lecroy system. It was not possible to shorten the decay time while at the same time maintaining a reasonable gain, and so the diode was mounted inside the target chamber, alongside the reference diode, to allow its relative response to be determined by measuring the direct charge output. Both the reference diode and the signal diode had, for these measurements, vanadium filters in front of them to select water window x-rays. The diode responses, for bias voltages of −5V and −10V, are shown in figures 2 and 3 (preliminary analysis). Linearity is good up to higher signal levels than will be used in practice for both voltages whereas the resolution (the ratio of the standard deviation of the signal to the mean) is improved with a higher negative bias. This is more marked at lower signal levels which are closer to those which will be obtained in the microscope.

Because of the lower than usual source output and of the pulse amplification problems, it was not possible to test the noise reduction schemes as planned. These schemes, which involve electrical screening and temperature reduction (using an array of Peltier coolers), will now be tested at King's where, however, the environment is different.

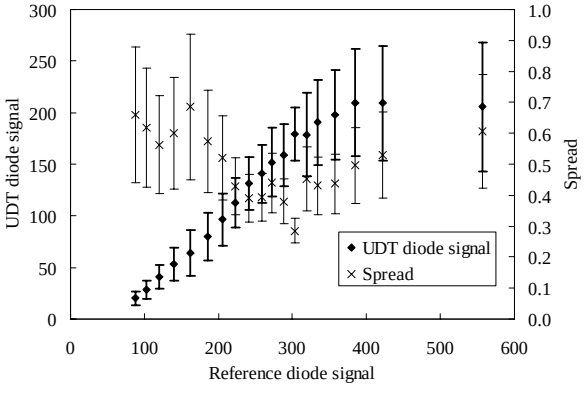

Figure 2. The photodiode response at a bias of −5 V.

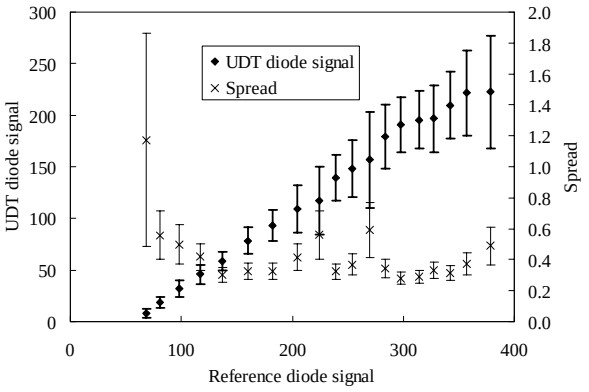

Figure 3. The photodiode response at a bias of −10 V.

ELECTRON MULTIPLIER

Because of the noise problems associated with the photodiode it is important to investigate other types of detector. One possibility is to use a modified photomultiplier. A Thorn EMI EM129 photomultiplier was removed from its glass vacuum envelope. The electron multiplier, without its photocathode, was then mounted on a flange with electrical feedthroughs and put into a purpose built compact vacuum vessel. The first dynode was coated with 100 nm of caesium iodide, which emits photoelectrons when irradiated with x-rays. The front flange of the vacuum vessel contained an aluminised silicon nitride window (0.5×0.5 mm and 0.1 µm thick); this maintained the vacuum, was opaque to light and about 50% transmitting to x-rays. The vessel was evacuated by a turbo pump and operated at a pressure of ~10^{-6} Torr.

The dynode chain was operated at negative voltages in the range 800–2000 V, giving a charge gain of 5×10^4–7×10^5 with a pulse width of ~20 ns. A preamplifier was used to provide extra gain to work comfortably within the range of the data acquisition electronics, and a number of comparisons between the reference diode and the multiplier system were recorded. Examples at voltages of −1147 V and −1850 V are shown in figures 4 and 5 (preliminary analysis). Although the spread is lower at the higher negative voltage the detector saturates at a lower signal level. This should not be a problem in practice as the signals used in the tests are much higher than will be the case in the microscope.

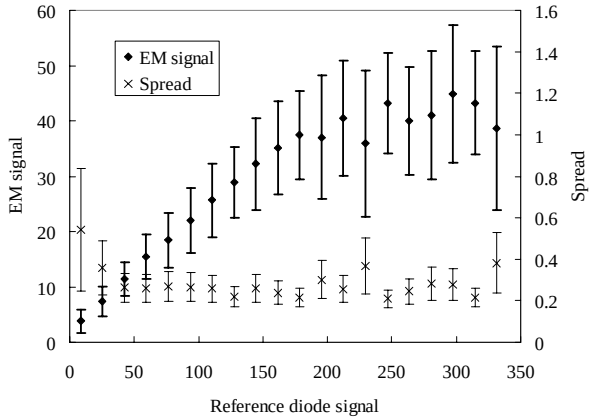

Figure 4. The electron multiplier response at −1147 V.

CONCLUSIONS

The results presented here are preliminary; the data obtained concerning each detector has yet to be fully analysed, and so it is not yet possible to conclude which will be the most appropriate for the scanning x-ray microscope. Although the response of the photodiode appears to be more linear than that of the electron multiplier, the spread is worse. However, it has not yet been possible to test the noise reduction schemes for the photodiode in the working environment; reduction of both electromagnetic and thermal noise should improve the spread considerably.

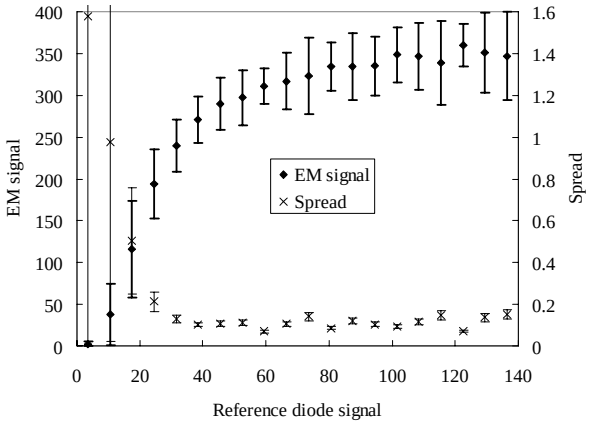

Figure 5. The electron multiplier response at −1850 V.

REFERENCES

1) A G Michette, R Fedosejevs, S J Pfauntsch and R Bobkowski Measurement Science and Technology, 5 555, (1994)

2) A G Michette, C J Buckley, S J Pfauntsch, N Khaleque, T English, M Folkard, B D Michael, G Schettino, I C E Turcu, R Allott and N Lisi
in: X-Ray Microscopy and Spectromicroscopy (Berlin: Springer) (in press, 1997)

REFLECTIVITY EXPERIMENTS WITH ULTRA-SHORT LASER PULSES

D Riley [1)], AJ Langley [2)], PF Taday [2)], W Shaikh [2)] and I McCormack [2)]

1) Queen's University of Belfast, Belfast BT7 1NN UK. Email d.riley@qub.ac.uk
2) Rutherford Appleton Laboratory Chilton, Didcot, Oxon, OX11 0QX, UK

INTRODUCTION

During the summer of 1996 an experiment was carried out to measure the reflectivity of solid targets irradiated at high intensity with ultra-short laser pulses from the Lasers For Science (LSF) 50 fs Ti-Sapphire facility. This experiment was a preliminary one designed to show the viability of the system for plasma physics based experiments. The experiment was successful in this respect and also in that the experimental results showed behaviour markedly different from what has been seen at longer pulse lengths.

THE EXPERIMENT

The results shown in this report are all taken from a single beam experiment. The output of the 50 fs Ti-Sapphire laser was focused onto both aluminium and silicon targets inside a vacuum chamber with f/2 optics. The pulses were incident at about 20 degrees to the normal and the specularly reflected light was collected with a second lens. Obtaining and monitoring a good focal spot was achieved by first illuminating the surface of the target with a strong white light source. The collection lens was then adjusted so that a small fraction of the collected light was reflected off a glass plate to form an image at x80 magnification at the image plane of a CCD camera. Good focusing was checked by the visibility of microscopic scratches on the target surface. The laser oscillator was then used to generate a rapid series of pulses which for viewing purposes was effectively a continuous wave beam. This was focused onto the target and the focal position adjusted so that the smallest possible spot was obtained in the centre of the viewing field of the collection lens/CCD system. This defined the best focal spot, which was measured on the captured CCD frame to be 8±0.5 μm in diameter. The collected light that was not reflected by the glass plate was incident on a diffusing glass plate in front of a photo-diode. This was used to measure the reflected energy from the target surface. The initial energy in the laser pulses was monitored by placing a further glass plate in the beam, before the focusing lens. This reflected a small fraction of the energy into an integrating sphere coupled to a photo-diode. The pulse energy could be controlled over a dynamic range of about 100 with a continuously variable thin glass ND filter. A calibrated power meter was used in the calibration of the photo-diode detector arrangements which were carried out *in-situ* with only the oscillator running. The absolute calibration of the energy was good to about 10%. The relative calibration between the photo-diodes showed a statistical fluctuation of about 3%, which indicates a similar level of confidence in the reflectivity measurements. Figure 1 shows a schematic of the experimental arrangement. Because the laser runs at 10 Hz, the output from the diodes was fed into oscilloscopes with the capability of automated boxcar integration. This meant that data could be collected automatically from each shot and stored electronically. The data presented here are averages over 10 actual laser shots

The pulse length was measured at the start of the experiment and the glass block in which the chirped pulse is recompressed was adjusted to give the shortest pulse at the target surface This was necessary as the glass plate, lens, ND wheel and glass plate all contribute to the dispersion of the pulse, and need to be corrected for. The best pulse was approximately 60 fs FWHM. Three target types were used. The first was an aluminium tape that was run like a cassette tape across the focus so as to present a fresh surface to each laser shot.. The second was an optical blank coated with one micron thick layer of aluminium to form a high quality mirror–like surface. This target was rotated as the laser was fired at 10 Hz. The third target was a polished silicon wafer that was mounted and rotated in a manner similar to the aluminium mirror. In all three cases, the focal spot was monitored so as to check that the motion of the target was small enough that the surface plane was always within the focal depth of the laser.

RESULTS

Figure 2 shows results for the silicon wafer. This should show the most marked change with irradiance since the reflectivity starts off at a low value (35%) and is expected to rise to over 80% with the formation of a high density plasma [1)]. The data at low irradiance was collected using the oscillator only. As can be seen there is no evidence for any real change in reflectivity with intensity. This was true also for the aluminium targets, i.e. there was no evidence of an increase in reflectivity due to plasma formation. For the latter case the evidence is not so conclusive since the reflectivity was already at 80% for the low irradiance

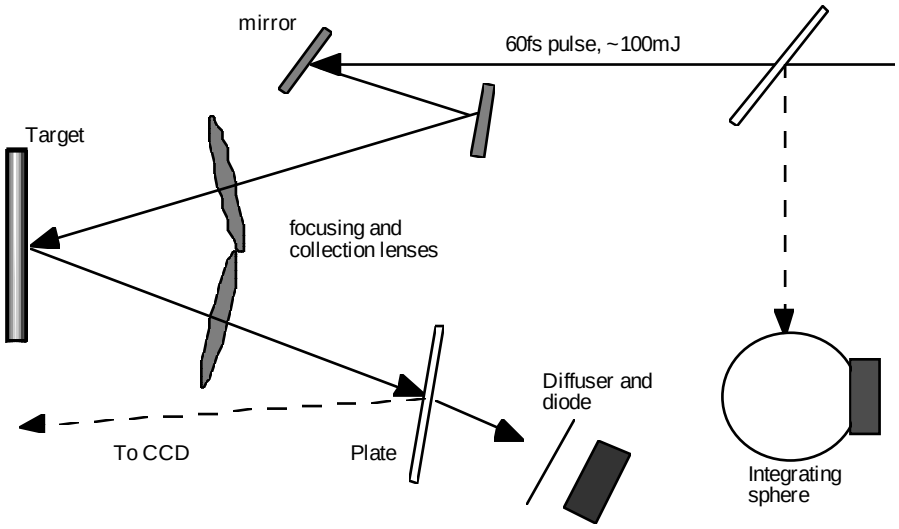

Figure 1 Schematic of the experimental arrangement. The lenses were nominally f/2 but the smaller beam diameter led to f/5 focusing

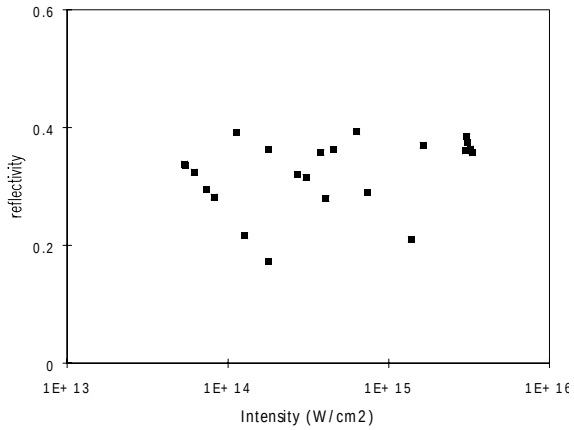

Figure 2 Reflectivity of the Si target as a function on intensity. Each point is averaged over 10 shots.

case and statistical fluctuations would mask an increase of a few percent. In the case of silicon, it may be argued that the absorption depth for 800 nm light is quite long (4 μm) and so the energy dumped may not be sufficient for plasma production. However, at the highest intensities using a 4 μm depth we can calculate that the energy density dumped is approximately $3x10^5$ J/cm^3, in other words about 40 eV per atom. This is more than enough to vaporise and ionise the silicon. Evidence of melting can be seen in figure 3 which is an Atomic Force Microscope (AFM) image of a damage spot on the silicon left by one shot at $4x10^{15}$ Wcm^{-2}. As can be seen a wide ring (~50 μm) of damage is created with ripples of several microns peak height. This is strong indication of melting due to thermal diffusion from the focal spot and shock generation.

DISCUSSION

The evidence is clearly that there is no change in reflectivity during the main part of the pulse. This is despite evidence that the pulse deposits enough energy to not only damage the target but heat it to very high temperature. This is not so surprising as it is known that the lattice in a solid may take several hundred femtoseconds to disassemble after initial heating. In the case of aluminium, there are free electrons already present and the conductivity (and hence reflectivity) of the target depends on maintaining the lattice structure.

In the case of silicon, it is not clear how many free electrons are created. For 800 nm light the promotion of electrons from the valence to the conduction band by photon absorption needs to be phonon assisted to cross the band gap. For silicon, the longitudinal-optical mode (LO) phonon vibrational period is 70 fs which is longer than the laser pulse length [2]. Exactly, how much this affects the absorption depth and thus the temperature attained, is not clear to the authors. However, it is clear that melting does occur and that it must occur after the pulse, since the reflectivity of molten Si is over 70%.

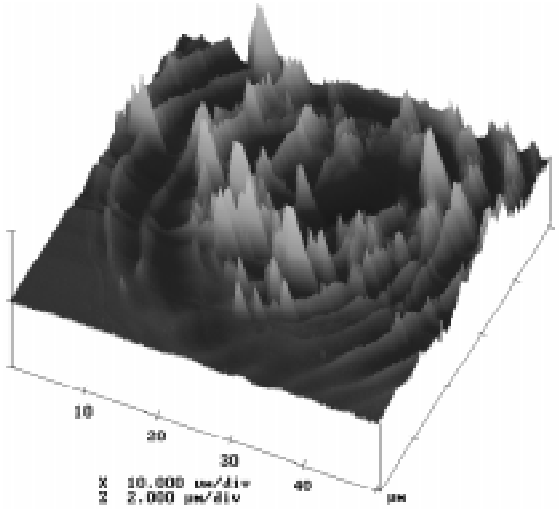

Figure 3 AFM picture of a typical shot. The vertical scale is expanded five times compared to horizontal. The focal spot was originally 8 microns in diameter

Previous work [2,3] on the response of silicon to ultra-fast laser pulses has shown that the lattice melts on a time scale of ~ 1ps. Thus our present conclusions may not appear to be surprising. However, it has also been shown that cubic order can be lost on a 150 fs timescale due to intense (>10^{12} Wcm^{-2}) laser excitation [3]. The focused intensities used here are much higher and the laser pulses are shorter. This is an important difference as it has been predicted that such short pulses may be used to generate very high harmonics of the laser when incident on solids at higher irradiances [4] and may even be used to generate coherent keV X-rays [5]. Both of these phenomena rely on the lattice of the solid remaining intact during the laser pulse, which from our data appears to be the case.

CONCLUSIONS

We have shown that the reflectivity of solid targets remains essentially constant when irradiated with 60 fs laser pulses at 800 nm. This appears to be the case even for focused intensity up to $4x10^{15}$ Wcm^{-2}. This is encouraging for the prospects of two mechanisms that have been advanced as methods of generating XUV and X-ray photon sources.

The authors would like to thank Dr Albert Turner for use of the Atomic Force Microscope and the staff of the target preparation facility at RAL for fabrication of targets.

REFERENCES

1) M M Murnane, H C Kapteyn, S P Gordon and R W Falcone
Appl. Phys. B 58 261, (1994)

2) C V Shank, R Yen and C Hirlimann
Phys.Rev.Lett. 50 (6) 454, (1983)

3) H W K Tom, G D Aumiller and C H Brito-Cruz
Phys.Rev.Lett. 60 (6) 1438, (1988)

4) S Hüller and J Meyer-ter-Vehn
Phys.Rev.A 48 3906, (1993)

5) P Kàlman and T Brabec
Phys. Rev. A 51 R21, (1995)

AN INVESTIGATION OF THE BEHAVIOUR OF GROUND STATE AND VIBRATIONALLY EXCITED CO_2 IN INTENSE FEMTOSECOND LASER PULSES

J. H. Sanderson[1)], R. V. Thomas[1)], W. A. Bryan[1)], W. R. Newell[1)], I. D. Williams[2], P. F. Taday[3)], A. J Langley[3)]

1) University College London, Gower Street, London WC1E 6BT
2) Department of Pure and Applied Physics, Queens University of Belfast , BT7 1NN
3) Rutherford Appleton Laboratory, Chilton Didcot, Oxfordshire OX11 0QX

In a number of experiments carried out at RAL we have studied the fragmentation of the CO_2 molecule using laser pulses of 60 fs at 750 nm producing field intensities of ~ 7×10^{15} W/cm^2. To date all work on laser fragmentation of molecules has been concerned with molecules initially in the lowest vibrational level, but in the present work we have also excited the molecules to upper vibrational levels (n, n, n) and measured the fragmentation spectra.

The laser employed in the present work is a 55 fs system[1)] operating at a centre wavelength of 750 nm with a pulse energy of 60 µJ and a repetition rate of 10 Hz. The incident laser beam enters the vacuum system through a fused silica window which stretches the pulses to 60fs and is reflection focused using an f/2 parabolic mirror into the interaction region giving a near diffraction limited spot size, calculated to be 4.2µm. The intensity was calculated from the spot size and the pulse energy yielding a peak value of 7×10^{15} W/cm^2 which was confirmed by measuring the charged states of Xe[2)]. The laser focus was situated in the central plane equidistant from two parallel grids separated by 20mm, which form the source region of a Wiley-McLaren type time-of-flight (TOF) mass spectrometer. The spectrometer has a total flight path of 12.53cm with a pair of microchannel plates of 25mm diameter used to detect the ions. To measure angular distributions, a 1mm diameter aperture is placed in front of the channel plates. The apparatus has an ultimate background pressure of around 4×10^{-10} torr, and the test gas is introduced into the interaction region by a hypodermic needle, the tip of which is situated 10mm from the laser focus. Vibrationally excited molecules are produced through thermal excitation, by heating the hypodermic needle with a kanthanol wire heating element which surrounds it. In a supplementary experiment, a thermocouple was used to determine the temperature of the tip of the needle which was found to be 200^o C.

The ion signal is fed through a preamplifier into an EG&G turbo multi-channel-scalar (MCS). The MCS has a channel width of 5ns with zero dead time between channels and is capable of counting more than one event per channel.

To ensure that there is no more than a 10% fluctuation in the energy of the laser pulses entering the experiment, the start pulse to the MCS is gated by monitoring the reflection from the input window with a photodiode. The photodiode pulse height having previously been calibrated against the laser pulse energy and found to be linearly proportional to it. The photodiode pulses are amplified and passed through a single channel analyser which has a window set to ±10% of the desired pulse height. The pulses which are within the chosen range are used to provide the start pulse for the MCS. The laser pulse shape is also monitored with an autocorrelator so that any drift in pulse width can be detected; the pulse to pulse variation in width is less than ± 5fs.

An ionic TOF spectrum obtained for both hot and cold CO_2, with the polarisation parallel to the TOF axis, is shown in Fig. 1, the prominent contamination features H_2O^+, OH^+, O^+ and O^{++} are detected. These features arise from the ionisation and dissociative ionisation of H_2O, evaporated from surfaces by the action of the heater. Apart from these contamination peaks, the differences between the hot and cold CO_2 spectra in Figure 1 are due to the vibrational excitation of the CO_2 molecules.

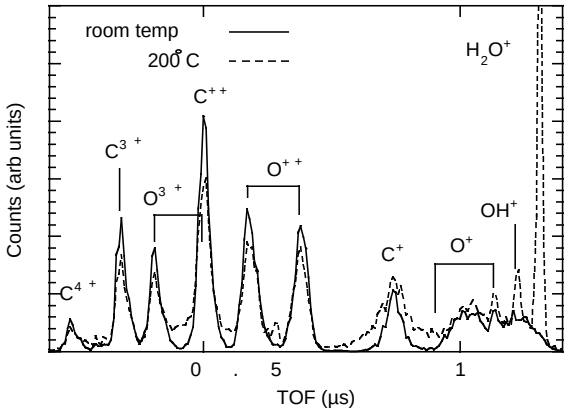

Fig. 1 TOF spectrum for fragment ions of ground state and vibrationally excited CO_2

The behaviour of ground state CO_2 in intense laser radiation has been well characterised experimentally, in the infra red wavelength region, by several groups; using the technique of covariance mapping, to identify the allowed channels of multielectron-dissociative-ionisation (MEDI)[3)] or to identify modifications to the linearity of the coulomb exploding molecule[4),5)]

In the present work the CO_2 molecules were non-selectively excited to the vibrational modes of the ground electronic state by resistive heating of the hypodermic needle. At the temperature of 200^{o}C used in this experiment 26% of all the molecules will be in excited vibrational states and assuming the normal Boltzmann distribution then 19% of the CO_2 molecules will be in the first excited vibrational level at 83meV. This level is a bend mode (010) which is non-symmetric in contrast to the ground state symmetric mode (000). In the (010) mode the central carbon atom oscillates in a direction perpendicular to the C_n axis, giving a maximum OCO angle of 175^o .

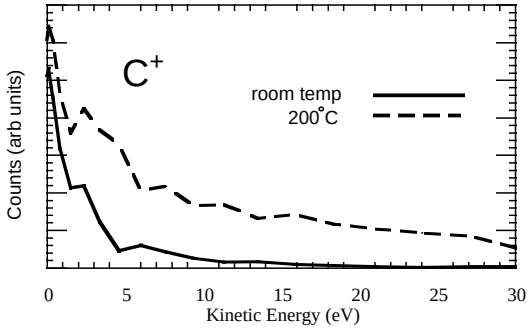

Fig.2 Kinetic energy distribution for C^+ ion resulting from coulomb explosion of CO2 both in ground state and vibrationally excited

The TOF spectrum recorded at 200^o shows two obvious changes when compared with the ground state spectrum in Fig. 1. Firstly the amounts of O^+ and particularly C^+ have increased, while the amounts of the higher stages of ionisation have decreased. Secondly, the widths of the C^+ and C^{2+} peaks have increased, with the width of the C^+ peak more than doubled in the time spectrum.

The FWHM of the energy distribution of C^+ in Figure 2, has increased from 1.5 to 5 eV while the tail has increased to kinetic energies of greater than 30 eV (the C^+ energy cannot be measured at higher energies as the C^+ peak merges with the O^{++} TOF peaks at around 30eV). Modifications to the oxygen ion kinetic energies are small.

The modifications to the TOF spectra which are primarily associated with the carbon ions may at first seem anomalous, but are a good indicator of how the laser field has interacted with the CO_2 molecule, excited predominately to the (010) mode. When initially in the ground state mode the CO_2 molecule will preferentially distort along the C_n axis, rotate by virtue of the induced moment and dissociate with the C_n axis parallel to the laser polarisation direction. We have observed this alignment of the molecule by measuring the signal for the various ion fragments, as a function of angle. Fig. 3 shows a polar plot for the O^{++} fragment (produced from ground state CO_2) showing strong alignment with the laser field direction, (parallel with the horizontal axis). Bending of CO_2 initially in the ground state can be seen by observing the angular distribution of the C^{++} ion in Fig. 4. Unlike the O^{++} ion the distribution is peaked at 90^o to the laser field direction, such a distribution can only results from the coulomb explosion of a bent molecule aligned with the laser field[4), 5)]

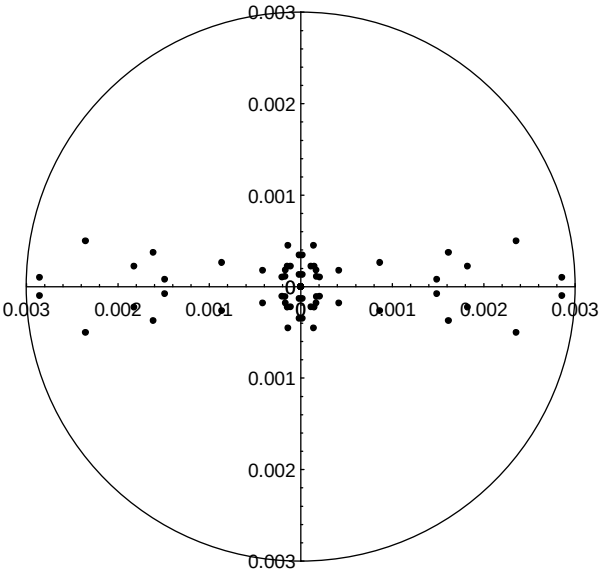

Fig. 3 polar plot of O^{++} ion distribution, with the laser field direction parallel to the horizontal axis

In the case of the initially vibrationally excited CO_2 it is reasonable to expect that the non-symmetric bending vibration, which has a dipole moment, allows the molecule to couple more strongly with the laser field. The dipole moment associated with the (010) bending mode will allow the molecule to align with the principal C_n axis perpendicular to the laser polarisation. If this is the case the CO_2 molecule will then tend to bend further.

When coulomb explosion takes place, the energy which the carbon ion gains is large compared to that of the oxygen ions, due to conservation of momentum. The result is a modification to the TOF spectrum (recorded parallel to the laser field) in the form of wider carbon ion peaks, but with no significant change to the oxygen peaks, this is exactly the pattern observed in Fig. 1. Evidence for this process also comes from the results of an experiment using SO_2, which is a bent molecule[6)]. The $O^+ + S^+ + O^{Z+}$ (Z=1,2) channel was shown to exhibit an almost

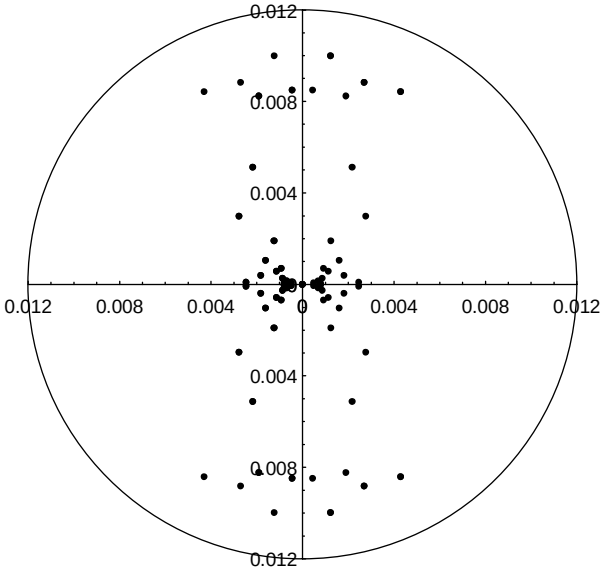

Fig. 4 polar plot of C^{++} ion distribution, with the laser field direction parallel to the horizontal axis

elliptical island, or more precisely an atoll on a covariance map produced with laser polarisation parallel to the detector axis. Cornaggia *et* al showed that the elipticity was due to the bend in the molecule, and consistent with an OSO angle of 120^o , which is the known molecular bend. The fact that the atoll was complete indicates that SO_2 was ionised with its central axis perpendicular to the laser field, as deduced in the present experiment for CO_2.

We can calculate the effect of a bent configuration on the C^+ kinetic energy. If we assume that the molecule is aligned with the O - O axis perpendicular to the laser polarisation, and that the equilibrium C - O bond length of 1.16 is constant, and the C^+ ions result from the $O^+ + C^+ + O^+$ channel, we can vary the OCO angle and calculate the coulomb energies which result. For an angle of 90^o it is possible to generate an energy of 13.7eV, which is in the tail of the C^+ energy distribution.

In conclusion we have made the first observation of laser induced fragmentation of a vibrationally excited molecule, and have also directly observed bending of ground state CO_2 during the dissociation process.

REFERENCES

1) A J Langley, W J Noad, I N Ross, and W Shaikh,
Applied Optics 33, 3875 (1994)

2) S Augst, D Strickland, D D Meyerhofer, S L Chin, and J H Eberly
Phys.Rev.Lett. 63, 2212 (1989)

3) L J Frasinski, P A Hatherly, K Codling, M Larsson, A Persson, and G G Wahlström
J.Phys.B: At.Mol.Opt.Phys. 27, L109 (1994)

4) C Cornaggia, M Schmidt, and D Normond
J.Phys.B: At.Mol.Opt. 27, L123 (1994)

5) C Cornaggia
Phys.Rev.A. 54, 2555 (1996)

6) C Cornaggia, F Salin and C Le Blanc
J.Phys.B: At.Mol.Opt. 29 L749 - 754 (1996)

TWO-COLOUR PHASE-CONTROL OF DISSOCIATIVE IONISATION OF H_2 WITH INTENSE Ti-SAPPHIRE LASER PULSES

M R Thompson, J H Posthumus, M K Thomas, L J Frasinski and K Codling

J J Thomson Physical Laboratory, University of Reading, Whiteknights, Reading RG6 6AF, United Kingdom

INTRODUCTION

In a recent letter, Sheehy *et al* (1995) reported on phase control in two-colour photodissociation of HD^+. In the experiment, the authors used the relative phase between the fundamental (1053 nm) and second harmonic (527 nm) of a 50 ps Nd:YLF laser to control the spatial asymmetry of the dissociation channels, H + D^+ and H^+ + D. To their surprise, the positive ions were preferentially emitted in the counter-intuitive direction, i.e. opposite that in which the maximum of the combined two-colour laser *E*-field points.

In this paper we report on a similar experiment on H_2 performed with laser pulses which are three orders of magnitude shorter and ten times more intense. Despite these large differences, and shorter wavelengths as well, we find qualitatively the same spatial asymmetry, i.e. counter-intuitive. However, in contrast to Sheehy *et al* (1995), we do not observe any other phase modulation, apart from the asymmetry. For example, the H_2^+ ion yield did not modulate as a function of phase, in disagreement with tunnelling and over-the-barrier models.

The first ion spectra of H_2 in the intense, *short* pulse regime were presented by Codling *et al* (1988), but the at that time available theoretical and experimental techniques did not allow for a correct interpretation. A few years later Frasinski *et al* (1992) subjected H_2 to intense 3 ps pulses of 600 nm wavelength and showed, using covariance mapping (Frasinski *et al* 1989), that the most energetic H^+ ions (1 to 6 eV, peaking at 2.4 eV) were due to the $H^+ + H^+$ channel. This confirmed that the double ionisation was a sequential process; the second ionisation step must have occurred at a larger internuclear separation, because Coulomb explosion from the equilibrium distance of H_2 would yield much higher kinetic energies. Zavriyev *et al* (1993) used 160 fs pulses at 769 nm wavelength and observed structure in the Coulomb explosion peak and ascribed this to trapping in a light-induced potential well (see e.g. the topical review on the dynamics of H_2^+ in intense laser fields by Giusti-Suzor *et al* 1995). We are unable to reproduce this structure.

A classical field ionisation, Coulomb explosion model to describe the multi-electron dissociative ionisation of diatomic molecules in intense laser fields was developed (Codling *et al* 1989, Posthumus *et al* 1995, 1996a). The model has been combined with trajectory calculations to produce fragment ion energies that are in good agreement with experiments, especially on I_2 (Posthumus *et al* 1996a). The most important aspect of the model is the enhanced ionisation probability at the critical internuclear distance R_c. This phenomenon has also been identified quantum-mechanically (Seideman *et al* 1995, Zuo and Bandrauk 1995).

With the ADK tunnelling model (Ammosov *et al* 1986) one can easily show that, for *sub-picosecond* pulses, the ionisation process does not saturate until the *classical* appearance intensity is reached (see Posthumus *et al* 1996c). The classical appearance intensity is calculated from the laser *E*-field that is required to let the active electron classically escape over the potential barrier. For H_2 it is about 2×10^{14} Wcm^{-2}. At this intensity the ionisation probability of H_2^+, when it dissociates through R_c, is extremely high, leading almost inevitably to further ionisation. It was therefore suggested that the stability of the neutral molecule, not trapping in H_2^+, lies at the origin of the strong Coulomb explosion signal (Posthumus *et al* 1996b). The data presented in this paper underline this explanation.

LASER OPTICS

The Ti-Sapphire laser plus three-stage dye amplifier provided laser pulses of 100 μJ at 750 nm (Langley *et al* 1994). The stretcher and compressor of the CPA system were adjusted to minimise the pulse length in the experiment, which was 55 fs. The second harmonic was created by a 0.2 mm thick BBO crystal. In order to determine the pulselength at λ = 375 nm, we led the beam through a Michelson interferometer and slowly stepped it whilst measuring an ion signal in the experimental set-up. The signal, in this case of N_2^+ ions, as a function of optical path difference in the interferometer, is shown in figure 1. Due to the finite stepsize, the interference is sampled in discrete steps, adding to the irregularity of the interferogram. We expect the ion signal to be nearly proportional to the focal volume, which itself is proportional to $I_{max}^{1.5}$, where I_{max} is the peak intensity of the laser pulse. The best fit to the interferogram was obtained with an 85 fs Gaussian pulse and an $I_{max}^{2.2}$ power law.

The 1 cm diameter laser beam was focused by a parabolic mirror of 4 cm focal length. The 62 cm long ion spectrometer, with a 5 V/cm ion extraction field, was placed parallel to the linear polarisation of the laser *E*-field. The analog signal of the channel plates was digitized by an oscilloscope with a 400 MHz sampling rate and averaged over generally several thousand laser pulses. The actual size of the laser focus is usually larger than the one calculated from the diffraction limit of a Gaussian beam profile, especially for short focal lengths. Since we could not measure the spot size directly, we calibrated the intensity with Xe^+ and the ADK model, which gives the correct saturation intensity at the fundamental wavelength of the Ti-Sapphire laser (Telebpour *et al* 1996). We found that the actual intensity was three times smaller than the calculated one. For the second harmonic, the focal spot area is in principle four times smaller. However, since the diffraction limit is harder to reach at shorter wavelengths, we assumed it was only twice as small, i.e. we have divided the calculated intensity by a factor of six. The background pressure was 10^{-9} mbarr. The target gas pressure was up to 10^{-5} mbarr for the lowest intensities, but always kept low enough to avoid space charge effects. The limiting factor in the energy resolution is thought to be Doppler-broadening.

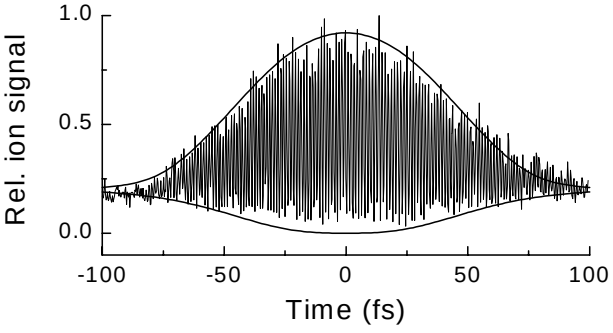

Figure 1. Interferogram, showing the N_2^+ ion signal as a function of time delay between two pulses at the second harmonic frequency. A pulse width of 85 fs is deduced, see envelope.

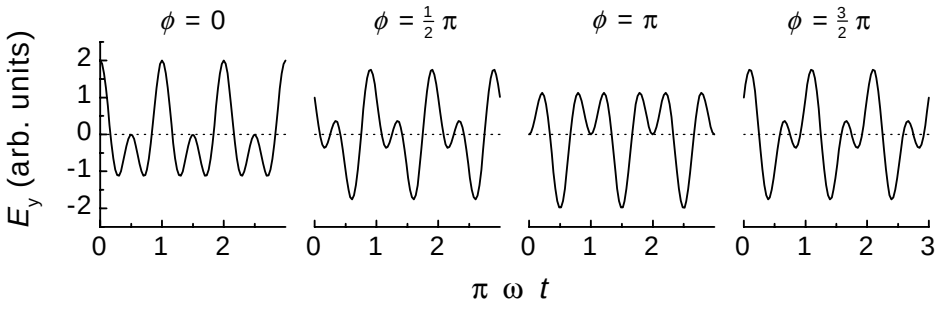

Figure 2. The two colour laser *E*-field, $\cos(\omega t) + \cos(2\omega t + \phi)$, for equal intensities and four different phases

COHERENT TWO-COLOUR PULSES

Two phase-locked pulses of different colour allow us to investigate spatial asymmetry in the H + H^+ dissociation channel. Sheehy *et al* (1995) used the relative phase between the fundamental (1053 nm) and second harmonic (527 nm) of a 50 ps Nd:YLF laser to control the spatial asymmetry of the dissociation channels, H + D^+ and H^+ + D. The positive ions were preferentially emitted in the counter-intuitive direction, i.e. opposite that in which the maximum of the combined two-colour laser *E*-field points. The phase modulation of the forward/backward ratio was largest when the intensity at both wavelengths was very nearly equal. The combined laser intensity was 2×10^{13} Wcm^{-2}. The total ion signal modulated at twice the frequency of the spatial asymmetry modulation. This is a clear sign of tunnel-ionisation, as can be appreciated from figure 2: whilst the phase goes through one cycle, the peak *E*-field has a maximum twice, namely at $\phi = 0$ and $\phi = \pi$.

In the present two-colour experiment, the electron drift tube was located opposite of the ion drift tube. The extraction field, therefore, directed both types of particles simultaneously towards their respective detectors. The collection efficiency of the electron drift tube was significantly enhanced by an axial magnetic field. Because of this and the variable ponderomotive shift, the electron energy resolution was relatively poor. However, the setup is perfectly suited for distinguishing between general 'forward' and 'backward' electrons.

Figure 3 shows three ion spectra for three different relative phases between two overlapping pulses of equal peak intensity, namely 10^{14} Wcm^{-2}. Like Sheehy *et al* (1995) we use the asymmetry in the electron spectra for calibration of the absolute phase. However, the short pulse regime does not allow for a direct comparison with the data of Schumacher *et al* (1994), nor does it advocate an absolute calibration of the phase. We trust, therefore, that a phase of $\phi = 0$ leads to a preponderance of forward electrons (see figure 3). Apart from an overall asymmetry, which is due to a higher collection efficiency of forward ions, an unmistakable interference of the dissociation channel can be observed, i.e. modulation of the $(2\omega_1 + \omega_2)$ peak.

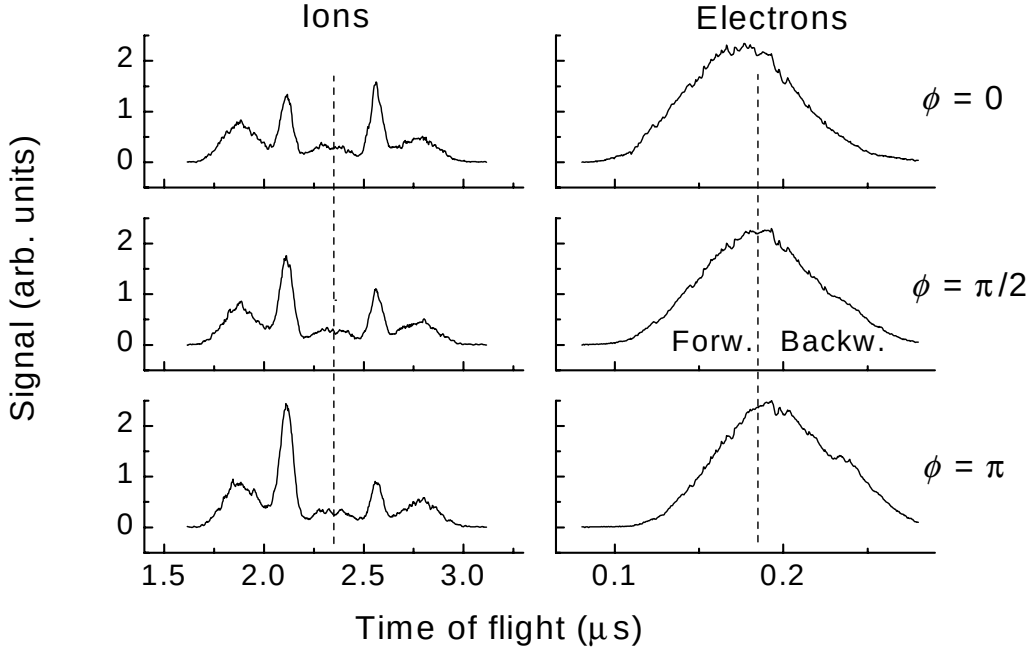

Figure 3. Ion spectra and electron spectra, clearly showing the control of spatial asymmetry by adjustment of the relative phase between overlapping short pulses of the Ti-Sapphire laser at the fundamental and second harmonic frequency.

CONCLUSIONS

The counter-intuitive asymmetry in the photodissociation of HD^+, measured by Sheehy *et al* (1995) with a Nd:YLF laser, has been reproduced with Ti-Sapphire laser pulses that are three orders of magnitude shorter and ten times more intense. For further understanding of this two-colour experiment, a comprehensive study of H_2 subject to laser pulses at the fundamental and second harmonic frequency has been made. Some of the findings are:

- Undulations are observed in the Coulomb explosion peak at λ = 375 nm. The present classical model predicts one critical distance, whereas quantum calculations predict two. The new observation could be a sign of two critical distances.
- At λ = 750 nm, the H_2^+ ion signal saturates just below 2×10^{14} Wcm^{-2}, in line with the ADK tunnelling model. At λ = 375 nm, the ionisation is in the multiphoton regime and the rate is considerably higher.
- After H_2 has been ionised, a constant fraction of the H_2^+ ions dissociate straight away via one photon absorption. This suggests that the appearance intensity of the ω_1 channel is determined by the appearance of H_2^+ ions.
- The angular distributions broadened for increasing laser intensity as well as shorter wavelength in this limited study. A more systematic study is required.
- The elongated shape of H_2 introduces only a very small alignment, due to the very short internuclear separation. For molecules with a large internuclear separation, e.g. I_2, this primary alignment will be substantial.

Although the spatial asymmetry turns out to be qualitatively the same as before, i.e. counter-intuitive, no modulations were observed in the 'forward plus backward' sum yields. It looks as though the asymmetry is added on at the end of the ionisation or dissociation process.

ACKNOWLEDGEMENTS

This work was made possible thanks to financial support from the Engineering and Physical Science Research Council. The dedicated assistance of Drs. A J Langley and P F Taday of the Rutherford Appleton Laboratory, where the experiments were performed, is greatly appreciated. Finally, we mention with pleasure the fruitful discussions with Drs. J McCann, M Plummer and L Madsen from the University of Durham.

REFERENCES

Ammosov M V, Delone N B and Krainov VP
1986 *Sov. Phys. JETP* **64** 1191
Charron E, Giusti-Suzor A and Mies F H
1994 Phys. Rev. Lett. 71 692
—— 1994 *Phys. Rev.* A **49** R641
—— 1995 *J. Chem. Phys.* **103** 7359
Codling K, Frasinski L J and Hatherly P A
1988 *J. Phys B: At. Mol. Opt. Phys.* **21** L433
—— 1989 *J. Phys B: At. Mol. Opt. Phys.* **22** L321
Constant E, Stapelfeldt H and Corkum P B
1996 *Phys. Rev. Lett.***76** 4140
Frasinski L J, Codling K and Hatherly P A
1989 *Science* **246** 1029
Frasinski L J, Stankiewicz M, Hatherly PA, Cross G M, Codling K, Langley A J and Shaikh W
1992 *Phys. Rev.* A **46** R6789
Freeman and Bucksbaum
1991 *J. Phys B: At. Mol. Opt. Phys.* **24** 325
Giusti-Suzor A, Mies F H, DiMauro L F, Charron E and Yang B
1995 *J. Phys B: At. Mol. Opt. Phys.* **28** 309
Helm H, Dyer M J and Bissantz H
1991 Phys. Rev. Lett. 67 1234
Langley A J, Noad W J, Ross I N and Shaikh W
1994 Appl. Opt. 33 3875
Plummer M and McCann J F
1996 *J. Phys B: At. Mol. Opt. Phys.* **29** 4625
—— 1997 *J. Phys B: At. Mol. Opt. Phys.* (submitted)
Posthumus J H, Frasinski L J, Giles A J and Codling K
1995 *J. Phys B: At. Mol. Opt. Phys.* **28** L349
Posthumus J H, Giles A J, Thompson M R, Frasinski L J, Codling K, Langley A J and Shaikh W
1996a *J. Phys B: At. Mol. Opt. Phys.* **29** L525
Posthumus J H, Giles A J, Thompson M R and Codling K
1996b *J. Phys B.* **29** 5811
Posthumus J H, Thompson M R, Frasinski L J and Codling K
1996c *Multiphoton Processes 1996, Proceedings of ICOMP VII, IOP Conference Series No 154*
Posthumus J H, Thompson M R, Giles A J and Codling K
1996d *Phys. Rev.* A **54** 955
Schumacher D W, Weihe F, Muller H G and Bucksbaum P H
1994 *Phys. Rev. Lett.***73** 1344
Seideman T, Ivanov M Yu and Corkum P B
1995 *Phys. Rev. Lett.***75** 2819
Sheehy B, Walker B and DiMauro L F
1995 *Phys. Rev. Lett.***74** 4799
Telebpour A, Chien C-Y and Chin S L
1996 *J. Phys B: At. Mol. Opt. Phys.* **29** L677
Telebpour A, Larochelle S and Chin S L
1997 *J. Phys B: At. Mol. Opt. Phys.* **30** L245
Walsh T D G, Ilkov F A and Chin S L
1997 *J. Phys B: At. Mol. Opt. Phys.* **30** 2167
Zavriyev A, Bucksbaum P H, Muller H G and Schumacher D W
1990 *Phys. Rev.* A **42** 5500
Zavriyev A, Bucksbaum P H, Squier J and Saline F
1993 *Phys. Rev. Lett.***70** 1077
Zuo and Bandrauk
1995 *Phys. Rev.* A **52** R2511

VUV RADIATION FROM LASER-PRODUCED PLASMAS: APPLICATIONS TO MOLECULAR PHOTOIONISATION AND ION-PAIR PRODUCTION

S.L.Wang[1)], K.P.Lawley[1)] , R.J.Donovan[1)] , K.W.D. Ledingham[2)], T.McCanny[2)], R.P.Singhal[2)], R. Allott[3)], N.Spencer[3)], W.Shaikh[3)] and I.C.E. Turcu[3)]

1) Department of Chemistry, The University of Edinburgh, King's Buildings, West Mains Road, Edinburgh EH9 3JJ, Scotland, UK. Email: K.P.Lawley@ed.ac.uk.
2) Department of Physics and Astronomy, University of Glasgow, Glasgow G12 8QQ, Scotland, UK
3) Rutherford Appleton Laboratory, Chilton, Didcot, Oxon, OX11 0QX, UK.

INTRODUCTION

Vacuum ultraviolet (VUV) radiation has been utilised for many decades[1,2] to study molecular electronic structure, ionisation thresholds of atoms and molecules, quantum yields of photoionization and photodissociation processes, autoionization structure, and ion-pair production[3-4]. Different methods for producing VUV, especially synchrotron radiation, have been widely used.

It has been known for some time that continuum VUV and extreme ultraviolet (XUV) radiation can be generated by laser-produced plasmas[5]. XUV radiation has been investigated extensively and applied to inner shell photoexcitation studies of atoms and ions[6]. However, no application for molecular photoabsorption and photoionization have been reported.

A table-top, high average power laser plasma x-ray source was developed at RAL using a picosecond excimer laser system[7]. This system demonstrated very high (11%) conversion efficiency from laser energy to 1 nm (Cu L shell) x-ray radiation by using a very high laser power density (~ 10^{15} W/cm^2) on target. This work investigates the suitability of this system, used at moderate on-target irradiance, to generate continuum VUV radiation. Some preliminary results using this new VUV generation technique for molecular photoionization and ion-pair production studies in the region of first ionisation threshold (around 10 eV for most molecules interested) are described.

EXPERIMENTAL

A schematic diagram of the experimental set-up is shown in Fig. 1. The plasma was generated by interaction of a 8-pulse train picosecond excimer laser system with continuously moving copper tape target. A Spectra Physics-375 synchronously pumped mode locked dye laser operating at 82 MHz produced a 7 ps pulse at 746 nm which were then converted to the third harmonic at 248 nm. This laser pulse pass a multiplexer to form a 8-pulse train of picosecond pulses separated by 1.85ns. This pulse train was then amplified by double pass in a KrF excimer laser operating at 248 nm, each train having an average energy of 120 mJ (15 mJx8).

The 248 nm laser beam was passed through a 1-meter normal-incidence vacuum spectrograph and focused by a 0.5 meter lens on the continuously moving copper tape target located at the position of the entrance slit. The spot diameter on the tape target is estimated to be about 70 μm. The VUV radiation from the laser plasma was dispersed by a 1-meter normal-incidence vacuum spectrograph with a 1200 lines/mm concave grating. The radiation was introduced into the parallel-plate ionisation chamber through which the gaseous molecules to be studied were flowed.

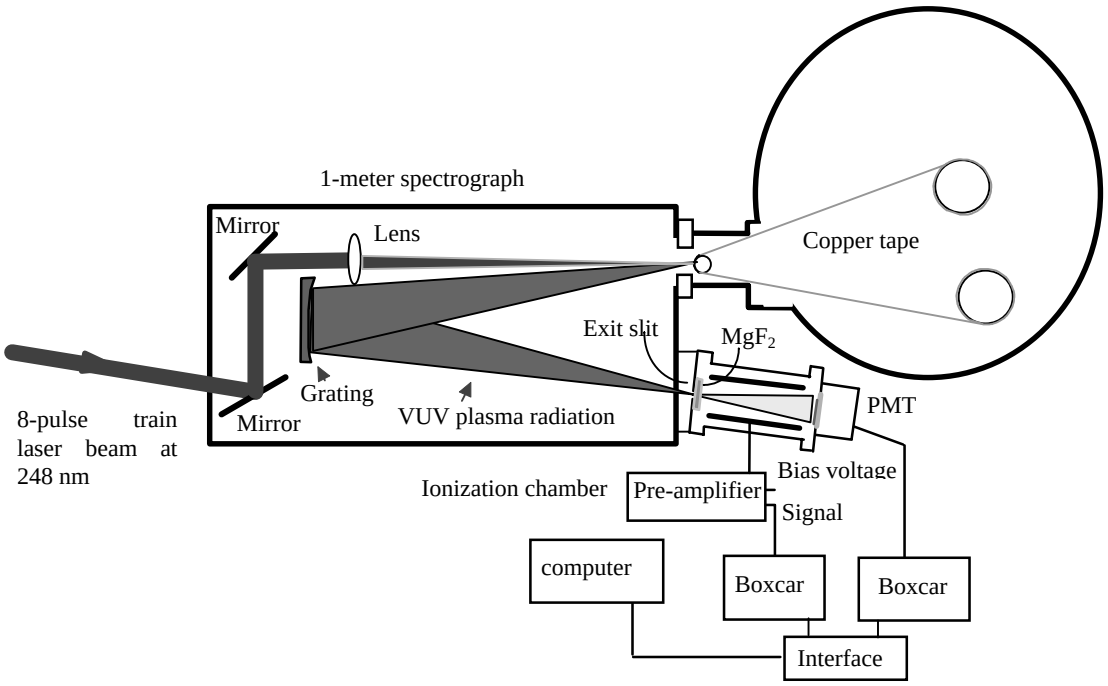

Fig.1 VUV experiment set-up

RESULT AND DISCUSSION

Photoionization of NO was investigated as an example to demonstrate the potential of this new technique. The VUV spectrum of NO obtained in the present experiment (Fig.2) shows a sharp step function at the ionization potential upon which is superimposed vibrational levels of the NO^+ ground state. The data presented here is very similar in quality and resolution to that presented by Erman et al[8] using synchrotron radiation.

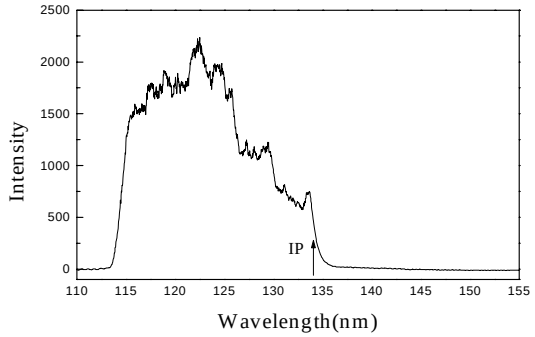

Fig.2 VUV single-photon excitation spectrum of NO which shows a sharp step function at ionization threshold upon which is superimposed vibrational levels of the NO^+ ground state.

Ion-pair formation from CH_3Br was also investigated. The observed threshold of 130.4 nm agrees well with the theoretical value of 130.5 nm estimated from available thermodynamic data. The spectrum of CH_3Br showed several broad peaks which are tabulated in Table I. The first four peaks A, B, C and D in the spectrum coincide with the four strong absorption peaks of the VUV absorption spectrum obtained by Hochmann et al[9] and Causley and Russel[10] who identified them as the 7s, 7p, 8s and 9s Rydberg states. In our experiment these act as doorway states to the ion-pair dissociative continuum. The intensity of ion-pair signal is about 1% of the ionisation signal above the ionisation threshold.

Peak	This work	Causley and Russell[10]	Hochmann et al[9]
A	78125±305	77869(7s)	77985(7s)
B	79460±315	79542(7p)	79554(7p)
C	80840±457	80509(8s)	80548(8s)
D	81840±334	81869(9s)	81927(9s)
E	83008±344	82713(10s) 83264(11s)	83070(8s′)

Table 1 Comparement between Peaks observed in ion-pair production spectrum using VUV radiation from laser-produced plasma and Rydberg states of CH_3Br. The state with prime is belong to [1/2] core while others [3/2]core.

CONCLUSION

It has been shown that continuum VUV radiation can be generated from laser-produced plasma using a table-top picosecond laser system. By combining with a 1-meter spectrograph this VUV radiation source can now be used for low resolution photoionization and ion-pair production survey studies of molecules. By optimising the present experimental arrangement or using a better spectrograph this VUV source might be used for high resolution molecular VUV spectroscopy studies.

REFERENCES

1) J.A.R.Samson
Techniques of Vacuum Ultraviolet Spectrocopy (Wiley, New York, 1967).

2) J.Berkowitz
Photoabsorption, photoionization and photoelectron spectroscopy (Academic Press, New York, 1979)

3) A.J.Yencha, D.K.Kela, R.J.Donovan, A.Hopkirk and A.Kvaran
Chem.Phys.Lett. 165, 283(1990)

4) A.Kvaran, A.J.Yencha, D.K.Kela, R.J.Donovan and A.Hopkirk
Chem.Phys.Lett. 179, 263(1991).

5) C.Breton and R.Papoular
J.Opt.Soc.Am. 63, 1225(1973).

6) E.T.Kennedy, J.T.Costello, J-P Mosnier, A.A.Cafolla, M.Collins, L.Kiernan, U.Koble, M.H.Sayyad, M.Shaw, B.F.Sonntag, R.Barchewitz
Opt. Eng. 33, 3984(1994).

7) I.C.E.Turcu, I.N.Ross, P.Trenda, C.W.Wharton, R.A.Meldrum, H.Daido, M.S.Schultz, P.Fluck, A.G.Michette, A.P.Juna, J.R.Maldonado, H.Shields, G.J.Tallents, L.Dwivedi, J.Krishnan, D.L.Stevens, T.J.Jenner, D.Batani, and H.Goodson
Proc.SPIE 2015, 243(1994).

8) P.Erman, A.Karawajczyk, E.Rachlew-Kallne, and C.Stromholm
J.Chem.Phys. 102, 3064(1995).

9) P.Hochmann, P.H.Templet, H.-t.Wang, and S.P.McGlynn
J.Chem.Phys. 62, 2588(1975).

10) G.C.Causley and B.R.Russell
J.Chem.Phys. 62, 848(1975).

THE EFFECT OF LASER PULSE LENGTH AND THE USE OF A TAPE TARGET ON THE DEPOSITION OF METALLIC FILMS BY PULSED LASER DEPOSITION

A M Widdowson[1)], S B Palmer[1)], R M Allott[2)], I C E Turcu[2)], N Lisi[2)], N Spencer[2)]

1) Department of Physics, University of Warwick, Coventry, CV4 7AL, UK. Email a.m.widdowson@csv.warwick.ac.uk
2) Rutherford Appleton Laboratory, Chilton, Didcot, OXON, OX11 0QX, UK.

INTRODUCTION

One of the difficulties encountered in the pulsed laser deposition (PLD) of metallic films is the production of droplets. These droplets are molten material expelled from the target and deposited onto the film surface at the substrate. The presence of droplets is detrimental to films for magnetoresistive application and therefore undesirable. In order to reduce droplets we expect that molten material on the target must be avoided.

The ablation process is driven by the amount of energy deposited per unit volume into the target. This volume is defined by the optical absorption depth α^{-1} and the thermal diffusion length L_{th}, where $\alpha^{-1} \propto \lambda$, the laser wavelength, and $L_{th} \propto (\tau_p)^{1/2}$, the laser pulse length. It is L_{th} that determines the diffusion of heat into the target influencing the amount of molten material produced during the laser pulse. Thus by altering the laser pulse length we can observe the effects of heating the target in terms of the number of droplets produced on the film. Hence we show the effect of laser pulse length on the production of droplets by comparing films deposited using nanosecond (ns) and picosecond (ps) pulse lengths.

It is standard in the PLD technique to use a bulk target for the deposition of films. As a result of the facilities available in the Laser Plasma X-ray laboratory at the Central Laser Facility we were able to investigated the use of a spooled metallic tape as a target. With the laser focused onto the tape a hole was punctured through it. It was suggested that unwanted debris would be ejected through the rear of the tape rather than being expelled perpendicular to the tape along with the plasma and thus prevent droplets being deposited onto the film.

EXPERIMENTAL DETAILS

The deposition of Ag films was carried out using excimer lasers lasing at 248nm with a repetition rate of 20Hz. Two pulse lengths, 20ns and 5ps were available. The 5ps pulses were achieved by selecting one pulse from the ps pulse train configuration in the Laser Plasma X-ray laboratory[1]. The laser beams were focused onto bulk targets using a 0.4m focal length lens and were incident upon the target at 45°. This is a standard geometry for the PLD technique[2]. Depositions were carried out in vacuum of 1×10^{-6}mbar. Deposition rates were measured using a quartz crystal monitor and film thicknesses were confirmed using a Talystep stylus instrument. The pulse energy of the lasers was converted to energy fluences at the target by taking the size of the damaged region at the target as the area over which the laser energy was incident.

Films deposited using the tape spooling mechanism were carried out as for the laser plasma generation of x-rays using the ps pulse train[1]. The chamber was evacuated and a substrate was placed 6cm in front of the tape to allow for the deposition of films.

VARIATION OF LASER PULSE LENGTH

A comparison of Ag films deposited using 20ns and 5ps pulse lengths are shown in figure 1 and 2 respectively. The films are

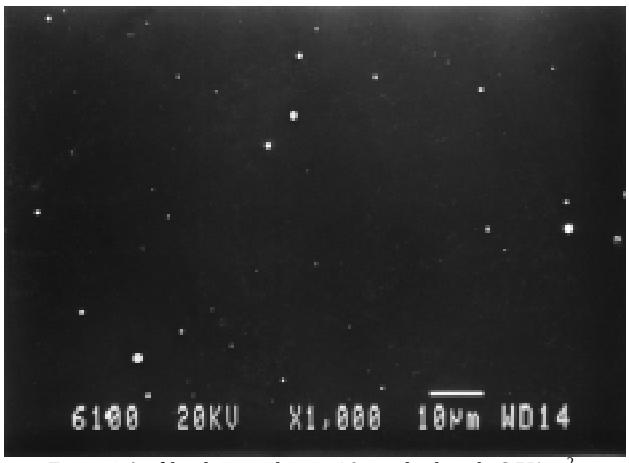

Figure 1 Ag film deposited using 20ns pulse length, 6.5J/cm^2.

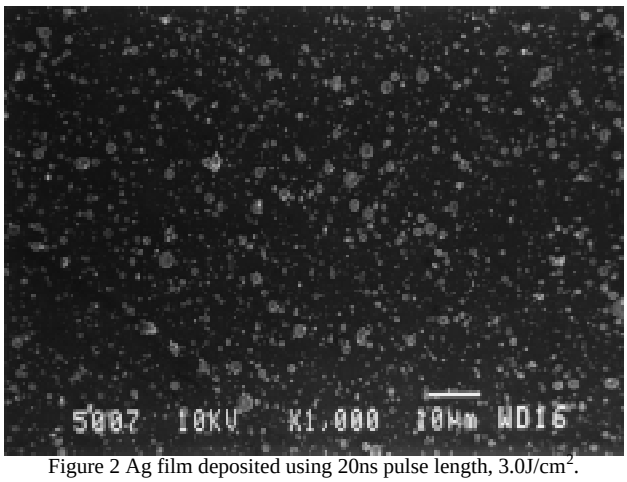

Figure 2 Ag film deposited using 20ns pulse length, 3.0J/cm^2.

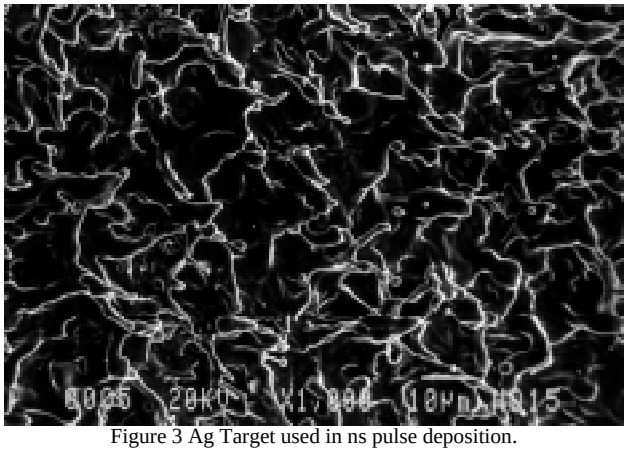

Figure 3 Ag Target used in ns pulse deposition.

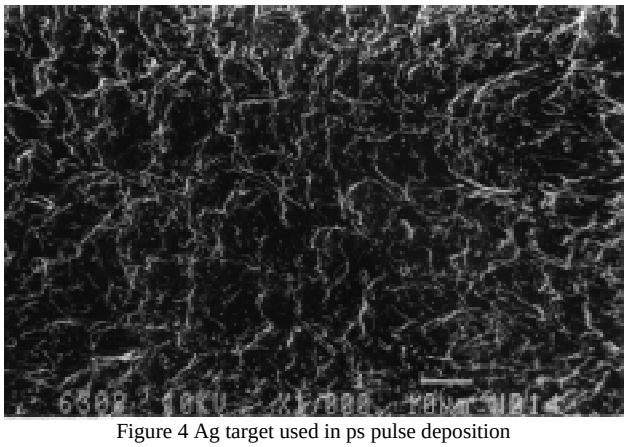

Figure 4 Ag target used in ps pulse deposition

10±2nm thick and were both deposited at an energy fluence of figure 1 that there are far more droplets on the film deposited 6.5±0.5 J/cm^2 and 3.0±0.5 J/cm^2 respectively. It is clear from using ps pulse length despite depositing at a lower energy fluence. The increased number of droplets on the film deposited using ps pulses is mirrored in the condition of the targets shown in figures 3 and 4. The turbulence on the target used for ps pulse deposition is far greater than that on the target used for depositing in the ns regime.

The model for laser-metal interaction needs to be examined to determine why droplets are still present in the ps pulse regime. Incident laser radiation is absorbed by the excitation of free electrons through inverse brehmmstralung. The excited electrons thermalise rapidly by electron-electron collisions, with a characteristic relaxation time, τ_e. Energy from the electron gas is then transferred to the lattice by electron-phonon interactions characterised by τ_l, where $\tau_e << \tau_l$. If the pulse length τ_p is varied three situations can arise.

- $\tau_e << \tau_p << \tau_l$ i.e. where femtosecond pulses are used for deposition the pulse length is shorter than the electron-phonon relaxation by three orders of magnitude. In this regime L_{th} is confined to the surface and heat conduction into the target can be neglected within the time duration of the pulse.
- $\tau_e << \tau_l \approx \tau_p$ i.e. for ps pulses the pulse length is at least comparable with the electron-phonon relaxation time. In this regime $L_{th} \approx 10$nm for metals and heating of the target may no longer be negligible thus allowing molten material to form at the target.
- $\tau_e << \tau_l << \tau_p$ i.e. for ns pulses the pulse length is sufficiently long for extensive heating of the target resulting in a large molten zone.

Thus in metals when using shorter pulse lengths for deposition the transfer of energy to the lattice which heats the target and causes melting needs to be taken into consideration. For Ag $\tau_l \sim 1$ps[3] hence with a 5ps pulse significant heating of the target can occur within the duration of the pulse. Thus molten material is still present on the target and leads to droplets being expelled onto the film. Work on the laser drilling of metallic samples using ns, ps and fs pulses indicates less melting of metals at shorter pulse lengths[4,5,6]. This suggests that moving to even shorter pulse lengths could be advantageous in avoiding droplet production. However this would be at the expense of a high deposition rates[7].

Despite the expected reduction in melting gained by using ps pulse lengths it remains that there are more droplets on the films deposited in this regime than for the film deposited using ns pulses and that the target correspondingly shows more turbulence. Recoil pressure arising from the atoms leaving the melt may explain the increase in droplets in the ps regime since this increases with decreasing laser pulse length[8].

DEPOSITION USING CU TAPE TARGET

Figure 5 shows a 16nm thick Cu film deposited with a fluence of 125J/cm^2 using a spooled Cu tape as the target. It is clear that droplets are still present on the film. Figure 6 shows the damaged region of the tape. Again there is evidence of melting and of molten material being ejected forward from the tape with the ablation plasma. The tape is 25μm thick and can therefore be considered as a bulk sample as $L_{th} \sim 10$nm. Within the ps pulse train regime there is sufficient time for molten material to form and be ejected by the recoil pressure of the ablated material. Ejection of the melt is expected to be completed within ~5ns[8] and the separation of the pulses in the train is ~1ns, with larger separation between trains.

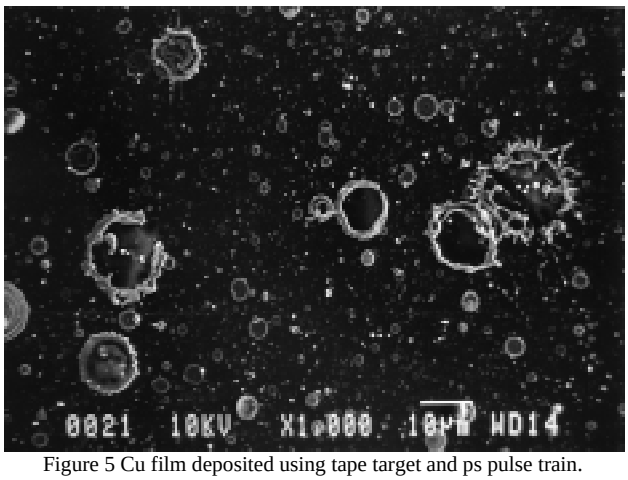

Figure 5 Cu film deposited using tape target and ps pulse train.

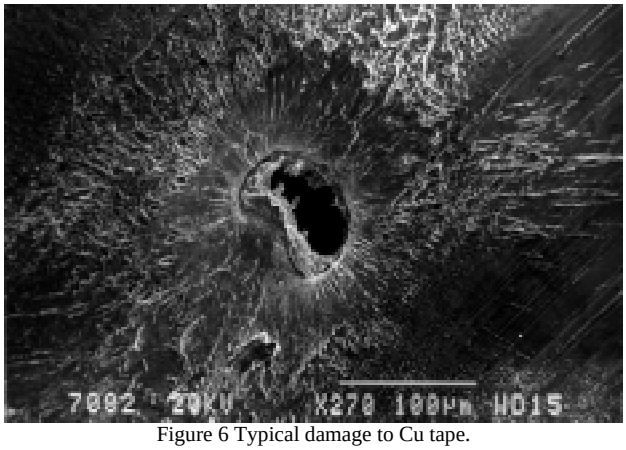

Figure 6 Typical damage to Cu tape.

CONCLUSIONS

In summary this work has looked at the effect of ns and ps pulse lengths on the deposition of metallic films using PLD. The aims were to access whether ps pulse lengths were sufficiently short to obtain smooth droplet free films by reducing melting at the target. The results show that droplets are still present on the films and that molten material still forms at the target. This is in agreement with work carried out on the laser drilling of metals. In addition we find that the use of a tape target does not allow unwanted debris to pass through the tape to reduce droplet numbers at the deposited film.

REFERENCES

1) I C E Turcu et al
Applications in Laser Plasma Radiation 2015 243 (1994)

2) T J Jackson and S B Palmer
J. Phys. D: Appl. Phys. 27 1581 (1994)

3) R H M Groneveld, R Sprik and A Ladendijk
Phys. Rev. B 51 11433 (1995)

4) A Luft, U Franz, A Emsermann and J Kaspar
Appl. Phys. A63 93 (1996)

5) B N Chichkov, C Momma, S Nolte, F von Alvensleben and A Tunnermann
Appl. Phys. A63 109 (1996)

6) J Jandeleit, G Urdasch, H D Hoffmann, H -G Treusch and E W Kreutz
Appl. Phys. A63 117 (1996)

7) S Preuss, A Demchuk, and M Stuke
Appl. Phys. A61 33 (1995)

8) O Bostanjoglo, R Niedrig and B Wedel
J. Appl. Phys. 76 3045 (1994)

TIME-RESOLVED RESONANCE RAMAN SPECTROSCOPY OF THE CARBONATE RADICAL

R. H.Bisby[1)], S.A.Johnson[1)], S.M.Tavender[2)], A.W.Parker[2)]

1) Department of Biological Sciences, University of Salford, Salford M5 4WT, UK
2) Rutherford Appleton Laboratory, Chilton, Didcot, Oxfordshire, OX11 0QX, UK.

INTRODUCTION

The carbonate radical is a powerful oxidant with a one electron reduction potential of 1.59 V at pH 12 [1], and is capable of the one-electron oxidation of several amino acids and proteins [2,3]. It has been suggested [4] that in phagosomes, which contain high levels of bicarbonate (≥25 mM), the carbonate radical formed from scavenging of hydrogen peroxide-derived $OH^{\cdot}$ might be a significant contributor to radical mediated damage. Peroxynitrite, an important contributor to oxidative stress, reacts fairly rapidly with carbon dioxide [5,6] and the carbonate radical has also been suggested as a possible product of this interaction [6,7].

The carbonate radical has been identified by flash photolysis as a transient species with a broad featureless absorption (λ_{max} 600 nm and $\varepsilon \approx 200$ dm^2 mol^{-1}) which is invariant between pH 8-13. Data from the Hoffman group, using flash photolysis of $Co(NH_3)_4CO_3^+$ as a source of carbonate radicals, showed a 90% increase in reactivity with indole-3-propionic acid on increasing pH between 7 and 13 [8, 9]. Studies of the kinetic salt effect on the rate of reaction between carbonate radicals and indole-3-propionic acid showed no ionic strength effect at pH 7, but a substantial effect at pH 12, indicating zero charge for the carbonate radical at pH 7 and unit negative charge at pH 12 [8]. These data were interpreted as showing a pK_a of 9.6 for equilibrium (1).

$$HCO_3^{\cdot} \rightleftharpoons CO_3^{-\cdot} + H^+ \quad \text{.....(1)}$$

Clifton and Huie [10] also point out that the second order rate constant for reaction of the carbonate radical with methanol obtained by Chen et al [8] at pH 6.4 is about half of their value obtained at pH 12.8. This supports the expectation that the $CO_3^{-\cdot}$ would be a more reactive oxidant than $HCO_3^{\cdot}$. Conversely, it was found that the reactivity of carbonate radical(s) with indole, which is uncharged and does not undergo deprotonation in the relevant pH region, is invariant with pH over the range 6-13 [9]. Eriksen, Lind and Merenyi [11] have investigated the possible protonation of the carbonate radical by pulse radiolysis, and obtained a tentative estimate for $pK_a(1)$ of 7.9.

There therefore appears to be confusion over whether the carbonate radical does undergo protonation in the pH range 6-13, and of the possible value of $pK_a(1)$. Since carbonate radical ionisation would affect one-electron reduction potential, reactivity and diffusion in biological systems, we have undertaken an examination of the carbonate radical(s) using time-resolved resonance Raman (TR^3) spectroscopy which is a powerful technique for the investigation of inorganic and organic free radicals [12].

MATERIALS AND METHODS

The carbonate radical was produced by laser flash photolysis of solutions of sodium persulphate (50 mM) and either sodium carbonate (0.5 M) or sodium bicarbonate (1 M). When required, the pH of the solutions was adjusted by addition of sodium phosphate. Water was obtained from a Millipore Milli Q apparatus and chemicals were either AnalaR grade or similar.

A frequency-doubled dye laser (Lambda-Physik FL3002) pumped by a Lumonics XeCl excimer laser was used to generate the pump laser pulse at 250 nm (ca. 2 mJ, 10 ns pulse length). A Continuum Scanmate OPO was used to generate the probe laser pulse at 620 nm (ca. 1.5 mJ, 5 ns) on the red edge of the carbonate radical absorption spectrum.

RESULTS AND DISCUSSION

In our experiments radicals were formed by laser flash photolysis of sodium persulphate (50 mM) at 250 nm, causing decomposition to the sulphate radical ($SO_4^{-\cdot}$). Carbonate radicals are formed by rapid electron transfer reaction either with carbonate (reaction (3) at pH ca. 13 [13]) or with bicarbonate (reaction (4) [10]).

$$S_2O_8^{2-} + h\nu \rightarrow 2\ SO_4^{-\cdot} \quad \text{..... (2)}$$

$$SO_4^{-\cdot} + CO_3^{2-} \rightarrow SO_4^{2-} + CO_3^{-\cdot} \quad \text{..... (3)}$$

$$SO_4^{-\cdot} + HCO_3^{-} \rightarrow SO_4^{2-} + CO_3^{-\cdot} + H^+ \quad \text{..... (4)}$$

Figure 1 shows the Raman spectra obtained from a solution of sodium persulphate (50 mM) and sodium carbonate (0.5 M) at pH 12.2. Spectrum A is that obtained with only the probe laser at 620 nm. It contains bands at 835 cm^{-1} and 1074 cm^{-1} which separate experiments showed were the normal (i.e. non-resonant) Raman bands of the persulphate ion. Similarly the 1065 cm^{-1} band, which strongly overlaps the 1074 cm^{-1} persulphate band, is due to the carbonate (CO_3^{2-}) symmetric C-O stretch (ν_1 (A1')) [14,15]. Since the CO_3^{2-} anion has D_{3h} symmetry, three Raman active vibrations are expected [14]. The very much weak bands at 1380 and 1460 cm^{-1} due to the antisymmetric C-O stretch (ν_3) are not evident in this spectrum, and the wavenumber range shown here does not include the weak antisymmetric CO_2 stretch (ν_4) at 684 cm^{-1}. Spectrum B (Figure 1) was obtained using both a pump pulse (250 nm) and a probe pulse (620 nm) delayed by 1 μs. Subtraction of A from B reveals spectrum C due to the transient carbonate radical. Spectrum C contains a strong band at 1063 cm^{-1} ascribed to the symmetrical C-O stretch of the radical and weaker bands at ca. 1180 cm^{-1} and 1400 cm^{-1} assigned to antisymmetric C-O stretching modes. Analysis of the depolarisation ratios indicates loss of D_{3h} symmetry in the radical, consistent with the ESR spectra of $CO_3^{-\cdot}$ in the solid state [16].

Figure 2 shows the similar set of spectra obtained from a

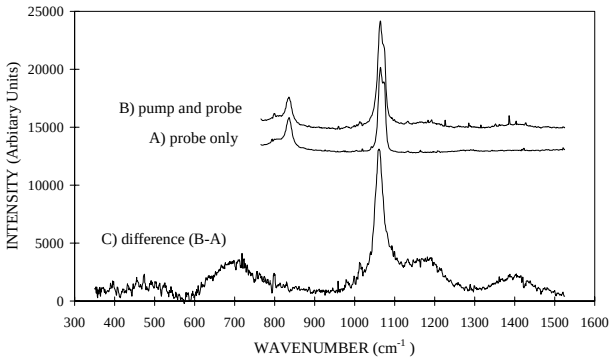

FIGURE 1 - Raman spectra obtained from solutions of sodium carbonate (0.5 M) and sodium persulphate (50 mM at pH 12.2. Spectrum A is probe only, spectrum B pump and probe and C the difference spectrum. The pump and probe wavelengths were 250 and 620 nm respectively with a time delay between pulses of 1 μs in spectrum B.

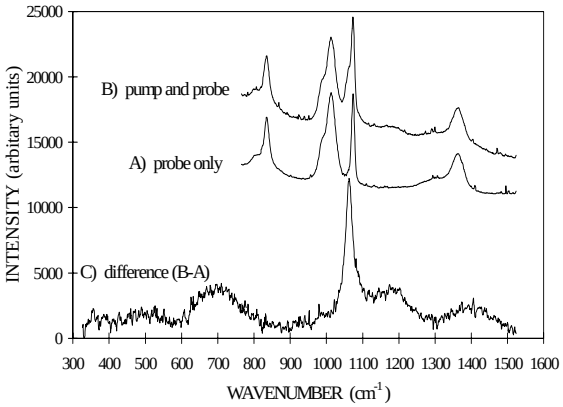

FIGURE 2 - Raman spectra from solutions of sodium bicarbonate (1 M) and sodium persulphate (50 mM) at pH 7.6. Spectrum A is probe only, B pump and probe and spectrum C the difference spectrum attributed to the transient radical. Pump and probe wavelengths were 250 and 620 nm respectively with a delay of 1 μs between pulses in B.

solution of sodium persulphate (50 mM) and sodium bicarbonate (1 M) buffered to pH 7.6 with phosphate. In addition to the persulphate bands described above, spectrum 2A (probe only) shows the strong C-O symmetric stretch (ν_3) at 1360 cm^{-1} and the C-OH stretch (ν_5) at 1017 cm^{-1} of bicarbonate. The Raman spectra clearly allow differentiation between carbonate with D_{3h} symmetry (Figure 1) and bicarbonate with C_{2v} symmetry (Figure 2). The difference spectrum (Figure 2C) from subtraction of probe only from the pump and probe spectrum reveals the transient resonant Raman spectrum of the carbonate radical which is indistinguishable from that measured at pH 12.2 (Figure 1C). On this basis, there is no evidence for protonation of the carbonate radical on reducing the pH from 12.2 to 7.6. Further spectra in D_2O at pH 7.6 (data not shown) were found to be identical, providing additional evidence for lack of protonation of the carbonate radical near neutral pH.

The lack of protonation implies that there is a different one-electron reduction potential, and therefore reactivity, of the radical at neutral pH from that expected if $pK_a(1) = 9.6$ as previously proposed. Using the reduction potential of 1.59 V measured at pH 12 [1] and pK_a's for carbonic acid of 6.34 and 10.37, the mid-point potential (E_{mi}) at other pH values can be readily calculated [17]. Figure 3 shows calculated curves of E_{mi} versus pH for assumed pKa(1) values of 9.6 and 2.0. Also shown is the reduction potential at pH 7.0 as a function of $pK_a(1)$. A change in $pK_a(1)$ from 9.6 to <<7 results in an increase in the reduction potential at pH 7 by 150 mV, sufficient to cause a substantial change in reactivity over and above any effect caused by the difference in charge on the radical.

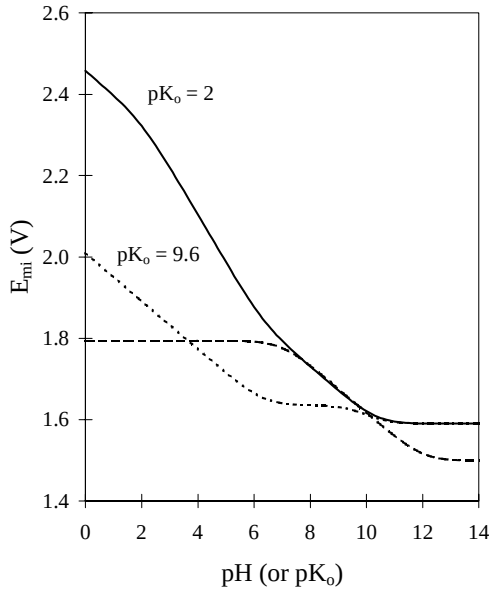

FIGURE 3 - Full line: reduction potential as a function of pH for carbonate radicals assuming $pK_a(1)=2.0$; dotted line reduction potential versus pH assuming $pK_a(1)=9.6$. The dashed line shows the standard reduction potential at pH 7.0 plotted versus $pK_a(1)$ for the carbonate radical.

ACKNOWLEDGEMENTS

The work was supported by grants from the Biotechnology and Biological Research Council (BBSRC) and Engineering and Physical Sciences Research Council (EPSRC) and was performed at the Rutherford Appleton Laboratories (Central Laboratory of the Research Councils, CCLRC). We thank Dan Balsom for technical assistance.

REFERENCES

1) R.E.Huie, C.L.Clifton and P.Neta
Radiat.Phys.Chem., 38, 477 (1991).

2) G.E.Adams et al
Radiat.Res., 49, 278 (1971).

3) S-C.Chen and M.Z.Hoffman
Radiat.Res., 56, 40 (1973); *ibid* 62, 18 (1975).

4) S.V.Lymar and J.K.Hurst
Chem.Res.Toxicol., 8, 833 (1995).

5) S.V.Lymar and J.K.Hurst
J.Am.Chem.Soc., 117, 8867 (1995).

6) R.M.Uppu, G.L.Squadrito and W.A.Pryor
Arch. Biochem.Biophys., 327, 335 (1996).

7) A.Denicola, B.A.Freeman, M.Trujillo and R.Radi
Arch. Biochem.Biophys., 333, 49 (1996).

8) S-C.Chen, V.W.Cope and M.Z.Hoffman
J.Phys.Chem., 77, 1111 (1973).

9) S-C.Chen and M.Z.Hoffman
J.Phys.Chem., 78, 2099 (1974).

10) C.L.Clifton and R.E.Huie
Int.J.Chem.Kinet., 25, 199 (1993).

11) T.E.Eriksen, J.Lind and G.Merenyi
Radiat.Phys.Chem., 26, 197 (1985).

12) G.N.R.Tripathi
Time Resolved Spectroscopy, eds. R.J.H.Clark and R.E.Hester, Wiley, New York, 157 (1989).

13) R.E.Huie and C.L.Clufton
J.Phys.Chem., 94, 8651 (1990).

14) A.R.Davis and B.G.Oliver
J.Solution Chem. 1, 329 (1972).

15) N.Wen and M.H.Brooker
J.Phys.Chem. 99, 359 (1995).

16) G.W.Chantry, A Horsfield, J.R.Morton and D.H.Whiffen
Mol.Phys., 5, 589 (1962).

17) P.Wardman
J.Phys.Chem.Ref.Data, 18, 1637 (1989).

THE ULTRAFAST PHOTODYNAMICS OF A VITAMIN E ANALOGUE IN WATER

R.H. Bisby[1], M Towrie[2], P. Matousek[2], G. Gaborel[2], A.W. Parker[2]

1) Department. of Biological Sciences, University of Salford, Salford, M5 4WT, UK.
2) Rutherford Appleton Laboratory, Chilton, Didcot, Oxfordshire, OX11 0QX, UK.

INTRODUCTION

The new ultrafast spectroscopy apparatus has been used to probe the dynamics for the formation of radicals following photoexcitation and photoionisation. The focus in most of these investigations has been the production and subsequent solvation of the electron. The solvation time for the electron in liquid water at room temperature is of the order of 200 fs, as determined by the blue shift in the near infra red absorption spectrum[1]. A further point of interest is the geminate recombination of the resulting electron-hole radical ion pair which occurs in competition with escape from the solvent cage into the bulk solvent. This is the same process that is observed after photo-induced electron transfer between donor-acceptor pairs. The timescale for geminate recombination process varies widely from ca. 1 ps for the electron-$H2O^{+\cdot}$ formed by direct photoionisation of liquid water, to ca 1 ns for other radical ion pairs.

Electron transfer reactions are of obvious importance in biology, being the basis for photosynthesis and oxidative phosphorylation as well as a multitude of other enzymic and non-enzymic reactions in biochemical pathways. Electron transfer reactions involving free radicals are particularly rapid and are involved in the pathways of lipid oxidation and the actions of antioxidants such as tocopherols (vitamin E), ascorbate (vitamin C) and uric acid. There have been many physico-chemical studies of antioxidant activity and some have focused on the mechanism of the reaction. The discrimination between hydrogen atom or electron plus proton transfer in reactions between a lipid peroxyl radical and ascorbate has been discussed previously (see references cited in reference 2). Before becoming more deeply involved in such studies using femtosecond spectroscopy we have undertaken an investigation using photoionisation as perhaps the simplest means of generating the tocopheroxyl radical. We have previously shown that laser photolysis at 308 nm is a valuable means of generating the radical[3]. Measurements made in acid solution[4] reveal that the pKa of the tocopheroxyl radical cation ($TOH^{+\cdot}$) is -1.4 and so deprotonation in neutral solution is expected to occur on the picosecond timescale. We report our initial findings on the study of water soluble derivatives of vitamin E using both transient absorption measurements with the new 40 kHz OPA system described in reference 5 and time resolved resonance Raman measurements with he new picosecond OPA facilities detailed elsewhere in this annual report.

The first studies investigated the photoionisation of Trolox C, a water soluble α-tocopheroxyl (vitamin E) analogue. Scheme 1 shows how in biological membranes and lipoproteins vitamin E is oxidised by the lipid peroxyl radical ($LOO^{\cdot}$) and therefore arrests the very damaging chain reaction of the lipid peroxidation Our ultimate goal is to study the details of electron transfer reactions involving vitamin E.

RESULTS

The kinetics of hydrated electron formation from Trolox C in a buffered neutral aqueous solution were observed after photo-ionisation with a 300 fs pulse at 277 nm. The lower curve in Figure 1 shows that the electron is formed in two steps: about half of the absorbance is formed within the risetime of the 300 fs pulse, whereas the remaining absorbance grows in with an approximately 5 ps time constant. The electron absorbance then decays with a lifetime of about 25 ps before reaching a value which is stable on the nanosecond timescale. Both the 5 ps and 25 ps processes show a kinetic isotope effect with a value for k_H/k_D of about 2.3. This strongly indicates that these processes are linked to the transfer of a proton.

We tentatively suggest that the delayed electron formation is due to deprotonation of the excited phenol followed by autoionisation of the excited phenolate anion. The picosecond decay is believed to be due to the electron recombining with the radical cation or the nascent proton.

The rate of deprotonation of the radical cation has been estimated by measuring the decay of the neutral and cation radicals using picosecond-TR[3] spectroscopy. Our results again correlate the rate of deprotonation to the rate of electron decay. Scheme 2 summarises our proposed mechanism for the photodynamics of Trolox C following photoexcitation.

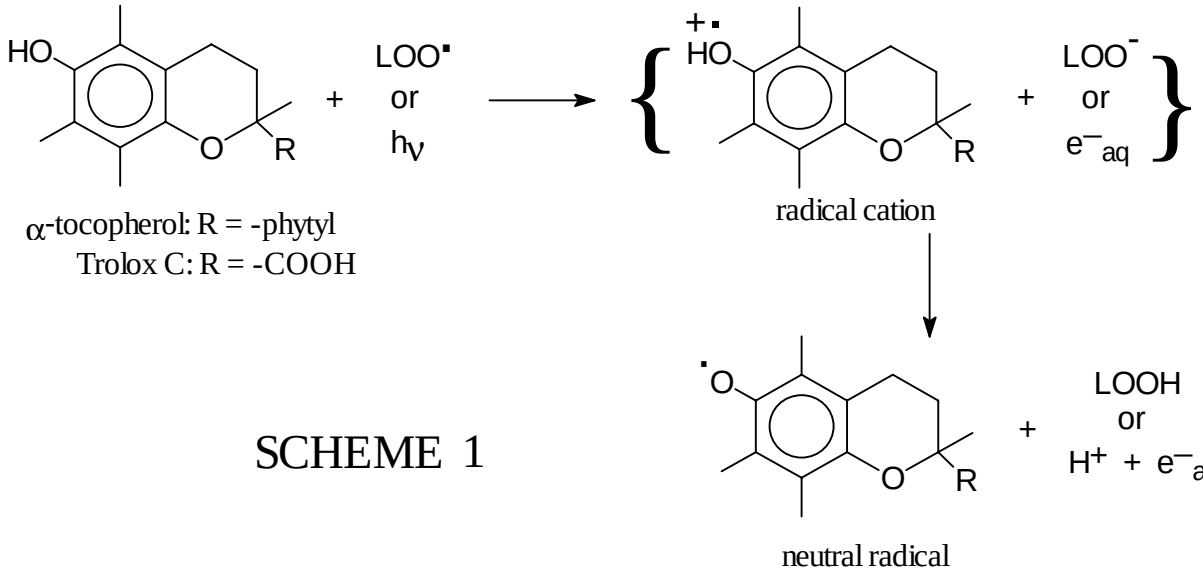

α-tocopherol: R = -phytyl
Trolox C: R = -COOH

SCHEME 1

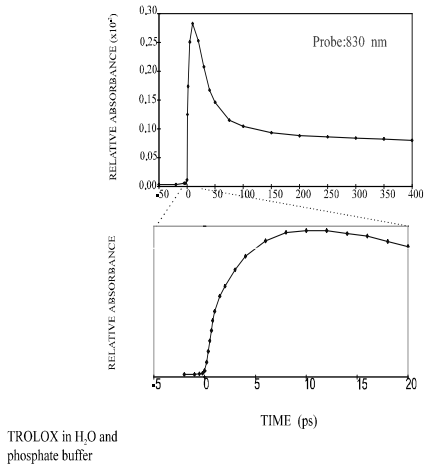

FIGURE 1: Transient absorption of the aqueous electron pumping at 277 nm and probing at 830 nm.

TR^3 spectra obtained for Trolox in neutral aqueous solution are shown in Figure 2. The insert shows the TR^3 spectra obtained with pump and probe wavelengths of 283 and 425 nm (i.e. third and second harmonics respectively of the Ti:sapphire fundamental.) With 425 nm as the probe wavelength both neutral and cation radicals are in resonance, $\varepsilon_{425} \approx 4 \times 10^3$ dm^3 mol^{-1} cm^{-1}. For a 10 ps time delay between pump and probe pulses the spectrum consists mainly of the 1620 cm^{-1} peak attributable to the C=C (ν_{8a}) stretching mode of the tocopheroxyl radical cation[4] but at 1 ns delay the spectrum contains two peaks representing the C-O (ν_{7a}) stretch at *c.* 1490 cm^{-1} and the C=C (ν_{8a}) stretch at 1600 cm^{-1} for the neutral tocopheroxyl radical. Further data show that the growth of the lower frequency band is complete after 100 ps, and correlates with the electron decay observed in the transient absorption experiments illustrated in Figure 1. The probe wavelength used to generate the main spectrum was obtained using the OPA system and the Figure illustrates that spectra of good quality may be obtained using the parametric amplification system. At

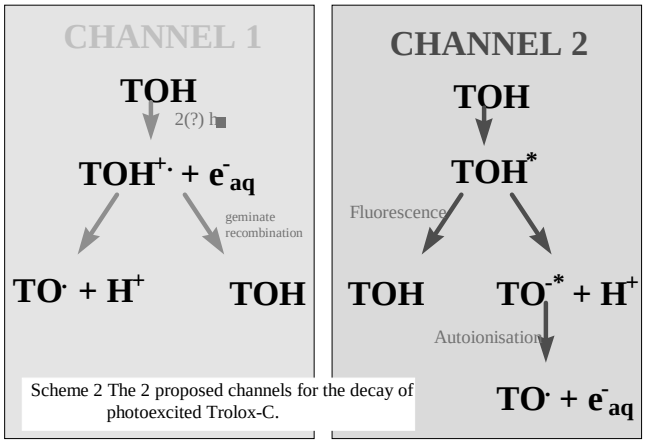

Scheme 2 The 2 proposed channels for the decay of photoexcited Trolox-C.

490 nm the radical cation, ε_{490} *c.* 10^4 dm^3 mol^{-1} cm^{-1}. A small shift to higher frequency was discernible between the *c.* 1620 cm^{-1} band seen in this spectrum and that of the insert spectrum at 10 ps despite the approximately similar bandwidth of the probe pulse and the expected shift of 20 - 25 cm^{-1} in the C=C band upon deprotonation of the radical cation. Further work is now in progress in order to extract kinetic information from these time resolved resonance Raman spectra.

REFERENCES

1) Y. Gaudel
J. Mol. Liquids 63, 1 (1995)

2) R.H. Bisby and A.W. Parker
(1995) Arch. Biochem. Biophys. 317, 170, (1995)

3) R.H. Bisby and A.W. Parker
FEBS Letters 290, 205 (1991)

4) A.W. Parker and R. H. Bisby
J. Chem. Soc. Faraday Trans. 89, 2873 (1993)

5) P. Matousek, A.W. Parker, P.F. Taday, W.T. Toner, M. Towrie
Opt. Comm. 127, 307 (1996)

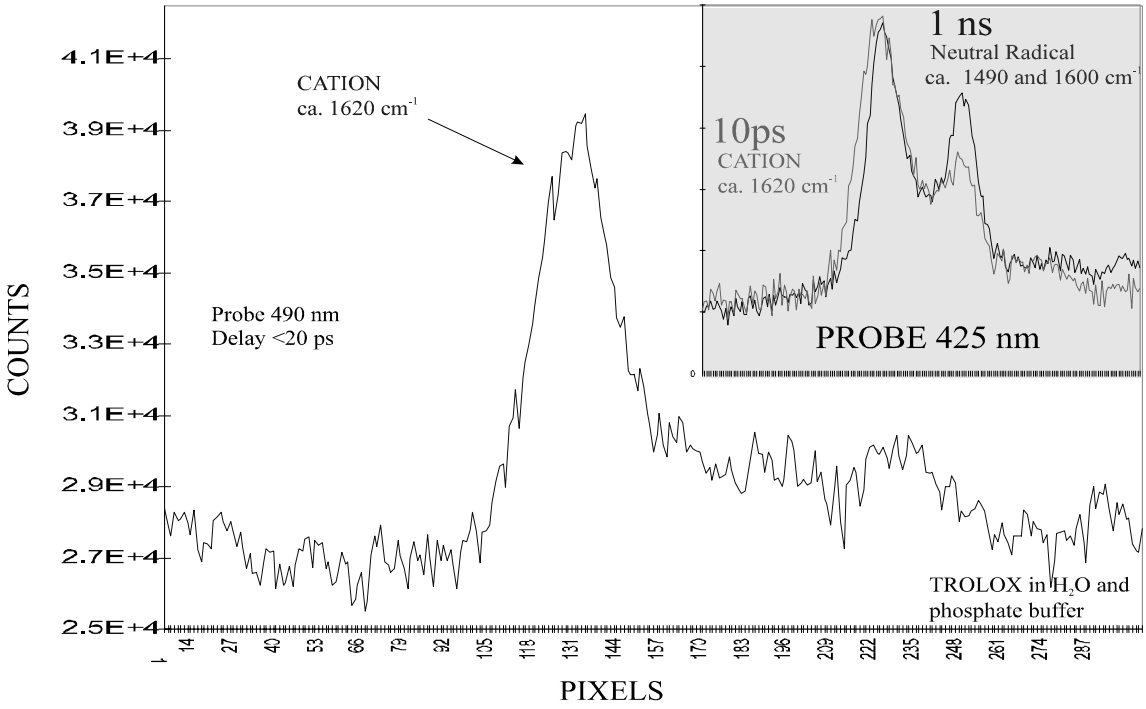

FIGURE 2: TR^3 of the Trolox-C radical cation in water. Pump 277 nm probe 490 nm, pump-probe time delay 20 ps. Insert shows the changes in the TR^3 spectrum on deprotonation of the radical cation (10 ps delay) to the neutral radical (>200 ps delay) Pump 283, nm probe 425 nm.

TIME-RESOLVED SPECTROSCOPY OF PROTEIN-RADICAL ENZYMES

R.H.Bisby[1)], S.A.Johnson[1)], S.M.Tavender[2)] and A.W.Parker[2)]

1) Department of Biological Sciences, University of Salford, Salford M5 4WT, UK.
2) Rutherford Appleton Laboratory, Chilton, Didcot, Oxfordshire, OX11 0QX, UK.

INTRODUCTION

In previous reports [1,2] we have described our progress in the study of the free radical site in pea seedling copper amine oxidase. This enzyme is unusual in containing a trihydroxyphenylalanine (TOPA) quinone residue which acts as a redox cofactor together with a cupric ion in the enzyme mechanism [3,4]. Amine oxidases from E.coli and pea seedling have recently been characterised by X-ray crystallography [5,6] showing that the TOPA quinone are very close within the protein structure, but that that the TOPA quinone is not a ligand to the cupric ion. Despite these advances there remain details of the enzyme mechanism which are still to be elucidated. Anaerobic incubation of PSAO with substrate leads to the accumulation of a TOPA-derived semiiminoquinone radical with a characteristic straw-yellow colour. Reoxidation of this intermediate by molecular oxygen completes the catalytic cycle and it is the order and mechanisms of this part of the cycle which are least well understood. We are investigating properties of the radical site in PSAO using resonance Raman spectroscopy. Radicals formed by one electron oxidation of 4-aminoresorcinol (4-AR) have been used as models for the enzyme radical site. In order to obtain time-resolved spectra of the enzyme free radical, several caged amine substrates have been synthesised and investigated. In the TR^3 experiment the pump laser pulse will uncage amine substrate and the probe laser pulse interrogates the transient intermediate(s) in the enzyme cycle.

RADICALS FROM 4-AMINORESORCINOL AS MODELS FOR THE ACTIVE SITE IN PSAO

The radical form of PSAO has an absorption maximum at 464 nm. In our pulse radiolysis experiments we have found that the one-electron oxidised form of 4-AR has λ_{max} at 430 nm at low pH and at 450 nm at neutral pH. Careful measurements of the intensity of the 450 nm absorption as a function of pH have reavealed that the semiiminoquinone undergoes deprotonation reactions with pK_a values of 3.4 and 6.4. The singly and doubly deprotonated radicals have very similar absorption spectra but undergo second order decay at different rates. We have now obtained time-resolved resonance Raman spectra of each of the three different protonated forms of the radical which exist between pH 2 and pH 8. In the laser experiments triplet duroquinone was used as the sensitiser. Figure 1 shows the TR^3 spectra obtained for each radical obtained from one-electron oxidation of 4-AR after subtraction of the duroquinone radical spectra which are also in resonance with the probe wavelengths (410 - 460 nm) used in these experiments. Also shown is the steady state resonance Raman spectra of the PSAO radical site reported by us previously [1]. Comparison indicates that the spectrum of the enzyme radical site is most like that of the 4-AR radical measured at pH 5 in the singly deprotonated form. The C=C stretch at this pH is at 1648 cm^{-1}, very close to that in the enzyme radical at 1647 cm^{-1}, whereas this vibration in the neutral 4-AR radical is at 1629 cm-1 at pH 1.2, and 1628 cm-1 in the doubly deprotonated form at pH 8.0 [7]. This is in agreement with our previous conclusion from the effect of deuteriation that the radical contains a strongly bound proton.

PHOTOCEMISTRY OF CAGED AMINES

We have synthesised and investigated caged amines based on conventional 2-nitrobenzyl photochemistry. Three amines, benzylamine, phenethylamine and N'N'-dimethyl-1,3,-propylamine, have been caged by reaction with

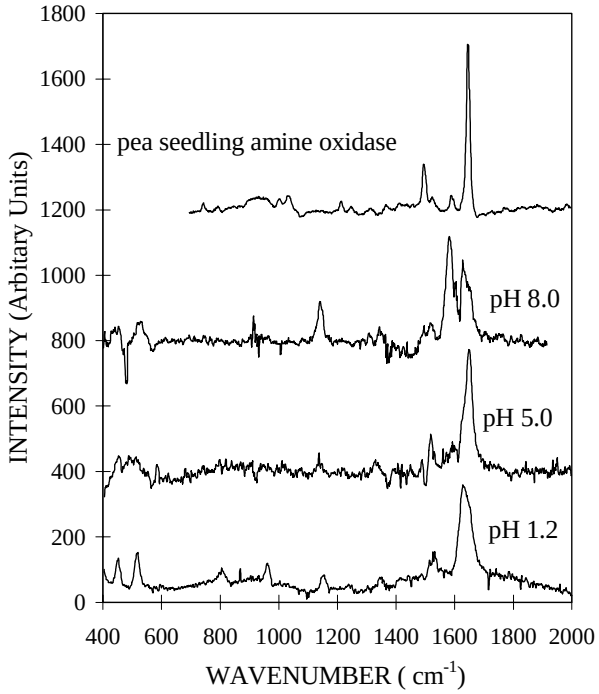

Figure 1 - Resonance Raman spectra of radicals from 4-aminoresorcinol in each protonated form, compared with the resonance Raman spectrum of the radical site in pea seedling amine oxidase obtained by anaerobic incubation with substrate.

2-nitrobenzaldehyde or 2-nitroacetophenone to form the Schiff base and subsequent reduction with borohydride. Data concerning these amines and caged amines are shown in Table 1. Although widely used in assays of PSAO activity, benzylamine is a poor substrate compared with N'N'-dimethyl-1,3,-propylamine. The higher turnover number (k_{cat}) of the latter substrate should allow better time resolution in the TR^3 experiments. Using 2-nitrobenzylamine as the caging group results in compounds having quantum yields (ϕ) for uncaging of ca 0.5% for benzylamine and phenethylamine and of about 2.5% for N'N'dimethyl-1,3,-propylamine. This variation in yield probably reflects the differing extent of stabilisation of photochemical reaction intermediates by the phenyl ring of the caged amine. Caging of N'N'dimethyl-1,3,-propylamine with 2-nitroacetophenone gives a compound having a quantum yield for uncaging of nearly 10%.

The rates of uncaging ($k_{uncage,}$ shown in Table 1)have been measured by laser flash photolysis using the XeCl excimer laser at 308 nm and taking advantage of the transient absorption of the *aci*-nitro intermediate which at 380 nm has excess absorption over the final 2-nitrosobenzaldyde product. In all cases the uncaging reaction occurs on a submicrosecond timescale. The increase in uncaging rate in compounds derived from caging with 2-nitroacetephenone is well known [8]. During these experiments it was noted that the yield of the 380 nm transient was very pH dependent . The intensity of the transient absorption measured for solutions of N-(2-nitrobenzyl)benzylamine (CBZ) 30 μs after the laser flash is shown plotted against pH in Figure 2. The data were found to fit well to a double pK_a curve with pK_a values of 6.74 ± 0.15

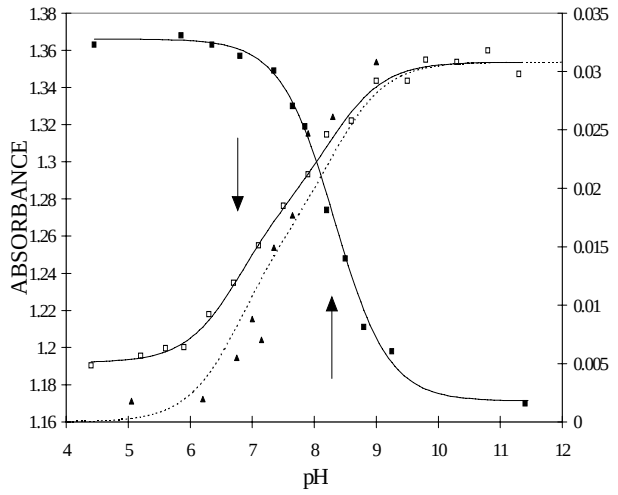

Figure 2 - Effect of pH on the yield of the *aci*-nitro intermediate, measured at 380 nm and 30 μs after the laser flash, from solutions of CBZ (, right-hand scale). The solid squares (■, left-hand scale) show the effect of pH on the absorbance of CBZ at 262 nm. Also shown is the relative quantum yield (▲) for uncaging of CBZ fitted (dotted line) to the same pK values, indicated by the arrowheads, as derived from the transient absorbance measurements.

and 8.28 ± 0.15. The latter value obviously represents the pK_a for the secondary amine group in CBZ since spectrophotometric titration of CBZ reveals a similar pK_a of 8.30 ± 0.03. The lower pK_a value may be tentatively attributed to the pK_a of the *aci*-nitro intermediate. The laser wavelength of 308nm is not at an isobestic point in the absorption spectra of CBZ so that the change in absorbance contributes in part to the increasing yield of intermediate. The steady state quantum yield for uncaging was also measured as a function of pH in experiments using a high pressure Xenon lamp and 313 nm interference filter. The results are included in Figure 2 and show a good correlation with the intensity of the *aci*-nitro transient intermediate.

The activity of PSAO is found to depend on deprotonation of a group identified as Asp 383 which has a pK ~ 5 [9] and so the enzyme is most active at pH ≥ 7. It is fortuitous that the quantum yield for uncaging of amine substrate is also greatest in slightly alkaline solution. These experiments therefore determine the optimal conditions for the TR^3 experiments.

ACKNOWLEGEMENTS

This work was undertaken with the support of BBSRC.

REFERENCES

1) S.A.Johnson, R.H.Bisby, S.M.Tavender and A.W.Parker FEBS Letts. 380, 183 (1996).

2) R.H.Bisby, S.A.Johnson, A.W. Parker and S.M.Tavender CLF Annual Report, 158 (1994-95).

3) J.P.Klinman and D.Mu
Ann.Rev.Biochem. 63, 299 (1994)

4) C.Anthony
Biochem.J. 320, 697 (1996).

5) M.R.Parsons et al
Structure 3, 1171 (1995).

6) V.Kumar et al
Structure 4, 943 (1996).

7) R.H.Bisby, S.A.Johnson, A.W Parker and S.M.Tavender
Laser Chem., *in press*.

8) D.Ramesh at al
J.Org.Chem. 58, 4599 (1993).

9) C.M.Wilmot et al
Biochemistry 36, 1608 (1997).

Caged amine	k_{cat} (s^{-1})	K_m (μmol dm^{-3})	$\phi \times 10^3$ (pH8.2)	k_{uncage} (s^{-1} at 25 C)	E_a kJ mol^{-1}
CBZ	5.1	30	4.55 ± 0.04	4.0×10^3	40
CPE	55	159	3.8 ± 0.2	6.4×10^3	40
CND	127	308	25.5 ± 1.0	6.3×10^3	---
CNAP	127	308	80.1 ± 3.4	$\geq 2 \times 10^4$	---

TABLE 1 Properties of the amine substrates with respect to reaction with pea seedling amine oxidase at pH > 8, and of the photochemical release of amines from their "caged" compounds.

Abbreviations for caged amines:

CBZ	N-(2-nitrobenzyl)benzylamine
CPE	N-(2-nitrobenzyl)phenethylamine
CND	N-(2-nitrobenzyl)N'N'dimethyl-1,3-propyldiamine
CNAP	N-(1-(2-nitrophenyl)-ethyl)N'N'dimethyl-1,3-propyldiamine

UNDERSTANDING IONIZATION DENSITY EFFECTS *IN VIVO* USING FOCUSED LASER-PLASMA X-RAYS.

M Folkard[1)], S J Pfauntsch[2)], P Schettino[1)], B.D Michael[1)] and A G Michette[2)]

1) Gray Laboratory Cancer Research Trust, PO Box 100, Mount Vernon Hospital, Northwood, HA6 2JR, UK.
2) King's College London, Strand, London WC2R 2LS, UK.

INTRODUCTION

We are proposing to develop a unique microprobe facility which will be capable of targeting mammalian cells *in vitro* individually using a finely focused (≤ 100 nm diameter) pulse of low-energy x-rays, produced using a pulsed laser-plasma x-ray source. This pulse will resemble the passage of a charged-particle, but with features that will allow us to critically evaluate the role of ionisation density in biological effect. Using this facility we can endeavour to resolve a number of key questions: (1) How is biological effect related to ionisation density and distribution *at the nanometer level*. (2) What *spatial* aspects of a charged-particle track account for its radiobiological properties. (3) What *temporal* aspects of a charged-particle track account for its radiobiological properties.

METHODS

We have performed a preliminary study to assess the suitability of using the laser-plasma x-ray source for this investigation. A prototype x-ray focusing and cell micro-alignment system was installed and evaluated. x-ray focusing was achieved using a zone-plate, which is a circular diffraction grating (~100 μm diameter) with radially increasing line density, such that diffracted x-rays are brought to an axial focus. The zone-plate is used in conjunction with an arrangement of masks which must be precisely micro-aligned to allow only first-order diffracted x-rays to reach the cell.

The initial phase of the experiment involved the installation, evaluation and optimisation of the zone-plate and mask alignment assembly. A schematic diagram of the experimental arrangement is shown in figure 1. The x-rays are produced by two excimer lasers, configured to deliver focused, intense single pulses (7 ps duration) of 248 nm light onto a moving carbon target. This generates a brief micron-size 'laser-plasma' which emits soft x-rays (predominately, the hydrogen-like L_α line at 367 eV). The target is contained within a chamber, filled with a helium/nitrogen mixture at low-pressure, which has favourable absorption properties for removing unwanted energies. The radiation emerges through a 100 nm thick silicon nitride window on the top surface of the chamber. An important requirement of the source is that the dose per pulse (delivered to a cell at the zone-plate focus) is sufficient to mimic that of a charged-particle. A calibrated window-less photo-diode was used to ascertain the dose per pulse. Maximising the measured dose critically depended on two factors; correct alignment of the masks and a proper flow of helium in the region between the exit window of the laser-plasma source and the focus. When optimised, the performance of the facility was highly favourable; the measured dose per pulse at the focus of the ZP was equivalent to 0.6–1.0 MeV deposited in the cell, which is sufficient for our proposed radiobiological experiments.

We were also able to install an arrangement for imaging and manually micropositioning the cells at the ZP focus. For cells to be irradiated, they are attached to a thin window that forms the base of a cell dish. A prototype cell dish that uses 100 nm thick silicon nitride windows was developed for this study. A three-axis microscope stage supports the cell dish such that each cell can be manually manoeuvred to the focus. The focus

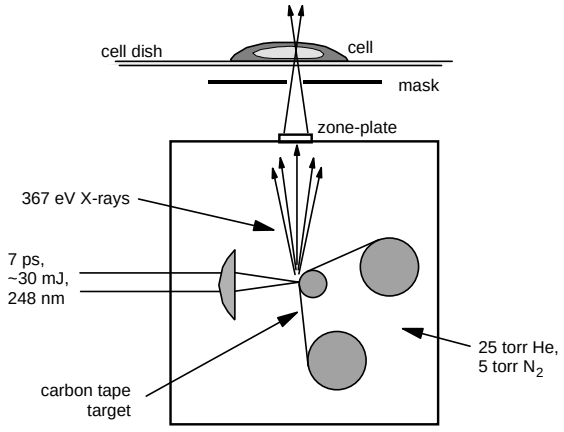

Figure 1. The arrangement for micro-irradiating cells (not to scale).

is established by measuring the output of the zone-plate while a 30 μm aperture (which also serves as the mask) is moved through the x-rays. The cell dish and zone-plate assembly are viewed from above using an epi-illuminating microscope, fitted with a CCD camera. A custom-built microscope objective mount enables the objective to be precisely positioned such that the microscope focus, and the zone-plate focus are in the same plane. This arrangement allows us to accurately position cells at the correct position for irradiation. Using this facility, we were successful in individually irradiating several hundred cells using a range of doses. Radiation damage to the cells was assessed by measuring the formation of micronuclei (indicative of lethal chromosome damage) after one cell division. The subsequent analysis showed that irradiated cells produced a significantly greater number of micronuclei than the controls (see figure 2).

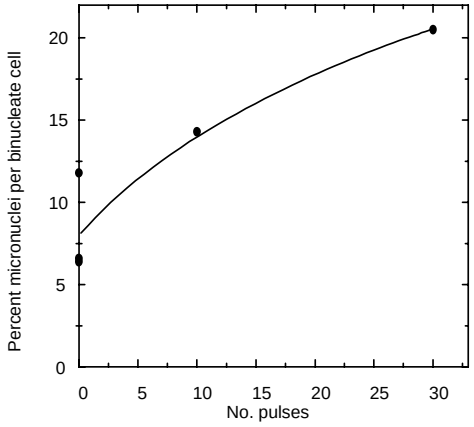

Figure 2. Preliminary data. The induction of micronuclei in mammalian cells.

CONCLUSIONS

As a result of this preliminary study, we are confident that the laser-plasma facility at RAL can be configured as a unique and powerful tool for targeting cells with sub-micron accuracy.

IRRADIATION OF DNA WITH 193NM LIGHT YIELDS FORMAMIDOPYRIMIDINE-DNA GLYCOSYLASE (FPG) PROTEIN SENSITIVE LESIONS.

T. Melvin[1)], S. Cunniffe[1)], P.O'Neill[1)], A.W. Parker[2)], T. Roldan-Arjona[3)]

1) MRC Radiation and Genome Stability Unit, Harwell, Didcot, Oxfordshire, UK.
2) Rutherford Appleton Laboratory, Chilton, Didcot, Oxfordshire, OX11 0QX, UK.
3) ICRF, Clare Hall Laboratories, Blanche Lane, Potters Bar, EN6 3LD, UK

INTRODUCTION

Exposure of DNA to ionising radiation results in chemical modifications caused by two different processes i) direct ionisation of the DNA molecule, the *direct effect*, and ii) damage from radical species produced in the vicinity of the DNA, the scavengeable (*indirect*) effect. The advent of short wave ultraviolet lasers has enabled the study of the direct ionisation processes to be studied without the interaction of the ionisation products of water.[1] Photoionisation of aqueous solutions of DNA with 193nm laser light results in the formation of a photoejected electron via a monophotonic process.[2] The DNA radicals formed by photoionisation are proposed precursors of low yields of single strand breaks (ssb),[1,3,4], which we have confirmed using Rayleigh light scattering experiments.[5] Based on the values for the extinction coefficients and quantum yield of ionisation of the mononucleosides[6], one would predict that a significant proportion of the radical cations are directly formed in DNA at guanine by the 193nm light. Further migration of the electron loss centres to guanine has been demonstrated thereby enriching the yield of guanine radicals.[7,8,9] Radical product(s) formed at guanine are indeed the precursor(s) of strand breakage[5,9,10], which occurs in yields of less than 1% of the photoionisation events.[2,11] Since, the majority of the damage, produced from photoionisation of DNA, is not prompt single strand breakage, the question arises as to whether base modifications are the major damages.

Spectroscopic studies of the one electron oxidation of the mononucleotide of guanine yields a radical cation with a pKa of 3.6,[7,12] and deprotonation, not hydrolysis, is suggested to be the reaction pathway. However recent results indicate that if the guanine radical cation is formed within a DNA matrix then hydration occurs yielding the stable product, 8-oxo-7,8-dihydroguanine.[13,14] In addition to 8-oxo-7,8-dihydroguanine, exposure of DNA to 193nm light also induces the formation of alkali labile damage.[4,15] One of the possible modifications of a guanine residue is 8-oxo-7,8-dihydroguanine, which is not a particularly alkali labile site in double stranded DNA[16-18] (*i.e.* is not cleaved efficiently by hot piperidine). However, a recent report suggests that hot piperidine causes scission at 8-oxo-7,8-dihydroguanine residues in short single stranded oligonucleotides. [19]

A method for quantitative determination of the base modifications formed within plasmid DNA was developed by Muller *et al.*,[20] using enzymes which are selective for different damage sites and create a single strand breakage at the site of the damage. The presence of repair enzymes which specifically recognise certain DNA base modifications and apurinic/apyrimidinic sites (sites of base loss) have been demonstrated in all cells investigated so far.[21,22] A number of guanine lesions are excised by the *Escherichia coli* formamidopyrimidine-DNA glycosylase (Fpg) protein.[23] The Fpg protein actively removes formamidopyrimidines (imidazole-ring opened purines), and 8-oxo-7,8-dihydroguanine from DNA.[23-25] Besides these DNA glycosylase activities, Fpg also nicks DNA at abasic sites by β-elimination reactions, and has a 5'-terminal deoxyribose phosphate excision activity.[26] However, the Fpg protein does not incise some of the reduced or oxidised abasic sites in DNA.[24,27]

Given the low yield of single strand breakage formed at the guanine residue as a result of exposure of DNA to 193nm light, a study was undertaken using purified Fpg protein to determine other modifications formed by exposure of DNA to 193nm light.

RESULTS

Aqueous solutions of plasmid DNA were irradiated with 193nm light, then assayed for yields of strand breakage, before and after treatment with the Fpg protein (For full experimental details see published results). Our results indicate that irradiation of plasmid DNA with 193nm light results in DNA lesions which are excised by the Fpg protein in yields that are about twenty times more abundant than those for prompt strand breakage.

Table: Quantum Yields of prompt and Fpg protein induced Strand Breaks.

Treatment	Argon saturated ($x10^{-4}$)	Air saturated ($x10^{-4}$)
Prompt strand breakage	0.9±0.1	1.5±0.1
Total strand breakage after treatment with Fpg protein	23.8±2.6	33.1±3.1

An aqueous solution containing a 5'-^{32}P-end labelled restriction cut fragment of double stranded DNA, of known sequence, was irradiated with 193nm light (for conditions see ref. 5). This results in prompt ssb exclusively at the deoxyguanosine moiety (lane 2). Damage, which is excised by Fpg to yield a gap (single-strand break) in the duplex (lane 3) (for enzyme conditions see ref. 28) also occurs exclusively at guanine.

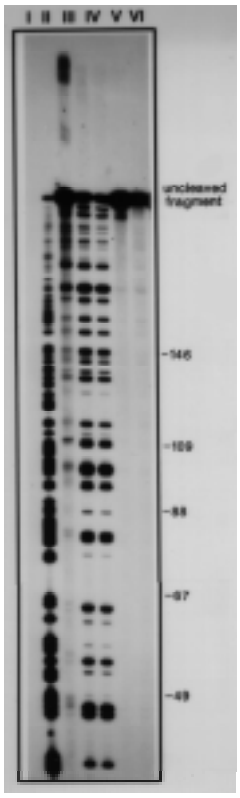

The effect of treatment by Fpg protein on the base specificity of ssb induction in the DNA fragment of known sequence by 193nm light.

I Maxam Gilbert (G/A) cleavage products,

II frank strand breakage (total fluence = 2mJ/cm^2).

III treated with Fpg (30ng/μg DNA),

IV treated with Fpg (150ng/μg DNA),

V no light,

VI no light, treated with Fpg (30ng/μg DNA).

Un-irradiated DNA samples have undetectable levels of ssb in the Fpg treated and untreated samples and a heat treated sample of Fpg does not cleave irradiated DNA. The electrophoretic mobility of the fragments of prompt ssb (lane 2) is marginally slower than for those treated by Fpg (lane 3), due to the presence of a damaged sugar remnant at the cleavage site of prompt ssb.[5]

The yields of ssb (as seen for the differences in band intensity), either in the form of frank ssb (lane 3) or resulting from damage excised by the Fpg protein (lane 3), is not equal for each deoxyguanosine site, but is influenced by neighbouring nucleobase sequence. However the sequence specificity for the relative yields of deoxyguanosine damage from prompt ssb (lane 2) and Fpg sensitive base modifications (lane 2) is approximately the same, suggesting that the products arise from a common precursor. The most likely candidate is the guanine radical cation, which yields prompt ssb in DNA.[5]

Fpg protein can efficiently excise purine modifications, including 8-oxo-7,8-dihydroguanine and 2,6-diamino-4-hydroxy-5-formamidopyrimidine (FapyGua),[23] and it additionally has a β-lyase activity that nicks DNA at apurinic/apyrimidic (AP sites).[29] Although Fpg protein incises 'regular' AP sites very efficiently, reduced and some oxidised AP sites are poor substrates of this DNA glycosylase.[26] Predicted guanine modifications could include the hydration products of the radical cation of guanine, such as 8-oxo-7,8-dihydroguanine and possibly also FapyGua (Scheme 1). 8-oxo-7,8-dihydroguanine, formed from the photosensitised oxidation of the guanine moiety within DNA is excised by the Fpg protein efficiently.[30]

The full spectrum of products that result from the guanine radical cation within DNA, in the absence and presence of oxygen, following photolysis with 193nm light have not, as yet, been determined. However, the products formed by photoionisation are, if chemically different, both excised by the Fpg protein to an equal extent. Model studies for the oxidation of DNA, using the photosensitiser riboflavin, indicate that the hydration of a guanine radical cation occurs to yield 8-oxo-7,8-dihydroguanine.[13] The results presented here, using plasmid DNA, indicate that there are large yields of guanine base damage compared with prompt strand breakage caused by photolysis with 193nm light.

REFERENCES

1) Schulte-Frohlinde, M. G. Simic and H. Görner
(1990) *Photochem. Photobiol.* 52, 1137-1151.

2) Görner, H., M. Wala and D. Schulte-Frohlinde
(1992) Photochem. Photobiol. 55, 173-184.

3) Gurzadyan, G. G., H. Görner
(1993) Photochem. Photobiol. 58, 71-80.

4) Kochevar, I. E., L. A. Buckley
(1990) Photochem. Photobiol. 51, 527-532.

5) Melvin, T., S.W. Botchway, A.W. Parker, P.O'Neill
(1996) J.Am.Chem.Soc., 118, 10031-10036.

6) Candeias L.P., S. Steenken
(1992) J.Am.Chem.Soc. 114, 699-704.

7) Candeias L. P., S. Steenken
(1993) J. Am. Chem. Soc. 115, 2437-2440.

8) Melvin, T., S.Botchway, A.W. Parker, P.O'Neill
(1995) J.Chem.Soc., Chem.Commun., 653-654.

9) Melvin, T., M.A. Plumb, S.W. Botchway, P.O'Neill, A.W. Parker
(1995) Photochem.Photobiol., 62, 584-591.

10) Melvin, T., M.A. Plumb, S.W. Botchway, A.W. Parker, P.O'Neill
(1995) Radiation damage in DNA: structure/function relationships at early times. (edited by A.F. Fuciarelli and J.D. Zimbrick) pp175-184. Battelle Press. Columbus, U.S.A.

11) Candeias L.P., P.O'Neill, G.D.D. Jones, S. Steenken
(1992) Int.J.Rad.Biol., 61, 15-20.

12) Willson, R.L., P. Wardman, K-D. Asmus
(1974) Nature (London), 252, 323-324.

13) Kasai, H., Z. Yamaizumi, M. Berger, J. Cadet
(1992) J. Am. Chem. Soc. 114, 9692-9694.

14) Cullis P.M., M.E. Malone, L.A. Merson-Davies
(1996) J. Am. Chem. Soc. 118, 2775-2781.

15) Gut, I. G., R. Farmer, R. C. Huang and I. E. Kochevar
(1993) Photochem. Photobiol. 58, 313-317.

16) Blazek, E. R., J. G. Peak and M. J. Peak
(1989) Photochem. Photobiol. 49, 607-613.

17) Devasagayam, T.P.A., S. Steenken, M.S.W. Obendorf, W.A. Schultz, H. Sies
(1991), Biochemistry, 30, 6283-6289.

18) Schneider, J.E., S. Price, L. Miadt, J.M.C. Gutteridge, R.A. Floyd
(1990), Nucleic Acids Res., 18, 631-635.

19) Chung, M-H, H. Kiyosawa, E. Ohtsura, S. Nishimura, H. Kasai
(1992) Biochem. Biophys. Res. Commun. 188, 1-7.

20) Muller, E, S. Boiteux, R.P. Cunningham, B. Epe
(1990), Nucleic Acids Res., 18, 5969-5973.

21) Wallace, S.S
(1988) Environ. Mol. Mutagen, 12, 431-477.

22) Lindahl, T
(1990) Mut. Res. 238, 305-311.

23) Boiteux, S., E. Gajewski, J. Laval, M. Dizdaroglu
(1992), Biochemistry, 31, 106-110.

24) Boiteux, S
(1993) J.Photochem.Photobiol. B., 19, 87-96.

25) Tchou, J., V. Bodepudi, S. Shibutani, I. Antioshichkin, J. Miller, A.P. Grollman, F. Johnson.
(1994) J.Biol.Chem. 269, 15318-15324.

26) Boiteux, S., T.R. O'Connor, F. Lederer, A. Gouyette, J. Laval
(1990) J.Biol.Chem. 265, 3916-3922.

27) Häring, M., Rudoger. H., Demple, B., Boiteux, S. and Epe, B
(1994) Nucleic Acids Res, 22, 2010-2015.

28) T. Melvin, S. Cunniffe, D. Papworth, T. Roldan-Arjona, P. O'Neill
Photochem, Photobiol,1997, 65, 660-665

29) O'Connor, T.R., J. Laval
(1989) Proc. Natl. Acad.Sci. U.S.A. 86, 5222-5226.

30) Ravanat, J.L., M. Berger, S. Boiteux, J. Laval, J. Cadet
(1993), J.Chem.Phys., 90, 871-879.

DI-SULPHONATED ALUMINIUM PHTHALOCYANINE INDUCED PHOTOSENSITISATION OF V79/4 CHINESE HAMSTER FIBROBLASTS-STEADY-STATE AND TIME-RESOLVED STUDIES

R.B. Ostler[3], A.D. Scully[1,3], A.Waite[3], K.Henbest[1], C. de Lara[4], D. Pattison[2], A.J. MacRobert[2] and D. Phillips[3] A.W. Parker[1]

[1]Rutherford Appleton Laboratory, Chilton, Didcot, Oxfordshire, OX11 0QX, UK.
[2]National Laser Medical Centre, UCL Medical School
[3]Department of Chemistry, Imperial College of Science, Technology and Medicine
[4]Medical Research Council, Harwell

INTRODUCTION

Selective photosensitisation of tumour cells offers a non-invasive alternative to major surgery in the treatment of cancer. Di-sulphonated aluminium phthalocyanine ($AlPcS_2$) is a second generation photosensitiser that shows particular promise, and which has been the subject of earlier investigations in the fluorescence microscopy laboratory at the Rutherford Appleton Laboratory.

In the present study, the localisation of $AlPcS_2$ prior to, during, and after photosensitisation, was investigated using steady-state confocal fluorescence microscopy (CFM). Possible changes in the sub-organelle environment were investigated using time resolved confocal fluorescence imaging microscopy (CFLIM).

STEADY-STATE MEASUREMENTS

Using the facilities at the Medical Research Council (MRC), V79/4 Chinese hamster fibroblasts were grown to log phase before staining with 25μM $AlPcS_2$ in phosphate buffered saline (PBS) at 37°C and 5% CO_2 for 30 minutes. CFM was carried out using the apparatus described in (2), with the Gated Optical Intensifier removed, and the image collected by focusing the fluorescence onto the chip of the CCD camera. An excitation wavelength of 610 nm was used for all measurements. The resolution in the x-y plane and in the axial direction was of the order of 1μM, as determined by calibration using 1μm fluorescent spheres.

Using a laser power of 10 Wcm^{-2}, changes in the localisation of $AlPcS_2$ were seen to occur very rapidly. In figure 1 the distribution of $AlPcS_2$ fluorescence in V79/4 cells acquired over a period of six seconds is shown. The small bright spots are endosomes and the large bright structure consists of membranes from the Golgi Body and Endoplasmic reticulum.

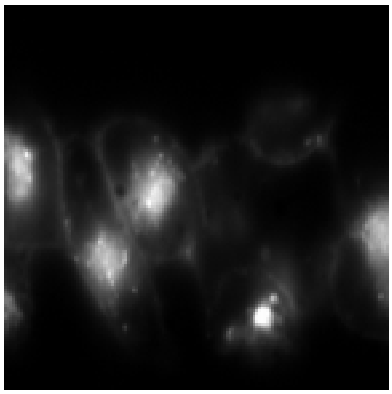

Figure 1. $AlPcS_2$ distribution in V79/4 cells.

After a further six seconds of irradiation profound changes in the localisation of $AlPcS_2$ are seen to occur; these changes are shown in figure 2. The bright ring seen around the nucleus is thought to arise from $AlPcS_2$ redistribution within the Golgi Body and nuclear envelope. The apparent expansion of the Golgi Body and Endoplasmic reticulum to fill the entire cell, we ascribe to the loss of structural integrity of these organelles occuring on photosesitisation.

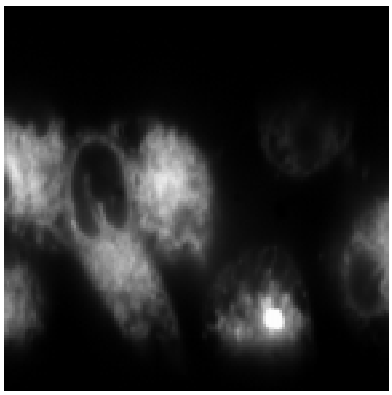

Figure 2. $AlPcS_2$ distribution in V79/4 cells after photosensitisation.

The sequence of events occuring during the early stages of photosensitisation of V79/4 cells, stained with 10μM $AlPcS_2$ for 30 minutes, and employing a much lower laser power, of 1 Wcm^{-2}, were recorded, and are shown in figure 3.

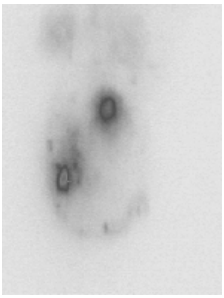

Figure 3a: 45s irradiation

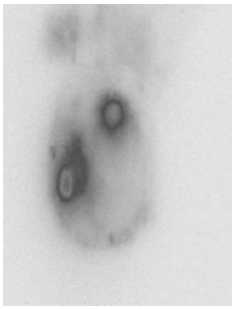

Figure 3b: 135s irradiation

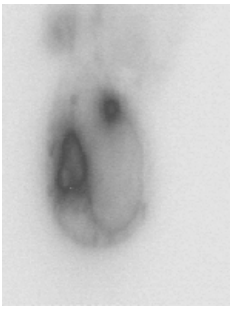

Figure 3c: 270s irradiation

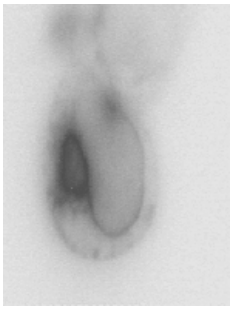

Figure 3d: 450 irradiation

It can be seen that the fluorescence (shown as darker regions in these images) begins to spread throughout the cell as photosensitisation proceeds, but is primarily associated with redistribution around the nucleus. We therefore propose that the initial stage of photosensitisation involves redistribution within the Golgi Body and possibly the nuclear envelope.

TIME RESOLVED STUDIES

Using the microscope in time gated mode has allowed changes in the fluorescence lifetime of $AlPcS_2$ to be monitored. Following from previous studies (1), we have demonstrated that the fluorescence lifetime of $AlPcS_2$ within v79/4 cells can, prior to photosensitisation be fitted exponentially, and a lifetime of

~4.5 ns obtained (figure 4). The fluorescence decay can however be fitted more accurately to two lifetime values, τ_1~ 2.0 ns and τ_2 ~ 5.0 ns (data not shown). Bi-exponentiality is expected from membrane localised A1PcS_2.This therefore suggests that $AlPcS_2$ has become membrane localised.

On further irradiation there is an increase in fluorescence intensity and an increase in the $AlPcS_2$ fluorescence lifetime to ~ 9.0 ns (figure 5). The reasons for an increase in fluorescence lifetime of intracellular $AlPcS_2$ are not known. However, the fluorescence lifetime of $AlPcS_2$ in lipid environments is longer than in aqueous environments, and it is possible that on photosensitisation there is a disintegration of the membranes giving a hydrocarbon milieu. At present, such suggestions are, however, tenuous.

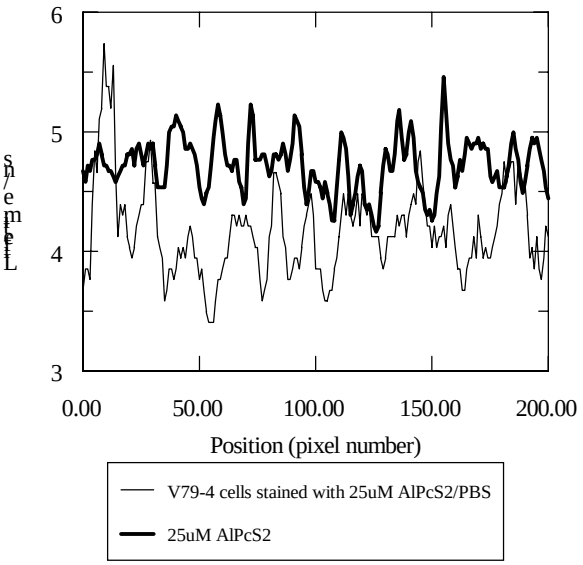

Figure 4. Cross-sections through fluorescence lifetime maps of A1PcS2/PBS and V79/4 cells stained with A1PcS2/PBS

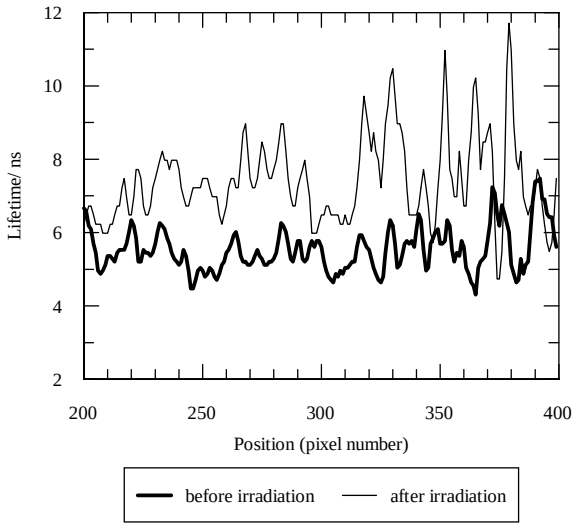

Figure 5. Cross-sections through fluorescence lifetime maps of V79-4 cells before and after irradiation

SUMMARY

The relocalisation of $AlPcS_2$, and the accompanying dramatic changes to the cell structure of V79/4 cells on photosensitisation have been demonstrated. Concomitant changes in the fluorescence lifetime of intracellular $AlPcS_2$ have been observed, and it is tentatively proposed that this results from the release of lipid moieties from the cell membranes as a result of photodamage.

REFERENCES

1) Intracellular Fluorescence Lifetime Imaging of Di-sulphonated Aluminium Phthalocyanine CLF Annual Report, 1995-96.

2) Development of a Laser Confocal Fluorescence Microscope having sub-nanosecond time resolution CLF RAL Annual Report 1995-96.

3) M Ambroz, A J MacRobert, J Morgan, G Rumbles, M S C Foley and D Phillips
Time-resolved fluorescence spectroscopy an intracellular imaging of disulphonated aluminium phthalocyanine, J Photochem Photobiol B: Biol 22 105-117 (1994).

TIME RESOLVED FLUORESCENCE MICROSCOPY OF CYANOBACTERIA

R.W. Sparrow [1)], W. Lu [2)], S.M. McColl [2)], E.H. Evans [2)], A. Scully [3)]

1) Bromley College, Rookery Lane, Bromley, Kent, BR2 8HE, UK
2) School of Biomolecular Sciences, Liverpool John Moores University, Byrom Street, Liverpool, L3 3 AF, UK
3) Rutherford Appleton Laboratory, Chilton, Didcot, Oxon, OX11 0QX, UK

INTRODUCTION

There are very few methods of measuring the physiological state of intact bacterial cells. Increasingly, in biotechnological processes, bacteria are used in fermentations, the control of which relies on substrates and products measured externally to the cells. In the environmental field, the microbial populations of water courses, in particular, give information on their status and development. All bacteria and all photosynthetic cells contain intrinsic fluorescent molecules which can be measured as a way of monitoring the physiological state of the cells. In this study we have concentrated on measurements of cyanobacteria under different nitrogen status, using photosynthetic pigments as fluorescent probes.

Cyanobacterial populations are major contributors to both freshwater and marine ecosystems. In recent years, there has been considerable publicity about growth of toxic cyanobacteria in freshwater lakes and reservoirs, and these organisms make a major contribution to marine productivity. The cyanobacteria are obligate photoautotrophs, and photosynthesis can be monitored by measuring the fluorescence of the photosynthetic pigments [1,2)]. The majority of fluorescence is associated with the light harvesting complexes (LHC) and Photosystem 2 (PS2). In cyanobacteria the bulk of the light harvesting complexes are phycobilins which fluoresce at wavelengths discrete from that of chlorophylla, (chl.a), allowing greater ease of discrimination of measurements of PS2. In *Anabaena cylindrica*, the organism described here, under conditions of nitrogen starvation a specialised cell, the heterocyst, is formed. This cell is proposed to be the site of nitrogen fixation, based on experiments on heterocysts isolated mechanically from vegetative cells. These latter experiments suggest that PS2 is inactive or absent, and that only PS1 may be active, (see 3 for review). In this paper we describe *in vivo* measurements on *A. cylindrica* of phycobilin and chl.a fluorescence.

RESULTS AND DISCUSSION

Measurements were taken of *A. cylindrica* cultures grown in the presence and absence of fixed nitrogen using a fluorescence microscope at RAL. The configuration of the microscope was as previously described [4)], except that fluorescence emission was monochromated at 660 nm by interference filter or above 670 nm by a glass filter, Kodak Wratten 70.

Figure 1 shows a typical light microscope photograph of *A. cylindrica* showing a heterocyst in a filament of vegetative cells. Figure 2 shows a similar culture viewed under the fluorescence microscope monitoring emission at 660 nm.

Although the vegetative cells either side of the heterocyst are visible, the heterocyst emits no fluorescence. This is consistant with the findings of other workers (see 3), and indicates the absence or extremely low level of phycobilins within the cell. Fluorescence emission above 670 nm is shown in Figure 3 of a similar filament of *A. cylindrica*.

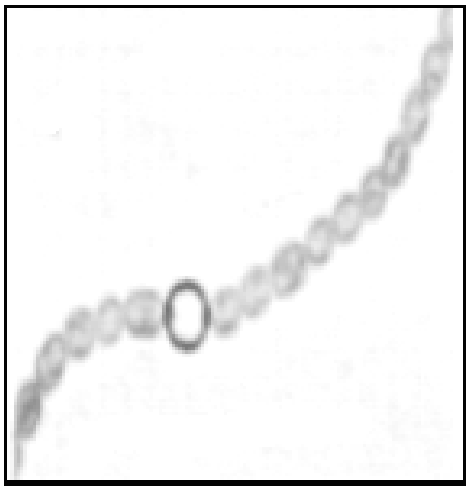

Figure 1: *A. cylindrica* x 300
Large cell is heterocyst, remainder vegetative cells.

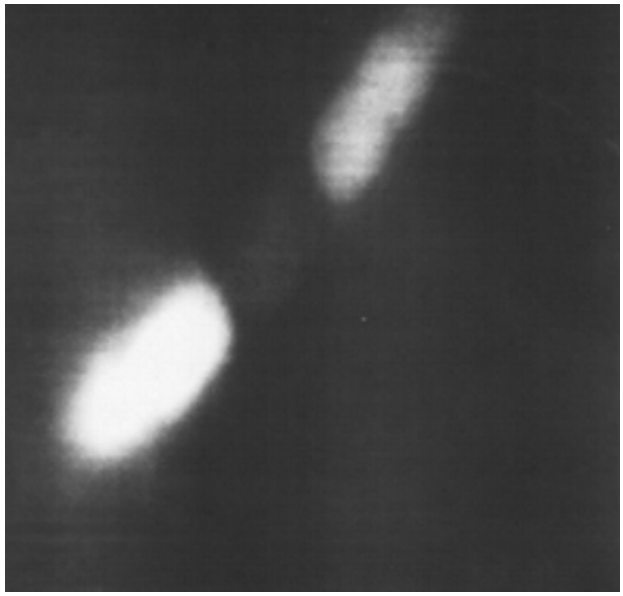

Figure 2: *A. cylindrica* x 1200
Fluorescence excited at J90 nm, emission measured at 660 nm.

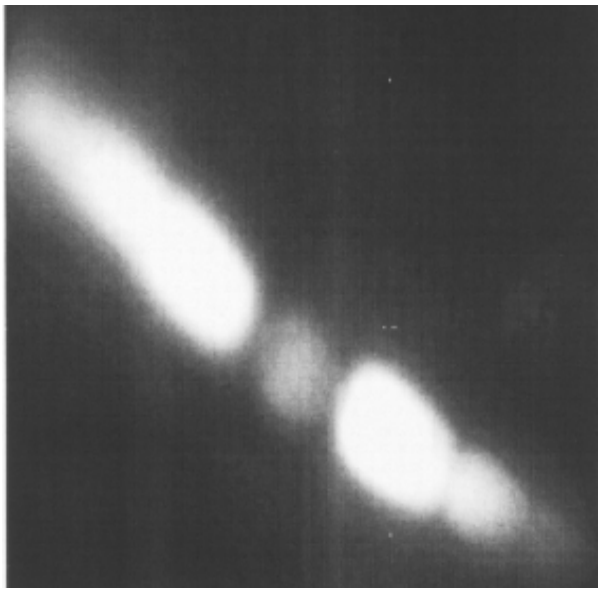

Figure 3: *A. cylindrica* x 1200
Fluorescence excited at 590 nm, emission measured at 680 nm.

The heterocyst is now visible, but less fluorescent than the vegetative cells. Chl.a is thus present and fluorescent, although at a lower level than the associated vegetative cells. There is thus a strong likelihood that photosynthesis is taking place but whether this involved PS2 as well as PS1 is difficult to establish. The fluorescence yield of PS1 is about 1% of PS2 [1)], but unfortunately, precise emission comparisons of these cells are technically impossible at this time. This is, however, the first demonstration of photosynthesis in heterocysts undisturbed within the filament of cells.

Time resolved fluorescence decay measurements can give further information about photosynthetic activity. The decay in both phycocyanin and chlorophyll fluorescence is multiexponential and the origins of individual components have been discussed [5)]. Energy transfer between pigments is extremely fast, exciton equilibration in the antennae appearing to take place in less than 15 ps, whilst terminal emitters of, for example, the phycobilin-containing phycobilisomes have much longer lifetimes in the ns. timescale. Disruption of energy transfer causes increased lifetimes [2)]. In the fluorescence microscope, time resolved fluorescence decay can be gated between 100 ps. and 1 ns, giving a short and a longer lived decay, as shown in Figure 4. There are clear indications that areas of the vegetative cells shown exhibit predominantly one

Figure 4: *A. cylindrica* x 1200 Fluorescence excited at 600 nm
Pink 100 ps decay Blue 1 ns decay

decay or the other. This may reflect heterogeneous activity within the cells. Such a likelihood has been suggested in higher plant chloroplasts on the basis of indirect methods of analysis [6)].

The results described above indicate that measurements of photosynthetic activity in individual cells are possible. Technical developments to allow fluorescence intensity comparisons and further resolution of fluorescence decays would allow detailed measurements to be made.

REFERENCES

1) G.H. Krause & E. Weis
Ann Rev. Plant Physiol. Plant Mol. Biol. 3l3, (1991).

2) E.H.Evans & R.G. Brown
J. Photochem, Photobiol. B. Biol, 22, 95, (1994)

3) J.R. Gallon & A.E. Chaplin
In : Biochemistry of the Algae and Cyanobacteria
(Ed. L.J. Rogers & J.R. Gallon) O.U.P. (1988)

4) A.D. Scully, A.J. MacRobert, S. Botchway, P.O'Neill, A.W. Parker, R.B. Ostler and D. Phillips
CLF. RAL. Annual Report, p.155 (1995-96)

5) A.R. Holzwarth
In: The Chlorophylls (Ed. H. Scheer) CRC Press Boca Raton, 1125, (1991)

6) J.K. Hoober
Chloroplasts, Plenum, N.Y. (1984).

SELECTIVE, LAYERED, X-RAY IRRADIATION OF YEAST CELLS

E Turcu[1)], R Allot[1)], N Lisi[1)], M Milani[2)], M Costato[3)], A Pozzi[3)], F Salsi[3)], G Baroni[4)], D Batani[4)], S Cozzi[4)], L Ferraro[4)], A Masini[4)], F Previdi[4)] and M Ballerini[4)]

1) Rutherford Appleton Laboratory, Chilton, Didcot, Oxfordshire, OX11 0QX, UK.
2) Dipartimento di Scienza dei Materiali, Universitàdi Milano, I.
3) Dipartimento di Fisica, Università di Modena, I.
4) Dipartimento di Fisica, Università di Milano, I.

INTRODUCTION

Yeast cells provide a simple easy-to-manipulate model system for studying flipping proteins that mark prion-associated diseases in mammals[1] and more in general cellular metabolic dynamics [3]. They represent a good stuff for the mammalian and a laboratory for the investigation of nonlinearities in biological systems and in particular for homeostasis,one of the most intriguing open problems in immunology[2]. The characterization of metabolism in *Saccharomyces cerevisiae* is helped by the simultaneous presence of two major ways, fermentation and respiration, that are driven by external conditions (for instance nutrients or atmosphere composition) and have different spatial locations. Soft X rays allows to differently affect these two metabolic pathways (both resulting in carbon dioxide production, nutrient consumption and energy storage), providing a deeper knowledge of their structure, loops, competition and relevant physical parameters. General features of the experiment and preliminary results have been illustrated in ref.4.

THE RADIATION SOURCE

Soft X-rays generated by laser-plasma interaction with suitable filters and target provide two different ranges of energies: 0.6 KeV (teflon target) and 1.2 KeV (copper target), whose spectral analysis has been investigated by spectrometer recording.

DOSIMETRY

A detailed investigation of the biological target structure gives two distinct pictures of energy release following irradiation at two distinct energies. The softer radiation will be stopped at the level of the membrane-cell wall complex (that in yeast cells has been evaluated to be around 200 nm); the harder one will be able to overcome the membrane-cell wall complex and will stop in the cytoplasm without inducing significant damages in nuclear DNA. Both radiation will severely interfere directly with metabolic processes, and indirectly since they will activate damage repair processes. An overall picture is given in fig.1 where the connections are shown between X-ray energy, depth penetration and energy deposition range, cellular structures and major metabolic pathway location.

Fig.1 Yeast cell morphology and energetic

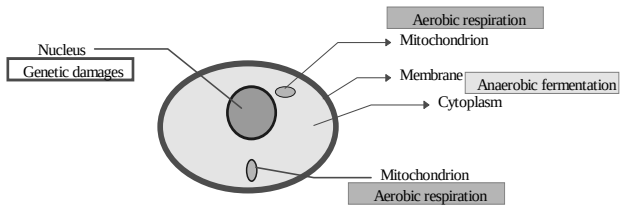

Typical recorded parameters are:

Average radius	3-4 microns
Membrane thickness	100-200 nm
Nucleus size	≈ 2 microns

In fig. 2 a layout of the experiment is presented together with the input parameters and the observed variables.

Fig.2 Yeast cell metabolism, control parameters and major variables

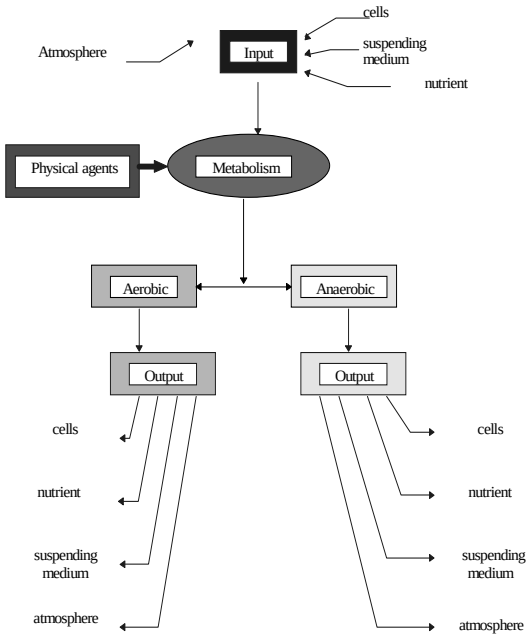

PREPARATION OF BIOLOGICAL SAMPLES

In order to obtain reproducible data, great attention has been devoted to cell characterization and sample preparation, trying to connect in the smoothest possible way the four major temporal phases of cell life during the experiment:

1. cell hydration and suspension preparation
2. cell deposition on filters
3. cell irradiation
4. cell detachment from filters and resuspension

Actually cells must be deposited (under sterile conditions) as a monolayer in order to ensurea reasonable homogeneous irradiation. This is achieved by using a Venturi tube. The subsequent step of esposure to soft X rays is ruled by exploiting a previously prepared robot, available at CLF, and using filter holders built out from teflon bars that can be inserted into the filter holder of the robot. A check of the structure of different filters, of the link between filters and cells, and of the organization of cells onto the filter surface can be easily obtained by Focused Ion Beam (FIB) inspection (see fig.3)

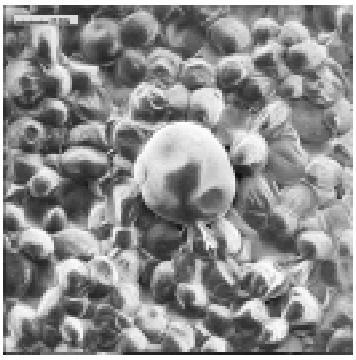

Fig.3 Organization of cells on filter surface

MEASUREMENT TECHNIQUES

Available measurement techniques during the experiments and related parameters, by which preliminary information has been obtained on the differential response of metabolism to the two colour soft X-ray irradiation are listed below:

1. CO_2 pressure (gauge sensor, absolute sensor);
2. Cell counting (Thoma-Neubauer chamber, plus videorecorder and image printer, spectro photometer);
3. Cell morphology (SEM, TEM, SXCM [Soft X-ray Contact Microscopy], FIB [Focused Ion Beam]);
4. Cell division (optical microscopy, FIB);
5. Oxygen consumption (mass spectrometer) and atmosphere composition;
6. Glucose consumption (chemical reaction plus spectrophotometer);
7. Ethanol production (mass spectrometer, solid state sensor);
8. pH (pH-meter);
9. Metabolism follow-up of released gas analysis (mass spectrometer, FTIR [Fourier Transform InfraRed]);
10. Metabolic oscillations (gauge sensor plus data analysis software);
11. Nuclear Magnetic Resonance (NMR) tracking of adenine nucleotides in cells;
12. Delayed Luminescence.

PERFORMANCES AND RESULTS

The analysis performed by the team during the experiment at RAL has highlighted:

1) Yeast cell metabolism does respond in a different manner to changes in soft X-ray dose and wavelength.
2) Nonlinear response to dose is observed (Fig.4).
3) Metabolic oscillations are present in non-irradiated samples, and depend on metabolic parameters (Fig.5).
4) Metabolic oscillations exhibit a clear-cut dependence on the irradiation parameters(Fig.6,7).
5) The presence of metabolic oscillations can be observed on samples monthes after the irradiation.
6) The frequency of oscillations is stable against the time lapse variation occurring between irradiation and metabolism monitoring.
7) Self recovery mechanism has been highlighted in a resumption of a standard metabolic activity following a time lag depending on the irradiation parameters.
8) CO_2 production was correlated to other relevant effects associated to yeast metabolism, growth and duplication. The wealth of collected data under different conditions has permitted to draw a multi- causal matrix connecting different dynamical aspects of yeast metabolism.

Fig.4

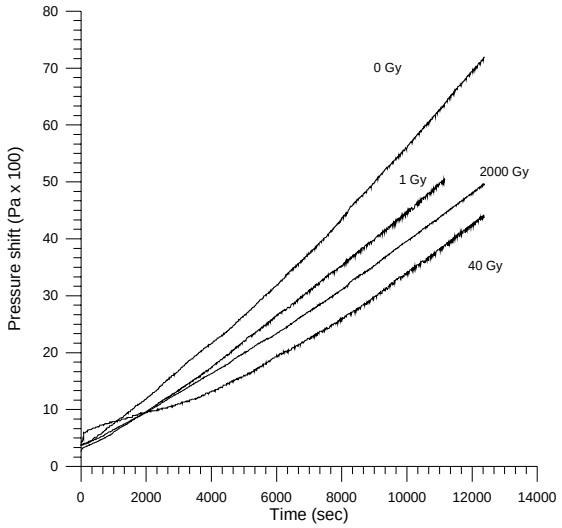

Fig.5

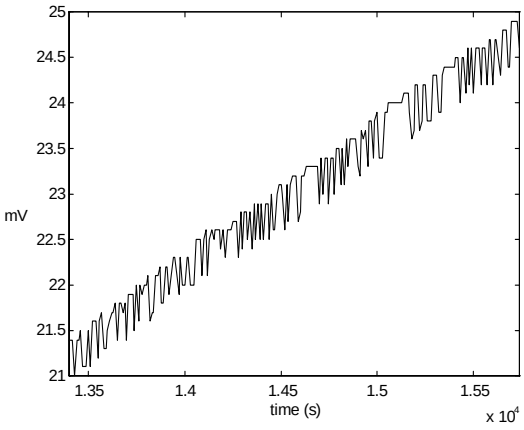

Fig.6

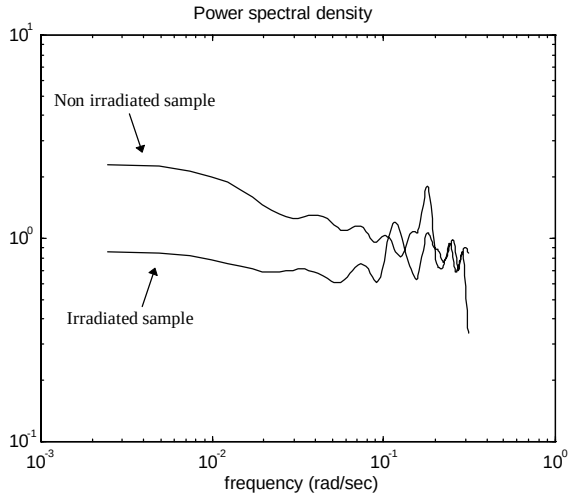

	mean (Hz)	**standard deviation (Hz)**
non irradiated	0.0278	0.0082
25 nC	0.0275	0.0081
1000 nC	0.0267	0.0079
50000 nC	0.0243	0.0079

Fig.7a

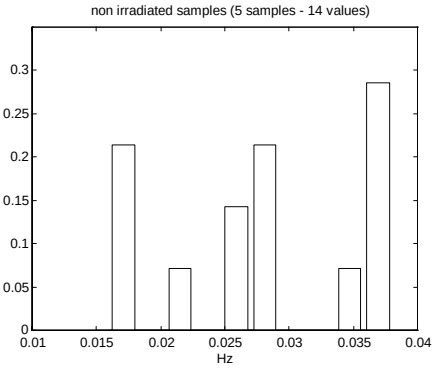

Fig.7b

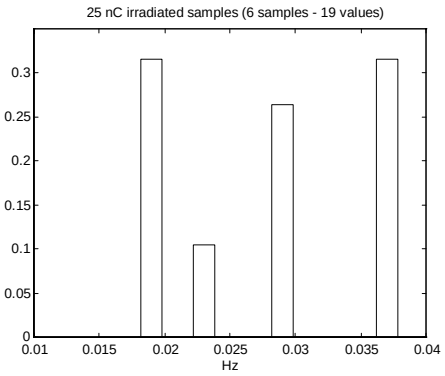

Fig.7c

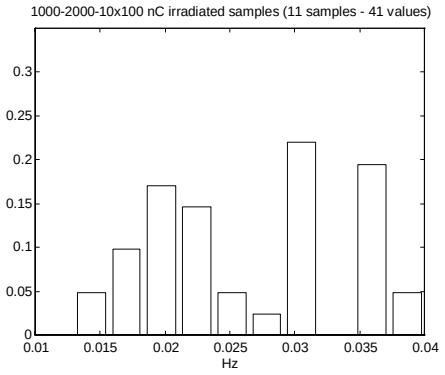

Fig.7d

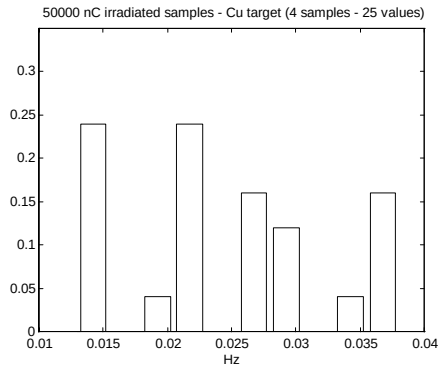

CONCLUSIONS

The experimental activity performed show s that soft X ray radiation affects the metabolic dynamics in a nonlinear way. The on-line measurement of pressure variations by differential pressure sensors has proven to be very effective and reproducible; the possibility of continuous monitoring allows the identification of peculiar oscillations and their frequency.

This turns out to be of great importance: actually the global pressure developed in sealed bottles strictly depends among the other parameters, on the total cell number, while the frequency of metabolic oscillations do not depend on such a variable thus resulting in an enhancement of statistical significance of the results (the yeast cell cellular cycle is of the order of 90 minutes, while measurements can last up to 100 hours).

The overall cross-linked measurements make us confident that similar experiments can be performed on mammalian cells, in particular those responsible for the immune response, where membrane related processes of recognition and defense are of the utmost importance. Their metabolism can be checked in the same way and the overall experimental set up seems to fit the general requirements as it has been confirmed by preliminary investigations. The two critical points will be related to the different structure and thickness of lymphocyte membrane: a detailed investigation is necessary of penetration depth and of the actual damages of nuclear material.

REFERENCES

1) Special News Report, Putting Prions to the Test Science 273 (1996) 184

2) K Nasmyth Viewpoint: Putting the Cell Cycle in Order, Science 274 (1996) 1643

3) B Gallagher Population Biology of Lymphocytes, Science 276 (1997) 1817

4) I C E Turcu et al Metabolic interference of soft X-rays on yeast cells, CLF-RAL Annual Report 1995-96 p.152

THE 'FRONT END' FOR THE PETAWATT UPGRADE OF VULCAN

J Collier, C Hernandez-Gomez, C Danson, D Hitchcock, J Walczak

Rutherford Laboratory, Chilton, Didcot, Oxon, OX11 0QX: j.collier@rl.ac.uk

INTRODUCTION

A completely new CPA Front End for VULCAN has been designed and implemented for the Phase I PetaWatt Upgrade. This comprises 3 new ultra short pulse oscillators, a new variable length pulse stretcher based on an aspheric design, a completely new optical 'switchyard' for input / output selection, a new suite of diagnostics and the ability to accurately frequency lock two CPA oscillators opening up the possibility of dual CPA operations through time multiplexing. These systems are individually detailed below.

OSCILLATORS

Three CPA oscillators are currently available in the Front End. These are

1. The Ti:S Oscillator - The *Tsunami* is a commercial Kerr Lens Modelocked (KLM) oscillator using Ti:Sapphire as the active medium. It is pumped by all lines of a pointing stabilised Argon Ion laser. The 80 MHz cavity produces 5 nJ pulses of duration 120 fs.

2. The SAM Oscillator - The GLX-100 is a commercial oscillator with Nd:Glass as the active medium. It is mode locked by a state of the art device known as a SEmiconductor Saturable Absorber Mirror (SESAM). The 80 MHz cavity produces 170 fs pulses at 1nJ per pulse. The SESAM is mounted on an intracavity piezo which is in turn mounted on a picomotor. The position of the piezo and picomotor are determined by a microprocessor controlled phase locked loop that is synchronised to an externally applied RF signal.

3. The YLF2 Oscillator - The final oscillator is an in house designed Nd:YLF Additive Pulse Modelocked (APM) oscillator similar to the other Nd:YLF oscillator (YLF1) that has been in use for a number of years. It is a coupled cavity oscillator that produces pulses of 1.8 ps duration at 1 nJ per pulse.

STRETCHER

As part of the Phase I PetaWatt upgrade the grating separation in the TAW compressor has been increased from 2.8 m to 3.5 m and the output bandwidth of VULCAN nominally increased from 2 nm to 4 nm. A new stretcher system has been designed to accommodate these changes and additional new features have been introduced.

The stretcher, shown in Figure 1, is a refractive confocal telescopic design operated in a double pass mode using aspheric optics. The two lenses have a focal length of 1.5 m, about the minimum focal length possible to match the 3.5 m compressor length. Both lenses are plano-convex manufactured from BK7. Lens 1 has a diameter of 70 mm and Lens 2 a diameter of 150 mm. The spherical aberration of Lens 2 means that, if not corrected, there will be a residual angular dispersion at the output of the system. Therefore Lens 2 is of an aspheric design with a conic coefficient of -1.07 to correct for this aberration.

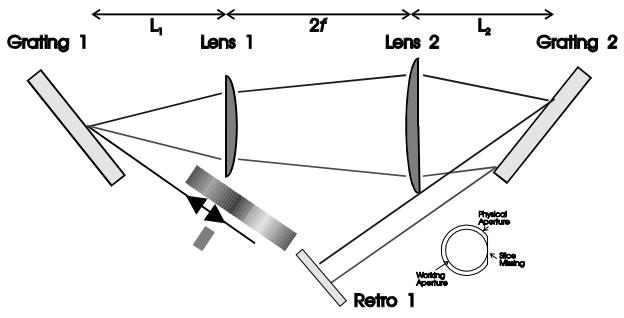

Figure 1 : The TAW Stretcher

The maximum bandwidth that the system can pass at 1053 nm is 16 nm. This is 4 times the expected output bandwidth of VULCAN after the upgrade has been completed. This is also about the maximum bandwidth that could be passed by a refractive design without 3rd order phase distortions from chromatic aberrations becoming important. The stretcher bandwidth has been maximised for the given lens aperture by optimising the distances L_1 and L_2 and grinding a flat on one side of Lens 2 thereby reducing the physical aperture to the working aperture at that point. This has ensured that the double sided clip imposed on the dispersed beam by Lens 2 en route to Grating 2 occurs at the same spectral point as the single sided clip occurring after diffraction from Grating 2.

One final important feature of the stretcher is the ability to vary the effective grating separation without changing the beam alignment.

With reference to Figure 2, this has been achieved by mounting Grating 2 and the retroreflector on a separate 'L' shaped breadboard which is in turn mounted on a Hepco rail system. This allows significantly easier tuning of the pulse compression which gives the option of adjustment in the Front End as well as the Target Area. This also provides the ability to 'dial up' a User specified pulse length up to 20 ps which can be positively or negatively chirped.

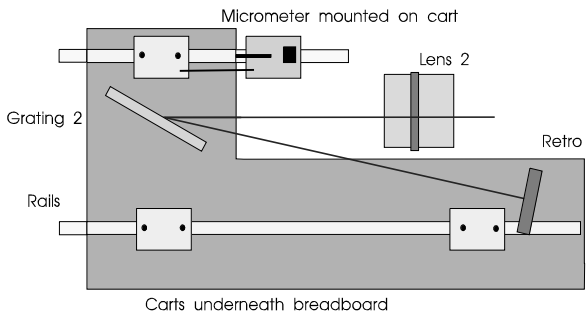

Figure 2 : The variable length stretcher configuration

OPTICAL SWITCHING

The use of three oscillators, a stretcher for each target area and a number of possible output directions has meant a new system to provide the necessary switching. A scheme has been devised based on McNielle polarizers which transmit or reject a beam based on its polarization. The special feature of a McNielle polarizer is the transmission and rejection directions are at 90 degrees with respect to each other which make them ideally suited for use on optical tables. The relevant beams are then switched by a combination of drop in beam blocks and wave plates. This drop in nature is achieved by mounting these components on a rotary solenoid. A miniature switch picks up the status of the mount. The solenoids are driven and read by a specially developed unit that can interface to the main VULCAN control computer system. The stretcher and input / output switching are housed on a single 3mx1.5m optical table.

DIAGNOSTICS

A number of fixed diagnostics have been implemented to improve the speed of alignment between the Front End and the main VULCAN system. Each oscillator has its own low resolution spectrometer to confirm wavelength and the modelocked status. The SAM oscillator has an additional monitor to confirm the frequency locking status. There is an Input Near Field and an Input Far Field monitor which determine the position and pointing of each oscillator into the stretcher system. A second Near Field and Far Field pair is located at the exit of the Front End to determine position and pointing into VULCAN. All four outputs are available on a single monitor using a quadrant framer. A high resolution spectrometer is used on the stretcher input line to diagnose any oscillator problems such as low level double pulsing. All of the outputs from these diagnostics are displayed in the Main Control Room. There are a number of temporary diagnostics which have been developed that are used on a transient basis, such as the 2nd order autocorrelator for pulse length measurement, the scanning 3rd order cross correlator for an instant measurement of pulse contrast and a 2nd order cross correlator for the measurement of the quality of oscillator frequency locking.

PRE-AMP

An integral part of the Front End for the PetaWatt upgrade is the development of an alternative mechanism of amplification covering the first 6 orders of gain. This is currently performed by a series of Nd:glass amplifiers, with the drawback that a significant amount of gain narrowing occurs, ultimately limiting the minimum pulse duration available at the end of the system. There are a number of possible solutions that are currently being evaluated. These are

- A Regenerative Amplifier operating at 1053 nm using Ti:S as the gain medium
- An Optical Parametric Amplifier operating at near degeneracy and seeded with the chirped pulse
- A diode pumped Ytterbium Fibre Amplifier with possibly a bulk Yb:glass amplifier following
- A Regenerative Amplifier operating at 750 nm, pulse compression and the generation of a 1053 nm pulse by an Optical Parametric Generator

PLAN

A schematic of the Front end for the Phase I PetaWatt Upgrade is shown in Figure 3.

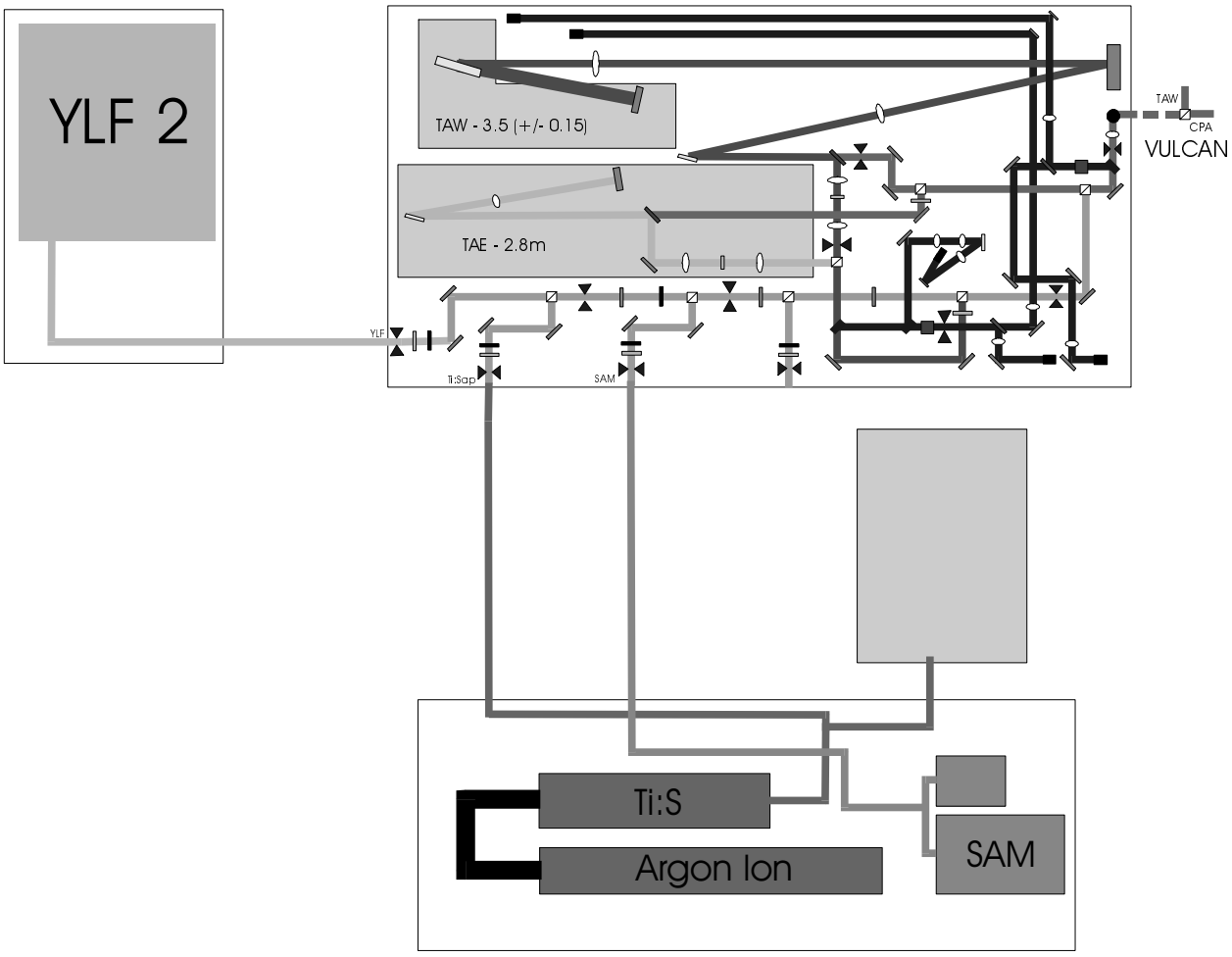

Figure 3 : Schematic of the Front End

PULSE CONTRAST MEASUREMENTS OF THE VULCAN CPA FRONT END OSCILLATORS

J Collier, D Hitchcock, C Danson, K Weingarten[1)]

Rutherford Appleton Laboratory, Chilton, Didcot, OXON: j.collier@rl.ac.uk
1)Time Bandwidth Products, Technoparkstrasse, CH-8005 Zurich, Switzerland

INTRODUCTION

When operating in CPA mode, the VULCAN laser system is capable of producing an on target power density of 10^{19} W.cm^{-2}. An important aspect in this mode of operation is the contrast of the pulse that is delivered to target with respect to any low level activity that may be present. This arises because low level activity can have sufficient intensity to cause the breakdown of the target before the arrival of the main pulse. The ultimate limiting factor in the low level activity is the Amplified Spontaneous Emission (ASE) from the laser chain. For VULCAN, the ASE intensity on target is of the order 10^{11} W.cm^{-2}, some 8 orders of magnitude below the main pulse intensity. This is in the threshold region that will cause a solid target to break down and as such any activity or pre pulse above this level is therefore very likely to cause plasma formation on target ahead of the main interaction pulse. One possible source of pre pulses is the ultra short pulse oscillator that is used to seed the amplifier chain. We have therefore conducted an examination of the pre pulse activity from two of the ultra short pulse oscillators that are used to seed the chain covering a 10^7 dynamic range.

The two shortest pulse oscillators that are used in the Front End of the VULCAN CPA system are the Tsunami (referred to as the Ti:S) from Spectra Physics and the GLX-100 (referred to as the SAM) from Time Bandwidth products. Both produce Fourier Transform limited pulses of Full Width Half Maximum (FWHM) duration 120 fs and 170 fs respectively. The Ti:S uses Ti:Sapphire as the active medium and the SAM uses Nd:Glass. Both oscillators are passively modelocked; the Ti:S employing a soft apertured Kerr Lens Modelocking (KLM) technique and the SAM utilising a specially designed semiconductor saturable absorber layer grown on one of the end cavity mirrors. The pulse contrast of the two oscillators has been measured over an extended time range using two different techniques. The contrast of the Ti:S was measured using a 3rd order cross correlation technique[1] and that of the SAM using a 2nd order autocorrelation technique[2].

Ti:S CONTRAST

Referring to Figure 1, the 3rd order cross correlation technique used provides an auto correlation between a pulse at its fundamental wavelength and the same pulse at its second harmonic wavelength.

A main advantage of using a 3rd order technique is the initial frequency doubling process, being non linear, effectively 'cleans up' the incident pulse with any low level pulse activity being effectively removed. Therefore, the auto correlation process becomes asymmetrical and effectively provides a cross correlation of a pulse sequence with a single 'clean' pulse. This enables one to determine whether any detected low level pulse activity occurs in front of or behind the main pulse in addition to providing a more accurate measurement of pulse shape. A secondary advantage of this technique is that one detects the third harmonic light derived from the frequency mixing of the first and second harmonic input pulses. This is therefore a technique capable of high dynamic range operation since the mixing crystal phase matching condition and the detection systems can be configured to be sensitive to third harmonic light only.

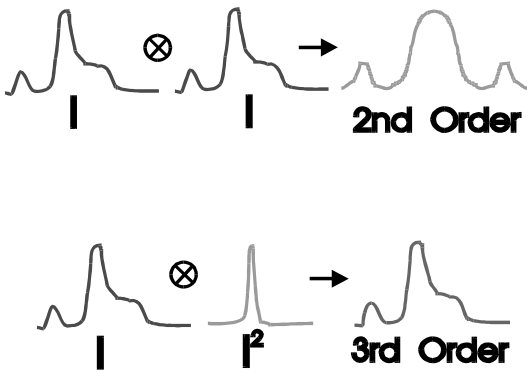

Figure 1 : 2nd and 3rd order cross correlation

A schematic of the device is shown in to Figure 2. The 400 mW incident beam at 1053 nm (80 MHz, 100 fs) is partially converted into a 526 nm beam with an approximate 20% conversion efficiency. The frequency doubling is performed in a 1mm length of Lithium Tri-Borate (LBO) used in a confocal geometry and non critically phase matched by heating the crystal to 163 °C. The 1053 nm and 526 nm beams are then separated using a di-chroic separator and directed to a focusing lens by appropriate mirrors. The 526 nm beam is directed via a retro-reflector as shown to provide variability of arm length and thus the scanning range. The two beams are

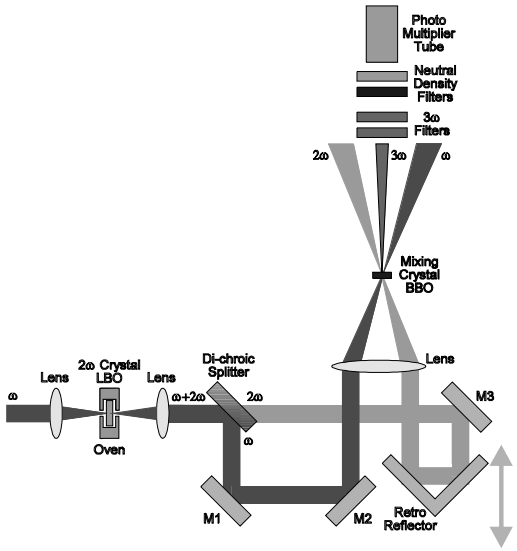

Figure 2 : A third order cross correlator

focused into a correctly cut β-Barium Borate (BBO) frequency mixing crystal and phased matched by angle tuning. The 3rd harmonic mixed signal is detected by a Photomultiplier tube. The input aperture to the tube is filtered by narrowband 351 nm filters with a 10^{-12} off centre extinction. Additional calibrated filtration is used to ensure the detector operates within fixed limits over the full dynamic pulse contrast range of interest. The output of the photomultiplier is processed by a Boxcar signal averager to improve the signal to noise ratio. Figure 3 show the results for the Tsunami oscillator over a 40 ps and a 5 ps range respectively. Points were taken every 66 fs. The plethora of low level pulses in Figure 3(a) are Fresnel reflections generated within the instrument from the frequency doubling crystal, the mixing crystal and the splitter. The source of each one has been identified. The short time scale trace 3(b) shows slight wings in the pulse starting at the 10^{-4} level. This is consistent with previous observations in KLM cavities indicating an incorrect amount of negative dispersion.

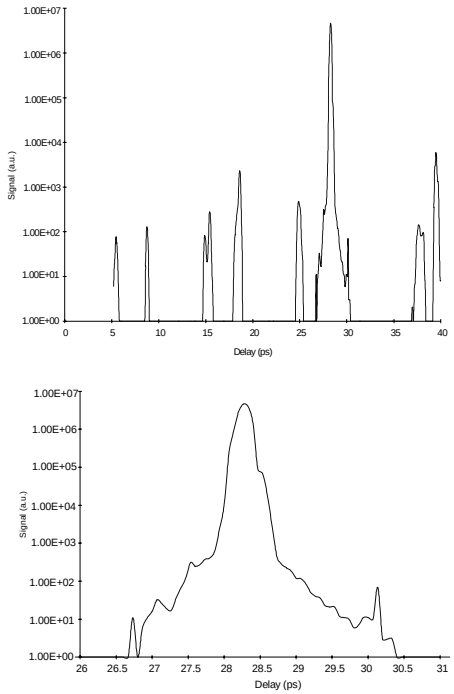

Figure 3 : Ti:S cross correlation

SAM CONTRAST

The pulse contrast of the SAM Oscillator was measured using a background free 2nd order technique. Referring to Figure 4, the input 70 mW beam (80 MHz, 200 fs) was equally split into 2 separate beams that were recombined in a thin frequency mixing crystal correctly cut for phase matching the two 1053 nm beams to 526 nm. The two beams were arranged to cross at a slight angle so that the any 2nd harmonic light generated by either beam could be prevented from entering the detector system by means of an appropriate aperture. The mixing signal (autocorrelation) is emitted at the half angle and passes through the aperture and into the detector system. The dynamic range of this technique is intrinsically limited to about 10^5 by the scattering of 2nd harmonic radiation generated by either of the two beams into the detector system off the mixing crystal.

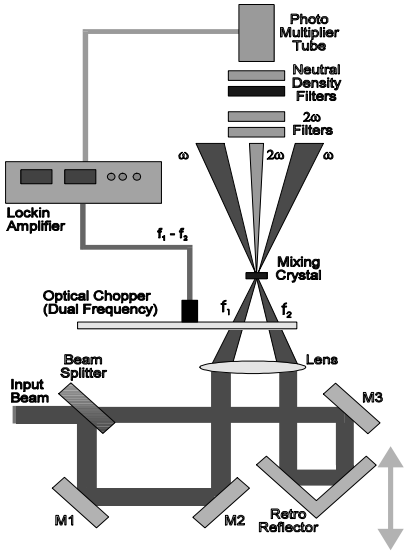

Figure 4 : 2nd order cross correlator

However, this range can be increased by using an optical chopper that chops each of the incident beams at a different frequency f_1 and f_2.. The mixing signal will then occur at the sum and difference frequencies f_1+f_2 and f_1-f_2. A lockin amplifier is used to lock to the mixing signal at, in this instance, the difference frequency f_1-f_2. Approximately two additional orders of magnitude can be obtained in the dynamic range of the instrument by this method. However, even though this technique exhibits a large dynamic range it remains a 2nd order process and it is therefore not possible to deduce whether any activity is before or after the main pulse.

The long time scale and short time scale results for the SAM oscillator are shown in Figure 5. The long time scale trace is significantly cleaner than that for the Ti:S but this is to be expected given the lower number of optics involved in the measurement technique. The single low level pulse is due to the beam splitter. An examination of the short time scale situation shows a pulse shape that adheres quite closely to that of a sech^2 type shape

CONCLUSION

A measurement of pulse contrast for both of the main CPA oscillators used on VULCAN has been performed. Over a long time scale both oscillators have been shown to be pre-pulse free

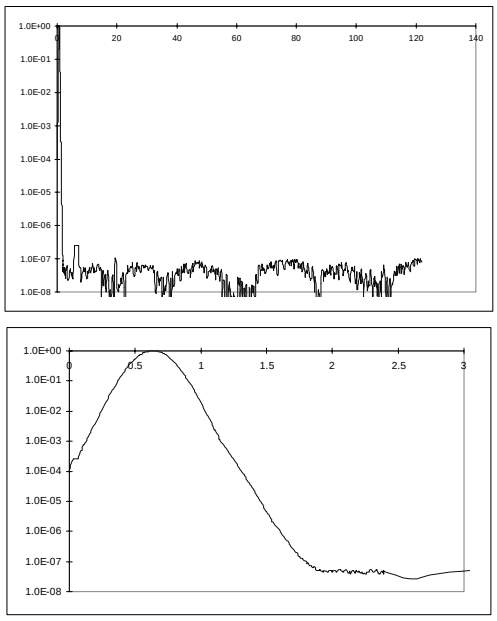

Figure 5 : SAM autocorrelation

over 7 orders of magnitude. The pulse shapes are slightly different but is not of significant consequences because the pulse shape that is ultimately produced at the end of VULCAN is dictated by the significant gain narrowing that occurs during amplification, asymmetric spectral clipping in the pulse compressor and the accumulation of non linear phase through self phase modulation.

REFERENCES

1) S Luan, M H R Hutchinson, R A Smith, F Zhou Meas Sci Technol, 28 (1) 426, (1993)

2) A Braun, J V Rudd, H Cheng, G Mourou, *et al* Optics Letters, 20 (18) 1889, (1995)

PHASE 1 PETAWATT CHAMBER CONFIGURATION AND DESIGN

D Neely, S Angood, A Damerell, C Danson, C Edwards, P Norreys and B Wyborn

Central Laser Facility, Rutherford Appleton Laboratory, Chilton, Didcot, Oxon, 0X11 0QX

INTRODUCTION

The Phase 1 PetaWatt Vulcan upgrade will provide a 200 TW sub ps Chirped Pulse Amplified (CPA) beam in Target Area West (TAW) for ultra high intensity (10^{20} Wcm^{-2}) laser plasma interaction experiments. This will be achieved by delivering a larger CPA beam of shorter pulse duration to the interaction region. Requirements also include the provision for frequency doubling the CPA beam and the simultaneous use of a multi-joule frequency shifted CPA probe beam and of the six full energy 108 mm diameter long pulse (80 ps - 1.5 ns) beams in either cylindrical, spherical, cluster or line focus geometry. This report will concentrate on the design of the grating compressor chamber and a new interaction chamber to accommodate these requirements. The developments to the laser, transport system and diagnostics are detailed in separate sections elsewhere in this document.

CHAMBER GEOMETRY

The optimum Phase 1 PetaWatt chamber design selected to fulfil all the experimental requirements was a cylinder of diameter 1.8 m, length 0.95 m and wall thickness 0.075 m, as shown in figure 1. It is constructed from mild steel and is electroless overcoated with a protective 25 micron nickel film. Two large 0.8 m diameter flat end section hinged doors are provided for internal access. When necessary, the doors can be replaced by the existing six ϕ 108 mm beam cluster or line focus housings normally used on Target Area East.

CHAMBER STABILITY AND OPTICAL ISOLATION

Finite element analysis has shown that significant movement of the main vacuum vessel wall will occur as the chamber is pumped. Measurements have confirmed that the centre of the end flange deflects by 1.75 mm and the rectangular side flange moves by 0.3 mm. To eliminate this wall movement from effecting the optical beam path, all critical optics are mounted on an internally vacuum isolated assembly onto which a number of smaller bread-boards are added as appropriate. The internal bread-boards are removable and interchangeable. This allows a user group to initially pre-align externally and then afterwards, store a given set-up between experiments saving on rebuilding time for a future use. All internal optics and alignment systems are supported from this table and tests have shown that angular deflections between air and vacuum are below the 0.05 mrad level.

PORT DESIGN

Experimental design requirements and engineering considerations demonstrated that rectangular ports are optimum for the side wall of the main chamber body. Circular ports require significantly increased chamber wall thickness compared to rectangular ports and give less beam access.

An equally spaced symmetrical port geometry was initially considered, however, after examining the options for 6, 8, 12 and 16 fold port layouts none were found suitable. The final optimised design incorporates 12 rectangular ports centred at 0º, ±25º, ±50º and ±90º w.r.t. the horizontal. Each port has a beam clearance of 600 mm (width) and 300 mm (height). These ports allow two ϕ108 mm beams to enter at angles of up to ± 5.8° from port centre in the same vertical plane. For two such ϕ108 mm beams entering at 11.6° separation a minimum F optic of F7 may be used to focus at chamber centre, or the existing f10 optics located just external to the chamber wall. and pillar mounted to the floor to avoid vacuum displacement.

ADDITIONAL PORTS

Twelve small circular ports are located at ± 20° from the top and bottom of the cylinder and these are used mainly for alignment systems and internal table vacuum isolation. An additional set of eight equally spaced ϕ300 mm circular ports are located in each of the end sections of the chamber. These are intended primarily for diagnostics purposes however, drive beams can enter through these ports.

GRATING CHAMBER

In a similar fashion to the previous CPA configuration, the first recompression grating will be in air and the second grating placed in a purpose built vacuum vessel as shown in figure 2. A 30 mm thick BK7 anti-reflection coated vacuum interface window will be located close to the first grating to minimise B-integral problems. To avoid misalignment problems during pump down and let-up the second grating and turning mirror are supported on mechanically isolated mounts tied to the floor. A gate valve containing a ϕ100 mm circular plane parallel BK7 window is located between the grating and main chamber. This

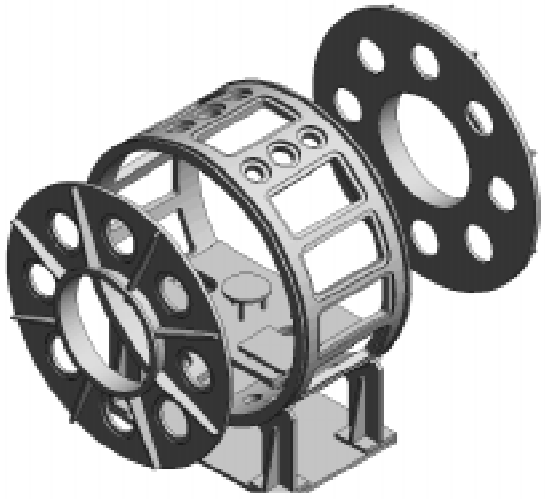

Figure 1 3D view of the interaction chamber.

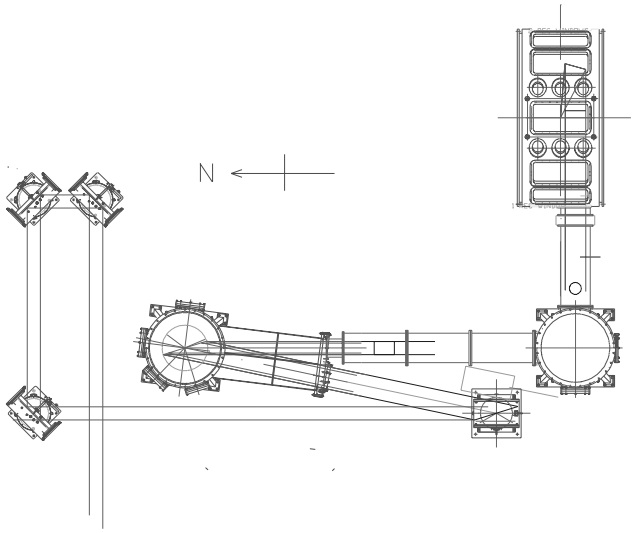

Figure 2 Plan view showing layout of grating, interaction chamber and timing slide in Target Area West.

enables an alignment beam to propagate through the grating compressor and onto the chamber optics whilst the main chamber is at atmospheric pressure and the grating under vacuum. Tests have shown that the vacuum isolation of the grating and turning mirrors ensure that between air and vacuum the interaction beam suffers less than 0.1 mrad deflection, which is significantly less than with previous hardware.

BEAM CONFIGURATION

There are four main configurations for the CPA and long pulse beams which the chamber has been designed to accommodate. These are, spherical, cluster, cylindrical and line focus. The following paragraphs detail the necessary beam configurations.

Spherical 6 beam geometry four of the ϕ108 mm beams would be brought in through the side wall rectangular ports, four at ± 45° and the remaining two beams through the end flanges as shown in figure 3. The f10 focusing optics would be located externally to the chamber and random phase plates internally. The CPA OAP would be located along the EW axis, with the beam focusing to within 12 degrees of the EW axis.

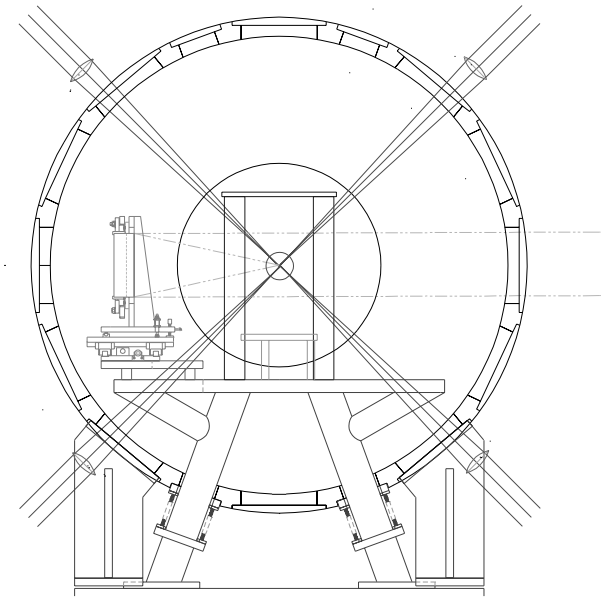

Figure 3 End view showing the interaction chamber configured for six beam spherical geometry with the CPA drive beam.

Cylindrical 6 beam geometry five of the ϕ108 mm beams would be brought in through the side wall rectangular ports, four at ± 30° and one at + 90° from the horizontal. The f10 focusing optics would be located externally to the chamber, with random phase plates placed inside of the chamber to avoid problems of bulk damage in the windows. The remaining ϕ108 mm beam would be brought in through a window (vertically below chamber centre) in one of the end flanges with the f10 and turning mirror located inside the chamber. The CPA Off Axis Parabola (OAP) would be located along the NS axis with the beam focusing axis orthogonal to the cylindrical beams. A ~39° steering mirror located inside the main chamber would deflect the input beam onto the OAP. The OAP mount would be supported on a bolt on extension to the central table.

Cluster geometry, the standard f10 ϕ108 cluster focusing optics can be attached to one of the CPA chamber end flanges and the six ϕ108 beams brought to a focus at chamber centre. Alternatively, the two existing cluster flanges can be attached to either end of the CPA chamber and three beams brought in on each. The CPA focused beam axis can either be along the cluster axis or orthogonal to it by using suitable beam steering mirrors.

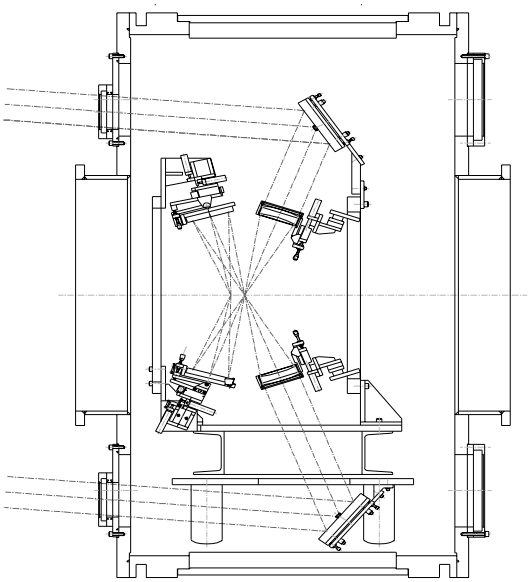

Figure 4 Side view showing two of the six beams used in the line focus set-up.

Line focus geometry is generated using the existing F2.5 internal optics for the ϕ108 mm beams. Four of the ϕ108 mm beams are brought in through the side wall rectangular ports, at ± 30° and the remaining two beams through the end flanges at ± 90°. The internal optics consist of a set of six aspheric doublets and concave mirrors mounted on two supporting rings which can be used to produce line foci between 0.5 - 40 mm in length. Figure 4 shows a schematic of the geometry. The CPA beam enters on the horizontal and is focused by an OAP before being re-imaged using a spherical mirror.

CONCLUSION

A new Phase 1 PetaWatt grating and experimental chamber giving access to higher interaction intensities and new more flexible geometries has been constructed. All design criteria as detailed in a user consultation document have been satisfied and commissioning detailed in an accompanying report.

PHASE 1 PETAWATT TARGET AREA COMMISSIONING

D Neely, C Danson, R Allott, S Angood, A Damerell, C Edwards, J Govans, P Hatton,
H Hutchinson, R Wyatt, B Wyborn

Central Laser Facility, Rutherford Appleton Laboratory, Chilton, Didcot, Oxon, 0X11 0QX

INTRODUCTION

An ultra high intensity ~ 10^{20} Wcm^{-2} laser plasma interaction facility has been built in Target Area West (TAW) as part of the PetaWatt Phase 1 Vulcan upgrade. Design and commissioning of this new area, beam transport system and associated diagnostics are reported in this document. The interaction and grating chamber design are detailed elsewhere in this report.

AREA AND BEAM REQUIREMENTS

Target Area West has been reconfigured to work with all eight of the Vulcan laser beams. This consists of two Chirped Pulse Amplified (CPA) lines (beams 7 and 8) and six 108 mm diameter long pulse lines (beams 1-6). The area is organised to provide maximum flexibility and chamber access whilst optimising experimental choice and maintaining a safe working environment.

The maximum CPA beam energy on target is primarily determined by the damage characteristics and area of the recompression gratings. Using new 300 x 150 mm, 1740 lines per mm, 1053 nm blazed gratings, the energy deliverable to target will be immediately increased from 30 J to 40 J. Larger gratings of substrate size 420 x 210 mm with a ruled surface area of 378 x 190 mm are on order. When installed they will give a final output beam size of 111 x 190 mm. Previous efficiency measurements of similar gratings at an identical input angle of 72.9 degrees have shown first order diffraction efficiencies of 89 %. Combining this with a peak damage threshold of 500 mJ cm^{-2} for the gold overcoated gratings will allow in excess of 80 J to be delivered to the focal plane. To fill the grating aperture, the main CPA line (beam 8) diameter will be expanded from 135 mm to 205 mm in the laser area using a vacuum lens relay assembly. New larger 360 x 260 mm 40 mm thick mirrors with RAL designed mountings will be used in the target area to transport the beam.

The first CPA recompression grating is situated in air and the second grating placed in a specifically designed mechanically isolated vacuum vessel as shown in figure 1. After leaving the second grating the beam is steered with a 99.6 % efficiency 45 degree mirror into the interaction chamber and the 0.4 % leakage used for diagnostic purposes. Provision for frequency doubling the 1054 nm CPA beam after recompression and using additional mirrors to reject the unconverted light (which will significantly enhance the pulse contrast ratio) is also included in the design. Once compressed, the CPA beam is transported to target and focused using only dielectric coated reflective optics to minimise B-integral and maintain focusability. Point foci will be generated using either a 0.225 m ON Axis Parabola (ONAP), a 0.6 m focal length Off Axis Parabola (OAP), a 3 m OAP or a 5.0 m focal length spherical mirror. A line focus of length 5 to 20 mm can be generated using an OAP and a tilted spherical mirror. The chamber design and optical layout is such the CPA and long pulse beams can be simultaneously overlapped in line, spherical, point or cluster geometries.

The secondary 150 x 89 mm CPA beam line (beam 7) is primarily intended for plasma diagnostic uses requiring a few mJ to J of energy with pulse lengths which can be tuned from 1 to 20 ps independently of the main CPA beam. To maintain experimental flexibility, the recompression gratings for this line will be mounted in air on a single level table. The beam will be transported and frequency doubled, quadrupled or Raman frequency shifted before entering the vacuum chamber through a thin glass window.

AREA LAYOUT

A series of TAW floor plans depicting the path layouts for the main CPA line (beam 8), the secondary CPA line (beam 7) and a long pulse line (beam 3) are shown in figures 1-3.

All Vulcan laser beams enter through the North TAW wall. The two CPA beams are brought in through 280 mm diameter 25 mm thick AR coated windows located in the western corner of the north wall at a height of 1.3 m above floor level. The six long pulse beams enter through 145 mm diameter 15 mm thick AR coated windows located on the centre of the north wall on a three level system.

After beam 8 enters the area it is reflected off a matching mirror onto a timing slide with up to 1.5 m of travel, as shown in figure 1. The beam is then injected onto the first grating from a mirror which can be moved in concert with the grating to maintain both the near and far field during grating tuning. A 0.3 % leakage from the final mirror prior to the recompression gratings is fed into a 4 m focal length lens and onto a CCD system to provide a far field pointing reference. On full shots an uncoated mirror is injected into the far field system to reflect a fraction of the beam, providing a full shot equivalent focal plane monitor, with 2 μrad resolution. The matching mirror is an in house design and has been modified to rotate through 90 degrees so that a 150 mW CW diode pumped YLF can be injected into the beam line for local alignment purposes. This novel arrangement which uses a rotating mirror as both the main beam steering mirror and local beam injection element is

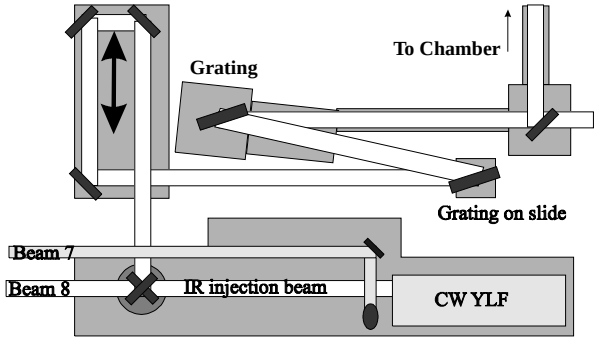

Figure 1. Schematic layout showing beam line 8 - the main CPA line

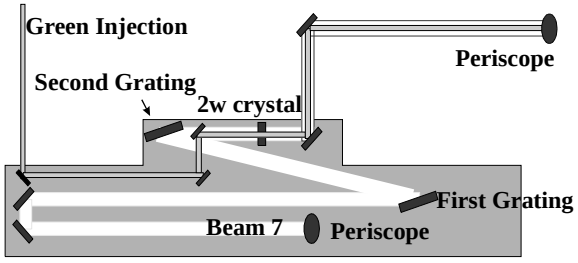

Figure 2. Schematic layout showing beam line 7 - the secondary CPA line used for optical probing

highly space efficient and only requires that the mirror rotates exactly about the centre point of its optical face and that both the laser and local beams coincide there also.

After entering the area beam 7 is reflected onto the lower level of the CPA bench where two recompression gratings, a 4 m timing slide and alignment systems are situated, as shown in figure 2. A linear injection slide is used to inject the same 150 mW CW alignment beam as beam 8 into this line as required. When frequency doubling, quadrupling or shifting techniques are employed, space has been left on the lower level for additional injection and pointing systems to be installed.

Beam lines 1-6 all have similar configurations to beam line 3 as shown in figure 3. The pointing systems, timing slides, frequency doubling crystals and alignment systems for all six beams are situated on the two three level tables located beside the North wall of the target area. The beams can be used at either the fundamental or frequency doubled wavelength and can be injected into the main chamber using external plinths to accommodate the required experimental geometry.

DIAGNOSTICS

The 0.4 % leakage from the final turning mirror which injects the CPA beam into the main chamber is fed through a 30 mm thick window onto two turning mirrors and then into the diagnostics chain. A commercial 250 mm aperture Schmidt Cassegrain telescope monitors the 0.2 % leakage through the first turning mirror to ensure that the pointing direction of the

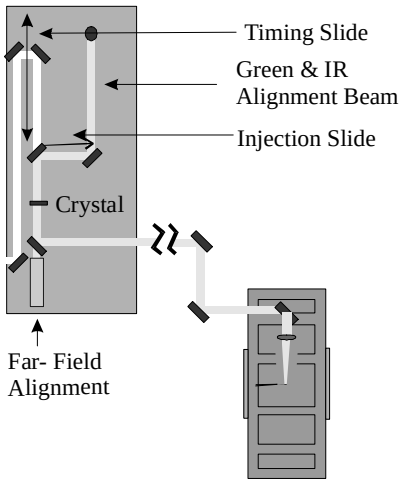

Figure 3. Layout showing beam 3 - a long pulse beam line

beam onto the gratings and between them is always maintained. This is essential during all grating tuning and optic replacement operations. After the turning mirrors, the beam is spatially demagnified by a factor of 6.7 using a Gallilean telescope comprising of two lenses of focal lengths + 4 m and - 0.6 m. Between low and full energy shots, a 75 mm diameter uncoated front surface mirror and a 50 mm diameter 25 % reflective mirror are injected into the telescope in such a manner that the path between the elements of the telescope is unchanged. These mirrors are used to control the intensity into the negative element of the telescope, avoiding B-integral effects causing any measurable pulse degradation. The beam from the telescope is then fed into two diagnostics tables where near field, far field, spectrum and pulse duration are measured on every shot.

The reduction in pulse length and increase in grating size for the Phase 1 PW upgrade requires more stringent recompression grating alignment tolerances. New alignment techniques must be considered to minimise beam shear, pedestal and pulse lengthening effects. After surveying the gratings into position, optical alignment using the zero and first order reflection from the grating surface of a near diffraction limited convergent visible laser beam was employed to set the grating surfaces and grooves in the vertical plane. Then, the grating surfaces were set parallel to each other in the horizontal plane at an input angle matched to the stretcher using precision surveying. A low energy 3-4 nm broad bandwidth beam was then injected into the grating recompression pair and their alignment adjusted to obtain a minimum far field spot size, giving an alignment parallelism accuracy of 0.4 mrad. After the recompression gratings were aligned, tuning to obtain the shortest possible CPA pulse was initially carried out using an optical streak camera. The autocorrelators were then used to fine tune this and the results are shown below in figure 4. These results were confirmed at full shot energies with pulses of 700 fs duration and power > 40 TW being achieved.

To avoid beam shear and pulse lengthening effects, which will become critical in the future when the pulse length is reduced from its present value of ~1 ps to less than 400 fs, the grating surfaces must be set more accurately to within 50 μrad parallelism. It is intended that orthogonally sampling autocorrelators will be used to set the grating parallelism to better than 50 μrad which corresponds to optimum system performance.

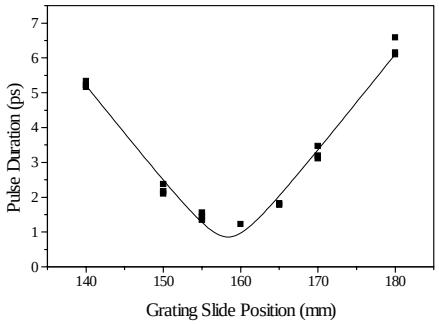

Figure 4. Grating tuning curve

CONCLUSION

Target area West has now been built and commissioned for use with the increased CPA capabilities of the Vulcan Phase 1 PetaWatt system. This will provide higher intensities and greater experimental flexibility than previously possible.

VULCAN PETAWATT MIRROR/GRATING MOUNT DESIGN

S M Angood, P E Hatton, B E Wyborn

Central Laser Facility, Rutherford Appleton Laboratory, Chilton, Didcot, Oxon, OX11 0QX, UK.

INTRODUCTION

The reduction in pulse length, increase in grating size and grating tuneability requirements for the Phase 1 PetaWatt upgrade required more stringent recompression grating alignment tolerances i.e. during grating tuning which involves changing the separation of the grating pair parallelism needs to be maintained at ≤ 0.050 mrad. In addition the upgrade required that a significant number of large optics had to be supported, manipulated and accurately aligned during routine operations with a number of different motional requirements.

In order to achieve these requirements a new mirror/grating mount was designed and installed which met these criteria and was also easy to handle, reliable and flexible in operation.

DETAILS

The mirror/grating mounts comprise of three major sub assemblies namely:

1. The Optics Handling Frame
2. The Mid Level Swivel Assembly
3. The Base Assembly

The optic is mounted into the handling frame and held securely in position. The frame is equipped with carrying handles and is located in the mid level swivel assembly by two dowels.

The mid level swivel assembly is kinematically mounted on to the base assembly and locked in position with two bolts. A fine adjustment screw is fitted to tilt the optic in the vertical plane.

Two Hepco 90^0 slide segments are incorporated into the mid level swivel assembly to allow for tilting the optic in the vertical plane, with movement provided either by fine adjustment screws that are manually operated or by a motorised micro positioner.

The base assembly incorporates a Hepco 360^0 slide ring and grooved bearings giving a full 360^0 rotation of the optic in the horizontal plane. The optic can be locked in any segment and finely adjusted about the vertical axis using either a fine adjustment screw or a motorised micro positioner.

An important feature of the design of the mirror/grating mount assembly is that all movements of the optic are about the optic front face centre.

Movement of 10 arc seconds can be achieved on all axiis.

The modularity of the design means that a number of variations are achievable to cater for different optical operational needs.

Various optics handling frames have been designed to accommodate different optics i.e. gratings 360mm x 250mm (as shown in the figure below), 235mm ϕ and 169mm ϕ beam mirrors. The grating mount can accommodate up to 500mm circular gratings if required.

The base assembly can be fitted to an additional stage to facilitate x y movement.

Two assemblies have also been mounted on a stage which has been adapted to run on a 3metre long Hepco rail system to enable precise beam timing to be carried out.

One assembly has been specially adapted to give a full 180^0 motorised drive capability for a beam injection mirror thus minimising the space requirements for this optic.

CONCLUSIONS

In all some twelve optic mount assemblies have been manufactured, two to house gratings and ten for mirrors.

The design of the mount assembly is modular leading to its being able to be adapted to a number of optic holding and manipulating parameters.

The design is based on proprietary high accuracy slide systems.

The mounts have been tested in TAW and found to be operationally highly successful.

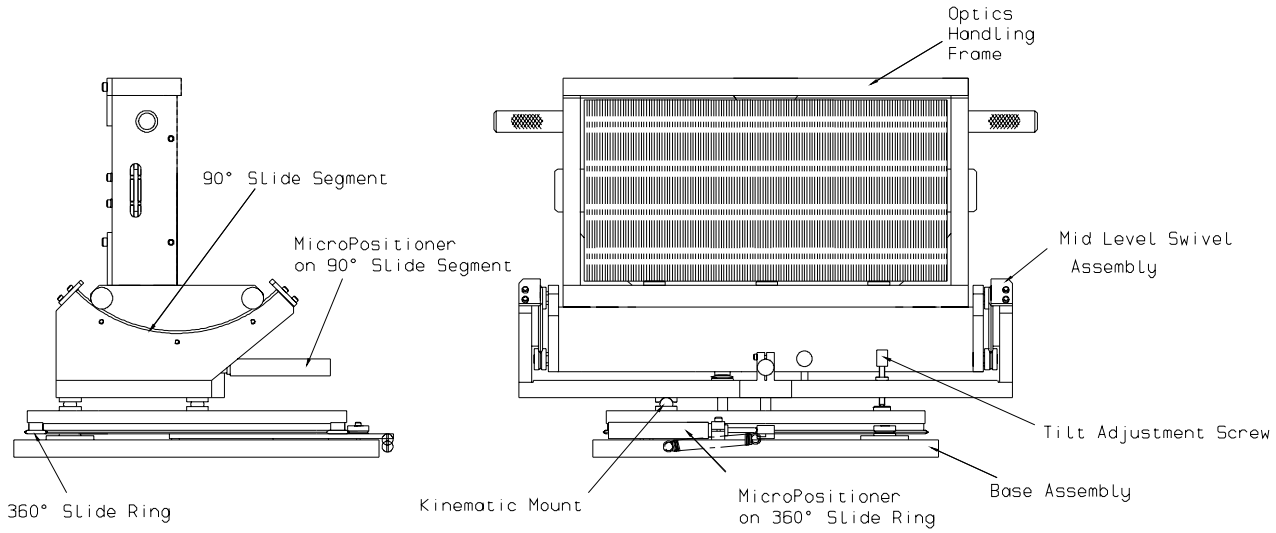

Fig. 1 Grating Mount Assembly

VULCAN PETAWATT VACUUM SYSTEM

J A C Govans, P E Hatton, W J Lester, D A Rodkiss, B E Wyborn, P Flintoff, R Allot, D Neely, C Danson

Rutherford Appleton Laboratory, Chilton, Didcot, Oxon, OX11 0QX, UK.

INTRODUCTION

The need for a large volume target chamber and grating chamber operating under vacuum conditions and requiring a quick pump down and let up cycle for the Phase 1 Petawatt upgrade resulted in the specification and instalment of a new upgraded vacuum system in TAW as described below.

SPECIFICATION

Routine vacuum operation involves letting the target chamber up to atmospheric pressure, replacing targets and diagnostics and repumping to 10^{-4} mbar within the 20 minute duty cycle of the Vulcan laser. The volume of the target chamber is 2.5 m^3 and the grating chamber 1.5 m^3.

In order to design the pumping system to achieve its specification the complete vacuum system was modelled on a computer simulation package. This enabled the optimum combination of vacuum pumps to be determined interactively.

Pumping is achieved using a combination of rotary, booster and turbo pumps and a cryogenic cold finger (see figure 1).

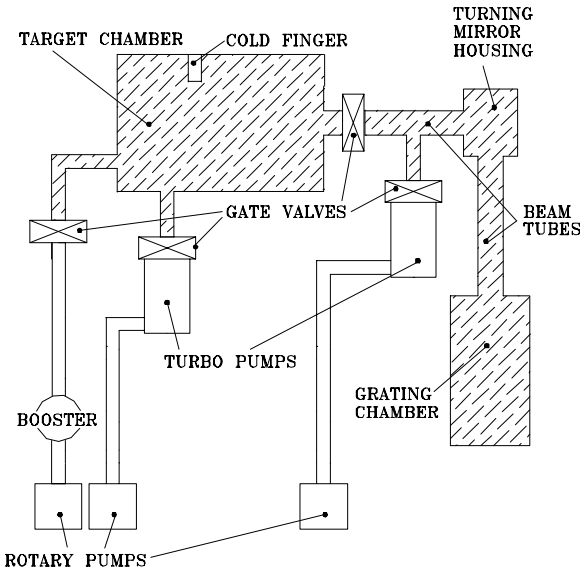

Fig 1 Schematic of Vacuum System

To achieve the necessary pump down times the grating chamber is normally constantly maintained at 10^{-4} mbar and only the target chamber volume cycled to atmospheric pressure with dry nitrogen.

The vacuum system is controlled from either a control panel, which has pump down and let up controls only, or via a table driven computer program that has further controls and drives a mimic diagram. The pump down and let up sequences are automatic, the appropriate valves etc., opening when required.

The target and grating chambers are initially both pumped through a 501 m^3h^{-1} booster pump and a 170 m^3h^{-1} rotary roughing pump. These are connected to the chamber through a 6 m long 160 mm ϕ pipe connected to the bottom port on the target chamber. As these pumps produce significant noise, air eating and turbulence when running both pumps are located in a sealed soundproofed underfloor services pit which has forced ventilation to the exterior of the room. This avoids possible interference with the beam paths and makes the operational conditions acceptable.

After initial pump-down to 0.5 mbar, two 1000 ls^{-1} turbo pumps are brought on. One turbo pump is located on the target chamber and the other is located between the final turning mirror housing and the pneumatically operated beam gate valve to the target chamber. This configuration ensures that no oil or debris contamination can propagate from the main chamber to the grating chamber during chamber let ups for target changes etc. These turbo pumps are backed by a $46m^3h^{-1}$ rotary pump and lower the pressure to 10^{-4} mbar. It is important that the grating chamber pressure is never lower than the target chamber pressure when the gate valve is open so the control system ensures that the target chamber turbo pump comes on before the grating chamber turbo pump.

Residual gas analysis showed that water is a primary contaminant. This is removed by cooling a thin walled metal tube of surface area 0.05 m^2 to liquid nitrogen temperatures after a pressure of 0.1 mbar has been attained. This cold finger is located in the target chamber and is replaced on each cycle.

A gate valve containing a 100 mm ϕ plane parallel BK7 window is located between the grating chamber and target chamber. This enables an alignment beam to propagate through the grating compressor and onto the chamber optics whilst the target chamber is at atmospheric pressure.

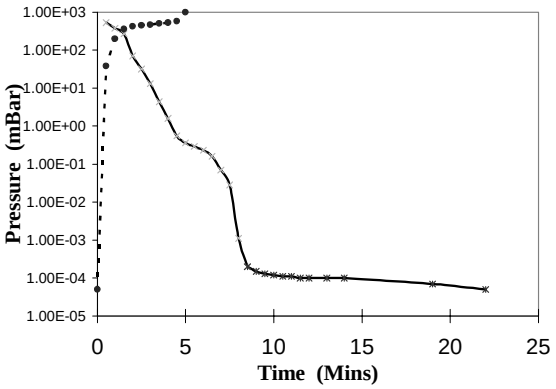

Fig 2 Typical pump down and let up curves

CONCLUSIONS

The complete system has been installed and commissioned satisfactorily and operational experience to date shows that the system meets its design requirements. Typical pump down and let up curves are shown in figure 2. The actual pump down curve agrees very closely to that predicted by the computer simulations. Tests have also shown that the vacuum isolation of the grating and turning mirror ensure that between air and vacuum the interaction beam suffers less than 0.1 mrad deflection.

OPTIMISATION OF A CHIRPED PULSE AMPLIFICATION NEODYMIUM GLASS LASER

I N Ross, M Trentelman, C N Danson

Central Laser Facility, Rutherford Appleton Laboratory, Chilton, Didcot, Oxon OX11 0QX, E-mail: I.N.Ross@rl.ac.uk

INTRODUCTION

The technique of chirped pulse amplification (CPA) and recompression [1)] has enabled Nd:glass laser systems to reach very high levels of brightness and provide pulses well below 1ps. [2,3,4,5)] The three principal indicators of performance of such a system are the brightness (or focused intensity), the pulse duration and the pulse contrast ratio (or prepulse intensity level). The achievement of the highest possible performance requires an analysis and optimisation of the various factors which affect these parameters. Such an analysis, which has relevance to a variety of laser systems, has been carried out for the CPA VULCAN Nd:glass laser, [6)] and takes account of the pulse degradation arising from the finite size of the gratings in the compressor, [7)] and gain narrowing in the amplifiers. It has been suggested that the use of mixed phosphate-silicate glass amplifiers [8)] would increase the amplified bandwidth and hence reduce the pulse duration. A quantitative comparison has been made between phosphate and mixed glass in the VULCAN laser to show how much the performance is expected to improve by the use of an optimum glass mix.

Before discussing these various aspects in more detail it is useful to introduce the parameters which control and limit the maximum performance from a CPA laser system:

a) Energy. Unlike most laser systems the maximum energy is likely to be determined by the damage threshold of the compressor gratings rather than the limits within the laser. A practical limit on the energy, as determined by available gratings (current maximum size ≈ 40 x 20 cm and damage threshold ≈ 0.5 J/cm^2 at 1053 nm), is approximately 200J with some further loss within the compressor due to the diffraction efficiency and spectral clipping (as discussed later). One implication is that, for maximum focused intensity after the compressor it is best to fill the first grating.

b) Pulse duration. Pulse duration in a CPA system is primarily determined by the laser output spectrum and the ability of the compressor to properly reconstruct the Fourier transform of this spectrum.

The laser output power spectrum can be represented by:

$$P_{OUT}(\lambda) = P_S(\lambda) \cdot T_{STR}(\lambda) \cdot G(\lambda) \cdot T \qquad 1$$

where: $P_S(\lambda)$ = input power spectrum; $T_{STR}(\lambda)$ = spectral transmission of stretcher; $G(\lambda)$ = gross gain of amplifiers; T = passive transmission of system

c) Focal spot area. The minimum spot size is not only set by diffraction (≈ Fλ, where F = F-number of the focusing optic) and by beam aberrations, but also (as discussed in more detail below) by the finite size of gratings in the compressor

d) Contrast ratio. For many experiments the main pulse interaction is adversely affected if there is a prepulse intensity (and fluence) on target in excess of a critical value. In consequence, as the main pulse intensities are increased with improving system design, so also must be the contrast ratio.. A figure of 10^{10} W/cm^2 is frequently used as a limit to the amplified spontaneous emission (ASE) and prepulse intensity on target.

In addition temporal shape irregularities on the main pulse may also significantly degrade the effective pulse contrast ratio. The exact shape of the temporal profile of the main pulse is dependent upon the exact shape of the laser output spectral profile and the limiting effects of the compressor.

OPTIMISATION

All the factors listed above must be included in any consideration of optimisation of the complete CPA system It is convenient to consider the system in two parts. The first considers the influence on the CPA performance of both the laser parameters and possible changes to the laser design, and the second considers effects arising from the grating compressor geometry.

LASER OPTIMISATION

The important feature of the laser is its output spectrum calculated using equation 1. For the purposes of comparison between different designs the magnitude of the gain spectrum is adjusted to maintain the integrated output energy at a value known to be available from the laser:

$$E_{OUT} = \int_t \int_\lambda P_{OUT}(\lambda) \cdot d\lambda \cdot dt = \text{Constant} \qquad 2$$

Equation 1 was evaluated for phosphate and mixed glass and the results given in Figure 1. The output spectra were all calculated for a fixed output energy of 100 J (Equation 2), for a fixed energy of 4 mJ in 8 nm from the regenerative amplifier, and using as gain spectra for phosphate and silicate glass the experimentally measured curves from the literature. [9)] For a mixed glass system the output spectral profile depends only on the ratio of gain exponents for the two glasses ($\ln G_{SIL}/\ln G_{PHOS}$) but for convenience we use a parameter (k) which varies from 0 (all silicate) to 1 (all phosphate) and is given by:

$$\frac{1-k}{k} = 1.6 \frac{\ln G_{SIL}}{\ln G_{PHOS}} \qquad 3$$

The factor 1.6 is the ratio of the peak stimulated emission cross-sections for the two glasses.

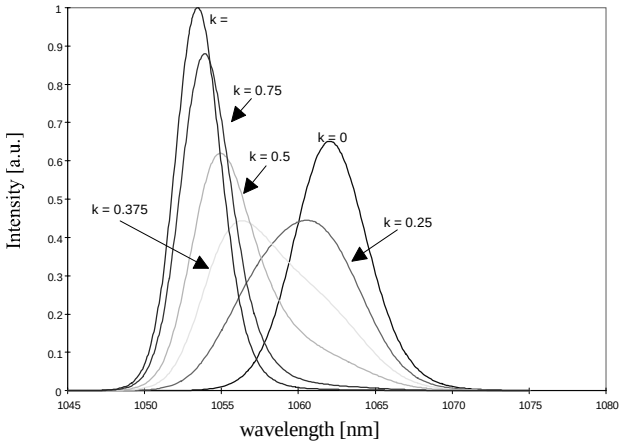

Figure 1 Spectral profile of the laser output pulse for different phosphate/silicate glass mixtures

Figure 1 plots the sequence of output spectra showing their respective spectral position and spectral shape for different phosphate/silicate glass mixtures from pure phosphate (k=1) to pure silicate (k=0). The maximum FWHM spectral bandwidth is 9.5 nm, a factor 2.7 higher than that for a pure phosphate glass system.

The shortest achievable pulse durations are found by taking the Fourier transform of the output spectra of figure 1. Due to changes in the spectral shape with glass mix, especially close to the optimum where it is very 'top hat' in shape, the shortest pulse duration using mixed glass is not as short as might be expected from the bandwidth at FWHM, but a reduction by a factor of 1.60 to 196fs still represents a significant improvement.

The estimated ASE intensity for the optimised mixed glass was 3.10^{13} W/cm^2 which may be too high for some experiments and may require the use of additional suppression.

COMPRESSOR EFFECTS

This section will consider the effects resulting from the limiting aperture of the gratings, which modify both the focal intensity on target and the pulse contrast ratio. Modelling of these effects has already been discussed. [7]

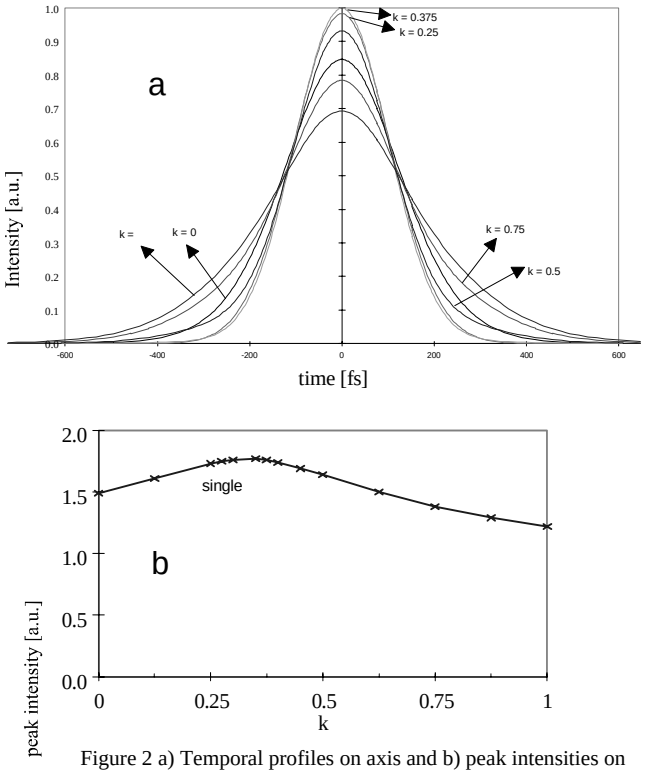

Figure 2 a) Temporal profiles on axis and b) peak intensities on axis for the recompressed and focused pulse for different phosphate/silicate glass mixtures

Figure 2a shows computed axial focal intensity time profiles for the laser output spectra of figure 1 representing phosphate glass and several mixes of phosphate/silicate glass. These curves are for gratings 450 mm long. The shortest pulse duration is 237 fs for a mix for which k = 0.375 (lnG_{SIL}/lnG_{PHOS} = 1.2 for gain values corresponding to the peaks of the phosphate and silicate gain curves respectively), as compared to a pulse duration of 380 fs for phosphate alone. These values can be compared to the values of 196 fs and 313 fs for a 'perfect' compressor. The reduction in pulse duration by a factor of 1.60 due to the use of mixed glass does not lead to the expected 60% higher focal intensity however because the clipping effects in the compressor also result in an energy loss and an increase in focal spot width. Figure 2b plots the focal intensity as a function of glass mix and shows that the best improvement in intensity achievable using mixed glasses instead of phosphate alone is a factor 1.44.

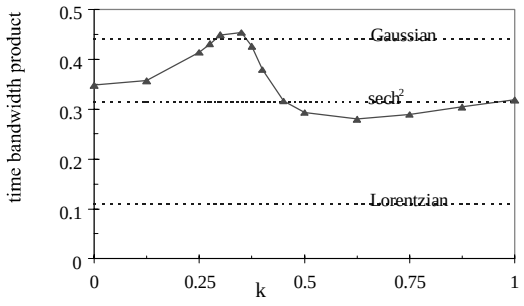

Figure 3 Time-bandwidth product for different glass mixtures

It appears that the potential advantages of using mixed phosphate/silicate glasses are not as great as might be expected due partly to the spectral shapes which (figure 3) give considerably higher time-bandwidth products than for phosphate alone and also to the spectral clipping effects in the compressor.

Figure 4 shows logarithmic plots of the focal intensity distributions of figure 4a along with that of a true sech^2 so that the pulse contrast can be seen down to the 10^{-8} level. It is immediately apparent that the real profiles have somewhat higher wings than the sech^2 pulse and that there is very little change in pulse contrast using mixed glasses.

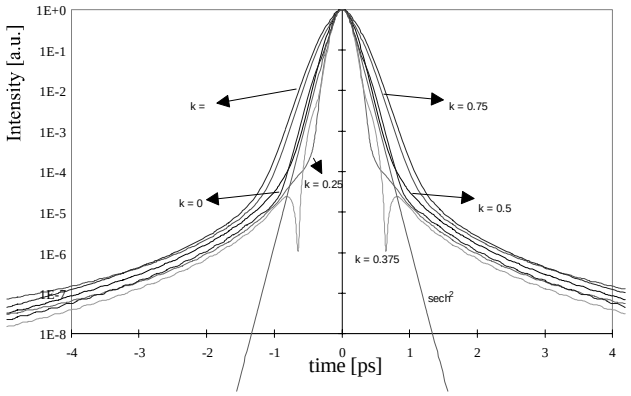

Figure 4 Pulse temporal profiles for different glass mixtures on a log-log plot to show the contrast in the pulse wings

REFERENCES

1) D Strickland and G Mourou
Opt. Comm. 56, 219, (1985)

2) F G Patterson, R Gonzales and M D Perry
Opt.Lett. 16, 1107, (1991)

3) C Rouyer et al
Opt Lett 18, 214, (1993)

4) I N Ross et al
Opt.Comm. 109, 288, (1994)

5) C P J Barty, C L Gordon and B G Lemoff
Opt.Lett. 19, 1442, (1994)

6) C N Danson et al
Opt.Comm. 103, 392, (1993)

7) M Trentelman, I N Ross and C N Danson
RAL Annual Report, RAL-TR-96-076, 85, (1996)

8) N Blanchot et al
Opt.Lett. 20, 395, (1995)

9) LLNL and commercial glass data sheets

VULCAN ROD AMPLIFIER FLASHLAMP DEVELOPMENT

R W W Wyatt [1], D A Pepler [1], R A Wellstood [1], J Littlechild [2]

1)Rutherford Appleton Laboratory, Chilton, Didcot, Oxon, OX11 0QX, UK
2)ILC Q-Arc Ltd, Saxon Way, Bar Hill, Cambs., CB3 8SL, UK

Early in the year the VULCAN facility suffered a pronounced increase in rod amplifier lamp failure, especially in the 45 mm (diameter) amplifiers which deploy twelve lamps in close proximity. Remedial action became essential to reduce running costs and restore VULCAN's good operational record.

To an increasing extent amplifier failure involved one or more lamps breaking on ignition, which on occasion resulted in 'end plate', and amplifier 'rod element' damage. Some common aspects in the failure scenarios were evident. It was found that electrodes became detached from the respective internal support, and amid the strong electric fields present these could become missiles thereby increasing the damage factor. The resin used for the glass to electrode support became soft weakening the lamp support mechanism. This suggested there had been a change in the type of resin used, as immersion in the amplifier coolant had not previously been a problem.

Our lamp manufacturers were invited to the facility to review the situation. It was agreed that the explosions were not related to any significant change in the electrical parameters of the pulsed power supplies; and two areas for possible improvement were identified to be the 'electrodes' and the 'glass to end support mechanism'.

From this combined concerted effort Q-Arc very quickly provided a new form of lamp, with the electrode support improved and the resin bonding replaced with a completely revised end section potted to the glass with a silicone solution as in the larger lamps used in our disc amplifiers.

A test batch was produced and put into service under close monitoring. Some failed, but not in a catastrophic manner, in the main they simply fractured and the Xenon gas was replaced by the water / glycol coolant. Since there were no explosions, collateral damage was minimum, but a question on lamp failure remained.

It had long been a view that unnecessary mechanical stress on lamps would be a contributing factor to failure, but it was difficult to identify where or how any unwanted forces were being applied to the lamps. With this in mind close inspection for lateral displacement of the end supports of the lamp and amplifiers was made. In the case of the lamps we simply rolled them on a surface table and measured the end displacement. In some cases this was found to be over 3 mm. This was significant since the amplifier geometry is such that the clearance available for the 'O' ring seal around the lamp ends is 0.2 mm and cannot accommodate deviations of this proportion. Such a large error would put great strain on a lamp in it's quiescent state. In response to our findings the manufacturer agreed to modify production technique and tighten QA to impose acceptable limits of axial alignment of the lamp end support units. We in turn introduced more stringent codes of practice for amplifier end plate alignment during construction with the use of machined rods to simulate the lamps during assembly and ensure critical alignment of the end plates before inserting the lamps. It was also considered beneficial to equalise electric fields by alternating the lamps such that current flow was opposite through adjacent lamps rather continue with a unidirectional system. This is in fact in keeping with the original Quantel amplifiers in which shorter lamps were fired in series pairs and the lamp current flowed down the first and returned back along the second lamp. The same criteria also applies in the disc amplifiers.

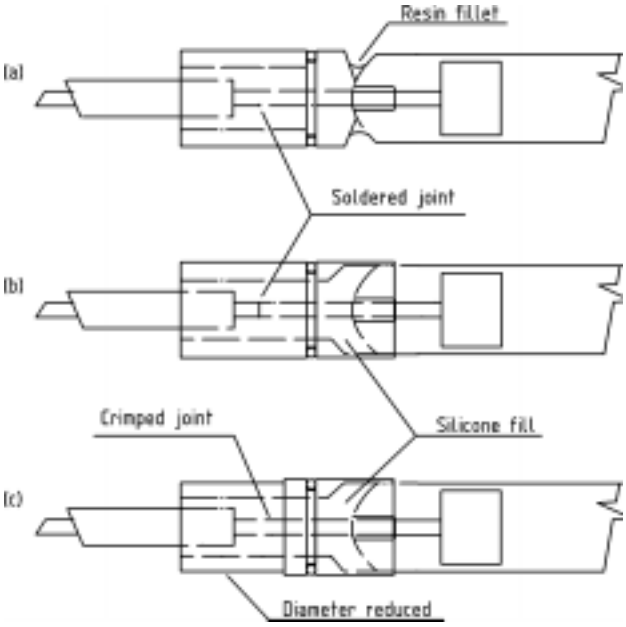

Figure 1 Schematic of the three flashlamp variants used on VULCAN.

Subtle detail changes that have improved the reliability of the lamps are shown in Fig.1.

The use of a resin to fill between the end support and the glass tube (a) was superseded by an extended Peek end cap which encapsulated the ends of the tube (b), providing more positive support to the lamp without excessive rigidity by virtue of the silicone interface between the two components.

The change from (b) to (c) allowed for positive supporting of the lamp with a greater degree of clearance in the amplifier housing, thereby reducing the possibility of contact with the lamp extremities applying undesirable lateral forces. The electrical connection within the supporting element was changed from soldered to crimped joint because solder 'run back' caused stiffening of the flexible HT wire, which could eventually break through work hardening induced by movement of the wire during operation.

These actions and precautions provided a very positive improvement in the lamp failure rate when all amplifiers had the intermediate design lamp (b) installed. Since then a 25 mm amplifier carrying a test batch of lamps made to the latest specifications (c), has been fired successfully without any failures, nearly three thousand times. These results have provided confidence enough for us to confirm acceptance of the latest configuration of lamp, which will be installed in all the amplifiers in due course.

HIGH PRESSURE WATER CLEANING SYSTEM

T B Winstone, C N Danson, D A Rodkiss, A Frackiewicz, J Govans, M Pitts, R A Wellstood, B Wyborn

Rutherford Appleton Laboratory, Chilton, Didcot, Oxon, OX11 0QX, UK

Since the introduction of glass laser disc amplifiers to the VULCAN laser system in 1977, their components have been cleaned prior to assembly using a chlorofluorocarbon (CFC) based cleaning system, and a high pressure spray system since 1983. All mechanical components, from small nuts up to the full chassis, an aluminium cylinder of 350 mm diameter and 1650 mm long, and large optical components have previously been successfully cleaned in this spray system. Following the signing of the Montreal Protocol on Substances that Deplete the Ozone Layer, cutting back markedly on the emission of CFC's and halting production by the year 2000, it became necessary to find a suitable alternative. A study was undertaken to evaluate commercially available systems to replace the CFC based technology. Most of these relied upon ultrasonic cleaning methods, and would require the purchase of several baths capable of holding the largest mechanical components. These existing systems were complex and relatively expensive.

An alternative solution would be to adapt the CFC based system to run using a different solvent. The overriding factors in the choice of a replacement solvent were cleaning power and safety. The solvent should not be highly flammable, should not be an asphyxiant, and should be stable under pressure and at room temperature. These requirements ruled out many of the possible contenders such as ethanol and acetone.

The only known solvent used in the building of glass laser disc amplifiers, other than CFC, is deionised water used for some time in the assembly of amplifiers for the GEKKO XII laser at Osaka, Japan[1)]. The Osaka system was considered to be more complex than would be required, with several filtration stages, as well as the deionisation stage. Historically, the components of the NOVA Laser at the Lawrence Livermore National Laboratory[2)] were cleaned using CFC. The Lawrence Livermore team were about to change to a relatively simple deionised water cleaning system using all the mechanics of the CFC system.

THE RAL CLEANING SYSTEM CHANGEOVER

Based on our research, tests were run on the RAL high pressure pump to ascertain whether it would provide suitable performance and hence produce similar cleaning with water as it did with CFC. These tests indicated that the cleaning with CFC and with water were similar, indicating that it would be possible to change the cleaning system for low cost.

The stainless steel water tank can hold a total of 900 litres when full. The tank was filled with prefiltered water with a conductivity of less than 1 mS/cm. The water in the tank is kept continually circulating through the deionisation column using a low pressure pump, ensuring the water is in it's purest state when required for spraying.

The high pressure spray gun worked well during the tests on the high pressure pump, emitting water at a pressure in the order of 1100 lb/in^2.

An advantage of using the CFC based system is that any standing liquid would evaporate rapidly at low pressure leaving the item free from drying marks. When the high pressure water spray system was used large quantities of water were left clinging to the cleaned mechanical components. The solution was to introduce heat into the system. For small items a drying cabinet was placed close to the spray booth. Once the small items had been sprayed they were removed using gloves then placed inside the pre-warmed drying cabinet at 70^{o}C. The drying cabinet would dry these components within 20 minutes.

An experiment was tried to dry the larger items in the spray booth by increasing the air flow over the components. A large volume air pump was sourced, and placed with an air intake from the ultra clean class 100 clean assembly area of the cleanroom. The pump is capable of pumping up to 430 cubic ft/min at a pressure in excess of 12.75 kPa to the spraybooth for the drying of the large items, this was then placed in series with a 3 kW electric heater, thus bringing the drying times down to < 30 minutes. The drying time was further lowered to < 20 minutes by the use of 80 psi nitrogen guns to remove the standing water from the surfaces and in particular from inside drilled and tapped holes.

The drying process described above worked well for large metallic items, but not for the disc protection plates (sheets of K5 type glass measuring ~1.5 m long by 250 mm wide by 6 mm thick). This was overcome by the introduction of two air-knives[3)], fed by the high volume air pump. The air-knives were separated by approximately 15 mm, facing each other. The piece of glass, mounted vertically, was drawn slowly between the two air-knives. The water was dispersed rapidly across the surface of the glass before the air-knives and was finally blown off the end of the sheet.

CONCLUSION

The high pressure water spray cleaning system has been in use in the building of several disc amplifiers since the changeover from CFC and has proven to be a successful viable alternative.

REFERENCES

1) Private communication Institute of Laser Engineering, Osaka University.

2) G Edwards
Private communication, Lawrence Livermore National Laboratory

3) Secomak Ltd, Stanmore, Middlesex, England. HA7 1BE

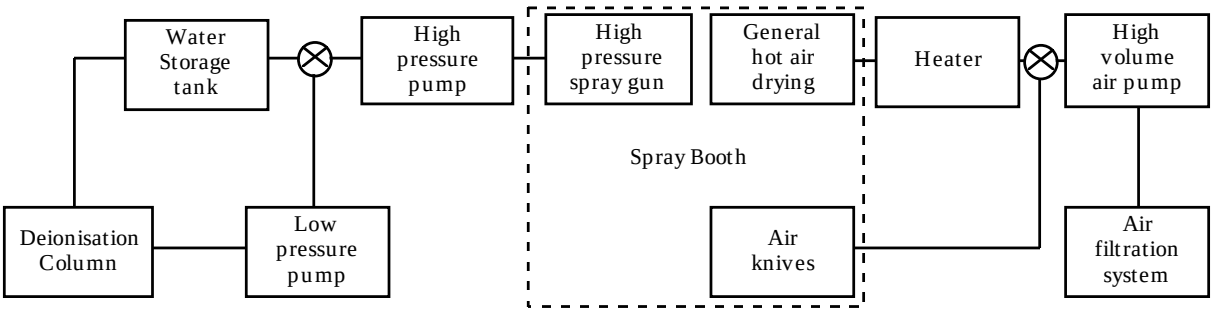

Fig. 1 Schematic of the water based high pressure cleaning system.

TITANIA CPA PERFORMANCE

J M D Lister, E J Divall, G J Hirst, T M J Kendall, A K Kidd and I N Ross

Rutherford Appleton Laboratory, Chilton, Didcot, Oxon. OX11 0QX, UK

INTRODUCTION

In April 1996, the first full laser shot was fired on the Titania laser system. The initial configuration was as a Chirped Pulse Amplification (CPA) system, and three scheduled plasma physics experiments were carried out in the following year.

SYSTEM CONFIGURATION

The Titania laser uses the same oscillator used on Sprite (an Argon-ion pumped Tsunami Ti:Sapphire laser). The main differences relative to the Sprite CPA system are that the pulses are chirped (stretched) and recompressed at different wavelengths, and that the required gain in the KrF lasers has been reduced by increasing the energy output from the 746nm amplifiers. The new configuration is shown schematically in figure 1. The oscillator produces pulses of around 120fs duration at 746nm. These pulses are then chirped in a folded, double passed grating stretcher to a duration of over 100ps. At the output of the stretcher the pulse energy is a few nanojoules. This is amplified to a few microjoules in a single pass dye amplifier, and then to about 20mJ in a multipass Ti:S amplifier. Both of these amplifiers are pumped by a frequency doubled Nd:YAG laser synchronised to the short pulse at a repetition rate of 8 Hz.

The output from the Ti:S amplifier is then frequency tripled in two BBO crystals. The doubler is 0.5mm thick and converts about 10% of the fundamental frequency to the second harmonic at 373nm. Frequency mixing crystals of 0.25 and 0.4mm thickness were used to produce the third harmonic at 249nm. The efficiency of the thicker crystal was greater, but the bandwidth of the output pulse was reduced, increasing the minimum pulse duration that could be achieved on target. In practice, the gain narrowing in the KrF amplifiers was such that the effect of using the thicker crystal on the final bandwidth was small. The energy of the 249nm pulse using this crystal was typically 200μJ.

This pulse is then amplified in two passes of each of the electron beam pumped KrF amplifiers Sprite and Titania, before being recompressed by a pair of large aperture diffraction gratings inside a vacuum vessel connected to the target chamber.

SYSTEM PERFORMANCE

The ultimate performance of large CPA laser systems (particularly at UV wavelengths) is predominantly limited by the performance of the diffraction gratings in the compressor. The size, efficiency and damage threshold of the gratings set an upper limit to the amount of energy that can be delivered to target. This limit was already well below the energy obtainable in a single pulse from the old Sprite system.

The optical quality of the diffraction gratings largely determines the minimum size of focal spot at the target, and hence the maximum achievable intensity. Although the flatness of the substrate used may be adequate, it is typical for the optical quality of the diffracted first order beam to be significantly worse than that of the zero order.

Given these constraints, the performance of the Titania CPA system could only be improved above the level already achieved by Sprite in two ways. Firstly, an increase in the size of the diffraction gratings would allow more energy to be delivered to target without increasing the energy density incident on the first grating. Secondly, an increase in the bandwidth of the final output pulse of the system allows a shorter pulse duration after recompression.

The Titania CPA system design called for gratings 200mm in diameter. If gratings of this size, and with a similar efficiency and damage threshold, were used then the energy obtained on target could be increased over that from the Sprite system by a factor of 2.25. In practice, the largest size gratings available at an acceptable cost were slightly smaller than this.

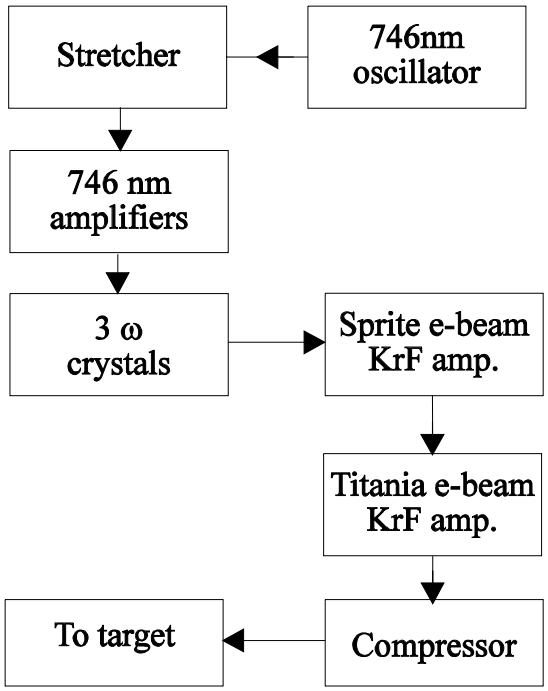

Figure 1 Titania CPA system schematic

Furthermore, without any spares (again due to cost considerations) it was necessary to be more conservative in approaching the damage threshold on the first grating. As a result, the energy that could be delivered to target was less than a factor of two greater than that achieved from Sprite.

By increasing the amount of gain in the 746nm amplifiers, and hence reducing the gain required from the KrF system, the overall gain narrowing was reduced (since the bandwidth of the Ti:S amplifier is much greater than that of the KrF amplifiers). Measurements (using a single shot cross-correlator) did not however show the expected reduction in the recompressed pulse duration. Measurements of the oscillator pulse duration are reported in detail in another section. Only a small amount of data was recorded of the final pulse duration, but the measurements suggest significant structure on the pulse extending over a time of up to 1 ps, with a large post-pulse. It is believed that this pulse structure was due to non-linear effects, either in the amplifier chain itself (which would affect the pulse duration on target), or in the path between the compressor and the cross-correlator (which would not).

BEAM QUALITY

The beam path in the Titania CPA system is long (over 150m) and there are a large number of optics. The optical quality of these optics, and of the air and laser gases through which the beam passes, is highly critical, particularly at UV wavelengths, where a typical good quality laser optic of $\lambda/10$ at 633nm is equivalent to only $\lambda/4$ at 249nm. Consequently, it is very difficult to maintain a near diffraction limited beam through the system, particularly where the beam size is large. We did however find that by reducing the aperture through the e-beam amplifiers it was possible to obtain such a beam. In a saturating amplifier, reducing the beam size will, of course, reduce the energy, but as it was necessary to attenuate the beam after the final amplifier in order not to damage the first diffraction grating, this did not significantly affect the energy reaching the target. Figure 2 shows the far-field beam profile obtained on a full energy shot, using a compound lens system with a focal length of >100m, the focal spot directly illuminating a UV sensitive CCD camera.

Figure 2 Far-field beam profile

The central spot has a FWHM of the less than 2 times the diffraction limit, and contains about 30-35% of the total beam energy. It should be noted that this diagnostic splits off a fraction of the beam energy before the diffraction gratings, so that the effect of the gratings and subsequent beam delivery optics (including the off-axis parabolic focusing mirror) is not taken into account. Measurements using only the low power oscillator beam do suggest, however, that these optics do not significantly degrade the beam.

As with the Sprite system, it was found that in order to maintain the beam quality on full energy shots, the laser could only be fired at approximately 10 minute intervals. Firing the laser more frequently than this over extended periods would lead to a severely broken up far-field profile. This effect is believed to be due to heating of the laser gas, resulting in turbulence disrupting the phase of the beam. Work is planned to eliminate, or at least significantly reduce this effect by improving the gas circulation and cooling systems on the electron beam amplifiers.

INTENSITY ON TARGET

Given that there are some uncertainties in the measurement of the pulse duration, and to a lesser extent the fraction of energy contained within the central spot, it is difficult to be precise about the intensity at the focus. The energy reaching the target for the shot whose far-field is shown in figure 2 was 250mJ. The pulse duration is believed to be between 350 and 800fs, depending on whether the structure in the measured pulse was due to effects in the laser itself, or in the measurement. The focal spot size was 1.5μm FWHM, with about 30% of the energy contained within that area. This gives us an intensity on target of between 5×10^{18} and 1×10^{19} W cm^{-2}.

SUMMARY

The performance of the Titania front end oscillator and amplifiers is as expected and meets the requirements of the system. The output energy from the e-beam amplifiers was below the predicted level, but the energy reaching the target was still limited by the damage threshold of the gratings. Further investigation is required to determine the pulse duration accurately, and also to measure the pre-pulse level. Modifications to the single shot cross-correlator should make this diagnostic easier to set up so that more data can be collected on the pulse duration, shape and pre-pulse level. Any significant improvement in the performance of the Titania CPA system will require the development of improved diffraction gratings in terms of optical quality, efficiency and, most importantly, damage threshold.

DETERMINATION OF TEMPORAL SHAPE AND CONTRAST OF TITANIA CPA PULSES

K Osvay [1,2] , I N Ross [2], J M D Lister [2], C J Hooker [2]

1) On leave from Dept. of Optics & Quantum Electronics, JATE University, Szeged, Hungary
2) Rutherford Appleton Laboratory, Chilton, Didcot, Oxon, OX11 0QX, UK. Email K.Osvay@RL.AC.UK

INTRODUCTION

The theory of temporal contrast measurement of ultrashort UV pulses by cross correlation via difference frequency mixing has been discussed along with preliminary results of multiple-shot measurements [1,2]. In this paper we describe the modification of the multiple-shot cross correlator to a single-shot one. Since no full CPA shot was really available for pulse duration measurement at that time, we report the results on the compressed seed pulse of Titania CPA. Moreover, we make an estimation of the best achievable pulse contrast from the Fourier analysis of the measured spectra of Titania CPA.

SINGLE SHOT CROSS CORRELATION

The modification of the cross correlator for single-shot measurements has two requirements. One has a smaller time window (2.1 ps) for which the temporal shape of the main KrF pulse (i.e. the duration) can be recorded while for the other the pulse structure (i.e. the contrast ratio) is to be measured by scanning with the larger time window (8.5 ps). The time windows are introduced along a line focus by use of pulse front tilts from a prism (quartz, 45°) and from the prism and a grating (1200 l mm^{-1}), respectively (Fig. 1).

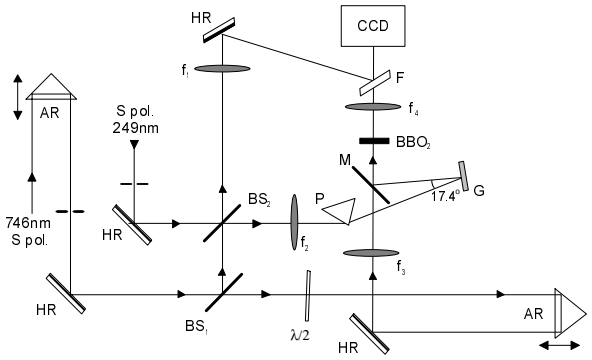

Figure 1 The layout of the single-shot cross correlator

The generating pulse at 745 nm originates directly from the Titania oscillator as before [1]. The KrF pulse to be measured was the seed pulse sent through the whole Titania CPA system steered back to the multiplexer room from the target area.

Since the technique of single-shot measurement is very sensitive to the spatial inhomogeneity of the incoming beams, the monitoring of the spatial beam distribution along the focal line is necessary. To do this 4 % of the beams are split off and imaged onto the CCD camera. The final mirror used is the filter BG39 which eliminates the generating beams from the difference frequency (DF) signal in the main arm. Recording then the line of DF along with the two generating beams, the cross correlation curve is obtained by dividing the DF line point-by-point with the generating lines.

An average of five shots of Titania seed pulse is seen in Fig.2. The cross correlation width is 479 fs. Taking into account the pulse length of the fundamental pulse in eq.4 of Ref.1 and the GVD in the optical elements of the beam pipe between the cross correlator and the CPA compressor, the pulse length of the KrF seed pulse at the BBO crystal is 348 fs. As a result of pulse front tilt a pulse can be considerably lengthened [3] moving away from the dispersive element as prism or grating. In the case of the cross correlator, calculating with the correct geometry and with the introduced pulse front tilt, the width of the Gaussian (sech^2) Titania seed pulse is 161 fs (152 fs) and transform limited (negatively chirped, 1.22 × transform limit).

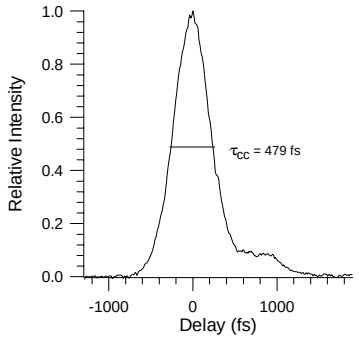

Figure 2 Measurement of the Titania CPA seed pulse width

MEASUREMENT OF SPECTRA - FOURIER ANALYSIS

The temporal shape of an ultrashort pulse is ultimately determined by its spectral shape. The temporal and spectral intensity distributions are related by Fourier transform (FT) of their amplitudes. Hence, measuring the spectra and assuming transform limited pulses (i.e. no relative phase shift along the spectrum), one obtains the best possible temporal pulse shape.

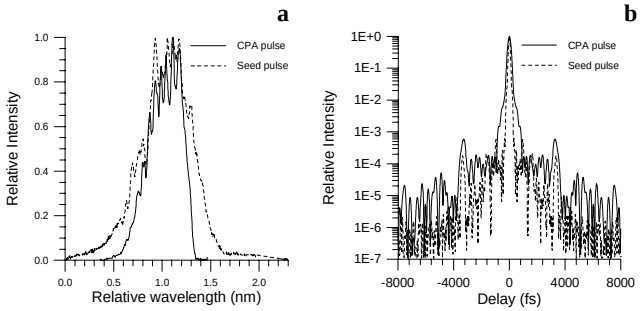

Figure 3 The measured spectra (a) and the corresponding Fourier transforms (b) of the amplified and seed pulses of Titania CPA

The spectra of the seed pulse and the full Titania CPA pulse (Fig. 3a) have been measured by a home made spectrograph in the front end room and an Exitech one in the multiplexer room, respectively. The corresponding FTs are displayed in Fig.3.b. As might have expected from Sprite CPA, the amplified pulse has been degraded considerably (see Table 1). More detailed analysis of the properties of FT on different spectral shapes has proved that the subpeaks at 3.3 ps of both the CPA and seed pulses are resulted in the spectra and not in the FT.

	Seed Pulse	CPA Pulse
Duration	124 fs	252 fs
$\Delta\tau\Delta\nu$	0.341	0.494
Subpeak	3rd @ 3364 fs	1st @ 3288 fs

Table 1 Parameters of the "best obtainable" pulses calculated from the measured spectra by Fourier transform

REFERENCES

1) K Osvay et al
CLF Annual Report 1996, RAL-TR-96-076, p.104, (1996)

2) K Osvay, I N Ross, J M D Lister and C J Hooker
2nd Gr-I Conference, SPIE, Ancient Olympia, Greece, (1997)

3) O E Martinez
JOSA B, 3 929, (1986)

TITANIA STOKES BEAMLINE DESIGN

C J Hooker, S Hancock

Rutherford Appleton Laboratory, Chilton, Didcot, Oxon., OX11 0QX, UK. Email C.J.Hooker@RL.AC.UK

In the original design of the Titania Raman system[1], it was proposed to deliver four Stokes beams to target in a new target chamber. At a later date it was decided to limit the startup system to a single Stokes beam in the original target chamber, while ensuring the optics and the mechanical components were compatible with a later upgrade to four-beam operation. This report describes the design of the single Stokes beamline.

The Stokes beam path from the front end room consists of five main sections: the optical delay line which compensates for the long beam paths into and out of the KrF amplifiers; an expanding diffraction-limited spatial filter to form a high-quality beam into the Raman preamplifier (RAT2); the preamplifier itself, a further diffraction-limited spatial filter to isolate the main Raman amplifier (RAT3) from the preamplifier and maintain the beam quality, and finally the main Raman amplifier. Of these, only the delay line has been used previously in its present form. The increased path length of the Titania KrF chain means that nine passes of the 12-metre long delay line are now required, plus some extra delay in the front end room, to synchronize the Stokes with the pump at RAT2.

Much of the optical design work concentrated on the two vacuum spatial filters, which are also beam expanders. The first takes the 7 mm oscillator beam and expands it to 50 mm before RAT2, and the second expands it up to 150 mm before RAT3. Both VSFs have a three-element design in which the output lens is a telephoto combination: the input positive lens and the negative component of the telephoto form the vacuum windows, and the positive lens of the telephoto pair is mounted separately some distance away. The lengths of the vacuum sections are limited by the time delay between the two Raman amplifiers, but are made as long as possible to maximize the spot size and reduce pinhole erosion. The path length between the amplifiers is 45.9 metres, corresponding to 153 ns, but since the Stokes beam traverses the two Raman amplifiers in the same direction, the maximum length of the vacuum sections is half this distance, and it was decided to make both 18 metres in length to allow space for the additional beam manipulation required in the four-beam system. The telephoto lenses were based on a design used previously in the Sprite Raman upgrade[2], and were optimized using the Beam 4 ray-tracing code[3]. All but one of the six lenses are simple plano types; the negative lens of the second VSF is a meniscus, ray-tracing having shown that this minimized the spherical aberration in the beam to RAT3. The diffraction-limited pinhole diameters are 650 microns in VSF1 and 160 microns in VSF2: each VSF has an array of pinholes, drilled in a 1 mm thick tantalum plate mounted on a motorized x-y stage. Each plate also has one 2†mm hole for alignment purposes.

RAT2 uses the cell from the old RA3, with a new 6 cm x 6 cm lightguide. RAT3 has a 16 cm x 16 cm lightguide and required a new cell; both guides are constructed from 10 mm thick float glass glued with epoxy adhesive. The glass is left uncoated because the laser fluence is close to the damage level for aluminium. There is a small loss of pump energy because the reflectivity of glass at 3 degrees incidence in P-polarization is only 60%; however, only half of the beams have this polarization, and in RAT3 only 1/4 of the area of those beams is reflected from the guide, so the net loss is approximately 5%. Selected Hoya plates[4] were used as windows for RAT2, but at 16 cm the aperture of RAT3 is larger than any standard plates. The gas windows described in last year's report[5] will be installed on this amplifier once they have been assembled and fully tested; for the start-up experiments, silica windows 180†mm diameter and 3 mm thick were used.

To minimize B-integral effects in the path to target, the Stokes output from RAT3 propagates mostly in an evacuated beam pipe, which it enters through a calcium fluoride window situated 5.5 metres away from the amplifier. This distance allows all the residual pump beams to separate from the Stokes, thus avoiding non-linear interactions at the window. Between the amplifier and the window the beam travels in a helium-filled beam pipe fitted with baffles to absorb the residual pump radiation.

REFERENCES

1) S Angood et al
Internal Report RAL-94-014, (1994)

2) D C Wilson et al
CLF Annual Report 1993, RAL-93-031, pp.111-112, (1993)

3) Stellar Software Inc, Berkeley CA, USA

4) Hoya Corporation, part no QZ-5W65-000-SE

5) C J Hooker et al
CLF Annual Report 1996, RAL-TR-96-076, pp.99-100, (1996)

ENGINEERING OF THE TITANIA RAMAN SYSTEM

D A Bates, P A Brummitt, A R Damerell, J A C Govans, K Gregory, S Hancock, M R Harman, A R Jackson, W J Lester, M R Pitts, D A Rodkiss, D Wood and B E Wyborn

Rutherford Appleton Laboratory, Chilton, Didcot, Oxon, OX11 0QX, UK.

INTRODUCTION

Last year the engineering work for the installation of the Titania CPA system was reported[1, 2, 3, 4].

This year has seen the operation of Titania in CPA mode and the grant funded installation of the new Raman system.

The installation of the Raman system involved a large amount of engineering work, namely: the design and installation of the frameworks and mirror mounts to facilitate the multiplexing, propagation and demultiplexing of 22 beams through the KrF amplifiers and onto the Raman amplifiers; the design and installation of the Raman amplifiers; the design and installation of the associated Raman and Stokes beam line components; and the design, installation and modification of a number of supporting sub-systems.

A major philosophy during the design phase was to produce a new facility which would be functional, meet the design specification and have potential for future development.

The installation work took place in the spring of 1997 with the majority of the design and planning work taking place in 1996. The primary aim throughout the installation phase was to minimise the down time of the laser as an operational machine.

More detail about what has been achieved is given in the following paragraphs.

FRONT END

A minimal amount of work was carried out to the front end of Titania. A discharge laser (LPX 105) was installed, into the Front End Room, along with two methane Raman cells, one for Raman generation and the other as the first stage of Raman amplification (RAT1). These were installed together with their associated gas, water, electrical and gas leak detection services.

KRF MULTIPLEXING AND DEMULTIPLEXING

The design of the buildings and the beamlines installed last year for the CPA system had already taken into account the requirements for the Raman system. The design of the complex multiplexing and demultiplexing arrangement to get all the beam path lengths and angles correct, using a state of the art 3D CAD package, has been reported earlier[5].

Figure 1 shows an isometric view, from the NE direction, of the equipment installed in the Titania Multiplexer Area after the upgrade. To give some idea of scale, the two lines of equipment shown are each approximately 25 m long and the frameworks in the foreground are approximately 2 m high. The work and equipment are described in more detail in the following paragraphs.

A pair of surface tables were installed for the multiplexing of the seed beam fed from the Front End Room.

The large frameworks were then surveyed into position in the Multiplexing Area prior to being secured to the floor.

Finally the optics mounting sub-systems, which included 105 of the novel flexure mirror mounts[3], were assembled and installed.

It's worth noting that on the Titania feed array it has been possible to pack the flexure mounts very closely. This was necessary in order to facilitate the required beam geometries.

The Titania splitting and turning array splits the original 12 beams into 24.

Beams 13 - 24 have an extended beam path length for timing reasons and therefore need the extra extended feed array as shown.

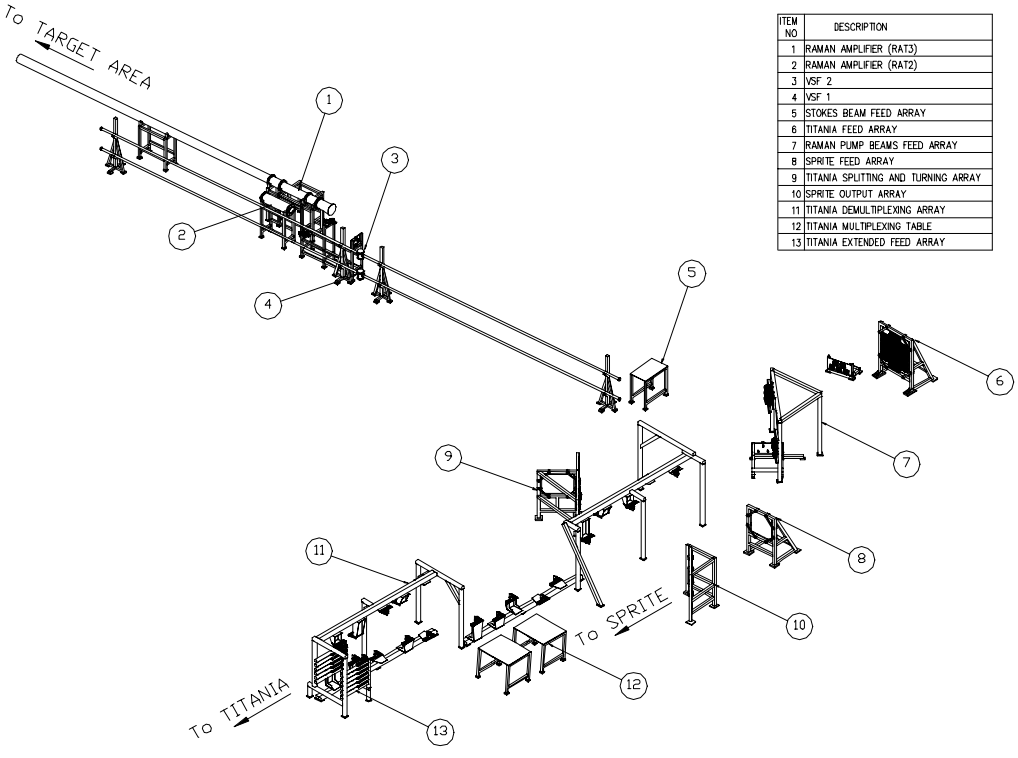

ITEM NO.	DESCRIPTION
1	RAMAN AMPLIFIER (RAT3)
2	RAMAN AMPLIFIER (RAT2)
3	VSF 2
4	VSF 1
5	STOKES BEAM FEED ARRAY
6	TITANIA FEED ARRAY
7	RAMAN PUMP BEAMS FEED ARRAY
8	SPRITE FEED ARRAY
9	TITANIA SPLITTING AND TURNING ARRAY
10	SPRITE OUTPUT ARRAY
11	TITANIA DEMULTIPLEXING ARRAY
12	TITANIA MULTIPLEXING TABLE
13	TITANIA EXTENDED FEED ARRAY

Figure 1 View of Titania Multiplexer Area from the NE

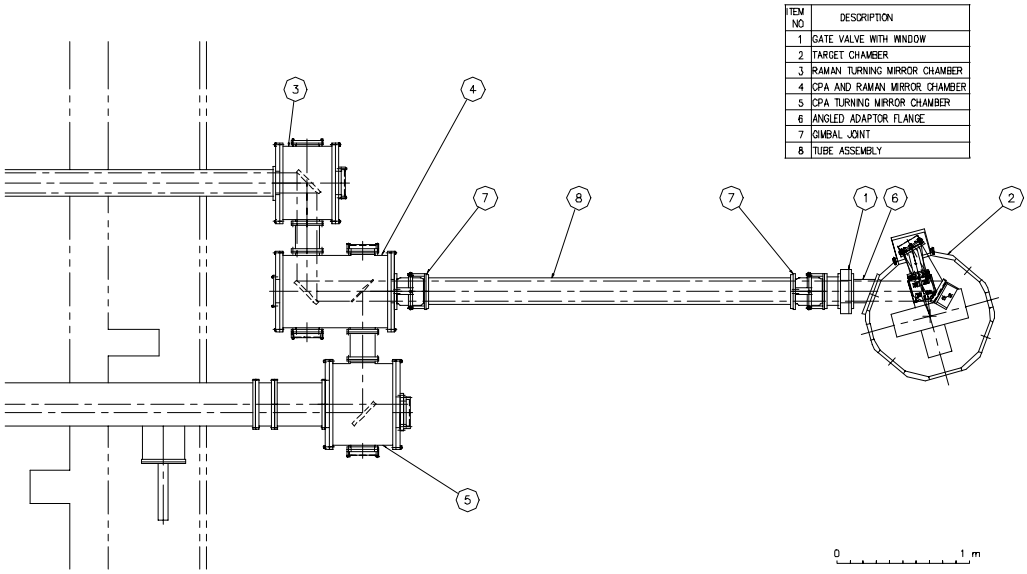

Figure 2 Raman and CPA beam delivery system to Target Chamber

The demultiplexing array incorporates the optics on slides so that fine timing tuning is possible between all the beams.

The existing delay line was altered for dual Raman and CPA operation.

Two long equivalent focal length VSFs were also installed.

A tip tilt mirror has been installed just before the 1st VSF. The beam position is measured against a reference and then any errors corrected by feedback to the automatically controlled tip tilt mirror.

The final Raman pump feed array ensures that the 22 KrF pump beams arrive at the Raman amplifiers at the correct time and position in space.

It should be noted that the flexure mounts have proved themselves to be very stable in the subsequent operational phase.

RAMAN AMPLIFIERS

An existing Raman amplifier but with new internals (RAT2) and a completely new amplifier (RAT3) were installed.

RAT3 was designed for operation with gas windows[6], but initially installed with thin solid silica windows. It has a 160 mm square aperture. Incorporated into its mounting frame is the ability to slide the amplifier into and out of the beam so that the alignment beam is available to the Target Area when the gas windows are closed. A final baffle tube has been included to absorb any remaining KrF pump beams.

TARGET AREA

The new layout in the Target Area is shown in figure 2.

The existing CPA turning mirror chamber was modified to increase the diameter of the two side ports.

A new Raman turning mirror chamber was designed and installed.

A further chamber was designed and installed which was designed to give easy change over from Raman to CPA operation and the option for future co-axial propagation of CPA and Raman beams.

The three chambers were all designed with a bellows vacuum isolation mounting system to minimise any movement due to vacuum loads during pump down.

A new increased diameter beam transport tube and gate valve, with associated gimbals/ bellows units, were installed.

To deliver the new Raman beam to target the existing target chamber needed to be reconfigured. An adapter was manufactured for the target chamber to take a 150 mm diameter beam and a F3.5 parabola. The chamber was also rotated and repositioned.

ANCILLARY SERVICES

In addition to the above pieces of equipment ancillary services such as gas lines, vacuum lines, gas leak detection systems, beam pipes and electrical supplies were all installed.

CONCLUSIONS

The design, manufacture and installation of the Titania Raman system has involved a lot of engineering design, planning and sheer hard work. This opportunity should be taken to thank everyone for their contribution during the last year.

REFERENCES

1) S Angood et al
CLF Annual Report 1995-6, RAL-TR-96-076, p.93, (1996)

2) A R Damerell
CLF Annual Report 1995-6, RAL-TR-96-076, p.95, (1996)

3) S Hancock
CLF Annual Report 1995-6, RAL-TR-96-076, p.96, (1996)

4) C J Reason et al
CLF Annual Report 1995-6, RAL-TR-96-076, p.97, (1996)

5) S Hancock and C J Hooker
CLF Annual Report 1994-5, RAL-TR-95-025, p.111, (1995)

6) C J Hooker et al
CLF Annual Report 1995-96, RAL-TR-96-076, p.99, (1996)

CONFIGURATION OF TITANIA FOR MATERIALS PROCESSING

G J Hirst, E J Divall, A K Kidd, J M D Lister

Central Laser Facility, Rutherford Appleton Laboratory, Chilton, Didcot, Oxon., OX11 0QX, UK Email G.J.Hirst@RL.AC.UK

INTRODUCTION

Titania is normally configured as an ultra-high power system but it is also capable of very high energies, in principle up to 1 kJ per pulse. Such pulses can be used for large-area materials processing where the requirements are typically for tens of nanoseconds pulse duration, fluences up to 1 J cm^{-2} and maximum fluence uniformity at the target[1]. This article describes a provisional design for delivery of this performance.

DESIGN PRINCIPLES

The pulse duration was chosen to be 20 ns FWHM since this was readily available from the KrF discharge laser in the Front End Room. It was decided to use the existing Sprite/Titania optics[2] as far as possible to minimise the disruption when the configuration was changed. The technique of image-relaying[3] was employed to maximise the fluence uniformity.

The existing Raman pump optics conveniently deliver overlapped beams to a plane near the entrance of the RAT3 Raman amplifier[2]. Setting this as the target plane fixed the positions of all of the intermediate image planes back through Titania and Sprite and, once the target size (125 mm diameter) and field angle were decided, it also fixed the beam sizes. A geometric optics model was constructed using Mathcad5.0[4] to calculate these and to check for vignetting. The model showed that the beam diameter in the Titania amplifier was approximately twice that at the target, so a target fluence of 1 J cm^{-2} would require a fluence in the amplifier of 0.25 J cm^{-2}. Assuming a Titania output intensity of 5 MW cm^{-2} (roughly $3 \times I_{sat}$) the fluence available from a single 20 ns pulse would be 0.1 J cm^{-2} so it would be necessary to overlap three pulses on target. The optical layout needed to do this is shown in figure 1. Independent relay lenses, L1-L3, are required since the paths into Sprite and out of Titania have different lengths in each channel. A further lens, L4, relays the light from the discharge laser into the multiplexer.

The existing demultiplexing optics constrained the inter-pulse interval to be a multiple of 6 ns. 24 ns was chosen to provide adequate pulse separation while staying within the Sprite temporal gain profile.

If the gain in Sprite does not saturate then Sprite and Titania can be treated as a single saturating amplifier and the required input energy can be calculated[5] in terms of the known small-signal gain length product and the output energy. Previous measurements[6] suggest that a total gain length product of more than 14.5 should be available. Even allowing for static losses of 50% the energy required from the discharge laser would then be only 3 mJ per pulse. This should allow it to be operated with no output coupler ie as a double-pass ASE source, the angular divergence of which should be sufficient to fill the amplifier chain.

REFERENCES

1) M Stehle
Laser Focus World, 32 (5) 101, (May 1996)

2) S Hancock and C J Hooker
CLF Annual Report 1994-5, RAL-TR-95-025, p.111, (1995)

3) J M D Lister, M J Shaw, C J Hooker and E C Harvey
CLF Annual Report 1991, RAL-91-025, p.83, (1991)

4) MathSoft Inc., 101 Main St., Cambridge, MA 02142, USA

5) A E Siegman
"Lasers", Chapter 7, publ. Oxford University Press (1986)

6) A K Kidd, C J Hooker, A P Visser and M J Shaw
CLF Annual Report 1994-5, RAL-TR-95-025, p.108, (1995)

7) A K Kidd, M H Key and C J Hooker
2nd KrF Laser Technology Workshop, Banff, Canada, (1990)

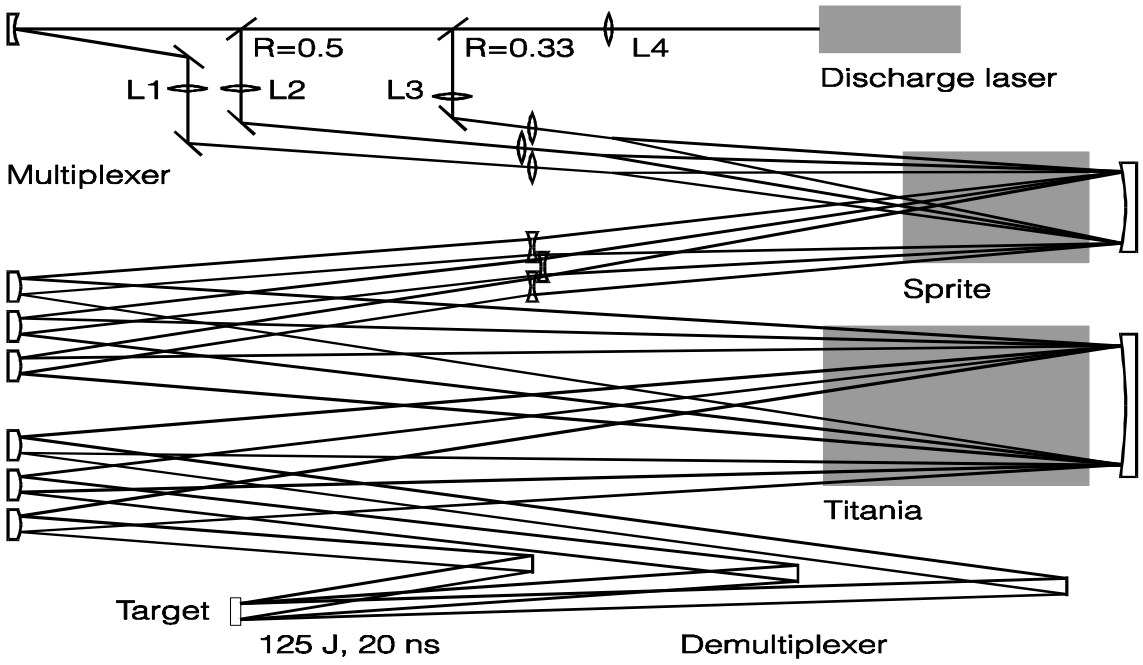

Figure 1 Optical layout of the three-channel multiplexed Titania materials processing system

THE 'TRAVELLING WAVE' FOCUS ON VULCAN

J Collier[1)], D Pepler[1)], C Danson[1)], J Warwick[2)], C Lewis[2)], D Neely[1)]

1)Rutherford Appleton Laboratory, Chilton, Didcot, Oxon, OX11 0QX
2)Queens University, Belfast, BT7 1NN

INTRODUCTION

This paper concerns the creation of a travelling wave focus on VULCAN for the efficient pumping of an X-ray laser. The X-ray laser scheme uses a pre-formed plasma in a line focus geometry that is pumped by an ultra short 2 ps pulse to create the longitudinally distributed population inversion that is required for laser gain. The travelling wave focus ensures that the pump pulse propagates along the line focus at the speed of light coincident with the X-ray laser photons.

THE LINE FOCUS

The creation of the line focus geometry uses the optical aberration that is introduced by a spherical mirror when operated at an angle with respect to the optic axis. The scheme used is illustrated in Figure 1.

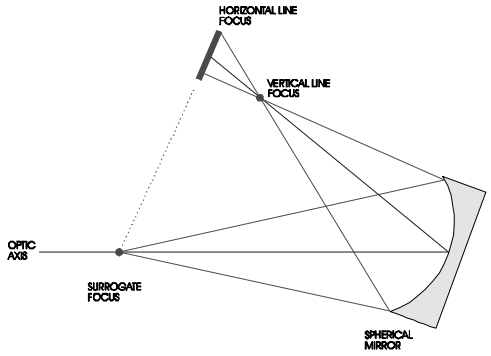

Figure 1: The line focus geometry

The incoming laser beam is focused to a point using an off axis parabolic mirror. This point source is referred to as the *surrogate focus*. The spherical mirror, operating at an angle to the optic axis, then images this point source to the target plane. The angled operation of the spherical lens introduces a large astigmatism into the beam producing two 1 dimensional images which are line foci. One is formed perpendicular to the plane of incidence and is produced closer to the mirror while the other one is a line contained in the plane of incidence that is produced further away from the mirror. An extrapolation of the line focus lying in the plane of incidence will intersect the surrogate focus and it is this line focus that is used.

The line focus always points toward the surrogate point and due to the geometry there is an inherent optical path difference between rays arriving on one side of the line with respect to the other. This optical path difference can be appreciable and becomes especially relevant when the incoming 'beam' is an ultra short pulse as used in the X-ray laser scheme detailed above. This difference means that the incident laser pulse will propagate from one side of the target to the other with a finite time that is normally several times the speed of light. This pulse propagation velocity (PPV) increases rapidly with reduced incidence angle. The existence of this PPV partially aids the X-ray laser process. The line lengths used are typically 10 mm which means that the X-ray laser photon transit time from one end to the other is tens of picoseconds. However, the X-ray laser gain only lasts for a few picoseconds so if the pumping (gain) were to be delivered at the same time everywhere along the line length (infinite PPV as would be generated if a cylindrical lens were used to produce the line focus) then the gain at the end of the line will have dissipated by the time the X-ray photons arrive. The optical path difference inherent in this line focus scheme means there is a finite PPV and the longitudinal pumping rate along the length of the line is sufficiently reduced such that the X-ray laser photons experience gain over a longer length than they would do in its absence. The typical PPV's encountered in this focusing geometry are of the order 2-3 *c*. In the travelling wave scheme this is reduced to exactly *c* ensuring that the X-ray photons always see the peak of the available gain throughout the whole length of the line focus.

MATCHING THE PPV TO *c*

The matching of the PPV to *c* can achieved by the use of a diffraction grating. The dispersive nature of a diffraction grating means that an incident laser beam will experience an optical path length from an input to an output plane that is a function of a spatial co-ordinate. Again, if the input 'beam' is an ultra-short pulse this results in a lateral time shear upon diffraction. This can be seen in Figure 2 where the transit time of an input pulse though the grating system is dependant on its spatial location in the input beam. The transit time difference $d\tau$ for a spatial separation dx is given by

$$d\tau = \frac{N_t \lambda}{c \cos\phi} \cdot dx \qquad \text{..... 1}$$

where N_t is the grating line density, λ is the wavelength, c the speed of light and ϕ is the input angle. Thus, by correct choice of the diffraction grating and insertion parameters an additional optical path length difference can be imposed spatially on the pulse that will add to the inherent optical path difference that the pulse will experience at the line focus. This will then ensure that the PPV can be reduced to the speed of light. This

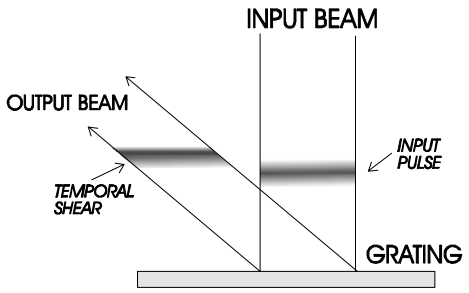

Figure 2 : Diffraction Grating and Temporal Shear

optimised PPV is known as a *travelling wave* focus.

IMPLEMENTATION ON VULCAN

The PPV slowing scheme described above was implemented on VULCAN for a specific set of experimental parameters. These parameters were used to determine the correct grating line density required to bring the PPV to *c* at the line focus when the grating was inserted at a specific point in the laser system. This grating insertion point was chosen to be at the end of the rod amplifier chain just before the last 45 mm rod amplifier primarily dictated by grating availability and its associated damage threshold. The grating line density required at this point was determined as follows.

Recalling Figure 1, the surrogate focus produced in the target area was formed using an off axis parabola with a focal length of 450 mm and beam dimensions entering the parabola of 88 mm in the grating dispersion plane and 130 mm in the non dispersion plane. The spherical mirror located 350 mm from the

surrogate had a 350 mm focal length and was operated at an incidence angle of 15.5°. This gives a surrogate to line focus centre distance of 195 mm. This focusing system was modelled by the optical design program ZEEMAX which indicated an intrinsic PPV in a 12.0 mm length line focus of 2.5 *c* giving a pulse propagation time of 15.9 ps. For matching to *c* a propagation time of 40 ps is required which equates to an additional 7.2 mm optical path length difference required across the 88 mm input beam. Due to the system magnification of 3.8 the size of the 88 mm beam at the grating insertion point is 23.3 mm, and it is this that must be used for the beam size. The grating line density required is then determined from Equation 1 to be 294 lines mm^{-1} when operated at approximately normal incidence. A 300 lines mm^{-1} is used at the expense of introducing a slight increase in the path difference.. This is however compensated for by the slight change in beam size as a result of the diffraction. These factors result in an additional path difference of 7.0 mm which gives a nominal overall path difference of 11.77 mm and a PPV of 1.02 *c*. It is possible to fine tune the PPV by changing the incidence angle onto the spherical mirror. The table below illustrates the range possible.

Incidence Angle	Line focus length (mm)	Pulse velocity
14.5°	10.24	0.95 c
15.5°	12.00	1.02 c
16.5°	13.87	1.08 c

Table 1 : PPV tuning

GRATING RETUNING

Following the introduction of the diffraction grating into the system to produce the travelling wave, it becomes necessary to readjust the compressor grating separation to recover the shortest pulse duration. The reason for this can be understood by reference to Figure 3.

Considering rays passing through a small aperture *A* placed at the output of the compressor, it is clear that in order to pass through the aperture different wavelengths must originate

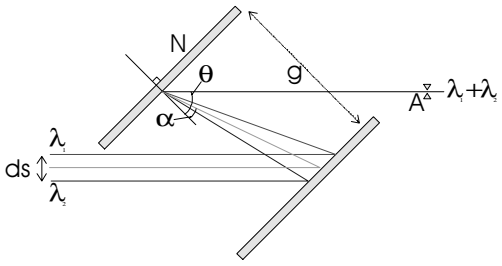

Figure 3 : Grating Compressor

spatially separated on the input beam by *ds* given by

$$ds = \frac{Ng\cos\theta}{\cos^3\alpha}\cdot d\lambda \qquad \text{..... 2}$$

where $d\lambda=(\lambda_1 - \lambda_2)$, *N* is the compressor grating line density and *g*, θ and α are as defined in the figure. The corresponding separation of these wavelengths at the travelling wave grating insertion point is however reduced by the system magnification *M* to $dx = ds / M$. Furthermore, because these wavelengths do not propagate exactly co-parallel through the system but have a slight relative angle due to the dispersion of the travelling wave grating, this adds to *dx* an amount *dx'* given by

$$dx' = \pm\frac{LN_t}{M^2\cos\varphi}\cdot d\lambda \qquad \text{..... 3}$$

where N_t is the travelling wave grating line density, φ is the diffracted angle from the travelling wave grating and *L* is the location of the image plane of the travelling wave grating formed by the VULCAN system measured from the compressor. The sign of *dx'* depends on the sign of the magnification. The spatial separation of these wavelengths at the travelling wave grating means they have necessarily experienced a different transit time through the travelling wave grating system as discussed earlier. Recalling Equation 1, this time difference Δτ is equal to

$$\Delta\tau = \frac{N_t\lambda}{c\cos\phi}\left(dx \pm dx'\right)$$

$$= \frac{N_t\lambda}{c\cos\phi}\left(\frac{Ng\cos\theta}{M\cos^3\alpha} \pm \frac{LN_t}{M^2\cos\varphi}\right)\cdot d\lambda$$

$$= \kappa^{\pm}\cdot d\lambda \qquad \text{..... 4}$$

where $\kappa^{\pm}$ is a constant for the configuration that can have two possible values depending on the magnification sign. The variation of transit time as a function of wavelength for light passing through the aperture *A* represents an additional linear chirp that can be compensated for by a compressor grating separation adjustment Δz equal to

$$\Delta z = \frac{\kappa^{\pm}c\cos^2\alpha}{N^2\lambda} \qquad \text{..... 5}$$

Using values of *N* = 1740 mm^{-1}, N_t = 300 mm^{-1}, θ=73°, α=61°, $\phi \approx \varphi \approx 0°$, M=3.8, g=1.7 and *L*≈50 m (determined by Zeemax) this gives values for Δz of either 7.0 cm or 2.2 cm. In the implementation the actual grating separation was changed by 6.0 cm to achieve the shortest pulse duration.

VERIFICATION

The verification of the travelling wave was conducted using an streak camera with a sub picosecond resolution. Two metal spikes were positioned in the line focus and separated by 6.75 mm. The scattered light from these spikes was imaged onto the streak camera. The results are presented in Figure 4. The left

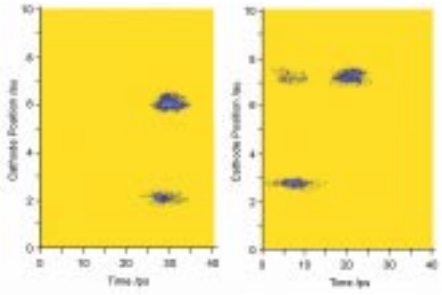

Figure 4 : Streak Records

image is taken with no grating and the right image with the grating. The temporal separation of the spikes in the upper image is 1 ps but should however be 9 ps due to the intrinsic PPV. The fact that it is not is due to the non normal imaging of the line focus onto the streak camera and this must be taken into account. The separation in time of the spikes in the lower image is about 14 ps. A further 8 ps (9 ps - 1 ps) must be added to this to yield a 22 ps difference for 6.75 mm giving a PPV of 1.02 *c*.

A NEW TARGET ALIGNMENT SYSTEM FOR TITANIA

D Neely[1)], J M Knott[1)], R J Clarke[1)], A R Damerell[1)], E Divall[1)], P F Gray[2)], G Hirst[1)], S J Morrall[1)]

1)Central Laser Facility, Rutherford Appleton Laboratory, Chilton, Didcot, Oxon, 0X11 0QX
2)Space Science Division, Rutherford Appleton Laboratory, Chilton, Didcot, Oxon, 0X11 0QX

INTRODUCTION

A target chamber alignment system was required to position laser interaction targets to better than the Rayleigh range (20 µm) of the Titania laser focusing parabola for high intensity interaction experiments. The alignment system was required to work in both the visible, for initial alignment of targets and the UV, to check the laser beam's size and position using low intensity shots. The system must also be mechanically stable, allow good access to the target and be highly reproducible over the period of an experiment ~ 4 weeks.

DESIGN

A two arm microscope imaging system giving near orthogonal views of the target plane was considered to be a suitable solution, the target plane being defined by the bisection of their foci. As each arm of the microscope system was required to work simultaneously in both the UV and visible, a reflective design which is free from chromatic aberrations was adopted. Due to the chamber size, target accessibility and laser beam paths, no components of the microscopes could be within 200 mm of the object plane. A long focal length microscope consisting of a Schwarzschild collection objective and parabolic mirror was selected to fulfil these requirements as shown in figure 1. The Schwarzschild collection objective is set to produce a parallel beam which can be fed through a quartz vacuum interface window into a standard Newtonian telescope and CCD detector.

Figure 1 Schematic diagram showing the components of the long working distance microscope system.

The Schwarzschild collection objective uses only spherical mirrors and is theoretically free from primary spherical aberration, coma and astigmatism. Higher order aberrations were reduced and image quality over the field of view optimised by adjusting the mirror curvatures and separation. The final design used a 250 mm diameter concave mirror located at a distance of 403.5 mm from the target with a curvature of 308.25 mm. The second 50 mm diameter convex mirror had a curvature of 117.485 mm and was located 190.58 mm from the first mirror. The telescope system outside the chamber is a standard Newtonian astronomical telescope using a 0.6 m parabolic mirror.

The residual theoretical wavefront aberration of the Schwarzschild microscope objective is less than $\pm\lambda/20$ at λ = 633 nm over the required high resolution part of the field of view (± 0.5 mm at the object plane). The two mirrors were interferometrically aligned to an accuracy of ± 5 µm, producing an actual residual wavefront error of about $\pm\lambda/6$ at λ= 633 nm, mainly arising from the residual errors of alignment, departures from the sphericity in the mirrors and minor deformations of the mirrors by their support structure.

TESTING AND RESULTS

The MTF (Modulation Transfer Function) of the imaging system was measured with uniform white light illumination using a binary resolution target. In Figure 2, the theoretical diffraction limited MTF produced using a ray tracing program is compared with the MTF obtained using monochromatic light. The measured MTF is lower than anticipated probably due to

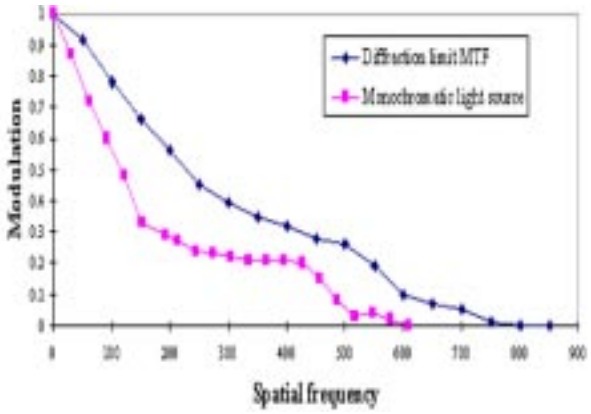

Figure 2 Theoretical and measured Modulation Transfer Function (MTF) of the long working distance microscope system.

diffraction caused by the mechanical supports and scattering from the mirror surfaces. However, with >20% MTF at spatial frequencies of 400 l/mm the system is still within operational requirements.

Targets were aligned using two long focal length microscopes set ~75° to each other. A 10 µm wide Aluminium cross was put in the centre of the target so it could be positioned such that the cross was in focus on both microscopes. The target was then translated orthogonally to the focal plane to a suitable region of its surface. The image from each microscope system was formed on a CCD camera of pixel size 5.5 µm. This was ideally matched when capturing an image on a framestore type system, but is difficult to align using only a monitor. To overcome this, an additional x5 objective was added to magnify the image onto the CCD detector.

Using an electronic measuring system, tests were carried out to estimate the relocation accuracy to which a target could be positioned. The accuracy of repositioning the target was to within ±3 µm of the defined location, which was ideal, considering that the Rayleigh range of the Titania Raman beam with a 0.5 m focusing parabola is ~ 20 µm.

CONCLUSION

This design of Schwarzschild collection objective coupled to a Newtonian telescope provided the required resolution and mechanical stability to reliably position targets within the focal volume of the Titania laser system.

PLASTIC FOIL PRODUCTION FOR LASER INTERACTION EXPERIMENTS

P Griffiths[1)], E Wolfrum[2)], C Brown[1)], D Neely[1)], N Prior[1)], B Wyborn[1)]

1)Central Laser Facility, Rutherford Appleton Laboratory, Chilton, Didcot, Oxon, 0X11 0QX
2)Clarendon Laboratory, Department of Physics, University of Oxford, Oxford, OX1 3PU

INTRODUCTION

An important aspect of inertial confinement fusion is the study of Rayleigh-Taylor growth. Recent advances in the soft X-ray laser field now permit the study of Rayleigh-Taylor growth in 5-20 µm thick CH foils using soft X-ray laser backlighting. To facilitate such an experiment, foils of surface roughness ~ 10 nm were requested by the Oxford group of J. Wark. This report details surface roughness measurements of foils produced by two manufacturing processes at the CLF.

FOIL PRODUCTION

Hydro-Carbon (CH) foils are routinely produced at the Target Preparation Laboratory of the CLF, using a vapour deposition technique on glass substrates. This technique can produce foils of typical thickness 0.1 - 30 µm. The surface finish of two samples were analysed using an Atomic Force Microscope (AFM). The samples analysed were (1) a 6.5 µm thick CH coating on a HOYA glass plate substrate and (2) a 12 µm thick CH coating on microscope glass slide substrate. Both, the growth side and the side which was initially on the glass, have been investigated. The maximum area, that can be sampled by the AFM, is 64.29 x 76.92 µm. All images (figures 1 - 3) shown have these dimensions. Table 1 below clearly shows that the surface roughness of the growth side is much poorer than the side against the glass and that the roughness increases with foil thickness. Such foils are unacceptable for experimental purposes due to their high surface roughness.

glass side	growth side	CH thickness
6.2 ± 1.9 nm	33 ± 3 nm	6.5 µm
7.5 ± 1.9 nm	106 ± 16 nm	12 µm

Table 1 The rms surface roughness measurements for two different thicknesses of CH foils.

An alternative method for producing flat plastic foils suggested by LLNL was successfully tested at RAL. Here, commercially available plastic foils are placed between two HOYA glass

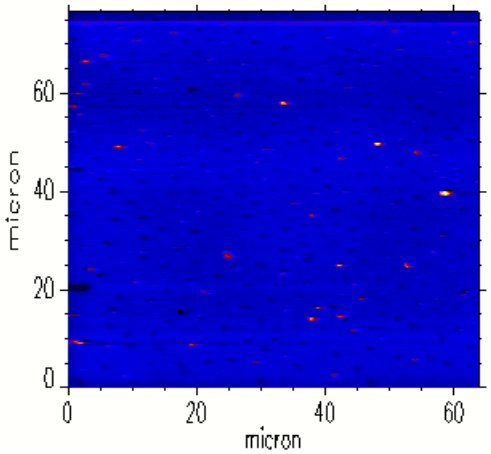

Figure 1. AFM image of the side initially on the glass of a 6.5 µm thick CH coating on a HOYA glass plate.

plates (~20 x 20 mm) separated by 10 µm tungsten wires. The glass plates together with the CH foil are heated on a hotplate to ~ 100° C and loaded with a weight (2.2 kg) for 60 to 90

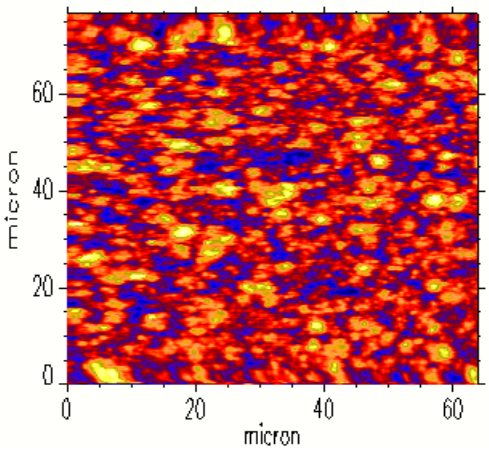

Figure 2. Image of the growth side of a 12 µm CH coating on a glass microscope slide, with surface roughness 106 nm.

minutes. The CH foil is thus pressed to a final thickness of 11.7 ± 0.9µm. Unlike vapour deposited CH foils, there is no difference between surface roughness of the two sides.

Various foils prepared in this manner have been investigated with the AFM. Most of the sampled areas exhibit a surface roughness of 4 - 5 nm rms (cf. figure 3), some areas (< 10%) show scratches and dust leading to a value of 8 - 10 nm rms.

CONCLUSION

The vapour deposition technique was shown to produce foils

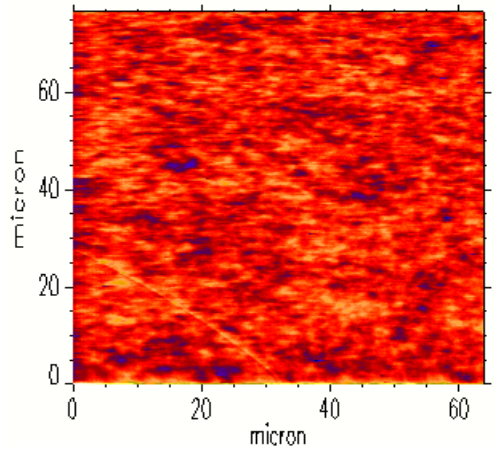

Figure 3. Typical AFM image of a compressed CH foil. The surface roughness is 4.9 nm rms.

over large areas (30x30 mm) with thickness uniformity of 2 %. However, the rms roughness was demonstrated to be > 100 nm for foils of >10 µm thickness. The alternative technique of compressing a foil whilst heated between two flat glass plates was shown to produce the desired quality of <10 nm rms roughness and was used for the experimental run.

DEVELOPMENT OF AN ADAPTIVE OPTICS SYSTEM FOR LASER PHASEFRONT CONTROL

M J Shaw, C J Hooker, C J Reason, T Kanèko

Rutherford Appleton Laboratory, Chilton, Didcot, Oxon, OX11 0QX, UK

INTRODUCTION

A major increase in focal irradiance from the CLF's high power lasers could be obtained by reducing their spatial phase errors. Both Vulcan and Titania operate with beams which are several times diffraction limited so, in principle, factors of 10 or more improvement in irradiance may be possible by the use of adaptive optics (AO) to reduce phase errors. Such AO systems have been known about for some time and are increasingly being used in astronomy and are proposed for the NIF and MegaJoule fusion laser systems[1]. At RAL we have developed a prototype AO system which uses a deformable mirror, a wavefront sensor based on a simple Hartmann plate and a computer control system for phase front curvature correction.

EXPERIMENTAL SETUP

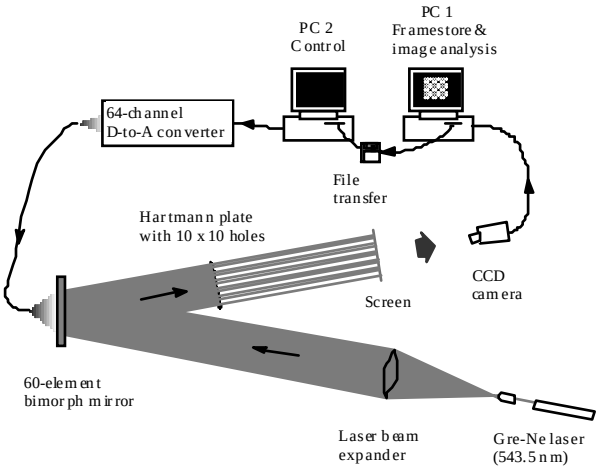

Figure 1. Experimental layout for characterising and controlling spatial phase with a deformable mirror.

The experimental set-up is shown in Fig. 1. A Gre-Ne laser beam is expanded and reflected from a deformable mirror and the wavefront of the resulting beam is analysed using a Hartmann plate. The type of deformable mirror chosen works on the bimorph principle, whereby a sandwich is made between a thin mirror substrate and a piezoceramic plate. A voltage applied across the thin dimension of the plate causes an expansion or contraction in the plane of the plate and bends the substrate in a manner analogous to a bimetallic strip. If the thickness of the piezoceramic is small compared to the substrate, the curvature produced is given approximately by:

$$R^{-1} = \frac{6 d_{31} E_p (1 - \sigma_g)}{E_g t_g^2} V \qquad (1)$$

where d_{31} is the transverse piezoceramic strain constant, E_p and E_g are the Young's moduli for the piezo and glass plate respectively, σ_g Poisson's ratio for glass and t_g the glass plate thickness. V is the applied voltage and, as can be seen from (1), the local curvature is proportional to the locally applied voltage. Thus bimorph mirrors are ideally suited to curvature control. An array of electrodes screen-printed onto the piezo plate using conductive ink allows spatial variation of the voltage in a controlled manner. In our prototype mirror shown in Fig. 2, 60 control elements (an 8x8 array with the corners removed) are printed onto a 70 mm square x 0.2 mm thick PZT plate which is glued to a 100 mm dia x 1.5 mm thick Pyrex mirror substrate. Pyrex was chosen since it has an expansion coefficient close to that of PZT and so reduces the sensitivity of the construction to temperature variation. After attachment of the PZT, the mirror was polished flat to λ/4 and coated with an aluminium reflective coating for testing. The useful controllable aperture of the mirror is 50 mm.

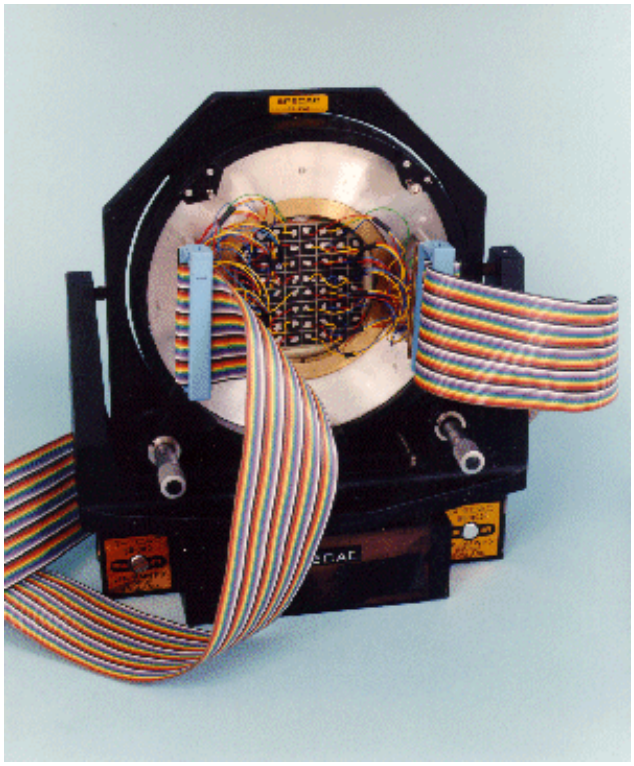

Figure 2. Photograph of rear side of the bimorph mirror showing control electrodes.

The control voltages are derived from a 64 channel driver which is addressed from the computer I/O bus. Each channel has a 10 bit D/A converter which is followed by a push-pull transistor amplifier giving ± 64 volts output with a 10 mA peak current. The set voltage on the 2 nF control electrodes is achieved in about 100 µs which is well within the mechanical response time of the mirror.

CENTROIDING

The wavefront sensor chosen was a Hartmann plate with an 10 x 10 array of 2 mm diameter holes on a 5 mm pitch. The beamlets propagated 4.2 m to a screen which was imaged by a CCD camera. The Hartmann plate was chosen because of its simplicity, ease of changing sensitivity and the fact that it gives wavefront slopes directly. Curvature is obtained after a very simple derivative calculation whilst integration gives the optical path difference (OPD). The captured image is an array of spots

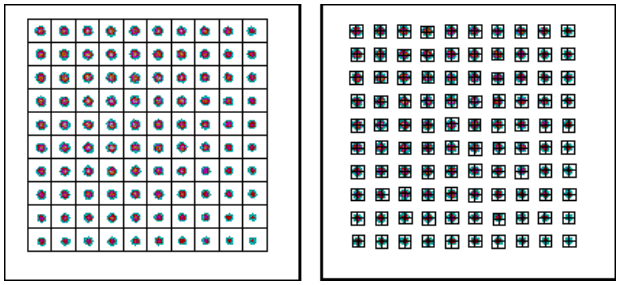

Figure 3. The Hartmann image is first divided into cells, each containing a spot. The spots are then enclosed by a nucleus which define the extent of the spots.

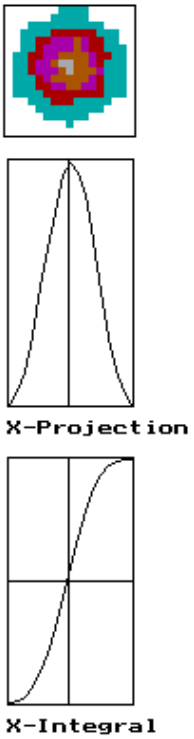

Figure 4. Typical spot showing the projection on the *x*-axis and its integral to give the *x* component of the centroid from the median.

and the first task is to locate the centroid of each spot. Both the areas between the spots and the spots themselves contained interference patterns. An array of Fresnel lenses, which was tested as an alternative to a Hartmann plate exhibited even more interference between the spots, though the spots themselves were smaller and brighter. The centroiding algorithm must be capable of locating the centroids of the spots to within a fraction of a pixel, be suitable for either optical arrangement, and above all be robust, even at the expense of computing time.

Firstly, the operator is asked to specify the corner spots of the Hartman image, then the image is divided by an equally spaced grid into cells that should each contain a single spot (Fig. 3).

Each cell is scanned for the brightest group of nine pixels, whose central element is a good estimate of the spot's centroid to the nearest pixel. Now the spots need to be extracted from the background and this is done by boxing each spot in a nucleus which is centred on the approximate centroid (see Fig. 3). The operator can adjust the size of the nucleus to define the edge of the spots. The measurement is refined to a fraction of a pixel by projecting the intensity of the spots in one direction to smooth the data, the medians are then taken to be the centoid coordinates (see Fig. 4). This centroiding algorithm has been running reliably with a precision of around 0.1 pixel but is also the time-limiting factor; the time taken to obtain the centroids for a 10×10 array is around two seconds with the program running under Turbo Pascal on a 200 MHz Pentium PC.

WAVEFRONT ANALYSIS

To find the horizontal (x) and vertical (y) components of the wavefront slopes, the coordinates of the centroids from a test image, are compared with those from a reference image taken with a perfectly flat wavefront. Global tilt is removed at this stage by averaging all the centroid coordinates for each image, then the two images are mapped on to each other using the difference of the average coordinates as the translation vector.

The two orthogonal components of the wavefront slopes at aperture (i, j) of the Hartmann plate are given by

$$S^x_{i,j} = \Delta x_{i,j} / L \quad , \quad S^y_{i,j} = \Delta y_{i,j} / L \, , \qquad (2)$$

where ($\Delta x_{i,j}$, $\Delta y_{i,j}$) is the shift of the spot's centroid between the test and reference image, and L is the separation between the Hartmann plate and the screen.

The wavefront curvature follows directly from the slopes using the equation:

$$\overline{R}^{-1}_{i,j} = \frac{1}{4h}\left(S^x_{i+1,j} - S^x_{i-1,j} + S^y_{i,j+1} - S^y_{i,j-1}\right) \qquad (3)$$

Where $\overline{R}^{-1}_{i,j}$ is the mean curvature (ie. average curvatures in x and y directions) at Hartmann aperture number (i, j), and h is the separation of the holes.

For OPD reconstruction (which is not a necessary stage for closed loop operation), we used a numerical algorithm proposed by Southwell [2], which appears to return fairly accurate estimates of the OPD.

CURVATURE CONTROL

The curvature values calculated at the locations fixed by the Hartmann array need to be mapped onto the actuator array so that the appropriate control voltages can be calculated. This was done by applying a voltage to each actuator in turn within the aperture and measuring the resulting spot deflections. Our initial efforts to map actuators fitted various shapes to the curvature and OPD data and proved to be surprisingly inaccurate. It proved to be far more sensitive to use the slope data directly and obtain the (Hartmann) x and y coordinates of the actuator centres from the intersections of the slopes near the zero crossing point shown in Fig. 5. (The fact that the slopes do not intersect at zero in this case means that this actuator applies an overall tilt to the mirror).

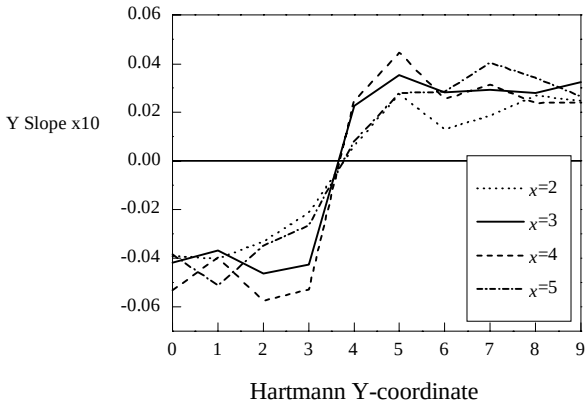

Figure 5. Y-slopes measured along various columns (x = const) in the Hartmann grid with a voltage applied to a single actuator. The intersection of the slopes near to zero gives the y-coordinate of the activated actuator.

The curvature at the actuator positions can now be calculated by interpolation from the values at the nearest Hartmann grid points. A typical curvature-voltage plot for a single actuator is shown in Fig. 6. The effect of hysteresis is clear, as is the approximate linearity between curvature and voltage. The average slope $\beta = R^{-1}/V$ was found to vary little between actuators but was considerably less than that given by Eqn (1). Ansys computations, which included the effect of the ~ 100 μm thick epoxy glue layer, showed much better agreement with measurements. For application of control voltages to correct the curvature under closed loop conditions it was found that a control factor somewhat less than β was necessary to avoid over

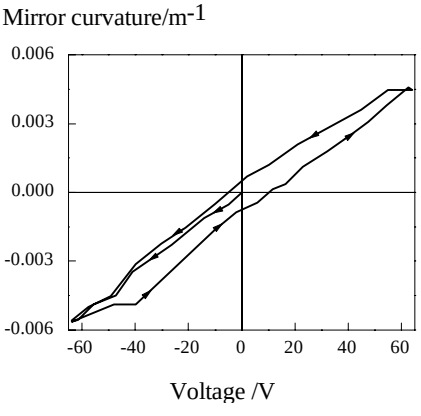

Figure 6. Measured curvature of mirror as a function of applied voltage, showing effect of hysteresis.

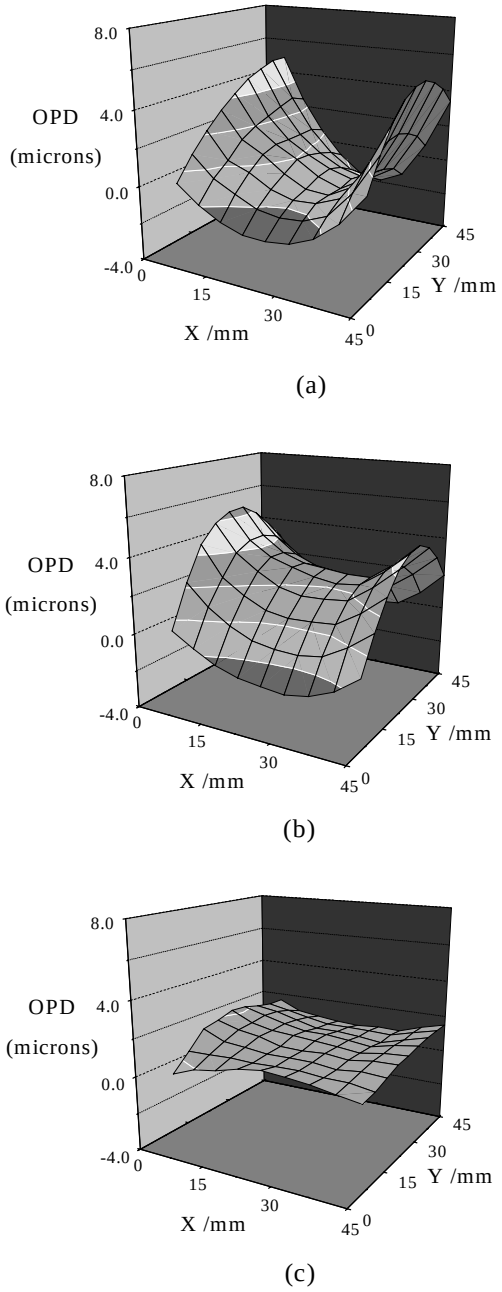

Figure 7. a) Measured OPD of aberrated beam with deformable mirror nominally flat. b) resulting OPD after two passes through the control loop applying curvature correction to actuators within the optical aperture. c) OPD resulting from applying voltages manually to actuators outside the optical aperture to apply correct edge slopes. Curvature correction re-run for two passes.

correction. No attempt was made to compensate for the hysteresis.

CLOSED LOOP TEST

In principle, the correction of curvature solves Poisson's equation within the optical aperture. The solution we arrive at however, may not be the correct one because we have taken no account of the boundary conditions at the aperture perimeter. A unique solution would be obtained if we also apply correct normal slopes at the boundary (Neumann conditions). At present, although we measure slopes at the boundary, we have not yet developed a control algorithm to apply this correction automatically, but it can be done manually.

These features are illustrated in a closed loop test of the system with a static aberrator. Fig. 7(a) shows the OPD of an aberration which was introduced into the beam by placing a piece of melted perspex before the adaptive mirror. After two cycles of automatic curvature correction, the OPD was as in Fig. 7(b) where the average curvature is clearly reduced but is of opposite sense in the *x* and *y* directions. This can only be corrected by applying the correct opposite slopes to the x and y edges of the beam. This was done manually by applying voltages to rows of actuators outside the optical aperture. Fig. 7(c) shows the result which is much flatter and amounts to a five-fold reduction in the OPD of the aberrated beam.

ACKNOWLEDGEMENTS

The authors gratefully acknowledge the work of Dick Carter, Technology Dept. for designing the multi-channel driver and of Leigh Perrot of ISIS Department. for Ansys modelling of bimorph structures.

This work is supported in part by the US Naval Research Laboratory under Contract No N68171-96-C-9099 and in part by AWE, Aldermaston under contract No RCH.0249.

REFERENCES

1) J T Salmon et al.
Proc. SPIE **2633**, 105-113 (1995)

2) W H Southwell
J. Opt. Soc. Amer. **70**, 998-1005 (1980)

EXPERIMENTS ON CHIRPED-PULSE RAMAN AMPLIFICATION

C J Hooker, M J Shaw, J M D Lister
Rutherford Appleton Laboratory

INTRODUCTION

This paper describes experiments on the amplification of chirped pulses using stimulated Raman scattering. Such a process is potentially of interest to all areas of the CLF. For example, production of ultrashort pulses at different wavelengths is useful in both the high and low power laser facilities. In the Vulcan amplifier chain Raman shifting could be used to reduce ASE background and gain narrowing by transferring the bulk of the amplification to the peak of the TiS gain band (806 nm) before Raman shifting (in methane) to 1054 nm for power amplification in glass. On Titania, lower background and better beam quality on the CPA beam would be obtained if chirped pulses could be amplified in the Raman chain. There have been previous reports of Raman generation using chirped pulses[1,2] and work on fibre Raman amplifiers e.g.[3] where chirp is a consequence of g.v.d., but there appears to have been no investigations of Raman amplifiers where chirped pulses are used with bandwidths considerably greater than the Raman linewidth. In principle, such a situation should not affect Raman gain providing the chirped pump and Stokes maintain a constant frequency difference $\omega_R = \omega_P(t) - \omega_S(t)$ centred on the Raman frequency. We undertook these experiments to see if this were so.

EXPERIMENT

We used the CPA oscillator of the Titania laser system as a source of chirped pulses at 249 nm. This gives pulses of 50 ps duration with a bandwidth of 80 cm^{-1} capable of recompression to 250 fs. Two beams were split off and sent to a KrF discharge laser operating at 8 Hz and synchronised with the pump laser of the Ti:sapphire amplifier. After the first pass of amplification, one of the beams was used to drive the Raman generator, while the other beam was further amplified in a second pass through the discharge laser to provide a pump beam for the Raman amplifier. The layout of the KrF discharge laser and the Raman generator and amplifier is shown in Figure 1. The Raman medium was pressurised methane at up to 3.5 bar.

For most of the measurements the input energy to the generator was adjusted so that three or four Stokes orders were produced, as this was found to yield the most consistent energy in the first Stokes. The beam emerging from the generator was dispersed using a prism. The first Stokes was selected with a 1 mm pinhole, then spatially filtered and collimated to give a diffraction-limited beam of 4 mm diameter at the input to the amplifier. The Stokes was injected into the amplifier through a dichroic mirror having about 80% transmission at 268 nm, which was also the final steering mirror for the pump beam. This ensured the two beams could be made collinear. A prism immediately after the amplifier separated the two wavelengths so their energies could be measured individually.

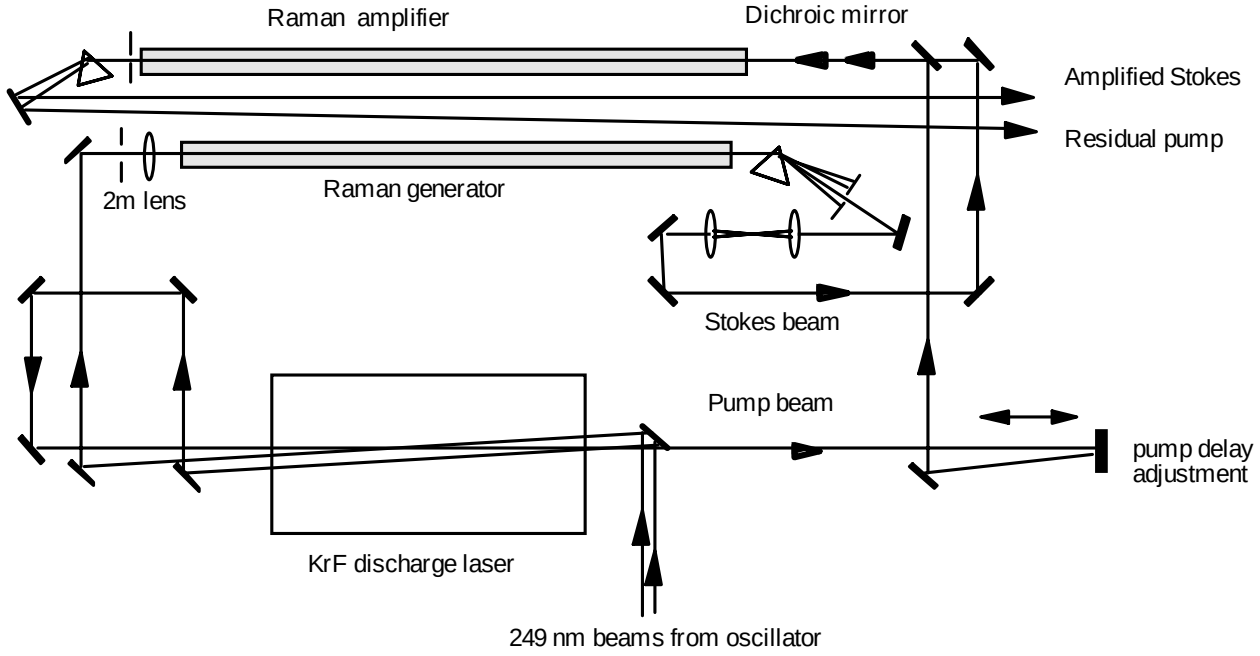

Fig. 1. Experimental set-up

RESULTS

We measured the threshold for Raman generation with chirped pulses by reducing the input to the generator. With a x2 attenuating filter in the input beam, an iris was adjusted until the first Stokes was seen only very rarely when the input energy was abnormally large. Repeated trials consistently gave iris diameters between 1.7 and 2.0 mm. When the filter was removed, the first Stokes was seen on almost every pulse, indicating that the threshold lay between the two energies defined by the presence and absence of the filter. The average (116 μJ) of these two values was taken to be the threshold. The methane pressure used for this measurement was 3.5 atmospheres.

For comparison, we measured the threshold for unchirped pulses of 60 ps duration with near transform-limited bandwidth under similar experimental conditions (3.3 bar pressure) and using the same technique. The result (93 μJ) was essentially equal to the chirped pulse threshold within the rather large margins of error of these measurements.

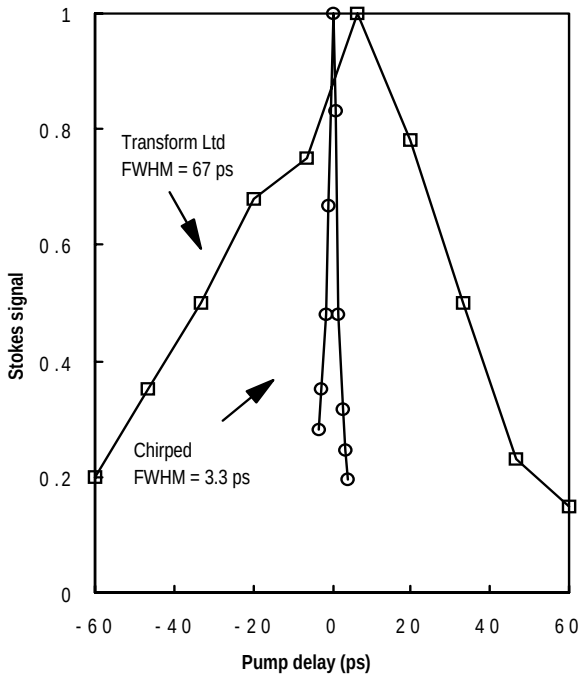

Fig. 2. Timing curves for the Raman amplifier for transform limited and chirped pulses

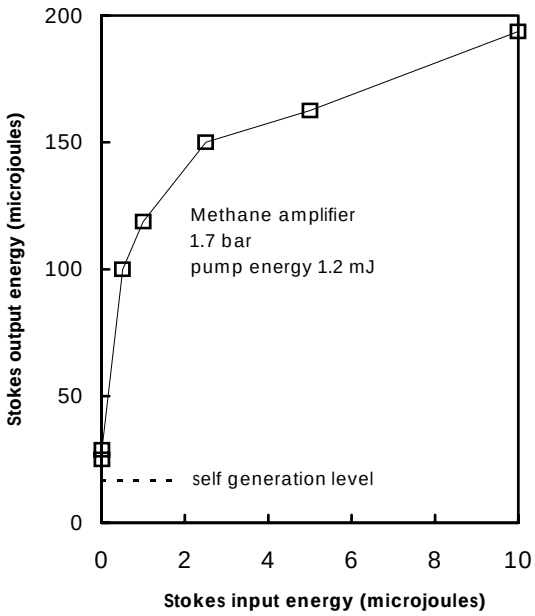

Fig. 3. Saturation curve for the chirped-pulse Raman amplifier at optimum timing

As might be expected, in order to see gain in the amplifier with chirped pulses the delay between pump and Stokes had to be adjusted quite precisely. Figure 2 shows typical timing curves for the amplifier for both transform limited pulses and chirped pulses. Timing curves for chirped pulses were measured under a variety of conditions of methane pressure, pump energy and Stokes input and yielded values for the FWHM of between 1 and 3.5 ps. Unfortunately, the signals were rather noisy and we could not take enough data to discover a systematic variation, if any, with these parameters.

Finally, we measured the saturation curve and extraction efficiency of the amplifier. Figure 3 shows the Stokes input/output characteristic obtained at a methane pressure of 1.7 bar. The amplifier is clearly driven into saturation but the best overall conversion efficiency is still quite low being about 15%. This efficiency is averaged across the whole beam. The local efficiency in the beam centre measured through an iris was found to be 25%. Measurements at 3.5 bar gave a somewhat higher overall conversion efficiency in the region of 20%.

CONCLUSIONS

Raman generation from chirped pulses is perfectly feasible and has essentially the same threshold as for equivalent transform limited pulses. Chirped-pulse Raman amplifiers have a stringent requirement on timing between pump and Stokes. The conversion efficiency of the amplifier although useful, was rather lower than expected from theory (see elsewhere in this report).

REFERENCES

1) N J Everall, J P Partanen, J R M Barr and M J Shaw
Optics Comm. (64), 393 (1987)

2) C Jordan, K A Stankov, G Marowsky and E J Canto-Said
Appl. Phys. (B 59), 471 (1994)

3) C Headley and G P Agrawal,
JOSA (B 10), 2383 (1993)

THEORY OF CHIRPED-PULSE RAMAN AMPLIFICATION

G H C New

Laser Optics & Spectroscopy Group, Department of Physics, Imperial College, LONDON, SW7 2BZ

Chirped-Pulse Raman Amplification (CPRA) is a close counterpart to the well-known process of Chirped-Pulse Amplification (CPA). In a KrF-Raman system, chirped 249 nm pulses would be amplified in the normal way, but dechirping would take place ***after*** Raman conversion rather than before. Naturally, for this process to work successfully, the Raman process would have to take place with chirped pump pulses generating chirped Stokes pulses; if there were hidden problems in this step, they would have to be overcome before CPRA could become viable.

This report outlines the results of a theoretical feasibility study of the CPRA process. The key point to note at the outset is that, for pump and Stokes pulses that are initially chirped in an identical fashion, and that remain in step throughout the generation process, the results are exactly the same as for unchirped pulses with the same envelope. This follows from the structure of the standard coupled-wave equations for Stimulated Raman Scattering (SRS)[1)] where the phonon wave is driven by the field combination $E_pE_s^*$ in which identical frequency modulation on the pump and Stokes waves evidently cancels out. At the same time, the equations for the pump and Stokes fields are driven by the respective combinations E_sQ and E_pQ^*, so the phases match here too.

Only two possible problems can therefore arise. If the pump and Stokes waves do not have same initial frequency modulation and/or the waves get significantly out of step either in the angled-beam geometry of the Raman amplifiers or through group velocity dispersion, the Raman conversion process will be impaired. Fortunately, the process of phase-pulling[1-2)] works strongly to correct phase discrepancies in SRS, and the entire problem therefore boils down to the question whether the experimental deficiencies are sufficiently severe to elude the healing properties of phase-pulling.

One aspect of the problem that cannot be avoided is the fact that the initial Stokes pulse is generated from noise and is moulded to match the pump pulse by the phase-pulling process. But this is no more of a problem in CPRA than in the standard Raman process, because the accuracy of phase replication is unaffected by the fact that in one case the pump pulse is chirped and in the other it is not.

Pilot experiments[3)] already conducted at RAL have involved essentially collinear pump and Stokes beams. We have therefore focused our attention on the timing precision needed to ensure good conversion efficiency with chirped pump and Stokes pulses. The 50 ps pump pulses typically contained 900 μJ and had a bandwidth of 80 cm^{-1}; this corresponds to a frequency sweep of 50 GHz/ps. The Stokes pulse energy was around 13 μJ but are assumed to be the same as the pump pulses in other respects. The beam diameter was 4 mm, the methane cell length 3 m, and the methane pressure 1.7 bar.

Since the Raman bandwidth is around 30 GHz (T_2 = 27.9 ps in methane), a rough calculation suggests that the timing accuracy needs to be better than a picosecond (≈ 30 GHz/50 GHz ps^{-1}). This expectation is confirmed in fig. 1 which shows the conversion efficiency as a function of the relative pump/Stokes timing. The upper curve is for the full 3 m length of the Raman cell, while the lower is at half that distance. The width of the latter is approximately 600 fs, exactly as predicted, whereas saturation has broadened the upper curve to over 1 ps. Making approximate allowance for group velocity dispersion between the pump and Stokes pulses lowers the efficiency by about 10%, but leaves the timing curve basically unchanged.

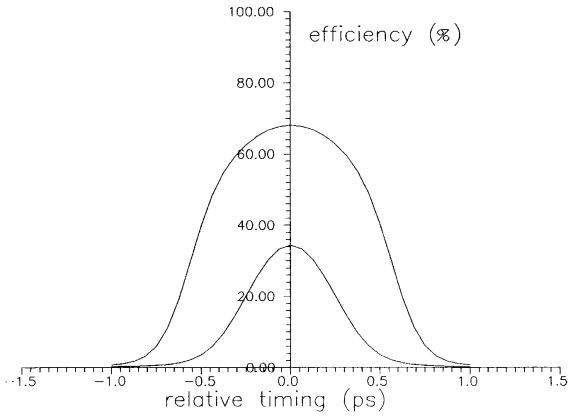

Fig. 1 Timing curve for CPRA

A convenient performance test of the CPRA process is to look at the quality of the Stokes pulse after compression. Our code calculates the frequency sweep of the Stokes pulse coming out of the Raman cell and attempts to compute the optimal compression factor. A typical example is shown in fig. 2 which shows the initial pump profile (broad solid curve), the final pump (dotted), the output Stokes (lower solid curve), the compressed Stokes the peak of which is off-scale. The FWHM in this case is 320 fs which compares with the figure of 250 fs which would apply if the full bandwidth of the pump could be utilised.

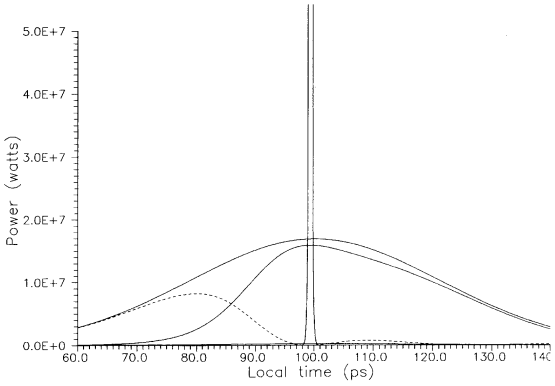

Fig. 2 Pulse profiles showing the dechirped Stokes

Simulations of the Stokes pulse generation process have also been performed. We have demonstrated the growth from noise of Stokes pulses driven by an accurately-chirped pump pulse. Transient effects ensure that the Stokes profiles lie towards the rear of the pump and hence, for an up-chirped pump, are slightly biased towards higher frequencies. The bandwidth is also lower than that of the pump for the same reason and this will present a further slight limitation on the width of the final Stokes profile after compression.

1) K.E. Hill, G.H.C. New, P.A. Rodgers and K.Burnett, Opt. Commun., 87, 315 (1992).

2) M.D. Duncan, R. Mahon, L.L. Tankersley, G. Hilfer and J. Reintjes
J. Opt. Soc. Am. B, 7, 202 (1990).

3) C. Hooker, M J Shaw, J M D Lister
See elsewhere in this Report.

THE ULTRAFAST SPECTROSCOPY LABORATORY PICOSECOND OPA SYSTEM

M. Towrie, P. Matousek, W. Shaikh, G. Gaborel

Rutherford Appleton Laboratory, Chilton, Didcot, Oxon, OX11 0QX, UK.

INTRODUCTION

Many ultrafast time-resolved techniques require two broadly and independently tunable, synchronised light pulses. Recent advances in short pulse laser technology and non-linear crystal materials such as BBO have encouraged the rapid development of optical parametric oscillators (OPOs) and traveling wave optical parametric amplifiers (OPAs) capable of meeting the needs of ultrafast spectroscopists. We have developed kilohertz repetition rate OPA systems providing a stable, high repetition rate, high spectral brightness laser source tunable through the UV and visible wavelengths[1]. The system is optimised for femtosecond/picosecond, pump and probe time-resolved absorption, reflectance and resonance Raman spectroscopies.

DESCRIPTION OF THE SYSTEM

The OPA system is based on two type I BBO (5mm, 27°) crystals which are pumped by a single Spectra-Physics titanium sapphire regenerative amplifier system operating at 1 kHz repetition rate around 800 nm, 600-800μJ pulse energy and ~1 ps pulse width (figure 1)[2]. Figure 2 is a more detailed diagram of the narrow linewidth OPA. A three stage pump arrangement is used in each OPA. The first stage generates seed light by optical parametric generation, OPG, ('superfluorescence' generation). A 60 cm lens, f1, focuses a ~20 μJ split of 400 nm pump light into the BBO crystal. Tilting this lens creates an aberrated focus elongated in the direction of angle walk-off between pump signal and idler within the crystal. Since the total gain is a stronger function of effective crystal length than of pump intensity this enhances the OPG process. For the second stage the same pump beam and the OPG light are retro-reflected back to the crystal. The pump beam is re-focused into the crystal using lens f2. Group velocity mismatch accrued in the OPG stage is compensated by a 'magic' mirror. The output from this stage is a beam with several 10's of nJ of energy and provides good quality seed light for the final amplifier stage. Both OPAs use this configuration but OPA 1 uses a grating dispersion element, G, to spectrally filter the pulse prior to injection into the final amplification stage. This filter also reconstitutes the beam with

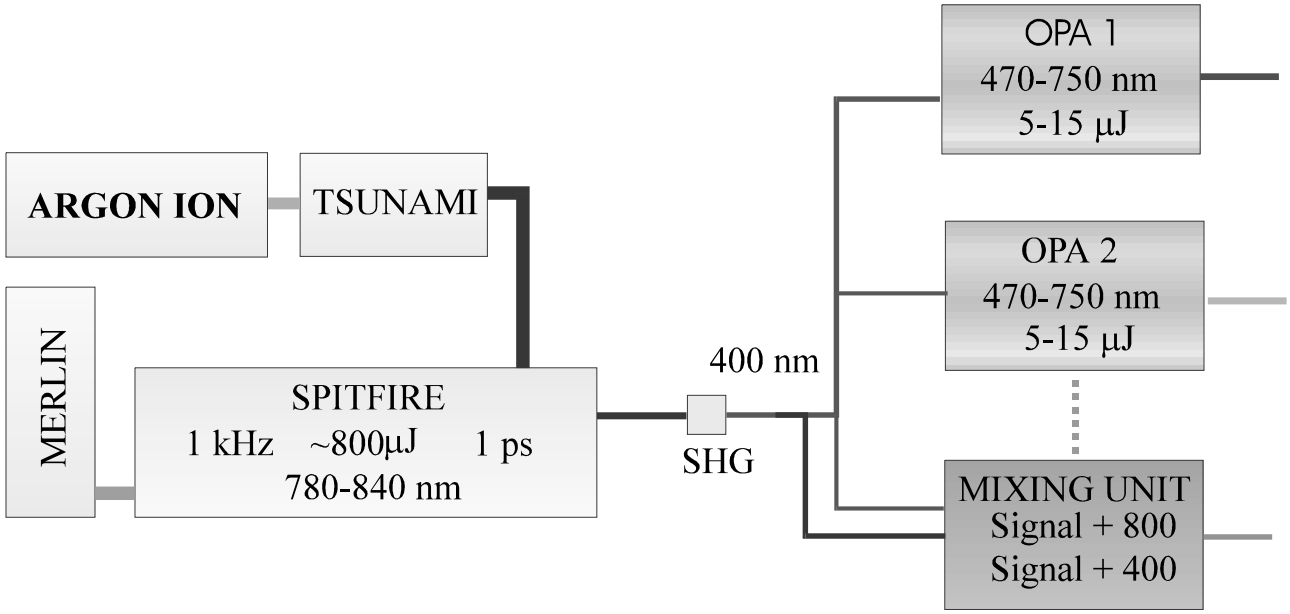

Figure 1: The Ultrafast Spectroscopy Laboratory picosecond OPA system

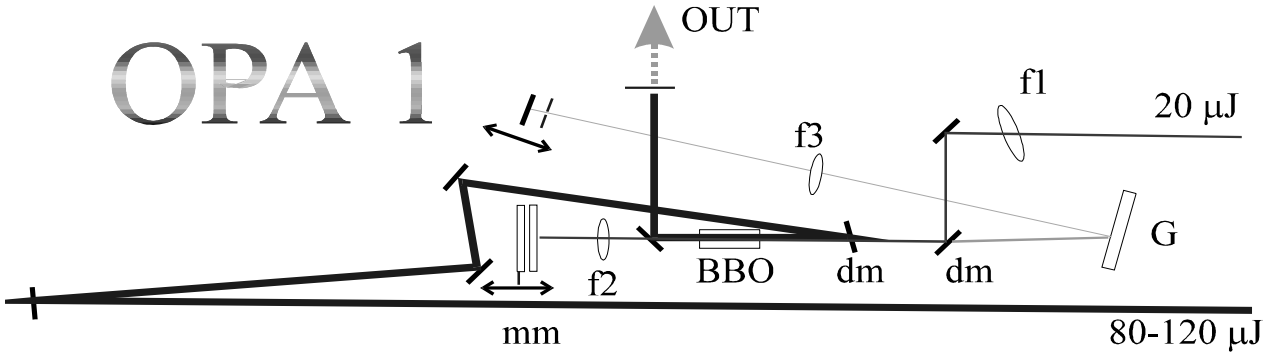

Figure 2: Expanded view of OPA 1. BBO = type I beta barium borate crystal, f1,2 and 3 are focusing lenses. DM are dichroic mirrors. G is a 600 l/mm grating. mm is a 400 nm dichroic mirror and broadband mirror combination with variable separation.

no spatial chirp before final amplification and lifts the seed beam in the vertical plane so that the amplified light can be picked off.

For the last stage the pump beam energy in OPA1 is typically 80-120 μJ and in OPA2 60-80 μJ. Care is taken to maintain good spatial beam quality in the pump and to minimise beam divergence because these have adverse effects on efficiency and linewidth. The overall pump to signal conversion efficiency of OPA1 and OPA2 is 10 % and 15 % respectively.

Typical performance curves for the OPAs are shown in Figure 3. Using both OPAs and a combination of non-linear conversion processes continuous tuning from 220 - 2200 nm at > 0.1-1 μJ at the sample is possible. We estimate the spatial beam quality to be < 2 times diffraction limited and the time bandwidth product 1.8 times that of a Gaussian pulse. Shot to shot stability is around ± 10% but constant output is routinely maintained over 10 hours or more greatly facilitating the acquisition of weak Raman signals.

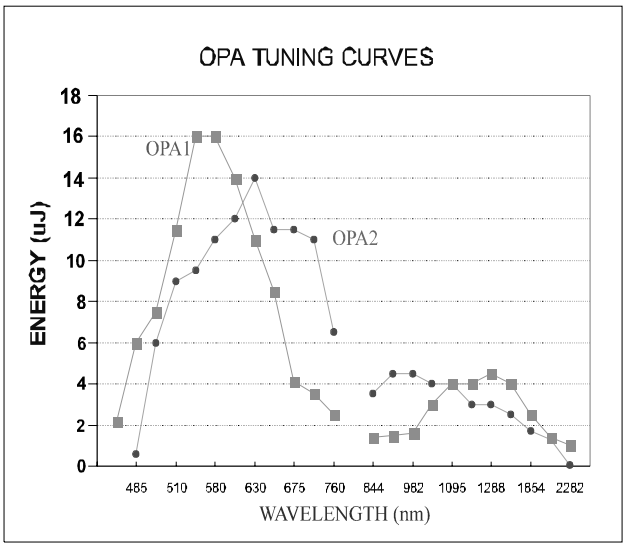

Figure 3: Signal and idler tuning curves.

For some applications where the ps TR^3 spectroscopy may require higher spectral resolution the OPA beams can be further spectral filtered using another external grating pulse shaper like the one used before the third stage of OPA1.

SPECTROSCOPIC APPARATUS

The Ultrafast Spectroscopy Laboratory houses apparatus designed for time resolved resonance Raman (TR^3) spectroscopy and complimentary transient absorption and gain spectroscopy. An optical delay up to 6 ns controls timing between pump and probe to a level of better than 50 fs. For the TR^3 experiments, beams are overlapped at the sample in a crossed beam arrangement of a few degrees using broadband aluminium mirrors and individually adjustable focusing lenses. Overlap at the sample is made using an achromatic equivalent plane imaging system consisting of a thin beam splitter, a 50 μm dye cell containing a near IR dye and a CCD with microscope objective to image the fluorescence from the pump and probe beams. The sample is renewed shot to shot by flowing the sample in an open jet. Raman scatterer light is collected in a conventional spectrometer with high quality liquid nitrogen cooled CCD.

TR^3 PERFORMANCE

The power of this new facility is demonstrated by high quality data obtained from recent experiments. More detailed of the research can be found in the Proceeding of the Conference on Time Resolved Vibrational Spectroscopy VIII[3,4,5] recently hosted by RAL and in this report.

Figure 4 shows the spectra of the S_1 excited state of quaterphenyl taken using the frequency mixed output from OPA2 at 300 nm to pump and 605 nm probe generated in OPA1. Recent experiments on quaterphenyl[3] show this to have remarkably simple electronic state features in its excited state and new dynamics hitherto not observed.

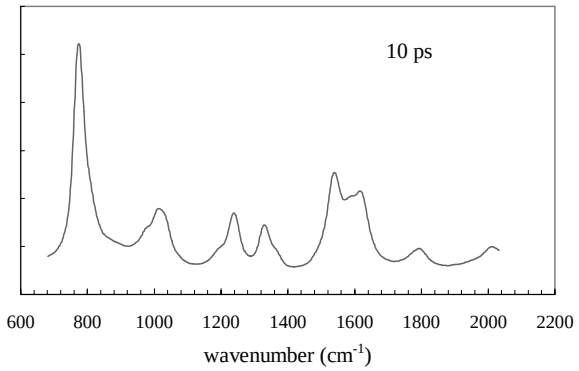

Figure 4: TR^3 spectrum of S_1 quaterphenyl pumped at 300 nm and probed at 605 nm.

Carotenes are known to play a major role in photosynthetic processes. They undergo rapid internal conversion on a femtosecond to picosecond time scale from an initially excited S_2 state to close by S_1 excited state. Truscott (Keele) has used TR^3 to study the evolution of electronic and vibrational mode coupling between these states in different solvents immediately after excitation. The carotenes were pumped at 400 nm and 475 nm and probed between 480 -700 nm using both OPAs. Analysis of data is in progress.

An example that uses only one OPA and the third harmonic of the amplifier is the study of *cis*-stilbene[4]. This molecule has been much studied by conventional pump/probe spectroscopies. It is a model system used to study isomerism from an excited state. The new OPA system has made it possible to probe this process by TR^3. This system has never been studied by this technique before because of its very short lifetime of approximately 1 ps and the difficulty in accessing its pump and probe wavelengths. Excellent spectra were obtained and these cast new light on the fast relaxation pathways taken by this molecule.

REFERENCES

1.P. Matousek, A.W. Parker, P.F. Taday, W.T. Toner, M. Towrie. Optics Communications **127** (1996) 307-312

2.M. Towrie, P. Matousek, A.W. Parker, W. Shaikh. *Submitted Meas. Sci. Tech.*

3.W.T.Toner, P. Matousek, A.W. Parker, M.Towrie *TRVS VIII* (To be published)

4.P.Matousek, A.W.Parker, D.Phillips, W.T.Toner, M.Towrie, G.Scholes *TRVS VIII (To be published)*

5.G. Scholes, P. Matousek, A.W.Parker, D. Phillips, M. Towrie *TRVS VIII (To be published)*

SCHEDULES AND OPERATIONAL STATISTICS

VULCAN OPERATIONAL STATISTICS

D. A. Pepler

Rutherford Appleton Laboratory, Chilton, Didcot, Oxon, OX11 0QX, UK. Email D.A.Pepler@RL.AC.UK

In this reporting period (March '96 to March '97) a major facility development programme (comprising a CPA characterisation study and the commencement of the Phase I Petawatt upgrade), and sixteen experiments have been conducted using all four target areas. Twelve of the experiments were for the EPSRC and four for the EU TMR Large Scale Facilities access programme. A broad range of experiments have taken place with a high level of laser shots. The majority of the experiments have been in the two main target areas; west (TAW) and east (TAE).

A total of 9706 shots were fired during the year with 5027 shots into the laser area for test or alignment purposes and 4679 shots being to the target areas. These are comparable to last year's totals (4616 into the laser area and 4704 into the target area) but the ratio of set-up to target shots has been improved. The total number of shots has risen by a little more than 4% but the actual number of disc shots to target has risen by almost 16%. A total of 1742 disc amplifier shots were fired for laser-plasma interaction studies.

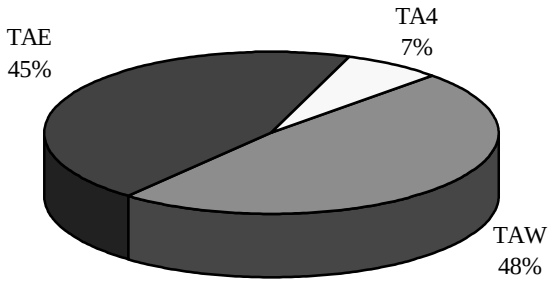

Chart 1 Relative number of shots per area

Experimental set-ups continue to increase in complexity and about 60% of the shots into the target areas were required to establish beam timings, crystal tunings and to set-up and calibrate the instruments and experimental conditions.

Table 1 indicates the full statistics for the experimental programme giving totals for the number of shots fired, target shots (disc shots) and failed target shots for each individual experiment and area. Chart 1 indicates the relative breakdown of the target shots fired into each area.

No significant down time was experienced during the year with only a day or so being lost due to capacitor bank or rod amplifier problems. There were also a number of spurious building fire alarms which caused temporary evacuation of the facility.

EXPERIMENTAL PERIOD Mar '96 - Mar '97	EXPERIMENT (Total number of shots - Target shots - Failed target shots)		
	TAE	TAW	TA4 / TA2
25 Mar - 7 Apr	Heat-flow dynamics (436 - 170 - 4)	Relativistic plasma waves (328 - 118 - 3)	
8 Apr - 5 May			Dense cool plasma studies (42)
13 May - 2 June	RT studies using Hohlraums (370 - 86 - 3)	Self generated magnetic fields (500 - 158 - 0)	
3 June - 16 June			Biological imaging (45)
17 June - 23 June			
8 July - 28 July	XUV radiography (215 - 126 - 2)	Wakefield acceleration (332 - 110 - 2)	
29 July - 18 Aug			
26 Aug - 15 Sep	X-ray scattering (267 - 106 - 1)	E4 Nickles X-ray laser (249 - 187 - 0)	
16 Sep - 7 Oct			
15 Oct - 4 Nov	CPA characterisation studies (762 - 143 - 0)		
5 Nov - 25 Nov	X-ray laser (259 - 223 - 1)	Overdense propagation (510 - 112 - 0)	
26 Nov - 23 Dec			
13 Jan - 2 Feb	Radiation transport (465 - 129 - 3)	E2 Batani Laser shock compression (262 - 142 - 1)	
3 Feb - 9 Feb			E3 Cefalas (42)
10 Feb - 23 Feb			E6 Resendes
24 Feb - 30 Mar	Phase I Petawatt upgrade (26 - 0 - 0)		
Totals	(2012 - 840 - 14)	(2538 - 902 - 6)	(129)

Table 1 VULCAN statistics for the year ending March '97

TITANIA OPERATIONS

E J Divall, G J Hirst, T M J Kendall, A K Kidd and J M D Lister

Rutherford Appleton Laboratory, Chilton, Didcot, Oxon., OX11 0QX, UK

INTRODUCTION

The Titania system started its operational life on 1st April 1996 running in the CPA mode. Four experimental slots were scheduled. The first was used by RAL staff to characterise the laser and the others were taken by external users. The remaining time was used for implementation and testing of the new Raman system.

SCHEDULED OPERATIONS

Titania was initially reconfigured in the CPA mode, primarily to reduce the time and cost of bringing the system back on line. Conversion to the Raman operation was planned for the first year and time scheduled to install and test the new hardware.

Compared to the last year of Sprite's operation the number of scheduled user weeks had fallen significantly to 22. The main reason for this was that later in the year a long period was set aside to implement and test the new Raman configuration. The remaining time was scheduled for routine maintenance and shutdown.

Three plasma physics experiments were run by the Oxford, Imperial and Athens/RAL groups (see Table 1). Full details of each can be found in the 'Science from High Power Lasers' sub-chapter of this report. Between the second and third experiments time was scheduled to install the majority of the large Raman frames. The final hardware set-up and testing was left until after the last experiment to avoid unnecessarily reconfiguring the CPA system. Testing the Raman system took the remaining weeks to the end of the year.

Experiment	Institution(s)	Dates (inc. set-up)	Laser Configuration	Pulse Duration	Typical Energy	Number of Target Shots
Titania Characterisation	RAL	1.4.96-28.4.96	CPA	350fs	300mJ	171
High Harmonic Generation	Oxford Univ.	17.6.96-28.7.96	CPA	350fs	300mJ	210
Solid Target Interactions	Imperial College	5.8.96-15.9.96	CPA	350fs	300mJ	193
Solid High Harmonics	Athens/RAL	18.11.96-19.1.97	CPA	350fs	300mJ	83

Table 1 Scheduled experiments on Titania

LASERS *for* SCIENCE FACILITY (LSF): OPERATIONS AND DEVELOPMENT REPORT

R M Allott, D Balsom, T Fournier, A Foulds, G Gaborel, I Gray, K Henbest, A J Langley, N Lisi, P Matousek, A W Parker, A D Scully, W Shaikh, N Spencer, P F Taday, S M Tavender, M Towrie, I C E Turcu

Rutherford Appleton Laboratory, Chilton, Didcot, Oxfordshire, OX11 0QX, UK.

ULTRAFAST SPECTROSCOPY LABORATORY

The commissioning of the 1 kHz OPA TR^3 system was completed, as scheduled, in January 1997. The upgrade of the OPA system provides pulses of higher spectral brightness needed for ps-TR^3 spectroscopy. This was achieved by decreasing the repetition rate of the regenerative amplifier from 40 kHz to 1 kHz and increasing the pulse duration from 100 fs to 1 ps. The pulse duration was chosen as the best compromise between the spectral and time-resolution for TR^3 spectroscopy. Two picosecond OPA units were developed at the laboratory and replaced existing 100 fs/40 kHz OPAs. The performance of the 1 kHz system meets all and exceeds some of the projected parameters and has lead to an improvement of up to three orders of magnitude in TR^3 signal to noise over the previous 40 kHz system. This enables a wider range of experiments which previously were not feasible. Since the beginning of February 1997 the apparatus has been scheduled for user experiments which confirmed the excellent performance of the system. The twin-OPA TR^3 concept has proved to be an ideal solution to a long standing problem of generating pairs of independently and widely tunable, high energy pulses, synchronised on femtosecond timescale for ps-TR^3 spectroscopy. The new system with its specifications and flexibility now represents a cutting-edge technology in picosecond TR^3 spectroscopy and related picosecond and femtosecond pump and probe techniques. An additional option was provided to operate the system in femtosecond mode. This configuration gives output pulse duration of 200 - 250 fs and may also be used in fs-transient absorption measurements. More details on the apparatus layout and performance can be found in the Development Section of this Report.

The previous 40 kHz twin-OPA system was successfully applied to a range of LSF experiments comprising of ps-time-resolved resonance Raman (TR^3) and femtosecond transient absorption measurements. These experiments are reported in the Chemistry Section of this Report.

FEMTOSECOND SCIENCE LABORATORY

This has been a most successful year for the Femtosecond Science Laboratory. Highlights included the success of Prof. Codling's group from Reading in overcoming the many technical difficulties associated with two-colour superposition experiments. This has enabled them to study and control the dissociation dynamics of hydrogen. A new user group to the Femtosecond laboratory, led by Dr Langridge-Smith from the University of Edinburgh, carried out a highly successful mass spectroscopy study of the photodissociation of large molecules (>600 amu) using 50 fs pulses. Dr Dave Riley from Queen's University Belfast, also a new user, carried out feasibility absorption measurements on plasmas created at solid (aluminium and silicon) surfaces. Technically these experiments were highly successful and demonstrated our capability of carrying out reflectivity experiments, including pump and probe, on surface generated plasmas. These and other reports from this laboratory are covered in more detail elsewhere in this year's Annual Report.

The most exciting development of the year was EPSRC's funding to upgrade the femtosecond laser to the terawatt level. The proposal was a collaborative venture between RAL and 6 University groups. The upgrade will enable these groups to carry out a range of experiments in femtosecond mass spectrometry, molecular dissociation in intense fields, femtosecond plasma physics and to study high harmonic generation in various environments.

During the year 10 experiments were conducted in the Femtosecond Science Laboratory in 42 weeks of scheduled time. A total of 7 refereed papers were published and at least 5 conference presentations were made by users of the facility. The CCLRC mounted an exhibition stand at the Institute of Physics Congress (Leeds, Spring 1997) for which the LSF provided material and the femtosecond upgrade was highlighted.

LASER MICROSCOPY LABORATORY

The development of the confocal laser scanning microscope (CLSM) was completed in September 1996. The new optical design, presented in this Annual Report, has demonstrated the capability of sub-micron optical sectioning. The first steady-state fluorescence images were generated in November. The microscope is capable of generating gated fluorescence images with durations as short as 120ps and has been used to carry out time-resolved fluorescence lifetime imaging experiments. In a recent experiment the intracellular fluorescence lifetime of the sensitizer disulphonated aluminium phthalocyanine was mapped (Phillips/MacRobert) , enabling the determination of the intracellular distribution of the drug. Future work will include imaging experiments to determine intracellular distribution of physiologically important ions such as H^+ and Ca^{2+}.

For two weeks in January the laser microscopy lab hosted an EU funded experiment as part of a collaboration between researchers from Loughborough and Lisbon Universities. Fluorescence lifetime measurements of cyanine dyes in cellulose matrixes were studied. Interesting time resolved fluorescence data suggested the evidence of a photo-isomer produced at the surface, confirming previous steady state data. A contribution to the RAL annual report has been submitted and the researchers have applied for further laser time in the Autumn in the Microscope and Ultra Fast Spectroscopy laboratories.

The single photon counting apparatus was rebuilt during March and April. The work has been carried out by Dr Anita Jones/Peter Jennings (Edinburgh) and Mike Towrie (RAL). The system included a new monochromator and sample holder designed in Edinburgh. The acquisitions and data analysis software will be upgraded in the near future. The current instrument response is ~120ps. The system will be used for the measurement of the ~1-5 ns lifetimes of electro-polymerised indoles excited at 300nm.

The picosecond dye laser energy and beam quality had been deteriorating over a period of months. The laser was replaced with the identical spare and the system realigned. Service engineers have optimised the Spectron YAG (pump) and the dye laser to give a much improved system. Specifications of 2.2 W from the YAG and 100mW at 600nm have now been achieved. A Pentium computer with CD writer was installed with a 2 G byte hard drive. This will be used as an analysis computer and is interfaced to the data acquisition computer. The OFA software for the microscope is being upgraded for automated z-sectioning with a series of programmable delays.

LASER-PLASMA X-RAY AND UV LABORATORY

The team running the laboratory this year was composed of Edmond Turcu (manager), Ric Allott (deputy), Nicola Lisi (EU fellow) and Nick Spencer (student). At the end of the year Ric moved to Vulcan and Waseem Shaikh has taken on the responsibilities of being deputy for this area. Nicola moved to CERN-Geneva and was replaced by Nobuyuki Takeyasu (scholarship from Kyushu University - Japan).

During the year a total of 12 scheduled experiments were carried out in 39 weeks. 1 week was used for maintenance and 2 weeks for the installation of the new Lumonics (PM846) excimer laser (25W @ 100Hz @ λ = 308nm) which replaces a seven year old Questek laser, to pump the picosecond laser dye amplifiers.

The new VUV beamline, continuously tuneable from 30nm to 250nm, has demonstrated an output of 10^{13} photons/s/cm^2/1% Bandwidth at the user cell, using the $\Delta\lambda/\lambda$ =1% grating spectrometer. For higher resolution spectroscopy a 1m grating spectrometer/UV beamline with $\lambda/\Delta\lambda$ =0.1% was used. The Universities of Edinburgh and Glasgow experiment obtained high resolution single photon ionisation spectra and ion-pair spectra.

A new "imaging X-ray fluorescent spectrometer" for low Z elements, using the plasma source, was demonstrated by the University of Leicester group. The fluorescent image of a composite Al/Ni target was resolved with very low X-ray exposure (even single shot).

The CRC-Gray Lab experiment has demonstrated the feasibility of performing simultaneously, both <100nm space resolved and 10ps time resolved cell radiobiology with soft X-rays (3.37nm) using Zone-Plate optics and a single 10ps X-ray pulse from the plasma source.

The Universities of Milan and Modena experiment (European Large Scale Facility Project) have successfully used the new "two colour" X-ray technique for differential X-ray exposure of the membrane and nucleus of the yeast cell, which was correlated with a change in the cell metabolic response.

The MRC Harwell experiment concluded that the major DNA damage brought about by 193 nm irradiation results from radical ions with the damage focusing on guanine cations.

The University of Warwick experiments successfully used laser deposition to grow up to 40 multilayers of Ni/Ag thin films for the study of giant magneto-resistance effect with applications in high sensitivity magnetic read/write devices.

The large amount of new scientific information was disseminated through: 14 papers in refereed journals and conference proceedings, 1 patent, 12 conference presentations, 10 lectures in the UK and abroad and 5 articles in specialist magazines.

NANOSECOND SCIENCE LABORATORY

The year has been a very busy one resulting in 11 published papers from work carried out in the nanosecond laboratories. The new OPO technology has proved somewhat problematic with four major breakdowns during the year. A contract has now been established to service the system every 3 months and we are confident this will maintain output specifications. The possibility of pumping a dye laser with the 355 nm output of the YAG is also being investigated.. The OPO frequency doubling unit was successfully installed and a major benefit of the new optical layout is that no re-alignment is required when only the fundamental is required. Conversion is 10% of fundamental with two BBO crystals used in parallel, one acting as doubler and the second as compensator. A beam alignment system which allows easy interchange between the dye and OPO laser beams for Raman experiments has been designed and installed and uses a diode laser to back-align the Raman system from the sample chamber to the lasers which are sited 5 m away in a different laboratory. Finally, safety screens were installed to give dedicated workstations for the TR^3 and LFP experimental set-ups.

In July the nanosecond laboratories played host to the CREST (Creativity in Science and Technology) scheme - a national award scheme to place sixth form students into leading research facilities and so give them first hand knowledge of working in a research environment. The six students were given a crash course in photochemistry and spent a week carrying out experiments to measure the lifetime of phthalocyanines (which they first had to purify) using the laser flash photolysis apparatus and also ran ground state Raman experiments of alcohol mixes.

Scientific highlights from the nanosecond laboratories include the Phillips (IC) group with their investigations of the electron and energy transfer reactions in polar and non-polar solutions indicating that it is the dielectric constant of the solvent medium that determines which relaxation mechanism will occur. Bisby (Salford) has continued his successful programme on the radical enzyme pea seedling amine oxidase as well as investigating the structure of the carbonate radical, a powerful oxidant which acts as an intermediate in free radical mediated damage in biological systems. Interestingly, Truscott (Keele) have been independently investigating the isoelectronic NO_3 radical using TR^3. Simpson (Oxford) used the polarised OPO beam to probe desorbed NO from the dielectric surface and found a clear polarisation effect which determined the rotational energy of the desorbed molecule i.e. if it rotated like a 'cartwheel' or a 'helicopter' which is related to the J vector of the molecule. These results are described in more detail elsewhere in this year's annual report.

LASER LOAN POOL

The major highlight has been EPSRC's full support of the Loan Pool Facility for the next 4 years. The Review panel recognised the User Community's scientific excellence and high quality of support provided by the LSF. The award includes marginal funding to maintain Loan Pool lasers at less than 5 years of age, as recommended in the Longaire Review (1995). The recently completed Loan Pool upgrade places the Loan Pool in an extremely strong position to fulfil its role. We thank the user community for their support.

Over the last 4 years the facility has provided lasers for around 60 loan periods with over 31 different researchers in a wide range of chemistry, physics, engineering and medical experiments. During this period demand for loan lasers exceeded laser availability by nearly 1.5. About 50 % of laser time was allocated to grant holders and the remainder to non-grant associated projects. The total of 79 publications stemming from the Loan Pool over the last 4 years represents excellent value for money and use of resources.

This year's highlights include the investigations by Smith (Birmingham) who used the tunable nanosecond IR and UV lasers to study the reaction kinetics of low temperature gases. He made the observation that rates stay or become fast as the temperature is dropped to very low temperatures (*c.* 20 K). Simons (Oxford) has begun to investigate the structure and photophysical behaviour of (bio)organic molecules in small clusters. This approach probes the direct interaction between solute and solvent and is of primary importance in understanding the nature of chemical reactivity in condensed matter.

The CW lasers have supported research in the area of communications, optical processing and storage, short wavelength laser diodes, ultrashort pulse generation and as a probe for laser drilling. For example, Eason (Southampton) has found new diode laser compatible photorefractive materials with high phase conjugate reflectivities permitting coupling between two laser beams. This will provide distortion control of laser beams. Wilkinson (Southampton) has reported on investigations into the design and potential uses of tunable integrated waveguide lasers. These miniature devices may be built on wafers and can be modulated in amplitude, phase or may be made to produce very short pulses by Q-switching or mode-locking techniques by controlled application of voltages.

In developing the Loan Pool we always note the views of the user community. There remains much interest in OPO and other new technologies such as diode pumped lasers. We are still cautious about the use of OPO systems within the Loan Pool environment and believe that the technology needs another year or two to reach the required reliability. However, we will constantly review developments throughout the grant. In the immediate future it seems appropriate to replace ageing lasers with similar conventional systems. Later this year the aged PDL2 lasers will be replaced, and possibly one or both of the WEX units. As anticipated, the introduction of a mode-locked fs titanium sapphire laser into the Loan Pool was strongly endorsed. This is to be made available in late 1997 and will be pumped by the Millennia diode pumped laser. The grant also provides additional funding for purchasing of hardware to support experimenters. We see laser beam diagnostics to characterise laser output as a priority and will be purchasing a high quality wavemeter and 2 fast (500 M samples/s) digital scopes.

LSF OPERATIONS FACTS AND FIGURES

This year a total of 55 RAL-based experiments were carried out over 164 weeks of laser time. LSF Loan Pool lasers were loaned for 6.3 years of time to 17 university research groups.

The table below shows LSF usage by sponsor for both RAL-based facilities and the Laser Loan Pool.

Sponsor	Scheduled time	Total per sponsor	%
RAL based experiments:	**Weeks**		
BBSRC			
Grant approved	13	19	11
Feasibility experiments	6		
EPSRC			
Grant approved	66	133	76
Unfunded Programme	6		
Feasibility experiments	55		
Division head's allocation	6		
EU	6	6	3
MRC	5	5	3
NERC	1	1	1
Other			
Maintenance		9	5
CREST		1	1
Total		174	
Loan Pool Experiments:	**Months**		
EPSRC			
Grant approved	28.6	71.8	95
Non-grant associated	43.2		
NERC	4	4	5
Total		75.8	

ACKNOWLEDGEMENT

Thanks to the engineering and support staff for their outstanding support of the science programme namely; Chris Reason, Andy Fracwiecz, John Govans, Bill Lester, Cyril Brown, Garry Williams, Alison Brown, Chris Naboulsi and Katharine Hale.

SCHEDULE OF RAL-BASED EXPERIMENTS AT THE LASERS *for* SCIENCE FACILITY 1996/97

Week start	X-RAY LABORATORY	NANOSECOND LABORATORY	FEMTOSECOND SCIENCE LABORATORY	ULTRAFAST SPECTROSCOPY LABORATORY	LASER MICROSCOPY LABORATORY	Week start
11 Mar			**LEDINGHAM/ SINGHAL/ KOSMIDIS/SMITH** (Glasgow/RAL)	COMMISSIONING EXPERIMENTS FOR ULTRAFAST SPECTROSCOPY FACILTY		11 Mar
18 Mar	**O'NEILL/MELVIN/ CULLIS/PARKER** (MRC/Leicester/RAL)	**FOURNIER/PHILLIPS/ SCHOLES/PARKER** (Imperial College/RAL)				18 Mar
25 Mar	Time resolved studies on photoionisation of DNA	Electron transfer: a ns time resolved resonance Raman study	Femtosecond laser mass spectrometry as an ultra-sensitive analytical technique FL04P3/95			25 Mar
1 Apr	XU06M3/95					1 Apr
8 Apr	MAINTENANCE	NL03C3/95	**DONOVAN/ SHAIKH/ FLEXEN** (Edinburgh/RAL)	DEVELOPMENT FOR TRANSIENT ABSORPTION AND PICOSECOND RAMAN APPARATUS		8 Apr
15 Apr	**ALLOTT/TURCU/ LEDINGHAM** (RAL/Glasgow)	**SIMPSON/TOWRIE** (Oxford/RAL)				15 Apr
22 Apr	Spectral characterisation of a laser-plasma source in the vacuum UV	The dynamics of the photolysis and desorption of physisorbed nitrites and carbonyls	High harmonic generation for XUV spectroscopy			22 Apr
29 Apr	XU01P3/95	NL05C3/95	FL01C3/95			29 Apr
6 May	**ALLOTT/TURCU/ LEDINGHAM** (RAL/Glasgow)	**SIMPSON/TOWRIE** (Oxford/RAL) Photofragmentation spectroscopy and photofragment spectroscopy and the	**NEWELL/WILLIAMS** (UCL/QUB)		DEVELOPMENT OF CONFOCAL MICROSCOPE	6 May
13 May	VUV development	dynamics of photolysis of molecules on a dielectric Surface NL06C1/96	Multiphoton dissociation of excited molecules by femtosecond laser interactions	**TONER et al** (Oxford/RAL)		13 May
20 May	XU5P1/96	**McGARVEY/ TRUSCOTT/ WAYNE/TAVENDER** (Keele/RAL)		Pico and femtosecond time resolved resonance raman studies of the relaxation of photo-excited molecules in solution		20 May
27 May	**MANN/CRONIN/ CAIRNS** (RAL/Bath/Dundee)	A TR^3 study of the reactions of the nitrate radical with organic molecules in solution	FL02P1/96			27 May
3 Jun	Resist and Mask Preparation	NL03C1/96	**RILEY/LANGLEY/ SHAIKH/TADAY** (QUB/RAL)	US05C1/96		3 Jun
10 Jun	Optimisation for Deep/High Resolution X-ray Lithography	**FOURNIER/PHILLIPS/ SCHOLES/PARKER** (Imperial College/RAL)	Pulse-probe absorption measurements	**SCHOLES/PHILLIPS/ PARKER** (IC/RAL)		10 Jun
17 Jun	XU04P1/96	A time resolved resonance Raman study of TICT	on plasma generated at solid surfaces	Picosecond time resolved		17 Jun
24 Jun	**WYBREW** (Oxford) VUV experiment XU6P1/96	Molecules		resonance raman studies of solvent re-organisation after charge separation		24 Jun
1 Jul	**TURCU/ALLOTT/ LISI/ROSS/WHITE/ WILLIAMS/ KHRUSCHEV** (Bath/RAL)	NL04C1/96	FL03P1/96	US04C1/96		1 Jul
8 Jul	Laser-Plasma X-ray Source Research and Development	**CREST**	**FRASINSKI/ CODLING** (Reading)	**BISBY/PARKER** (Salford/RAL)		8 Jul
15 Jul		**PHILLIPS/OLDHAM/ OSTLER** (Imperial College) Photophysics of urocanic acid and	Coherent control of the dissociation dynamics of diatomic molecules in intense laser fields	Picosecond dynamics of de-protonation of α-tocopheroxyl radical cation		15 Jul

Continued....

Week start	X-RAY LABORATORY	NANOSECOND LABORATORY	FEMTOSECOND SCIENCE LABORATORY	ULTRAFAST SPECTROSCOPY LABORATORY	LASER MICROSCOPY LABORATORY	Week start
22 Jul	XU03P1/96	singlet oxygen luminescence from model biological particles NL05C1/96	FL01P1/96	US01B1/96	**SOUTAR/SWANSON** (Lancaster) Investigation of miscibility	22 Jul
29 Jul	**PALMER/ WIDDOWSON/ ALLOTT/TURCU** (Warwick/RAL)	**BISBY** (Salford)				29 Jul
5 Aug	Effect of laser pulse length and tape target on the formation of droplets during	Time resolved resonance Raman and laser flash photolysis of protein radical enzymes		**HESTER/MOORE/ LEDNEV** (York)		5 Aug
12 Aug	the growth of thin magnetic films by laser deposition	NL01B1/96		Ultrafast spectroscopy of azobenzene	**EVANS** (John Moores) Detection of phytobilisome and chlorophyll	12 Aug
19 Aug	XU02P1/96	INSTALLATION OF SAFETY SCREENS				19 Aug
26 Aug	MAINTENANCE			US03C1/96		26 Aug
2 Sept	**WHYBREW/ ALLOTT/TURCU** (Oxford/RAL)	**FOURNIER/ SCHOLES/ PHILLIPS/ PARKER** (IC/RAL)	**LANGRIDGE-SMITH/ MAIER/ HOLLINGSWORTH** (Edinburgh)		**SCULLY/OSTLER/ PHILLIPS** (Imperial College)	2 Sept
9 Sept	Xe^{2+} auger laser at 109nm, pumped by a KrF laser generated	An ns TR^3 study of	Femtosecond mass spectrometry of large biological molecules		Determination of intracellular ion concentrations using	9 Sept
16 Sept	plasma XU06B2/96	electron transfer: comparison between the diffusion-controlled process and the direct	FL4C2/96		time- resolved fluorescence microscopy ML03C2/96	16 Sept
23 Sept	**O'NEILL/CULLIS/ PARKER** (MRC/Leicester/RAL)	excitation of ground-state electron-donor complexes NL04C2/96				23 Sept
30 Sept	The influence of base sequence on DNA strand breakage	**SIMPSON/TOWRIE** (Oxford/RAL)	**NEWELL/WILLIAMS/ SANDERSON** (UCL/QUB)			30 Sept
7 Oct	XU05B2/96	The dynamics of the photolysis of physisorbed carbonyls following	Multiphoton dissociation of excited molecules			7 Oct
14 Oct	**GOODHEAD/ STEVENS/HILL/ KADHAM** (MRC)	($\pi^* \leftarrow \pi$) and ($\pi^* \leftarrow$n) excitations	by short pulse laser interactions	**DEVELOPMENT GRANT** GR/J763692	**GOODALL** (York)	14 Oct
21 Oct	The biological consequences of high-intensity pulsed x-ray exposures	NL04C2/96	FL03P2/96		Direct observation of analyte dynamics in capillary electrochromatography	21 Oct
28 Oct	comparable to high-LET particle traversal times	**BISBY** (Salford)	**FRASINSKI/ CODLING** (Reading)		ML01C2/96	28 Oct
4 Nov	XU02B2/96	Time-resolved resonance Raman and laser flash photolysis of protein-radical enzymes				4 Nov
11 Nov	**ALLOTT/TURCU** (RAL)	NL01B2/96	Wavelength dependence of the dissociation dynamics of diatomic molecules		**MACROBERT/ PHILLIPS** (Imperial College)	11 Nov
18 Nov	Development of VUV beamline	**PEMBLE** (Salford)	FL01P2/96		Time-gated fluorescence bioimaging studies	18 Nov
25 Nov	XU01P2/96	2ω - resonance enhanced optical SHG from adsorbate-modified metal surfaces.	**LEDINGHAM/ SINGHAL/KOSMIDIS** (Glasgow)		ML02C2/96	25 Nov

Continued....

Week start	X-RAY LABORATORY	NANOSECOND LABORATORY	FEMTOSECOND SCIENCE LABORATORY	ULTRAFAST SPECTROSCOPY LABORATORY	LASER MICROSCOPY LABORATORY	Week start
2 Dec	**MICHAEL/ FOLKARD/PRISE/ MICHETTE** (Gray Lab/Kings College)	NL06C2/96	Femtosecond laser mass spectrometry as an ultra sensitive analytical technique		**SOUTAR/SWANSON** (Lancaster)	2 Dec
9 Dec	Radiobiological effects of single-pulse doses of focussed soft X-rays			**COMMISSIONING EXPERIMENTS**	Investigation of miscibility in synthetic polymer blends using 2-photon fluorescence microscopy	9 Dec
16 Dec	XU03B2/96		FL02P2/96		ML04C2/96	16 Dec
6 Jan	**MILANI/BATANI** (Milan Italy)	RAMAN DEV			**FERREIRA/ WILKINSON** (CQPM, Italy/Loughborough)	6 Jan
13 Jan	Study of soft X-ray irradiation effects on yeast cells			**OPA COMMISSIONING EXPERIMENTS**	Photophysics of cyanine dyes at surfaces NL02C2/96	13 Jan
20 Jan		**SIMPSON/TOWRIE** (Oxford/RAL)				20 Jan
27 Jan	XU4B2/96					27 Jan
3 Feb	**FRASER//TURCU/ HOLLAND** (Leicester/RAL)	Photofragment spectroscopy and photolysis studies of adsorbed NO dimers		**MATOUSEK** (RAL)		3 Feb
10 Feb	Imaging X-ray fluorescence spectrometer XU04P3/96	NL05C3/96	**FRASINSKI/CODLING** (Reading)	Picosecond TR^3 spectroscopy of S_1 cis-stilbene US02C3/96	**MACROBERT/ PHILLIPS** (UCL/Imperial College)	10 Feb
17 Feb	**FACILITY DEVELOPMENT**		Coherent control of H_2 studied using electron-ion coincidence techniques	**PHILLIPS** (IC) Picosecond TR^3 studies of structural reorganisation accompanying intramolecular charge separation US03C/96	Time-resolved fluorescence bioimaging	17 Feb
24 Feb	Installation. of new XeCl excimer laser and R&D	**BISBY** (Salford)				24 Feb
3 Mar	**TURCU/ALLOTT/ LAWLEY/DONOVAN/ MICHAEL** (RAL/Edinburgh)	Time-resolved resonance Raman spectroscopy and laser flash photolysis of protein-radical enzymes	FL02P3/96		LM04B3/96	3 Mar
10 Mar	**FACILITY DEVELOPMENT**	NL01B3/96		**BISBY/PARKER** (Salford/RAL) Deprotonation of radicals formed by photoionisation of alpha-tocopherol and analogues studied by ultra-fast spectroscopy US01C3/96	**SPC DEVELOPMENT**	10 Mar
17 Mar	VUV development	**PEMBLE** (Salford)	**NEWELL/WILLIAMS/ SANDERSON** (UCL/QUB)			17 Mar
24 Mar		2ω-resonance enhanced optical SHG from adsorbate-modified metal surfaces	Multiphoton interactions with diatomic and polyatomic molecules FL03P3/96			24 Mar
31 Mar		NL06C2/96				31 Mar

SCHEDULE OF THE LASERS *for* SCIENCE FACILITY'S LASER LOAN POOL 1996/97

Date	NSL1 GCR-11/PDL-3	NSL2 Spectron SL805G/PDL-2	NSL3 Spectron SL805/PDL-2	NSL4 Continuum 8010/ND6000	NSL5 Fluoride excimer	CWL1 2025 Argon	CWL2 3900 Ti:S
April 1							
8	**PEMBLE** **Salford** **LP03C3/95**	**BROWN/** **WHITHAM** **Oxford** **LP01C3/95**	**PFAB** **Heriot-Watt** **LP04C2/95**		**ASHFOLD** **Bristol**	**WALSH** **Reading** **LP05C3/95**	**KACZMAREK/** **SMITH/** **EASON** **ORC**
15					Investigation		
22					into diamond		
29			IR-VIS 2 Photon		film depositing	Time-Resolved	
May 6	Resonant-		Photochemistry		and cutting	Studies	
13	Enhanced	Electronic	of Jet			of the gas phase	
20	Optical SHG	Spectroscopy					
27	from	of Involatile,	Cooled Methyl			Kinetics of	
June 3	Metal &	Metal	Nitrites			Germanium	
10	Semiconductor	Compounds in a				& Tin	
17	Surfaces	Jet Free				Containing	
24		Expansion.	24 wks			Transients	24 wks
July 1			DFG				
8	16wks		INSTALLATION				
15							
22			**PFAB**	**SIMS/SMITH**			**KACZMARE K**
29	**SIMONS/**	16 wks	**Heriot-Watt**	**Birmingham**			**/SMITH**
Aug. 5	**DICKINSON**			**LP05C1/95 &**			**EASON**
12	**Oxford**		IR-VIS 2 Photon	**LP05C2/95**	16 wks		**ORC**
19		**TAYLOR**	Photochemistry				Characterisation
26	Laser	**IC**	of Jet	Relative			Of period poled
	spectroscopy						
Sept. 2	of amide and	**LP8 C2/96**	Cooled Methyl	Inelastic		**WALSH**	photo-conduct
9	amino		Nitrites	Processes in a	**HEAL**	**Reading**	materials &
16	acid-water			Gas	**Edinburgh**		Investigations of
	clusters						
23				Phase at Ultra-		Time-Resolved	New IR
Oct. 7		State selective		Low	**LP02C3/95**	Studies	Sensitive Photo-
14		hydrogen		Temperatures		of the gas phase	Refractive
21		desorption from				Kinetics of	Materials
28		Si(001)			UV detection &	Germanium	
Nov. 4		surfaces	16 wks		Kinetics of	& Tin	
11	16wks				peroxy Radicals	Containing	**KACZMAREK**
18					in Dimethyl	Transients	**/ SMITH**
25					Sulphide		**EASON**
Dec. 2		16 wks	**WHITEHEAD**		Oxidation		**ORC**
9	**HECHT/**		**Manchester**				
16	**BARRON**		**LP9 C2/96**		16 wks		Loan
23	**Glasgow**	**ORR-EWING**					Continuation
30	**LP3 C2/96**	**Bristol**				**FRENCH**	
Jan. 6		**LP6 C2/96**			**McKENDRICK**	**Liverpool**	
13			IR spectroscopy		**Edinburgh**	**LP1M3/96**	
20	Optical activity		of		**LP5 C2/96**		
27	studies		Hydrogen				
Feb. 3	of chiral	A tunable	bonding				
	isotropic						
10	surfaces	photolysis	and solvation in		The dynamics of	Laser Percussion	
17	with non-linear	source	aqueous		elementary	drilling	
24	light	for	clusters		reactive and		
Mar. 3	scattering	photoinitiated	16 wks		inelastic		
10	16 wks	bimolecular			collision		**WHITHNALL**
17		reactions			processes		**Greenwich**
24			**WHITEHEAD**	2x24 wks			**LP3B3/96**
31		16 wks	**Manchester**				

PUBLICATIONS

SCIENCE - HIGH POWER LASER PROGRAMME

JOURNAL PUBLICATIONS AND PUBLISHED CONFERENCE PROCEEDINGS

F N Beg, A R Bell, A E Dangor, C N Danson, A P Fews, M E Glinsky, B A Hammel, P Lee, P A Norreys, M Tatarakis
A study of picosecond laser-solid interactions up to 10^{19} W cm^{-2}
Physics of Plasmas **4**, 447-457 (1997)

A Behjat, J Lin, G J Tallents, A Demir, M Kurkcuoglu, C L S Lewis, A G MacPhee, S P McCabe, P J Warwick, D Neely, E Wolfrum, S B Healy, G J Pert
The effects of multi-pulse irradiation on x-ray laser media
Institute of Physics Conference Series **151**, 247-249 (1996)

A Behjat, J Lin, G J Tallents, A Demir, M Kurkcuoglu, C L S Lewis, A G MacPhee, S P McCabe, P J Warwick, D Neely, E Wolfrum, S B Healy, G J Pert
The effects of multi-pulse irradiation on X-ray laser media
Optics Comm **135**, 49-54 (1997)

A Benuzzi, T Lower, M Koenig, B Faral, D Barani, D Beretta, C Danson, D Pepler
Indirect and direct laser-driven shock-waves and applications to copper equation of state measurements in the 10-40 Mbar pressure range
Phys Rev E **54**, 2162-2165 (1996)

M Borghesi, A Giulietti, D Giulietti, L A Gizzi, A Macchi, O Willi
Characterization of laser plasmas for interaction studies: Progress in time-resolved density mapping
Phys Rev E **54**, 6769-6773 (1996)

M Borghesi, A J MacKinnon, L Barringer, R Gaillard, L A Gizzi, C Meyer, O Willi, A Pukhov, J MeyerterVehn
Relativistic channeling of a picosecond laser pulse in a near-critical preformed plasma
Phys Rev Letts **78**, 879-882 (1997)

G F Cairns, S B Healy, C L S Lewis, D Neely, G J Pert, E Robertson
Spectroscopy studies of the resonance line emission in the Ge XXIII XUV laser
Institute of Physics Conference Series **151**, 380-382 (1996)

G F Cairns, S B Healy, C L S Lewis, G J Pert, E Robertson
A time-resolved spectroscopy study of the resonance-line emission in the Ge-XXIII xuv laser
J Phys B-Atomic Molecular and Optical Physics **29**, 4839-4854 (1996)

D M Chambers, S G Preston, M Zepf, M CastroCelin, M H Key, J S Wark, A E Dangor, A Dyson, D Neely, P A Norreys
Imaging of high harmonic radiation emitted during the interaction of a 20 TW laser with a solid target
J Appl Phys **81**, 2055-2058 (1997)

J P Connerade, C H Keitel
High harmonic-generation in a static magnetic-field
Phys Rev A **53**, 2748-2751 (1996)

H Daido, K Murai, R Kodama, G Yuan, M S Schulz, M Takagi, Y Kato, D Neely, A Macphee, C L S Lewis
Collisional exitation soft-x-ray laser at 236 nm in a laser-produced cylindrical target
Appl Phys B-Lasers and Optics **62**, 129-133 (1996)

H Daido, S Ninomiya, T Imani, R Kodama, M Takagi, Y Kato, K Murai, J Zhang, Y You, Y Gu
Nickel-like soft-x-ray lasing at the wavelengths between 14 and 79 nm
Optics Letters **21**, 958-960 (1996)

A Demir, G J Tallents, P Zeitoun, E Fill, G Jamelot, Y L Li, M Nantel, G J Pert, B Rus, D Schlogl
Spectroscopic analysis of Li-like Ti and Ca X-ray laser media
Institute of Physics Conference Series **151**, 383-385 (1996)

A Demir, P Zeitoun, G J Tallents, E Fill, G Jamelot, Y L Li, M Nantel, G J Pert, B Rus, D Schlogl
Detailed comparison of experimental and theoretical heliumlike Ti and Ca satellite line spectra emitted from a laser-produced plasma
Phys Rev E **55**, 1827-1835 (1997)

A Djaoui
Pulse shaping for ignition and gain of an indirectly driven target
Physics Of Plasmas **3**, 4677-4682 (1996)

A Dyson, A E Dangor, A K L Dymoke-Bradshaw, T Ashfarrad, P Gibbon, A R Bell, C N Danson, C B Edwards, F Amiranoff, G Matthieusent, S J Karttunen, R R E Salomaa
Observations of relativistic plasma-waves excited by a 1064 μm and 1053 μm laser beat
Plasma Physics and Controlled Fusion **38**, 505-525 (1996)

D L Foulis, S J Rose, T D Beynon
Multicenter wavefunctions in opacity calculations for dense plasmas
Laser and Particle Beams **14**, 555-560 (1996)

F I Gauthey, C H Keitel, P L Knight, A Maquet
Phase of harmonics from strongly driven two-level atoms
Phys Rev A **55**, 615-621 (1997)

L A Gizzi, A J Mackinnon, D Riley, A M Viano, O Willi
Measurements of thermal transport in plasmas produced by picosecond laser-pulses
Laser and Particle Beams **14**, 529 (1996)

D H Kalantar, L B DaSilva, S G Glendinning, B A Remington, F Weber, S V Weber, M H Key, N S Kim, D Neely, E Wolfrum, J Zhang, J S Wark, A Demir, J Lin, R Smith, G J Tallents, C L S Lewis, A MacPhee, J Warwick, J P Knauer
Extreme ultraviolet probing of laser imprint in a thin foil using an x-ray laser backlighter
Rev Sci Instruments **68**, 802-805 (1997)

D J Heading, J S Wark, R W Lee, R Stamm, B Talin
Comparison of the semiclassical and modified semiempirical method of spectral calculation
Phys Rev E 56, 936-946 (1997)

D Hoarty, A Iwase, C Meyer, J Edwards, O Willi
Characterization of laser driven shocks in low density foam targets
Phys Rev Letts **78**, 3322-3325 (1997)

D H Kalantar, M H Key, L B DaSilva, S G Glendinning, B A Remington, J E Rothenberg, F Weber, S V Weber, E Wolfrum, N S Kim, D Neely, J Zhang, J S Wark, A Demir, J Lin, R Smith, G J Tallents, C L S Lewis, A MacPhee, J Warwick, J P Knauer
Measurements of direct drive laser imprint in thin foils by radiography using an x-ray laser backlighter
Physics of Plasmas **4**, 1985-1993 (1997)

C H Keitel
Ultra-energetic electron ejection in relativistic atom-laser field interaction
J Phys B-Atomic Molecular and Optical Physics **29**, L873-L880 (1996)

C H Keitel
Vacuum modified resonance fluorescence in intense laser fields
Journal Of Modern Optics **43**, 1555-1562 (1996)

M H Key, T W Barbee, J W Blyth, K Burnett, G F Cairns, A E Dangor, T Ditmire, A Djaoui, L B DaSilva, A Demir, A Dyson, A P Fews, E Fill, P Gibbon, P Lee, S Healy, M G Holden, D Kalantar, N Kim, C L S Lewis, Y Li, J Lin, P Loukakos, A McPhee, I Mercer, S Mousta
Development and application of ultra-bright laser and harmonic XUV sources
Institute of Physics Conference Series **151**, 9-16 (1996)

N S Kim, A Djaoui, M H Key, D Neely, S G Preston, M Zepf, C G Smith, J S Wark, J Zhang, A A Offenberger
Extreme-ultraviolet line emission at 247 nm from Li-like nitrogen plasma produced by a short KrF excimer-laser pulse
Appl Phys Letts **69**, 884-886 (1996)

A Klisnick, S Sebban, A Carillon, P Jaegle, G Jamelot, M Nantel, B Rus, P Zeitoun, F Albert, D Ros, A McPhee, C L S Lewis, P J Warwick, I Weaver, G J Tallents, A Demir, M G Holden, J Krishnan
Progress in the control and optimization of the 212 nm zinc laser
Institute of Physics Conference Series **151**, 47-49 (1996)

D G Lappas, A Sanpera, J B Watson, K Burnett, P L Knight, R Grobe, J H Eberly
2-electron effects in harmonic-generation and ionization from model He atom
J Phys B-Atomic Molecular and Optical Physics **29**, L 619-L 627 (1996)

A Lorenz, A K L Dymoke-Bradshaw, A E Dangor
Optical multi-frame system with one gated intensifier as a diagnostic for high-speed photography
Measurement Science & Technology **8**, 676-678 (1997)

A G MacPhee, A Behjat, G F Cairns, S B Healy, M H Key, N Kim, M E Kurkcuoglu, M J Lamb, C L S Lewis, S P McCabe, D Neely, G J Pert, J Plowes, G J Tallents, P J Warwick, E Wolfrum, J Zhang
Improving the efficiency of collisionally excited X-ray lasers using multiple 100ps pulses
Institute of Physics Conference Series **151**, 250-254 (1996)

A G MacPhee, C L S Lewis, P J Warwick, I Weaver, P Jaegle, A Carillon, G Jamelot, A Klisnick, B Rus, P Zeitoun, M Nantel, P Goedkindt, S Sebban, G J Tallents, A Demir, M Holden, J Krishnan
The influence of prepulse level on the 3p-3s XUV laser output from Ne-like ions of Zn, Cu and Ni
Optics Commun **133**, 525-533 (1997)

V Malka, A Modena, Z Najmudin, A E Dangor, C E Clayton, K A Marsh, C Joshi, C N Danson, D Neely, F Walsh
Second harmonic generation and its interaction with relativistic plasma waves driven by forward Raman instability in underdense plasmas
Physics of Plasmas **4**, 1127-1131 (1997)

O Meighan, A Gray, J P Mosnier, W Whitty, J T Costello, C L S Lewis, A MacPhee, R Allott, I C E Turcu, A Lamb
Short-pulse, extreme-ultraviolet continuum emission from a table-top laser plasma light source
Appl Phys Letts **70**, 1497-1499 (1997)

T Mocek, B Rus, P Zeitoun, A Demir, S Sebban, G Jamelot, A Klisnick, G J Tallents
Spectroscopy of Zn and Cu line plasmas generated on slab target by irradiances 10^{10}-10^{11} Wcm^{-2}
Institute of Physics Conference Series **151**, 399-401 (1996)

A Modena, Z Najmudin, A E Dangor, C E Clayton, K A Marsh, C Joshi, V Malka, C B Darrow, C N Danson
Observation of Raman forward scattering and electron acceleration in the relativistic regime
IEEE Transactions on Plasma Science **24**, 289-295 (1996)

S D Moustaizis, E Bakaresos, F N Beg, A E Dangor, A Dyson, P Lee, N Papadogiannis, M Tatarakis
Laser based, intense, high rep-rate x-ray source (1keV-10keV) from nsec to subpsec
Institute of Physics Conference Series **151**, 475-479 (1996)

M Nantel, A Klisnick, G Jamelot, P B Holden, B Rus, A Carillon, P Jaegle, P Zeitoun, G Tallents, A G Macphee, C L S Lewis, S Jacquemot, L Bonnet
Spectroscopic characterization of prepulsed x-ray laser plasmas
Phys Rev E **54**, 2852-2862 (1996)

K Nazir, S J Rose, A Djaoui, G J Tallents, M G Holden, P A Norreys, P Fews, J Zhang, F Failles
X-ray spectroscopic studies of hot, dense iron plasma formed by subpicosecond high-intensity KrF laser irradiation
Appl Phys Letts **69**, 3686-3688 (1996)

P A Norreys, M Zepf, M Bakarezos, M Castro-Colins, D Chambers, C N Danson, A Dyson, A P Fews, P Gibbon, M H Key, P Lee, P Loukakos, S Moustaizis, D Neely, S G Preston, F N Walsh, J S Wark, J Zhang, A E Dangor
Extreme ultraviolet harmonic generation from ultra-intense picosecond laser-solid interactions: Results and perspectives
Institute of Physics Conference Series **154**, 211- 220 (1997)

P K Patel, J S Wark, D J Heading, A Djaoui, S J Rose, O Renner, A Hauer
Simulation of X-ray line transfer in a cylindrically expanding plasma
J Quant Spectrosc & Radiative Transfer **57**, 683-694 (1997)

M Protopapas, C H Keitel, P L Knight
Relativistic mass shift effects in adiabatic intense laser field stabilization of atoms
J Phys B-Atomic Molecular and Optical Physics **29**, L 591-L 598 (1996)

M Protopapas, C H Keitel, P L Knight
Atomic physics with super-high intensity lasers
Reports on Progress in Physics **60**, 389 (1997)

M Protopapas, D G Lappas, C H Keitel, P L Knight
Recollisions, bremsstrahlung, and attosecond pulses from intense laser fields
Phys Rev A **53**, R2933-R2936 (1996)

U W Rathe, C H Keitel, M Protopapas, P L Knight
Intense laser-atom dynamics with the two-dimensional Dirac equation
J Phys B-Atomic Molecular and Optical Physics **30**, L531-L539 (1997)

S J Rose
Compton-scattering in inertial confinement fusion plasmas
J Quant Spectros & Radiative Transfer **55**, 707-713 (1996)

B Rus, P Zeitoun, T Mocek, S Sebban, M Kalal, A Demir, G Jamelot, A Klisnick, G J Tallents
Investigation of prepulse plasmas for collisional excitation X-ray lasers
Institute of Physics Conference Series **151**, 394-398 (1996)

A Sanpera, J B Watson, M Lewenstein, K Burnett
Harmonic-generation control
Phys Rev A **54**, 4320-4326 (1996)

C G Smith, M H Key, G Cairns, L Dwivedi, J Krishnan, C L S Lewis, A G Macphe, D Neely, S A Ramsden, G Tallents
Study of beam aberrations in a germanium-XXIII xuv laser-amplifier
Optics Commun **130**, 69-74 (1996)

G J Tallents, A Behjat, A Demir, M G Holden, J Krishnan, J Y Lin, P Zeitoun, G Cairns, C L S Lewis, S P McCabe, A G MacPhee, P J Warwick, J Zhang, D Neely, E Wolfrum, G Jamelot, M Nantel, B Rus, E Fill, Y L Li, D Schlogl, S B Healy, G J Pert
Spectroscopic investigations of X-ray laser media
Institute of Physics Conference Series **151**, 372-379 (1996)

M Tatarakis, F N Beg, P Lee, A E Dangor, S Moustaizis
X-ray emission from plasmas generated by 450 femtosecond excimer laser pulses
Physica Scripta **55**, 651-653 (1997)

U Teubner, I Uschmann, P Gibbon, D Altenbernd, E Forster, T Feurer, W Theobald, R Sauerbrey, G Hirst, M H Key, J Lister, D Neely
Absorption and hot-electron production by high-intensity femtosecond uv-laser pulses in solid targets
Phys Rev E **54**, 4167-4177 (1996)

J Wark
Time-resolved x-ray-diffraction
Contemporary Physics **37**, 205-218 (1996)

J S Wark, S J Rose, P K Patel, A Djaoui, O Renner, A Hauer
Astrophysically relevant experiments on radiation transfer through plasmas with large velocity gradients
Physics of Plasmas **4**, 2004-2010 (1997)

P J Warwick, A Demir, D H Kalantar, M H Key, N S Kim, C L S Lewis, J Lin, A G MacPhee, D Neely, B A Remington, S J Rose, R Smith, G J Tallents, J S Wark, S V Weber, E Wolfrum, J Zhang
Radiography measurements of direct drive imprint in thin Al foils using a bright XUV laser
Institute of Physics Conference Series **151**, 509-511 (1996)

J B Watson, A Sanpera, D G Lappas, P L Knight, K Burnett
Nonsequential double ionization of helium
Phys Rev Letts **78**, 1884-1887 (1997)

J B Watson, A Sanpera, K Burnett, D G Lappas, P L Knight
Double ionisation of helium: Beyond the single active electron approximation
Institute of Physics Conference Series **151**, 132-141 (1996)

J B Watson, A Sanpera, K Burnett, P L Knight
Wave-packet recollision and pulse-shape effects in high-harmonic generation
Phys Rev A **55**, 1224-1233 (1997)

J B Watson, A Sanpera, X Chen, K Burnett
Harmonic-generation from a coherent superposition of states
Phys Rev A **53**, R1962-R1965 (1996)

J B Watson, C H Keitel, P L Knight, K Burnett
Entropic measure of wave-packet spreading and ionization in laser-driven atoms
Phys Rev A **54**, 729-735 (1996)

I Weaver, C L S Lewis
Aspects of particulate production from metals exposed to pulsed-laser radiation
Applied Surface Science **96**, 663-667 (1996)

I Weaver, C L S Lewis
Polar distribution of ablated atomic material during the pulsed-laser deposition of Cu in vacuum - dependence on focused laser spot size and power-density
J Appl Phys **79**, 7216-7222 (1996)

N C Woolsey, A Asfaw, B Hammel, C Keane, C A Back, A Calisti, C Mosse, R Stamm, B Talin, J S Wark, R W Lee, L Klein
Spectroscopy of compressed high-energy density matter
Phys Rev E **53**, 6396-6402 (1996)

N C Woolsey, J S Wark
Modeling of time resolved x-ray diffraction from laser-shocked crystals
J Appl Phys **81**, 3023-3037 (1997)

W Yu, J Zhang
An estimate of resonance absorption of picosecond laser pulses by fibre targets
Optics Comm, **134**, 91-94 (1997)

W Yu, J Zhang, J X Ma, B F Shen, Q K Lu, Z Z Xu
Electron synchrotron radiation generated by ultrastrong laser fields
Institute of Physics Conference Series **151**, 460-462 (1996)

M Zepf, M Castrocolin, D Chambers, S G Preston, J S Wark, J Zhang, C N Danson, D Neely, P A Norreys, A E Dangor, A Dyson, P Lee, A P Fews, P Gibbon,S Moustaizis, M H Key
Measurements of the hole boring velocity from doppler-shifted harmonic emission from solid targets
Physics Of Plasmas **3**, 3242-3244 (1996)

J Zhang, A E Dangor, C N Danson, A Demir, A Dyson, A P Fews, E Fill, P Gibbon, M G Holden, M H Key, P Lee, C L S Lewis, Y L Li, A G MacPhee, S Moustaizis, D Neely, P A Norreys, D Schlogl, J Steingruber, G J Tallents, F Walsh, J S Wark, P Zeitoun, M Zepf
High gain recombination XUV lasers and efficient XUV harmonics from ps laser pulse interactions with solid targets
Institute of Physics Conference Series **151**, 122-129 (1996)

J Zhang, A G MacPhee, J Lin, E Wolfrum, R Smith, C N Danson, M H Key, C L S Lewis, D Neely, J Nilsen, G J Pert, G J Tallents, J S Wark
A saturated X-ray laser beam at 7 nanometers
Science **276**, 1097-1100 (1997)

J Zhang, A G MacPhee, J Nilsen, J Lin, T W Barbee, C N Danson, M H Key, C L S Lewis, D Neely, R M N O'Rourke, G J Pert, R Smith, G J Tallents, J S Wark, E Wolfrum
Demonstration of saturation in a Ni-like Ag x-ray laser at 14 nm
Phys Rev Letts **78**, 3856-3859 (1997)

J Zhang, E E Fill, Y Li, D Schlogl, J Steingruber, M Holden, G J Tallents, A Demir, P Zeitoun, C N Danson, P A Norreys, F Walsh, M H Key, C L S Lewis, A G McPhee
High-gain x-ray lasing at 111 nm in sodium-like copper driven by a 20-J, 2-ps Nd-glass laser
Optics Letters **21**, 1035-1037 (1996)

Y Zhang, J Zhang, S H Pan, Y X Nie
A simple model for electron temperature and penetration depth in interaction of ultra-short laser pulses with solid targets
J Phys D-Applied Physics **30**, 655-660 (1997)

Y Zhang, J Zhang, S H Pan, Y X Nie
An estimate of threshold intensity of the leading-edge of ultrashort laser-pulses in interaction with solid targets
Optics Communications **126**, 85-88 (1996)

J Zhang, M Zepf, P A Norreys, A E Dangor, M Bakarezos, C N Danson, A Dyson, A P Fews, P Gibbon, P Lee, P Loukakos, M H Key, S Moustaizis, D Neely, F N Walsh, J S Wark
Spatial and temporal coherence measurements of harmonics of a 1053 nm, 25 ps laser interacting with solid surfaces
Institute of Physics Conference Series **151**, 452-454 (1996)

J Zhang, M Zepf, P A Norreys, A E Dangor, M Bakarezos, C N Danson, A Dyson, A P Fews, P Gibbon, M H Key, P Lee, P Loukakos, S Moustaizis, D Neely, F N Walsh, J S Wark
Coherence and bandwidth measurements of harmonics generated from solid-surfaces irradiated by intense picosecond laser-pulses
Phys Rev A **54**, 1597-1603 (1996)

J Zhang, P A Norreys, G J Tallents, C N Danson, L Dwivedi, M Holden, P B Holden, M H Key, C L S Lewis, A G Macphee, D Neely, G J Pert, S A Ramsden, S J Rose, F N Walsh, Y L You
Characteristics of rapidly recombining plasmas suitable for high-gain x-ray laser action
Laser And Particle Beams **14**, 71-79 (1996)

J Zhang, P J Warwick, E Wolfrum, M H Key, C N Danson, A Demir, S Healy, D Kalantar, N Kim, C L S Lewis, J Lin, A MacPhee, D Neely, J Nilsen, G J Pert, R Smith, G J Tallents, J S Wark
Characterisation of a saturated single frequency Ne-like Ge XUV laser on the J=0->1 transition at 196 nm
Institute of Physics Conference Series **151**, 56-58 (1996)

J Zhang, P J Warwick, E Wolfrum, M H Key, C N Danson, A Demir, S Healy, D H Kalantar, N S Kim, C L S Lewis, J Lin, A G Macphee, D Neely, J Nilsen, G J Pert, R Smith, G J Tallents, J S Wark
Saturated output of a Ge-XXIII x-ray laser at 196 nm
Phys Rev A **54**, R4653-R4656 (1996)

INTERNAL PUBLICATIONS

A Bennuzzi, T Lower, M Koenig, B Faral, JM Boudenne, D Batani, D Berretta, C Danson and D Pepler
Mesure de l'equation d'etat du cuivre dans le domaine 10-40 Mbars avec des ondes de choc generees par irradiation directe et indirecte
Rapport Scientifique 1995, LULI, Ecole Polytechnique, Palaiseau, p 138-146, July 1996

A Giulietti, M Borghesi, O Willi, D Giulietti, LA Gizzi, A Macchi, C Danson and D Neely
Preformed Plasma Studies with CPA VULCAN Pulses: I Progress in Plasma Characterisation for Interaction Studies; II Propagation of Ultra-Short Pulses through Underdense Plasmas
RAL Technical Report RAL-TR-96-078

S Moustaizis, M Bakarezos, P Loukakos, P A Norreys, D Neely, F N Walsh and C N Danson, M Zepf, J Zhang and J S Wark, P Lee, A Dyson and A E Dangor, A P Fews and P Gibbon
Efficient XUV Harmonics Generated from Picosecond Laser Pulse Interactions with Solid Targets
RAL Technical Report RAL-TR-96-071

CONFERENCE PRESENTATIONS

24th Annual UK IOP Plasma Physics Conference, University of Leeds, March 24-27, 1997

D Neely, P Norreys, A Damerell, R Parker and C Danson
A high efficiency soft X-ray and optical spectrometer

P A Norreys, C N Danson, D Neely, F N Beg, A R Bell, A Dyson, P Lee, M Tatarakis, M Zepf, A E Dangor, A P Fews, M Catsro-Colin, D Chambers, S G Preston, J Zhang, J S Wark, M Glinsky, B A Hammel, M Bakarezos, P Loukakos, S Moustaizis and P Gibbon
A Study of Picosecond Laser Pulse Interactions with Solid Targets up to 10^{19} Wcm^{-2}

OSA Topical Meeting on the Applications of High Field and Short Wavelength Sources, Sante Fe, New Mexico, March 19-22, 1997

P V Nickles, M P Kalachnikov, M Schnurer, W Sander, V N Shlyaptsev, C Danson, D Neely, E Wolfrum, M Key, A Behjat, A Demir, G Tallents, G J Pert, J Warwick and C Lewis
A Short-long pulse excitation of [Ne]-like Ti and Ge has succeeded in saturated short pulse lasing at 326 nm and 196 nm with low pump energy level

5th International Conference on X-ray Lasers, Lund, Sweden, June 10-14, 1996

J Zhang, A E Dangor, C N Danson, A Demir, A Dyson, A P Fews, E E Fill, P Gibbon, M Holden, M H Key, P Lee, C L S Lewis, Y L Li, P Loukakos, A G MacPhee, S Moustasis, D Neely, P A Norreys, D Schlogel, J Steingruber, G J Tallents, F N Walsh, J S Wark, P Zeitoun and M Zepf
Research on high gain recombination XUV lasers and efficient XUV harmonics from ps laser pulse interactions with solid targets

J Zhang, J Warwick, E Wolfrum, M H Key, T W Barbee, C N Danson, A Demir, S Healy, D Kalantar, N S Kim, C L S Lewis, J Lin, D Neely, L Nilson, G J Pert, R Smith, G J Tallents and J Wark
Characteristation of a saturated Ne-like Ge X-ray laser on the J=0-1transition at 196 nm

J Zhang, M Zepf, P A Norreys, A E Dangor, M Bakarezos, C N Danson, A P Fews, P Gibbon, P Lee, P Loukakos, S Moustasis, D Neely, F Walsh and J S Wark
Measurements of coherence and bandwidth of harmonics generated from ps laser pulse interactions with solid targets

24th ECLIM, Madrid, Spain, June 3-7, 1996

M Borghesi, A J MacKinnon, L Barringer, L Gizzi, C Meyer, O Willi
Propagation of a short laser pulse in preformed plasmas at relativistic intensities

T Ceccotti, P Angelo, H Derfoul, P Gauthier, E Leboucher-Dalimier, A PoquÇrusse, P Sauvan, A Giulietti, D Giulietti and C Danson
Over dense plasma x-ray emission enhancing through beam smoothing techniques

C Danson, L Barzanti, N Bradwell, J Collier, C Edwards, C Johnson, M Key, D Neely, M Nightingale, D Pepler, I Ross, P Ryves, N Thompson, M Trentelman, F Walsh and R Wyatt
Characterisation of the VULCAN Nd:glass laser for multi-TW operation

M Dunne, J Edwards, T Afshar-rad, O Willi
Hydrodynamics of x-ray ablated targets - a comparison of measured and simulated density profiles

D Hoarty, A Iwase, C Meyer, J Edwards, O Willi
Characterisation of laser driven shocks in low density foam targets

A Iwase, J H Barringer, R Gaillard, O Willi, R Watt, T Hurry
Observations of Rayleigh-Taylor instability in cylindrical geometry

M Kalal, B Rus, P Zeithoun, T Mocek, S Sebban, A Demir, G Jamelot, B Kralikova, L Pina, J Skala, G Tallents
Studies in the phenomena involved in the prepulse pumping of collisional x-ray lasers by optical interferometry

D H Kalantar, L B Da Silva, S G Glendinning, F Weber, B A Remington, S V Weber, M H Key, D Neely, E Wolfrum, A Demir, J Lin, R Smith, G J Tallents, N S Kim, J S Wark, J Zhang, C L S Lewis, A McPhee, J Warwick, J P Knauer
Measurements of laser imprint by XUV radiography using an x-ray laser

M H Key, D Neely, E Wolfrum, D H Kalantar, T W Barbee Jr, L B Da Silva, S G Glendinning, F Weber, B A Remington, J Lin, S V Weber, A Demir, R Smith, G J Tallents, N S Kim, J S Wark, J Zhang, C L S Lewis, A McPhee, J Warwick, J P Knauer
Control of hydrodynamic perturbations in directly driven implosions.

N S Kim, A Djaoui, M H Key, J S Wark
Numerical modelling of the optical field ionised nitrogen recombinant XUV laser scheme

C Meyer, T Afshar-rad, O Willi, H Croso, F Mucchielli
Heat wave propagation in low density foam targets

A Modena, Z Najmudin, A E Dangor, C E Clayton, K A Marsh, C Joshi, V Malka, C N Danson, D Neely and F N Walsh
Observation of Raman Forward Scattering and Electron Acceleration in the Relativistic Regime

P A Norreys, A P Fews, F N Beg, A R Bell, M D Cable, C N Danson, B A Hammel, P Lee, M Nelson, H Schmidt, M Tatarakis and A E Dangor
A study of picosecond laser pulse interaction with solid targets in the range 10^{17}-10^{19} W cm $^{-2}$

O Renner, D Salzmann, P Sondhauss, E Forster, A Djaoui, E Krousky, K Eidmann
Search for plasma shifts in higher transition lines of aluminium Lyman series

R Taylor, C Meyer, S Nuruzzaman, O Willi
Short wavelength Rayleigh-Taylor studies using hohlraum radiation drive

O Willi, T Afshar-rad, M Borghesi, M Desselberger, M Dunne, M Jones, A Iwase, C Meyer, R Taylor, R G Watt, H Croso, F Mucchielli, C Reverdin
Reduction of laser imprinting using the foam buffered direct scheme

E Wolfrum, D Neely, M H Key, A Demir, J Lin, R Smith, G J Tallents, N S Kim, J S Wark, J Zhang, C L S Lewis, A McPhee, J Warwick, D H Kalantar, B A Remington, S V Weber
Measurement of a single-mode laser imprint by XUV radiography

P Zeithoun, S Sebban, G Jamelot, A Carrillon, P Jaegle, A Klisnick, F Albert, D Ros, B Rus, T Mocek, A Demir, G J Tallents, M Kalal, A G McPhee, C L S Lewis
Investigation into the effects of low intensity prepulses on x-ray lasing

M Zepf, P A Norreys, M Bakarezos, A E Dangor, A Dyson, P Lee, A P Fews, P Gibbon, P Loukakos, S Moustaizis, J S Wark, J Zhang
XUV harmonic generation from picosecond laser pulses from solid targets

IOP Plasma Physics Conference, Crieff, Scotland, 1-4 April 1996

F N Walsh, S Angood, C N Danson, L J Barzanti, J Collier, M H Key,
A Damerell, C B Edwards, D Neely, P A Norreys, D A Pepler, D Rodkiss, I N Ross, M Trentleman, E Wolfrum and R Wyatt
Progress towards 10^{20} Wcm^{-2} on VULCAN

PhD THESES

Andrew Garrick MacPhee
Queens University Belfast
Development of CCD Detectors for Study and Applications of VUV Lasers

R Taylor
Imperial College
Stability and hydrodynamics of targets driven by laser or soft x-ray radiation.

Abbas Behjat
Univesity of Essex
Investigations of the uniformity of X-ray laser media

SCIENCE - LASERS *for* SCIENCE FACILITY PROGRAMME

JOURNAL PUBLICATIONS AND PUBLISHED CONFERENCE PROCEEDINGS

D Batani, A Conti, A Masini, M Milani, M Costato, A Pozzi, ICE Turcu, R Allott, N Lisi, F Musumeci, A Triglia,
Biosystem response to soft x-rays irradiation: nonmonotonic effects in the relevant biological parameters of yeast cells
Nuovo Cimento **18D**, 657-662 (1996)

D Batani, M Milani, G Leoni, A Conti, A Masini, F Pisani, M Costato, A Pozzi, ICE Turcu, R Allott, N Lisi, F Cotelli, C Lora Lamia Donin, M Moret
Yeast cells response to soft x-rays from laser-plasmas
Vouto, Science and Technology, in press

A Beeby, A W Parker, C F Stanley
E*limination of fluorescence contributions to singlet oxygen measurements using a novel electronic switch*
Photochem Photobiol B, **37**, 267-271 (1996)

J Bezant, D D Turner, G Dormer, A M Ellis
A new discharge nozzle for spectroscopic studies in supersonic jets
J Chem Soc Faraday trans, **92** (17), 3023-3028 (1996)

S Bishop, A Beeby, H Meurnier, A W Parker, M Foley
The photophysics of disulphonated metallophthalocyanines upon complexation with fluorides
JChem Soc Farad Trans, **92**, 15 2689-95 (1996)

P Bocherel, L B Herbert, BR Rowe, I R Sims, I W M Smith, D Travers
Ultra-low temperature kinetics of CH($X^2\Pi$) reactions: Rate coefficients for reactions with O_2 and NO down to 13 K, and with NH_3 down to 23 K
J Phys Chem, **100**, 3063-3069 (1996)

I S Borthwick, K D Ledingham, R P Singhal, R Zheng, M Campbell
Diagnostic and analytical study of post ablation ionization of neutral atoms of major and minor constituents from a low alloy steel
Spectrochimica Acta **B51**, 127-137 (1996)

R A Brownsword, L B Herbert, I W M Smith, D W A Stewart
Pressure and temperature dependence of the rate constants for the association reactions of CH radicals with CO and N_2 between 202 and 584 K
J Chem Soc Faraday Trans, **92**, 1087-1094 (1996)

R A Brownsword, I R Sims, I W M Smith, D W A Stewart, A Canosa, B R Rowe
The radiative association of CH with H_2: A mechanism for loss of CH in interstellar clouds
Astrophys J, **485**, 1, 195-202 (1997)

R A Brownsword, A Canosa, B R Rowe, I R Sims, I W M Smith, D W A Stewart, A C Symonds, D Travers
Rate constants for the reactions of CH(v = 0) with H_2, D_2 and for the removal of CH(v = 1) by H_2, D_2 over a wide range of temperature
J Chem Phys, **106**, 7662-7677 (1997)

A N Brunton, G W Fraser, W B Feller, P L White, R M Allott, I C E Turcu, N S Kim, N Lisi
Recent development of MCP collimators for X-ray lithography of semiconductor devices
Optics for Science and New Technology Eds J-S Chang, J-H Lee, CH Nam, SPIE **2778**, 1193-4 (1996)

N Cain, M O'Neill, J E Nicholls, T Poirek, W E Hagston, P Chen, S Chalk, D E Ashenford, A J Langley, P F Taday
Electron-tunneling in CdTe/CdMnTe double-barrier Structures
J Crystal Growth, **159,** 818-821 (1996)

N Cain, M O' Neill, J E Nicholls, T Stirner, W E Hagston, D E Ashenford
Photoluminescence of highly excited CdTe/CdMnTe quantum wells
Proceeds European Quantum Electronics Conference, Paper QM23, 1996

A Canosa, I R Sims, D Travers, I W M Smith, B R Rowe
Reactions of the methylidene radical with CH_2, C_2H_2, C_2H_4, C_2H_6 and but-1-ene studied between 23 and 295 K with a CRESU apparatus
Astron Astrophys, **323**, 2, 644-651 (1997)

K Codling, L J Frasinski
Molecules in intense laser fields: an experimental viewpoint
Struct Bonding **86**, 1–26 (1996)

J A Dickinson, P W Joireman, R W Randall, E G Robertson and J P Simons
Conformational structures in 3-phenyl-1-propionic acid, its p-hydroxy derivative and its hydrated clusters
J Phys Chem, **101**, 4, 513-521 (1997)

T Fournier, G Scholes, D Phillips, S Tavender, A W Parker
Competitive energy and electron transfer reactions of the triplet state of 1-nitronaphthalene: A laser flash photolysis and Time-Resolved Resonance Raman Study
J Phys Chem A, **101**, 29, 5320-53 (1997)

L J Frasinski, A J Giles, P A Hatherly, J H Posthumus, M R Thompson, K Codling
Covariance mapping and triple coincidence techniques applied to multielectron dissociative ioniosation
J Electron Spec, **79**, 367-71 (1996)

P A Hepworth, J McCombie, J P Simons, J F Pfanstiel, J W Ribblet, D W Pratt
High resolution electronic spectroscopy of molecular conformers: methyl- and ethyl-3 aminobenzoic acid esters
Chem Phys Letts, **249**, 341-350 (1996)

L Herbert, I R Sims, I W M Smith, D W A Stewart, A Canosa, B R Rowe
Rate constants for the relaxation of CH($X^2\Pi$, v = 1) by CO and N_2 at temperatures from 44 to 593 K
J Phys Chem, **100**, 14928-14935 (1996)

P L James, I R Sims, I W M Smith
Rate coefficients for the vibrational self-relaxation of NO($X^2\Pi$, v = 3) at temperatures down to 7 K
Chem Phys Letters, **276**, 5-6, 423-429 (1997)

P L James, I R Sims, I W M Smith
Total and state-to-state rate coefficients for rotational energy transfer in collisions between NO($X^2\Pi$) and He at temperatures down to 15 K
Chem Phys Letters, **272**, 412–8 (1997)

J A Joireman, R T Kroemer, D W Pratt, J P Simons
Conformationally induced rotations of a molecular electronic transition moment
J Chem Phys, **105**, 6075-6077 (1996)

M Kaczmarek, P Hribek, R W Eason
Characterization of photorefractive properties of blue Rh-$BaTiO_3$ via nonlinear-wave mixing
J Mod Optics, **43**, 9, 1817-1827 (1996)

M Kaczmarek, P Hribek, R W Eason
Near-infrared incoherent coupling and photorefractive response time of 'blue' Rh:$BaTiO_3$
Opt Comm, 136, 277-282 (1997)

M Kaczmarek, P Hribek, R W Eason, M J Damzen, R Ramos-Garcia, M H Garrett
Intensity-dependent absorption and its modeling in infrared-sensitive rhodium-doped $BaTiO_3$
J Opt Comm **126**, 1-3, 175-184 (1996)

N Khaleque, A G Michette, C J Buckley, S J Pfauntsch, S D Saville, G S Demody
Development of a laboratory based scanning x-ray microscope
Cell Vision **4,** 114-115 (1997)

H S Kilic, K W D Ledingham, C Kosmidis, T McCanny, R P Singhal, S L Wang, D J Smith, A J Langley, W Shaikh
Multiphoton ionisation and dissociation of nitromethane using femtosecond laser pulses at 375 and 750 nm
J Phys Chem A, **101**, 817-823 (1997)

H Kilic, K W D Ledingham, C Kosmidis, T McCanny, R P Singhal, A J Langley, W Shaikh
The Photo-dissociative pathways of nitromethane using femtosecond laser pulses at 375 nm
Resonance Ionization Spectroscopy 1996, Eds NWinograd and JEParks AIP Conference Proceedings **388,** 395-398 ISBN 1-56396-611-5, (1997)

C Kosmidis, K W D Ledingham, H S Kilic, T McCanny, R P Singhal, A J Langley, W Shaikh
On the Fragmentation of nitrobenzene and nitrotoluene isomers induced by a femtosecond Laser at 375 nm
J Phys Chem A, **101**, 2264-2270 (1997)

G Meaden, P G Partridge, M N R Ashfold, E D Nickolson, A Wisbey
Laser cutting of diamond fibres and diamond fibre/titanium metal matrix composites
Diamond and Rel Mats **5**, 825-8 (1996)

P Matousek, A W Parker, P F Taday, W T Toner, M Towrie
Two independently tunable and synchronised femtosecond pulses generated in the visible at the repetition rate 40 kHz using optical parametric amplifiers
Optics Comm, **127**, 307-12 (1996)

G Meaden, P G Partridge, MNR Ashfold, ED Nickolson, A Wisbey
Laser ablation of diamond fibres and laser fibre metal matrix
J Mat Sci **31**, 11, 2801-5, (1996)

O Meighan, A Grey, J-P Mosnier, W Whitty, J T Costello, C L S Lewis, A MacPhee, R Allott, I C E Turcu, A Lumb
Short-pulse, extreme-UV continuum emission from a table-top laser-plasma light source
Appl Phys Lett, **70,** 1497-9 (1997)

T Melvin, S Botchway, P O'Niell, M Plumb and A W Parker
Induction of strand breaks in single stranded polynucleotides and DNA by photoionisation: one electron oxidised nucleobase radicals as precursors
J Am Chem Soc, **118**, 10031-6 (1996)

M Milani, D Batani, A Conti, A Masini, M Costato, A Pozzi, I C E Turcu,
Soft x-ray controlled dose deposition in yeast cells: techniques, model and biological assessment
SPIE **2925**, 206-15, (1996)

A G Michette
Projected advances in laboratory soft x-ray systems and their applications
J X-ray Sci Technol (in press)

A G Michette
X-ray microscopy: the state of the art and future prospects
Cell Vision **4**, 113-114 (1997)

S W Moon, C M Mann, B J Maddison, I C E Turcu, R Allott, S E Huq, N Lisi
Terrahertz waveguide components fabricated using a 3D x-ray microfabrication technique
Electronics Letters **32**, 1794-5 (1996)

C L Ning, J Pfab
Generation and 355 nm laser photodissociation of nitrous acid (HONO) and HONO-water clusters
J Phys Chem, A, **101**, 34, 6008-6014 (1997)

K B Ozanyan, J E Nicholls, L May, J H Hogg, W E Hagston, B Lunn, D A Ashenford
Optically pumped stimulated emission in ZnS/ZnCdS multiple quantum wells, MBE Grown on GaP
Solid-State Comm, **99**, 407-411 (1996)

K B Ozanyan, J E Nicholls, M O'Neill, L May, J H Hogg, W E Hagston, B Lunn, D A Ashenford
Spectroscopic evidence for the excitonic lasing mechanism in UV ZnS/CdZnS multiple quantum well lasers
Appl Phys Lett, **69** , 4230-2 (1996)

K B Ozanyan, J E Nicholls, M O'Neill, L May, J H Hogg, W E Hagston, B Lunn, D A Ashenford
Stimulated emission at 333 nm frm ZnS/CdZnS multiple quantum wells, grown on GaP by MBE
Proceeds XXIII Int Conf Phys Semiconductors, Berlin, 1996

J H Posthumus, A J Giles, M R Thompson, L J Frasinski, K Codling, A J Langley, W Shaikh
The dissociation dynamics of diatomic molecules in intense laser fields
J Phys B, **29**, L525–L531 (1996)

J H Posthumus, M R Thompson, A J Giles, K Codling
Spatial asymmetry in the photofragmentation of diatomic molecules using coherent control
Phys Rev A, **54**, 955–957 (1996)

J H Posthumus, A J Giles, M R Thompson, K Codling
Field-ionisation, coulomb explosion of diatomic molecules in intense laser fields
J Phys B, **29**, 5811–5829 (1996)

J H Posthumus, K Codling, L J Frasinski, M R Thompson
Field ionisation of molecules in intense laser fields
Laser Physics, **7**, 3, 813-825 (1997)

J H Posthumus, M R Thompson, L J Frasinski, K Codling
Molecular dissociative ionisation using a classical over-the-barrier approach
Proceedings of the 7th International Conference on Multiphoton Processes Eds P Lambropaulus and H Walther, IOP Conference Series No **154**, 298–307 (1996)

C M Reeves, I C E Turcu, P D Prewett, A M Gundlach, J T Steventon, A J Walton, A W S Ross, R A Lawes, P Anastasi, R Burge, P Mitchell
Fabrication of 200nm field effect transistor by x-ray lithography with laser-plasma x-ray source
Electronics Letters, **31**, 2218-9 (1996)

C M Reeves, I C E Turcu, J T M Stevenson, A W S Ross, A M Gundlach, P Prewett, R A Lawes, P Anastasi, R Burge, P Mitchell
Fabrication of 200nm field effect transistors by x-ray lithography using a laser plasma source
Microelectronic Engineering, **30**, 187-190 (1996)

J Sanderson, R V Thomas, W A Bryan, W R Newell, P F Taday, A J Langley
Multielectron-dissociative-ionization of SF_6 by intense femtosecond laser pulses
J Phys B, **30**, 20, 4499-4507 (1997)

A D Scully, R Ostler, D Phillips, P O'Neill, K Townsend, A W Parker, A MacRobert
Applications of fluorescence lifetime imaging spectroscopy to the investigation of intracellular PDT mechanisms
Bioimaging **5**, 9-18 (1997)

I R Sims
Reaction Kinetics at Extremely Low Temperatures
In press, Research in Chemical Kinetics, RG Compton and G Hancock, Eds, Blackwell Science, Oxford, **4** (1997)

C J S M Simpson, P T Griffiths, H L Wallaart, M Towrie
Photodissociation of alkyl nitrites adsorbed on a MgF_2 surface
Rotational and translational energy distributions of product $N_{(v,J)}$ molecules
Chem Phys Letts,**263**, 19-24 (1996)

R P Singhal, H S Kilic, K W D Ledingham, C Kosmidis, T McCanny, A J Langley, W Shaikh
Multiphoton ionisation and dissociation of NO_2 by 50 fs laser pulses
Chem Phys Letts, **253**, (1-2), 81-86 (1996)

I W M Smith
Reaction between neutral species at low temperatures: Laboratory results and astrophysical modelling
Proceeds of IAU Symposium 178: Molecules in astrophysics, Probes and Processes, **178**, 253-269 (1997)

I W M Smith
Kinetics and energy partitioning in complex-forming reactions between simple neutral species
Berichte Der Bunsen-Gesellschaft Phys Chem/Chem Phys, **101**, 516-523 (1997)

I W M Smith
Molecules in Space: The Chemical Laboratory at the End of the Universe
Chemistry Reviews, 1997, in press

I W M Smith
Neutral-Neutral Reaction without barriers: Comparisons with Ion-Molecules systems and their possible role in the chemistry of interstellar clouds
Int J Mass Spec Ion Proc, **149**, 190-200 (1996)

I W M Smith, B R Rowe, I R Sims
Kinetics at ultra-low temperatures: Non-Arrhenius behaviour and applications to the chemistry of interstellar clouds
Gas-Phase Chemical Reaction Systems, Experiments and Models 100 Years After Max Bodenstein, ed J Wofrum, H-R Volpp, R Rannacher and J Warnatz (Springer Series in Chemical Physics) **61,** 190-200 (1996)

I W M Smith, B R Rowe, I R Sims
Gas-Phase Reactions at Low Temperatures: Towards Absolute Zero Chemistry:A European Journal, in press (1997)

G Sweeney, A Watson, K G McKendrick
Rotational and Spin -Orbit effects in the dynamics of $O(^3P_j)$ + Hydrocarbon Reactions I:Experimental Results
Submitted J Chem Phys

G Sweeney, A Watson, K G McKendrick
Rotational and Spin -Orbit effects in the dynamics of $O(^3P_j)$ + Hydrocarbon Reactions II: Models for Spin-Orbit Propensities
Submitted J Chem Phys

H Thorogood, T R Waters, A W Parker, C W Wharton, B A Connolly
Resonance Raman spectroscopy of 4-thiothymidine and oligodeoxynucleotides containing this base both free and bound to the restriction endonuclease EcoRV
Biochem **35**, 8732-8733 (1996)

M Towrie, P Matousek, A W Parker, P F Taday, W T Toner
Two 40 kHz repetition rate independently tunable synchronised femtosecond pulses generated in the visible using optical parametric amplifiers
Proceedings of the XVth International Conference on Raman Spectoscopy, Ed P Stein & S A Asher, 150

M Towrie, P Matousek, A W Parker, P F Taday, W T Toner
Two 40 kHz repetition rate independently tunable synchronised femtosecond pulses generated in the visible using optical parametric amplifiers
Technical Digest of the 1996 Conference on Lasers and Electro-Optics Europe, 142

I C E Turcu, C M Mann, S W Moon, R Allott, N Lisi, B J Maddison, S E Huq, N S Kim
Deep, three dimensional lithography with a laser-plasma x-ray source at 1nm wavelength
Micro-electronic Engineering, **35**, 541-4 (1997)

I C E Turcu, M C Gower, P Huntington
Measurement of KrF breakdown threshold in gases
Optics Comm **134**, 66-68 (1997)

I C E Turcu, I N Ross
1 W plasma x-ray source for lithography at 1 nm wavelength
Rev Scien Inst, **67**, 3245-7 (1996)

I C E Turcu, I N Ross, C M Reeves, C M Mann, B J Maddison, S W Moon, R Allott, J T M Stevenson, A W S Ross, A M Gundlach, P Prewett, N S Kim, S E Huq, B Koek, P Mitchell, N Lisi, P Anastase
High average power KrF laser-plasma x-ray source for lithography at 1nm wavelength
Optics for Science and New Technology Eds J-S Chang, J-H Lee, CH Nam, SPIE **2778**, 1193-4 (1996)

I C E Turcu, B Dance
X-Rays from laser-plasmas: Generation and applications
John Wiley & Sons, in press

S L Wang, K W D Ledingham, W J Jia, R P Singhal
Studies of silicon nitride (Si_3N_4) using laser ablation mass spectrometry
Appl Surf Sci, **93**, (3), 205-210 (1996)

S L Wang, K W D Ledingham, R P Singhal
Observation of the hypermatalic molecule K_2CN by laser ablation mass spectrometry
J Phys Chem, **100**, (27), 11282-11284 (1996)

F Wilkinson, D Worrall, J Hobley, L Jansen, S Williams, A Langley, P Matousek
Picosecond time resolved spectroscopy of the photocolouration reaction of photochromic naphthoxazine-spiro-indolines
JChem Soc Farad Trans, **92**, 8 1331-6 (1996)

R Zheng, M Campbell, K W D Ledingham, W Jia, C T J Scott, R P Singhal
Diagnostic study of laser ablated $YBa_2Cu_3O_y$
Spectrochim Acta, **52**, 3, 339-352 (1997)

CONFERENCE PRESENTATIONS

Institute of Physics Meeting on Topics in Spectroscopy, Leeds, March 1997

T McCanny, K W D Ledingham, D J Smith, C Kosmidis, H S Killic, R P Signal, W X Peng, S Wang, A J Langley, P F Taday
Ultrafast laser mass spectroscopy

A Hollingsworth, R R J Maier, P R R Langridge-Smith, A J Langley, P F Taday
Femtosecond photoionisation dynamics of large molecules

RAL/Daresbury Joint Optics Seminar Coseners House, Abingdon, September 1996

A J Langley
Femtosecond optics in the CLF

IOP Atomic, Molecular and Optical Physics, Oxford, April 1996

A J Langley, W Shaikh and P F Taday
Femtosecond science at the Central Laser Facility

Conf of Micro- and Nano-Engineering MNE96, Glasgow, Sept 1996

I C E Turcu, C M Mann, S W Moon, R Allott, N Lisi, B J Maddison, S E Huq, N S Kim
Deep, three dimensional lithography with a laser-plasma x-ray source at 1nm wavelength

17th Congress of the Int Comission for Optics ICO17, Taejon, Korea, August 1996

I C E Turcu, I N Ross, C M Reeves, C M Mann, B J Maddison, S W Moon, R Allott, J T M Stevenson, A W S Ross, A M Gundlach, P Prewett, N S Kim, S E Huq, B Koek, P Mitchell, N Lisi, P Anastase
High average power KrF laser-plasma x-ray source for lithography at 1nm wavelength

A N Brunton, G W Fraser, W B Feller, P L White, R M Allott, I C E Turcu, N S Kim, N Lisi
Recent development of MCP collimators for X-ray lithography of semiconductor devices

European Symposium on Lasers, Optics, and Vision for Productivity in Manufacturing II (EUROPTO96), Besancon, France, June 1996

I C E Turcu
X-ray generation using excimer lasers

Workshop on Advanced Technologies for Generating VUV Radiation Today and in the Future, Daresbury Laboratory, Warrington, February 1997

R M Allott, I C E Turcu, N Lisi
Bright, continuously tunable laser plasma VUV Source

15th General Conference of European Physical Society Condensed Matter Division", Stresa, Italy, April 1996

I C E Turcu, R Allott, N Lisi, A Conti, D Batani, A Masini, F Pisani, M Milani, G Leoni, M Coastato, A Pozzi, M Koenig
Characterisation of a soft x-ray laser-plasma source for yeast biophysics studies

IEE Colloquium on wide gap semiconductor light emitters

JE Nicholls
Room temperature UV lasing from photo-pumped ZnCdS/ZnS quantum wells

Condensed Matter and Materials Physics Conference, York University, 17-19 December 1996

A M Widdowson, S B Palmer, R Allot, I C E Turcu, N Lisi, N Spencer
The Effect of Laser Pulse Length on the Production of Droplets During the Pulsed Laser Deposition of Metallic Films

International Symposium on Atomic Physics Methods in Modern Research, Heidelberg 1996

W T Toner, P Matousek, A W Parker, M Towrie
Resonance Raman Studies of photoexcited molecules in Solution on the picosecond timescale

Fast Reactions In Solution 96, Royal Society of Chemistry, Graz, Austria, Sept 1996

R H Bisby, S A Johnson, A W Parker and S M Tavender
Free Radicals formed by one-electron oxidation of 4-aminoresorcinol as models for the intermediate in copper amine oxidase

Biochemical Society Postgraduate symposium, Liverpool 1996

S Johnson, R Bisby, A W Parker and S Tavender
Protein-radical enzymes - a TR^3 study

IUPAC - International Conference on Photochemistry, Helsinki, August 1996

T Fournier, S M Tavender, A W Parker, G D Scholes, D Phillips
A time-resolved resonance Raman Spectroscopy study of electron transfer intermediates: 1-nitonaphthalene triplet excited state, radical anion and reaction with trans-stilbene

Laser Applications to Chemical and Environmental Analysis, Orlando, Florida, March 1996

P Matousek, A W Parker, M Scully, P F Taday, W T Toner and M Towrie
Doubly Tunable Femtosecond Pulses Generated in the Visible using Optical Parametric Amplifiers for Time-resolved Spectroscopy

Ultrafast Spectroscopy Workshop, University of Manchester, March 1996

M Towrie, P Matousek, A W Parker, M Scully, P F Taday and W T Toner
Doubly tunable OPA for pump and probe spectroscopy

X-ray microscopy and spectroscopy, Berlin

A G Michette, C J Buckley, S J Pfauntsch, N Khaleque, T English, M Folkard, B D Michael, G Schettino, I C E Turcu, R Allott, N Lisi
Applications of laboratory soft x-ray systems

X-Tech 96: International Workshop on Industry Related EUV and Soft X-ray Technology

A G Michette
Formation and application of soft x-ray micoprobes

Conference on Lasers and Electro-Optics, Europe & European Quantum Electronics Conference 1996, September 1996USA

M Towrie, P Matousek, A W Parker, P F Taday and W T Toner
Two 40 kHz repetition rate independently tunable, synchronised femtosecond pulses generated in the visible using optical parametric amplifiers

***Mini-Symposium on the Generation of Coherent XUV and X-ray Radiation,* 17–20 June 1996**

M R Thompson
Dynamics of Molecules in Intense Laser Fields

***ICOMP VI* September 1996**

M R Thompson, J H Posthumus, L J Frasinski, A J Giles, K Codling
Orientation effects in the multiphoton ionisation and dissociation of small molecules

J H Posthumus, A J Giles, M R Thompson, L J Frasinski, K Codling
Field Ionisation, Coulomb explosion of diatomic molecules in intense laser fields

CLEO/QUELS97 QFA1 (1997)

R M Allott, I C E Turcu, N Lisi
Bright, continuously tunable, VUV plasma source generated by a high repetition rate picosecond KrF laser

Institute of Physics Meeting on Topics in Spectroscopy, Leeds, March 1997

T McCanny, K W D Ledingham, D J Smith, C Kosmidis, H S Killic, R P Signal, W X Peng, S Wang, A J Langley, P F Taday
Ultrafast laser mass spectroscopy

A Hollingsworth, R R J Maier, P R R Langridge-Smith, A J Langley, P F Taday
Femtosecond photoionisation dynamics of large molecules

PhD THESES

N Cain (University of Hull)
An invesigation of the optical nonlinearities in CdTe/CdMnTe quantum well structures

L Mulroy (University of Keele)
Pulsed radiation studies of photo-protective systems

PATENT APPLICATIONS

I C E Turcu, B J Maddison, C M Mann, "Deep pattern micro-lithography"
International Patent Application, No PCT/GB96/00421, (1996)

ICE Turcu, IN Ross, F O'Neill, " Laser excited X-Ray source"
International patent 93089811 (1993), filing in USA, Japan and Europe (1996)

FACILITY DEVELOPMENTS

JOURNAL PUBLICATIONS AND PUBLISHED CONFERENCE PROCEEDINGS

E J Divall, C B Edwards, G J Hirst, C J Hooker, A K Kidd, J M D Lister, R Mathumo, I N Ross, M J Shaw, W T Toner, A P Visser, B E Wyborn
Titania - a 10^{20} w cm^{-2} ultraviolet-laser
J Mod Optics, **43**, 1025-1033 (1996)

P Matousek, A W Parker, P F Taday, W T Toner, M Towrie
Two independently tunable and synchronised femtosecond pulses generated in the visible at the repetition rate 40 kHz using optical parametric amplifiers
Optics Comm, **127**, 307-12 (1996)

K Osvay, I N Ross
Broad-band sum-frequency generation by chirp-assisted group-velocity matching
J Opt Soc Am B-Optical Physics, **13**, 1431-1438 (1996)

I N Ross, K Osvay
Efficient broad-bandwidth frequency mixing in dispersive media
Optical and Quantum Electronics **28**, 83-86 (1996)

I N Ross, P Matousek, M Towrie, A J Langley, J L Collier
The prospects for ultrashort and ultrahigh intensity using optical parametric chirped pulse amplifiers
Optics Comm, **144**, 1-3, 125-133 (1997)

D N J Shannon, P W Smith, P J Dobson, M J Shaw
Dual mode electron emission from ferroelectric ceramics
Appl Phys Letts, **70**, 1625-1627 (1997)

M J Shaw, E J Divall, G J Hirst, C J Hooker, J M D Lister, I N Ross, A Kvaran, K Osvay
On the origin of the dip in the KrF laser gain spectrum
J Chem Phys, **105**, 1815-1824 (1996)

M J Shaw
Prospects for High Average Power Electron-Beam-Pumped KrF Lasers for Inertial Confinement Fusion and Industrial Applications
Proc SPIE **3092,** 154-160 (1997)

CONFERENCE PRESENTATIONS

24th Annual UK IOP Plasma Physics Conference, University of Leeds, March 24-27, 1997

C N Danson, S Angood, L Barzanti, J Collier, A Damerell, C B Edwards, S Hancock, P Hatton, M H R Hutchinson, M H Key, W Lester, C McCoard, D Neely, P A Norreys, D A Pepler, C Reason, D A Rodkiss, I N Ross, W Toner, M Trentelman, F N Walsh, T B Winstone, E Wolfrum, R W W Wyatt and B E Wyborn
The VULCAN Nd:Glass Laser: A Unique System to give Focused Intensities of up to 10^{20} Wcm^{-2} for Laser/Plasma Interaction Studies

IOP Half-Day Technical Meeting, Advances in Solid State Lasers, London, November 20, 1996

C N Danson, S Angood, L Barzanti, N Bradwell, J Collier, A Damerell, C B Edwards, C Johnson, M H Key, D Neely, M Nightingale, D A Pepler, D A Rodkiss, I N Ross, P Ryves, N Thompson, M Trentelman, F N Walsh, E Wolfrum and R W W Wyatt
VULCAN: an ultra-high intensity Nd:glass laser interaction facility

2nd Annual International Conference on Solid State Lasers for Application to Inertial Confinement Fusion (ICF) Paris, France, October 22-25, 1996

C N Danson, S Angood, L Barzanti, N Bradwell, J Collier, A Damerell, C B Edwards, C Johnson, M H Key, D Neely, M Nightingale, D A Pepler, D A Rodkiss, I N Ross, P Ryves, N Thompson, M Trentelman, F N Walsh, E Wolfrum and R W W Wyatt
Design and Charcterisation of the VULCAN Nd:glass Laser to give focussed intensities of $>10^{19}$ W cm^{-2}

IAEA Technical Committee Meeting on Drivers for Inertial Confinement Fusion, Osaka , 10 - 14 March 1997

M J Shaw, I N Ross, C J Hooker, J M Dodson, G J Hirst, J M D Lister, E J Divall, A K Kidd, S Hancock, A R Damerell and B E Wyborn
Ultrahigh-brightness KrF laser system for fast ignition studies

Second Gr-I conference on New Laser Technologies and Applications, 1997, Ancient Olympia, Greece

K Osvay, I N Ross, J M D Lister and C J Hooker
High dynamic range measurement of the temporal contrast of ultrashort UV pulses

20th Seminar on Laser-Matter Interactions, 17th - 21st March 1997, Aussois, France

G J Hirst
Developpements au RAL

PANEL MEMBERSHIP &
CLF STRUCTURE

PANEL MEMBERSHIP

HIGH POWER LASER PANEL 1996/97

Professor C Lewis (Chairman)
Department of Pure and Applied Physics
Queen's University Belfast

Dr H C Barr
Department of Physics
University of Essex

Professor R Burge
Department of Physics
Kings College London/Cambridge University

Dr A Giulietti
Istituto di Fisica Atomica E Moleculare
Pisa, Italy

Dr C Smith
AWE
Aldermaston

Prof. S Tendler
Department of Pharmaceutical Sciences
The University of Nottingham

Professor O Willi
Department of Physics
Imperial College

Dr J S Wark
Clarendon Laboratory
University of Oxford

LASERS FOR SCIENCE FACILITY PANEL 1996/97

Professor D Phillips (Chairman)
Department of Chemistry
Imperial College

Dr R Bisby
Department of Biological Sciences
University of Salford

Dr C Wharton
Department of Biochemistry
University of Birmingham

Professor T M McCaffrey
School of Chemistry and Molecular Sciences
University of Sussex

Professor K Codling
Department of Physics
University of Reading

Professor F Wilkinson
Department of Chemistry
Loughborough University

Professor J A Cairns
Department of Applied Physics and Electronic and Mechnical Engineering
University of Dundee

Dr R Devonshire
Department of Chemistry
Sheffield University

CLF EURO EXPERIMENTS PANEL

Professor C L S Lewis (Chairman)
Department of Pure and Applied Physics
Queen's University of Belfast

Professor C Fotakis
Institute of Electronic Structure and Laser
FORTH, Greece

Professor D Phillips
Department of Chemistry
Imperial College

Dr E Rachlew-Kallne
Department of Physics
Royal Institute of Technology, Sweden

Dr G Matthieussent
Laboratoire Physique Gaz et Plasmas, Universite Paris XI - CNRS, France

Dr R Sigel
Max-Planck-Institut fur Quantenoptik
Garching, Germany

CENTRAL LASER FACILITY STRUCTURE